Transactions of the ASME

HEAT TRANSFER DIVISION
Chairman, R. K. SHAH
Secretary, A. S. ADORJAN
Senior Technical Editor, G. M. FAETH
Technical Editor, J. V. BECK
Technical Editor, I. CATTON
Technical Editor, R. GREIF
Technical Editor, H. R. JACOBS
Technical Editor, P. J. MARTO
Technical Editor, D. M. McELIGOT
Technical Editor, R. H. PLETCHER
Technical Editor, W. A. SIRIGNANO
Technical Editor, R. VISKANTA
Technical Editor, M. M. YOVANOVICH

BOARD ON COMMUNICATIONS
Chairman and Vice President
K. N. REID, JR.

Members-at-Large
W. BEGELL
J. T. COKONIS
W. G. GOTTENBERG
M. KUTZ
J. R. LLOYD
T. C. MIN
R. E. NICKELL
C. F. PHILLIPS
R. E. REDER
F. W. SCHMIDT

President, N. D. FITZROY
Executive Director,
PAUL ALLMENDINGER
Treasurer,
ROBERT A. BENNETT

PUBLISHING STAFF
Mng. Dir., Publ., J. J. FREY
Dep. Mng. Dir., Pub.,
JOS. SANSONE
Managing Editor,
CORNELIA MONAHAN
Production Editor,
VALERIE WINTERS
Editorial Prod. Asst.,
MARISOL ANDINO

The Journal of Heat Transfer (ISSN 0022-1481) is published quarterly for $100 per year by The American Society of Mechanical Engineers, 345 East 47th Street, New York, N Y 10017. Second class postage paid at New York, NY and additional mailing offices. POSTMASTER: Send address changes to The Journal of Heat Transfer, c/o THE AMERICAN SOCIETY OF MECHANICAL ENGINEERS, 22 Law Drive, Box 2300, Fairfield, NJ 07007-2300.
CHANGES OF ADDRESS must be received at Society headquarters seven weeks before they are to be effective. Please send old label and new address.
PRICES: To members, $24.00, annually; to nonmembers, $100.00.
Add $6.00 for postage to countries outside the United States and Canada.
STATEMENT from By-Laws. The Society shall not be responsible for statements or opinions advanced in papers or . . . printed in its publications (B7.1, para. 3).

INDEXED by Engineering Information

Journal of Heat Transfer

Published Quarterly by The American Society of Mechanical Engineers

VOLUME 108 • NUMBER 3 • AUGUST 1986

ANNOUNCEMENTS

TECHNICAL PAPERS

TECHNICAL NOTES

DISCUSSION

Heat Transfer Around Sharp 180-deg Turns in Smooth Rectangular Channels

D. E. Metzger
Fellow ASME

M. K. Sahm[1]
Mechanical and Aerospace Engineering Department, Arizona State University, Tempe, AZ 85287

Measured Nusselt numbers are presented for forced convection within and around sharp 180-deg turns in smooth channels of rectangular cross section. Separately determined top wall, bottom wall, and side wall values are presented individually along with azimuthal averages. The geometry of the channels and connecting turn is characterized by the parameters W*, *the ratio of upstream and downstream channel widths;* D*, *the nondimensional channel depth; and* H*, *the nondimensional clearance at the tip of the turn. Results from nine combinations of these parameters are presented at several values of channel Reynolds number to illustrate the effect of turn geometry on the heat transfer distributions.*

Introduction

In various types of heat exchange equipment, straight sections of flow channels are connected by 180-deg bends, and it is well known that both the nature of the flow and the associated convection heat transfer are usually significantly altered in and around the bend. In general, the centrifugal forces present in a turning flow induce secondary flows [1]. This has the effect of both augmenting heat transfer in the streamwise direction and creating azimuthal variations in heat transfer. The augmentation in average heat transfer is usually desirable, but the variation in heat transfer around the cross section is often not. This is particularly true for internal cooling passages of high-temperature gas turbine engine components, where 180-deg bends are common, usually in channels with rectangular cross sections. In such applications, variations in convection heat transfer rates occurring over small distances can lead to increased thermal stresses and decreased component life.

Thus designers of heat exchange equipment, and especially designers of internally cooled turbomachines, are interested in the rate of change of both axial and azimuthal heat transfer in and around channel turns. Despite the need for such information, relatively few investigations of heat transfer in passage turns through angles of less than 360 deg have been made in the past. Most prior studies are restricted to the fully developed conditions which are established well downstream from the start of bends, usually after more than a full 360-deg turn [2–4]. Until recently, the small amount of information available on heat transfer in 90 and 180-deg turns has been confined to flow channels of circular cross section [5, 6]. Even there, results are often contradictory and provide only limited help to the designer. For example, for virtually identical geometries, the maximum observed azimuthal variation in heat transfer coefficients ranges from 150 to 400 percent, depending on the reference consulted. In all cases, the highest coefficients occur along the turn outer radius, and the lowest occur along the turn inner radius.

The developing region near the start of turns in square and rectangular cross-section channels has received increased attention during the past few years [7–12]. A recently reported study of local heat transfer in a 180-deg bend with square cross section [9] reports a maximum observed azimuthal variation of about 2:1, also generally with the lowest coefficients at the inner radius wall and the highest coefficients at the outer radius wall. Another recent study of local heat transfer in 90-deg bends with rectangular cross-section channels [10] reports a maximum observed azimuthal variation of 170 percent, also with the lowest coefficients at the inner radius wall. The coefficients at the outer radius wall, however, were also found to be generally lower than those on the top and bottom walls. In this latter study, the rectangular channel aspect ratio was 3:1, with the short side on the curved walls.

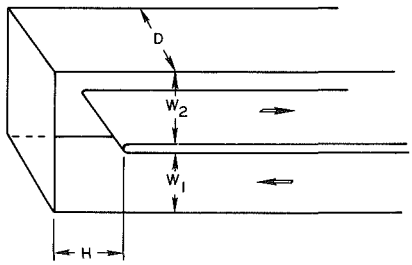

Fig. 1 Turn geometry and nomenclature

The preceding brief discussion of developing heat transfer in channel turns has only limited relevance to the present situation of interest. In all of the studies referenced, the turn geometries have relatively large radii of curvature at both the inner and outer channel radius and have little, if any, flow separation at the inner radius. In contrast, the 180-deg turns employed in gas turbine component cooling passages are usually extremely sharp, with the inner turn radius provided by a divider rib, as shown in Fig. 1.

In this configuration, there obviously will be flow separation at the divider tip, and flow visualization in a study [11] preliminary to the present work confirms this expectation. In [11] the length of the recirculating flow region on the downstream side of the divider is shown to be strongly dependent on both W^* and H^*. The separated flow length was observed to vary from approximately 1.5 to 3.5 times the width W_2 of the downstream channel. Pressure loss coefficients were also determined over the ranges $0.67 \le W^* \le 1.5$, $0.4 \le H^* \le 0.6$, and were found to be most sensitive to changes in H^*.

Recently, heat transfer results obtained in a 180-deg turn geometry like that of Fig. 1 have been presented [12]. Both smooth wall and rib-roughened wall heat transfer coefficients have been obtained for a single channel geometry, $W_1 = W_2 = H = D$. In addition, in [12] only the top and bottom channel walls were heated. This boundary condition is undesirable because secondary flow will transport fluid to near the heated measuring surface from unheated regions, a situation not found in most applications of interest. Also in [12], a single thermocouple was used to determine a single localized heat transfer coefficient at each streamwise position. If there is a strong azimuthal variation in heat transfer coeffi-

[1] Present address: Pratt & Whitney Aircraft, East Hartford, CT.

Contributed by the Heat Transfer Division for publication in the JOURNAL OF HEAT TRANSFER. Manuscript received by the Heat Transfer Division April 4, 1985. Paper No. 85-GT-122.

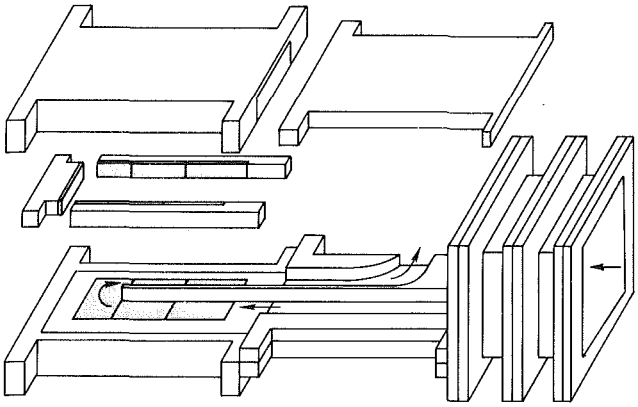

Fig. 2 Exploded view of test section components

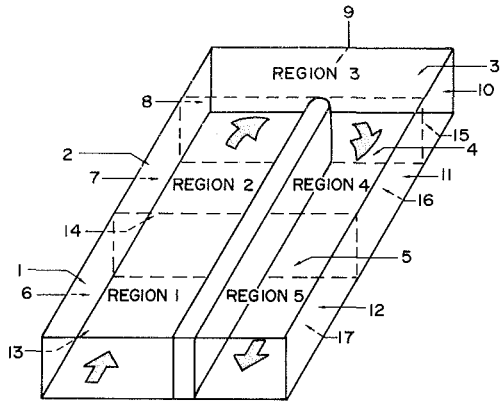

Fig. 3 Surface segment and flow region numbering

cient, the single measured value may not be representative of the overall channel heat transfer behavior.

The present experimental program was designed to provide information on both streamwise and azimuthal heat transfer behavior for a variety of different turn geometries. The investigation thus far has been restricted to the case of smooth channel walls in order to provide a well-established baseline for future measurements with roughened walls.

Experimental Apparatus

A special test rig was constructed for the present study, designed with interchangeable component parts in order to permit assemblies covering a range of different combinations of W^*, H^*, and D^*. Further design objectives were to create, as close as possible, a uniform wall temperature thermal boundary condition, and to obtain a measure of both the streamwise and azimuthal variations in heat transfer.

The resulting rig consists of two main sections, a heated test section and an entrance/exit section. The components and their assembled relationship are shown in exploded view in Fig. 2. Air is used as the test fluid and is supplied to the test rig from one of several laboratory compressors, depending on the desired mass flow rates. Compressor output, filtered and dried, is measured in an ASME standard orifice installation and routed to a plenum chamber located immediately upstream of the inlet/exit section. The plenum contains a series of screen sections to settle the flow prior to its entry through a contraction ratio of approximately 80:1 to the channel on the upstream side of the turn.

The heated test section, when assembled, consists of seventeen separate copper segments, each with its own foil resistance heater and thermocouple. The copper segments are shown shaded in Fig. 2. The copper plates are all 0.64 cm thick but vary in size and shape depending on location. The thickness of the plates, together with their high thermal conductivity, insures excellent surface temperature uniformity with the test conditions used in the present study.

Five of the copper segments, mounted in a 3.2-cm-thick basswood frame, form the channel top walls. The segments are thermally insulated from each other with 0.127-cm-thick balsa wood strips topped with a thin layer of acrylic plastic. The plastic prevents erosion of the soft balsa and allows final machining of the epoxy-bonded top wall section to a smooth finish. The section forming the channel bottom walls is a mirror image of the top wall configuration and both are mounted in aluminum frames which provide rigidity and enable accurate repeated assembly.

The channel side wall is in three sections, one each for the entrance side wall, the exit side wall, and the turn or end wall. The entrance and exit side wall sections each contain three heated copper plates; the end wall section contains a single heated plate. All three side wall sections have construction similar to that of the top and bottom wall sections, with basswood backing used together with balsa and plastic inserts to thermally separate the heater plates.

The 17 heated panels are numbered as shown in Fig. 3. Segments 1-5 are on the top surface, segments 6-8 are on the entrance side wall, segment 9 is on the end or turn wall, segments 10-12 are on the exit side wall, and segments 13-17 are on the lower surface.

The machined 0.64-cm-thick basswood dividing rib between the inlet and exit channels is of one-piece construction and extends from an attachment point in the entrance/exit section into the turn region, eliminating possibility for leakage across the rib at a joint. In addition, the top and bottom edges of the rib are grooved for O-rings to provide an effective seal at these locations. For reasons previously mentioned, a heated rather than passive rib would be desirable, but was not possible within the rib thickness dictated by passage modeling considerations. Fortunately, in the present geometry the wetted area on the rib is only approximately ten percent of the total wetted area. Use of basswood with its low thermal conductivity limits the heat transfer at the rib surface to less than one percent of the azimuthal total at any streamwise location. The junctions between the side walls and top and bottom walls are also sealed with O-rings, as are all other possible air leakage routes. The mating parts are positioned accurately through the use of locator pins, so that the resulting channel geometry is accurate and repeatable upon reassembly.

Nomenclature

A = heat transfer area
c_p = fluid specific heat
D = channel depth
D_h = hydraulic diameter of inlet channel
D^* = $D/(W_1 + W_2)$
H = divider tip-to-wall clearance
H^* = $H/(W_1 + W_2)$
$\dot{m}$ = mass flowrate
Nu_i = segment Nusselt number
Nu_j = regional peripheral average Nusselt number
$\dot{q}$ = convective heat transfer rate
t_m = fluid mixed mean temperature
t_s = surface temperature
Re = entrance channel Reynolds number = $\rho V D_h/\mu$
V = entrance channel mean velocity
W_1 = entrance channel width
W_2 = exit channel width
W^* = W_1/W_2
Δ = $(\mathrm{Nu}_{i,\mathrm{lower}} - \mathrm{Nu}_{i,\mathrm{upper}})/\mathrm{Nu}_{,\mathrm{upper}}$
μ = fluid dynamic viscosity

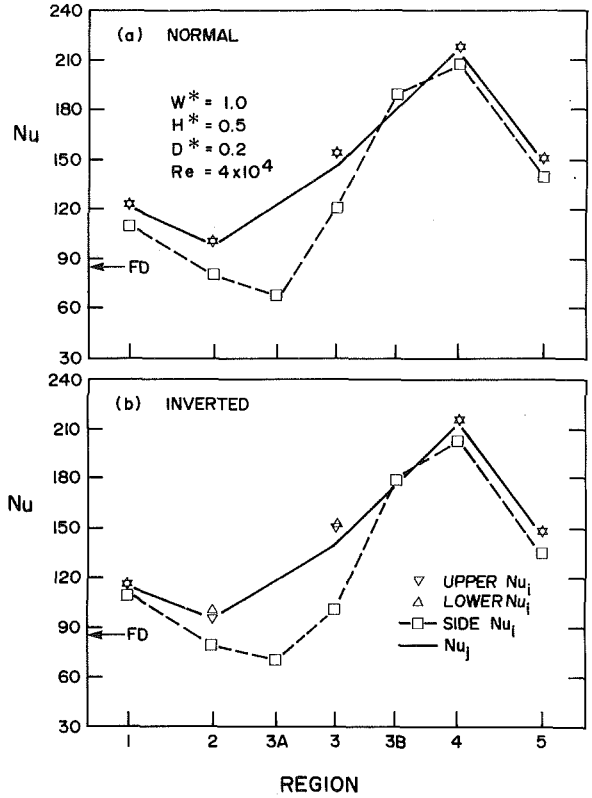

Fig. 4 Comparison of Nu_i values for (a) normal and (b) inverted test section orientation

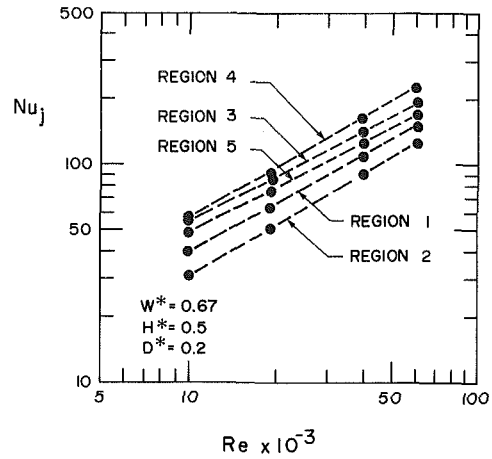

Fig. 5 Typical Nu_j versus Re results

Provision is made in the test section design for assembly at three different ratios of inlet to outlet channel widths, $W^* = 0.67$, 1.0, and 1.5 ($W_1 + W_2 = 6.35$ cm for all three configurations). In addition, three values of the nondimensional divider tip-to-wall clearance, $H^* = 0.4$, 0.5, and 0.6 ($H = 2.54$, 3.18, and 3.81 cm), can be assembled at each value of W^*. Changes in channel depth are also possible, but require a separate set of side walls for each depth. For the present study, a single value, $D^* = 0.2$ ($D = 1.27$ cm), was used.

For all test configurations, flow from the plenum into the test section begins with sharp-edged entrance into the $W_1 \times D$ inlet channel and proceeds 31.5 cm before encountering the first heated segments (segments 1, 6, and 13). This first set of heated segments is 7.62 cm long in the mean flow direction, followed by a second identical 7.62-cm-long set (segments 2, 7, and 14). The two sets of heated segments in the exit channel are both also 7.62 cm long in the mean flow direction. Further details of the apparatus can be obtained from [13].

Data Acquisition and Reduction

Each of the 17 heaters is individually controlled with an autotransformer. Acquisition of thermocouple and heater power information is accomplished with a digital data logger used in conjunction with a CRT display to assist in setting desired temperature boundary conditions over the test surface. Heating element resistance varies with heater temperature, and heater power is therefore most accurately determined by separately measuring both the voltage drop across and current through the individual heaters. A rotary stepping switch is used to sequentially switch the individual heater circuits into a measuring configuration where the voltage drop across a calibrated 0.01 percent resistor is used to determine the heater current. Heater current and voltage measurements are conditioned by a solid state a-c/d-c converter.

All testing is carried out at steady-state conditions and utilizes the segment temperatures and heater power measurements to determine area-averaged convective heat transfer rates for each of the 17 segments. In all cases an isothermal wall boundary condition is used with individual heaters adjusted to equalize all the segment temperatures. In a typical test, steady isothermal conditions are generally achieved on all segments to within ± 0.2°C, and on adjacent segments to within ± 0.1°C. This uniformity is achieved through manual control of the individual autotransformers, assisted by graphical displays on the CRT.

Each channel geometry tested was investigated at nominal Reynolds numbers of 10^4, 2×10^4, 4×10^4, and 6×10^4, based on inlet channel hydraulic diameter. For a particular flow rate and turn geometry, power levels were usually set to provide a nominal difference of 25°C between the surface and mixed mean temperatures. Some tests were repeated at three additional values of this driving potential: 7°C, 12.5°C, and 50°C.

At each test condition, the measured segment electrical powers are corrected for conduction losses from the back and ends of the segments and for intersegment conduction across the insulating spacers. Separate auxiliary experiments have been conducted to determine these correction terms, and they are generally small due to the low conductivity supporting structure and the outer insulation wrap. The close segment-to-segment temperature uniformity maintained in the present tests insures a negligible intersegment conduction correction. The backside and end loss ranges from less than 2 percent of the heater power input (at high flow rates) to 7 percent (at the lowest flow rates). The local mixed mean temperature is determined from an energy balance on the flow done regionally throughout the test section. As shown in Fig. 3, five regions were used, corresponding to the boundaries between adjacent segments. The total heat input to a given region is

$$\dot{q}_j = \sum_{i=1}^{n} \dot{q}_i \tag{1}$$

where the summation is over the number of segments bounding the region. For example, region 1 is bounded by segments 1, 6, and 13, region 2 by segments 2, 7, and 14, and so on for all five regions as indicated in Fig. 3. An energy balance then expresses the region-to-region change in mixed mean temperature

$$t_{m,j} = t_{m,j-1} + \frac{\dot{q}_j}{\dot{m} c_{p,j}} \tag{2}$$

$$\mathrm{Nu}_i = \frac{\dot{q}_i D_h}{A_i k_j (t_{s,i} - t_{m,j})} \tag{3}$$

All properties are determined at a regional average film temperature, defined as the arithmetic mean of the average region surface temperature and the average region mixed mean temperature.

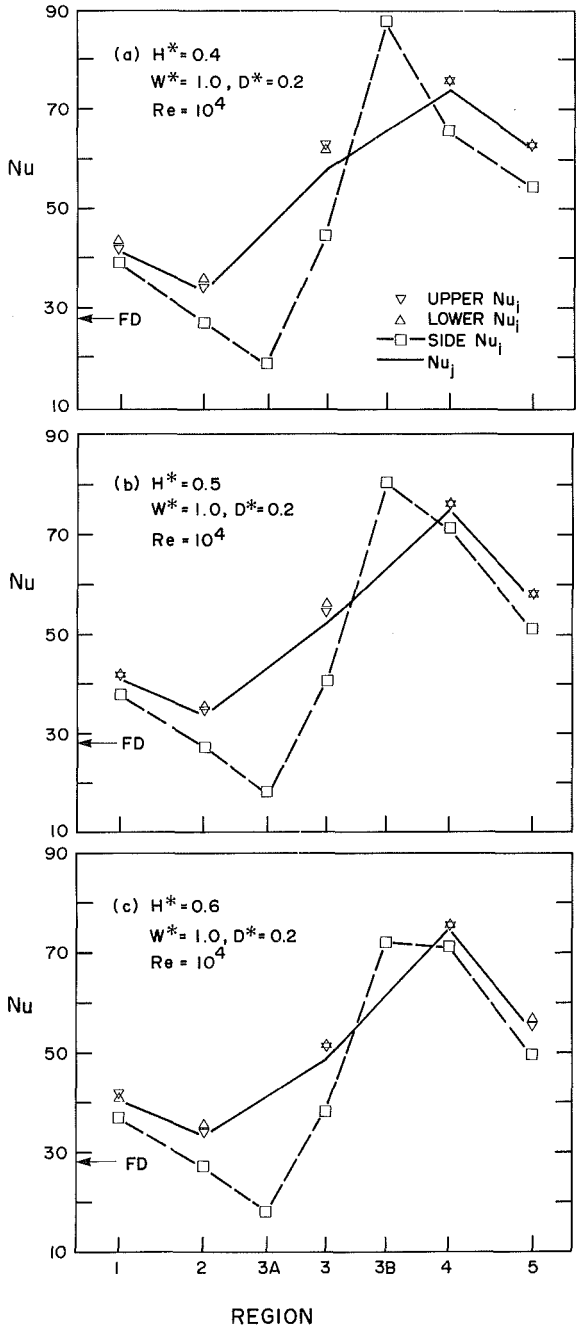

Fig. 6 Effect of H^* at $W^* = 1.0$

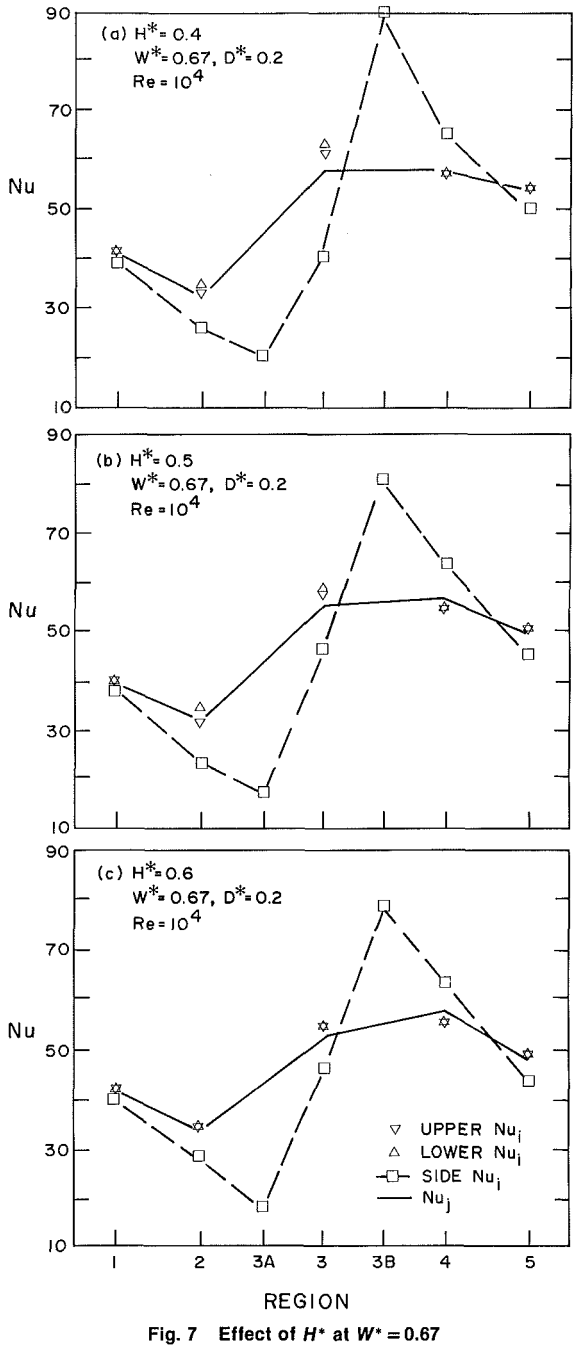

Fig. 7 Effect of H^* at $W^* = 0.67$

Results and Discussion

The test rig design allows tests to be repeated with the heated test section inverted, in effect interchanging the position of the segments from top to bottom and from inlet to exit. Several such repeated tests have been conducted and a typical comparison of the Nu_i values is shown in Figs. 4(*a*) and 4(*b*). The Nusselt number agreement in these paired tests was generally within experimental uncertainty on individual segments, and even closer for peripheral average Nusselt numbers. Experimental uncertainty is estimated to be ±8 percent, based on the methods of Kline and McClintock [14]. The fact that results can be successfully repeated after disassembly and reassembly with interchanged components provides confidence in the apparatus.

The results shown in Fig. 4 illustrate general characteristics observed throughout the present test program. First, the Nusselt numbers in regions 1 and 2 are above those predicted by fully developed tube flow correlations (indicated by FD on the figures). This behavior is expected for the thermal entry conditions present in the tests. The proximity of region 2 Nusselt numbers to fully developed values indicates the flow is close to fully developed conditions at the end of the entrance channel, although this was not independently verified with velocity measurements in the present tests. Side wall Nusselt numbers in the entrance channel are, as expected, lower than those of the upper and lower walls, by an amount that agrees with previous findings in a channel of similar aspect ratio [10].

Flow visualization for the present turn geometries was previously conducted [11] using an ink-dot matrix and solvent film technique described in [15]. The visualized surface streamlines show strong secondary flow that begins to become apparent about one channel width upstream of the divider tip. Throughout Region 3, there is a strong radially inward flow indicated on the top and bottom wall surfaces. The necessary balancing radially outward flow along the channel center

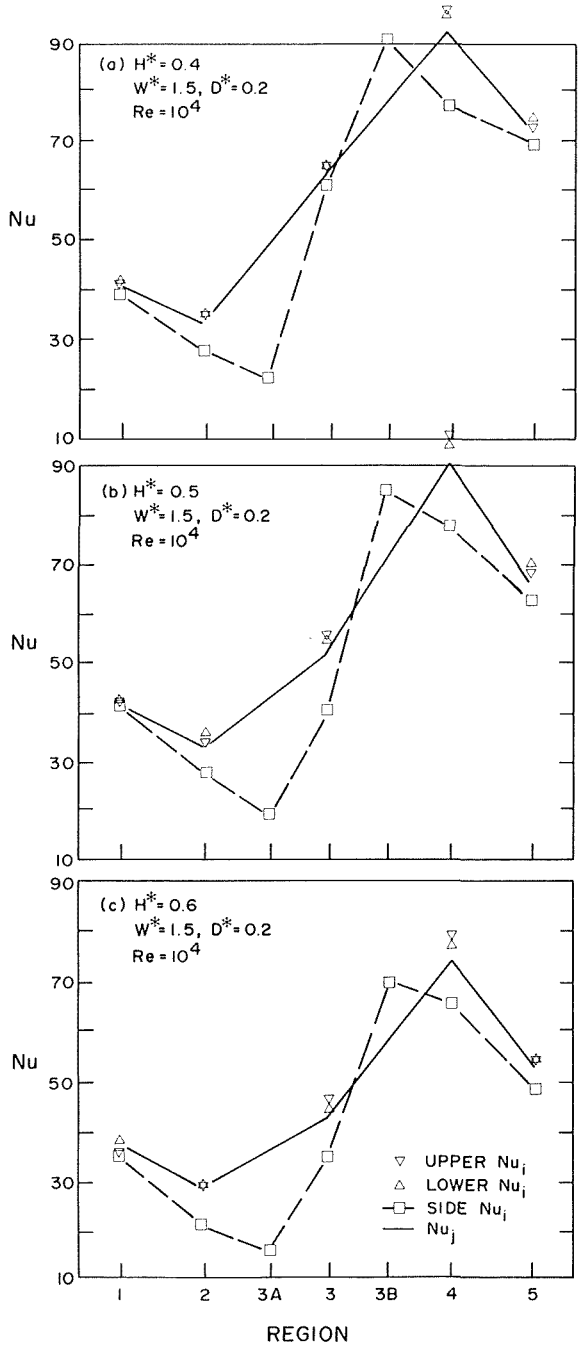

Fig. 8 Effect of H^* at $W^* = 1.5$

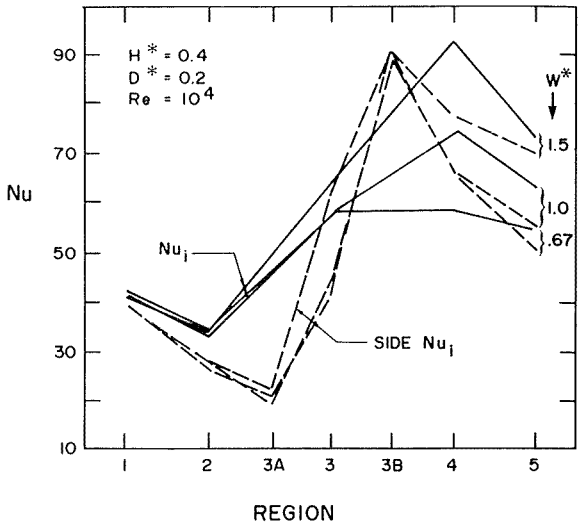

Fig. 9 Effect of W^* at $H^* = 0.4$

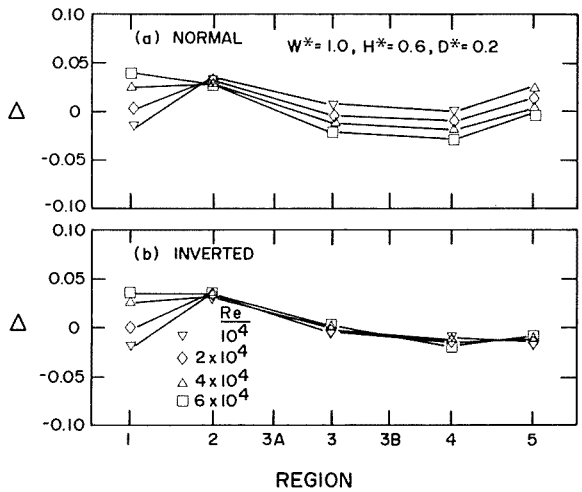

Fig. 10 Bottom-to-top Nu_j deviations

plane would be expected to produce elevated Nusselt numbers on the outer side walls. This expectation has been generally observed for both circular and square cross-section curved tube flows, for both fully developed and entry conditions. The present side wall behavior shown in Fig. 4 is in sharp contrast to this expectation. Already lower than the lower and upper wall Nusselt numbers, the side wall Nusselt number continues to drop on the entrance side wall in the turn region (segment 8, labeled region 3A in the figures). Although subtle deviations from the simple cellular secondary flow pattern and its corresponding Nusselt number distribution have been observed before [9], in the present case it is more plausibly a result principally of flow separation and the creation of a low-velocity recirculating flow zone in the upstream corner, observed in the flow visualizations. The effect continues on the far side wall (segment 9, labeled region 3 in the figures), and only at the exit side wall in the turn region (segment 10, labeled region 3B in the figures) does the side wall Nusselt number level finally reach the levels of the upper and lower walls.

The results of Fig. 4 are also typical in showing that the highest heat transfer levels generally occur in region 4, downstream of the turn. Figure 5 illustrates this with a typical Nu_j set for a single geometry over the four nominal values of Reynolds number used in the testing.

In order to facilitate comparisons between different geometries at identical values of Reynolds number, least-square fits of the form $Nu_j = a\ Re^b$ were obtained for each region. The a, b coefficient sets also provide a compact way of accurately presenting all of the Nu_j results. Table 1 lists the coefficients, those of Fig. 5, and also those of the other eight turn geometries.

From the tabulated coefficients, the distribution of Nu_j around the turn can be obtained accurately at any desired value of Reynolds number within the test range of $10^4 \le Re \le 6 \times 10^4$. Similar coefficient pairs have been obtained for Nu_i for each of the individual heated segments, but space limitations prevent listing all of them here. Instead, the salient features of the Nu_i behavior will be illustrated graphically with a few typical results; the complete set of coefficient pairs is available in [13].

Figure 6 shows effects of changes in H^* at $W^* = 1$. In this case inlet and outlet channel widths are equal. In Fig. 6(*b*), $H^* = 0.5$, the divider tip-to-wall clearance is also equal to the

Table 1

W*	H*	Region	a	b
0.67	0.4	1	0.04360	0.7420
		2	0.02495	0.7757
		3	0.08364	0.7105
		4	0.03619	0.7992
		5	0.09037	0.6940
0.67	0.5	1	0.04022	0.7493
		2	0.02275	0.7839
		3	0.09320	0.6926
		4	0.04128	0.7845
		5	0.08221	0.6943
0.67	0.6	1	0.04883	0.7324
		2	0.03025	0.7577
		3	0.06622	0.7265
		4	0.05907	0.7469
		5	0.09201	0.6786
1.0	0.4	1	0.04371	0.7450
		2	0.02396	0.7847
		3	0.12350	0.6717
		4	0.07339	0.7546
		5	0.12109	0.6784
1.0	0.5	1	0.03699	0.7613
		2	0.02421	0.7849
		3	0.05790	0.7375
		4	0.06487	0.7651
		5	0.07621	0.7164
1.0	0.6	1	0.03571	0.7633
		2	0.02603	0.7763
		3	0.07289	0.7059
		4	0.07246	0.7536
		5	0.07939	0.7092
1.5	0.4	1	0.03429	0.7718
		2	0.02408	0.7857
		3	0.14491	0.6542
		4	0.12281	0.7210
		5	0.08377	0.7334
1.5	0.5	1	0.04513	0.7449
		2	0.02729	0.7731
		3	0.12321	0.6610
		4	0.10515	0.7350
		5	0.06917	0.7465
1.5	0.6	1	0.01988	0.8188
		2	0.00843	0.8827
		3	0.01630	0.8581
		4	0.01830	0.9033
		5	0.01710	0.8720

channel width. As tip clearance is reduced (Fig. 6*a*), Nu_i and Nu_j in region 3 are increased, particularly Nu_i on the downstream sidewall (3B). The opposite effect is seen in Fig. 6(*c*) where the tip clearance has been increased relative to Fig. 6(*b*). Here Nu_i and Nu_j in region 3 are decreased.

Figures 7 and 8 present similar graphic presentations of the effect of H^* on the Nusselt number distributions for $W^* = 0.67$ and 1.5, respectively. Again, reducing tip clearance increases Nusselt numbers in region 3. The effect is most pronounced for $W^* = 1.5$. For $W^* = 1.5$, decreasing H^* also has a significant effect on heat transfer in regions 4 and 5, whereas the effect of H^* on these regions is minor for $W^* = 0.67$ and 1.0.

In general, the effect of decreasing W^* below 1.0 is to create more nearly uniform Nusselt number distributions in the streamwise direction. In these cases, the tendency of the turn-induced secondary flow to enhance heat transfer is apparently partially offset by the lowered mean velocities present in the enlarged downstream cross section.

In contrast, the result of increasing W^* above 1.0 is that the effects of secondary flow and streamwise mean flow acceleration both work together to create a high degree of Nusselt number increase through the turn. In the most pronounced example, Fig. 8(*a*) with $W^* = 1.5$, $H^* = 0.4$, the value of Nu_j in region 4 is some 60 percent higher than that of region 3, and nearly three times higher than the Nu_j value in region 2.

The independent effect of W^* at constant H^* can be viewed by comparing the appropriate curves in Figs. 6-8; for example, Fig. 9, which combines Figs. 6(*a*), 7(*a*), and 8(*a*), shows the effect of W^* at $H^* = 0.4$. In all such comparisons, it can be observed that the effect of W^* on the side wall heat transfer is

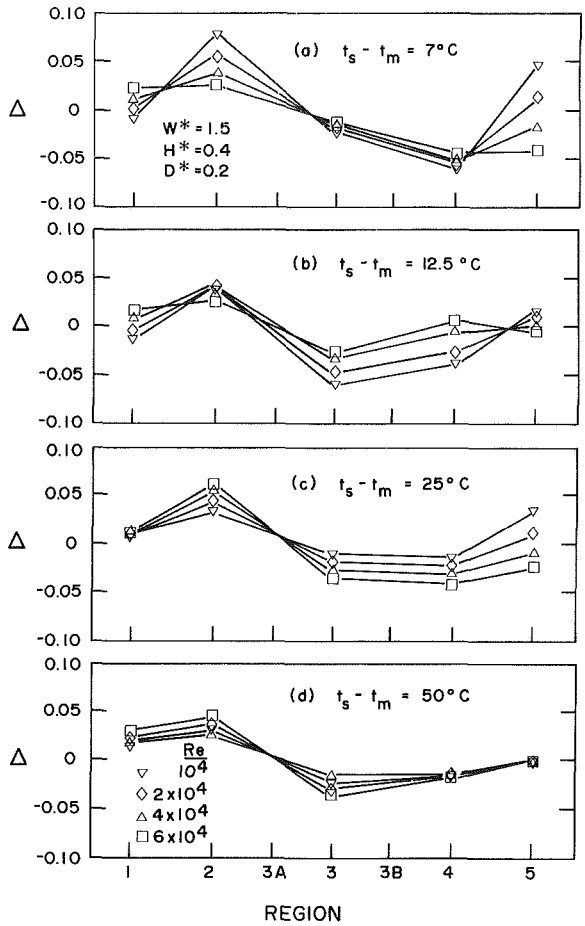

Fig. 11 Effect of $(t_s - t_m)$ on Nu_i deviations

minor compared with the effect of W^* on the top and bottom walls. The net result is small peripheral variation in Nu_i at large W^*, and very large peripheral variation at small W^*. Thus with relatively small adjustments in the turn geometry parameters, both the streamwise and peripheral heat transfer distributions can be tailored to best fit the needs of a given application.

Close examination of all of the acquired Nu_i values shows that there is a small but remarkably consistent difference between the lower surface values and the corresponding upper surface values. Figure 10 shows typical deviations over the full Reynolds number range, for both normal and inverted test rig orientation. The good match between the normal and inverted results strongly indicates that the deviation is not an artifact of the test rig, but rather is an actual flow phenomenon.

Approximately 95 percent of all the results obtained in the present study exhibit a deviation pattern similar in both shape and magnitude to that of Fig. 10, with positive deviations in the upstream channel and negative deviations in the downstream channel. In about 90 percent of the cases, the maximum deviations are 5 percent or less; in the remaining cases the deviations do not exceed 10 percent.

Grashof numbers in these tests are large enough to raise the possibility of free convection effects as a cause of the deviations. In order to test, within the temperature capabilities of the test rig, whether different driving potentials would affect the deviations, a few tests were carried out at both lower and higher differences between the surface and mixed mean temperatures, as mentioned in the data acquisition section. Figure 11 shows that the pattern and magnitude of the deviations are changed only slightly as driving potential is changed. A satisfactory explanation of this phenomenon will probably require detailed velocity and temperature field measurements;

but at the present time, the effect seems to be of minor importance in applications.

Closure

The study provides a measure of both the streamwise and azimuthal distributions in convection heat transfer rates for sharp 180-deg bends. Nine different geometries were investigated to explore the effects on heat transfer of changes in the ratio of inlet to outlet channel width and from changes in the divider tip-to-wall clearance. Considerable variation in heat transfer distributions, both streamwise and azimuthal, results from what are rather minor changes in geometry. Considerable care has been taken in the apparatus design and data acquisition, and also in the verification of the repeatability and test-rig independence of the results. Consequently, the study should not only provide guidance for the design of heat exchange equipment, but, in addition, should provide useful data for assessing future attempts at numerical prediction of such flows.

References

1 Dean, W. R., "Fluid Motion in a Curved Channel," *Proc. Royal Society of London*, Series A, Vol. 121, 1928, pp. 402–420.

2 Mori, Y., and Nakayama, W., "Study on Forced Convective Heat Transfer in Curved Pipes (1st Report, Laminar Region)," *International Journal of Heat and Mass Transfer*, Vol. 8, 1965, pp. 67–82.

3 Mori, Y., and Nakayama, W., "Study on Forced Convective Transfer in Curved Pipes (2nd Report, Turbulent Region)," *International Journal of Heat and Mass Transfer*, Vol. 10, 1967, pp. 37–59.

4 Mori, Y., and Nakayama, W., "Study on Forced Convective Transfer in a Curved Channel With a Square Cross Section," *International Journal of Heat and Mass Transfer*, Vol. 14, 1971, pp. 1787–1805.

5 Ede, A. J., "The Effect of a Right Angled Bend on Heat Transfer in a Pipe," *Proceedings, 4th International Heat Transfer Conference*, Vol. 2, FC-4, 1970.

6 Stradden, P. W., and Tailby, S. R., "The Influence of 90° and 180° Pipe Bends on Heat Transfer From an Internally Flowing Gas Stream," *Proceedings, 4th International Heat Transfer Conference*, Vol. 2, FC-4, 1970.

7 Humphrey, J. A. C., Whitelaw, J. H., and Yee, G., "Turbulent Flow in a Square Duct With Strong Curvature," *J. Fluid Mechanics*, Vol. 103, 1981, pp. 443–463.

8 Chang, S. M., Humphrey, J. A. C., and Modavi, A., "Turbulent Flow in a Strongly Curved U-Bend and Downstream Tangent of Square Cross Section," *Physico-Chemical Hydrodynamics*, Vol. 4, 1983, pp. 243–269.

9 Johnson, R. W., and Launder, B. E., "Local Heat Transfer Behavior in Turbulent Flow Around a 180 deg Bend of Square Cross Section," ASME Paper No. 85-GT-68, 1985.

10 Metzger, D. E., and Larson, D. E., "Use of Melting Point Surface Coatings for Local Convection Heat Transfer Measurements in Rectangular Channel Flows With 90 Degree Turns," ASME Paper No. 84-HT-23, 1984.

11 Metzger, D. E., Plevich, C. W., and Fan, C. S., "Pressure Loss Through Sharp 180 Degree Turns in Smooth Rectangular Channels," ASME *Journal of Engineering for Gas Turbines and Power*, Vol. 106, 1984, pp. 677–681.

12 Boyle, R. J., "Heat Transfer in Serpentine Passages With Turbulence Promoters," ASME Paper No. 84-HT-24, 1984.

13 Sahm, M. K., "Heat Transfer in Smooth 180° Sharp Turns," MS Thesis, Arizona State University, 1983.

14 Kline, S. J., and McKlintock, F. A., "Describing Uncertainties in Single Sample Experiments," *Mechanical Engineering*, Vol. 75, Jan. 1953.

15 Langston, L. S., and Boyle, M. T., "A New Surface-Streamline Flow-Visualization Technique," *Journal of Fluid Mechanics*, Vol. 125, 1982.

ERRATA

Corrections to "The Exchange Factor Method: An Alternative Basis for Zonal Analysis of Radiating Enclosures," by M. E. Larsen and J. R. Howell, published in the November 1985 issue of the ASME JOURNAL OF HEAT TRANSFER, pp. 936–942.

There was a sign error in equation (44). The correct form is as follows:

$$\left(\frac{\partial T}{\partial x}\right)_w = \frac{9\,T_\gamma - 8T_w - T_{\gamma+\Delta x}}{3\Delta x} \qquad (44)$$

Calculations reported in the article were obtained using the correct form of the equation.

An Experimental and Analytical Investigation of Friction Factors for Fully Developed Flow in Internally Finned Triangular Ducts

H. Chegini
Graduate Teaching Assistant.

S. K. Chaturvedi
Associate Professor.

Mechanical Engineering and Mechanics,
Old Dominion University,
Norfolk, VA 23508

Friction factors for fully developed flow in triangular ducts with fins of various height and width are investigated for Reynolds numbers ranging from 150 to 90,000. Two triangular ducts having apex angles of 60 and 38.8 deg are studied. Results are presented in the form of standard plots of friction factor as a function of Reynolds number. Friction factor values for the smooth triangular duct cases are in good agreement with the existing results. For the finned-duct cases, the fully developed axial velocity profiles in laminar flow are determined by solving the x-momentum equation iteratively by the Gauss–Seidel finite-difference technique. The theoretically determined friction factors for these cases are in good agreement with the experimental values of friction factors based on pressure drop measurements.

Introduction

The fluid flow characteristics of noncircular ducts have been studied extensively in the past three decades owing to wide applications in compact heat exchanger design. Many researchers investigating the pressure drop and heat transfer characteristics in ducts with noncircular cross section have found that the pressure drop in fully developed turbulent flow can also be estimated as a first approximation from turbulent flow correlation for circular duct if the diameter is replaced by the hydraulic diameter of that particular cross section. This is particularly true for fully developed turbulent flow in equilateral triangular ducts for which only minor deviation from the circular tube correlations for friction factor has been reported [1]. However, significant deviation from the circular duct correlation have been reported for the sharp cornered ducts such as isosceles triangular ducts with narrow apex angle [2]. In their investigation, Eckert and Irvine [3] have found that for Newtonian fluids in narrow triangular ducts, laminar and turbulent flows can coexist side by side over a wide range of Reynolds number. Leonhardt [4] performed measurements of friction factors for Newtonian and non-Newtonian fluids and found them to be in good agreement with theoretical solutions of Shah and London [5] for laminar flow in isosceles triangular ducts. Aly et al. [6] have numerically predicted the secondary flow patterns in the cross-sectional plane, mean axial velocity, and pressure drop in fully developed turbulent flow in an equilateral triangular duct. To solve for these quantities, the turbulence kinetic energy (K)–turbulence length (l) model was employed. They also compared the predicted pressure drop values with experimental values and found a reasonable agreement between the two. Gosman and Rapley [7] used an algebraic stress model for predicting the fully developed turbulent flow in ducts of triangular cross section and found the theoretically predicted results in good agreement with experimental results.

The application of internally finned ducts in high-performance heat exchangers has provided impetus for the development of such systems. The performance of conventional heat exchangers can be substantially improved by a number of techniques [8] which involve heat transfer augmentation by providing extra heat exchange area in the form of fins. Bergles et al. [9] have analyzed the turbulent flow in a finned circular duct. They found that the largest increase in heat transfer occurs with short spiral fins. Hilding and Coogen [10] found that the use of continuous straight fins of large length resulted in good heat transfer performance in circular ducts. Hu and Chang [11] analytically solved for the fully developed laminar flow in a circular tube having longitudinal rectangular fins equally spaced along the wall. Also, Chen [12] extended the work reported in [11] by considering longitudinal fins within square and hexagonal ducts. Date [13] solved the problem of fully developed laminar and turbulent flow in a tube containing a twisted tape. Aggarwala and Gangal [14] and Gangal and Aggarwala [15] studied the heat transfer performance of internally finned rectangular and square ducts for the case of combined free and forced convection in fully developed laminar flow. Masliyah and Nandakumar [16, 17] analyzed fully developed laminar flow through a circular tube having triangular fins equally spaced along the wall. They employed a finite element method to obtain solutions for velocity and temperature profiles. Patankar et al. [18] studied turbulent flow and heat transfer characteristics in internally finned tubes and annuli; and Soliman et al. [19] analyzed laminar heat transfer in internally finned tubes with uniform outside wall temperature. Recently, Scott and Webb [20] extended the work related to laminar flow in internally finned circular tubes [11] to turbulent flows. They examined the problem both theoretically and experimentally. Prakash and Patankar [21] numerically solved the problem of combined free and forced convection in vertical tubes with radial internal fins.

Present Work

The literature review pursued prior to the initiation of this work indicated that friction factor data for the finned triangular duct were not available in the literature. The main objective of this study is to determine the effect of longitudinal internal fins on the friction factor for fully developed flow of a Newtonian fluid such as air. Two test sections of triangular cross section with different apex angles were fabricated so that the effect of apex angle on friction factor could also be analyzed. Parameters such as Reynolds number, size of fins, and number of fins are also varied in the present study. Since no comparable analytical solutions or experimental data exist for finned triangular ducts, the analytical solutions for the laminar flow are developed to check the accuracy of the experimentally obtained friction fac-

Contributed by the Heat Transfer Division for publication in the JOURNAL OF HEAT TRANSFER. Manuscript received by the Heat Transfer Division September 24, 1984.

Table 1 Dimensions and friction factors for various cases

Cases	α, deg	L, cm	a, cm	d_H^{**}, cm	h, cm	t, cm	C_L	C_T
1	60	5.080	5.080	2.934	0.0	0.0	53.3	0.305
2	60	5.080	5.080	2.934	0.415	0.317	75.7	0.345
3	60	5.080	5.080	2.934	0.415	0.635	87.7	0.486
4	60	5.080	5.080	2.934	0.831	0.317	123.1	0.539
5	60	5.080	5.080	2.934	0.831	0.635	165.3	0.721
6	38.8	4.143	6.177	2.934	0.0	0.0	53.2	0.312
7	38.8	4.143	6.177	2.934	0.415	0.317	73.3	0.340
8	38.8	4.143	6.177	2.934	0.415	0.635	82.9	0.596
9	38.8	4.143	6.177	2.934	0.831	0.317	110.1	0.421
10	38.8	4.143	6.177	2.934	0.831	0.635	138.7	0.583
11*	60	5.080	5.080	2.934	0.831	0.317	92.6	0.472

*For this case, fins are located on one side as shown in Fig. 7.
**Smooth duct hydraulic diameter is used for calculating f and Re even for finned duct cases.

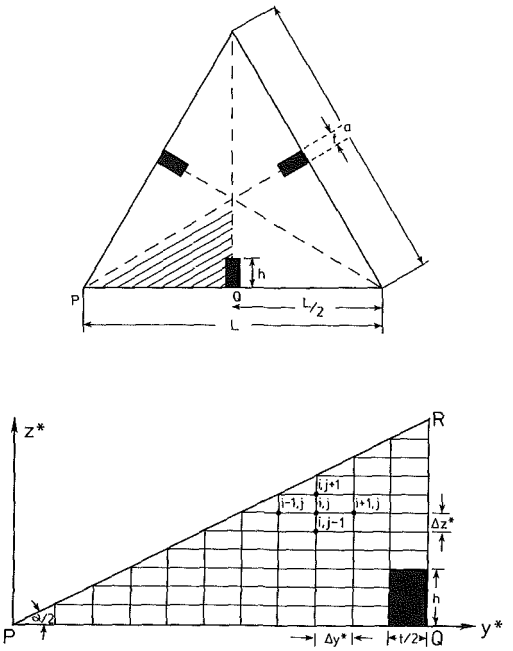

Fig. 1 Duct geometry and grid network for numerical computation

tors. Utilizing the relationship between the friction factor, Reynolds number, and the nondimensional volumetric flow rate, the theoretical friction factors are computed and compared with experimental results.

Experimental Apparatus and Procedure

An experimental apparatus was designed and fabricated to study the pressure drop characteristics of flows in finned triangular ducts [22]. Experiments were performed with two different test sections each having the same hydraulic diameter but different apex angles (60 and 38.8 deg). A typical cross-sectional view is shown in Fig. 1. The dimensions of each cross section are given in Table 1. In order to achieve fully developed flow, an entrance region of approximately 120 hydraulic diameters was chosen. This length was considered sufficient for the incoming flow to become fully developed in both laminar as well as turbulent regimes [23, 24].

The quantities measured in a typical experimental run were the volumetric flow rate of the air and the time-averaged pressure drop between pressure taps located in the fully developed region. The volumetric flow rate of air was measured by an orifice plate meter whose pressure taps were located one diameter upstream and 0.3 diameter downstream [25]. The pressure drop per unit length of the duct was measured by an electronic pressure transducer connected to two pressure taps at a given distance apart. The resulting raw data were used as inputs to a computer program which determined the Reynolds number, friction factor, least square fit to the data, and the experimental uncertainty in the measurements. For most runs, the experimental rms uncertainty for the friction factor ranged from 3.8 to 8.0 percent, and from 2 to 3.1 percent for the Reynolds number [22].

Each triangular duct has four pressure taps located at various locations along the axial direction. At any given axial location, the taps were also located in the circumferential direction to sense any pressure variation in that direction. This effect was investigated for the equilateral cross section, and the results showed that the circumferential pressure variations were well within the overall uncertainty of the experiment.

The experimental data are presented in the standard form of friction factor as a function of Reynolds number defined as

$$\mathrm{Re} = \frac{\rho \bar{u} d_H}{\mu} = \frac{\dot{m} d_H}{\mu A} \tag{1}$$

where the hydraulic diameter is defined as

$$d_H = \frac{4A}{p} \tag{2}$$

Nomenclature

A = cross-sectional area, cm^2
A_0, B_0 = intercept and slope of correlation given by equation (8)
a = duct interior dimension (Fig. 1), cm
C_L = laminar friction coefficient $= f \cdot \mathrm{Re}$
C_T = turbulent friction coefficient $= f \cdot \mathrm{Re}^{0.25}$
d_H = hydraulic diameter of smooth duct, cm
f = Darcy friction factor
h = height of the fin, cm
L = characteristic reference length (Fig. 1), cm
$\dot{m}$ = mass flow rate, kg/s
P = pressure, Pa
p = wetted perimeter, cm
$\dot{Q}$ = volumetric flow rate, m^3/s
$\dot{Q}^*$ = nondimensional volumetric flow rate
Re = Reynolds number, defined in equation (1)
t = thickness of the rectangular fin, cm
$\bar{u}$ = average velocity in axial direction, m/s
u^* = dimensionless velocity
x, y, z = Cartesian coordinates, m
y^*, z^* = dimensionless y and z coordinates
μ = dynamic viscosity, Pa•s
ρ = density, kg/m^3

Subscripts

n = index for normal direction
i = index for x direction
j = index for y direction

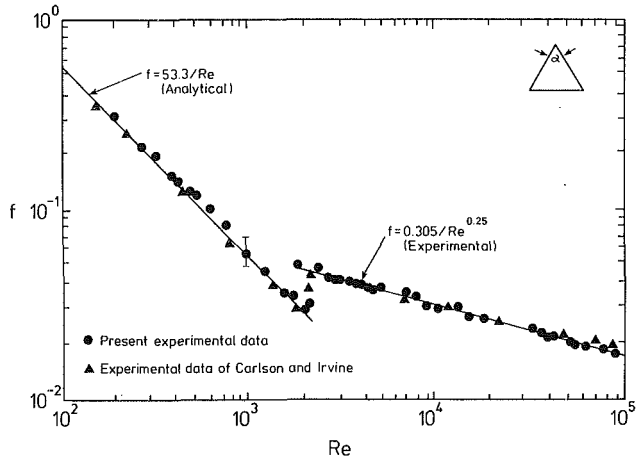

Fig. 2 Presentation of friction factor versus Reynolds number for a smooth triangular duct with $\alpha = 60$ deg

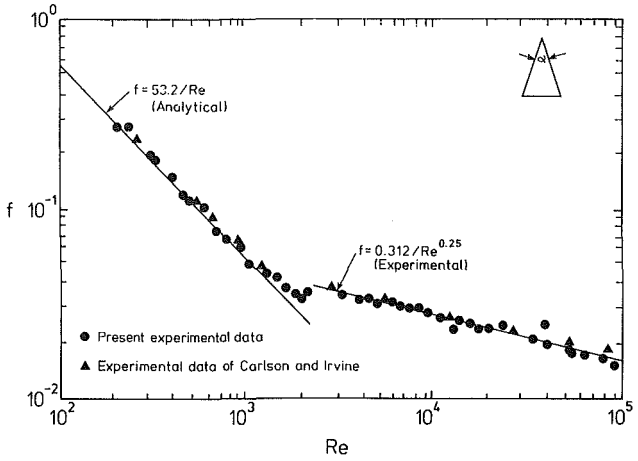

Fig. 3 Presentation of friction factor versus Reynolds number for a smooth triangular duct with $\alpha = 38.8$ deg

The symbol p designates the wetted perimeter and A is the cross-sectional area of the duct. The friction factor f, also known as Darcy friction factor in the literature, is defined as

$$f = \frac{2d_H}{\rho \bar{u}^2} \frac{dP}{dx} = \frac{2d_H \rho A^2}{\dot{m}^2} \frac{dP}{dx} \tag{3}$$

The term dP/dx is the pressure drop per unit length of the duct.

Numerical Calculation of Friction Factors

The governing equation for the nondimensional axial velocity in fully developed region can be written in the following form

$$\frac{\partial^2 u^*}{\partial y^{*2}} + \frac{\partial^2 u^*}{\partial z^{*2}} = 1 \tag{4}$$

where $y^* = y/L$, $z^* = z/L$, and $u^* = u/(-L^2/\mu)(dP/dx)$. The symbol L is the nondimensional characteristic length, shown in Fig. 1.

Poisson's equation (4) is solved by an iterative finite difference technique known as the Gauss-Seidel method with overrelaxation [26]. The Cartesian grid network for the numerical scheme is illustrated in Fig. 1 for the case of equilateral triangular duct with internal fins. Due to apparent symmetry in this case, the solution needs to be determined in only a one-sixth portion of the geometry shown in Fig. 1. Since the flow is symmetric about boundaries QR and PR, the boundary condition representing vanishing normal velocity gradient $\partial u/\partial n = 0$ is enforced at all points along those two boundaries that do not coincide with a solid surface. A central difference approximation is adopted to determine the finite difference analog for the second-order partial derivatives of the u^* velocity. A uniform grid with $\Delta y^* = \Delta z^* = 0.0125$ was used for all numerical calculations.

Following the determination of the velocity field, the volume flow rate is computed from the expression

$$\dot{Q}^* \equiv \frac{\dot{Q}}{-\frac{1}{\mu} dP/dx L^4} = \int_{A^*} u^* dA^* \tag{5}$$

where $\dot{Q}$ and $\dot{Q}^*$ are the dimensional and nondimensional volumetric flow rates, respectively. It should be noted here that $\dot{Q}^*$ is a function of duct shape only. Using the definitions of Re, $\dot{Q}$, $\dot{Q}^*$, and friction factor f, the following expression for $f \cdot \mathrm{Re}$ can be obtained

$$f \cdot \mathrm{Re} = \frac{2A d_H^2}{L^4 \dot{Q}^*} \tag{6}$$

A typical numerical solution gives the value of Q^*, from which the quantity $f \cdot \mathrm{Re}$ can be computed. The friction factor calculations for laminar flow in ducts reported by Shah and London [5] are well known. The relationship they used is of the type $f \cdot \mathrm{Re} = C_L$, where C_L is a constant dependent only on the apex angle for the smooth duct geometry. However, for the case of a finned duct this constant C_L will also depend on the size and number of fins. Similarly, for turbulent flow, the well-known Blasius formula $f \cdot \mathrm{Re}^{0.25} = C_T$ is commonly used for correlating the frictional pressure drop data. As we shall see in the next section, most of the experimental data for the finned geometry correlated well with the above two expressions.

Discussion of Results

Prior to taking extensive data for complex cross-sectional shapes, the pressure drop data were initially obtained for simple cross-sectional shapes so that the experimental and numerical techniques used in the present study could be validated. As shown in Figs. 2 and 3, the experimental data for smooth equilateral triangular cross section were found to be in good agreement with the experimental data of Carlson and Irvine [27] for both laminar and turbulent flows. The numerical results obtained in the present study for laminar friction factors are shown by solid lines in Figs. 2 and 3. They are also in good accord with the present experimental data as well as with the previously reported work of Shah and London [5] for a smooth equilateral triangular geometry. The experimental rms uncertainty of the friction factor is also shown for a typical data point in Fig. 2 to illustrate the close agreement between the numerical and experimental results.

To ascertain the validity of the hydraulic-diameter rule for noncircular geometries, i.e., the application of circular tube results with appropriate hydraulic diameter, the friction factor values for several finned equilateral and isosceles triangular cases ($\alpha = 38.8$) were plotted as a function of Reynolds number [22]. For all these cases the actual hydraulic diameter of the finned duct geometry is used (i.e., $d_H = 4A/p$). The failure of various finned geometry data to collapse on a single curve indicated that for the finned duct cases, the hydraulic-diameter rule for computing friction factor carries large and unacceptable uncertainty for laminar as well as turbulent regimes. It should be noted that the isosceles triangular duct data showed a much larger scatter compared to the equilateral triangular case. The failure of turbulent flow data to collapse on the circular duct data is somewhat unexpected in view of limited success of hydraulic-diameter rule for such noncircular duct shapes as the smooth equilateral and the wide-angled isosceles triangles. Since secondary flows exist in noncircular ducts, the

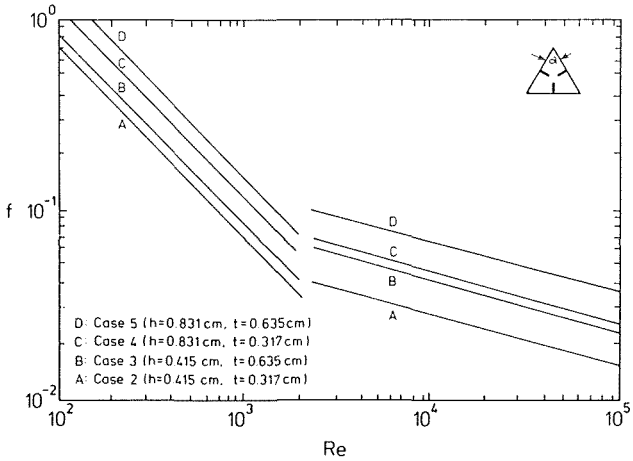

Fig. 4 Presentation of friction factor versus Reynolds number for various finned duct geometries for triangular duct with $\alpha = 60$ deg

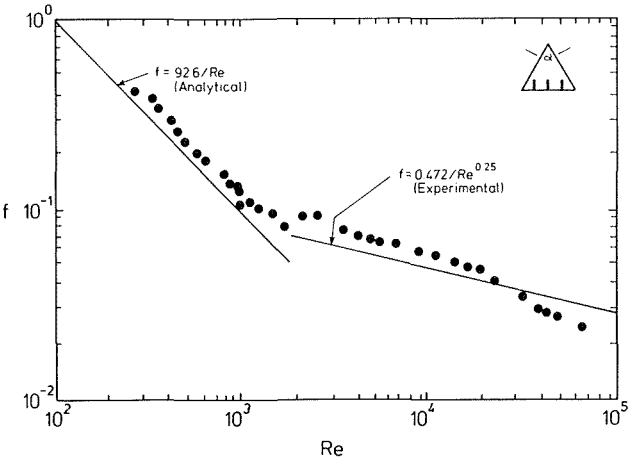

Fig. 5 Presentation of friction factor versus Reynolds number for a finned duct with $\alpha = 60$ deg

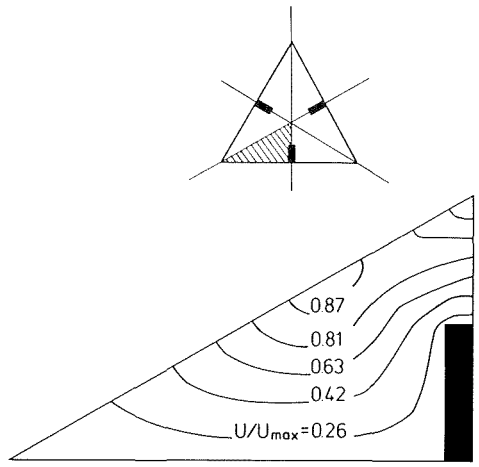

Fig. 6 Velocity contours for finned equilateral triangular duct with $h = 0.831$ cm and $t = 0.317$ cm

presence of thick fins in a duct perhaps causes the turbulent flow characteristics to depart significantly from those of an equivalent circular-shaped duct. As we shall see subsequently, the shape and the location of fins have significant influence on the friction factor characteristics. For the laminar case, even for the smooth noncircular duct shapes, the friction factor results are not governed satisfactorily by the hydraulic-diameter rule [1]. In fact, addition of fins has significant influence on the velocity contours which, despite retaining some symmetry, as in the case of equilateral triangular geometry, depart significantly from those of the equivalent circular geometry case.

Finned Equilateral Cross Section. In veiw of the large uncertainty involved in the use of hydraulic-diameter rule, the effects of fin height and width on friction factors are illustrated by employing the hydraulic diameter of the smooth duct for calculating f and Re, even for the finned geometry cases. Experiments were performed for fins with two different thicknesses and two different heights for each triangular duct shape. The majority of data obtained in the present study correlated well with $f \cdot \mathrm{Re} = C_L$ for laminar cases, and with $f \cdot \mathrm{Re}^{0.25} = C_T$ for the turbulent cases. The least-squares fits through the data for all four finned geometries are shown in Fig. 4. The parameters characterizing the duct shape and the fin geometry are given in Table 1, along with corresponding values of C_L and C_T.

In the laminar regime, the agreement between the numerical and the experimental data was always within the experimental uncertainty for all four finned geometries. It is interesting to note that whereas for a fixed fin height, doubling the fin thickness from 0.317 to 0.635 cm (cases 2 and 3) resulted in only a 16 percent increase in the value of the laminar coefficient C_L, doubling of the fin height from 0.415 to 0.831 cm for a fixed thickness (cases 2 and 4) resulted in about a 62 percent increase in C_L value. Comparison of cases 3 and 4 also shows that despite the same fin area, the fin with higher height resulted in 40 percent higher friction factor value in case 4 as compared to case 3. For taller fins, the axial velocity contours are greatly perturbed, and this leads to much higher velocity gradients and higher friction factor [22].

For the turbulent cases, the value of C_T ranged from 0.305 for smooth duct case to 0.721 for the case with maximum fin dimensions (case 5). In the turbulent regime, the results are qualitatively similar to the results for the laminar regime. For example, the fin height variation exerts a stronger influence on friction factor as compared to fin thickness variation. However, the effect of fin geometry is definitely weaker for the turbulent flow cases. For example, in cases 3 and 4, the fin area is kept the same by doubling the height and halving the thickness. The turbulent friction factor changes by less than 11 percent, as compared to 40 percent change in the laminar case.

For one particular equilateral triangular duct geometry, all three fins of equal size were mounted on one side of the duct at an equal distance apart (case 11). The dimensions of these fins are given in Table 1. The theoretical predictions of the laminar friction factor, along with the experimental data for this particular case, are given in Fig. 5. It can be seen that the theoretical solution of laminar coefficient of $C_L = 92.6$ is underestimated by approximately 7 percent when it is compared with the corresponding experimental data. Also, the value of $C_T = 0.472$ represents the least-squares linear fit through the turbulent data points with a slope of $-1/4$. Clearly, for this case, a curve fit of the type $f = C_T\,\mathrm{Re}^{-0.25}$ is a poor representation of the turbulent experimental data. Comparison of this particular case (Fig. 5) with the similar case of three fins of same size located on each side of a triangular duct (Fig. 4) shows a reduction of 24.8 percent in the laminar friction factor and a reduction of about 13 percent in the turbulent friction factor.

To further explore the difference between the above two cases, the axial velocity contours are plotted in Figs. 6 and 7. A comparison of the symmetric case (Fig. 6) with a similar case in which the same fins are located on one side of the duct (Fig. 7) shows that the flow patterns are disturbed more by the former configuration. The point at which the maximum velocity occurs in Fig. 7 is still near the point where the three

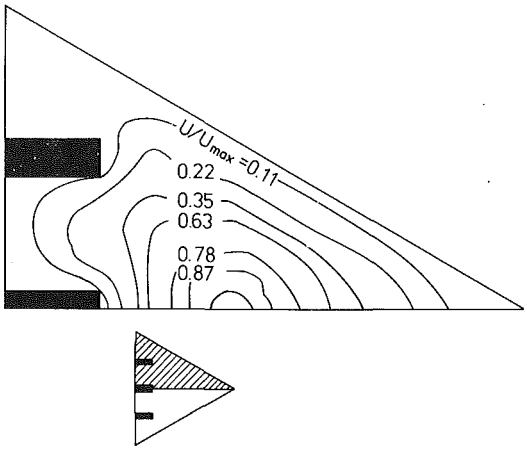

Fig. 7 Calculated velocity contours for finned equilateral triangular duct with $h = 0.831$ cm and $t = 0.317$ cm, with all fins located on one side

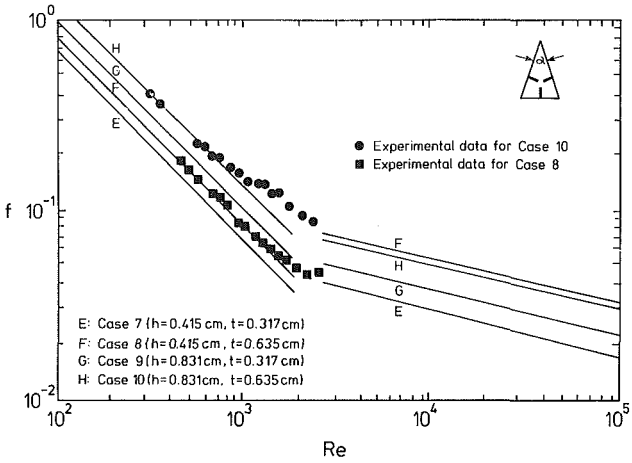

Fig. 8 Presentation of friction factor versus Reynolds number for various finned duct geometries for triangular duct with $\alpha = 38.8$ deg

bisectors meet. In contrast, locating fins on three different sides generates velocity contours with several near-maximum points. This leads to a higher velocity gradient and consequently a larger friction factor when compared to the case where all three fins are located on the same side.

Isosceles Cross Section. Experimental results for the finned isosceles triangular duct with apex angle 38.8 deg were also obtained for the same four finned geometries as in the case of equilateral duct. The dimensions of the duct and the fins are given in Table 1. The least-squares fits through the data for all four finned cases are shown in Fig. 8. For the fins corresponding to cases 7 and 9 in Table 1, experimental data are in excellent agreement with numerically predicted value of C_L for the laminar regime. Also, a curve fit of the type $f \cdot \mathrm{Re}^{0.25} = C_T$ resulted in reasonable agreement with data in the turbulent regime. However as seen in Fig. 8, for the fins with greatest width (cases 8 and 10), not all the laminar experimental data fell on the numerically predicted values of $C_L = 82.9$ and 138.7. It seems that transition from laminar to turbulent flow occurs at approximately $\mathrm{Re} \geq 900$ for cases 8 and 10 with wider fins. It should be remarked that in the present work, the transition from laminar to turbulent flow for all cases occurred in the range $1900 \leq \mathrm{Re} \leq 3200$, except for cases 8 and 10.

It is also interesting to note that for the laminar case with the largest size fin, the friction factor is about 16 percent lower for the isosceles cross section as compared to the corresponding equilateral case. For the turbulent case the two differ by 19 percent. As in the case of equilateral geometry, the fin height appears to be a more dominant parameter in the laminar regime. For example, doubling the height from 0.415 cm to 0.831 cm (cases 7 and 9) resulted in roughly a 50 percent increase in the value of C_L. In contrast the variation of width from 0.317 cm to 0.635 cm (cases 7 and 8), resulted in only 13 percent increase in the value of C_L.

A Correlation for the Laminar Friction Factor for Finned Equilateral Geometry. The next step during the investigation was to determine a correlation between the laminar friction factor and other nondimensional parameters that govern it. In the present case, the application of the Buckingham Pi theorem resulted in the following relationship between laminar friction factor f, the apex angle α, and the nondimensional thickness and height

$$f \cdot \mathrm{Re} = G(t/d_H, h/d_H, \alpha) \tag{7}$$

The following correlation was obtained from experimental data for laminar flow in finned equilateral cross section

$$f \cdot \mathrm{Re} = A_0 + B_0(t/d_H) \tag{8}$$

where A_0 and B_0, using a quadratic fit to the data, are given by the following expressions [22]

$$A_0 = 53.3 + 214.6\ (h/d_H) - 138.2\ (h/d_H)^2 \tag{9}$$

$$B_0 = 575.3\ (h/d_H) + 1883.7\ (h/d_H)^2 \tag{10}$$

Conclusions

Some of the prominent conclusions of this study can be summarized as follows:

1 The hydraulic-diameter rule for calculating friction factors for finned triangular ducts apparently produces a large error for both laminar and turbulent flows, especially for the thicker and longer fins. The equilateral duct has much smaller scatter of friction factor data compared to the isosceles duct.

2 In the laminar regime, the experimental data for most finned geometries were in excellent agreement with numerical results, well within the uncertainties of experimental data.

3 The theoretically determined correlation $f = C_L/\mathrm{Re}$, with C_L ranging from 53.2 for the smooth duct to 165.3 for the finned duct geometries, provided a good fit to the laminar data. The only exceptions were the isosceles triangular duct cases 8 and 10. For these cases, apparently the transition to turbulent flow occurs at lower Reynolds numbers.

4 For the turbulent cases, the friction factor data were well represented by the relationship $f = C_T\ \mathrm{Re}^{-0.25}$, with C_T ranging from 0.305 (for smooth triangular ducts) to 0.720 for the largest finned triangular duct. The only exception was for the equilateral triangular duct with all the three fins located on the same side. For this case, the above correlation is a poor representation of the turbulent data.

5 It is interesting to note that locating all three fins on the same side of an equilateral triangle resulted in lower values of friction factor, as compared to the case where all three fins of same size are located on three different sides.

6 To illustrate the effect of the fin size on the laminar friction factor for a duct with equilateral triangular cross section, a nondimensional correlation between the laminar coefficient ($C_L = f \cdot \mathrm{Re}$) and height and thickness ratios of the fins was obtained. Although the range of validity of this correlation is limited to the range of parameters covered in this study, it is hoped that due to its nondimensional nature, it may still be valid for other finned equilateral triangular duct cases not considered in the present study.

Acknowledgments

The authors wish to acknowledge the financial support of

the Mechanical Engineering Department and Old Dominion Research Foundation in carrying out this research project.

References

1 Nikuradse, J., "Investigation of Turbulent Flow in Tubes of Non-circular Cross-Section," *Engineering Archive* (*Ingen. Arch.*), Vol. 1, 1930, pp. 306–332.

2 Eckert, E. R. G., and Irvine, T. F., "Flow in Corners of Passages With Noncircular Cross-Sections," *Trans. of ASME*, Vol. 78, 1956, pp. 709–718.

3 Eckert, E. R. G., and Irvine, T. F., Jr., "Simultaneous Turbulent and Laminar Flow in Ducts With Noncircular Cross-Sections," *Journal of the Aeronautical Sciences*, Vol. 22, 1955, pp. 65–66.

4 Leonhardt, W. J., "Experimental Friction Factors for Fully Developed Flow of Dilute Aqueous Polyethylene-Oxide Solutions in Smooth Wall Triangular Ducts," in: *Heat and Mass Transfer Sourcebook: Fifth All-Union Conference, Minsk, 1976*, M.A. Styrikovich et al., eds., Wiley, New York, 1977.

5 Shah, R. K., and London, A. L., *Laminar Flow Forced Convection in Ducts*, Academic Press, New York, 1978, pp. 227–232.

6 Aly, A. M. M., Trupp, A. C., and Gerrard, A. D., "Measurements and Prediction of Fully Developed Turbulent Flow in an Equilateral Triangular Duct," *Journal of Fluid Mechanics*, Vol. 85, Part 1, Mar. 1978, pp. 57–83.

7 Gosman, A. D., and Rapley, C. W., "A Prediction Method for Fully Developed Flow Through Noncircular Passages," *Royal Society Proceedings*, Vol. 116, 1969, pp. 271–285.

8 Bergles, A. E., Webb, R. L., Junkhan, G. H., and Jensen, M. K., "Bibliography on Augmentation of Convective Heat and Mass Transfer," Report HTL-19, ISU-ERI-AMES-79206, Iowa State University, May 1979.

9 Bergles, A. E., Brown, G. S., Jr., and Snider, W. D., "Heat Transfer Performance of Internally Finned Tubes," ASME Paper No. 71-HT-31.

10 Hilding, W. E., and Coogen, C. H., Jr., *Heat Transfer and Pressure Loss Measurements in Internally Finned Tubes, Symposium on Air-Cooled Heat Exchangers*, ASME, New York, Feb. 1964, pp. 57–85.

11 Hu, M. H., and Chang, Y. P., "Optimization of Finned Tubes for Heat Transfer in Laminar Flow," ASME JOURNAL OF HEAT TRANSFER, Vol. 95, 1973, pp. 332–338.

12 Chen, D. T. W., "Flow and Heat Transfer in Internally Finned Tubes of Non-circular Cross-Section," Ph.D. Thesis, University of New York at Buffalo, 1973.

13 Date, A. W., "Prediction of Fully Developed Flow in a Tube Containing a Twisted-Tape," *International Journal of Heat and Mass Transfer*, Vol. 17, 1974, pp. 845–859.

14 Aggarwala, B. D., and Gangal, M. K., "Heat Transfer in Rectangular Ducts With Fins From Opposite Walls," *Journal of Applied Mathematics and Mechanics* (*ZAMM*), Vol. 56, 1976, pp. 253–266.

15 Gangal, M. K., and Aggarwala, B. D., "Combined Free and Forced Laminar Flow in Internally Finned Squate Ducts," *Journal of Applied Mathematics and Physics* (*ZAMP*), Vol. 28, 1977, pp. 86–96.

16 Nabdajynarm, J., and Masliyah, J. H., "Fully Developed Viscous Flow in Internally Finned Tubes," *Chemical Engineering Journal* (Lousanne), Vol. 10, 1975, pp. 113–120.

17 Masliyah, J. H., and Nandakumar, K., "Heat Transfer in Internally Finned Tubes," ASME JOURNAL OF HEAT TRANSFER, Vol. 98, 1975, pp. 257–261.

18 Patankar, S. V., Ivanovic, M., and Sparrow, E. M., "Analysis of Turbulent Flow and Heat Transfer in Internally Finned Tubes and Annuli," ASME JOURNAL OF HEAT TRANSFER, Vol. 101, 1979, pp. 29–37.

19 Soliman, H. M., Chau, T. S., and Trupp, A. C., "Analysis of Laminar Heat Transfer in Internally Finned Tubes With Uniform Outside Wall Temperature," ASME JOURNAL OF HEAT TRANSFER, Vol. 102, 1980, pp. 598–604.

20 Scott, M. J., and Webb, R. L., "Analytical Prediction of the Friction Factor for Turbulent Flow in Internally Finned Channels," ASME JOURNAL OF HEAT TRANSFER, Vol. 103, 1981, pp. 423–428.

21 Prakash, C., and Patankar, S. V., "Combined Free and Forced Convection in Vertical Tubes With Radial Internal Fins," ASME JOURNAL OF HEAT TRANSFER, Vol. 103, 1981, pp. 566–572.

22 Chegini, H., "An Experimental and Analytical Investigation of Friction Factors for Fully Developed Flow in Internally Finned Triangular Ducts," M.S. Thesis, Old Dominion University, Norfolk, VA, 1984.

23 Kays, W. M., and Crawford, M. E., *Convective Heat and Mass Transfer*, McGraw-Hill, New York, 1981.

24 Fox, R. W., and McDonald, A. T., *Introduction to Fluid Mechanics*, Wiley, New York, 1978.

25 Tuve, G. L., and Sprenkle, R. E., "Orifice Discharge Coefficients for Viscous Liquids," *Instruments*, Vol. 6, 1933, pp. 201–205.

26 Nogotov, E. F., *Application of Numerical Heat Transfer*, Hemisphere, Washington, D.C., 1978.

27 Carlson, L. W., and Irvine, T. F., "Fully Developed Pressure Drop in Triangular Shaped Ducts," ASME JOURNAL OF HEAT TRANSFER, Vol. 84, 1961, pp. 441–444.

Mean-Parameter Modeling of Oscillating Flow

D. Gedeon
Principal, Gedeon Associates,
Athens, OH 45701

After looking at the exact solution for laminar incompressible oscillating flow between parallel plates with a longitudinal temperature gradient, the momentum and energy equations are recast in terms of mean (section average) velocity and temperature. It is shown that fluid shear stress and normal temperature gradient at the wall are amplified and phase shifted compared to the steady-flow case and some practical equations for friction factor and Nusselt number are given. However, the mean-parameter solution differs from the exact solution in regard to net advected energy, thereby prompting the introduction of an apparent enhanced fluid conductivity to account for the difference.

There are important differences between steady and oscillating flow. Recent papers [1–4] have appeared which cover the subjects of thermal and mass diffusion in oscillating flow. Compared to steady flow, oscillating flow can produce large enhancements of apparent diffusion. These enhancements are due to the interaction of the bulk fluid flow and the boundary layer.

This paper examines the energy and momentum equations of oscillating flow from the point of view of someone needing heat transfer and pressure drop correlations to insert into a one-dimensional computational model. In a one-dimensional model, fluid parameters are averaged in the cross section normal to the principal flow direction and the fluid-dynamic equations expressed in terms of these mean parameters. Steady flow heat exchangers, for example, are often successfully treated as one-dimensional problems thanks to a wealth of steady-flow literature which correlates heat transfer and pressure drop in terms of section-averaged flow parameters. This paper shows that it is also possible to treat oscillating flow as a one-dimensional problem by extending the usual definitions of Nusselt number and friction factor and modifying the usual one-dimensional energy and momentum equations.

Definition of Problem

To simplify the analysis as much as possible, attention is restricted to incompressible flow oscillating sinusoidally between parallel plates. Fluid flow is assumed laminar and parallel; velocity is in the x-coordinate direction only and varies only in the y-coordinate direction normal to the plate faces. Velocity and temperature do not depend on the z direction, which is therefore ignored in the analysis. Figure 1 shows the coordinate system. Parallel flow implies that entrance effects are negligible, which is a fair approximation to reality when the flow oscillation amplitude and the plate separation are both small compared to the plate length. The time-averaged temperature profile of both the fluid and plates is assumed linear in x which will give rise to important results regarding fluid-to-wall heat transfer and advected energy in the x direction.

Parallel plates were chosen instead of circular tubes because the flow solutions involve exponential functions rather than Bessel functions. Exponential functions are easier to deal with and the fundamental results for parallel plates are likely to be similar to those for tubes.

Momentum Equation

The Navier–Stokes equations for an incompressible fluid are given by Schlichting [5]. When simplified to the case of parallel flow the momentum equation becomes

$$U_{yy} - U_t/\nu = P_x/(\nu\rho) \tag{1}$$

Partial derivatives are denoted by subscripts in equation (1). Introducing the dimensionless variables $\xi = (x/a)$, $\eta = (y/a)$, $\tau = (\omega t)$, and the Womersley number $\alpha = a\sqrt{\omega/\nu}$, equation (1) becomes

$$U_{\eta\eta} - \alpha^2 U_\tau = \alpha^2 P_\xi/(\rho a\omega) \tag{2}$$

For the case where P_ξ is sinusoidal in time with angular frequency ω, the solution of equation (2) can be written in the form (see Kurzweg [3])

$$U = U_0 \text{Real}(f(\eta)e^{i\tau}) \tag{3}$$

where U_0 is the center line velocity amplitude and f is a complex-valued function given by

$$f = \frac{\cosh(A\eta) - \cosh(A/2)}{1 - \cosh(A/2)} \tag{4}$$

Equation (4) can be readily simplified for the cases of small and large α. For small $|z|$, $\cosh(z)$ can be approximated as

$$\cosh(z) \simeq 1 + z^2/2 \tag{5}$$

which when applied to equation (4) results in the approximation

$$f \simeq 1 - 4\eta^2; \qquad \alpha << 1 \tag{6}$$

giving the familiar parabolic velocity profile for steady flow. For large $|z|$ (Real$(z) > 0$), $\cosh(z)$ can be approximated as

$$\cosh(z) \simeq \frac{1}{2} e^z \tag{7}$$

which when applied to equation (4) results in the approximation

$$f \simeq 1 - e^{-A(1/2-\eta)}; \qquad \alpha >> 1 \text{ and } \eta \geq 0 \tag{8}$$

showing that the velocity distribution tends to slug flow except for a thin boundary layer at the wall. For $\eta < 0$ the fact that f is an even function of η can be used to evaluate f.

Energy Equation

Once the velocity distribution is solved, the fluid energy

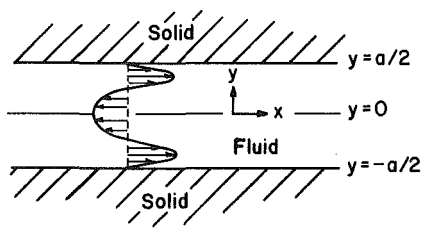

Fig. 1 Coordinate system used for analysis of parallel plate flow showing indication of velocity profile

Contributed by the Heat Transfer Division for publication in the JOURNAL OF HEAT TRANSFER. Manuscript received by the Heat Transfer Division August 8, 1985.

equation can be used to solve for the temperature distribution. Again, the derivation for the energy equation in incompressible flow can be found in Schlichting [5]. For the parallel flow problem at hand, simplification is possible and the resulting energy equation is

$$T_t + UT_x = \kappa(T_{xx} + T_{yy}) \tag{9}$$

The viscous dissipation term νU_y^2 has been neglected in equation (9) which limits applicability of this analysis to problems where viscous heating of the fluid is small compared to advected energy (cUT_x). Since U is known and T_x is assumed constant, an approximation ϵ to the ratio of viscous heating and advected energy can be found. For the case $\alpha >> 1$ of interest

$$\epsilon \simeq \alpha\nu U_0/(2c\,|T_x|a^2) \tag{10}$$

For equation (9) to be valid, ϵ must be small.

Expressed in terms of dimensionless variables ξ, η, and τ, equation (9) can be written

$$T_\tau + U/(a\omega)T_\xi = (T_{\xi\xi} + T_{\eta\eta})/(\alpha^2 \mathrm{Pr}) \tag{11}$$

The general solution to equation (11) is not needed; a restricted solution which applies to linear time-averaged longitudinal temperature distributions suffices for the problem at hand (see Kurzweg [3])

$$T/T_0 = \gamma[\xi + \mathrm{Real}(g(\eta)e^{i\tau})] \tag{12}$$

where T_0 is a normalization temperature, γ is a real constant, and g is a complex function given by ($\mathrm{Pr} \neq 1$):

$$g = B\left[\frac{C}{(1-\mathrm{Pr})}\cosh(\sqrt{\mathrm{Pr}}A\eta) - \frac{\mathrm{Pr}}{(1-\mathrm{Pr})}\cosh(A\eta) - \cosh(A/2)\right] \tag{13}$$

where

$$B = \frac{i\zeta}{|\langle f\rangle|[1-\cosh(A/2)]} \tag{14}$$

$$C = \frac{[\sigma\cosh(A/2) + \sqrt{\mathrm{Pr}}\sinh(A/2)]}{[\sigma\cosh(\sqrt{\mathrm{Pr}}A/2) + \sinh(\sqrt{\mathrm{Pr}}A/2)]} \tag{15}$$

In other words the fluid temperature distribution is the sum of a linear time-independent term and a time-varying term which is a function of distance from the wall. The function g at $\mathrm{Pr} = 1$ can be obtained by taking the limit of equation (13) as Pr approaches 1.

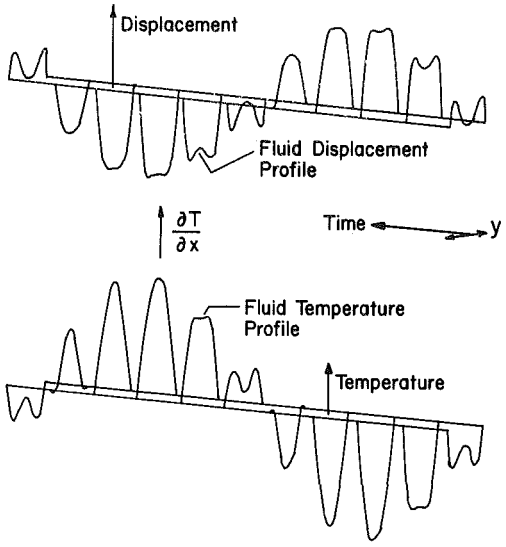

Fig. 2 Displacement and temperature profiles of exact solution at equally spaced time intervals: $\alpha = 10$, $\sigma = \infty$, $\mathrm{Pr} = 0.7$, $\zeta = 1$

Equation (11) applies to the solid as well if the advection term is set to zero and solid properties are substituted. The temperature solution (12) is also valid for the solid if g is replaced by g_s given by

$$g_s = De^{-[a\sqrt{i\omega/\kappa_s}(\eta - 1/2)]} \tag{16}$$

where

$$D = \frac{-B}{(1-\mathrm{Pr})}[\cosh(A/2) - C\cosh(\sqrt{\mathrm{Pr}}A/2)] \tag{17}$$

Plot of Exact Solution

Figure 2 shows an exact solution for the fluid displacement and temperature profiles at ten equally spaced time intervals over the course of one period. In both plots, the closely spaced parallel line segments represent the plates ($y = \pm a/2$) at $x = 0$. In the upper plot, the curves show the displacement function (integral of U) for the fluid; the curves are successive positions of a tracer line moving with the fluid. The bottom plot shows the temperature distribution at $x = 0$. There is a uniform temperature gradient in the direction of displacement. The

Nomenclature

a = plate spacing, m
A = $\sqrt{i}\,\alpha$
B = constant; see equation (14)
c = fluid specific heat, J/kgK
c_s = solid specific heat, J/kgK
C = constant; see equation (15)
d = $2a$ = hydraulic diameter, m
D = constant; see equation (17)
f = fluid velocity profile function; see equation (4)
F = generalized friction factor; see equation (25)
g = fluid temperature profile function; see equation (13)
g_s = solid temperature profile function; see equation (16)
G = constant; see equation (58)
h = ρcUT = advected energy per unit area, exact solution, W/m^2
h_b = $\rho c\langle U\rangle\langle T\rangle$ = advected energy per unit area, mean solution, W/m^2
h_c = $\rho c\langle U\rangle T_c$ = advected energy per unit area, steady-flow comparison solution, W/m^2
H = generalized film coefficient; see equation (35), W/m^{2}K
i = $\sqrt{-1}$
k = fluid conductivity, W/mK
k_s = solid conductivity, W/mK
Nu = generalized Nusselt number; see equation (33)
P = pressure, N/m^2
Pr = ν/κ = Prandtl number
q = $-kT_x$ = fluid heat conduction per unit area, W/m^2
r = apparent conductivity enhancement factor
S = wall shear factor; see equation (23)
t = time, s
T = temperature, K
T_c = temperature for mean-parameter solution using steady flow Nusselt number, K
T_0 = normalization temperature, K
U = fluid velocity, m/s
U_0 = fluid velocity amplitude at $y = 0$, m/s

temperature gradient in the y direction varies with time and position and sometimes even changes sign several times within the gap. It is the heat conduction driven by the y component of the temperature gradient which interacts with the fluid displacement profile to give a net advection of energy over the course of a cycle.

Equivalent Mean-Parameter Formulation

Mean-parameter forms of the oscillating-flow momentum and energy equations are now derived by taking section averages of the exact equations. In effect, the dependence on the y coordinate is removed, leaving one-dimensional equations involving mean flow parameters $\langle U\rangle$ and $\langle T\rangle$. The known exact solutions are then used to express wall shear stress and normal temperature gradient as functions of Womersley number. A comparison with steady-flow wall shear stress and normal temperature gradient is realized by taking the limit as Womersley number approaches zero.

Integrating the momentum equation (1) with respect to η between the wall limits (denoted by $\langle\rangle$) and observing that $\langle U_{yy}\rangle = (2/a)U_y(a/2)$ and that P_x is independent of y, the following mean-parameter momentum equation is obtained

$$\rho\langle U_t\rangle = -P_x + (2\rho\nu/a)U_y(a/2) \tag{18}$$

The second term on the right of equation (18) is the instantaneous force per unit volume due to wall shear stress. Using equation (3), it is possible to express $\langle U\rangle$ as

$$\langle U\rangle = U_0 \text{ Real } (\langle f\rangle e^{i\tau}) \tag{19}$$

Similarly, $\langle U_\tau\rangle$ can be expressed as

$$\langle U_\tau\rangle = -U_0\text{Imag}(\langle f\rangle e^{i\tau}) \tag{20}$$

and $U_y(a/2)$ as

$$U_y(a/2) = (U_0/a)\text{Real}(f'(1/2)e^{i\tau}) \tag{21}$$

Using equations (19) and (20), it is easy to verify that equation (21) can be written

$$U_y(a/2) = -(1/a)[\langle U\rangle\text{Real}(S) + \langle U_\tau\rangle\text{Imag}(S)] \tag{22}$$

where

$$S = \frac{-f'(1/2)}{\langle f\rangle} \tag{23}$$

A restricted form of the mean-parameter momentum equation, valid for sinusoidally oscillating mean flow velocity $\langle U\rangle$, is obtained by substituting equation (22) (with $\langle U_\tau\rangle$ replaced with $\langle U_t\rangle/\omega$) into equation (18) and simplifying

$$[\rho + (2\rho/\alpha^2)\text{Imag}(S)]\langle U_t\rangle = -P_x - (2\rho\nu/a^2)\text{Real}(S)\langle U\rangle \tag{24}$$

It is perhaps expected that the real part of S should appear in the right side of equation (24) in the wall stress term. More striking is the imaginary part of S in the bracketed quantity on the left side which plays the role of a modified density.

For those who prefer to see the momentum equation in terms of a conventional friction factor, define F by

$$F = |16\nu/\langle U\rangle d|S \tag{25}$$

where $d = 2a$ is the hydraulic diameter. Using equation (25), it is easy to verify that equation (24) can be written

$$[\rho \pm \rho\text{Imag}(F)\langle U\rangle/(2\omega d)]\langle U_t\rangle = -P_x \mp \text{Real}(F)\rho\langle U\rangle^2/(2d) \tag{26}$$

In equation (26) the upper signs are taken for $\langle U\rangle$ positive and the lower signs for $\langle U\rangle$ negative. It turns out that in the limit as α approaches zero, F reduces to the usual steady-flow friction factor and the second term on the left of equation (26) vanishes since Imag(S) approaches zero. Either equation (24) or (26) can be used as practical working equations for solution of engineering problems such as, for example, predicting pressure gradient P_x in terms of a known sinusoidally oscillating mean velocity $\langle U\rangle$.

The energy equation (9) can also be integrated with respect to η between the wall limits in order to obtain the following mean-parameter energy equation

$$\rho c\langle T_t\rangle + \rho c\langle U\rangle T_x = (2k/a)T_y(a/2) \tag{27}$$

The term on the right side of equation (27) is the total heat flux per unit volume into the fluid from both walls. Defining the difference between mean fluid temperature and deep wall temperature as

$$\theta = \langle T\rangle - \gamma\xi T_0 \tag{28}$$

and using equation (12) it follows that

$$\theta = \gamma T_0 \text{ Real}(\langle g\rangle e^{i\tau}) \tag{29}$$

and

$$\theta_\tau = -\gamma T_0\text{Imag}(\langle g\rangle e^{i\tau}) \tag{30}$$

Also, directly from equation (12)

$$T_y(a/2) = (\gamma T_0/a)\text{Real}(g'(1/2)e^{i\tau}) \tag{31}$$

Nomenclature (cont.)

W = pumping dissipation per unit volume; see equation (42), W/m^3
x = coordinate in flow direction, m
y = coordinate normal to plate faces, m
α = $a\sqrt{\omega/\nu}$ = Womersley number
γ = $(a/T_0)T_x$ = dimensionless temperature gradient
δ = $(U_0/\omega)|\langle f\rangle|$ = tidal amplitude of mean flow, m
ϵ = small parameter; see equation (10)
ζ = δ/a = dimensionless tidal amplitude
η = y/a = dimensionless y coordinate
θ = mean fluid to deep-wall temperature difference; see equation (32)
κ = $k/(\rho c)$ = fluid thermal diffusivity, m^2/s
κ_s = $k_s/(\rho_s c_s)$ = solid thermal diffusivity, m^2/s
ν = fluid kinematic viscosity, m^2/s
ξ = x/a = dimensionless x coordinate
ρ = fluid density, kg/m^3
ρ_s = solid density, kg/m^3
σ = $\sqrt{(k_s\rho_s c_s)/(k\rho c)}$
τ = ωt = dimensionless time coordinate
ω = angular frequency, rad/s
$\langle\ \rangle$ = section average:

$$\langle f\rangle = \int_{-1/2}^{1/2} f d\eta$$

$\{\ \}$ = time average over one period:

$$\{f\} = \frac{1}{2\pi}\int_0^{2\pi} f d\tau$$

$'$ = derivative of a single-variable function: $f'(\eta) = df/d\eta$

Subscripts

x, y, t, η, ξ, τ = denote partial differentiation: $U_t = \partial U/\partial t$, etc.

The following operations are defined on a complex number $z = a + bi$:

Real(z) = a
Imag(z) = b
z^* = $a - b_i$
$|z|$ = $\sqrt{zz^*}$

Using equations (29) and (30) it is possible to express $T_y(a/2)$ in terms of θ and θ_τ in a manner analogous to the way U_y was written in terms of $\langle U\rangle$ and $\langle U_\tau\rangle$ in the mean-parameter momentum equation

$$T_y(a/2) = -[\theta\,\mathrm{Real(Nu)} + \theta_\tau\,\mathrm{Imag(Nu)}]/(2a) \tag{32}$$

where

$$\mathrm{Nu} = \frac{-2g'(1/2)}{\langle g\rangle} \tag{33}$$

A restricted form of the mean-parameter energy equation – valid for sinusoidally oscillating mean flow velocity $\langle U\rangle$ and linear time-averaged longitudinal temperature distributions $\langle T\rangle$ – is obtained by substituting equation (32) into equation (27) and simplifying

$$[\rho c + (4/d)\mathrm{Imag}(H)/\omega]\langle T_t\rangle + \rho c\langle U\rangle T_x = -(4/d)\mathrm{Real}(H)\theta \tag{34}$$

where

$$H = (k/d)\mathrm{Nu} \tag{35}$$

H is understood as a generalized heat transfer film coefficient where Nu plays the role of a generalized Nusselt number. The factor $(4/d)$ in equation (34) is the wetted surface area per unit volume which is expressed in terms of hydraulic diameter d rather than the plate spacing a so that the equation can be applied universally.

It should be emphasized that the restrictions of sinusoidally oscillating mean flow velocity and linear time-averaged longitudinal temperature distribution are critical in the derivation of equation (34). It is beyond the scope of this paper to formulate a generalized Nusselt number for the case of nonlinear longitudinal temperature distribution.

The mean-parameter momentum and energy equations for oscillating flow are similar to their steady flow counterparts yet fundamentally different. In steady flow, the wall shear stress is proportional to the mean velocity and the normal temperature gradient is proportional to the mean temperature difference. In the oscillating flow situation the constants of proportionality are complex. That is, there is a phase shift between shear stress and mean velocity and between normal temperature gradient and mean temperature difference.

The quantities S and Nu defined by equations (23) and (33) can be simplified for the cases of small and large α. Using the approximating equations (6) and (8) for f, S can be written

$$S \simeq 6 \qquad \alpha << 1 \tag{36}$$

$$S \simeq (\sqrt{2} + \sqrt{2}\,i)\alpha/2; \quad \alpha >> 1 \tag{37}$$

Nu is more complicated to approximate since g is not as simple as f. In fact, g depends on C (equation (15)) which is a function of Pr and σ. It follows that Nu depends on the solid as well as fluid properties. Clearly, for an insulating wall ($\sigma = 0$) the normal fluid temperature gradient at the wall vanishes and therefore the generalized Nusselt number Nu vanishes. Using the defining equations (13)–(15) for g and a good deal of simplification, a few nontrivial approximations to Nu have been worked out

$$\mathrm{Nu} \simeq 10; \quad \alpha << 1, \quad \sigma >> 1 \tag{38}$$

$$\mathrm{Nu} \simeq \frac{\sigma}{(\sigma+1)} \frac{(\sqrt{\mathrm{Pr}} - \mathrm{Pr})}{(1-\mathrm{Pr})} (\sqrt{2} + \sqrt{2}\,i)\alpha; \quad \alpha \gg 1 \tag{39}$$

Of interest are the limiting cases for small α and large σ of S and Nu denoted S_0 and Nu_0. From equations (36) and (38)

$$S_0 = \lim_{\alpha \to 0} S = 6 \tag{40}$$

and

$$\mathrm{Nu}_0 = \lim_{\alpha \to 0} \mathrm{Nu} = 10 \tag{41}$$

Nu_0 is the Nusselt number for steady laminar flow between parallel plates under conditions of uniform heat flux and when the film coefficient is defined in terms of section-average temperature rather than bulk (velocity-weighted section average) temperature [6]. When S_0 is substituted for S in equation (25), F reduces to the familiar friction factor for steady laminar flow between parallel plates [7].

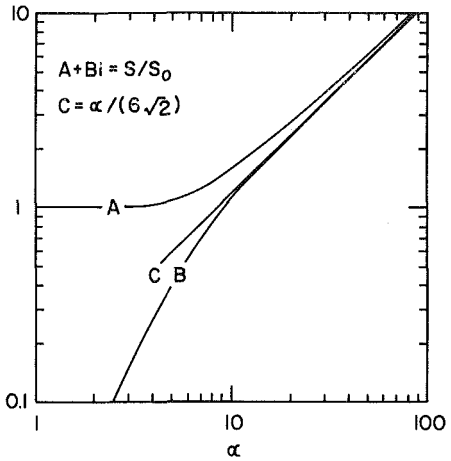

Fig. 3 Ratio of oscillating-flow shear stress at wall to steady flow shear stress at wall as a function of Womersley number α. Curve A is also the ratio of pumping power dissipation between the exact solution and a solution using the steady-flow friction factor. Curve C is the large α asymptote.

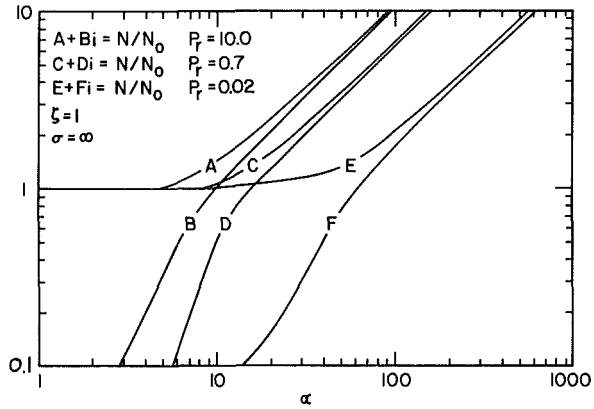

Fig. 4 Ratio of oscillating-flow normal temperature gradient at wall to steady flow normal temperature gradient at wall as a function of Womersley number α. In all cases $\sigma = \infty$, which is approached when solid conductivity is much larger than fluid conductivity.

For values of α and σ not covered in equations (38) through (41) one can resort to the defining equations (4) and (13) for f and g in order to calculate S and Nu. Alternatively, one can read S and Nu directly from the following graphs, at least in some cases. Figures 3 and 4 plot the real and imaginary parts of S/S_0 and $\mathrm{Nu}/\mathrm{Nu}_0$ against α. For simplicity, Fig. 4 considers only the case of $\sigma = \infty$ in which case the wall temperature is constant in time ($T = \gamma\xi T_0$; $|\eta| \geq 1/2$).

A useful engineering question is: What is the ratio of pumping power dissipation between a solution using the exact friction factor and a solution using the steady-flow friction factor? Based on the force balance shown in Fig. 5, the instantaneous rate of work per unit volume done on a volume element is

$$W = -UP_x + (\nu\rho)(U_y U)_y \tag{42}$$

To find the average of W in both t and y, first integrate W with respect to y between the wall limits and note that the last term on the right of equation (42) drops out because $U_y U$ is zero at the walls. Denoting time average with { } brackets and

recalling that $\langle\ \rangle$ brackets denote section average, it follows that

$$\{\langle W\rangle\} = -\{\langle UP_x\rangle\} \tag{43}$$

Since P_x is independent of y

$$\{\langle W\rangle\} = -\{P_x\langle U\rangle\} \tag{44}$$

Solving the mean-parameter momentum equation (24) for P_x and substituting into equation (44) gives

$$\{\langle W\rangle\} = \{(2\rho\nu/a^2)\text{Real}(S)\langle U\rangle^2 + [\rho + (2\rho/\alpha^2)\text{Imag}(S)]\langle U_t\rangle\langle U\rangle\} \tag{45}$$

Since U_t and U are orthogonal, the second term on the right of equation (45) drops out, leaving the final expression for average pumping dissipation per unit volume

$$\{\langle W\rangle\} = (2\rho\nu/a^2)\text{Real}(S)\{\langle U\rangle^2\} \tag{46}$$

For a solution using the steady-flow friction factor, a similar analysis would show that average pumping dissipation per unit volume would be given by

$$\{\langle W_0\rangle\} = (2\rho\nu/a^2)\text{Real}(S_0)\{\langle U\rangle^2\} \tag{47}$$

where S_0 is the steady-flow wall shear factor given by equation (40). Therefore, the ratio of pumping power dissipation between the exact solution and a solution using the steady-flow friction factor is

$$\{\langle W\rangle\}/\{\langle W_0\rangle\} = \text{Real}(S/S_0) \tag{48}$$

which is plotted in Curve A of Fig. 3.

Advected Energy of Mean-Parameter and Exact Solution

When the oscillating-flow solutions of the exact momentum and energy equations (1) and (9) are compared to the solutions of the mean-parameter equations (18) and (27), they are found to be similar in most, but not all, respects. The section averages of fluid variables such as U and T are of course identical. Furthermore, the average pumping dissipation for the exact solution turns out to be the same as the average pumping dissipation for the mean-parameter solution, as shown by inspection of equations (43) and (44). This result, which might seem trivial at first, is seen, upon closer examination, to be due to the fact that P_x is independent of y. Fate has not been so kind in the case of advected energy.

The advected energy through any plane normal to the x direction is proportional to the product of U and T evaluated at the plane. Since U and T are both functions of y, it does not follow that the section average of advected energy for the exact solution equals the advected energy for the mean-parameter solution. In fact, it will be seen that in the case of insulating walls, where there is no net advected energy over a cycle in the mean-parameter solution, there can nonetheless be a large net advected energy in the exact solution. This phenomenon was pointed out previously [1-3].

The average over y and t of advected energy per unit area in the exact oscillating-flow solution is

$$\{\langle h\rangle\} = \rho c\{\langle TU\rangle\} \tag{49}$$

Substituting for U using equation (3), T using equation (12), and switching the order of integration gives

$$\{\langle h\rangle\} = (\rho c\gamma T_0 U_0)\langle\{\text{Real}(ge^{i\tau})\text{Real}(fe^{i\tau})\}\rangle \tag{50}$$

Equation (50) can be further simplified by borrowing a result from complex analysis which states that for any complex numbers A and B

$$\{\text{Real}(Ae^{i\tau})\text{Real}(Be^{i\tau})\} = \frac{\text{Real}(AB^*)}{2} \tag{51}$$

where * denotes the complex conjugate. Applying equation (51) to equation (50) gives

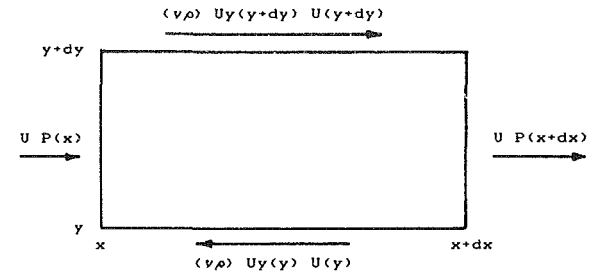

Fig. 5 Rates of work per unit time done on a fluid element by various forces

$$\{\langle h\rangle\} = (\rho c\gamma T_0 U_0/2)\text{Real}(\langle gf^*\rangle) \tag{52}$$

It is convenient to normalize advected energy by the energy flux per unit area due to simple conduction

$$q = -kT_x = -k\gamma T_0/a \tag{53}$$

Dividing equation (52) by (53) and simplifying gives

$$\{\langle h\rangle\}/q = \frac{\alpha^2\text{Pr}\zeta}{2|\langle f\rangle|}\text{Real}(-\langle gf^*\rangle) \tag{54}$$

Similarly, the time average for advected energy in the mean-parameter oscillating-flow solution is

$$\{h_b\} = \rho c\{\langle T\rangle\langle U\rangle\} \tag{55}$$

Substituting for T and U and simplifying as above gives

$$\{h_b\}/q = \frac{\alpha^2\text{Pr}\zeta}{2|\langle f\rangle|}\text{Real}(-\langle g\rangle\langle f^*\rangle) \tag{56}$$

Since $\langle gf^*\rangle$ is not generally equal to $\langle g\rangle\langle f^*\rangle$, equations (54) and (56) are not equivalent.

For comparison purposes it will also be useful to consider the time average for advected energy which results from the solution of the mean-parameter oscillating-flow energy equation (34) where the film coefficient H is based on the steady-flow Nusselt number Nu_0 instead of the generalized Nusselt number Nu. Denoting this solution by T_c it follows that

$$\{h_c\} = \rho c\{T_c\langle U\rangle\} \tag{57}$$

Assuming there is a complex constant G so that T_c is of the form

$$T_c/T_0 = \gamma[\xi + \text{Real}(Ge^{i\tau})] \tag{58}$$

it follows that

$$\{h_c\}/q = \frac{\alpha^2\text{Pr}\zeta}{2|\langle f\rangle|}\text{Real}(-G\langle f^*\rangle) \tag{59}$$

and G satisfies the equation

$$iG + \zeta = -\text{Nu}_0/(\alpha^2\text{Pr})G \tag{60}$$

Solving equation (60) for G and substituting into equation (59) gives the exact solution

$$\{h_c\}/q = \frac{\text{Nu}_0\alpha^4\text{Pr}^2\zeta^2}{2(\text{Nu}_0^2 + \alpha^4\text{Pr}^2)} \tag{61}$$

Approximations for $\{h_b\}/q$ and $\{\langle h\rangle\}/q$ have been worked out for the case of large α

$$\{h_b\}/q \simeq \frac{\sqrt{2}}{2}\frac{\sigma}{(\sigma+1)}\frac{(\sqrt{\text{Pr}}-\text{Pr})}{(1-\text{Pr})}\alpha\zeta^2; \quad \alpha >> 1 \tag{62}$$

$$\{\langle h\rangle\}/q \simeq \{h_b\}/q + \frac{\sqrt{2}}{2}\frac{(1-\sqrt{\text{Pr}})}{(1-\text{Pr}^2)} \cdot \frac{(\sigma+\sqrt{\text{Pr}})}{(\sigma+1)}\text{Pr}\alpha\zeta^2; \quad \alpha >> 1 \tag{63}$$

Figure 6 shows time-averaged normalized advected energies $\{\langle h\rangle\}/q$, $\{h_b\}/q$, and $\{h_c\}/q$ plotted against α. The plot is restricted to the case $\sigma = \infty$, $\text{Pr} = 0.7$, and dimensionless tidal

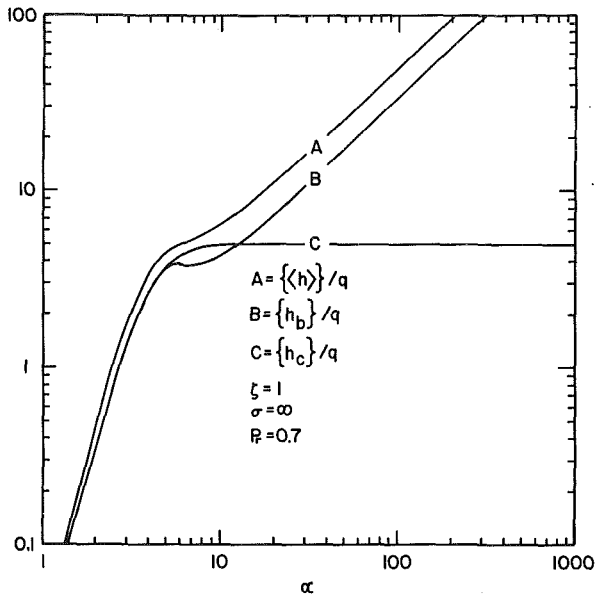

Fig. 6 Time-average advected energy/conduction for the exact solution (curve *A*), the mean-parameter solution using the generalized Nusselt number Nu (curve *B*), and the mean-parameter solution using the steady flow Nusselt number Nu_0 solution (curve *C*): $\sigma = \infty$, $Pr = 0.7$, $\zeta = 1$

amplitude $\zeta = 1$. All normalized advected energies are proportional to ζ^2 so it is a simple matter to obtain advected energies for other values of ζ. For other values of σ and Pr, however, there seems to be no short cut to the truth apart from the approximations already mentioned above: One is forced to use the defining equations (4) and (13) for f and g in order to compute advected energies.

It is seen in Fig. 6 that the exact and mean-parameter advected energies tend toward infinity for increasing Womersley number while the advected energy for the comparison solution levels off. In fact, for large α, $\{h_c\}/q$ is seen to approach $Nu_0/2$. However, below $\alpha \simeq 10$ (depending on σ and Pr) the steady-flow comparison solution is a reasonable approximation. The reason for the divergence of the exact versus comparison solution can be traced to the divergence in Nusselt number ratio Nu/Nu_0 shown in Fig. 4.

The mean-parameter solution can be made equivalent to the exact solution in all respects if an enhanced fluid conductivity is defined to make up for the difference in exact and mean-parameter advected energies $\{\langle h \rangle\}$ and $\{h_b\}$. In fact the apparent conductivity enhancement factor is simply

$$r = 1 + \frac{\{\langle h \rangle\} - \{h_b\}}{q} \tag{64}$$

It should be emphasized that defining an enhanced fluid conductivity is only a means to correct the advected energy deficit of the mean-parameter solution in a one-dimensional computational model; the need for an enhancement over molecular conductivity disappears when the exact two-dimensional energy equation is used. Nonetheless, an enhanced conductivity might be justified, for example, to correlate data from an experimental test rig sensitive only to mean parameters. An approximation for r in the case of large α is obtained from the difference of equations (62) and (63)

$$r - 1 \simeq \frac{\sqrt{2}}{2} \frac{(1-\sqrt{Pr})}{(1-Pr^2)} \frac{(\sigma+\sqrt{Pr})}{(\sigma+1)} Pr\alpha\zeta^2; \quad \alpha >> 1 \tag{65}$$

Conclusions

It has been shown that a mean-parameter formulation is possible for the momentum and energy equations of incompressible oscillating flow between parallel plates. Moreover, the solution of the mean-parameter equations can be made equivalent to the exact solution in all respects if an enhanced conductivity is defined in order to account for the discrepancy in advected energy.

Mean-parameter equations are likely to be useful for closed-form analytic, numerical, and experimental work. In numerical modeling of oscillating fluid flow, the two-dimensional computational grid which is required for the exact solution can be replaced by a one-dimensional grid. In experimental work, the equations can be used as a framework upon which to build empirical correlations.

Several unanswered questions remain. How does one handle oscillating flow that is turbulent, or compressible, or not quite sinusoidal, or for which entrance effects are significant or longitudinal temperature gradients nonlinear? What about flow in tubes or channels or porous matrices? An effort has been made to formulate the important equations in this paper in sufficiently general terms that they can serve as first approximations to these other cases. Thus, hydraulic diameter, generalized friction factor and generalized Nusselt number have been used. More accurate results should be possible, in at least some of the above cases, by modifying only the friction factor or Nusselt number in a manner analogous to the way laminar steady-flow equations are extended to turbulent flow. This is not to suggest that such modifications will be easy; significant extensions of idealized oscillating flow theory are likely to come only from a combined analytic and experimental effort.

References

1 Kurzweg, U. H., and Zhao, L. D., "Heat Transfer by High Frequency Oscillations: a New Hydrodynamic Technique for Achieving Large Effective Thermal Conductivities," *Physics of Fluids*, Vol. 27, Nov. 1984, pp. 2624–2627.

2 Kurzweg, U. H., "Enhanced Heat Conduction in Fluids Subjected to Sinusoidal Oscillations," ASME JOURNAL OF HEAT TRANSFER, Vol. 107, May 1985, pp. 459–462.

3 Kurzweg, U. H., "Enhanced Heat Conduction in Oscillating Viscous Flows Within Parallel-Plate Channels," *J. Fluid Mech.*, Vol. 156, 1985, pp. 291–300.

4 Watson, E. J., "Diffusion in Oscillatory Pipe Flow," *J. Fluid Mech.*, Vol. 133, 1983, pp. 233–244.

5 Schlichting, H., *Boundary-Layer Theory*, 7th ed., McGraw-Hill, New York, 1979, pp. 65–66, 265–268.

6 Jacob, M., *Heat Transfer*, Vol. 1, Wiley, New York, p. 467.

7 Knudsen, J. G., and Katz, D. L., *Fluid Dynamics and Heat Transfer*, McGraw-Hill, ch. 4.

Effect of Tip-to-Shroud Clearance on Turbulent Heat Transfer From a Shrouded, Longitudinal Fin Array

E. M. Sparrow

D. S. Kadle[1]

Department of Mechanical Engineering,
University of Minnesota,
Minneapolis, MN 55455

Experiments were performed to determine the response of the heat transfer from a longitudinal fin array to the presence of clearance between the fin tips and an adjacent shroud. During the course of the experiments, the clearance was varied parametrically, starting with the no-clearance case; parametric variations of the fin height and of the rate of fluid flow through the array were also carried out. Air was the working fluid, and the flow was turbulent. The fully developed heat transfer coefficients corresponding to the presence and to the absence of clearance were compared under the condition of equal air flowrate, and substantial clearance-related reductions were found to exist. For clearances equal to 10, 20, and 30 percent of the fin height, the heat transfer coefficients were 85, 74, and 64 percent of those for the no-clearance case. The ratio of the with-clearance and no-clearance heat transfer coefficients was a function only of the clearance-to-fin-height ratio, independent of the air flowrate, the fin height, and the fin efficiency model used to evaluate the heat transfer coefficients. The presence of clearance slowed the rate of thermal development in the entrance region.

Introduction

Although fins have long served as the primary means of enhancement in heat exchange devices, key issues about their performance remain to be resolved. The issue to be investigated here will be discussed with the aid of Fig. 1. To initiate the discussion, suppose that the surface labeled *shroud* is absent. What remains is a diagram of an array of longitudinal fins affixed to a baseplate – a diagram whose variants appear in all heat transfer textbooks. The textbook treatments of such a fin array neglect the tendency of the longitudinal flow to leak out of the interfin spaces into the ambient as it seeks the path of least resistance. In practice, to avoid such outleakage, which would diminish the rate of heat transfer, a shroud is positioned adjacent to the fin tips, as illustrated in Fig. 1.

A clearance between the fin tips and the shroud is frequently encountered in practice, either by design or by chance. For example, a configuration similar to that of Fig. 1 is employed in the cooling of computer components. When a clearance is present, the velocity distribution is more complex than for the no-clearance case, and similarly for the heat transfer.

The focus of the present experiments is to determine the response of the heat transfer from an array of longitudinal fins to the size of the clearance between the fin tips and the shroud. Two geometric parameters were varied during the course of the experiments: the relative clearance C/H and the relative fin height H/W. For each configuration defined by C/H and H/W, the rate of fluid flow passing through the array was varied by a factor of six within the turbulent regime. Air was the working fluid in all the experiments. The thermal boundary condition was uniform heat input per unit axial length and cross-sectionally uniform baseplate temperature. Heat was supplied via the baseplate, while the shroud was adiabatic.

In the presentation of results, primary attention will be given to the fully developed regime, but illustrative entrance region results will be presented showing the thermal response to variations of the clearance at a fixed airflow and to variations of the airflow at a fixed clearance. Fully developed heat transfer coefficients and Nusselt numbers were evaluated using two models for the fin efficiency, and the response of both sets of Nusselt numbers to parametric variations of the clearance will be highlighted. As the end result of a correlation effort, the ratio of the heat transfer coefficients in the presence and in the absence of clearance was found to be a unique function of C/H, independent of the airflow rate, the relative fin height, and the fin efficiency model.

From a search of the literature, no prior experimental work was found dealing with the effect of the fin tip to shroud clearance. Finite-difference solutions, restricted to laminar flow, are reported in [1] and [2], respectively, for forced convection and for mixed convection.

Experiments

Test Section Components and Configurations. To facilitate the description of the experimental apparatus, reference may be made to Fig. 2, which shows a cross section of one of the several test sections used in carrying out the experiments. The main components of the test section included

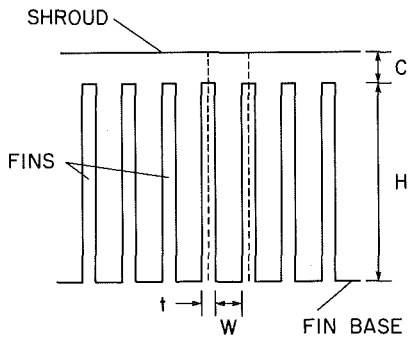

Fig. 1 Fin array with a clearance between the fin tips and an adjacent shroud

[1]Present address: Harrison Radiator Division, General Motors Corporation, Lockport, NY.

Contributed by the Heat Transfer Division for publication in the JOURNAL OF HEAT TRANSFER. Manuscript received by the Heat Transfer Division October 8, 1985.

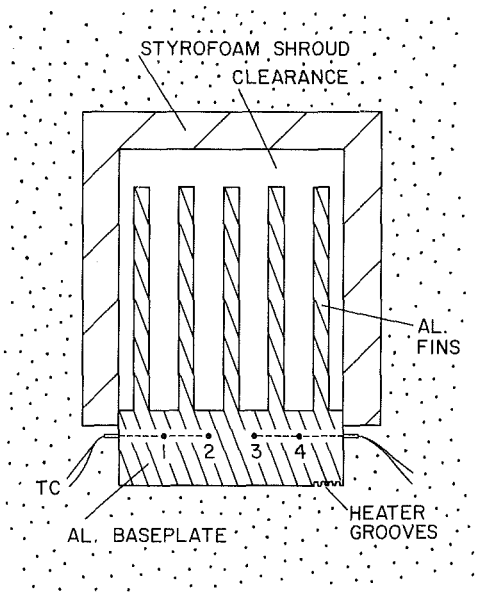

Fig. 2 Cross-sectional view of test section

an array of parallel longitudinal fins, a baseplate integral with the fins, and a shroud which served to confine the airflow. All told, eight different test sections were employed, encompassing two fin heights and, for each fin height, four different clearances between the fin tips and the shroud.

The fins were made integral with the baseplate to guarantee the absence of contact resistance, and the fin/baseplate assembly was fabricated from aluminum because of its high thermal conductivity, low emissivity, and easy machinability. For the fabrication, longitudinal grooves, which served as the interfin gaps, were milled into the upper face of a long rectangular aluminum bar having premachined external dimensions of 3.81 × 5.08 × 50.8 cm (width × height × axial length). Special fixtures and techniques were used to ensure that warpage did not occur as the successive grooves were cut and that the fins were straight and parallel. The fin height pictured in Fig. 2 is the larger of the two investigated heights. Once the experiments for this fin configuration had been completed, the fin height was reduced to half its initial value by a milling operation and additional experiments carried out.

To accommodate electrical resistance wire which served to heat the test section, shallow longitudinal grooves were milled into the lower face of the baseplate. The heater wire grooves were anodized to provide a thin, electrically insulating layer which supplemented the Teflon cladding of the wire as a defense against short circuits.

As seen in Fig. 2, the shroud used to confine the airflow was an inverted U-shaped shell which was attached to the outboard edges of the baseplate. The shroud material was chosen to minimize possible extraneous heat losses from the baseplate through the shroud. To this end, closed-pore, extruded polystyrene insulation (Styrofoam) was used not only because of its low thermal conductivity but also because of its structural stiffness and its capability of being machined to a smooth surface finish and to close tolerances. All surfaces of the Styrofoam which interfaced with the airflow were covered with self-adhering, plasticized contact paper to ensure hydrodynamic smoothness. Prior to the application of the contact paper, the Styrofoam was sealed to prevent possible infiltration. The bonding of the shroud to the baseplate was accomplished with silicone rubber adhesive, which also served as a sealant.

A different shroud was used for each of the eight investigated test section configurations. Each shroud was fabricated from a long barlike piece of premachined Styrofoam. With the aid of a milling machine, a channel was cut in the Stryrofoam to a depth equal to the sum of the fin height, the tip-to-shroud clearance, and the overlap needed for the bonding of the shroud to the baseplate. The width of the milled-out channel was identical to that of the baseplate. The overall axial length of the shroud was made equal to the combined lengths of the test section, the hydrodynamic development section, and the exit section (situated downstream of the test section).

The assembled test section, as shown in Fig. 2, included five fins. The interfin spaces formed four parallel flow passages, flanked on either side by a half-width flow passage bounded by the outboard fin and the shroud wall. The half-width flow passages were used to more closely model an infinite array of fins.

The investigated parametric variations of the tip-to-shroud clearance C and of the fin height H may be expressed in dimensionless form as

$$C/H = 0, 0.083, 0.165, 0.336 \tag{1}$$

$$H/W = 3.75, 7.5 \tag{2}$$

while the other geometric aspects of the test section are defined by: (*a*) flow passage width W = 0.508 cm, (*b*) fin thickness t = 0.254 cm, (*c*) thickness of shroud = 0.635 cm, (*d*) thickness of baseplate = 1.27 cm, and (*e*) axial length of test section = 50.8 cm. The clearance C was set with the aid of specially machined Teflon spacers placed between the fin tips and the shroud during the assembly process. Once the shroud had been bonded to the baseplate, the spacers were eased out of the clearance gap.

Heating and Temperature Aspects. As indicated earlier, heating of the test section was accomplished by Ohmic dissipation in electrical resistance wire embedded in longitudinal

Nomenclature

A'_{hL} = heat transfer surface area per unit axial length and per lane
B = coefficient in Nu versus $\dot{M}$ relation
C = tip-to-shroud clearance
c_p = specific heat
H = fin height
h = fully developed heat transfer coefficient, equation (4)
h_0 = value of h for no-clearance case
k = thermal conductivity
L = test section length
$\dot{M}$ = dimensionless mass flowrate $= \dot{m}_L/W\mu_{air}$
$\dot{m}_L$ = mass flowrate per lane
Nu = fully developed Nusselt number $= hW/k_{air}$
Nu_0 = value of Nu for no-clearance case
n = exponent in Nu versus $\dot{M}$ relation
Q'_L = heat transfer rate per unit axial length and per lane
Re = hydraulic-diameter Reynolds number
T_b = bulk temperature
T_w = baseplate temperature
t = fin thickness
W = width of interfin gap
x = axial coordinate
η = fin efficiency
μ = viscosity

Subscripts

fd = fully developed
0 = no clearance
x = at axial station x

grooves uniformly deployed along the bottom of the baseplate. The wiring was arranged so that there were three independently controlled circuits. The main heating circuit, the wiring for which occupied the central 23 grooves, was flanked at either side by a guard heater, each occupying five grooves. The guard heaters provided a means to compensate for possible end effects associated with the finiteness of the array. Power was supplied by a regulated a-c source which fed a separate autotransformer for each heating circuit. The heater voltage drops and current flows (measured as shunt voltages) were read with a true rms voltmeter.

The test section was instrumented with 52 thermocouples which were deployed in 26 cross sections, with two in each cross section. The thermocouple installation in a typical instrumented cross section is illustrated in Fig. 2. As seen there, the thermocouples were brought in from the sides, and the lead wires were laid along the dashed lines, which were expected to be (and actually were) isothermal. In any instrumented cross section, the thermocouple junctions were positioned either at points 1 and 3 or at points 2 and 4, with the 1/3 and 2/4 positioning alternating in successive cross sections. The thermocouples were made from precalibrated, 30-gage, Teflon-coated chromel and constantan wires.

The voltage settings for the individual heating circuits were guided by the thermocouple readings. It was found that if the heater voltages were set to provide a spanwise-uniform heat input, the two thermocouples in each cross section read the same to within the 1 μV resolving power of the instrumentation. This finding indicates that any end effects were too small to be detected.

The bulk temperature of the air entering the test section, needed for the data reduction, was measured in the hydrodynamic development section using three thermocouples situated in the air stream just upstream of the test section inlet. During any data run, the three thermocouples indicated the same value.

Other Apparatus Components. The hydrodynamic development section and the exit section, which respectively preceded and followed the test section, were both unobstructed rectangular ducts having respective lengths of 50.8 and 25.4 cm. These ducts were made of insulating materials, with the continuation of the Styrofoam shroud forming three sides of the rectangular cross section and a thin sheet of unlaminated fiberglass circuit board forming the fourth side.

The experimental apparatus was operated in the open-circuit mode and in suction. Air from the laboratory room was drawn through a flowmeter (a calibrated rotameter) into a plenum chamber, from which it passed successively through the hydrodynamic development section, the heated test section, and the exit section. The exit section interfaced with a circular pipe which contained a flow control valve and which delivered the air to the blower inlet. The hot discharge from the blower was ducted out of the building.

The development section, the test section, and the exit section were all situated within a large, closed, wooden-walled container (52.5 × 52.5 cm in cross section and 91.5 cm long) filled with silica aerogel powder insulation. The thermoconductivity of the silica aerogel is 15 percent smaller than that of air. To further minimize extraneous heat losses, the aforementioned components were suspended in the insulation container by nylon lines instead of being supported by rigid structural members. A finite-difference analysis of the conduction heat losses through the insulation demonstrated that they were entirely negligible [3]. Owing to the large volume of the insulation, about 8–10 hr were required to attain steady-state conditions during a data run.

Data Reduction

Heat transfer coefficients and Nusselt numbers were evaluated for the thermally developed regime. The attainment of thermal development was identified for each case by plotting the axial distributions of the baseplate temperature T_w and the fluid bulk temperature T_b. The baseplate temperatures were determined by direct measurement as described earlier, while the bulk temperature distribution was obtained by calculation. For the calculations, it was found convenient to work with a typical lane in the array, as illustrated by the pair of dashed lines in Fig. 1. If $\dot{m}_L$ denotes the mass flowrate of air per lane and Q'_L is the rate of heat transfer to the airflow per unit axial length and per lane, then

$$T_b = T_{bi} + (Q'_L/\dot{m}_L c_p)x \tag{3}$$

where T_{bi} is the inlet bulk temperature. For all cases, there was a portion of the test section where the wall and bulk temperature distributions were precisely parallel, yielding a uniform value of $(T_w - T_b)$, as will be documented later.

The fully developed heat transfer coefficient h was evaluated from the definition

$$h = Q'_L/A'_{hL}(T_w - T_b) \tag{4}$$

in which A'_{hL} is the heat transfer surface area per unit axial length and per lane, and the other symbols have already been defined. Based on purely geometric considerations, A'_{hL} is equal to $(W+2H+t)$ in the presence of tip-to-shroud clearance and to $(W+2H)$ when there is no clearance, as can be verified by inspection of Fig. 1. However, it is common practice in applications involving fins to de-rate the fin surface area by the efficiency η, so that

$$A'_{hL} = W + \eta(2H+t), \qquad C>0 \tag{5}$$

$$A'_{hL} = W + \eta(2H), \qquad C=0 \tag{6}$$

Two approaches were employed to evaluate η. One was to set $\eta = 1$. The second was to use the conventional one-dimensional fin model which can be found in any heat transfer textbook, i.e.,

$$\eta = [\tanh(\lambda H_c)]/\lambda H_c \tag{7}$$

where

$$\lambda = (2h/k_{\text{fin}}t)^{1/2} \tag{8}$$

and H_c is equal to $(H + t/2)$ in the presence of clearance and to H when there is no clearance.

An iterative procedure was required to implement the second approach, since the calculation of η from equations (7) and (8) necessitates that h be known. To begin, with η set equal to 1, the heat transfer area A'_{hL} was found from equations (5) or (6), and h was evaluated from equation (4) using the values of Q'_L and $(T_w - T_b)$ from experiment. With this h value as input, η was calculated from equations (7) and (8), enabling successive re-evaluations of A'_{hL} and h. The new h value was used to initiate another cycle of the iteration, and this process was continued until convergence, yielding both h and η. This approach to the evaluation of the fin efficiency was given considerable support in [4] where, for the no-clearance case, it yielded values that agreed well with those from finite-difference solutions of the governing conservation equations.

The fully developed heat transfer coefficients evaluated from both of the aforementioned fin efficiency models were recast in dimensionless terms via the Nusselt number

$$\text{Nu} = hW/k_{\text{air}} \tag{9}$$

The width W of the interfin gap was chosen as the characteristic dimension since it was fixed during the course of the experiments. Consequently, any change in Nu which occurred in response to the variations of the parameters is a true reflection of the changes in the heat transfer coefficient. The thermal conductivity appearing in equation (9) was evaluated at the mean bulk temperature in the fully developed regime

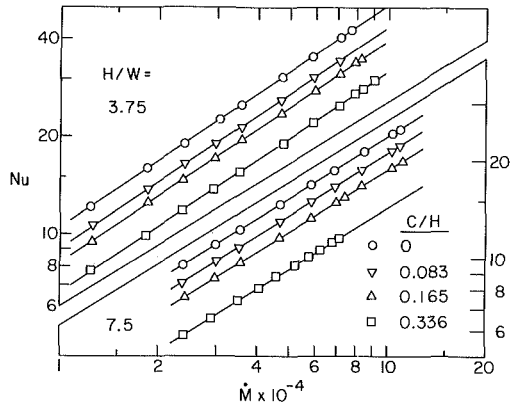

Fig. 3 Fully developed Nusselt numbers for with-clearance and no-clearance fin arrays. Fin efficiency model: $\eta = 1$.

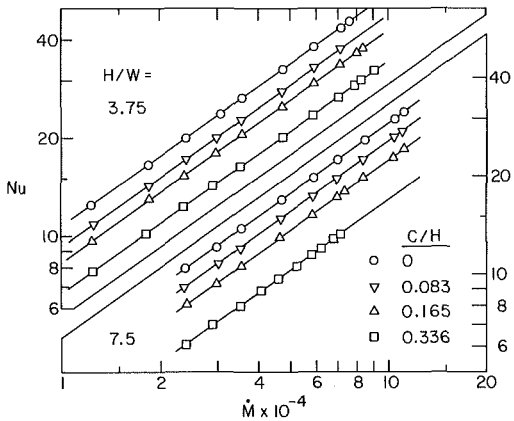

Fig. 4 Fully developed Nusselt numbers for with-clearance and no-clearance fin arrays. Fin efficiency model: equations (7) and (8).

(property variations were of little significance since the inlet-to-exit bulk temperature rise was only about 10°F).

In the forthcoming presentation of results, heat transfer coefficients corresponding to different tip-to-shroud clearances will be compared at a fixed air flowrate. To facilitate such a comparison, a dimensionless representation was sought which is a direct reflection of the air flowrate but does not depend on the clearance. These criteria are satisfied by the definition

$$\dot{M} = \dot{m}_L / W\mu_{\text{air}} \tag{10}$$

where the viscosity was evaluated at the same temperature used to evaluate k_{air}.

The conventional hydraulic-diameter Reynolds number depends both on the clearance and on the air flowrate and will, therefore, not be used in the presentation of results. It is, however, relevant to indicate the relationship between the $\dot{M}$ parameter and the Reynolds number. For example, for the no-clearance case, where the Reynolds number Re_0 (0 = no clearance) is given by $2\dot{m}_L/(H+W)\mu_{\text{air}}$,

$$\text{Re}_0 = [2W/(H+W)]\dot{M} \tag{11}$$

so that $\text{Re}_0 = 0.421\dot{M}$ and $0.235\dot{M}$, respectively, for H/W = 3.75 and 7.5.

Results and Discussion

The fully developed Nusselt number results are presented in Figs. 3 and 4. The first of these corresponds to the $\eta = 1$ fin efficiency model, while the second is for the $\eta < 1$ model embodied in equations (7) and (8). Each figure is a composite of two graphs. The upper graph conveys results for the shorter fins (H/W = 3.75), and the lower graph conveys the results for the longer fins (H/W = 7.5). Each graph contains four sets of data parameterized by relative clearances C/H equal to 0 (no clearance), 0.083, 0.165, and 0.336. In appraising the results presented in each graph, the no-clearance case (C/H = 0) will be regarded as a baseline against which the with-clearance cases will be compared.

Table 1 Values of B in equation (12)

		$\eta = 1$		$\eta < 1$	
C/H	H/W =	3.75	7.5	3.75	7.5
0		1.96	1.58	1.53	0.764
0.083		1.68	1.40	1.31	0.674
0.165		1.52	1.25	1.18	0.589
0.336		1.23	0.969	0.944	0.445

An overall examination of Figs. 3 and 4 shows that at any given mass flowrate $\dot{M}$, the Nusselt number decreases significantly as the clearance C/H increases. The extent of the Nusselt number decrease will be quantified and correlated shortly, but it is worth noting here that even a clearance as small as C/H = 0.083 causes a decrease in the 10–15 percent range. Since a decrease in the Nusselt number gives rise to a reduction in the rate of heat transfer, it follows that the presence of a clearance gap, either by design or by chance, degrades the heat transfer performance.

It is also seen that the Nu versus $\dot{M}$ data for a given clearance fall on a straight line with minimal scatter, so that the power-law repesentation

$$\text{Nu} = B\dot{M}^n \tag{12}$$

is appropriate, where B and n may be found from a least-squares fit. Furthermore, for a given fin height H/W, the straight lines for the various clearances are parallel.

For the Nusselt numbers evaluated with the η = 1 fin efficiency model, the exponents in the power-law representation are slightly different for the H/W = 3.75 and 7.5 fin heights, respectively n = 0.683 and 0.635. However, for the Nusselt numbers based on the fin efficiency model of equations (7) and (8), the exponents are virtually identical for the two H/W, namely, 0.712 and 0.716 for H/W = 3.75 and 7.5. The emergence of a common exponent lends strong support to the use of the fin efficiency model of equations (7) and (8). To complement the aforementioned n values, the constants B for equation (12) are listed in Table 1.

This tabulation provides the basis for correlating the heat transfer response to the presence of tip-to-shroud clearance. Consider an array of fins of fixed height H/W for which the clearance is varied parametrically at a given value of the dimensionless mass flowrate $\dot{M}$, and let Nu and Nu_0 denote the with-clearance and no-clearance Nusselt numbers. From equation (12),

$$\text{Nu} = B\dot{M}^n,\ \text{Nu}_0 = (B\dot{M}^n)_0 \tag{13}$$

Since n was found to be independent of C/H for a fixed fin height (i.e., $n = n_0$) and $\dot{M}$ is specified to be equal to $\dot{M}_0$, it follows that

$$\text{Nu}/\text{Nu}_0 = h/h_0 = B/B_0 \tag{14}$$

Thus, the B/B_0 ratio is a direct measure of the response of the heat transfer coefficient to the size of the tip-to-shroud clearance gap.

As seen in Table 1, the B/B_0 ratio is available for two fin heights and, for each fin height, for two fin efficiency models. The h/h_0 variations with C/H for these four cases are plotted in Fig. 5. The figure quantifies the extent of the degradation sustained by the heat transfer coefficient due to the presence of the clearance gap. For the largest clearance investigated here (C/H = 0.336), $h/h_0 \sim 0.6$, which corresponds to a 40

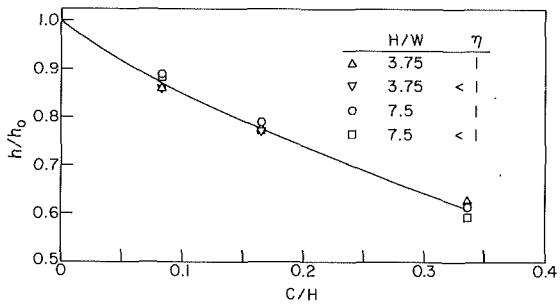

Fig. 5 Correlation of the with-clearance/no-clearance heat-transfer-coefficient ratio with the size of the clearance

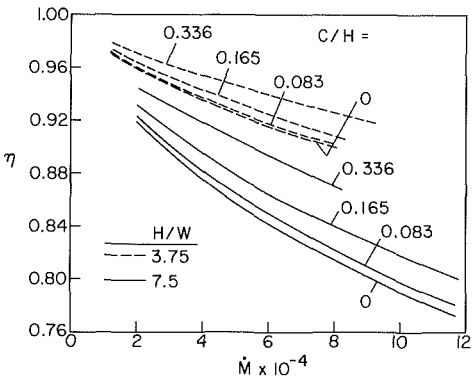

Fig. 6 Fin efficiencies for the operating conditions of the experiments evaluated from equations (7) and (8)

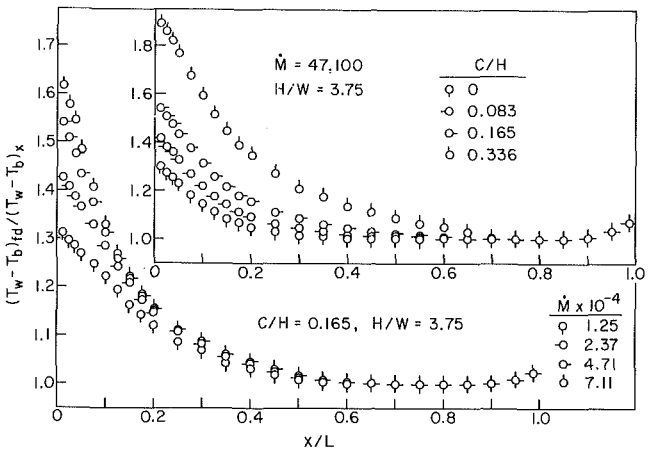

Fig. 7 Representative entrance region results

percent clearance-related decrease in the heat transfer coefficient.

Of considerable practical interest in Fig. 5 is the fact that the data for all four cases tend to fall together in a tight band, so that a single curve representing h/h_0 versus C/H is appropriate. This curve is independent of W/H, of the fin efficiency model, and of the air flowrate $\dot{M}$ in the investigated ranges. While it cannot be asserted that the h/h_0 versus C/H curve of Fig. 5 is totally universal, it does possess considerable generality and should be useful as a design tool. From this standpoint, Fig. 5 conveys the main results of the paper.

In connection with the generality of Fig. 5, it is relevant to point out that the data plotted there encompass fin efficiencies which cover a substantial range – extending from 0.78 to 1. In this regard, the fin efficiencies which emerge from the use of equations (7) and (8) in the data reduction are presented in Fig. 6. In the figure, η is plotted as a function of the dimensionless air flowrate $\dot{M}$ for parametric values of the clearance and for the two investigated fin heights.

Not unexpectedly, the efficiencies were substantially lower for the taller fins. In particular, the η values for the $H/W = 3.75$ fins generally exceeded 0.9, while values as low as 0.78 occurred for the $H/W = 7.5$ fins. It is also seen that the efficiency increased monotonically as the clearance increased at a fixed flowrate. This trend reflects the clearance-related decrease of the heat transfer coefficient that was set forth in Fig. 5. The monotonic decrease of η with $\dot{M}$ in evidence in the figure is due to the flowrate-related increase of the heat transfer coefficient.

Heretofore, the presentation of results has been focused on the fully developed regime. Now, attention will be turned to the thermal entrance region, the results for which will be conveyed via the temperature ratio

$$(T_w - T_b)_{fd}/(T_w - T_b)_x \qquad (15)$$

The denominator is the wall-to-bulk temperature difference at any axial station x, while the numerator is the axially unchanging wall-to-bulk temperature difference in the fully developed regime. At any station where the net axial conduction in the baseplate is zero or negligible, as in the fully developed region, the temperature-difference ratio of equation (15) is equal to the ratio of the local to the fully developed heat transfer coefficient.

Representative axial distributions of the temperature-difference ratio are plotted in Fig. 7 as a function of the dimensionless axial coordinate x/L (L = test section length). The results are presented from different perspectives in the two graphs which make up the figure. In the upper graph, the response of the results to parametric variations of the clearance is highlighted, while the lower graph displays the response to variations in the air flowrate.

The axial distributions of Fig. 7 all display a common shape which is identical to that for the distribution of the local heat transfer coefficient in a developing duct flow. Starting with a maximum value at the inlet, the distributions drop off with increasing downstream distance, rapidly at first and then more gradually. At a sufficient distance from the inlet, the distribution levels off, signaling the attainment of the thermally developed regime. Just upstream of the exit, the slight liftoff of the data reflects an end effect.

From the upper graph of Fig. 7, it is seen that the rate of thermal development is quite sensitive to the size of the tip-to-shroud clearance – the larger the clearance, the slower is the thermal development. Thus, for example, for an entrance length defined by $(T_w - T_b)_{fd}/(T_w - T_b)_x = 1.05$, the $(x/L)_{ent}$ values for $C/L = 0$ and 0.336 are 0.2 and 0.6, respectively. The relative enhancement of the heat transfer coefficient due to entrance effects (as indicated by larger values of the temperature-difference ratio) is seen to increase as the clearance increases. This is due, at least in part, to the lower fully developed heat transfer coefficients associated with larger clearances.

The lower graph of Fig. 7 shows that the entrance-region-related enhancement is greatest at lower flowrates, which is a well-established characteristic for conventional duct flows. The 5-percent entrance lengths are, however, a weak function of the flowrate, which is also in accord with available duct flow information.

Concluding Remarks

The work reported here is, seemingly, the first systematic experimental investigation of the response of the heat transfer from a longitudinal fin array to the presence of clearance between the fin tips and an adjacent shroud. The experiments were parameterized by the clearance, the fin height, and the rate of fluid flow passing through the array, all in dimen-

sionless terms. Air was the working fluid, and the flow was turbulent.

The fully developed heat transfer coefficients corresponding to the presence and to the absence of clearance were compared under the condition of equal air flowrate. These comparisons showed that clearance gave rise to significant reductions in the heat transfer coefficient. For example, for clearances equal to 10, 20, and 30 percent of the fin height, the heat transfer coefficients were 85, 74, and 64 percent of those for the no-clearance case.

The ratio of the with-clearance and no-clearance heat transfer coefficients was found to be a function only of the clearance-to-fin-height ratio, independent of the flowrate, the fin height, and the fin efficiency model used to evaluate the heat transfer coefficients. The resulting correlation is presented in Fig. 5. While it cannot be asserted that this correlation is totally universal, it does possess considerable generality and should be useful as a design tool.

The fully developed heat transfer results were supplemented by entrance region information, which showed that the presence of clearance slowed the rate of thermal development.

References

1 Sparrow, E. M., Baliga, B. R., and Patankar, S. V., "Forced Convection Heat Transfer From a Shrouded Fin Array With and Without Tip Clearance," ASME JOURNAL OF HEAT TRANSFER, Vol. 100, 1978, pp. 572–579.

2 Acharya, S., and Patankar, S. V., "Laminar Mixed Convection in a Shrouded Fin Array," ASME JOURNAL OF HEAT TRANSFER, Vol. 103, 1981, pp. 559–565.

3 Kadle, D. S., "Effect of Tip Clearance on Turbulent Heat Transfer for a Shrouded, Longitudinal Fin Array," Ph.D. thesis, Department of Mechanical Engineering, University of Minnesota, Minneapolis, MN, 1984.

4 Kadle, D. S., and Sparrow, E. M., "Numerical and Experimental Study of Turbulent Heat Transfer and Fluid Flow in Longitudinal Fin Arrays," ASME JOURNAL OF HEAT TRANSFER, Vol. 108, 1986, pp. 16–23.

T. Ota[1]
Professor.

H. Nishiyama[2]
Research Assistant.

J. Kominami
Graduate Student.

K. Sato
Graduate Student.

Department of Mechanical and Production Engineering, Akita University, Akita 010, Japan

Heat Transfer From Two Elliptic Cylinders in Tandem Arrangement

An experimental investigation has been conducted to clarify heat transfer characteristics of two elliptic cylinders having an axis ratio 1:2. They were placed in tandem arrangements and their angles of attack to the upstream uniform flow were identical. The testing fluid was air and the Reynolds number based on the major axis length c *ranged from about 15,000 to 80,000. The angle of attack was varied from 0 to 90 deg at 30 deg intervals and the nondimensional cylinder spacing* l/c *from 1.25 to 4.0, where* l *denotes the streamwise distance between the cylinder centers. It has been found that the heat transfer features vary drastically with the angle of attack and also with the cylinder spacing.*

Introduction

Explorations of high-performance heat exchangers for saving and making effective use of energy is a very important and urgent problem. Among many types of heat exchangers, those constructed of circular pipes have been used in many industries. Flow around pipes, however, is not necessarily normal to the pipe axis. In such a situation, the cross section of a pipe in the flow direction becomes an ellipse. An elliptic cylinder is a basic and general form, which becomes a flat plate and also a circular cylinder depending on its axis ratio. There have been many works on the flow around elliptic cylinders and it is well known that the flow characteristics change considerably with the axis ratio and the angle of attack. Furthermore it is found that their drag coefficient at small angles of attack is lower than that of a circular cylinder. This may be an advantageous feature when using elliptic tubes as a heat transfer surface element, since the pumping power needed for fluids to flow around them may become very small.

As far as forced-convection heat transfer characteristics of the elliptic cylinder are concerned, there have been only a few investigations. Boundary layer analyses were made by Eckert [1] and Chao et al. [2]. Their results, naturally, may be applicable only to the upstream surface of the elliptic cylinder on which a laminar boundary layer develops. Seban et al. [3] and Drake et al. [4] measured the local heat transfer coefficients on elliptic cylinders of axis ratio 1:4 and 1:3, respectively. Their main purpose, however, seemed to consist of confirming the applicability of boundary layer theory. The angle of attack examined by them was limited to 0, 5, and 6 deg, and the mean heat transfer coefficient was not measured. Reiher [5] reported the mean heat transfer coefficient for an elliptic cylinder at 0 and 90 deg, but its configuration was obscure. On the other hand, it is reasonable to consider that the heat transfer features of the elliptic cylinder vary remarkably with the angle of attack, since the flow behaviors change greatly, as previously noted.

From this standpoint, the present authors have conducted experimental studies of forced convection heat transfer from elliptic cylinders of axis ratio 1:2 and 1:3 [6–8]. The local heat transfer features are clarified and it is found that they are quite different from those of the circular cylinder. The mean heat transfer coefficient depends upon the axis ratio, the angle of attack, and the Reynolds number, and it is comparable to or higher than that of the circular cylinder over the Reynolds number range studied. In order to employ elliptic tubes as a heat transfer surface element of heat exchangers, it is basically important to examine the heat transfer characteristics of elliptic tube banks. However there has been little information on them.

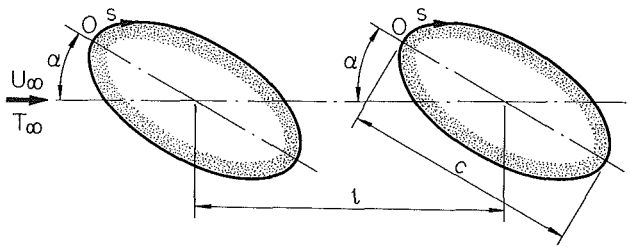

Fig. 1 Arrangement of two elliptic cylinders and coordinate system

The purpose of the present study was to investigate the local and overall heat transfer characteristics from two elliptic cylinders in tandem arrangement in a uniform flow of air. The elliptic cylinders examined have an axis ratio 1:2. Although an infinite number of arrangements could be considered, in the present study they are arranged in a following way. That is, a line through the centers of two elliptic cylinders is in line with the direction of the upstream uniform flow and their inclination angles between the major axes and the uniform flow direction (called "angle of attack" hereafter) are the same. The arrangement of two elliptic cylinders is represented in Fig. 1.

Experimental Apparatus and Technique

Experiments were conducted in a wind tunnel, which was the same as that in our previous work [6]. The working section at the tunnel exit is 150 mm wide, 400 mm high, and 800 mm long. One of the side walls of the test section was changed in order to be able to set two elliptic cylinders and to change their spacing. The free-stream velocity U_∞ was varied from about 4 m/s to 25 m/s and the corresponding Reynolds number Re based on the major axis length c of the elliptic cylinder was about 15,000 to 80,000. The highest velocity was limited by the power of the motor and the lowest one by the accuracy of the manometer. However, the lowest velocity was sufficiently high to be able to neglect effects of natural convection. The free-stream turbulence intensity was measured to be about 0.3 percent in the Reynolds number range described above.

The two elliptic cylinders examined have an axis ratio of 1:2, the major axis being 50 mm and the spanwise length 150 mm. They were made of fiber-reinforced plastics by the same procedure as in our previous report [6].

[1] Present address: Professor, Department of Mechanical Engineering, Faculty of Engineering, Tohoku University, Sendai 980, Japan.

[2] Presently, Lecturer.

Contributed by the Heat Transfer Division for publication in the JOURNAL OF HEAT TRANSFER. Manuscript received by the Heat Transfer Division January 29, 1985.

Experimental procedures were almost the same as in [6]; therefore, only the main points will be described. Heating of the cylinder surface was accomplished by means of an electric current passed through a stainless steel sheet wound helically around it; this provided the condition of constant heat flux. The heat flow rate was determined from the measured electric current and voltage to the stainless steel sheet and the heat loss by conduction and radiation was neglected in the following results. The wall temperature was measured with 49 copper-constantan thermocouples embedded on the cylinder surface of the central section. Thus the local heat transfer coefficient and the corresponding local Nusselt number were calculated for $h = q/(T_w - T_\infty)$ and $\mathrm{Nu} = hc/\lambda$, respectively. The mean Nusselt number was determined from graphic integration of the local Nusselt number distribution.

The uncertainty in the present data depends upon several factors: manufacturing accuracy of the elliptic cylinders, accuracy of the arrangement of the elliptic cylinders, local deviation of the condition of constant heat flux, heat loss, and reading error of thermoelectric voltage. The wall temperature varies along the cylinder surface. Therefore the electric resistance of the stainless steel sheet changes locally resulting in a variation of the local heat flow rate. In the present study, the temperature difference along the cylinder surface was at most 20 K and the deviation for the constant heat flux was estimated to be at most 10 percent. On the other hand, the temperature gradient along the cylinder surface produces the heat flow there, which diminishes the temperature difference. The heat conduction loss was estimated to be less than 10 percent. The position of zero angle of attack was carefully determined by comparing the local Nusselt numbers on two sides of the cylinder. Furthermore, comparisons of the results for each single cylinder confirmed a reasonable accuracy of two elliptic cylinders. Based on these considerations, uncertainty of the local Nusselt number was estimated to be less than ± 5 percent and that of the mean Nusselt number to be about ± 3 percent.

Although it was possible to heat two elliptic cylinders at the same time, only the measuring cylinder was heated in the experiments, since thermal interactions between two cylinders may lead to a difficulty in estimating the temperature of the oncoming flow, especially for the downstream cylinder. The cylinder spacing l, defined as the distance between two centers of the cylinders, was varied from 1.25 to 4 times the major axis length and the angle of attack α, described as (α, α) in the following figures, was changed from 0 to 90 deg at 30 deg intervals. The tunnel blockage ratio varies from 0.0625 at $\alpha = 0$ deg to 0.125 at $\alpha = 90$ deg and the aspect ratio of the present elliptic cylinders is 3. The present data, however, are uncorrected for the tunnel wall effects.

A flow visualization study was made with a water channel using floating aluminum powders [9] in order to determine flow features around the two elliptic cylinders. The Reynolds number examined was about 5000. This was much lower than those in the heat transfer study; however, it may be thought to be useful for understanding mutual correlations between the heat transfer and flow characteristics. The angle of attack ranged from 0 to 90 deg and the nondimensional cylinder spacing l/c from 1.3 to 4.0. Photographs presented later were taken at a shutter speed of 1/8 s.

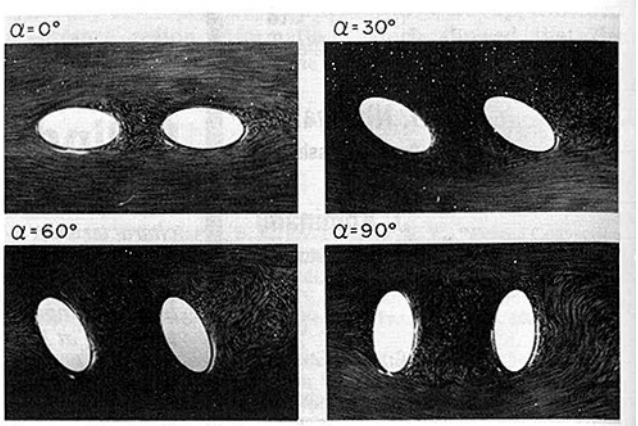

Fig. 2 Flow features for $l/c = 1.5$ and Re = 5000

Experimental Results and Discussion

Representative examples of the flow visualization photographs are shown for $l/c = 1.5$ and Re $\cong$ 5000 in Fig. 2. At $\alpha = 0$ deg, a laminar boundary layer developing on the upstream cylinder (called UC hereafter) separates near the point of minor axis. Then a separated shear layer attaches to the downstream cylinder (called DC hereafter), a boundary layer develops and separates closer to the trailing edge than on the UC. A vortex street is then formed in the wake of the DC. The flow between two cylinders is relatively stagnant and a pair of vortices is formed.

At $\alpha = 30$ deg, the flow on the UC separates near the leading and trailing edges and two separated shear layers attach to the DC near the leading edge and a point close to the minor axis. Two large vortices are formed between the UC and the DC. As α increases further, the separation point on the suction side of the UC is fixed near the major axis, although that on the pressure side moves downstream. Consequently the wake increases its width between the two cylinders. It brings about a violent motion of fluid therein as shown clearly in the photographs for $\alpha = 60$ and 90 deg. Two shear layers separated from the UC seem to roll up behind the DC and form a vortex street there. These flow features change naturally with the cylinder spacing [10]. However, the results for other spacings are omitted from this paper due to space limitations. The local and overall heat transfer characteristics of two elliptic cylinders are remarkably affected by the flow variations described above.

Typical examples of the local Nusselt number distribution for various arrangements of the two cylinders are shown in Figs. 3–6. It is noted here that the general characteristic features of the local Nusselt number distribution show no essential dependence upon the Reynolds number in the present experimental range, although some exceptions are found. In accordance with this fact, the results are presented only for

Nomenclature

c = length of major axis of elliptic cylinder
h = heat transfer coefficient $= q/(T_w - T_\infty)$
l = streamwise distance between two cylinder centers
Nu = local Nusselt number $= hc/\lambda$
Nu_m = mean Nusselt number
Nu_{ma} = arithmetic mean Nusselt number of two cylinders
q = heat flux per unit area and unit time
Re = Reynolds number $= U_\infty c/\nu$
s = surface distance from leading edge, taken as positive along upper side
T_w = wall temperature
T_∞, U_∞ = temperature and velocity of upstream uniform flow
α = angle of attack
λ, ν = thermal conductivity and kinematic viscosity of fluid at T_∞

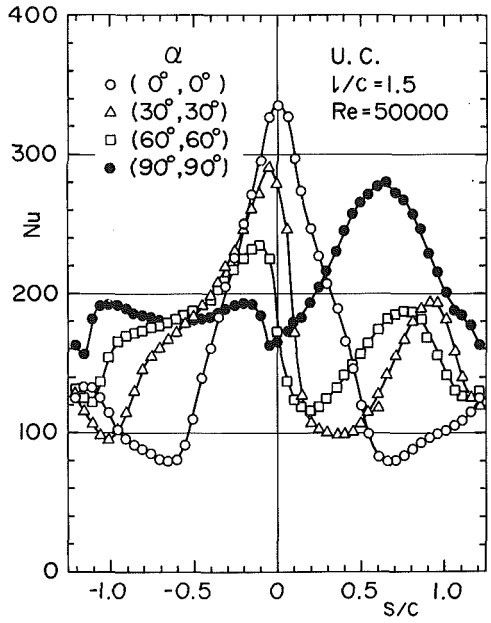

Fig. 3 Effect of α on local Nusselt number distribution for UC

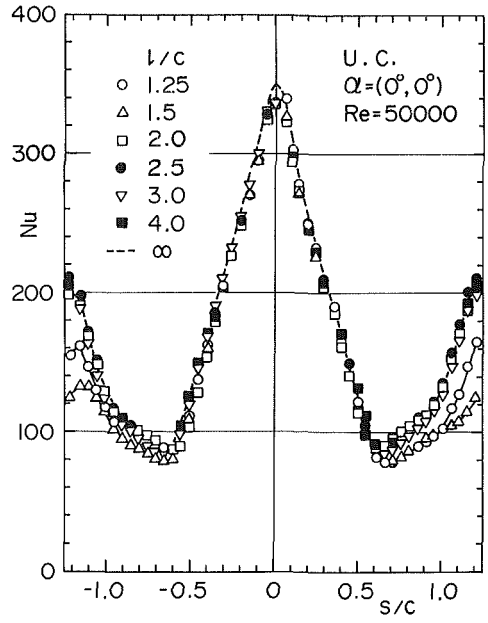

Fig. 5 Effect of *l/c* on local Nusselt number distribution for UC

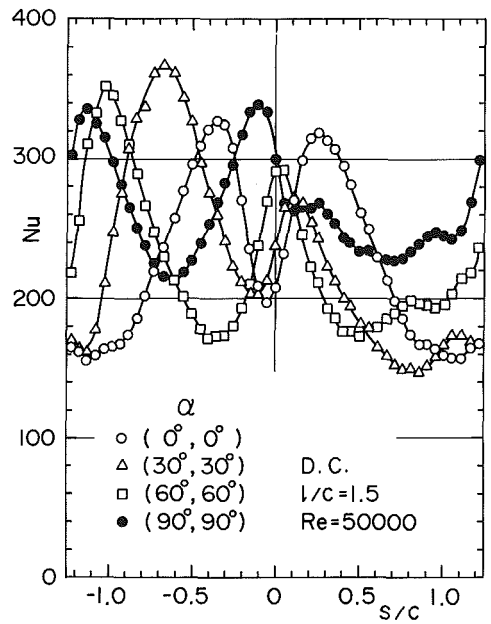

Fig. 4 Effect of α on local Nusselt number distribution for DC

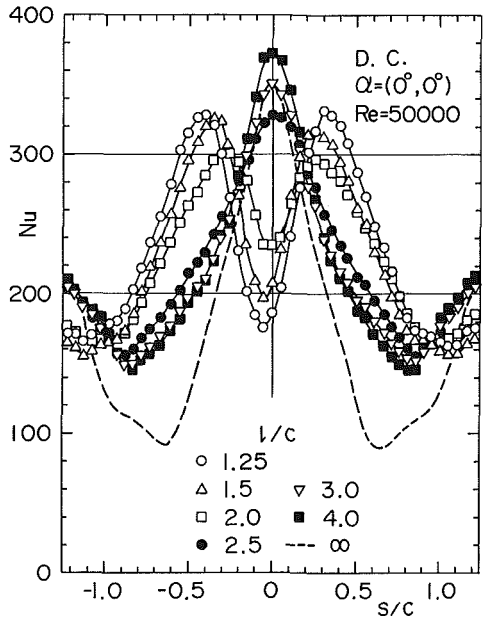

Fig. 6 Effect of *l/c* on local Nusselt number distribution for DC

typical Reynolds numbers in the following. The surface distance s from the leading edge of the cylinder is taken as positive along the upper side of the cylinder, as shown in Fig. 1.

Figures 3 and 4 show effects of the angle of attack upon the local Nusselt number distribution at $l/c = 1.5$ for the UC and the DC, respectively. The results for the UC are very similar to those for the single cylinder [6], although Nu in the wake region between two cylinders is affected by the existence of the DC. It may be interesting to note that the local maximum value of Nu is located near the major axis point independently of α. This suggests that it is not easy to estimate the flow field around the cylinder from only the local heat transfer distribution. The maximum of Nu near the major axis may be caused by the rapid acceleration of the flow there. Nu reaches a local minimum near the separation point on the pressure side, which moves downstream with an increase of α. Nu in the separated flow region generally increases with an increase of α because of the violent motion of fluid there.

As far as the DC is concerned, the local heat transfer distribution exhibits large variations with α, since the attachment point of the shear layer separated from the UC moves greatly on the surface of the DC with α. At $\alpha = 0$ deg, two separated shear layers attach to the DC at about $s/c = \pm 0.3$, respectively, where Nu attains maxima. In the separated flow region near the leading edge, Nu is low and becomes a local minimum at the leading edge. Downsteam of the attachment point, Nu decreases steeply as a boundary layer develops. A minimum is reached around $s/c = \pm 1.1$, where the flow may separate from the DC.

At $\alpha = 30$ deg, the attachment point on the pressure side shifts to about $s/c = -0.7$, where a maximum of Nu is obtained. Downstream of the attachment point, a boundary layer may develop, but it separates immediately near the trail-

Table 1 Values of A and n in equation (1)

		U.C.		D.C.	
l/c	$\alpha°$	A	n	A	n
1.25	0	0.152	0.676	0.581	0.521
	30	0.455	0.545	0.179	0.650
	60	0.332	0.577	0.169	0.667
	90	0.289	0.605	0.157	0.689
1.5	0	0.262	0.589	0.383	0.590
	30	0.288	0.585	0.176	0.663
	60	0.429	0.552	0.124	0.696
	90	0.245	0.622	0.174	0.678
2.0	0	0.450	0.547	0.217	0.644
	30	0.284	0.583	0.208	0.646
	60	0.308	0.589	0.260	0.631
	90	0.388	0.577	0.260	0.636
2.5	0	0.289	0.588	0.201	0.647
	30	0.340	0.564	0.183	0.657
	60	0.560	0.521	0.180	0.662
	90	0.305	0.590	0.157	0.678
3.0	0	0.357	0.568	0.474	0.565
	30	0.465	0.546	0.276	0.619
	60	0.512	0.549	0.225	0.637
	90	0.604	0.526	0.400	0.591
4.0	0	0.193	0.625	0.302	0.607
	30	0.396	0.559	0.169	0.664
	60	0.184	0.652	0.196	0.648
	90	0.272	0.616	0.335	0.602

ing edge. In accordance with such a flow feature, Nu decreases steeply therein. On the other hand, a local maximum of Nu located at about $s/c = 0.1$ is much lower than that found at $s/c = -0.7$. It may originate from an attachment of the inner part of the separated shear layer flowing at relatively low speed. It seems that downstream of that attachment point, a wake is immediately formed, as expected from the flow visualization photograph in Fig. 2. Therefore Nu decreases toward the center of the separated flow region. A minimum of Nu at about $s/c = 0.8$ may coincide with a downstream stagnation point in the separated flow region and a small hump found around $s/c = 1.1$ may be due to an attachment of a shear layer separated near the trailing edge as forming a small separation bubble. The results at $\alpha = 60$ deg show a generally similar trend to that at $\alpha = 30$ deg, though two attachment points of the shear layers separated from the UC are different from those at $\alpha = 30$ deg.

At $\alpha = 90$ deg, the inner parts of two separated shear layers seem to attach to the DC at about $s/c = -0.1$ and -1.1 where Nu reaches a maximum, but their greater parts roll up behind the DC forming a vortex street. The flow near the upstream surface bounded by two separated shear layers is very stagnant and Nu attains a minimum at the upstream stagnation point. On the downstream surface, a variation of Nu with the surface distance is relatively small and Nu becomes a local minimum at the downstream stagnation

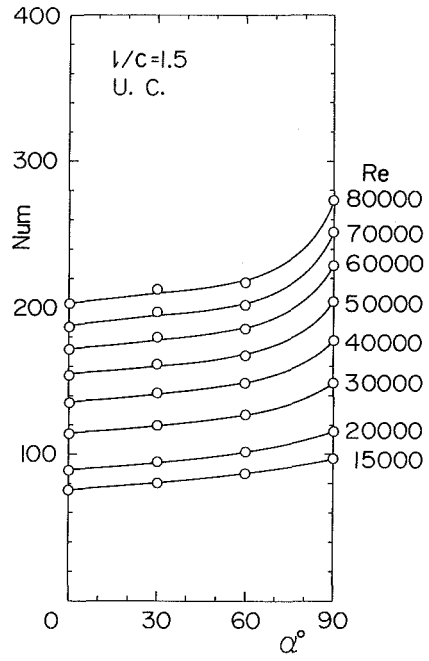

Fig. 7 Variation of Nu_m with α for UC

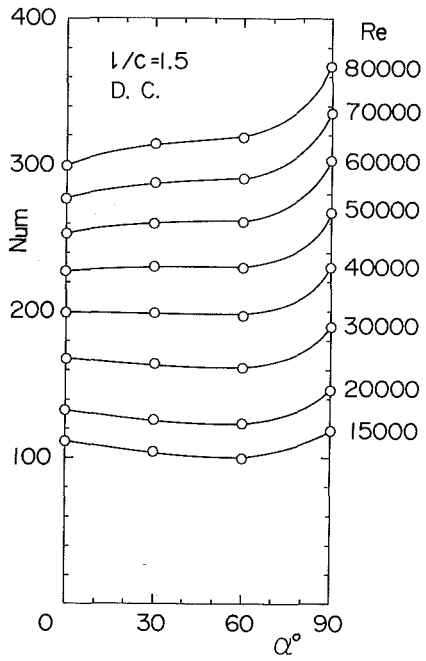

Fig. 8 Variation of Nu_m with α for DC

point. Such local heat transfer features of the DC are quite different from those of the UC exhibited in Fig. 3. The characteristic behavior of the local heat transfer coefficient corresponds well with the flow features presented in Fig. 2.

Figures 5 and 6 show the influences of the cylinder spacing upon the local heat transfer distribution. Only the results at $\alpha = 0$ deg are shown as a typical case. Figure 5 represents the results for the UC. It is very clear that Nu on the upstream surface, where a laminar boundary layer develops, exhibits no dependence upon the cylinder spacing and is almost equal to that for the single cylinder [6]. That is, Nu attains a maximum at the leading edge, decreases steeply with development of the laminar boundary layer, and subsequently reaches a minimum near the separation point. At $\alpha = 0$ deg and Re = 50,000, it seems that the location of the flow separation represents no

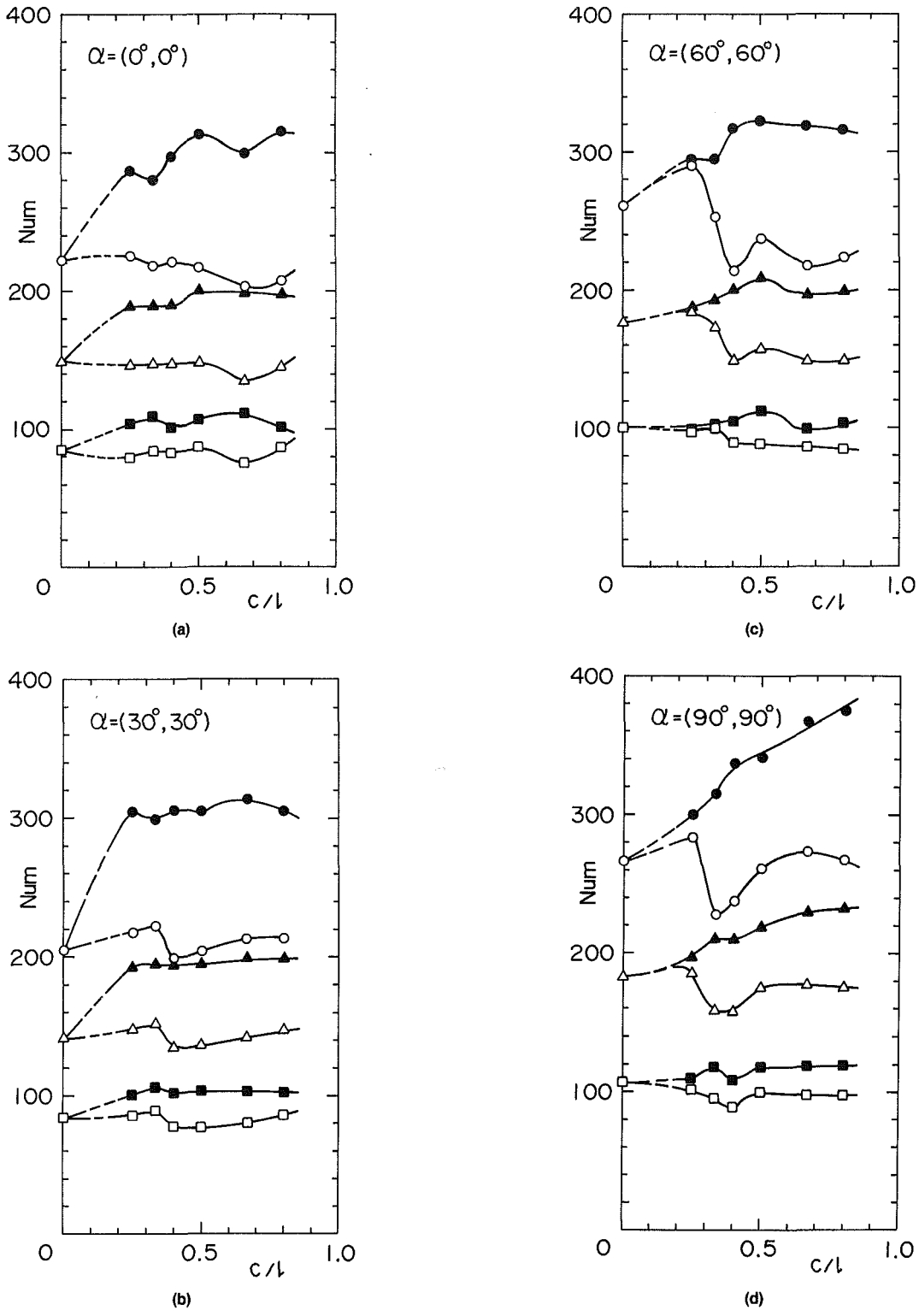

Fig. 9 Variation of Nu_m with l/c. Re: □, 15,000; △, 40,000; ○, 80,000. Open symbols: UC; closed symbols: DC.

essential dependence upon the cylinder spacing. On the other hand, Nu in the separated flow region is strongly affected by the cylinder spacing. As l/c increases from 1.25 to 1.5, Nu decreases. However when it increases from 1.5 to 2.0, Nu increases rather discontinuously and a further increase of l/c does not bring about an essential change of Nu distribution. This sudden variation may be caused by the so-called jumping phenomenon well known for two in-line circular cylinders [11]. That is, if the spacing between two cylinders is large enough, a vortex street is formed behind the upstream cylinder. Such a vortex street may stimulate the fluid motion in the wake, producing a higher heat transfer rate therein as detected in Fig. 5.

Shown in Fig. 6 are the results for the DC. Local heat transfer coefficient varies remarkably on the whole of the cylinder surface with the cylinder spacing. At a narrow spacing such as $l/c = 1.25$ and 1.5, two shear layers separate from the UC and attach to the DC. Nu attains a maximum at the at-

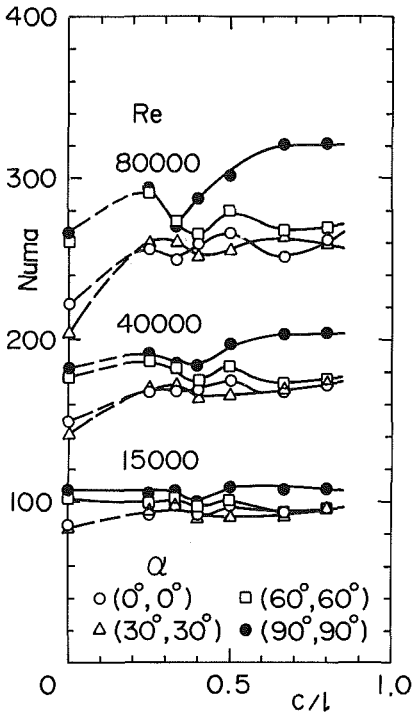

Fig. 10 Variation of Nu_{ma} with l/c

tachment point. The flow inside a wake region bounded by two cylinders and two separated shear layers is stagnant and then Nu is low. Downstream of the attachment point, Nu decreases with the surface distance because of a developing boundary layer, as inferred from the flow pattern in Fig. 2. Nu reaches a minimum near the separation point and then increases slightly in the separated flow region.

The profile of Nu at $l/c = 2.0$ is very similar to that at $l/c = 1.25$ and 1.5. However, an increase of l/c from 2.0 to 2.5 brings about a great variation of the heat transfer distribution, especially on the upstream surface. That is, Nu attains a maximum at the leading edge, decreases with the surface distance, and reaches a minimum. Subsequently Nu increases in the wake region. Such a drastic variation of Nu may be due to an occurrence of the jumping phenomenon for the wake from the UC as described previously. The separated shear layers from the UC roll up upstream of the DC and the main flow at free-stream temperature is entrained onto the upstream surface of the DC. This results in a higher heat transfer rate there. It is very interesting that the sudden variation of the local heat transfer rate occurs between $l/c = 1.5$ and 2.0 and for the UC and between 2.0 and 2.5 for the DC, respectively. It is not clear presently why such a difference of the streamwise distance for the sudden variation of Nu distribution occurs for the UC and the DC. At greater spacings than $l/c = 2.5$, the local heat transfer distribution becomes similar to that for the UC or the single cylinder, though Nu is generally higher on the DC than on the UC because of the highly turbulent flow.

Exemplified in Figs. 7 through 9 are characteristic variations of the mean Nusselt number Nu_m. Figures 7 and 8 represent a variation of Nu_m with α at $l/c = 1.5$. Nu_m for the UC, in general, increases monotonically with an increase of α at all the Reynolds numbers examined. Its rate of increase is quite large between $\alpha = 60$ and 90 deg. On the other hand, Nu_m for the DC shows a slightly different trend. This is, at Reynolds numbers higher than about 40,000, Nu_m increases monotonically as α increases. However at Reynolds numbers lower than about 30,000, Nu_m decreases slightly with an increase in α, becomes minimum around $\alpha = 60$ deg, and subsequently increases between $\alpha = 60$ and 90 deg. These characteristics of Nu_m, however, depend upon the cylinder spacing. The results for other spacings are omitted in this paper.

In general, Nu_m can be expressed as a function of Re as follows

$$Nu_m = A\mathrm{Re}^n \tag{1}$$

A and n in equation (1) depend upon both α and l/c. Summarized in Table 1 are their values, which were determined with the method of least squares. They are naturally valid only in the Reynolds number range examined in the present experiments, say $15{,}000 \leqq \mathrm{Re} \leqq 80{,}000$.

Typical examples of a variation of Nu_m with l/c are shown for $\alpha = 0$, 30, 60, and 90 deg in Fig. 9. In these figures, Nu_m for the UC is compared with that for the DC at Re = 15,000, 40,000, and 80,000. In general, Nu_m for the DC is much higher than that for the UC and its variation with l/c is quite different between them depending on α. Furthermore Nu_m for the UC shows a sudden change at the critical cylinder spacing. At the larger cylinder spacing beyond the critical one, Nu_m for the UC is comparable to or a little higher than that for the single cylinder. It seems that the critical cylinder spacing increases with increasing α. In general, Nu_m for the UC attains a minimum at a cylinder spacing just before the critical one.

On the other hand, Nu_m for the DC, in general, does not show a great change at the critical cylinder spacing, although the local heat transfer distribution exhibits a sudden variation, as previously described. Even at a large cylinder spacing such as $l/c = 4.0$, Nu_m for the DC is still much higher than that for the single cylinder, though some exceptions can be detected at low Reynolds numbers.

In order to use the elliptic tubes in heat exchangers, it is very important to estimate the overall heat transfer rate of the elliptic tube bank. As a preliminary examination, an arithmetic mean Nusselt number Nu_{ma} of Nu_m for the UC and the DC is evaluated in the present study. Figure 10 shows a variation of Nu_{ma} with l/c for $\alpha = 0$, 30, 60, and 90 deg at Re = 15000, 40,000 and 80,000. At a relatively low Reynolds number such as Re = 15,000, Nu_{ma} shows no essential change with l/c. Its value is nearly equal to that for the single cylinder at $\alpha = 60$ and 90 deg but is a little higher than that for $l/c = \infty$ at $\alpha = 0$ and 30 deg. At higher Reynolds numbers, Nu_{ma} varies greatly with l/c and its dependence upon α becomes severe. It may not be unreasonable to say from these results that the cylinder spacing is to be as small as possible for the higher heat transfer capability and for the compactness of the heat exchangers, although some exceptions can be detected.

Concluding Remarks

Local and overall heat transfer characteristics of two elliptic cylinders having an axis ratio 1:2 in tandem arrangements were determined experimentally in the present investigation. The main points obtained are summarized as follows.

The local heat transfer coefficient depends strongly upon the angle of attack and the cylinder spacing both for the UC and the DC, although Nu on the upstream surface of the UC exhibits no essential change with the cylinder spacing. There exists a critical cylinder spacing, at which the local heat transfer coefficient varies suddenly both for the UC and the DC and its variation is much greater for the DC than for the UC. The critical cylinder spacing seems to increase with an increase in the angle of attack.

The mean heat transfer coefficients were estimated as functions on the angle of attack, the cylinder spacing, and the Reynolds number. It was found that the mean Nusselt number shows great dependence upon these parameters. At the critical cylinder spacing, Nu_m suddenly changes for the UC but not for the DC. Furthermore, an arithmetic mean Nusselt number Nu_m for the UC and the DC was evaluated. Its variation was found to be a complicated function of the geometric and flow parameters.

Acknowledgments

The present authors express their sincere thanks to Mr. Nobuhiko Kon for his skillful support in the experiments.

References

1 Eckert, E., "Die Berechnung des Wärmeübertragangs in der laminaren Grenzschift umströmter Körper," *VDI Forschungsheft*, Vol. 13, 1942, pp. 1-44.

2 Chao, B. T., and Fagbenle, R. O., "On Merk's Method of Calculating Boundary Layer Transfer," *Int. J. Heat Mass Transfer*, Vol. 17, 1974, pp. 223-240.

3 Seban, R. A., and Drake, R. M., "Local Heat-Transfer Coefficients on the Surface of an Elliptic Cylinder in a High-Speed Air Flow," *Trans. ASME*, Vol. 75, 1953, pp. 235-240.

4 Drake, R. M., Jr., Seban, R. M., Doughty, D. L., and Levy, S., "Local Heat-Transfer Coefficients on Surface of an Elliptic Cylinder, Axis Ratio 1:3, in a High-Speed Air Flow," *Trans. ASME*, Vol. 75, 1953, pp. 1291-1302.

5 Reiher, H., *Handbuch der Experimentalphysik*, Vol. 9, Pt. 1, 1925, pp. 312.

6 Ota, T., Aiba, S., Tsuruta, T., and Kaga, M., "Forced Convection Heat Transfer From an Elliptic Cylinder of Axis Ratio 1:2," *Bull. JSME*, Vol. 26, 1983, pp. 262-267.

7 Ota, T., Nishiyama, H., and Taoka, Y., "Heat Transfer and Flow Around an Elliptic Cylinder," *Int. J. Heat Mass Transfer*, Vol. 27, 1984, pp. 1771-1779.

8 Ota, T., and Nishiyama, H., "Fouling Effects of Geothermal Water Scale Upon Heat Transfer Around an Elliptic Cylinder," *Wärme- und Stoffübertragung*, Vol. 19, 1985, pp. 93-100.

9 Ota, T., Asano, Y., and Okawa, J., "Reattachment Length and Transition of the Separated Flow Over Blunt Flat Plates," *Bull. JSME*, Vol. 24, 1981, pp. 941-947.

10 Ota, T., and Nishiyama, H., "Visualization Study on Flow Around Two Elliptic Cylinders in Tandem" (in Japanese), *Sci. Tech. Rep. of Mining College*, Akita Univ., Vol. 5, 1984, pp. 131-138.

11 Zdravkovich, M. M., "Review of Flow Interference Between Two Circular Cylinders in Various Arrangements," ASME *Journal of Fluids Engineering*, Vol. 99, 1977, pp. 618-633.

D. R. Jeng
Professor,
Department of Mechanical Engineering.
Mem. ASME

T. C. A. Chang
Graduate Assistant,
Department of Chemical Engineering.

K. J. De Witt
Professor,
Department of Chemical Engineering.

College of Engineering,
The University of Toledo,
Toledo, OH 43606

Momentum and Heat Transfer on a Continuous Moving Surface

An analysis has been carried out to determine the momentum and heat transfer occurring in the laminar boundary layer on a continuous moving surface which has an arbitrary surface velocity and nonuniform surface temperature. Merk series types of solutions are obtained for the momentum and heat transfer for an isothermal surface. The results are expressed in terms of universal functions. For a nonisothermal surface, the procedure begins with a consideration of the solution of the energy equation for a step discontinuity in the surface temperature by the introduction of appropriate transformation variables. Equations for the temperature profile and for the local heat flux are expressed explicitly in terms of the Prandtl number and the surface velocity parameter. Numerical examples for a power law surface velocity and a linearly stretching surface velocity with nonzero slot velocity are given for the isothermal surface. The accuracy of the present solutions is also discussed.

1 Introduction

Polymer sheets and filaments are manufactured by continuous extrusion of the polymer from a die to a windup roller which is located a finite distance away. The thin polymer sheet or filament constitutes a continuously moving solid surface with a nonuniform surface velocity and temperature through an otherwise quiescent fluid. This situation represents a different class of boundary layer problem which has a solution substantially different from that of boundary layer flow over a semi-infinite flat plate.

Sakiadis [1–3] was the first to recognize this new class of problem and, in a series of papers, presented analyses for the momentum transfer occurring in laminar and turbulent flow for two-dimensional and axisymmetric geometries for a constant surface velocity (rigid surface). For laminar flow, an exact solution was obtained numerically and an approximate solution arrived at by employing an integral method. For the turbulent flow case, an integral method using a one-seventh power velocity profile was employed in the analysis. Tsou et al. [4] later extended Sakiadis' work to include heat transfer, and verified the analytial results by experimental measurement. In their work, both the surface velocity and the temperature or heat flux were assumed to be constant.

More recently, Vleggaar [5] measured the surface velocity and temperature of a polyester monofilament being ejected from a die. Since polyester is a flexible material, the filament surface may stretch during the course of ejection and therefore the surface velocity deviates from being uniform. These nonuniformities in both surface velocity and temperature were measured by Vleggaar and are shown in Fig. 1 of [5]. In [5], Vleggaar analyzed the laminar boundary layer behavior on continuously accelerating surfaces for both two-dimensional and axisymmetric cases. A linear variation of surface velocity with respect to yarn path distance, i.e., $U_s = cx$, was employed, but the surface temperature was treated as isothermal.

Gupta and Gupta [6] extended Vleggaar's work to include suction and blowing over a stretching surface. To relax the assumption of an isothermal surface, Soundalegekar and Ramana Murty [7] used a power law surface temperature to investigate the heat transfer, but the surface velocity was treated as a constant. The heat transfer occurring on a continuous, linearly stretched surface with a power law surface temperature was recently investigated by Grubka and Bobba [8].

In view of the variable surface velocity and the nonuniform surface temperature which actually occur, it is the purpose of the present paper to develop a method to analyze the momentum and heat transfer for a continuously moving flat surface with an arbitrarily specified surface velocity and temperature. The restrictions of uniform or linearly varying surface velocity and power law surface temperature variation which were used in the previous analyses are relaxed.

For the momentum transfer analysis, the independent coordinate along the moving surface is transformed into a new coordinate by integrating the arbitrarily specified surface velocity in the same direction, such that the surface velocity is implicitly absorbed into the new variable. The momentum equation is then solved using a Merk series. Similarity is applied for obtaining the energy equation solution for the isothermal surface condition. For the nonisothermal case, the analysis begins with the consideration of a step discontinuity in surface temperature. A new series solution is proposed in terms of appropriate transformed variables with coefficients expressible in terms of universal functions. Because of the linearity of the energy equation, the solutions obtained for a step change in wall temperature may be readily applied to the situation of an arbitrarily specified surface temperature by simply using Duhamel's theorem or the superposition technique.

2 Problem Formulation and Method of Solution

The physical system under investigation is illustrated in Fig. 1. An x–y coordinate system is fixed in space, and at $x = y =$

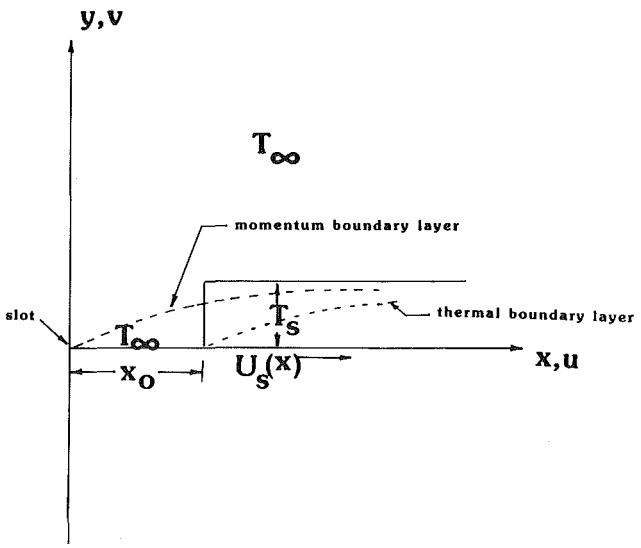

Fig. 1 Coordinate system and the description of the physical model

Contributed by the Heat Transfer Division and presented at the 23rd National Heat Transfer Conference, Denver, Colorado, August 1985. Manuscript received by the Heat Transfer Division April 11, 1985.

0 (die slot), a thin solid surface is extruded and moves in the x direction with an arbitrary surface velocity $U_s(x)$.

Assuming steady-state flow of an incompressible, Newtonian fluid at a large Reynolds number, the governing boundary layer equations are

Continuity

$$\frac{\partial u}{\partial x}+\frac{\partial v}{\partial y}=0 \tag{1}$$

Momentum

$$u\frac{\partial u}{\partial x}+v\frac{\partial u}{\partial y}=\nu\frac{\partial^2 u}{\partial y^2} \tag{2}$$

with the boundary conditions

$$\begin{aligned} &u=U_s(x),\ v=0 && \text{for } y=0\\ &u=0 && \text{for } y\to\infty \end{aligned} \tag{3}$$

where $U_s(x)$ is the velocity of the surface which can be constant or any function of x.

For the heat transfer analysis, two different cases are considered: an isothermal surface and the situation where a step change in surface temperature occurs, i.e., a portion of the surface from the slot $x = y = 0$ to an arbitrary distance x_0 is isothermal at the fluid temperature T_∞, and for $x > x_0$ the surface temperature has a step change to T_s.

The governing boundary layer energy equation for the problem is

Energy

$$u\frac{\partial T}{\partial x}+v\frac{\partial T}{\partial y}=\alpha\frac{\partial^2 T}{\partial y^2} \tag{4}$$

with

$$\begin{aligned} &T(x,0)=T_\infty+(T_s-T_\infty)1(x-x_0)\\ &T(x_0,y>0)=T_\infty\\ &T(x,\infty)=T_\infty \end{aligned} \tag{5}$$

where $1(x - x_0)$ is the Heaviside unit operator and has the values: for $(x - x_0) < 0$, $1(x - x_0) = 0$; and for $(x - x_0) > 0$, $1(x - x_0) = 1$. When $x_0 = 0$, this boundary condition reduces to that for an isothermal surface at T_s.

Since the fluid is incompressible, the momentum equation (2) and the energy equation (4) are decoupled and can be solved consecutively. The solution to the momentum equation will be considered first.

A stream function Ψ defined by

$$u=\frac{\partial\Psi}{\partial y}\qquad v=-\frac{\partial\Psi}{\partial x} \tag{6}$$

is introduced such that the continuity equation is identically satisfied. The original x, y coordinates are now transformed by

$$x\to\xi=\int_0^x U_s(x)dx \tag{7a}$$

$$y\to\eta=(2\xi\nu)^{-1/2}U_s y \tag{7b}$$

A dimensionless stream function is introduced by

$$\Psi(x,y)=(2\nu\xi)^{1/2}f(\xi,\eta) \tag{8}$$

so that, using equations (6), (7), and (8), the velocity components become

$$u=U_s\frac{\partial f}{\partial\eta} \tag{9}$$

$$v=-\frac{(2\xi\nu)^{1/2}}{2\xi}U_s\left[f+2\xi\frac{\partial f}{\partial\xi}+(\Lambda-1)\eta\frac{\partial f}{\partial\eta}\right] \tag{10}$$

where Λ is called a "surface velocity parameter" and is defined by

$$\Lambda=\frac{2\xi}{U_s}\frac{dU_s}{d\xi} \tag{11}$$

Substituting equations (9) and (10) into equation (2), the dimensionless stream function f satisfies the following transformed momentum equation

$$\frac{\partial^3 f}{\partial\eta^3}+f\frac{\partial^2 f}{\partial\eta^2}-\Lambda\left(\frac{\partial f}{\partial\eta}\right)^2=2\xi\left[\frac{\partial f}{\partial\eta}\frac{\partial^2 f}{\partial\eta\partial\xi}-\frac{\partial^2 f}{\partial\eta^2}\frac{\partial f}{\partial\xi}\right] \tag{12}$$

which is subject to the boundary conditions

$$f=0,\quad \frac{\partial f}{\partial\eta}=1 \qquad \text{for } \eta=0 \tag{13a}$$

$$\frac{\partial f}{\partial\eta}=0 \qquad \text{for } \eta\to\infty \tag{13b}$$

In general, the first boundary condition in (13a) should read $(f + 2\xi\partial f/\partial\xi) = 0$ as can be obtained from equations (3) and (10). However, for an impervious surface, we assign $f = 0$ at the surface and, therefore, $\partial f/\partial\xi$ also vanishes at the surface.

Using the above coordinate transformations, the nonhomogeneous surface velocity boundary condition in equation (3) has become homgeneous. Since ξ is only a function of x, as is Λ, there is a one-to-one correspondence between Λ and ξ. Hence one may regard Λ as a function of ξ or,

Nomenclature

$a(\xi)$ = $f''(\xi, 0)$
b = $\mathrm{Pr}^{1/2}$
$\mathrm{erfc}(x)$ = complementary error function
k = thermal conductivity
Nu_x = local Nusselt number
Pr = Prandtl number = $C_p\mu/k$
q_s = surface heat flux
Re_x = local Reynolds number
T = temperature
U_s = surface velocity
u = velocity component in x direction
v = velocity component in y direction
x = streamwise coordinate measured along surface from slot
x_0 = location in x direction where temperature step change occurs
y = coordinate normal to surface
α = thermal diffusivity
δ = momentum boundary layer thickness
δ_T = thermal boundary layer thickness
δ_1 = displacement thickness
δ_2 = momentum thickness
ζ = transformed dimensionless coordinate defined in equation (28b)
η = transformed dimensionless coordinate defined in equation (7b)
θ = dimensionless temperature defined in equation (19)
Λ = surface velocity parameter defined in equation (11)
μ = shear viscosity
ν = kinematic viscosity
ξ = transformed coordinate defined in equation (7a)
ρ = fluid density
χ = transformed dimensionless coordinate defined in equation (28a)

Subscripts

s = surface condition
∞ = condition of quiescent fluid

conversely, ξ as a function of Λ. The dependent variable f in equation (12) may thus be considered as a function of η and ξ, or of η and Λ.

The solution to equation (12) may be written in Merk series form as proposed by Chao and Fagbenle [9] as

$$f(\Lambda, \eta) = f_0(\Lambda, \eta) + 2\xi \frac{d\Lambda}{d\xi} f_1(\Lambda, \eta) + 4\xi^2 \frac{d^2\Lambda}{d\xi^2} f_2(\Lambda, \eta) + \left(2\xi \frac{d\Lambda}{d\xi}\right)^2 f_3(\Lambda, \eta) + \left(2\xi \frac{d\Lambda}{d\xi}\right)\left(4\xi^2 \frac{d^2\Lambda}{d\xi^2}\right) f_4(\Lambda, \eta) + \ldots \quad (14)$$

Upon substituting (14) into (12) and collecting terms free of $d\Lambda/d\xi$ and then terms common to $2\xi d\Lambda/d\xi$, $4\xi^2 d^2\Lambda/d\xi^2$, . . . , etc., a sequence of coupled ordinary differential equations is obtained. The first equation in the sequence is

$$f_0''' + f_0 f_0'' - \Lambda f_0'^2 = 0 \quad (15a)$$

with

$$f_0(\Lambda, 0) = 0, \quad f_0'(\Lambda, 0) = 1, \quad f_0'(\Lambda, \infty) = 0 \quad (15b)$$

The remaining differential equations are

$$f_1''' + f_0 f_1'' - 2(\Lambda + 1) f_0' f_1' + 3 f_0'' f_1 = \left(\frac{\partial f_0'}{\partial \Lambda} f_0' - \frac{\partial f_0}{\partial \Lambda} f_0''\right) \quad (16)$$

$$f_2''' + f_0 f_2'' - 2(\Lambda + 2) f_0' f_2' + 5 f_0'' f_2 = f_0' f_1' - f_0'' f_1 \quad (17)$$

$$f_3''' + f_0 f_3'' - (\Lambda + 2)[2 f_0' f_3' + f_1'^2] + 5 f_0'' f_3 + 3 f_1 f_1'' = \left(f_0' \frac{\partial f_1'}{\partial \Lambda} - f_1'' \frac{\partial f_0}{\partial \Lambda}\right) + \left(f_1' \frac{\partial f_0'}{\partial \Lambda} - f_0'' \frac{\partial f_1}{\partial \Lambda}\right) \ldots, \text{ etc.} \quad (18)$$

The boundary conditions for these three equations are: $f_i = f_i' = 0$ for $\eta = 0$ and $f_i' = 0$ for $\eta \to \infty$, where $i = 1, 2$, and 3. The primes in the above equations denote differentiation with respect to η.

Inspection of the above set of equations shows that for any x, Λ is fixed and, therefore, the above equations with their boundary conditions can be treated as simultaneous ordinary equations. Furthermore, all f_i' ($i = 0, 1, 2, 3, \ldots$) are universal in the sense that they depend only on a single parameter Λ and their solution can be tabulated once and for all for any specified value of Λ.

Numerical solutions have been obtained for equations (15*a*), (16), (17), and (18). For conservation of space, only the surface derivatives of the velocity functions are given in Table 1 since the calculation of the local surface shear requires only information about $f_i''(\Lambda, 0)$.

In order to solve the energy equation (4), we will first consider the isothermal surface case, i.e., $x_0 = 0$ in boundary condition (5). Defining a dimensionless temperature function as

$$\theta(\xi, \eta) = \frac{T - T_\infty}{T_s - T_\infty} \quad (19)$$

and using the variables in (6) through (8), the energy equation is transformed to

$$\frac{\partial^2\theta}{\partial\eta^2} + \Pr f \frac{\partial\theta}{\partial\eta} = 2 \Pr \xi\left[\frac{\partial f}{\partial\eta}\frac{\partial\theta}{\partial\xi} - \frac{\partial\theta}{\partial\eta}\frac{\partial f}{\partial\xi}\right] \quad (20)$$

with the boundary conditions

$$\theta(\xi, 0) = 1 \quad \text{for } \eta = 0$$
$$\theta(\xi, \infty) = 0 \quad \text{for } \eta \to \infty \quad (21)$$

Using a Merk type series analogous to (14), the solution to (20) can be written as

$$\theta(\Lambda, \eta) = \theta_0(\Lambda, \eta) + 2\xi \frac{d\Lambda}{d\xi} \theta_1(\Lambda, \eta) + 4\xi^2 \frac{d^2\Lambda}{d\xi^2} \theta_2(\Lambda, \eta) + \left(2\xi \frac{d\Lambda}{d\xi}\right)^2 \theta_3(\Lambda, \eta) + \ldots \quad (22)$$

Table 1 Surface derivatives of the velocity functions in the series

Λ	$f_0''(\Lambda,0)$	$f_1''(\Lambda,0)*10$	$f_2''(\Lambda,0)*10^2$	$f_3''(\Lambda,0)*10^2$
-0.10	-0.5815786	0.6086720	-0.3706994	0.9177400
0.00	-0.6275549	0.5519510	-0.7698450	0.7714337
0.10	-0.6714305	0.5030020	-0.6843336	0.6533740
0.20	-0.7134303	0.4604634	-0.6113127	0.5573080
0.30	-0.7537449	0.4232589	-0.5485497	0.4783739
0.40	-0.7925367	0.3905288	-0.4942804	0.4130906
0.50	-0.8299459	0.3615800	-0.4470959	0.3586298
0.60	-0.8660936	0.3358485	-0.4058614	0.3129822
0.70	-0.9010854	0.3128719	-0.3696561	0.2743759
0.80	-0.9350142	0.2922676	-0.3377263	0.2416550
0.90	-0.9679616	0.2737178	-0.3094513	0.2136481
1.00	-1.0000000	0.2569556	-0.2843165	0.1895002
1.10	-1.0311939	0.2417567	-0.2618925	0.1690515

Table 2 Surface derivatives of temperature function in the series (22) for isothermal surface

Pr	Λ	$\theta_0'(\Lambda,0)$	$\theta_1'(\Lambda,0)*10^2$	$\theta_2'(\Lambda,0)*10^3$	$\theta_3'(\Lambda,0)*10^3$
0.7	-0.10	-0.4989901	-0.3554633	-0.4198137	-1.1803667
	0.00	-0.4938941	-0.2811791	-0.5389336	-0.9849872
	0.10	-0.4890506	-0.2166163	-0.6385276	-0.8248271
	0.20	-0.4844422	-0.1602146	-0.7219964	-0.6920076
	0.30	-0.4800469	-0.1107154	-0.7920568	-0.5814725
	0.40	-0.4758457	-0.0670940	-0.8505277	-0.4891789
	0.50	-0.4718222	-0.0285089	-0.9002980	-0.4113306
	0.60	-0.4679618	0.0057361	-0.9417142	-0.3452891
	0.70	-0.4642516	0.0362220	-0.9763485	-0.2891081
	0.80	-0.4606806	0.0634357	-1.0051967	-0.2412892
	0.90	-0.4572384	0.0877886	-1.0290910	-0.2006831
	1.00	-0.4539162	0.1096302	-1.0487295	-0.1664783
	1.10	-0.4507057	0.1292585	-1.0647018	-0.1337091
1.0	-0.10	-0.6333432	-0.4284843	-0.3852784	-1.2948944
	0.00	-0.6275549	-0.3463207	-0.5178445	-1.0822178
	0.10	-0.6220564	-0.2748702	-0.6289888	-0.9074535
	0.20	-0.6168194	-0.2124049	-0.7224555	-0.7632014
	0.30	-0.6118195	-0.1575334	-0.8012299	-0.6437507
	0.40	-0.6070354	-0.1091233	-0.8677158	-0.5431915
	0.50	-0.6024489	-0.0662467	-0.9238627	-0.4589439
	0.60	-0.5980438	-0.0281360	-0.9712660	-0.3872348
	0.70	-0.5938059	0.0058477	-1.0112392	-0.3263876
	0.80	-0.5897227	0.0362408	-1.0448718	-0.2721137
	0.90	-0.5857830	0.0635503	-1.0732136	-0.2236322
	1.00	-0.5819767	0.0879929	-1.0965993	-0.1925514
	1.10	-0.5782949	0.1100630	-1.1160987	-0.1588944
5.0	-0.10	-1.6397855	-0.5971364	-0.3738427	-1.3965666
	0.00	-1.6318210	-0.4982324	-0.5271745	-1.1473961
	0.10	-1.6242326	-0.4126533	-0.6519953	-0.9572554
	0.20	-1.6169826	-0.3381641	-0.7619739	-0.7956253
	0.30	-1.6100386	-0.2729764	-0.8518008	-0.6593777
	0.40	-1.6033727	-0.2156412	-0.9274291	-0.5567196
	0.50	-1.5969608	-0.1649895	-0.9912100	-0.4610012
	0.60	-1.5907817	-0.1200605	-1.0150508	-0.3856168
	0.70	-1.5848170	-0.0800484	-1.0905320	-0.3223099
	0.80	-1.5790502	-0.0442966	-1.1289216	-0.2670306
	0.90	-1.5734669	-0.0122477	-1.1612828	-0.2206328
	1.00	-1.5680542	0.0165695	-1.1885016	-0.1790251
	1.10	-1.5628004	0.0425471	-1.2113036	-0.1476451
10.0	-0.10	-2.3847912	-0.6079891	-0.4313942	-1.3375775
	0.00	-2.3762936	-0.5076221	-0.5823731	-1.0900489
	0.10	-2.3681926	-0.4210858	-0.7074138	-0.8947154
	0.20	-2.3604478	-0.3460130	-0.8113847	-0.7284457
	0.30	-2.3530246	-0.2805170	-0.8981149	-0.6105924
	0.40	-2.3458935	-0.2230936	-0.9706119	-0.4967455
	0.50	-2.3390287	-0.1725080	-1.0313155	-0.4093060
	0.60	-2.3324078	-0.1277608	-1.0821684	-0.3376712
	0.70	-2.3260112	-0.0880165	-1.1247756	-0.2688540
	0.80	-2.3198217	-0.0525901	-1.1604304	-0.2178972
	0.90	-2.3138238	-0.0209121	-1.1901910	-0.1849290
	1.00	-2.3080039	0.0075080	-1.2149597	-0.1472112
	1.10	-2.3023500	0.0330747	-1.2354648	-0.1159836

Substituting (22) into (20) and equating terms of like coefficients leads to the following set of ordinary differential equations for the θ_i:

$$\theta_0'' + \Pr f_0 \theta_0' = 0 \quad (23a)$$

with

$$\theta_0(\Lambda, 0) = 1, \quad \theta_0(\Lambda, \infty) = 0 \quad (23b)$$

$$\Pr^{-1} \theta_1'' + f_0 \theta_1' - 2 f_0' \theta_1 = \left(f_0' \frac{\partial\theta_0}{\partial\Lambda} - \theta_0' \frac{\partial f_0}{\partial\Lambda}\right) - 3 f_1 \theta_0' \quad (24)$$

$$\Pr^{-1} \theta_2'' + f_0 \theta_2' - 4 f_0' \theta_2 = (f_0' \theta_1 - \theta_0' f_1) - 5 f_2 \theta_0' \quad (25)$$

$$\Pr^{-1} \theta_3'' + f_0 \theta_3' - 4 f_0' \theta_3 = \left(f_0' \frac{\partial\theta_1}{\partial\Lambda} - \theta_1' \frac{\partial f_0}{\partial\Lambda}\right) + \left(f_1' \frac{\partial\theta_0}{\partial\Lambda} - \theta_0' \frac{\partial f_1}{\partial\Lambda}\right) - 3 f_1 \theta_1' + 2 f_1' \theta_1 - 5 f_3 \theta_0' \quad (26)$$

etc. The boundary conditions for the last three equations are:

$\theta_i = 0$ for $\eta = 0$ and $\eta \to \infty$, where $i = 1, 2$, and 3. The numerical solutions for θ_i ($i = 0, 1, 2$, and 3) with the appropriate boundary conditions were obtained and the surface derivatives of the temperature functions are given in Table 2 for Pr = 0.7, 1, 5, and 10, respectively.

When the surface temperature experiences a step change as given by equation (5), the transformations (7) used for the isothermal case are no longer appropriate, and other variables must be used.

In order to find such variables, the problem will first be solved by using von Karman's integral technique. Using fourth-order and third-order polynomials respectively for the dimensionless velocity and temperature profiles, the dimensionless temperature gradient at the surface for large Pr was obtained as

$$\theta'(x, 0) = -0.5305\,\mathrm{Pr}^{1/2}\sqrt{\frac{U_s}{\nu x}}\left[1-\frac{x_0}{x}\right]^{-1/2} \tag{27}$$

For an isothermal surface, i.e., $x_0 = 0$, equation (27) reduces to that reported by Erickson et al. [10].

Returning to the solution of the energy equation (4) for a step change in surface temperature, further transformations are introduced

$$\xi \to \chi = \left[1-\frac{\xi_0}{\xi}\right]^{1/2} \tag{28a}$$

$$\eta \to \zeta = b\,\frac{\eta}{\chi} \tag{28b}$$

in which $\xi_0 = \int_0^{x_0} U_s(x)dx$ and b is a constant to be determined later. The transformations proposed in equations (28*a*, *b*) are motivated from the anticipation of developing a series solution in powers of χ such that when the Prandtl number becomes large, the first term of the series solutions shall dominate the result and, further, when the surface velocity becomes constant, the first term will be comparable with the integral solution given in equation (27).

Making use of equations (28*a*, *b*), the energy equation becomes

$$\frac{\partial^2\theta}{\partial\zeta^2}+\frac{\mathrm{Pr}}{b}\left\{\chi\left(f+2\xi\,\frac{\partial f}{\partial\xi}\right)+\left[\frac{1}{b}-\frac{\chi^2}{b}\right]\zeta\,\frac{\partial f}{\partial\eta}\right\}\frac{\partial\theta}{\partial\zeta} + \frac{\mathrm{Pr}\,(\chi^3-\chi)}{b^2}\,\frac{\partial f}{\partial\eta}\,\frac{\partial\theta}{\partial\chi}=0 \tag{29}$$

with

$$\theta(\chi, 0)=1, \qquad \theta(\chi, \infty)=0 \tag{30}$$

The ranges of the variables are $0 \le \chi \le 1$ and $0 \le \zeta \le \infty$. When $\xi = \xi_0$, χ becomes 0 and $\zeta \to \infty$ due to the form chosen for equation (28*b*). Therefore the entrance condition $T(x_0, y > 0) = T_\infty$ given in equation (5) merges into the second condition given by equation (30). For the isothermal surface, $\xi_0 = 0$ and $\chi = 1$ and thus equation (29) reduces to equation (20).

In order to solve equation (29) with the boundary conditions (30), the function f is first expanded in a power series of the form

$$f(\xi, \eta) = \sum_{n=1}^{\infty} a_n\,\frac{\eta^n}{n!} = \frac{\zeta}{b}\,\chi + \frac{a\zeta^2}{2b^2}\,\chi^2 + \frac{\Lambda\zeta^3}{3!b^3}\,\chi^3 + \ldots \tag{31}$$

in which the a_n can be obtained by substituting equation (31) into equation (12) and equating coefficients having the same power of η. This process yields

$$a_1 = 1; \quad a_2 = a; \quad a_3 = \Lambda; \quad a_4 = (2\Lambda-1)a + 2\xi a'$$
$$a_5 = 2\Lambda(\Lambda-1) + (2\Lambda-1)a^2 + 2\xi a a' + 2\xi\Lambda' \ldots \text{ etc.} \tag{32}$$

where $a = a_2 = \partial^2 f/\partial\eta^2|_{\eta=0}$ and numerical values of a and its derivatives for various values of Λ may be evaluated from equation (14) using the results tabulated in Table 1.

The solution to equation (29) is now proposed as

$$\theta = \sum_{n=0}^{\infty} \theta_n(\xi, \zeta)\chi^n \tag{33}$$

and

$$\theta_0(\xi, 0) = 1; \quad \theta_1(\xi, 0) = \theta_2(\xi, 0) = \ldots = 0 \tag{34a}$$

$$\theta_0(\xi, \infty) = \theta_1(\xi, \infty) = \ldots = 0 \tag{34b}$$

which satisfies the boundary conditions equation (30). The θ_n functions appearing in equation (33) can be obtained by solving a set of differential equations which result from direct substitution of equations (31) and (33) into (29) and equating coefficients of like powers of χ. In order to render the set of differential equations satisfied by the θ_n independent of the parameters of a particular problem, such as the Prandtl number, a, and Λ, it is necessary to further define

$$b = \mathrm{Pr}^{1/2}$$

$$\theta_1 = \frac{a}{\mathrm{Pr}^{1/2}}\,\bar\theta_1$$

$$\theta_2 = \frac{a^2}{\mathrm{Pr}}\,\bar\theta_{2,1} + \frac{\Lambda}{2\mathrm{Pr}}\,\bar\theta_{2,2} \tag{35}$$

$$\theta_3 = \frac{a^3}{\mathrm{Pr}^{3/2}}\,\bar\theta_{3,1} + \frac{a\Lambda}{2\mathrm{Pr}^{3/2}}\,\bar\theta_{3,2} + \frac{a}{\mathrm{Pr}^{1/2}}\,\bar\theta_{3,3} + \frac{2\xi a' + a}{2\,\mathrm{Pr}^{1/2}}\,\bar\theta_{3,4} + \frac{(2\Lambda-1)a + 2\xi a'}{6\,\mathrm{Pr}^{3/2}}\,\bar\theta_{3,5} \ldots, \text{ etc.}$$

By using (35), it is found that θ_0, $\bar\theta_1$ and the $\bar\theta_{m,n}$ satisfy the following equations

$$\theta_0'' + \zeta\theta_0' = 0 \tag{36}$$

$$\bar\theta_1'' + \zeta\bar\theta_1' - \bar\theta_1 = -\zeta^2\theta_0' \tag{37}$$

$$\bar\theta_{2,1}'' + \zeta\bar\theta_{2,1}' - 2\bar\theta_{2,1} = -\zeta^2\bar\theta_1' + \zeta\bar\theta_1 \tag{38a}$$

$$\bar\theta_{2,2}'' + \zeta\bar\theta_{2,2}' - 2\bar\theta_{2,2} = -\zeta^3\theta_0' \tag{38b}$$

$$\bar\theta_{3,1}'' + \zeta\bar\theta_{3,1}' - 3\bar\theta_{3,1} = -\zeta^2\bar\theta_{2,1}' + 2\zeta\bar\theta_{2,1} \tag{39a}$$

$$\bar\theta_{3,2}'' + \zeta\bar\theta_{3,2}' - 3\bar\theta_{3,2} = -\zeta^2\bar\theta_{2,2}' - \zeta^3\bar\theta_1' + 2\zeta\bar\theta_{2,2} + \zeta^2\bar\theta_1 \tag{39b}$$

$$\bar\theta_{3,3}'' + \zeta\bar\theta_{3,3}' - 3\bar\theta_{3,3} = -\bar\theta_1 + \zeta\theta_0' \tag{39c}$$

$$\bar\theta_{3,4}'' + \zeta\bar\theta_{3,4}' - 3\bar\theta_{3,4} = -\zeta^2\theta_0' \tag{39d}$$

$$\bar\theta_{3,5}'' + \zeta\bar\theta_{3,5}' - 3\bar\theta_{3,5} = -\zeta^4\theta_0' \tag{39e}$$

The associated boundary conditions are, respectively,

$$\theta_0(0) = 1,\ \bar\theta_1(0) = \bar\theta_{2,1}(0) = \bar\theta_{2,2}(0) = \bar\theta_{3,1}(0) = \bar\theta_{3,2}(0) = \bar\theta_{3,4}(0) = \bar\theta_{3,5}(0) = 0 \text{ and } \theta_0(\infty) = \bar\theta_1(\infty) = \bar\theta_{2,1}(\infty) = \bar\theta_{2,2}(\infty) = \bar\theta_{3,1}(\infty) = \bar\theta_{3,2}(\infty) = \bar\theta_{3,3}(\infty) = \bar\theta_{3,4}(\infty) = \bar\theta_{3,5}(\infty) = 0$$

The primes denote partial differentiation with respect to ζ. As can be seen from examining equations (36) to (39), no parameters are present so θ_0, $\bar\theta_1$, and the $\bar\theta_{m,n}$ are universal functions and, once obtained, can be tabulated once and for all. The solution to equation (36) can be obtained in closed form as

$$\theta_0(\zeta) = \mathrm{erfc}\left(\frac{\zeta}{\sqrt{2}}\right) \tag{40}$$

and has the surface derivative

$$\theta_0'(0) = -\sqrt{\frac{2}{\pi}} = -0.79788 \tag{41}$$

Equations (37), (38*a*, *b*), and (39*a*–*e*) were solved numerically and the results are presented in Table 3. The surface derivatives of these functions are required in order to evaluate the surface heat flux. These values are

Table 3 Universal temperature functions for (33), step change in surface temperature

ζ	θ_0	$\bar{\theta}_1$	$\bar{\theta}_{2,1}$	$\bar{\theta}_{2,2}$	$\bar{\theta}_{3,1}$	$\bar{\theta}_{3,2}$	$\bar{\theta}_{3,3}$	$\bar{\theta}_{3,4}$	$\bar{\theta}_{3,5}$
0.00	1.000000	0.000000	0.000000	0.000000	0.000000	0.000000	0.000000	0.000000	0.000000
0.20	0.841480	-0.049895	0.025100	-0.040147	-0.023733	0.056973	0.018950	-0.025228	-0.037998
0.40	0.689157	-0.098377	0.051180	-0.081510	-0.049113	0.118078	0.035248	-0.051026	-0.078896
0.60	0.548506	-0.142256	0.079094	-0.123960	-0.077449	0.186836	0.046878	-0.076065	-0.124894
0.80	0.423711	-0.177443	0.109256	-0.165317	-0.109727	0.265843	0.052860	-0.097761	-0.176306
1.00	0.317310	-0.200313	0.141150	-0.201642	-0.146620	0.355921	0.053321	-0.113378	-0.230559
1.20	0.230139	-0.208856	0.172929	-0.228363	-0.188334	0.454786	0.049280	-0.120998	-0.282163
1.40	0.161513	-0.203262	0.201429	-0.241760	-0.234226	0.555899	0.042265	-0.120098	-0.323945
1.60	0.109598	-0.185818	0.222806	-0.240180	-0.282257	0.648520	0.033887	-0.111614	-0.349154
1.80	0.071861	-0.160236	0.233572	-0.224534	-0.328625	0.719591	0.025516	-0.097580	-0.353567
2.00	0.045500	-0.130732	0.231711	-0.197967	-0.367950	0.757102	0.018093	-0.080553	-0.336763
2.20	0.027807	-0.101142	0.217348	-0.164933	-0.394263	0.753723	0.012100	-0.062908	-0.302116
2.40	0.016395	-0.074333	0.192742	-0.130067	-0.402571	0.709177	0.007637	-0.046610	-0.255664
2.60	0.009322	-0.051970	0.161638	-0.097236	-0.390442	0.630396	0.004547	-0.032812	-0.204395
2.80	0.005110	-0.034606	0.128268	-0.069002	-0.358907	0.529489	0.002551	-0.021977	-0.154598
3.00	0.002700	-0.021968	0.096393	-0.046534	-0.312295	0.420443	0.001345	-0.014021	-0.110777
3.20	0.001374	-0.013306	0.068657	-0.029855	-0.257071	0.315846	0.000663	-0.008529	-0.075291
3.40	0.000674	-0.007695	0.046390	-0.018238	-0.200177	0.224657	0.000304	-0.004951	-0.048593
3.60	0.000318	-0.004252	0.029761	-0.010618	-0.147488	0.151432	0.000128	-0.002744	-0.029815
3.80	0.000145	-0.002245	0.018142	-0.005895	-0.102870	0.096815	0.000048	-0.001453	-0.017399
4.00	0.000063	-0.001134	0.010517	-0.003123	-0.067962	0.058757	0.000015	-0.000736	-0.009669
4.20	0.000027	-0.000548	0.005802	-0.001579	-0.042558	0.033877	0.000003	-0.000356	-0.005120
4.40	0.000011	-0.000253	0.003048	-0.000763	-0.025278	0.018570		-0.000165	-0.002585
4.60	0.000004	-0.000112	0.001526	-0.000352	-0.014251	0.009685		-0.000073	-0.001245
4.80		-0.000048	0.000728	-0.000156	-0.007631	0.004808		-0.000031	-0.000572
5.00		-0.000019	0.000331	-0.000066	-0.003884	0.002274		-0.000013	-0.000251
5.20		-0.000008	0.000144	-0.000026	-0.001880	0.001025		-0.000005	-0.000105
5.40		-0.000003	0.000060	-0.000010	-0.000866	0.000440		-0.000002	-0.000042
5.60			0.000024	-0.000004	-0.000380	0.000181			-0.000016
5.80			0.000009		-0.000158	0.000071			-0.000006
6.00			0.000003		-0.000063	0.000026			-0.000002
6.20					-0.000024	0.000009			
6.40					-0.000009	0.000003			
6.60					-0.000003				

Table 4 Functions related to displacement thickness

Λ	$f_0(\Lambda,\infty)$	$f_1(\Lambda,\infty)*10$	$f_2(\Lambda,\infty)*10^2$	$f_3(\Lambda,\infty)*10^2$
-0.10	1.1616580	0.6397114	-1.1794360	1.0646657
0.00	1.1427733	0.5925261	-1.0787448	0.9343529
0.10	1.1249830	0.5506512	-0.9901750	0.8245072
0.20	1.1081769	0.5132896	-0.9118454	0.7314709
0.30	1.0922601	0.4797925	-0.8422305	0.6518635
0.40	1.0771507	0.4496260	-0.7800806	0.5835758
0.50	1.0627773	0.4223478	-0.7243648	0.5244141
0.60	1.0490773	0.3975884	-0.6742252	0.4731975
0.70	1.0359956	0.3750371	-0.6289439	0.4284974
0.80	1.0234836	0.3544303	-0.5879146	0.3890706
0.90	1.0114980	0.3355443	-0.5506246	0.3542873
1.00	1.0000000	0.3181863	-0.5166350	0.3230290
1.10	0.9889550	0.3021920	-0.4855714	0.2969041

Table 5 Integrals related to momentum thickness

Λ	I_1	I_2*10^1	I_3*10^2	I_4*10^2
-0.10	0.6459826	0.4607879	-0.7629907	0.8998153
0.00	0.6273391	0.4115521	-0.6694243	0.7537328
0.10	0.6101746	0.3694283	-0.5904731	0.6360961
0.20	0.5943079	0.3331467	-0.5233815	0.5407943
0.30	0.5795855	0.3016901	-0.4659998	0.4629735
0.40	0.5658766	0.2742637	-0.4166305	0.3982780
0.50	0.5530775	0.2502235	-0.3739198	0.3444175
0.60	0.5410860	0.2290452	-0.3367859	0.2993911
0.70	0.5298286	0.2103055	-0.3043454	0.2613851
0.80	0.5192296	0.1936501	-0.2758828	0.2287271
0.90	0.5092282	0.1787931	-0.2508115	0.2018328
1.00	0.4997767	0.1654876	-0.2286370	0.1782105
1.10	0.4908208	0.1535316	-0.2089570	0.1583593

$$\bar{\theta}_1'(0) = -0.250, \quad \bar{\theta}_{2,1}'(0) = 0.12467,$$
$$\bar{\theta}_{2,2}'(0) = -0.19947, \quad \bar{\theta}_{3,1}' = -0.11719,$$
$$\bar{\theta}_{3,2}'(0) = 0.28125, \quad \bar{\theta}_{3,3}'(0) = 0.097077,$$
$$\bar{\theta}_{3,4}'(0) = -0.12500, \quad \bar{\theta}_{3,5}'(0) = -0.18750 \tag{42}$$

3 Important Formula Relating to Momentum and Heat Transfer

Using the solutions for the f_i and θ_i obtained in the previous section, the calculation of the local surface shear, the development of the displacement and momentum thicknesses and the local Nusselt number becomes a simple matter. The necessary inputs are the surface velocity $U_s(x)$ and the temperature $T_s(x)$, which may be obtained from experiments. In this section some important formulas needed for the calculation are summarized.

The local friction coefficient may be expressed in terms of universal functions as

$$c_f = \frac{-\mu \left.\frac{\partial u}{\partial y}\right|_{y=0}}{\frac{1}{2}\rho U_s^2} = -\left(\frac{2\nu}{\xi}\right)^{1/2}\left\{f_0''(\Lambda, 0) + 2\xi \frac{d\Lambda}{d\xi} f_1''(\Lambda, 0) + 4\xi^2 \frac{d^2\Lambda}{d\xi^2} f_2''(\Lambda, 0) + 4\xi^2\left(\frac{d\Lambda}{d\xi}\right)^2 f_3''(\Lambda, 0) + \ldots\right\} \tag{43}$$

The displacement and momentum thicknesses for a continuous moving surface are defined by

$$\delta_1 = \frac{1}{U_s}\int_0^\infty u dy = \frac{(2\xi\nu)^{1/2}}{U_s}\left\{f_0(\Lambda, \infty) + 2\xi \frac{d\Lambda}{d\xi} f_1(\Lambda, \infty) + 4\xi^2 \frac{d^2\Lambda}{d\xi^2} f_2(\Lambda, \infty) + 4\xi^2\left(\frac{d\Lambda}{d\xi}\right)^2 f_3(\Lambda, \infty) + \ldots\right\} \tag{44}$$

$$\delta_2 = \frac{1}{U_s^2}\int_0^\infty u^2 dy = \left\{I_1(\Lambda) + 2\xi \frac{d\Lambda}{d\xi} I_2(\Lambda) + 4\xi^2 \frac{d^2\Lambda}{d\xi^2} I_3(\Lambda) + \left(2\xi \frac{d\Lambda}{d\xi}\right)^2 I_4(\Lambda) + \ldots\right\} \tag{45}$$

where

$$I_1 = \int_0^\infty f_0'^2 d\eta, \qquad I_2 = 2\int_0^\infty f_0' f_1' d\eta$$

$$I_3 = 2\int_0^\infty f_0' f_2' d\eta, \qquad I_4 = \int_0^\infty (f_1'^2 + 2f_0' f_3') d\eta$$

These boundary layer functions are also tabulated in Tables 4 and 5 for various values of Λ.

Two expressions for the local surface heat flux, one for a uniform surface temperature using a Merk type series, and the other for a step change in surface temperature, are given below.

For a uniform surface temperature

$$q_s = -k\frac{\partial T}{\partial y}\bigg|_{y=0} = \frac{k(T_s - T_\infty)U_s}{(2\nu\xi)^{1/2}}\left(-\frac{\partial\theta}{\partial\eta}\right)\bigg|_{\eta=0} \tag{46}$$

In terms of the local Nusselt number

$$\mathrm{Nu}_x = \frac{q_s\, x}{k(T_s - T_\infty)} = \frac{U_s\, x}{(2\nu\xi)^{1/2}}\left(-\frac{\partial\theta}{\partial\eta}\right)\bigg|_{\eta=0} \tag{47}$$

where

$$\left(-\frac{\partial\theta}{\partial\eta}\right)\bigg|_{\eta=0} = -\left[\theta_0'(\Lambda, 0) + 2\xi\frac{d\Lambda}{d\xi}\theta_1'(\Lambda, 0) + 4\xi^2\frac{d^2\Lambda}{d\xi^2}\theta_2'(\Lambda, 0) + \left(2\xi\frac{d\Lambda}{d\xi}\right)^2\theta_3'(\Lambda, 0) + \ldots\right] \tag{48}$$

For a step change in surface temperature

$$q_s = k(T_s - T_\infty)\frac{\mathrm{Pr}^{1/2}\, U_s}{(2\nu\xi)^{1/2}\chi}\left(-\frac{\partial\theta}{\partial\zeta}\right)\bigg|_{\zeta=0} \tag{49}$$

and the local Nusselt number for this case is

$$\mathrm{Nu}_x = \frac{\mathrm{Pr}^{1/2}\, U_s\, x}{(2\nu\xi)^{1/2}\,\chi}\left(-\frac{\partial\theta}{\partial\zeta}\right)\bigg|_{\zeta=0} \tag{50}$$

where

$$\left(-\frac{\partial\theta}{\partial\zeta}\right)\bigg|_{\zeta=0} = 0.79788 + \frac{0.25a}{\mathrm{Pr}^{1/2}}\chi + \left[\frac{0.0997\,\Lambda}{\mathrm{Pr}} - \frac{0.12467a^2}{\mathrm{Pr}}\right]\chi^2 + \left[\frac{0.125\xi a' - 0.03458a}{\mathrm{Pr}^{1/2}} + \frac{0.3750\xi a' - 0.4688a\Lambda - 0.1875a}{6\ \mathrm{Pr}^{3/2}} + \frac{0.11719a^3}{\mathrm{Pr}^{3/2}}\right]\chi^3 + \ldots \tag{51}$$

The dimensionless temperature profile equation (33) can be recast in terms of universal functions as

$$\theta(\Lambda, \zeta, \chi) = \theta_0(\zeta) + \frac{a}{\mathrm{Pr}^{1/2}}\bar{\theta}_1(\zeta)\chi + \left\{\frac{a^2}{\mathrm{Pr}}\bar{\theta}_{2,1}(\zeta) + \frac{\Lambda}{2\ \mathrm{Pr}}\bar{\theta}_{2,2}(\zeta)\right\}\chi^2 + \left\{\frac{a^3}{\mathrm{Pr}^{3/2}}\bar{\theta}_{3,1} + \frac{a\Lambda}{2\ \mathrm{Pr}^{3/2}}\bar{\theta}_{3,2} + \frac{a}{\mathrm{Pr}^{1/2}}\bar{\theta}_{3,3} + \frac{2\xi a' + a}{2\ \mathrm{Pr}^{1/2}}\bar{\theta}_{3,4} + \frac{(2\Lambda - 1)a + 2\xi a'}{6\ \mathrm{Pr}^{3/2}}\bar{\theta}_{3,5}\right\}\chi^3 + \ldots \tag{52}$$

Using the above information, the calculation of the friction coefficient and the surface heat transfer proceeds as follows. For a given function $U_s(x)$, the corresponding quantities ξ, Λ, $d\Lambda/d\xi$, . . . , etc., can be evaluated. For each value of x, the corresponding values of a and a' can be determined from Table 1 and the shear stress can be determined. For a specified x_0 and Prandtl number, the development of the temperature profile in the boundary layer downstream of the surface discontinuity can be readily obtained from equation (52) with the data provided in Table 3. The local surface heat flux can be evaluated from equations (46) or (49).

No approximations or limitations have been imposed in the above analysis, and higher order terms in the series solutions may be obtained by a straightforward calculation. The accuracy of using a finite number of terms in a series solution, however, depends upon the convergence of the series. Under certian conditions, the series may become semidivergent, in which case Euler's summation method [11] may be used for summing the series.

4 Examples and Discussion of Accuracy

In this section, two examples using different surface velocity distributions will be given in order to demonstrate the usefulness and the accuracy of the series solution presented in this paper. They include the power law surface velocity and the linearly stretching surface velocity with nonzero slot velocity. Whenever possible, the results for the velocity and the temperature fields are compared with results available in the literature.

Table 6 Comparison of $\mathrm{Nu}_x\ \mathrm{Re}_x^{-1/2}$ for isothermal surface; $\mathrm{Re}_x = U_s x/\nu$; $U_s = cx^m$

Pr	m	Number of Terms in Series, Eq. (50) 1	2	3	4	Eq. (47)	Ref. [4]	Upper Bound Error
0.7	0	0.4720	0.3611	0.3196	0.3255	0.3493	0.3492	-0.0681
	1	0.6676	0.4173	0.3875	0.4109	0.4539	-	-0.0947
10.0	0	1.7841	1.6732	1.6622	1.6769	1.6803	1.6804	-0.002
	1	2.5231	2.2731	2.2652	2.2990	2.3080	-	-0.004

Inspection of the series solution equations (49) or (50) reveals that the first term in the series mathematically represents the exact solution to the problem when the velocity profile in the boundary layer is linear. The remainder of the terms in the series may therefore be considered as corrections for the departure of the actual velocity profile from being linear. The boundary layer on the continuously moving surface originates at the slot and grows in the direction of motion of the surface. Therefore, for a large Prandtl number fluid and a constant surface temperature, the thermal boundary layer thickness is comparatively thinner than the momentum boundary layer and only the first term solution in the series of equations (49) or (50) is needed for an accurate result. For the case of a step change in surface temperature, the thermal boundary layer is thin for a short distance downstream of the point of temperature discontinuity (Fig. 1), regardless of the Prandtl number. For this region, corrections to the linear velocity profile results are small. At larger downstream distances where the thermal boundary layer has had significant development, the thermal boundary layer thickness, depending on the Prandtl number, may be much greater than the momentum boundary layer thickness.

4.1 Surface Velocity Proportional to a Power of Distance Measured From the Slot for an Isothermal Surface. Consider a surface velocity of the form

$$U_s = cx^m \tag{53}$$

in which c and m are constants.

For constant surface velocity, i.e., $m = 0$, $c_f\ \mathrm{Re}_x^{1/2} = 0.8875$ and $\mathrm{Nu}_x\ \mathrm{Re}_x^{-1/2} = 0.3493$ (for Pr = 0.7), which are in excellent agreement with the results reported in [2, 4].

The accuracy of equation (50) for a step change in surface temperature may be examined by comparing numerical values evaluated by using equation (50) for the isothermal case with those obtained from equation (47). The maximum error from using a finite number of terms in the series of equation (50) for a given Prandtl number will occur when $\chi = 1$, which is the largest value that χ can have for the isothermal case. A comparison was done for $\mathrm{Nu}_x\ \mathrm{Re}_x^{-1/2}$ for $m = 0$ and 1 and for Pr = 0.7 and 10 with the numbers of terms used in the series. The first term dominates the solution and the convergence of the series can be seen from the number of terms used in the calculation. In general, equation (50) underpredicts the local Nusselt number. As the Prandtl number increases, the error is expected to become smaller. To increase the accuracy for smaller Prandtl numbers, more terms may be required in the series of (50).

If the surface velocity is constant but the surface temperature has a step change at x_0, for $\mathrm{Pr} \to \infty$, equation (5) reduces to

$$\mathrm{Nu}_x\ \mathrm{Re}_x^{-1/2}\ \mathrm{Pr}^{-1/2} = 0.56419\left[1 - \frac{x_0}{x}\right]^{-1/2} \tag{54}$$

Table 7 $c_f\ \mathrm{Re}_x^{1/2}$ for surface velocity, $U_s/U_0 = 1 + x/L$, $\left(c_f = \dfrac{-\mu \partial u/\partial y|_{y=0}}{\frac{1}{2}}, \mathrm{Re}_x = U_0 x/\nu\right)$

Λ	x/L	Number of Terms in Series, Eq.(43) 1	2	3	4
0.1	0.0541	0.93696	0.92433	0.92365	0.92234
0.2	0.1180	0.98042	0.96018	0.95804	0.95723
0.3	0.1952	1.01746	0.99346	0.98974	0.98860
0.4	0.2910	1.04722	1.02246	1.01744	1.01618
0.5	0.4140	1.06829	1.04502	1.03926	1.03811
0.6	0.5811	1.07818	1.05811	1.05228	1.05139
0.7	0.8257	1.07209	1.05645	1.05128	1.05017
0.8	1.2361	1.03953	1.02878	1.02473	1.02444

which, if the constant 0.56419 is replaced by 0.5305, becomes identical to the results obtained using the integral method.

4.2 Linearly Stretched Surface With Nonzero Slot Velocity. In the previous example, the functional form chosen for the velocity profile give the unrealistic surface velocity at the slot ($x = 0$) to be zero, which is only an approximation to the real problem. In order to illustrate how a friction coefficient and Nusselt number can be evaluated for a linearly stretched surface with a nonzero slot velocity, the surface velocity functional form is taken as

$$\frac{U_s}{U_0} = 1 + \frac{x}{L} \tag{55}$$

where L is the inverse of the absolute magnitude of the velocity gradient $(d/dx)(U_s/U_0)$ and U_0 is the velocity of the surface at the slot. The surface velocity given by equation (55) is analogous to the velocity at the edge of the ordinary boundary layer in the accelerated flow over an inclined flat surface. The coordinates and the parameters corresponding to (55) are

$$\xi = U_0 L\left(\frac{x}{L} + \frac{x^2}{2L^2}\right), \qquad \Lambda = \frac{2\dfrac{x}{L}\left(1 + \dfrac{1}{2}\dfrac{x}{L}\right)}{\left(1 + \dfrac{x}{L}\right)^2}$$

$$2\xi\frac{d\Lambda}{d\xi} = \frac{4\left(\dfrac{x}{L} + \dfrac{1}{2}\dfrac{x^2}{L^2}\right)}{\left(1 + \dfrac{x}{L}\right)^4}, \qquad 4\xi^2\frac{d^2\Lambda}{d\xi^2} = -32\frac{\left(\dfrac{x}{L} + \dfrac{1}{2}\dfrac{x^2}{L^2}\right)^2}{\left(1 + \dfrac{x}{L}\right)^6} \tag{56}$$

The computed local surface friction data expressed as $c_f\ \mathrm{Re}_x^{1/2}$ are summarized in Table 7. In this table, data calculated using a different number of terms in the series are presented in order to illustrate the series convergence. It can be seen that the series is dominated by the first term. No data could be found in the literature for comparison with the present results.

The local heat transfer coefficient, expressed as $\mathrm{Nu}_x \cdot \mathrm{Re}_x^{-1/2}$, for an isothermal surface in a fluid of Prandtl number = 0.7, is summarized in Table 8. Again, no data could be found for comparison, and therefore the results are presented for the two equations obtained in this work. As shown in Table 8, the results are in reasonable agreement.

5 Conclusions

An analysis was made of the flow and heat transfer occurring in the laminar boundary layer on a continuously moving surface with arbitrary surface velocity. Two solution methods were presented for the energy equation, one for a uniform surface temperature and the other for a step change in surface temperature.

Table 8 Local heat transfer parameter, $\mathrm{Nu}_x\ \mathrm{Re}_x^{-1/2}$ for linearly stretched surface with nonzero slot velocity $U_s = U_0(1 + x/L)$, isothermal surface, Pr = 0.7

Λ	x/L	Eq.(47),4 terms	Eq.(50),4 terms
0.1	0.0541	0.35996	0.34336
0.2	0.11803	0.37246	0.35391
0.3	0.1952	0.38738	0.36684
0.4	0.2910	0.40598*	0.38301
0.5	0.4142	0.42933*	0.40373
0.6	0.5811	0.46796*	0.43134
0.7	0.8257	0.48260*	0.47048
0.8	1.23607	0.54810*	0.53234

* Euler's Summation

The appropriate series expansions for the velocity function f and the dimensionless temperature θ for uniform surface temperature are presented and the significant surface derivatives of the associated universal functions for the first four terms of the series have been tabulated for a wide range of the surface velocity parameter Λ and the Prandtl number. With the aid of these tables, the local friction coefficient and the heat transfer rate can be readily computed once the surface velocity distribution is specified. The evaluation of the displacement and the momentum thicknesses can also be readily accomplished using the tabulated integral functions.

The essential feature of the analysis for the nonisothermal surface is to first obtain the solution for a step change in surface temperature. New series solutions for the temperature profile and the surface heat flux are expressed in terms of the Prandtl number and the surface velocity parameter. It is shown that the local Nusselt number for a large Prandtl number is proportional to the one-half power of the Prandtl number. The solution obtained for a step discontinuity in surface temperature may be applied to obtain the solution to problems with any arbitrarily prescribed surface temperature variation by the use of Duhamel's integral or by numerical superposition [12]. However, the actual measurement of the filament surface temperature is very difficult to accomplish, and its prediction becomes very important for engineering applications. By the use of Duhamel's integral, the heat flux at the surface due to variable surface temperature $T_s(\xi)$ can be written as

$$-k\frac{\partial T}{\partial y} = k[T_s(0) - T_\infty]\frac{\mathrm{Pr}^{1/2}\,U_s}{(2\nu\xi)^{1/2}}\left(-\frac{\partial\theta}{\partial\zeta}\right)_{\zeta=0,X=1} + \frac{k\mathrm{Pr}^{1/2}\,U_s}{(2\nu\xi)^{1/2}}\int_0^\xi\left(-\frac{1}{\chi}\frac{\partial\theta}{\partial\zeta}\right)_{\zeta=0}\frac{dT_s}{d\xi_0}\,d\xi_0 \tag{57}$$

in which $T_s(0)$ is the surface temperature at the slot. Assuming the thickness of the moving surface is $2B(\xi)$ and using the energy balance equation for the filament with the neglection of heat conduction in the x direction, the surface temperature of the filament will satisfy the following integral equation

$$\frac{1}{2}\dot{m}_s C_{ps}[T_s(0) - T_s(\xi)] = \frac{k[T_s(0) - T_\infty]\mathrm{Pr}^{1/2}}{(2\nu)^{1/2}}\int_0^\xi\frac{1}{\xi^{1/2}}\left(-\frac{\partial\theta}{\partial\zeta}\right)_{\zeta=0,X=1}d\xi + \frac{k\mathrm{Pr}^{1/2}}{(2\nu)^{1/2}}\int_0^\xi\left[\int_0^\xi\left(-\frac{1}{\chi}\frac{\partial\theta}{\partial\zeta}\right)\frac{dT_s}{d\xi_0}\,d\xi_0\right]\frac{d\xi}{\xi^{1/2}} \tag{58}$$

where the Kernels, $(-\partial\theta/\partial\zeta)_{\zeta=0,X=1}$ and $(-\partial\theta/\partial\zeta)_{\zeta=0}$ can be obtained from equation (50). The mass ejection rate $\dot{m}_s = 2B\rho U_s$ is assumed to be constant.

Equation (58) is the general integral equation for predicting the surface temperature T_s, and can be solved by a finite difference numerical method. No attempt will be made in this paper to obtain the solution of (58). However, as one can see equation (58) together with the Kernel $(-\partial\theta/\partial\zeta)_{\zeta=0}$ obtained by the present analysis provides a much simpler means for obtaining the surface temperature as compared to the straightforward finite difference schemes of [10].

A great advantange of the present method is that one can refine the solution by obtaining more terms in the series in a straightforward manner, as described in the text.

For engineering calculations, it is recommended that the term a' appearing in the expression for $(-\partial\theta/\partial\zeta)|_{\zeta=0}$ in equation (50) can be neglected without introducing a significant error since it appears in the fourth term of the series. By using the data provided in the tables, the formulas presented in this paper provide a general and rapid calculation method for the local shear stress and heat flux for any prescribed surface velocity or temperature conditions as any yet presented in the literature.

References

1 Sakiadis, B. C., "Boundary-Layer Behavior on Continuous Solid Surfaces: I. The Boundary-Layer Equations for Two-Dimensional and Axisymmetric Flow," *AIChE Journal*, Vol. 7, Mar. 1961, pp. 26–28.

2 Sakiadis, B. C., "Boundary-Layer Behavior on Continuous Solid Surfaces: II. The Boundary-Layer on a Continuous Flat Surface," *AIChE Journal*, Vol. 7, No. 2, June 1961, pp. 221–225.

3 Sakiadis, B. C., "Boundary-Layer Behavior on Continuous Solid Surfaces: III. The Boundary-Layer on a Continuous Cylindrical Surface," *AIChE Journal*, Vol. 7, No. 3, Sept. 1961, pp. 467–472.

4 Tsou, F. K., Sparrow, E. M., and Goldstein, R. J., "Flow and Heat Transfer in the Boundary-Layer on a Continuous Moving Surface," *Int. J. of Heat and Mass Transfer*, Vol. 10, 1967, pp. 219–235.

5 Vleggaar, J., "Laminar Boundary-Layer Behavior on Continuous Accelerating Surfaces," *Chemical Engineering Science*, Vol. 32, 1977, pp. 1517–1525.

6 Gupta, P. S., and Gupta, A. S., "Heat and Mass Transfer on a Stretching Sheet With Suction and Blowing," *Canadian Journal of Chemical Engineering*, Vol. 55, No. 6, 1977, pp. 744–746.

7 Soundalgekar, V. M., and Ramana Murty, T. V., "Heat Transfer Past a Continuous Moving Plate With Variable Temperature," *Warme- und Stoffübertragung*, Vol. 14, 1980, pp. 91–93.

8 Grubka, L. J., and Bobba, K. M., "Heat Transfer Characteristics of a Continuous Stretching Surface With Variable Temperature," private communication, Oct. 1983.

9 Chao, B. T., and Fagbenle, R. O., "On Merk's Method of Calculating Boundary Layer Transfer," *Int. J. of Heat and Mass Transfer*, Vol. 17, 1974, pp. 223–240.

10 Erickson, L. E., Cha, L. C., and Fan, L. T., "The Cooling of a Moving Continuous Flat Sheet," AIChE Chemical Engineering Progress Symposium, Eighth National Heat Transfer Conference, Los Angeles, Calfornia, Aug. 1965.

11 Meksyn, D., *New Methods in Laminar Boundary-Layer Theory*, Pergamon Press, Oxford, 1961.

12 Kays, W. M, and Crawford, M. E., *Convective Heat and Mass Transfer*, 2nd ed., McGraw-Hill, New York, 1980.

H. J. Carper, Jr.
Department of Mechanical Engineering,
Texas Tech University,
Lubbock, TX 79409
Mem. ASME

J. J. Saavedra
Mechanical Engineering Department,
Intel Corporation,
Phoenix, AZ

T. Suwanprateep
Department of Mechanical Engineering,
Kasetsart University,
Bangkok, Thailand

Liquid Jet Impingement Cooling of a Rotating Disk

Results are presented from an experimental study conducted to determine the average convective heat transfer coefficient for the side of a rotating disk, with an approximately uniform surface temperature, cooled by a single liquid jet of oil impinging normal to the surface. Tests were conducted over a range of jet flow rates, jet temperatures, jet radial positions, and disk angular velocities with various combinations of three jet nozzle and disk diameters. Correlations are presented that relate the average Nusselt number to rotational Reynolds number, jet Reynolds number, jet Prandtl number, and dimensionless jet radial position.

Introduction

Impinging jets are used for heating and cooling purposes in numerous industrial applications, their principal advantage being that relatively high convective heat transfer coefficients can be obtained for a given mass flow rate. Many applications involve the submerged jet, where the surrounding environment is the same fluid as the jet, this fluid typically being air. Other applications involve an unsubmerged jet, where a jet of liquid impinges on a surface in a gaseous environment.

Due to the complex nature of the flow field associated with an impinging jet, most investigations have been experimental with the resulting correlations being used in schemes for predicting surface heat transfer rates. Examples of impingement surface and jet configuration combinations that have been investigated experimentally include a submerged jet, or an array of such jets, impinging on stationary flat or curved surfaces [1–6], a submerged jet impinging on a rotating disk [7], an unsubmerged liquid jet impinging on a stationary surface [8–10], and an unsubmerged liquid jet impinging on a rotating disk [10]. One practical application of this latter case, which is addressed by the present study, involves a common cooling technique employed in many power transmission gearing mechanisms where a jet of the liquid lubricant is directed to impinge on a frictionally heated component such as a bearing or gear. The mechanisms which employ this technique typically involve high rotational speeds where the bearings and gears are not immersed in the lubricant because of the prohibitively high churning losses that would result. The jet mass flow rate is generally much higher than that required to provide lubricant for the lubrication process, the main purpose of the relatively high flow rate being to provide the necessary cooling of the rotating component through convective heat transfer to the liquid lubricant. In order to design for adequate cooling, or to optimize the cooling in the interest of minimizing pumping power requirements and the size and weight of cooling system components, convective heat transfer coefficients associated with unsubmerged liquid jets impinging on rotating surfaces are needed. The work reported in [10] was undertaken as a first step toward providing such data.

Reference [10] presents results for the case of a single circular jet of oil impinging normal to the face of a disk rotating in an air environment, a configuration intended to represent impingement on the side of a rotating machine element such as a gear. In that study, tests were conducted for a range of jet mass flow rates and disk angular velocities with various combinations of jet nozzle diameter and disk diameter. The jet flow conditions were maintained such that the jet was laminar for all experiments. For the majority of the experiments, the axis of the jet was coincident with the axis of rotation of the disk (axisymmetric impingement), although limited experiments were conducted to determine the effect of locating the jet axis at other radial positions (asymmetric impingement). Jet Prandtl number Pr was held constant at 270, and the difference between the approximately uniform disk surface temperature T_s and the temperature of the impinging jet T_j was maintained small to minimize property variations in the oil layer flowing over the disk surface. The heat transfer being dominated by the relatively thin liquid layer flowing over the disk surface away from the stagnation region beneath the jet, and the adiabatic wall temperature being approximately equal to that of the jet, the average convective heat transfer coefficient for the side of the disk was defined as

$$\bar{h} = \frac{q}{A(T_s - T_j)} \tag{1}$$

It was found that the data could be reasonably well correlated with the Nusselt number based on disk diameter $\overline{\mathrm{Nu}}_D$, given in terms of the rotational Reynolds number Re_r and the jet Reynolds number Re_j. All three of these dimensionless variables were calculated using the oil properties evaluated at the temperature of the jet T_j. The present study was undertaken to determine the effect of Pr, to define more completely the effect of the radial location of the jet, and to include these variables, along with Re_r and Re_j, in a concise relationship for $\overline{\mathrm{Nu}}_D$.

Experimental Apparatus and Procedures

Test Facility. The experimental test facility is shown in Fig. 1. The facility employs an aluminum disk which rotates in a horizontal plane inside a stainless steel cylindrical enclosure, 0.603 m in diameter and 0.387 m high, fitted with a transparent cover. The disk is encased in thermal insulation around its periphery and on its bottom side, with the top side serving as the heat transfer surface. The insulated disk, instrumented with embedded thermocouples and a thin, circular, electrical resistance heater on its botton side, is held in an aluminum housing which is attached to a hollow drive shaft driven by a variable-speed electric motor. Leads from the thermocouples and heater are routed through the hollow drive shaft and attached to a mercury slip ring which is used to supply power to the disk heater and to transmit voltage signals from the disk thermocouples to a potentiometer for determining disk temperature. Wattmeters are provided to measure the power supplied to the disk heater, and an electronic counter is used to determine the angular velocity of the disk.

Oil is drawn from a heated, temperature-controlled reservoir by a positive displacement gear pump and is supplied to a

Contributed by the Heat Transfer Division for publication in the JOURNAL OF HEAT TRANSFER. Manuscript received by the Heat Transfer Division February 7, 1985.

thermally insulated plenum chamber mounted above the enclosure. A thermocouple is inserted into the plenum for determining the oil temperature in the plenum, and a pressure tap is provided for measuring plenum pressure with bourdon gages. Extending downward from the plenum is a nozzle from which the oil issues as a free jet and impinges on the top side of the disk. After flowing over the disk, the oil collects in the bottom of the enclosure, flows out a drain to a heat exchanger used for cooling the oil, and then returns to the reservoir. Jet mass flow rate is controlled by the use of valves and a bypass line arrangement.

Disks and Nozzles. Disks with diameter D of 10.0, 20.0, and 28.3 cm were employed in this study. All disks are 2.54 cm thick and were machined from the same piece of 7075-T6 aluminum, a material with a relatively high thermal conductivity of 121.4 W/m-K, which was chosen to provide a disk surface temperature as uniform as possible. The material used to insulate each disk is a nylon which has a relatively low thermal conductivity of 2.94 W/m-K. This nylon was machined to provide an insulation thickness of 1.27 cm both at the periphery and on the bottom of each disk.

For determining disk surface temperature, each disk is provided with three type K thermocouples, made from 0.254-mm-dia wire with a small spherical bead forming the junction. Each thermocouple bead is located within 1.6 mm of the heat transfer surface, having been inserted into a blind hole drilled from the bottom side of the disk, and is held in place with thermally conductive cement. For all disks, one of the three thermocouples is located within about 3 mm of the disk periphery. For the disks used in the experiments with axisymmetric impingement, the other two thermocouples are located at $r/R = 0$ and 0.5, while for the disks used in the experiments with asymmetric impingement they are located at $r/R = 0.33$ and 0.70. All thermocouples were checked prior to installation and were found to be accurate to within ± 0.3 K at 273 K.

The nozzle is a straight stainless steel tube, 0.305 m long, with constant internal diameter. Three different nozzles with diameter d of 0.2, 0.4, and 0.8 cm were used in the experiments. Each nozzle is flared at the entry to provide a smooth flow transition as the oil enters the nozzle from the plenum, and each nozzle is wrapped with thermal insulation over its length to minimize the temperature drop in the oil between the plenum and the nozzle exit. Calibrations were conducted to determine jet mass flow rate as a function of plenum pressure and temperature for all three nozzles over the complete range of operating conditions employed in the experiments.

Test Oil. The oil used in the experiments is a commercially available petroleum-base heat transfer fluid. Equations for the properties as a function of absolute temperature were determined from data supplied by the manufacturer. The oil temperature range employed in the present study, 320 K to 375 K, falls well within the range of temperatures for which the property data apply. The property equations are

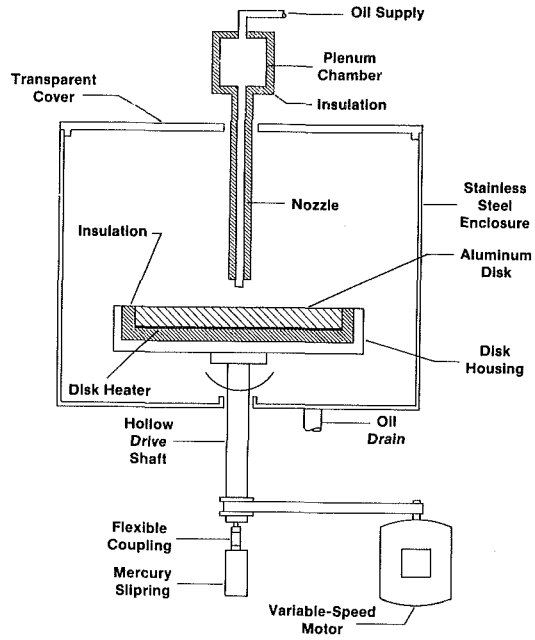

Fig. 1 Experimental test facility

$$k = 0.1623 - 1.383 \times 10^{-4} T \tag{2}$$

$$c_p = 686.4 + 3.833T \tag{3}$$

$$\nu = 10^{-6}\{\log^{-1}[\log^{-1}(9.937549 - 3.898842 \log T)]\} - 0.6\} \tag{4}$$

$$\rho = 1063.2 - 0.70964T \tag{5}$$

Experimental Procedures. For all experiments the free jet was maintained laminar with the spacing between the nozzle exit and the disk surface set to about 4 cm. It was experimentally determined that there was no effect of this spacing on disk heat transfer as long as the jet did not undergo transition from a laminar to a turbulent condition before impinging on the disk. Metzger et al. [9] also found no effect of jet exit-to-disk spacing over the range of from one to three nozzle diameters.

Each experiment was conducted at steady-state conditions, and the average convective heat transfer coefficient for the side of the disk $\bar{h}$ was obtained from equation (1). Due to the relatively low emissivity of the aluminum surface and the low disk temperatures involved, the radiation heat transfer loss from the disk surface is negligible in comparison with the convective heat transfer due to the impinging jet. The heat transfer through the disk insulation is also relatively small, but was accounted for by subtracting a small correction from the disk heater wattmeter reading to obtain q. This correction, which was determined in separate tests for each disk assembly, amounted to less than a 4 percent correction to $\bar{h}$.

For the case of axisymmetric impingement, the deviation

Nomenclature

A = disk surface area exposed to impinging jet
c_p = specific heat of test oil (equation (3)), J/kg-K
d = jet nozzle diameter
D = disk diameter
$\bar{h}$ = average convective heat transfer coefficient
k = thermal conductivity of test oil (equation (2)), W/m-K
$\overline{\mathrm{Nu}}_D$ = average Nusselt number $= \bar{h}D/k$
Pr = jet Prandtl number $= \mu c_p/k$
q = rate of heat transfer from disk surface by convection
r = radial coordinate of the impingement point
R = disk radius
Re_j = jet Reynolds number $= dU_j/\nu$
Re_r = rotational Reynolds number $= \omega D^2/\nu$
T = absolute temperature (equations (2-5)), K
T_j = jet temperature
T_s = disk surface temperature
U_j = average jet velocity
μ = absolute viscosity of test oil
ν = kinematic viscosity of test oil (equation (4)), m^2/s
ρ = density of test oil (equation (5)), kg/m^3
ω = angular velocity of disk

from the desired uniform disk surface temperature condition was spot checked over the complete range of operating conditions with all three disks. The temperature difference between the disk center and the edge was usually less than 1 K, the largest difference of about 1 K being observed with the 28.3-cm-dia disk. In most cases, the average of the three thermocouple readings was very nearly the same as the temperature indicated by the thermocouple at $r/R = 0.5$. Thus for all experiments with axisymmetric impingement, the temperature indicated by this thermocouple was taken as the average disk temperature T_s. For the case of asymmetric impingement, thermocouple readings from all three disk thermocouples, which agreed to within less than 1 K, were obtained for all tests, and the average was used for T_s. For all experiments, the difference between the average disk temperature and the jet temperature, the latter being taken to be the temperature of the oil in the plenum, was maintained at about 3 K. This relatively small temperature difference was chosen as a compromise between the desire to obtain reasonable accuracy in the determination of $\bar{h}$ and the desire to minimize property variations in the oil layer flowing over the disk.

An uncertainty analysis based on the methods of [11] was conducted which gave an uncertainty in $\bar{h}$ of approximately ± 13 percent. Further details concerning the experimental apparatus and procedures are contained in [12, 13].

Range of Experimental Parameters

Experiments were conducted for three nominal values of T_j of 375 K, 330.7 K, and 320.1 K resulting in nominal values of Pr of 87, 270, and 400, respectively. The lowest and highest values of Pr were fixed by the oil heating and cooling capabilities of the experimental apparatus when operating under a steady-state condition. The value of Pr of 270 was chosen for direct comparison with the results of [10]. At each Pr, experiments were conducted with various combinations of jet mass flow rate, nozzle diameter, disk diameter, disk angular velocity, and jet radial position. Table 1 presents the ranges of the dimensionless variables where the oil properties appearing in each variable have been evaluated at T_j. At each Pr, data were obtained for at least three values of Re_j, and for each combination of Pr and Re_j, from five to eight values of Re_r were selected over each range of Re_r shown in the table. The values for Pr and Re_j shown in the table are nominal values; actual values of these parameters varied from experiment to experiment by about ± 5 percent from the nominal. For all combinations of Pr, Re_j, and Re_r, data were obtained for axisymmetric impingement where the dimensionless jet radial position r/R is zero. For selected combinations of Pr, Re_j, and Re_r, data were also obtained for asymmetric impingement with values of $r/R = 0.2$, 0.4, 0.6, and 0.8.

Results for Axisymmetric Impingement

Effect of Rotational Reynolds Number and Jet Reynolds Number. Selected results for impingement with the nozzle axis at $r/R = 0$ are presented in Fig. 2 where, to show the effect of rotational Reynolds number, $\overline{\mathrm{Nu}}_D$ is plotted versus Re_r on logarithmic coordinates for the three values of Pr. For Pr = 87 (Fig. 2*a*), data are included for the minimum, the maximum, and one intermediate value of Re_j. For Pr = 270 (Fig. 2*b*) and 400 (Fig. 2*c*), data are included only for the minimum and the maximum Re_j, the data for intermediate Re_j having been omitted for clarity. The various combinations of D and d used to obtain these data are indicated in the figure. The best-fit straight line drawn for each Pr–Re_j combination is seen to fit the data reasonably well.

In Fig. 3, $\overline{\mathrm{Nu}}_D$ is plotted versus Re_j for the three values of Pr. For each Pr, data are presented for three values of Re_r, the highest and lowest being representative of the maximum and minimum values of Re_r employed in the experiments. Data for

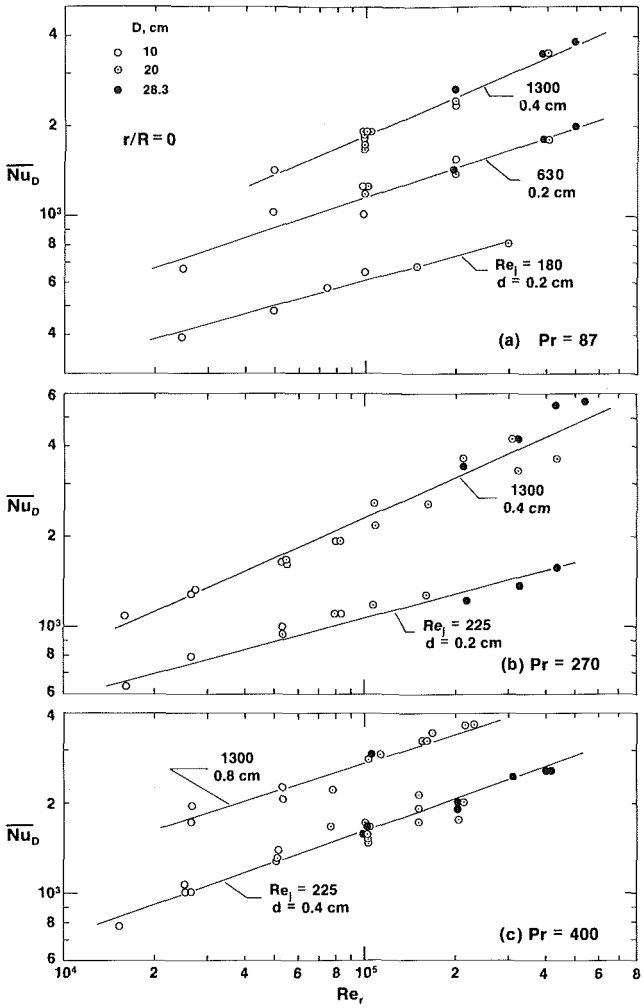

Fig. 2 Effect of Re_r on $\overline{\mathrm{Nu}}_D$ for various Re_j for three different Pr: (*a*) Pr = 87, (*b*) Pr = 270, (*c*) Pr = 400; $r/R = 0$

one intermediate value of Re_r are shown, the data for other intermediate Re_r again being omitted for clarity. The various combinations of D and d used to obtain these data are also indicated in the figure. The data were selected for the plot such that the Re_r for each data point does not deviate by more than ± 5 percent from the nominal Re_r indicated for each curve. Again, the best-fit straight line drawn for each Pr–Re_r combination fits the data reasonably well.

As seen in Fig. 3, for each of the three Pr there is a consistent tendency for the slope of the $\overline{\mathrm{Nu}}_D$ versus Re_j curves to increase as Re_r increases. A similar trend can be seen in Fig. 2 where for Pr = 87 and 270 the slope of the curves of $\overline{\mathrm{Nu}}_D$ versus Re_r increases as Re_j is increased. This trend is not observed for Pr = 400 in Fig. 2 probably because for the data obtained with $\mathrm{Re}_j = 1300$, the maximum value of Re_r employed for the tests with Pr = 400 was about half that employed for the tests with Pr = 87 and 270. This change in slope is probably the result of transition from laminar to turbulent flow in the oil layer flowing away from the stagnation region; however, no criterion for transition for this particular flow situation has been established. To establish such a criterion, which would most likely involve a dependence on both Re_j and Re_r, would require a more elaborate experimental setup that would enable the determination of local heat transfer coefficients as a function of the radial coordinate r.

Qualitatively, the behavior of $\overline{\mathrm{Nu}}_D$ with Re_r and Re_j at Pr = 270 is in agreement with the results of [10], in that the data are relatively well correlated through the use of Re_r and

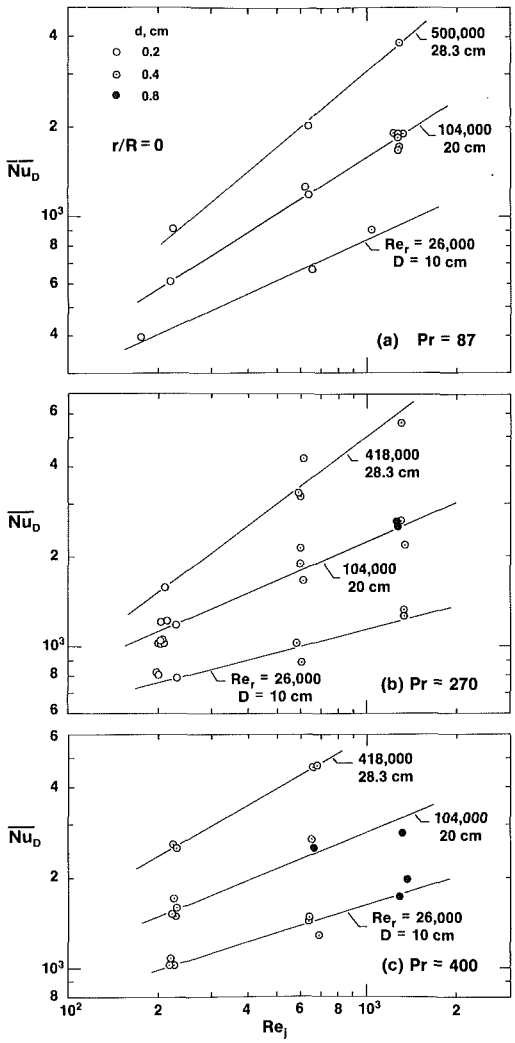

Fig. 3 Effect of Re_j on $\overline{Nu}_D$ for various Re_r for three different Pr: (*a*) Pr = 87, (*b*) Pr = 270, (*c*) Pr = 400; $r/R = 0$

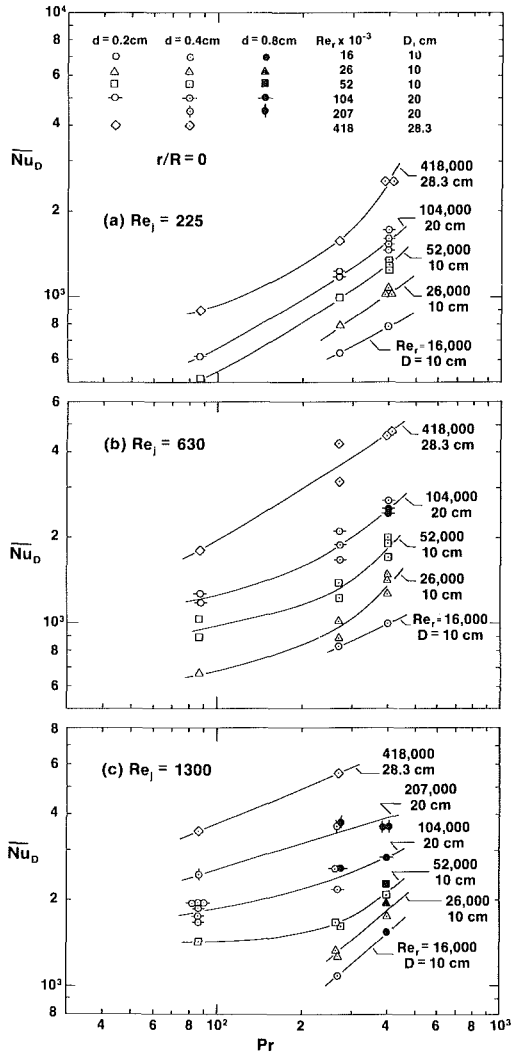

Fig. 4 Effect of Pr on $\overline{Nu}_D$ for various Re_r for three different Re_j: (*a*) Re_j = 225, (*b*) Re_j = 630, (*c*) Re_j = 1300; $r/R = 0$

Re_j, and $\overline{Nu}_D$ increases exponentially as either of these two dimensionless variables is increased while the other is held constant. A quantitative comparison between the results of the present study and those of [10] is given when the correlation of results is discussed.

Effect of Disk-to-Nozzle Diameter Ratio. Due to limitations on the maximum and minimum values of the disk angular velocity, the entire range of Re_r was not covered with any one disk diameter. Rather, as can be seen in Fig. 2, the lower values of Re_r were obtained with D = 10 cm, the intermediate values with D = 20 cm, and the higher values with D = 28.3 cm. However, it can also be seen in Fig. 2 that for most Re_j, the Re_r range obtained with D = 20 cm overlaps that obtained with D = 10 cm, the Re_r range obtained with D = 28.3 cm overlaps that obtained with D = 20 cm, and for many cases either two or all three disks were used to obtain approximately the same Re_r. Since, as indicated in Fig. 2, the data shown for each curve of constant Re_j were obtained with a single nozzle diameter, then in those cases where the same Re_r was obtained with different D there are represented two or three values of D/d. For the examples of these cases shown in Fig. 2, it can be seen that $\overline{Nu}_D$ is approximately the same regardless of the value of D/d. In fact, no effect of D/d was observed over any of the range covered by the present study which was $12.5 \leq D/d \leq 141.5$. That D/d has little or no effect over the range covered by the present study is in agreement with the work reported in [10], where the D/d range was $6.3 \leq D/d \leq 100$. This may be contrasted with the results presented by Metzger et al. [9], which for oil impingement on a stationary disk show that $\overline{Nu}_D$ increases with increasing D/d for $D/d \lesssim 25$. From the results of the present study, it appears that the effect of rotation is to reduce or eliminate the influence of D/d in this range.

Effect of Jet Prandtl Number. The effect of the jet Prandtl number for axisymmetric impingement is shown in Fig. 4 where $\overline{Nu}_D$ is plotted versus Pr for various Re_r for nominal values of Re_j of 225 (Fig. 4*a*), 630 (Fig. 4*b*), and 1300 (Fig. 4*c*). The data were selected for this plot such that the Re_r for each data point shown does not deviate by more than about ± 5 percent from the nominal Re_r indicated for each curve. The legend of the figure shows the various combinations of d and D used to obtain the data. The curves drawn through the data have been sketched in by eye.

The plot shows that for any Re_j–Re_r combination, $\overline{Nu}_D$ increases with an increase in Pr. However, for certain values of Re_r the effect of Pr is noticeably dependent upon Re_j. This can be seen for Re_r = 52,000 and 104,000 where in the range $87 \leq Pr \leq 270$ the effect of Pr continually decreases as Re_j is increased. Whether or not this trend prevails at lower Re_r is not known since, in general, data for Pr = 87 were not obtained at the two lowest values of Re_r for the various Re_j.

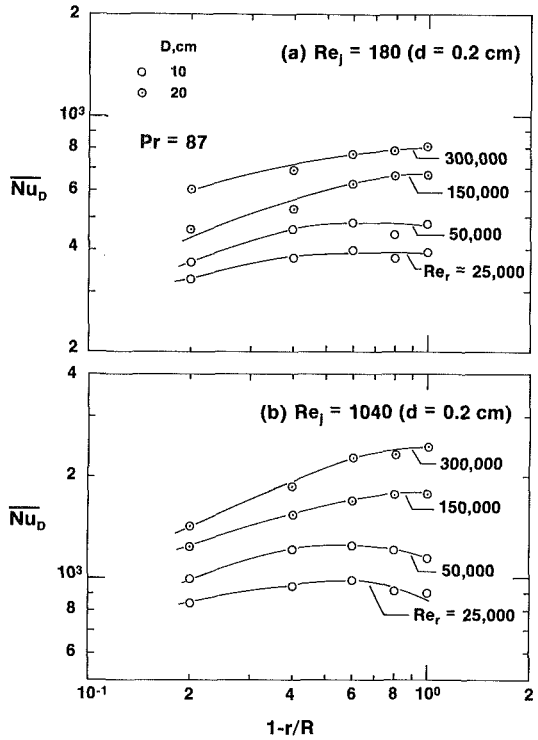

Fig. 5 Effect of r/R on $\overline{Nu}_D$ for various Re_r for two different Re_j: (*a*) Re_j = 180, (*b*) Re_j = 1040; Pr = 87

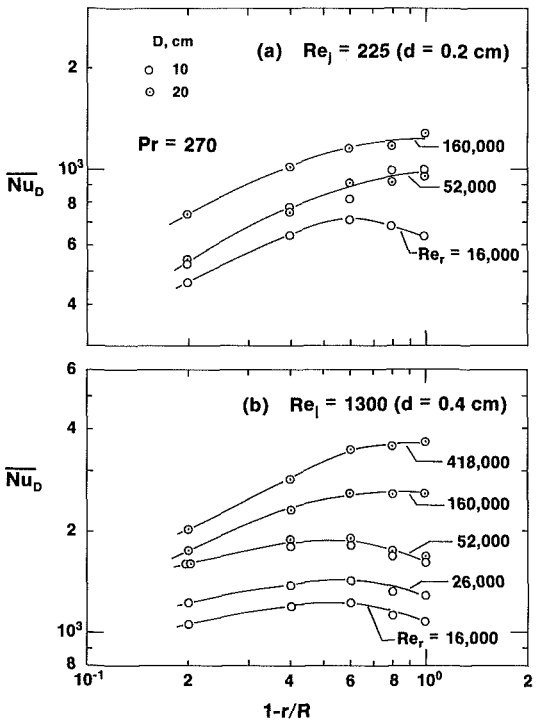

Fig. 6 Effect of r/R on $\overline{Nu}_D$ for various Re_r for two different Re_j: (*a*) Re_j = 225, (*b*) Re_j = 1300; Pr = 270

Results for Asymmetric Impingement

Examples of the variation of $\overline{Nu}_D$ with dimensionless jet radial position r/R are shown in Figs. 5, 6, and 7 where, in each figure, $\overline{Nu}_D$ has been plotted versus $1-r/R$ for various Re_r for two values of Re_j. Figure 5 is for Pr = 87 with Re_j = 180 and 1040, Fig. 6 is for Pr = 270 with Re_j = 225 and 1300, and Fig. 7 is for Pr = 400 with Re_j = 225 and 1300. The disk

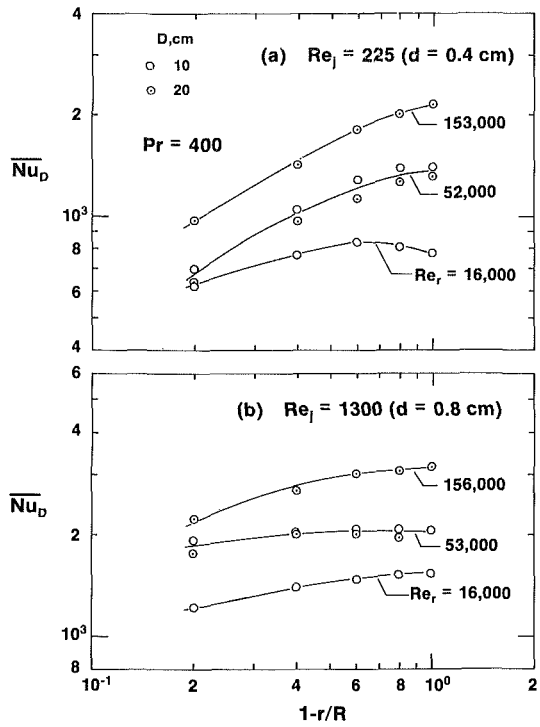

Fig. 7 Effect of r/R on $\overline{Nu}_D$ for various Re_r for two different Re_j: (*a*) Re_j = 225, (*b*) Re_j = 1300; Pr = 400

and nozzle diameters used to obtain the data are indicated in the figures. The curves drawn through the data have been sketched in by eye.

For these experiments where $r/R \neq 0$, data were obtained only with the 10- and 20-cm-dia disks. In general, as with the experiments conducted for $r/R = 0$, the smaller disk was used to obtain the lower values of Re_r, and the larger disk was used to obtain the higher values of Re_r. However, data were obtained in a few cases with the two disks being used to produce the same Re_r with the results indicating that the dimensionless radial position of the jet r/R can be used to correlate the data. These results can be seen in Figs. 6 and 7 for Re_r = 52,000.

Examination of Figs. 5, 6, and 7 shows that, in general, regardless of the values of Pr and Re_j, at low Re_r there is a nonmonotonic behavior of $\overline{Nu}_D$ with r/R, $\overline{Nu}_D$ first increasing to a maximum occuring at $r/R \simeq 0.4$, and then decreasing with further increase in r/R. The one exception to this is seen in Fig. 7(*b*) where at Re_r = 16,000, $\overline{Nu}_D$ decreases monotonically with increasing r/R. Figures 5, 6, and 7 also show that, again regardless of the values of Pr and Re_j, at higher values of Re_r, $\overline{Nu}_D$ decreases monotonically with an increase in r/R. Although not all the data have been presented here, for any given Pr and Re_j the nonmonotonic behavior was never observed for $Re_r \geq 100{,}000$, and the maximum value of $\overline{Nu}_D$ was always observed to occur at $r/R \simeq 0.4$.

The fact that the nonmonotonic behavior occurs only at low Re_r most likely indicates that at low Re_r the jet tends to dominate the heat transfer process, but that heat transfer can be enhanced by displacing the jet radially to introduce the beneficial effect of increasing the disk surface velocity beneath the jet. However, continuing to increase r/R eventually results in a starvation condition where some portion of the surface is not covered by the oil film. Visual observation of the oil film flowing over the disk surface verified that this occurs. On the other hand, at high Re_r the rotationally induced flow field tends to dominate the heat transfer process, and displacing the jet away from $r/R = 0$ results in a monotonic decrease in $\overline{Nu}_D$ as the disk surface is less effectively bathed by the oil film. For the range of variables employed in this study, the enhancement of the heat transfer process by radial displacement

Table 1 Ranges of experimental parameters

Pr	Re_j	Range of Re_r	Range of r/R
87	180	25,000–300,000	0–0.8
	225	50,000–510,000	0
	630	25,000–505,000	0
	630	25,000–300,000	0–0.8
	1040	25,000–300,000	0–0.8
	1300	50,000–500,000	0
270	225	16,000–440,000	0
	225	16,000–165,000	0–0.8
	580	16,000–435,000	0–0.8
	630	25,000–545,000	0
	1300	16,000–535,000	0
	1300	16,000–435,000	0–0.8
400	225	16,000–430,000	0
	225	16,000–155,000	0–0.8
	630	16,000–430,000	0
	630	16,000–155,000	0–0.8
	1300	16,000–230,000	0
	1300	16,000–160,000	0–0.8

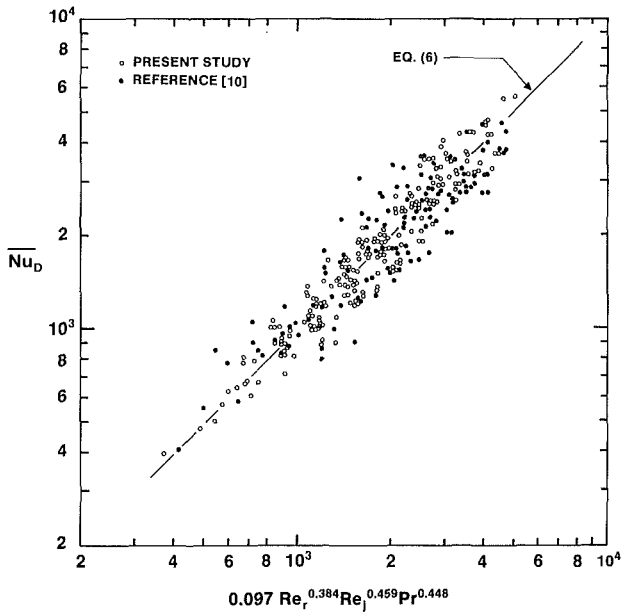

Fig. 8 Correlation of results for axisymmetric impingement

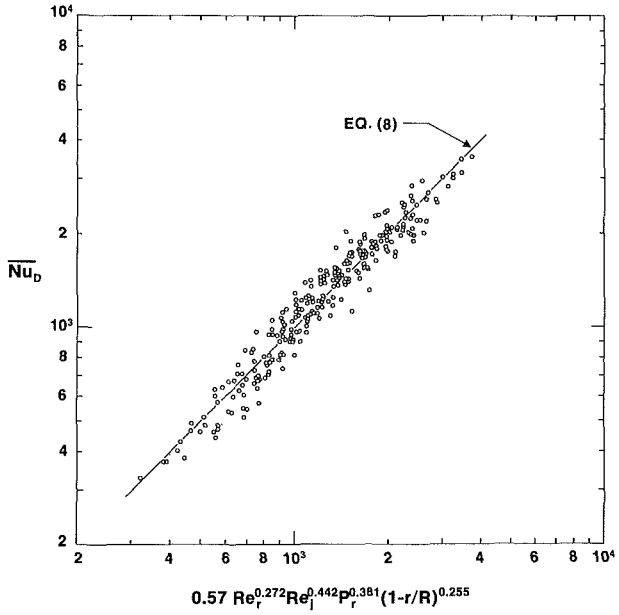

Fig. 9 Correlation of results for asymmetric impingement

of the jet is not very significant, the maximum value of $\overline{Nu}_D$ typically being less than 15 percent greater than that for $r/R = 0$. The data of Figs. 5, 6, and 7 also show that, similar to the case where $r/R = 0$, at any given value of $r/R \neq 0$, $\overline{Nu}_D$ increases monotonically with an increase in Re_r, Re_j, and Pr as any one of these three parameters is varied while the other two are held constant.

Correlation of Results

The data were analyzed in various ways in order to develop reasonably simple correlations of $\overline{Nu}_D$ in terms of the dimensionless variables of Re_r, Re_j, Pr, and r/R. The best representation of the data was obtained with two correlations, one for the axisymmetric case and one for the asymmetric case. For the axisymmetric case, a multiple linear regression analysis, which neglects the nonlinear behavior of $\overline{Nu}_D$ with Pr as seen in Fig. 4, yielded the correlating equation

$$\overline{Nu}_D = 0.097\ Re_r^{0.384}\ Re_j^{0.459}\ Pr^{0.448} \tag{6}$$

which represents 95 percent of the 200 data points to within ± 30 percent and is considered to be applicable for the ranges

$$16{,}000 \leq Re_r \leq 545{,}000$$

$$180 \leq Re_j \leq 1300$$

$$87 \leq Pr \leq 400$$

$$r/R = 0$$

The fit between all the data for $r/R = 0$ and equation (6) is shown in Fig. 8. Also shown in Fig. 8 are the data from [10], which were obtained with the same basic test apparatus, experimental procedures, and jet nozzles as used in the present study, but with different disk models with diameters of 5, 10, and 20 cm and a different petroleum-base oil. The ranges of the dimensionless variables in that study were $6250 \leq Re_r \leq 400{,}000$ and $230 \leq Re_j \leq 1800$. As mentioned previously, Pr was held constant at 270. The correlation obtained was

$$\overline{Nu}_D = 3.4\ Re_r^{0.413} Re_j^{0.250} \tag{7}$$

Comparison of equations (6) and (7) shows relatively good agreement as far as dependence of $\overline{Nu}_D$ on Re_r is concerned, but a noticeably different dependence of $\overline{Nu}_D$ on Re_j. This disagreement is at least partially explained by the increase in the slope of the $\overline{Nu}_D$ versus Re_j curves with an increase in Re_r as was seen in Fig. 3. Since in the present study the maximum Re_r is about 36 percent higher than the maximum employed in the work of [10], the effect is to increase the value of the exponent of Re_j in the overall correlation. A quantitative comparison shows that over the range $16{,}000 \leq Re_r \leq 400{,}000$, $\overline{Nu}_D$ predicted by equation (7) does not deviate from that pre-

dicted by equation (6) by more than 8 percent for the midrange Re_j of 630, nor by more than 16 percent for $Re_j = 1300$. The deviation is the largest for $Re_j = 225$ where it is 34 percent.

For the data obtained with $r/R \neq 0$, a multiple linear regression analysis, which neglects the nonmonotonic behavior of $\overline{Nu}_D$ with r/R, yielded the correlating equation

$$\overline{Nu}_D = 0.57\, Re_r^{0.272}\, Re_j^{0.442}\, Pr^{0.381}(1 - r/R)^{0.255} \qquad (8)$$

which represents 95 percent of the 264 data points to within ± 24 percent. The fit between equation (8) and the data is shown in Fig. 9. Equation (8) is considered to be applicable for the ranges

$$180 \leq Re_j \leq 1300$$

$$87 \leq Pr \leq 400$$

$$0.2 \leq r/R \leq 0.8$$

and for essentially the same range of Re_r given for equation (6). However, it should be noted in Table 1 that for $Pr = 87$ and particularly for $Pr = 400$, the maximum value of Re_r employed in the experiments for $r/R \neq 0$ was somewhat less than that for $r/R = 0$.

Acknowledgments

This material is based upon work supported by the National Science Foundation under Grant No. CME-7916252.

References

1 Gardon, R., and Cobonpue, J., "Heat Transfer Between a Flat Plate and Jets of Air Impinging on It," in: *International Developments in Heat Transfer*, ASME, New York, 1961, pp. 454–460.

2 Huang, G. C., "Investigations of Heat-Transfer Coefficients for Air Flow Through Round Jets Impinging Normal to a Heat-Transfer Surface," ASME JOURNAL OF HEAT TRANSFER, Vol. 85, 1963, pp. 237–245.

3 Gardon, R., and Akfirat, J. C., "The Role of Turbulence in Determining the Heat-Transfer Characteristics of Impinging Jets," *International Journal of Heat and Mass Transfer*, Vol. 8, 1965, pp. 1261–1272.

4 Gardon, R., and Akfirat, J. C., "Heat Transfer Characteristics of Impinging Two-Dimensional Air Jets," ASME JOURNAL OF HEAT TRANSFER, Vol. 88, 1966, pp. 101–108.

5 Metzger, D. E., Yamashita, T., and Jenkins, C. W., "Impingement Cooling of Concave Surfaces With Lines of Circular Air Jets," ASME *Journal of Engineering for Power*, Vol. 91, 1969, pp. 149–158.

6 Sparrow, E. M., Altemani, C. A. C., and Chaboki, A., "Jet-Impingement Heat Transfer for a Circular Jet Impinging in Crossflow on a Cylinder," ASME JOURNAL OF HEAT TRANSFER, Vol. 106, 1984, pp. 570–577.

7 Metzger, D. E., and Grochowsky, L. D., "Heat Transfer Between an Impinging Jet and a Rotating Disk," ASME JOURNAL OF HEAT TRANSFER, Vol. 99, 1977, pp. 663–667.

8 McMurray, D. C., Myers, P. S., and Uyehara, O. A., "Influence of Impinging Jet Variables on Local Heat Transfer Coefficients Along a Flat Surface With Constant Heat Flux," *Proceedings of the 3rd International Heat Transfer Conference*, Vol. II, Chicago, 1966, pp. 292–299.

9 Metzger, D. E., Cummings, K. N., and Ruby, W. A., "Effects of Prandtl Number on Heat Transfer Characteristics of Impinging Liquid Jets," *Proceedings of the 5th International Heat Transfer Conference*, Vol. 2, Tokyo, 1974, pp. 20–24.

10 Carper, H. J., and Deffenbaugh, D. M., "Heat Transfer From a Rotating Disk With Liquid Jet Impingement," *Proceedings of the 6th International Heat Transfer Conference*, Vol. 4, Toronto, 1978, pp. 113–118.

11 Kline, S. J., and McClintock, F. A., "Describing Uncertainties in Single Sample Experiments," *Mechanical Engineering*, Vol. 75, Jan. 1953, pp. 3–8.

12 Saavedra, J. J., "Effect of Prandtl Number on Impingement Cooling of Rotating Bodies," M.S. Thesis, Texas Tech University, Lubbock, TX, 1981.

13 Suwanprateep, T., "Effect of Jet Position and Shaft Obstruction on Impingement Cooling of Rotating Bodies," M.S. Thesis, Texas Tech University, Lubbock, TX, 1982.

Heat Transfer and Flow Visualization in Natural Convection in Rapidly Spinning Systems

L. Sobel
Research Assistant.

M. El-Masri
Associate Professor.

J. L. Smith
Professor.
Mem. ASME

Department of Mechanical Engineering,
Massachusetts Institute of Technology,
Cambridge, MA 02139

The design of airborne superconducting generators for intermittent duty requires the understanding of some unique free-convection processes in the spinning helium bath. Toward that end, some fundamental experiments on steady and transient free convection in rotating containers of representative geometries have been performed. Heat transfer data from heaters of various geometries mounted on the outer container surface to several fluids are reported. A correlation for steady-state Nusselt number is presented for a wide range of Rayleigh and Prandtl numbers. The heat transfer coefficient was found to be independent of heater size, geometry, and fluid viscosity. Heat transfer measurements during simultaneous thermal transients and sudden increases in rotational speed were also made. They show an enhancement of heat transfer due to the relative counterrotation of the fluid following the acceleration of the container. This persists for a period well below that for fluid spinup. A model based upon the submergence of the thermal boundary layer by the diffusive wave from the wall was successful in correlating this period. Quasi-steady flow visualization experiments indicate that the thermal plumes generate two-dimensional, axially invariant flow fields. Their trajectories are radial relative to the spinning container. Those observations are shown to be consistent with the fact that weak buoyant plumes in containers rotating at small Ekman numbers result in low Rossby number motions. Those are two dimensional according to the Taylor–Proudman theorem. It is shown that the Coriolis and pressure forces on such a thermal column are in azimuthal equilibrium, hence the radial trajectory. Flow visualization following impulsive acceleration in an off-axis, nonaxisymmetric container shows that the flow field is dominated by vortices expelled from corners. The fluid spinup time, however, was found to be the same as that for an on-axis circular cylinder of the same characteristic diameter.

Introduction

The operation of a superconducting generator [1] requires the removal of heat from within the rotating machine. These generators have a rotating field winding wound from superconducting wire immersed in a liquid helium bath. During normal steady-state generator operation the heat generated within the field winding will initiate a buoyancy-driven helium circulation. The hot fluid convected inward induces boiling in regions close to the axis of the spinning machine. Work has now begun on a prototype airborne superconducting generator [2] which will be operated intermittently. This generator will be spun to rated speed when there is a need for power and then operated for a short period of time. The rotor will normally be idled at a much lower speed. The demands on the cooling system for such a machine are naturally more severe than those of a conventional rotor because coolant flow and thermodynamic transients are coincident with significant transient heating in the field winding itself. The rotor must be fully operational in a time that is short compared with conventional rotor cooling system time constants.

The work reported here is most relevant to large pool natural convection initiated by isolated small thermal sources in rapidly spinning systems. Figure 1 is an example of the geometry shared by the various rotating apparatus constructed to model the transient thermal and fluid behavior of a helium-filled system. It shows a right circular annular cylinder filled with fluid. The cylinder is fitted with two radial baffles. A small heater is affixed to the outer cylinder wall and the heater surface is parallel to the axis of rotation. (The heater dimensions are not necessarily small compared to the dimensions of the container.) In the material to follow, pictures and surface heat transfer coefficient data will be presented which characterize the resulting flow in the container when the heater is turned on.

Natural convection flows have been observed in two different situations. In the first series of tests the heater was turned on a long time after the fluid in the container had come to be in solid body rotation (the fluid was motionless relative to the walls of the container). In the second series of tests the heater was energized just as the fluid-filled container was impulsively accelerated to a higher rotation rate. The purpose here was to assess the impact of the motion of the fluid relative to the walls of the container on the surface heat transfer coef-

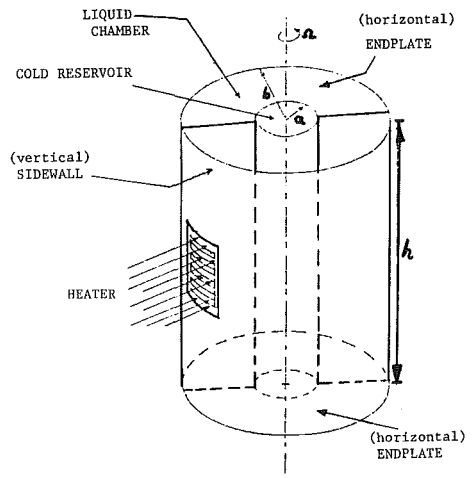

Fig. 1 Sketch of annular liquid reservoir with radial baffles and small heat source at the outer radius; heater surface is parallel to axis of rotation

Contributed by the Heat Transfer Division and presented at the ASME Winter Annual Meeting, New Orleans, Louisiana, December 9-13, 1984. Manuscript received by the Heat Transfer Division January 2, 1985.

ficient. The former class of experiments will be referred to as quasi-steady heat transfer tests in the discussion to follow. The test was quasi-steady because the bulk fluid in the container absorbed all the heater power, although the test duration was short enough (less than a minute in the longest test) to make bulk fluid temperature changes negligible. The latter class of tests will be referred to as transient spinup heat transfer tests. In this testing mode, heat transfer was a combination of natural convection and forced convection. The motion of the container radial walls initially imparted some additional irrotational motion to the fluid and this augmented the surface heat transfer coefficient.

The centrifugal accelerations in these experiments extended over a range of 27 to 120 times the earth's gravity. During the transient heat transfer tests the container acceleration rates were of the order of 100 rpm/s. The dynamics of fluid convection discussed in this paper were unaffected by the earth's gravity field. (Experiments with rotors spinning on a horizontal axis, however, revealed some interesting phenomena associated with air bubbles acted on by both gravity and rotational acceleration. These phenomena are described in [3].)

Quasi-Steady Heat Transfer Flow Visualization

Figure 2 shows a right square cylinder with an i.d. and axial height of 152 mm. The cylinder is fitted with a single, removable baffle. A small 40 ohm flat surface heater is attached to the outer wall. The container is filled with water to which a small amount of mica flakes coated with shiny titanium oxide have been added. These mica flakes are roughly 4 μm in diameter and tend to align themselves with strong shear stresses in the fluid within the container. The water-filled container is chucked up in a horizontal lathe and heater power is supplied via slip rings attached to the lathe spindle in the rear of the lathe. The lathe is then spun to 531 rpm and the container motion is observed by a strobe. When the fluid within the container is finally in solid body rotation the heater is turned on.

Figure 3(*a*) shows the starting plume as it accelerates away from the heater surface. Figure 3(*b*) shows the same plume a few moments later after the plume has reached the center of the container. Now these rather simple-looking plumes are quite extraordinary. It is surprising, first of all, to find that the plume is visible at all. The pictures shown in Fig. 3 are of fluid motions as seen through the front end plate of the rotating cylinder. The heater, however, is attached to the cylinder wall near the middle of the container (Fig. 2). Figure 3 therefore indicates that the hot fluid leaving the surface of the heater is dragging along a column of fluid that extends to the cylinder end plates where it can be seen and photographed. The hypothesis, subsequently proven with dyed fluid, was that a small slowly moving buoyant thermal creates a Taylor column

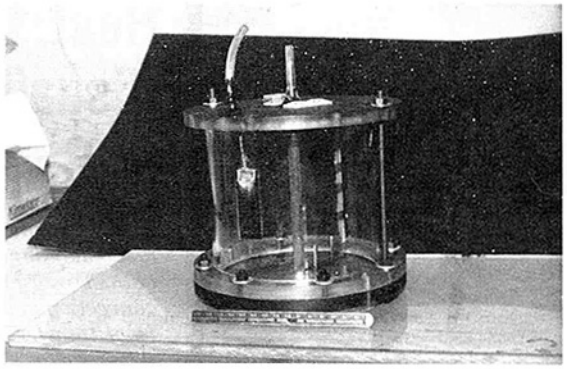

Fig. 2 Plexiglass cylinder with a small heater attached to the outer wall at container midheight

[4, 5], that is, a small amount of buoyant fluid will pull a column of nonbuoyant fluid inward just as if the heater had extended the full axial length of the container. This is illustrated in Fig. 4, where fluid path lines are made visible by electrolyzing a thymol blue/HCl solution, changing its color from amber to blue. The electrolyzing platinum wires, which generate the path lines, are distributed along the entire axial length of the spinning cylinder. Although the heater is at the axial midheight and is quite short, the entire motion is remarkably two dimensional. The fact that no fluid moves over or under the thermal (that no fluid changes in elevation) as the thermal moves inward can be explained as follows.

The buoyant plume moving radially inward assumes a velocity V and width b such that the buoyancy, inertia, and viscous forces acting upon it are all of the same order

$$\Delta\rho\omega^2 r \sim \frac{\rho V^2}{r} \sim \frac{\mu V}{b^2} \tag{1}$$

Those balances give the orders of magnitude for the dependent quantities V and b

$$\frac{V}{\omega r} \sim \sqrt{\frac{\Delta\rho}{\rho}}, \qquad \frac{b}{r} \sim \frac{E^{1/2}}{\left(\frac{\Delta\rho}{\rho}\right)^{1/4}} \tag{2}$$

where the Ekman number E is based on radius. Now in the experiments reported, the Ekman number E is on the order of 10^{-6} and the density ratio $(\Delta\rho/\rho)$ on the order of 10^{-3} near the heater, and falls with distance. This suggests that the motion generated should be of the form of a thin plume of low Rossby number,

$$\frac{b}{r} << 1, \qquad \mathrm{Ro} << 1 \tag{3}$$

Nomenclature

b = plume width, m
c = container characteristic radius, cylinder radius, m
cp = specific heat, J/kg K
E = Ekman number, $\nu/\omega h^2$
$\hat{e}_r$, $\hat{e}_\theta$ = unit vectors in the radial and tangential directions
F = force, N
h = container height, m; heat transfer coefficient, W/m^2 - K
k = thermal conductivity, W/m - K
l = heater length scale
Nu = Nusselt number = hl/k
Pr = Prandtl number = ν/α
p = pressure, N/m^2
Ra = Rayleigh number = $\omega^2 r \cdot \beta\Delta T l^3/\nu\alpha$
Rc = distance from center of rotation, m
Ro = Rossby number = $V/\omega r$
r = radius, m
u, v = radial and tangential velocity components, m/s
V = velocity relative to container, m/s
α = thermal diffusivity, m^2/s, angle
β = thermal expansion coefficient, 1/K, angle
δ = boundary layer thickness, m
Δ = difference
ν = kinematic viscosity, m^2/s
ρ = density, kg/m^3
τ = time constant(s), dimensionless time
ω = rotational speed, rad/s

Subscripts

r, θ = radial and tangential directions
ss = steady state
t = thermal
v = viscous

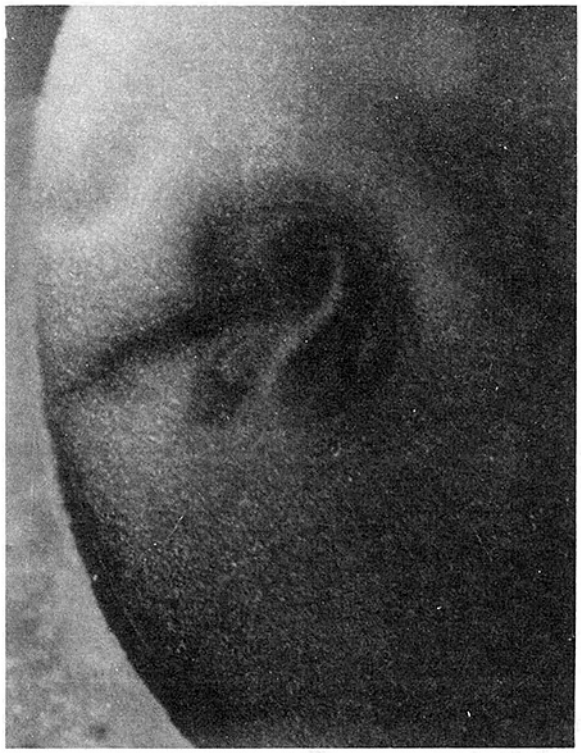

Fig. 3(*a*) Starting plume moving radially inward, produced by heater shown in Fig. 2; rotor speed 531 rpm

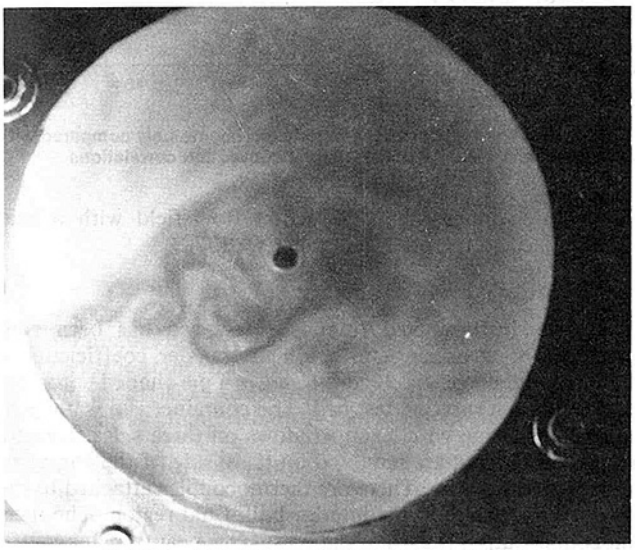

Fig. 3(*b*) Plume extending to centerline of rotor

In rotating flow theory, motions of low Rossby and Ekman numbers are known as geostrophic flows [6, 7]. The Navier–Stokes equations in the rotating frame simplify to a balance between Coriolis force and pressure gradient

$$2\omega \times \mathbf{V} = \frac{-\nabla p'}{\rho} \tag{4}$$

where

$$p' = p - \frac{1}{2}\rho\omega^2 r^2 \tag{5}$$

The inertia and viscous terms are of the order of Rossby and Ekman numbers and are negligible except for the thin, high shear regions. Taking the curl of equation (4) results in the Taylor-Proudman theorem

$$(\omega \cdot \nabla)\mathbf{V} = 0 \tag{6}$$

which implies that the velocity is invariant in the direction of

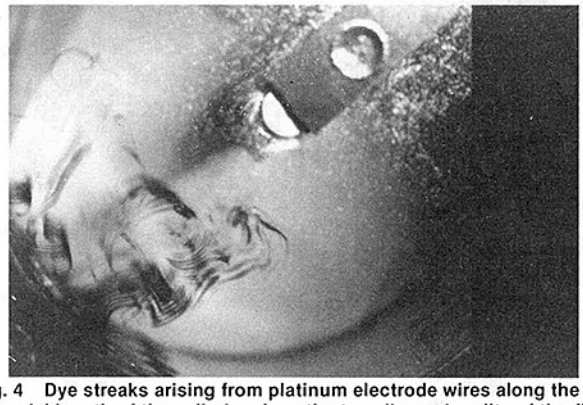

Fig. 4 Dye streaks arising from platinum electrode wires along the entire axial length of the cylinder show the two dimensionality of the flow generated by the short heater at axial midheight as shown in Fig. 2

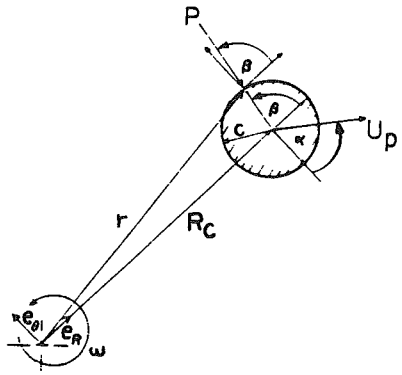

Fig. 5 Motion in an unbounded rotational fluid

ω, the axis of rotation, and the motion is therefore two dimensional in the (r, θ) plane since the end walls prevent axial velocities.

The second extraordinary feature of the plume photographed is that the trajectory is radial. A radial trajectory in a rapidly spinning system is only possible if there is a net force acting on moving fluid particles at right angles to their motion. This net force keeps the fluid within the plume from accelerating azimuthally relative to the walls of the container in order to conserve angular momentum. Many flow visualization experiments were performed with baffled as well as unbaffled cylinders (Figs. 3 and 4 show a plume in an unbaffled cylinder) and the plume trajectories have been the same. The trajectory is not a consequence of geometry. The external force acting on the buoyant column is supplied by the pressure field of the cold fluid streaming around the thermal.

This fact can be shown by considering an infinitely long solid cylinder moving normal to the axis of rotation with speed U_p relative to the fluid which is in solid body rotation (Fig. 5). This motion is resolved into components in the local coordinate system centered at the origin of the cylinder as follows

$$U_p = -U_p(\cos\alpha)\hat{e}_\theta + U_p(\sin\alpha)\hat{e}_r \tag{7}$$

where $\hat{e}_r$ is aligned with a radial line from the center of the spinning container and α is the angle between the direction of cylinder motion and the tangential as shown in Fig. 5. The fluid is incompressible, the flow two dimensional, and a stream function exists whose derivatives are the fluid velocity in the rotating frame

$$u = \frac{-\partial\psi}{r\partial\theta} \qquad v = \frac{\partial\psi}{\partial r} \tag{8}$$

The boundary condition at the surface of the cylinder gives

$$\frac{-\partial\psi}{c\partial\beta} = U_p \sin\alpha\cos\beta - U_p\cos\alpha\sin\beta \tag{9}$$

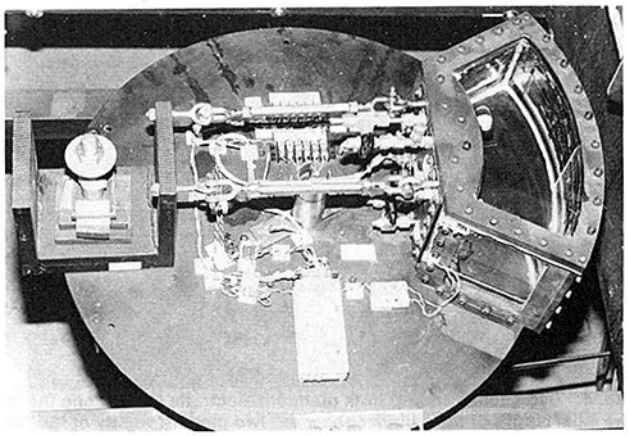

Fig. 6 Rotating apparatus consisting of water-filled aluminum/lexan container, electronics, and counterweight

The equation of motion for the inviscid flow streaming past the cylinder may be written as

$$\frac{d\mathbf{V}}{dt} = -\frac{1}{\rho}\nabla\left(p - 2\rho\omega\psi - \frac{\rho\omega^2 r^2}{2}\right) \tag{10}$$

It is convenient to decompose the pressure field into two components

$$p = p_1 + p_2 \tag{11}$$

such that the first component corresponds to an identical streaming flow in a nonrotating frame

$$-\frac{\nabla p_1}{\rho} = \frac{d\mathbf{V}}{dt} \tag{12}$$

and exerts no net force upon the cylinder. The remaining component due to rotation is thus given by equations (10), (11), and (12) as

$$\frac{p_2}{\rho} = 2\omega\psi + \frac{\omega^2 r^2}{2} + \text{const} \tag{13}$$

The net force exerted by the pressure field p_2 per unit length is given by its radial and tangential components as

$$\left.\begin{aligned} F_r &= \int_0^{2\pi} p_2 \cos\beta c d\beta \\ F_\theta &= \int_0^{2\pi} p_2 \sin\beta c d\beta \end{aligned}\right\} \tag{14}$$

Using equation (13) for the pressure p_2, together with the geometric relation

$$r^2 = R_c^2 + c^2 + 2R_c c\cos\beta \tag{15}$$

and noting that while ψ is unknown, its derivative given by equation (9) allows one to integrate equations (14) by parts to find

$$\left.\begin{aligned} F_r &= \rho\pi c^2(-\omega^2 R_c + 2\omega U_p \cos\alpha) \\ F_\theta &= \rho\pi c^2(2\omega U_p \sin\alpha) \end{aligned}\right\} \tag{16}$$

Thus the pressure field created by the fluid streaming past the cylinder has an asymmetric component p_2. This sets up forces opposite to the centrifugal and Coriolis forces on the cylinder. For the special case where the cylinder mass is the same as that of the fluid it displaces, the pressure field will exactly counterbalance the rotational forces on the moving cylinder. Since in our experiments the thermal front and the plume following it have an infinitesimal density deficit, their deflection from the radial is very small.

Flow visualization experiments have been performed with heaters of widely different shapes and cross sections. The plume trajectories were not radial in all cases. For sufficiently small heaters and sufficiently high surface heat fluxes the trajectories curve inward toward the centerline due to the larger value of $\Delta\rho/\rho$. It has not been possible, however, to generate a single three-dimensional convection flow field with a heat source fixed to the outer container wall.

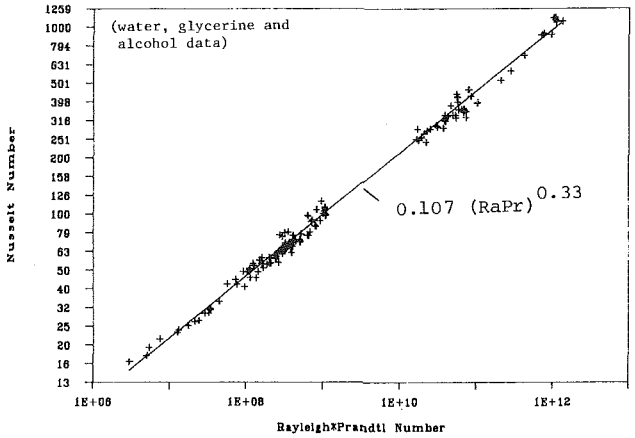

Fig. 7 Heat transfer data correlated with the Rayleigh number × Prandtl number product; data resulted from tests with water, a 40 percent glycerine/water solution, and alcohol

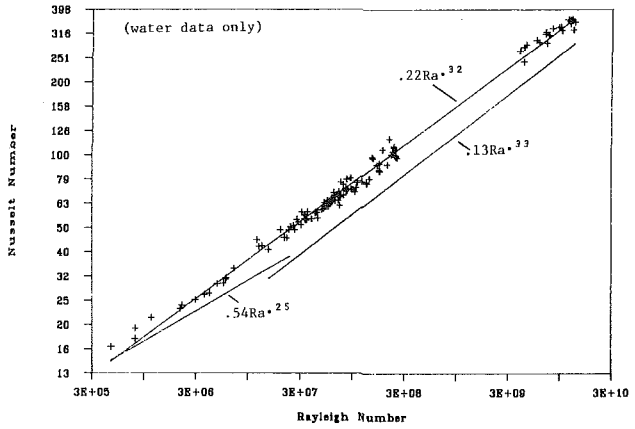

Fig. 8 Heat transfer data from water experiments only compared with standard laminar and turbulent natural convection correlations

Quasi-Steady Heat Transfer

A fully instrumented rotational test bed has been constructed for measuring surface heat transfer coefficients at high rotational speeds. Figure 6 shows a pie-shaped container mounted on a rotating test bed. The container is a watertight aluminum frame with lexan windows on three sides. Heaters of various shapes are mounted on the inside of the container outer lexan window. There are thermocouples attached to the heater surface and in the interior bulk fluid region. The thermocouple output is used to obtain surface heat transfer coefficients as a function of heat flux, fluid properties, and rotation rate. An onboard rotating data acquisition system multiplexes 11 analog thermocouple voltages from within the container, and converts each analog signal to a digital signal which is serially transmitted out of the rotating system with optical slip rings.

Over 150 quasi-steady heat transfer tests have been performed. Surface heat transfer coefficients as a function of heater power and rotation rate have been obtained for a glycerine/water solution, alcohol, and water. The range of centrifugal Rayleigh numbers (rotational acceleration $\omega^2 r$ substituted for g) covered in these tests is 10^5 to 10^{11}. The Prandtl number range was 4 to 40. The heat transfer data have been found to follow a relationship of the form

$$\text{Nu} = 0.107(\text{RaPr})^{0.33} \tag{17}$$

Figure 7 is a log–log plot of all the heat transfer data collected (water, water/glycerine, alcohol). The data include tests with

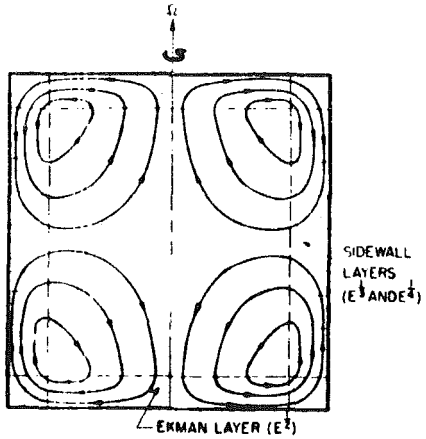

Fig. 9 Streamlines of spinup flow field; fluid acquires rotation after being flushed through Ekman layers on endplates

heaters of large and small axial extent (the dimension parallel to the axis of rotation) and heaters mounted in different places on the outer wall. Figure 8, on the other hand, is a logarithmic plot of the water data only compared with the standard laminar and turbulent natural convection correlations. The Rayleigh number in both figures is based on centrifugal acceleration. A linear regression of the water data alone yields a relationship of the form

$$\mathrm{Nu} = 0.22\mathrm{Ra}^{0.32} \tag{18}$$

The interesting implications of these two correlations (equations (17) and (18)) are as follows:

1 The conduction boundary layer is so thin at these high Rayleigh numbers that the surface heat transfer coefficient is not affected by the trajectory of the plume or the additional fluid dragged inward by the buoyant fluid.

2 The Nusselt number is apparently independent of fluid viscosity (the RaPr product cancels out the viscosity) indicating a conduction-dominated process of a sort associated with low Prandtl number fluids in Benard-like convection. This can be explained by the fact that the width scale of the fluid motion, b in equation (2), is much greater than the thermal boundary layer thickness over the heater.

3 The surface heat transfer coefficient is also independent of heater length, a fact related to the tendency of hot fluid to move radially inward all along the length of the heater; however, the competition of the disparate plumes trying to entrain ambient fluid causes these plumes to coalesce into a strong central plume rising off the center of the heater.

Spinup of a Homogeneous Fluid in a Nonaxisymmetric Geometry

An airborne superconducting generator will operate at rated speed only for short periods of time. The rotor, normally idling at low speed, will be accelerated at a rate of the order of 6000 rpm/s for 1 s when there is a sudden demand for power. Now it takes a finite amount of time for the on-board helium supply to come into solid body rotation. While the fluid is being spun up, the natural convection heat transfer coefficient will be smaller than the steady-state value corresponding to the instantaneous speed. This is because the fluid pressure gradient near the heater which drives the natural convection is not yet fully established. However, the relative motion of the fluid during spinup will augment the natural convection heat transfer coefficient h to an extent and in a manner that will be described below. The purpose of the investigation into spinup flows in general and the effect of fluid relative motion on the surface heat transfer coefficient in particular is thus to determine whether it is advantageous to exploit fluid relative motion with a generator reservoir design that inhibits fluid spinup.

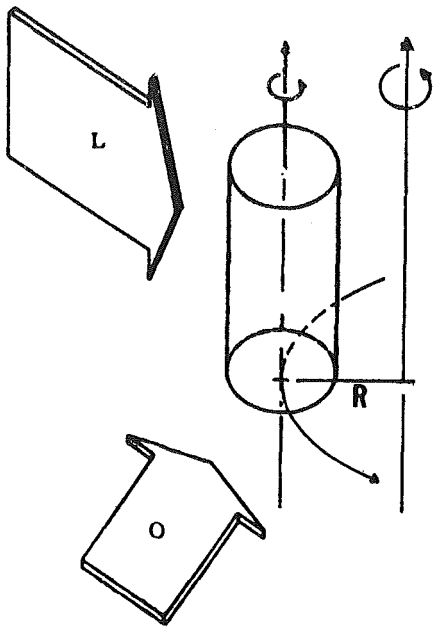

Fig. 10 Schematic for visualizing columnar evolution of fluid rotation. Observer is at right angles to vertical split source of light. Container can be spun up on axis or off axis and observer will see no difference, except the spinup off axis is visible only once per revolution.

When a right circular cylinder without radial baffles is suddenly rotated about its vertical axis the fluid comes to know of the motion of the cylinder because an imbalance in centrifugal pressure forces exists in different regions of the fluid. Unless the container geometry is small, spinup is not a simply diffusive (viscous) process. As the container begins to rotate fluid close to the top and bottom horizontal endplates of the cylinder is centrifuged radially outward. New fluid must then be drawn into the two endplate boundary layers from the interior fluid regions. To complete the flow circuit, fluid is drawn away from the outer wall region and into the interior. The latter fluid, however, is spinning. This fluid has come from regions close enough to the wall to have been acted upon by viscous stresses, and as this spinning fluid moves inward it spins faster to conserve angular momentum. The spinup is completed when the fluid in the interior is spinning at the same rate as the container. A schematic of this flow process is shown in Fig. 9. The time required for spinup is consequently determined by the time required to flush all of the interior region fluid through the endplate boundary layers and replace it with fluid drawn inward from the boundary layers on the vertical sidewalls of the cylinder [8]. These sidewall boundary layers are indicated in Fig. 9. This time scale is the Ekman time

$$\tau_E = \frac{h}{2\sqrt{\nu\omega}} \tag{19}$$

The spinup process can be neatly visualized in an experiment designed by Greenspan [6]. A right circular cylinder is seeded with shiny mica flakes and rotated on a vertical turntable (represented schematically in Fig. 10). A thin collimated light source is projected through the container, with the camera and the viewer positioned in front of the container and at right angles to the light source. Figure 11 is a sequence of photos illustrating a spinup using such an arrangement. The shiny column of fluid in the interior of the container is fluid that is nonspinning and is being slowly drawn into the top and bottom endplate boundary layers. The rest of the fluid in the container is spinning. The mica particles in this region are aligned with the rotation and are not visible to the observer. These particles reflect the incoming light back to the light source. A fraction of the incoming light, however, is not reflected back at the light source and is reflected from the in-

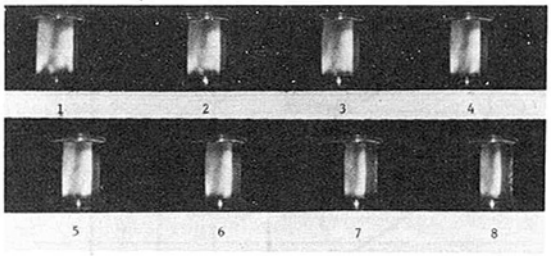

Fig. 11 Sequence of pictures taken during off-axis spinup. Note column of interior fluid getting thinner as spinup evolves. The last two pictures (numbered 7, 8) were taken with the turntable stopped. Unstable spindown is characterized by roll cells on outer container wall.

terior in the direction of the camera, showing the slowly diminishing core of nonspinning fluid.

Suppose instead that the same circular cylinder is made to rotate about a vertical axis not coincident with its vertical axis of symmetry (Fig. 10). It can be shown that the spinup process is still the same [3]. (The sequence of pictures in Fig. 11 actually shows an off-axis spinup.) The distance of the cylinder on the turntable from the axis of rotation affects only the pressure in the container. Pressure forces acting on a homogeneous fluid (no density gradients in the fluid) cannot create a torque on a fluid element, and so cannot by themselves impart rotation to the fluid. Furthermore, although the pressure in the fluid is different in an off-axis spinup the net pressure imbalance, which drives the secondary flow, is the same as in an on-axis spinup.

A homogeneous fluid in an enclosed container thus acquires rotation because it is slowly pumped into the viscous dominated endplate boundary layers. For very small times, fluid motion in the regions away from the endplates and sidewalls must be irrotational. This is true regardless of the shape of the container. When a right circular cylinder is impulsively accelerated to speed ω, the fluid initially appears in the reference frame of the container to counterrotate relative to the walls of the container at a rate equal to $-\omega$. Similarly, if a container of any shape is impulsively accelerated to some speed ω the fluid will always appear to counterrotate along streamlines having the horizontal contour of the fluid container itself at a rate equal to $-\omega$. The sum of this relative fluid rotation and the container rotation is zero, and the inertial motion of each fluid element is irrotational.

The relative motion of the fluid in an arbitrarily shaped container thus scales with ωc, where ω is the impulsive change in rotation rate, and c is a characteristic radius of the container. This result can be used to estimate the relative motion heat transfer enhancement. However, the inviscid irrotational flow just described is unstable for container geometries that are not circular. Decelerating boundary layers near the horizontal boundaries of the container will separate. Figure 12(a) shows the pie-shaped container of Fig. 6 seeded with mica flakes and impulsively accelerated from rest to 20 rpm. The direction of rotation is from right to left. Within two revolutions, the fluid in Fig. 12(b) can already be seen to have separated in the two opposing corners. Kinetic energy will be fed into the corner regions from the original irrotational flow field in each succeeding revolution until the vortices in the corners are of sufficient size to move out of the corners and into the interior of the container. It is most interesting to note that the initial flow field quickly evolves (within two revolutions) into two irrotational vortices which are now spinning in the same direction as the container. (A region of concentrated vorticity is clearly visible at the center of each of the two primary vortices.) These vortices continue to interact until the spinup evolves. Although the container in these pictures was rotating slowly, the flow field for impulsive accelerations to 500 rpm is not appreciably different. Although the number of eddies and their interactions are a function of container geometry and speed of

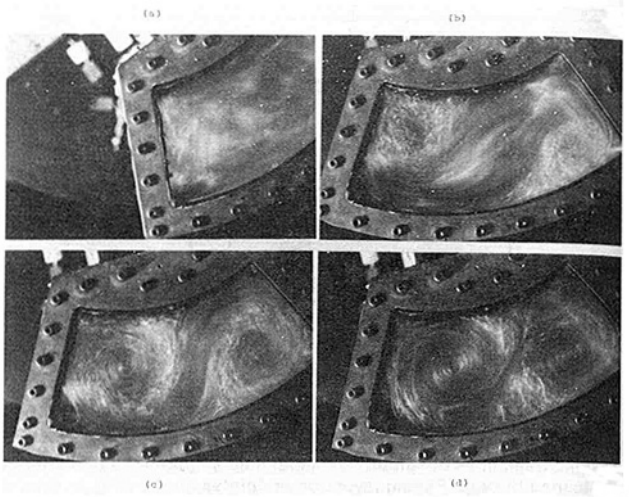

Fig. 12 Container is impulsively accelerated from right to left; flow separates in corners forming eddies

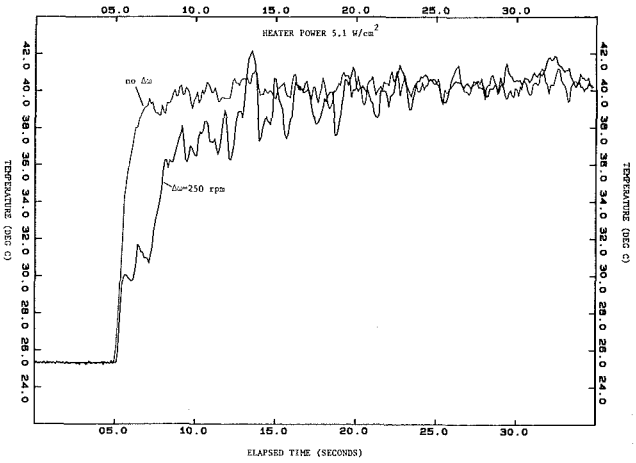

Fig. 13 Transient temperature histories compared. In the first curve, the heater is energized with the fluid in solid body rotation. In the second, the rotor was accelerated from 250 rpm to 500 rpm as the heater was energized. The lower temperature in the second curve reflects an enhanced heat transfer coefficient caused by relative fluid motion.

rotation, a most important result of observations of spinup in nonaxisymmetric containers is that the spinup is still an essentially two-dimensional process with a time constant of the same order as that in an unbaffled, symmetric container.

Transient Heat Transfer Tests

The effect of the initial irrotational fluid motion on the surface heat transfer rate has been measured. The pie-shaped rotor shown in Fig. 6 was idled at roughly 250 rpm until the fluid was in solid body rotation. The heater was energized and the rotor impulsively accelerated to, say, 550 rpm. The rotor reached 90 percent of its final rotation rate in less than 2 s (6 revs). (The spinup time constant for the fluid within this container for a final speed of 550 rpm was 13 s and the acceleration could be considered impulsive.)

Figure 13 is a recorded plot of the temperature history on the surface of a heater following an impulsive acceleration. Also shown in Fig. 13 is a plot of surface temperature during a quasi-steady test at 550 rpm. The heater power in both tests was the same. Figure 13 clearly shows that there is improvement in the heat transfer coefficient for some length of time, although that time is still short compared to the spinup time of the fluid in the container.

The unusual result that a quasi-steady heat transfer state is reached while there is still considerable relative motion in the interior of the container is explained as follows. The local sur-

face heat transfer coefficient is determined by the buoyancy based upon the local gradient in pressure and not upon the global pressure gradient. Although it takes a considerable amount of time to produce rotation in the interior of the container, a significant gradient is established early on in the regions very close to the sidewalls because of viscous diffusion. At high rotational rates the local thermal boundary layer is so small that it is quickly embedded within the spinup wall boundary layer and as the spinup boundary layer grows outward the net relative motion mass flux in the vicinity of the heater diminishes as well. Thus the time period during which the heat transfer is enhanced should be a function of the extent to which spun-up fluid has submerged the thermal boundary layer. To test this model, Figs. 14(*a*) and 14(*b*) have been plotted. The ordinate is the ratio of temperature difference between heater surface and fluid nondimensionalized by its steady-state value corresponding to the final rotation rate. This measures the extent of heat transfer enhancement by relative bulk motion. The abscissa is proportional to the ratio of the thickness of viscously spun-up fluid ($\sqrt{\nu t}$) to the momentum boundary layer thickness which corresponds to the steady-state heat transfer after spinup is completed $\delta_{v,ss}$

$$\tau = \frac{\sqrt{\nu t}}{\delta_{v,ss}} \tag{20}$$

This measures the time scale of heat transfer enhancement. Assuming the ratio of momentum to thermal boundary layer thickness at steady state is proportional to $\sqrt{\mathrm{Pr}}$, the time scale parameter for heat transfer enhancement can be written as

$$\tau = \frac{\sqrt{\alpha t}}{k/h_{ss}} = \frac{\mathrm{Nu}_{ss}}{l}\sqrt{\alpha t} \tag{21}$$

where the steady-state Nusselt number is given by equation (17). As Figs. 14(*a*) and 14(*b*) show, the data for a wide variety of conditions indicate a period of heat transfer enhancement due to spinup of approximately $\tau = 12$. The bumps and dips in the temperature curve of Fig. 14 are due to the swirling vortices which are interacting and scouring the container walls at the beginning of the spinup. This tends to suggest that a disordered spinup caused by the reservoir baffles which alter the geometry of the liquid reservoir and cause flow separation is preferable for heat transfer purposes, augmenting the effects of the relative fluid motion which would exist in a circularly symmetric container.

Conclusions

1 Weak buoyant plumes ($\Delta\rho/\rho << 1$) in a rapidly spinning container result in axially invariant, two-dimensional motions. This is true even when the thermal source is much shorter than the container in the axial direction.

2 The trajectories of such weak thermal plumes are radial relative to the spinning container.

3 The steady-state Nusselt number was found to correlate well with $(\mathrm{RaPr})^{0.33}$ and not $\mathrm{Ra}^{0.33}$ for the range of data obtained ($4 < \mathrm{Pr} < 40$ and $10^6 < \mathrm{Ra} < 10^{11}$). This implies that the heat transfer coefficient is independent of heater length scale and fluid viscosity.

4 In situations where the container is spun up simultaneously with application of heater power, the heat transfer coefficient is enhanced over its corresponding steady-state value due to relative motion of the bulk fluid. The time period for this enhancement, however, is short compared to the fluid spinup time. A model based upon the submergence of the steady-state boundary layer by the diffusive wave from the wall successfully correlates the enhancement times for the range of data obtained.

Acknowledgments

The work reported in this paper was sponsored by the U.S. Air Force through a subcontract from Westinghouse Corporation. The authors would like to thank Jim Parker and Phil Eckels of Westinghouse for their assistance during the course of this research.

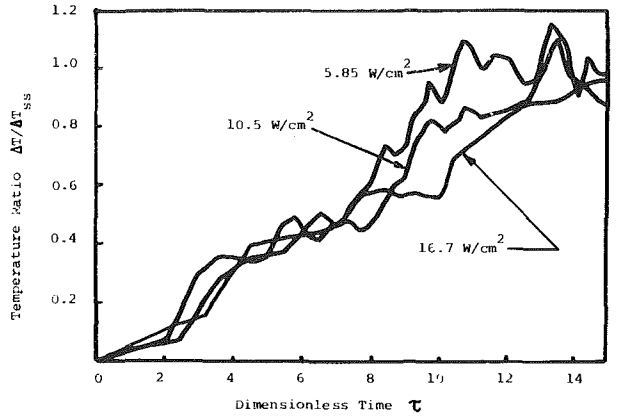

Fig. 14(*a*) Transient heat transfer data, all water, short heater (1.14 cm circumferentially × 12.9 cm axially)

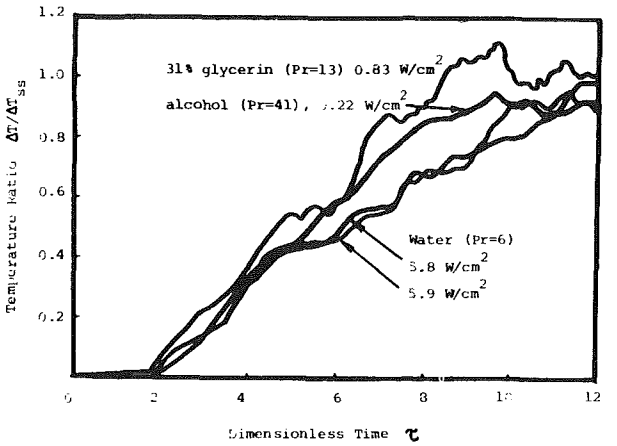

Fig. 14(*b*) Transient heat transfer data, with the long heater (12.9 cm circumferentially × 1.14 cm axially)

References

1 Smith, J. L., Jr., et al., "MIT-DOE Program to Demonstrate an Advanced Superconducting Generator," *IEEE Trans. on Magnetics*, Vol. MAG-15, No. 1, Jan. 1979, p. 727.

2 Gamble, B. B., and Kaim, T. A., "High Power Density Superconducting Generator," 15th Intersociety Energy Conversion Engineering Conference, Seattle, Washington, Aug. 18-22, 1980.

3 Sobel, L. D., "Heat Transfer and Flow Visualization in Natural Convection in Rapidly Spinning Systems," Ph.D. Thesis, MIT, May 1984.

4 Taylor, G. I., "Motion of Solids in Fluids When the Flow is Not Irrotational," *Proceedings of the Royal Society*, A, Vol. XCIII, 1917, pp. 99-113; *The Scientific Papers of Sir G. I. Taylor*, Vol. IV, G. K. Batchelor, ed., Cambridge University Press, 1971.

5 Taylor, G. I., "Experiments on the Motion of Solid Bodies on Rotating Fluids," *Proceedings of the Royal Society*, A, Vol. CIV, 1923, p. 213-218; *The Scientific Papers of Sir G. I. Taylor*, Vol. IV, G. K. Batchelor, ed., Cambridge University Press, 1971.

6 Greenspan, H. P., *The Theory of Rotating Fluids*, Cambridge University Press, Cambridge, 1980, Chap. 1.

7 Kreith, F., "Convection Heat Transfer in Rotating Systems," *Advances in Heat Transfer*, Academic Press, New York, 1968, Vol. 5, pp. 129-251.

8 Wedemeyer, E. H., "The Unsteady Flow Within a Spinning Cylinder," *J. Fluid Mech.*, Vol. 20, 1964, pp. 383-399.

9 Turner, J. S., "Buoyant Plumes and Thermals," *Annual Review of Fluid Mechanics*, Vol. 1, 1969, pp. 29-44.

10 Morton, B. R., Taylor, G. I., and Turner, J. S., "Turbulent Gravitational Convection From Maintained and Instantaneous Sources," *Proc. Royal Soc.*, A, Vol. 234, 1956, pp. 1-23.

11 Gebhart, B., "Instability, Transition, and Turbulence in Buoyancy-Induced Flows," *Annual Review of Fluid Mechanics*, Vol. 5, 1973, p. 213-246.

12 Morton, B. R., "Forced Plumes," *Journal of Fluid Mechanics*, Vol. 5, 1959, pp. 151-163.

13 Gebhart, B., "Natural Convection Flow, Instability, and Transition," ASME Journal of Heat Transfer, Vol. 91, 1969, pp. 293-309.

Experimental Investigation of Natural Convection in Partially Divided Enclosures

J. G. Symons
Division of Energy Technology,
Commonwealth Scientific and
Industrial Research Organization,
Highett, Victoria, Australia

An experimental study has been performed on natural convective heat transfer in inclined enclosures heated from below, and with partitions running in the up-slope direction (see Fig. 1). The influence of a clearance between the partitions and the lower heated isothermal surface is considered. This problem is of particular importance in solar collector design. Heat transfer rates have been measured for Ra < 10^7, enclosure inclination of 0, 30, 60, and 90 deg from the horizontal, and partition end clearances ranging from zero up to half the enclosure height. A flow visualization study which covers the same range of inclinations and end clearances is also reported. It is shown that introducing a small partition end clearance has no significant effect on the flow or heat transfer rates. However, a large end clearance allows up-slope rolls to be established in the unpartitioned region of the enclosure, resulting in an increase in the heat transfer rates. The natural convective heat transfer rates are found to be independent of both partition end clearance and enclosure inclination over certain ranges of these parameters. The convective heat transfer characteristics are also shown to be related to the flow.

Introduction

The partitioning of enclosures to enhance or suppress convection has received considerable attention in the recent heat transfer literature. The influence of across-slope partitions, up-slope partitions, and honeycombs on the convective heat transfer rates in inclined enclosures heated from below has been well documented [1–5]. One application for this work includes the suppression of convective heat losses from the absorber panel to the glass cover of a flat plate solar collector. To construct these low heat loss collectors, manufacturing tolerances require that a clearance be left between the lower extremity of the partitions and the heated absorber panel. Hereafter this space will be referred to as partition end clearance. It was postulated recently by Hollands and Iynkaran [6] that end clearance between the partitions and a low emittance isothermal surface can be advantageous in reducing overall heat transfer rates by decoupling the convective and radiative heat transfer modes near the isothermal surface. There is consequently a need for information on the rates of convective heat transfer within enclosures containing partitions with end clearance.

The problem being considered in this study is shown schematically in Fig. 1. The enclosure is inclined, and consists of four adiabatic side walls, a lower heated isothermal surface, an upper cooled isothermal surface, and an array of partitions running up-slope. This study is concerned with the influence of h, the partition end clearance, on the flow and convective heat transfer rates within the enclosure.

While many studies have considered inclined enclosures with partitions or honeycombs extending completely from the heated to the cooled isothermal surfaces, i.e., $h = 0$ at each surface, there have been very few studies dealing with enclosures containing partitions with end clearance, $h > 0$.

Nansteel and Greif [7], and others, have studied natural convection flows in an enclosure with the partition located parallel to the vertical isothermal surfaces. Edwards et al. [8] studied rectangular-celled honeycombs comprising both up-slope and across-slope partitions, with variable upper and lower end clearance. They measured Nusselt number Nu for $\theta = 0$, 15, and 30 deg, $h \leq 4.5$ mm, $H = 19$ mm, and Rayleigh number Ra up to 4×10^4 using silicone oils as the heat transfer medium. In a followup study, Wu and Edwards [9] considered varnished paperboard honeycombs with the same experimental equipment as Edwards, but for the extended range $\theta = 0$, 30, 60, and 90 deg, $H \approx 18$ and 37 mm, $h = 1.5$ mm and 3 mm, and Ra $< 2 \times 10^5$. From these studies, it was concluded that for end clearances up to 1.5 mm and $\theta \leq 30$ deg, there was no significant change in the natural convective heat transfer rates. For larger gaps, $h = 3$ mm, Nu did depart significantly from the value for $h = 0$. Hollands and Iynkaran [6] discussed polyester honeycombs with a 10.1-mm end clearance in an enclosure inclined at 45 deg to the horizontal. They found that the end clearance caused only a minor reduction in the Rayleigh number at which convection was established. References [6, 8, 9] are relevant for end clearances under honeycomb arrays, i.e., with partitions both up-slope and across-slope. While it has been shown by Symons and Peck [10] that up-slope partitions on their own can be very effective in suppressing natural convective heat transfer, there is no information currently available to determine the influence of end clearance in these enclosures. Nor is there any detailed information available for large clearances greater than 0.25 of the enclosure height, or where $h > 5$ mm. This paper aims to provide new experimental data and a description of the convective flows in enclosures with end clearance between the up-slope partitions and the heated isothermal surface.

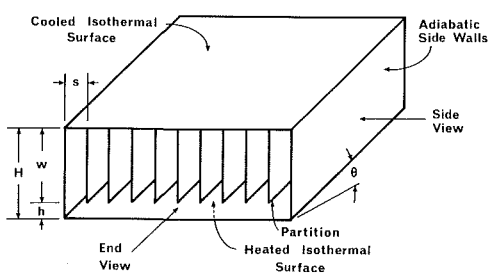

Fig. 1 Schematic of partially divided enclosure

Contributed by the Heat Transfer Division for publication in the JOURNAL OF HEAT TRANSFER. Manuscript received by the Heat Transfer Division December 20, 1984.

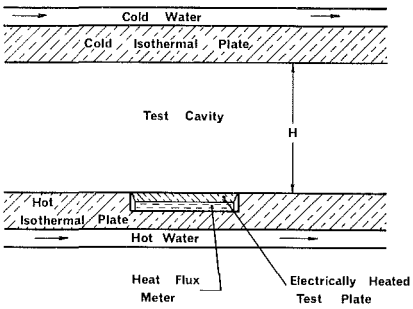

Fig. 2 Schematic of experimental equipment for measurement of convective heat transfer rates

Measurement of Natural Convection Heat Transfer Rates

The natural convective heat transfer rates from the heated isothermal surface to the cooled isothermal surface have been measured in a facility previously described in [11]. The equipment comprises two parallel copper plates measuring 450 mm × 450 mm × 10 mm, which were maintained at set temperatures by water circulating through tubes attached to the back of each plate. Each plate was uniform in temperature to within ± 0.03°C, and the plate temperature was measured with calibrated type T thermocouples. A small 125 mm × 125 mm electrically heated test plate and heat flux meter were inserted in the heated plate as shown in Fig. 2. Power to the small test plate was adjusted until the heat flux meter reading approached zero, indicating no heat flow between the heated isothermal plate and the small test plate. Under these conditions, all of the electric power supplied to the small test plate was dissipated into the enclosure by radiation, convection, and conduction. Heat transfer rates were only measured from the test plate to minimize boundary effects.

The perimeter of the isothermal plates was enclosed with aluminum foil on paper to give a linear temperature profile between the heated and cooled isothermal surfaces. The whole assembly was well insulated with fiberglass, and then installed in a pressure vessel charged with dry air. The temperatures of the heated and cooled isothermal plates were held constant at approximately 60°C and 30°C respectively during each experiment, and only the air pressure was varied to allow Ra to change from 10^3 up to 10^7, due to variations in the air properties. The experiment was allowed to stabilize for approximately 1 hr, following which the plate temperatures, heat flux meter voltage, power to the test plate, and pressure were logged over a test period of at least 40 min.

The first experiments were performed at low Ra so the convective heat transfer rate was insignificant. Under these conditions, heat is transferred from the heated to the cooled isothermal surfaces via radiation and conduction. In subsequent tests at higher Ra, the increase in heat transfer rate was due to the effect of natural convection. The convective heat transfer coefficient h_c was calculated as the convective heat transfer rate per unit area of test plate, divided by $(T_h - T_c)$.

The experimental facility included a microprocessor which performed the control and data logging functions. The overall system uncertainty was found to be 5 percent in the determination of Ra, and 7 percent in the determination of Nu [11].

The overall dimensions of the test enclosure were 450 × 450 × 60 mm for all tests. The isothermal surfaces were polished

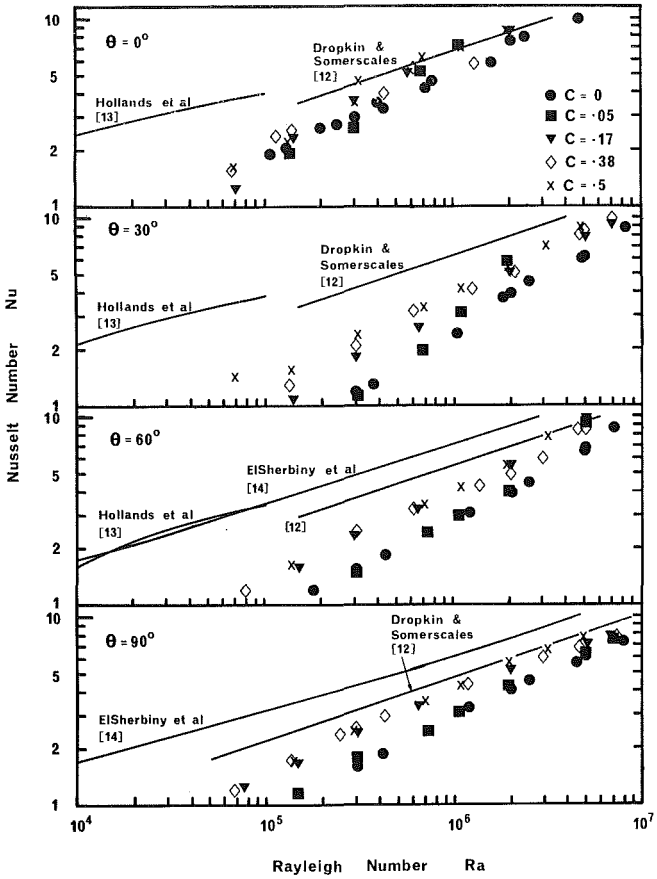

Fig. 3 Convective heat transfer results for various C: (a) θ = 0 deg, (b) θ = 30 deg, (c) θ = 60 deg, and (d) θ = 90 deg

Table 1 Details of enclosure dimensions, refer to Fig. 1 (H = 60 mm, and w/s = 6 in all cases)

End clearance h, mm	Dimensionless end clearance $C = h/H$
0(<1)	0
3	0.05
10	0.17
20	0.33
30	0.5

Nomenclature

a_1, a_2, a_3 = dimensions indicated in Fig. 11, mm
C = dimensionless end clearance = h/H
C_p = specific heat of air, J kg^{-1} K^{-1}
g = gravitational constant, m s^{-2}
h = partition end clearance, m
h_c = convective heat transfer coefficient, W m^{-2} K^{-1}
H = isothermal plate spacing, 0.06 m
k = thermal conductivity of air, W m^{-1} K^{-1}
Nu = Nusselt number = $h_c H/k$
Ra = Rayleigh number = $g\beta \cdot (T_h - T_c) H^3 \rho^2 C_p / \mu k$
s = partition spacing, mm
T_h = temperature of heated isothermal surface, K
T_c = temperature of cooled isothermal surface, K
w = partition height, mm
β = volumetric thermal coefficient of expansion for air, K^{-1}
θ = inclination of enclosure from horizontal, deg
μ = dynamic viscosity of air, Pa s
ρ = density of air, kg m^{-3}

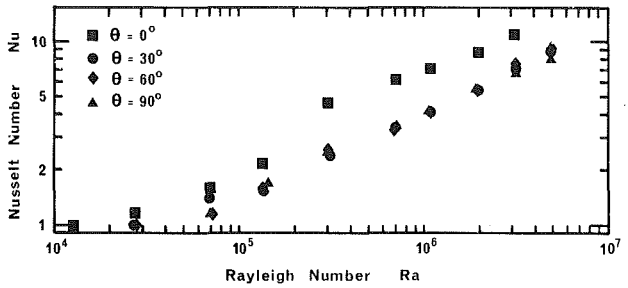

Fig. 4 Convective heat transfer results for $C = 0.5$ and various θ

to give an emittance of 0.05, and the aluminized paper side walls had an emittance of 0.05. The partitions were constructed of Teflon FEP type 50 A having a wall thickness of 13 μm and emittance of 0.31. This material is of particular interest for simultaneously suppressing convection and transmitting solar radiation in flat-plate solar collectors.

For the experiments, the end clearance dimension h was varied as listed in Table 1. The partition spacing s was varied to maintain the partition aspect ratio $w/s = 6$ for all tests. This ensured that the surface area of partitioning remained unaltered. By conducting the experiments in this manner, the influence of partition end clearance on Nu can be assessed alone, without introducing spurious effects relating to geometry of either the enclosure or the partitions. The inclination of the enclosure was varied from $\theta = 0$ deg (isothermal surfaces horizontal) to $\theta = 90$ deg (isothermal surfaces vertical) by rotating the entire pressure vessel. The partitions remained in the vertical plane for all θ.

The measured heat transfer rates are shown in Fig. 3 for various dimensionless end clearances C, and several angles of inclination θ. When the enclosure is oriented with the isothermal surfaces horizontal, $\theta = 0$ deg, Fig. 3(a) indicates that Nu is less for small end clearances, i.e., $C \leq 0.05$, and increases for larger end clearances. When the enclosure is inclined to $\theta = 30$ deg, the increase in Nu with increasing end clearance C becomes more pronounced. Figure 3(b) shows that there is approximate agreement between the results for $C = 0$ and 0.05, but as C is increased further, there is an increase in Nu. When $\text{Ra} = 10^6$ and $\theta = 30$ deg, increasing the end clearance from 0 to 0.5 causes an approximate 60 percent increase in Nu. The variation in Nu for $0 \leq C \leq 0.5$ is greater when $\theta = 30$ deg than for $\theta = 60$ deg as in Fig. 3(c). When $\text{Ra} = 10^6$ and $\theta = 60$ deg Nu increases by approximately 40 percent when C increases from 0 to 0.5. Figure 3(c) shows that for $0.17 \leq C \leq 0.5$, Nu is insensitive to partition end clearance. Again, as for all inclinations, the results for $C = 0$ and 0.05 are in close agreement. When $\theta = 90$ deg as shown in Fig. 3(d), the results are similar to those for $\theta = 60$ deg, i.e., Nu is insensitive to C when $0 \leq C \leq 0.05$, and Nu is insensitive to C when $0.17 \leq C \leq 0.5$.

The experimental arrangement did not allow C to be increased beyond 0.5 because the partition spacing s became very small. However, the limiting case of $C = 1$ can be obtained from previous experimental studies [12–14] as shown by the solid lines in Fig. 3.

When $\theta = 0$ deg and $\text{Ra} > 3 \times 10^5$, Fig. 3($a$) indicates the partitioned enclosure with $C = 0.5$ end clearance provides no convection suppression, i.e., no reduction in Nu over the unpartitioned enclosure, $C = 1$. For smaller Ra, the partitions do reduce the convection heat transfer rates by a small amount. When $\theta = 90$ deg as in Fig. 3(d), a small reduction in Nu is achieved with the inclusion of partitions for all values of C, and for the intermediate angles of 30 and 60 deg, an even greater reduction in Nu is found.

The maximum Ra at which convection is effectively suppressed, i.e., when $\text{Nu} \simeq 1$, could be described as a critical Rayleigh number. This value is of particular importance when designing partitions for convection suppression, and can be found by extrapolating the heat transfer results back to Nu = 1. When $\theta = 0$ deg, this critical Rayleigh number is only weakly affected by C and occurs at $\text{Ra} \simeq 2.4 \times 10^4$. When $\theta = 30$ deg the critical Rayleigh number decreases from about 2.4×10^5 when $C = 0$, down to about 5×10^4 when $C = 0.5$. For $\theta = 60$ deg, the critical Rayleigh number is reduced from about 1.4×10^5 when $C = 0$, to about 5×10^4 when $C = 0.5$. A similar effect is found when $\theta = 90$ deg.

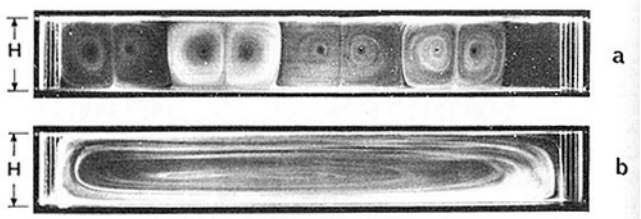

Fig. 5 Flow viewed from the side for $C = 0$, $\text{Ra} = 1.8 \times 10^5$: ($a$) $\theta = 0$ deg, (b) $\theta = 60$ deg

For all angles of inclination shown, the critical Rayleigh number was always greater when the partitions were installed in the enclosure, as compared with the enclosure without partitioning. The highest value of critical Ra was always for $C = 0$, and it was always reduced when $C \geq 0.17$.

The heat transfer results for $C = 0.5$ are shown in Fig. 4 for various angles of inclination. The results again fall into two groups, one for $\theta = 0$ deg, and the remainder for 30 deg $\leq \theta \leq$ 90 deg. This effect was previously reported by Symons and Peck [10] for $C = 0$, where it was shown that convective heat transfer rates were insensitive to θ over two ranges, viz., 0 deg $\leq \theta \leq$ 15 deg, and 25 deg $\leq \theta \leq$ 90 deg.

Flow Visualization

A facility has been constructed to enable flow visualization in small enclosures. This equipment was described in [15]. Two transparent isothermal plates were constructed from acrylic, and their temperatures were controlled to within 0.25°C by passing water through each one. A sheet of light from a quartz halogen lamp was directed through the enclosure to enable planes of the enclosure to be viewed from the side and end (see Fig. 1).

Two closely spaced outer walls of the enclosure were made from acrylic (to thermally isolate the test area from the environment), and the partitions were constructed from 1-mm-thick polycarbonate. These materials provided flat, rigid, and transparent boundaries which were free from optical distortion. The enclosure measured 445 mm × 80 mm × 60 mm high. This narrower enclosure allowed the convective patterns to be viewed and photographed from both the side and the end.

The experimental procedure consisted of setting the appropriate inclination angle and boundary temperatures, and allowing the flow to stabilize for at least 40 min. Cigar smoke was slowly introduced into the enclosure in a manner that would not disturb the flow. Photographs were taken from the side and end of the enclosure. End clearances of $C = 0$, 0.33, and 0.5 were studied, with $\text{Ra} = 1.8 \times 10^5$, using air as the heat transfer medium.

Figure 5 illustrates the flow when viewed from the side, for the case $C = 0$. In all photographs, the bottom edge represents the heated isothermal surface, and the top is the cooled isothermal surface. For $\theta = 0$ deg, the flow consists of multiple counterrotating cells, as shown in Fig. 5(a). The number of cells varied between experiments, being either 6, 8, or 10 without changing any of the variables. When θ was increased beyond about 25 deg, the flow changed to a single-cell circulation, as illustrated in Fig. 5(b). This effect is due to the purging of those cells which flow down the heated surface and up the cooled surface, i.e., counter to the buoyant forces [10]. The

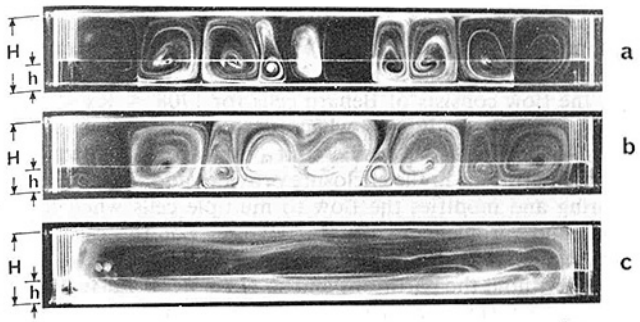

Fig. 6 Flow viewed from the side for $C = 0.33$, $Ra = 1.8 \times 10^5$: (*a*) θ = 0 deg, (*b*) θ = 10 deg, (*c*) θ = 30 deg

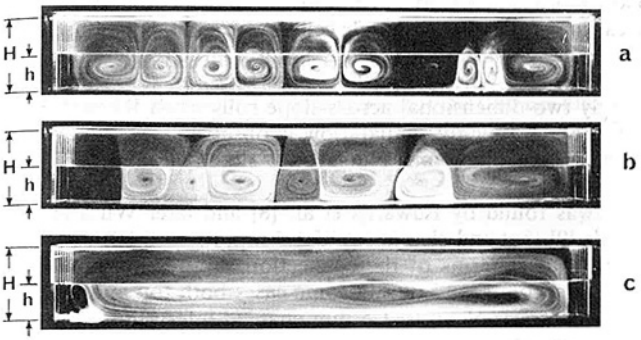

Fig. 7 Flow viewed from the side for $C = 0.5$, $Ra = 1.8 \times 10^5$: (*a*) θ = 0 deg, (*b*) θ = 10 deg, (*c*) θ = 30 deg

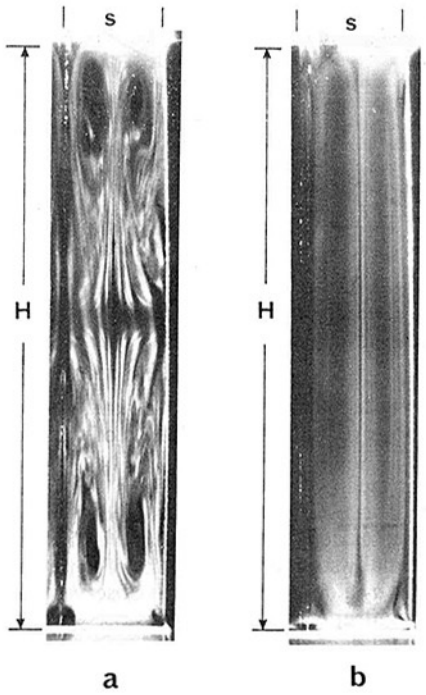

Fig. 8 Flow viewed from the end for $C = 0$, $Ra = 1.8 \times 10^5$ and θ = 0 deg: (*a*) plane of illumination through the center of one cell; (*b*) plane of illumination between two cells

remaining cells, which all rotate in the same direction, then coalesce to form one large cell.

The side view photographs for $C = 0.33$ are shown in Fig. 6. The horizontal white line visible through the flow represents the lower extremity of the partitions. For $\theta = 0$ deg, multiple counterrotating cells were again found, as shown in Fig. 6(*a*), but the center of rotation was lower than for $C = 0$. For θ = 10 deg, Fig. 6(*b*) shows that one set of cells has grown in size, and the remaining cells, which flow counter to the buoyant forces, have become smaller. When $\theta = 30$ deg (Fig. 6*c*), the small cells were purged, allowing the remaining cells to coalesce into a single cell. This single cell flow persists for θ up to 90 deg.

Figure 7 illustrates the flows as viewed from the side for the case $C = 0.5$, and the same trends were observed there. It was found for $C = 0.33$ and 0.5 that the transition from multiple-cell circulation to single-cell circulation occurred at $\theta \simeq 20$ deg.

The convective flows were also viewed from the end. Figure 8(*a*) illustrates the flow for $C = 0$, $\theta = 0$ deg, and with the plane of illumination passing through the center of one of the multiple cells. Recall that from Fig. 5(*a*) the side view indicated multiple cells when $\theta = 0$ deg. Figure 8(*a*) shows that there are two symmetric flows visible in the space between adjacent partitions. Figure 8(*b*) illustrates the same test conditions except that the plane of illumination was aligned with the boundary between two adjacent counterrotating cells.

When $\theta \geq 30$ deg and $C = 0$, no distinct flow pattern could be distinguished when viewed from the end.

When the partition end clearance was $C = 0.33$, counterrotating rolls were visible in the clearance region below the partitions, for $\theta = 0$ deg, as shown in Fig. 9(*a*). As the enclosure was inclined to $\theta = 30$ deg, these rolls with axis running up-slope were less well defined (Fig. 9*b*). For θ = 60 and 90 deg, the up-slope rolls were not distinguishable.

Figure 10 illustrates a similar set of photographs for C = 0.5. Again, when $\theta = 0$ deg rolls are visible in the clearance region (Fig. 10*a*), but weaken as θ increases until the rolls are not visible when $\theta = 90$ deg.

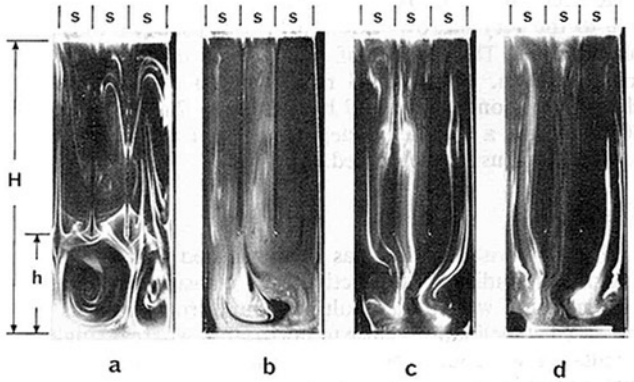

Fig. 9 Flow viewed from the end for $C = 0.33$, $Ra = 1.8 \times 10^5$: (*a*) θ = 0 deg, (*b*) θ = 30 deg, (*c*) θ = 60 deg, (*d*) θ = 90 deg

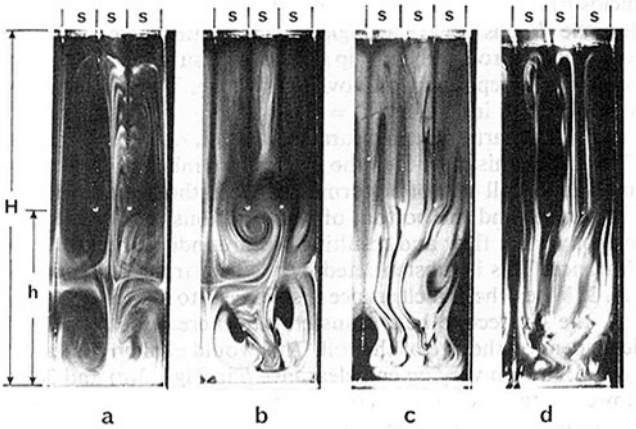

Fig. 10 Flow viewed from the end for $C = 0.5$, $Ra = 1.8 \times 10^5$: (*a*) θ = 0 deg, (*b*) θ = 30 deg, (*c*) θ = 60 deg, (*d*) θ = 90 deg

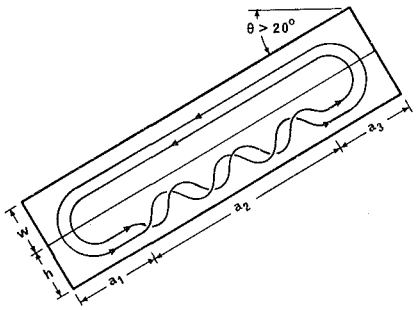

Fig. 11 Schematic of the up-slope roll, as observed for $\theta > 20$ deg

When $\theta = 0$ deg and $C \geq 0.33$, the rolls in the clearance region were observed over the full length of the enclosure, except where they were suppressed at the two ends. When the enclosure was inclined beyond 20 deg to the horizontal, the flow became a single cell with an added spiral in the end clearance region as depicted in Fig. 11. Over the length a_1, the flow was essentially straight up the slope of the heated surface, over the length a_2 a definite spiral was observed, and over the length a_3 straight up-slope motion was present. As θ was increased from 20 deg, the length a_1 also increased leaving a shorter length of roll. For $\theta = 60$ deg and above the roll had essentially disappeared.

After viewing many enclosures from the end, it was found that the height of the roll in the end clearance region extended completely from the heated isothermal surface to the lower extremity of the partitions. While Figs. 10(*a*) and 10(*b*) indicate four rolls, two wide and two high, this flow was not typical for wide enclosures. The four rolls in Fig. 10 are believed to be due to the very narrow width enclosures used for those end photographs. The number of rolls present in this equipment must be even. If only two rolls were to exist in the end clearance region, each would have to be $\simeq$ 7.5 mm wide and 30 mm high, a significant departure from the approximate square shape usually observed.

Discussion

The flow visualization has demonstrated that for all the enclosures studied, a convective flow transition occurred as the enclosure was tilted. Multiple counterrotating cells were observed at inclinations close to horizontal, whereas single-cell circulation was found for steeper inclines. The transition angle was approximately 25 deg when $C \leq 0.05$ but only 20 deg when $0.33 \leq C \leq 0.5$. This change in mode from multiple to single-cell flow causes the drop in Nu as shown in Fig. 4. As the flow speeds are visually similar for each flow type, the single-cell flow has a lower mass transfer rate across the enclosure, resulting in a lower Nu. For $C \geq 0.33$ and $\theta > 20$ deg, the flow is always a single-cell circulation sometimes incorporating a roll with axis up the slope, resulting in Nu being essentially independent of θ over this range. The same effects were observed in [10] for $C = 0$.

When the partition end clearance is small, i.e., $h \leq 3$ mm or $C \leq 0.05$ in this case, then the Rayleigh number based on h is small and a roll cannot be formed between the heated isothermal surface and the bottom of the partitions. Consequently, the convective flow and resulting Nu are independent of end clearance. This is substantiated by the heat transfer results in Fig. 3. When the end clearance is sufficient to accommodate a roll, the convective heat transfer rate increases, and Nu is dependent on the size of the roll. This would explain the variation in Nu with varying end clearance h in Figs. 3(*a*) and 3(*b*). However, for steeper inclinations, the end clearance roll disappears, and so Nu is independent of the end clearance (Figs. 3*c* and *d*).

The level of convection suppression achieved by the partitions at each angle of θ can be qualitatively understood by comparing the flows with and without the partitions. When there are no partitions in the enclosure ($C = 1$) and for $\theta = 0$ deg, the flow consists of Bénard cells for $1708 \leq \text{Ra} < 10^4$, changing to unsteady cells when $10^4 < \text{Ra} < 10^6$ and turbulence when $\text{Ra} > 10^6$, as described by Hart [16]. The placement of partitions in the enclosure provides additional viscous shearing and modifies the flow to multiple cells when Ra is small, and turbulence when Ra is large. For the case, say, when $\text{Ra} = 1.8 \times 10^5$ and $\theta = 0$ deg, unsteady cells can exist with or without the partitions and so Nu is weakly affected by their presence (Fig. 3*a*). When $\theta = 30$ and 60 deg, at $\text{Ra} = 1.8 \times 10^5$, the flow without partitions is unsteady up-slope rolls [16]. However these rolls cannot be accommodated between closely spaced partitions, resulting in up-slope rolls in the end clearance region, and a single cell between the partitions. This large change in the flow brings about a large reduction in Nu (see Fig. 3*b*). When $\theta = 90$ deg, the flow for no partitions is steady two-dimensional across-slope rolls when $\text{Ra} = 1.8 \times 10^5$ [16]. A roughly similar flow is observed when the partitions are in place and Nu is only slightly reduced by the partitions.

It was found by Edwards et al. [8] and later Wu and Edwards [9] that end clearances of 1.5 mm ($C = 0.08$) were not significant in terms of the convection suppression ability of the honeycomb, and that in some cases both top and bottom end clearances of up to 1.5 mm enabled intercellular flow to occur which reduced Nu. In those studies the end clearances were never sufficient to allow up-slope rolls to develop in the end clearance region. In the present study on up-slope partitions, end clearances of 3 mm ($C = 0.05$) have had no significant effect on the convective heat transfer rates. The present work goes beyond the range of end clearances used in [8, 9], and in no case in this study was Nu reduced by increasing the end clearance. For the enclosure considered in this paper, intercellular flow will not change Nu significantly.

Conclusions

Up-slope partitions with end clearance are effective in suppressing natural convective flows in inclined enclosures over the entire range of these experiments, i.e., $0 \text{ deg} \leq \theta \leq 90$ deg, $0 \leq C \leq 0.5$, and $\text{Ra} < 10^7$. The partitions are most effective in reducing Nu when $\theta > 20$ deg, and diminish in effectiveness when θ approaches 90 deg. Their ability to suppress Nu is due to the change in flow from up-slope rolls (when no partitions are used), to single-cell flow when $\theta > 20$ deg and $0.17 < C \leq 0.5$, or when $\theta > 25$ deg and $C \leq 0.05$.

The convective flows and Nu are unaffected by partition end clearances of up to 3 mm ($C = 0.05$). However, partition end clearances of 10 mm and beyond allow up-slope rolls to exist below the partition, resulting in an increase in Nu. The design of up-slope partitions for convection suppression requires that the end clearances be kept small to avoid the formation of these up-slope rolls. Multiple-cell flow was found for all values of partition end clearance studied, when the enclosure was inclined at less than 20 deg to the horizontal, and the flow changed to single cell when $\theta > 25$ deg. This transition was accompanied by a reduction in Nu for the steeper inclinations.

The convective heat transfer rates are found to be insensitive to enclosure inclination when $\theta > 25$ deg, for end clearances in the range $0 \leq C \leq 0.5$. Convective heat transfer is also found to be insensitive to partition end clearance when $\theta \geq 60$ deg.

Acknowledgments

The author wishes to thank M. K. Peck, L. H. Scott, and R. F. White for their contributions to the experimental work.

References

1 Cane, R. L. D., et al. "Free Convective Heat Transfer Across Inclined Honeycomb Panels," ASME JOURNAL OF HEAT TRANSFER, Vol. 99, 1977, pp. 86–91.

2 Smart, D. R., Hollands, K. G. T., and Raithby, G. D., "Free Convection Heat Transfer Across Rectangular Celled Diatherminous Honeycombs," ASME JOURNAL OF HEAT TRANSFER, Vol. 102, 1980, pp. 75–80.

3 Edwards, D. K., "Suppression of Cellular Convection by Heated Walls," ASME JOURNAL OF HEAT TRANSFER, Vol. 91, 1969, pp. 145–150.

4 Catton, I., Ayyaswamy, P. S., and Clever, R. M., "Natural Convection Flow in a Finite Rectangular Slot Arbitrarily Oriented With Respect to the Gravity Vector," *Int. J. Heat and Mass Transfer*, Vol. 17, 1974, pp. 173–184.

5 Meyer, B. A., Mitchell, J. W., and El-Wakil, M. M., "Natural Convection Heat Transfer in Moderate Aspect Ratio Enclosures," ASME JOURNAL OF HEAT TRANSFER, Vol. 101, 1979, pp. 655–659.

6 Hollands, K. G. T., and Iynkaran, K., "Proposal for a Compound-Honeycomb Collector," presented to the American Solar Energy Society, Los Angeles, CA, June 1984.

7 Nansteel, M. W., and Greif, R., "An Investigation of Natural Convection in Enclosures With Two and Three Dimensional Partitions," *Int. J. Heat and Mass Transfer*, Vol. 27, 1984, pp. 561–571.

8 Edwards, D. K., Arnold, J. N., and Catton, I., "End Clearance Effects in Rectangular Honeycomb Solar Collectors," *Solar Energy*, Vol. 18, 1976, pp. 253–257.

9 Wu, P. S., and Edwards, D. K., "Effect of Combined Tilt and End Clearance Upon Natural Convection in High L/D Rectangular Honeycomb," *Solar Energy*, Vol. 25, 1980, pp. 471–473.

10 Symons, J. G., and Peck, M. K., "Natural Convection Heat Transfer Through Inclined Longitudinal Slots," ASME JOURNAL OF HEAT TRANSFER, Vol. 106, 1984, pp. 824–829.

11 Peck, M. K., "An Apparatus for the Measurement of Natural Convection Heat Transfer in Enclosures," CSIRO Division of Energy Technology, Technical Report TR 4, Commonwealth Scientific and Industrial Research Organization, Melbourne, Australia, 1984.

12 Dropkin, D., and Somerscales, E., "Heat Transfer by Natural Convection in Liquids Confined by Two Parallel Plates Which Are Inclined at Various Angles With Respect to the Horizontal," ASME JOURNAL OF HEAT TRANSFER, Vol. 87, 1965, pp. 77–84.

13 Hollands, K. G. T., et al. "Free Convective Heat Transfer Across Inclined Air Layers," ASME JOURNAL OF HEAT TRANSFER, Vol. 98, 1976, pp. 189–193.

14 El Sherbiny, S. M., Raithby, G. D., and Hollands, K. G. T., "Heat Transfer by Natural Convection Across Vertical and Inclined Air Layers," ASME JOURNAL OF HEAT TRANSFER, Vol. 104, 1982, pp. 96–102.

15 Peck, M. K., and Scott, L. H., "Flow Visualization Apparatus for Natural Convection," *J. Physics E: Scientific Instruments*, Vol. 16, No. 4, 1983, pp. 251–252.

16 Hart, J. E., "Stability of the Flow in a Differentially Heated Inclined Box," *J. Fluid Mechanics*, Vol. 47, No. 3, 1971, pp. 547–576.

Interaction Between Film Condensation on One Side of a Vertical Wall and Natural Convection on the Other Side

D. Poulikakos
Department of Mechanical Engineering,
University of Illinois at Chicago,
Chicago, IL 60680

This paper reports a theoretical study of conjugate film condensation on one side of a vertical wall and boundary layer natural convection on the other side. Each phenomenon is treated separately and the solutions for each side are matched on the wall. The main heat transfer and flow characteristics in the two counterflowing layers, namely, the condensation film and the natural convection boundary layer, are documented for a wide range of the problem parameters. In addition, the wall heat flux and the wall temperature distribution resulting from the interaction of the two heat transfer modes (condensation and natural convection) are determined. Important engineering results regarding the overall heat flux from the condensation side to the natural convection side are summarized at the end of the study.

1 Introduction

Interaction between two different heat transfer mechanisms is a phenomenon of common occurrence in numerous thermal engineering applications. Many times, such interaction is inherent in the design of heat transfer apparatus. For example, the efficient performance of certain types of heat exchangers, thermal insulations, cryogenic equipment, nuclear reactors, and energy-efficient buildings is a direct result of man-induced enhancement or reduction of coupling between different heat transfer modes.

Relevant to the research reported in this paper is published work focusing on heat transfer through two boundary layers in thermal communication with one another. To this end, Lock and Ko [1] relied on finite differences to determine the coupling through a wall between two free convective systems. They found that, depending on the values of the problem parameters, the wall separating the two counterflowing boundary layers might exhibit temperature distributions drastically different from those given by the isothermal wall model whose detailed description is now well established in the literature.

In a recent sequence of three interesting papers [2–4] Anderson and Bejan investigated the problems of natural convection on both sides of a vertical wall separating two fluid reservoirs at different temperatures [2], two fluid-saturated porous reservoirs at different temperatures [3], and a porous reservoir and a fluid reservoir at different temperatures [4]. Their method of solution is based on the Oseen-linearization method used first by Gill [5] in the context of enclosure natural convection research. In the case of two fluid reservoirs, the results in [2] are in good agreement with those in [1]. Useful correlations for the overall heat transfer through the wall separating the two boundary layers are also reported in [2–4].

The importance of interaction between internal natural convection in a rectangular enclosure and an external natural convection boundary layer flow was examined by Sparrow and Prakash [6]. With the help of numerical simulations these authors proved that this interaction may result in flow and heat transfer characteristics in the enclosure markedly different from those exhibited by the classical enclosure model with two adiabatic horizontal walls and two isothermal differentially heated vertical walls.

The present paper examines the phenomenon of coupled (conjugate) film condensation on one side of a vertical wall and natural convection on the other side (Fig. 1). This problem is of fundamental value and, at the same time, it finds practical applications in heat exchangers, nuclear reactor cooling and, in general, in most engineering applications in which film condensation along a vertical wall takes place. To this author's knowledge analyses accounting for the conjugate nature of vertical plate condensation and natural convection do not exist in the literature. Of some relevance to the present paper is the work of Sparrow and Faghri [7] who studied the problem of Nusselt thin film condensation on the outside of a vertical pipe, triggered by fully developed forced convection of cold fluid inside the pipe.

The method of attack adopted to analyze the problem of interest in this paper consists of using the Oseen-linearization approach for the natural convection side following Gill [5], and thin film analysis for the condensation side. The solutions for the two sides are then matched at the wall [2–4]. It is worth noting that unlike the classical problem of vertical wall film condensation and natural convection [8], in the present study both the wall temperature and the wall heat flux are unknowns to be determined by the problem solution.

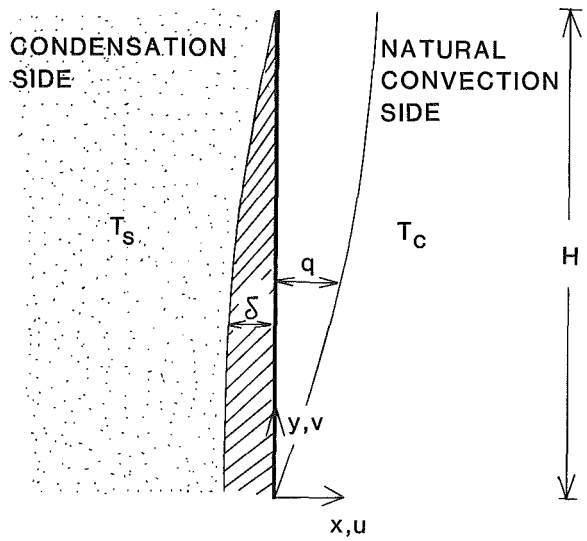

Fig. 1 Schematic representation of the system of interest: film condensation and natural convection coupled through a vertical wall

Contributed by the Heat Transfer Division for publication in the JOURNAL OF HEAT TRANSFER. Manuscript received by the Heat Transfer Division June 5, 1985.

2 Mathematical Formulation

The configuration of interest is shown in Fig. 1. A vertical impermeable wall separates two fluid reservoirs at different temperatures. The warmer of the two reservoirs contains vapor at saturation temperature. The cooling effect of the cold reservoir is felt by the vapor in the hot reservoir through the diathermal wall. We assume that this cooling effect eventually results in film condensation as shown in Fig. 1. At the same time, the heating effect of the hot side gives life to an upward-moving buoyancy-driven fluid jet at the wall vicinity in the cold side. The two fluid streams, i.e., the condensate in the film and the natural convection boundary layer, move in opposite directions while exchanging heat through the wall much like in a counterflow heat exchanger. To formulate the problem mathematically, the two sides need to be considered separately.

a **Natural Convection Side.** The dimensionless boundary layer equations governing the conservation of mass momentum and energy in the natural convection side of the system shown in Fig. 1 are

$$\frac{\partial u}{\partial x}+\frac{\partial v}{\partial y}=0 \tag{1}$$

$$\frac{1}{\mathrm{Pr}}\frac{\partial}{\partial x}\left(u\frac{\partial v}{\partial x}+v\frac{\partial v}{\partial y}\right)=\frac{\partial^3 v}{\partial x^3}+\frac{\partial T}{\partial x} \tag{2}$$

$$u\frac{\partial T}{\partial x}+v\frac{\partial T}{\partial y}=\frac{\partial^2 T}{\partial x^2} \tag{3}$$

The dimensionless quantities are defined as

$$x=\frac{\tilde{x}}{H\mathrm{Ra}^{-1/4}},\quad y=\frac{\tilde{y}}{H},\quad u=\frac{\tilde{u}}{\alpha/(H\mathrm{Ra}^{-1/4})},$$

$$v=\frac{\tilde{v}}{\alpha H/(H\mathrm{Ra}^{-1/4})^2},\quad T=\frac{\tilde{T}-\frac{1}{2}(T_s+T_c)}{T_s-T_c} \tag{4}$$

The above nondimensionalization was based on boundary layer scaling. A comprehensive treatment of boundary layer scaling in natural convection problems is presented in a recent heat transfer textbook [9]. Here, for the sake of brevity, the details that led to (4) are omitted. However, it is worth clarifying that the scale of the thickness of the boundary layer ($q\sim H\mathrm{Ra}^{-1/4}$, Fig. 1) was used to nondimensionalize the horizontal coordinate ($\tilde{x}$). The new parameters appearing in equations (1)–(4) are the Prandtl number and the Rayleigh number based on the wall height and the side-to-side temperature difference

$$\mathrm{Pr}=\nu/\alpha, \tag{5}$$

$$\mathrm{Ra}=\frac{g\beta H^3(T_s-T_c)}{\nu\alpha} \tag{6}$$

Equation (2) was derived by eliminating the pressure gradients between the $\tilde{x}$ and $\tilde{y}$ momentum equations after cross differentiating and subtracting these equations. In addition, equation (2) accounts for the Boussinesq approximation which states that the fluid density is constant everywhere except in the buoyancy term in the momentum equation where it depends on temperature according to

$$\rho=\rho_0[1-\beta(T-T_0)] \tag{7}$$

Here, β is the coefficient of thermal expansion and subscript 0 stands for a reference state. In the case where $\mathrm{Pr}>0(1)$ the inertia terms in the momentum equation are negligible compared to the viscous and the buoyancy terms. Hence, in this case, the momentum equation represents a balance between friction and buoyancy forces. It has been shown [2, 9] that omitting the inertia terms in equation (2) yields acceptable results (accurate within 10 percent) even for $\mathrm{Pr}=0(1)$. The present investigation focuses on Prandtl numbers of order unity or higher, on the natural convection side. Hence, the inertia terms in (2) are omitted to yield

$$\frac{\partial^3 v}{\partial x^3}=-\frac{\partial T}{\partial x} \tag{8}$$

The boundary conditions for the natural convection side read

$$\begin{aligned} u &= v=0,\ T=T_w(y) \text{ at } x=0 \\ v &= 0,\ T=-\tfrac{1}{2} \qquad \text{as } x\to\infty \end{aligned} \tag{9}$$

One more condition, namely the matching of the heat fluxes from the two sides at the wall, will be discussed after the mathematical formulation for the condensation side has been completed. Note that the wall temperature $T_w(y)$ is an unknown function of the vertical coordinate to be determined by the problem solution.

b **Condensation Side.** The classical solution of the film condensation problem from a vertical plate [8] yields

$$v^* = \left(\delta x_* + \frac{x_*^2}{2}\right) \tag{10}$$

Nomenclature

A = dimensionless parameter, equation (18)
B = dimensionless parameter, equation (15)
c_p = specific heat at constant pressure
g = gravitational acceleration
H = wall height
h_{fg} = latent heat of condensation
k = fluid thermal conductivity on the natural convection side
Nu = Nusselt number, equation (25)
Pr = Prandtl number, equation (5)
q = natural convection boundary layer thickness scale
Q = overall heat flux through the wall
Ra = Rayleigh number, equation (6)
Ra_f = film Rayleigh number, equation (14)
T_c = cold temperature
T_s = saturation temperature
T_w = wall temperature
T = dimensionless temperature, equation (4)
u = horizontal velocity component
v = vertical velocity component
x = horizontal Cartesian coordinate
y = vertical Cartesian coordinate
α = thermal diffusivity = $k/\rho c_p$
β = coefficient of thermal expansion
δ = condensation film thickness
λ = Oseen function
μ = viscosity
ν = kinematic viscosity
ξ = Oseen function
ρ = fluid density

Subscripts

* = dimensionless quantity for the condensation side
c = cold
f = film
l = liquid in the condensation side
s = saturation
v = vapor in the condensation side
w = wall

Symbols

~ = dimensional quantity for the natural convection side
- = quantity averaged in x

$$T = -(\tfrac{1}{2} - T_w(y))\frac{x_*}{\delta} + T_w(y) \tag{11}$$

$$\delta^3 \frac{d\delta}{dy} = -\frac{\tfrac{1}{2} - T_w(y)}{1 + B(\tfrac{1}{2} - T_w(y))} \tag{12}$$

Note that the derivation of equations (11) and (12) allows for altitude-dependent wall temperature. The dimensionless quantities for the condensation side are defined as follows

$$x_* = \frac{\tilde{x}}{H\mathrm{Ra}_f^{-1/4}},\quad \delta = \frac{\tilde{\delta}}{H\mathrm{Ra}_f^{-1/4}},$$

$$v_* = \frac{\tilde{v}}{\dfrac{g(\rho_l - \rho_v)}{\mu_l}[H\mathrm{Ra}_f^{-1/4}]^2} \tag{13}$$

where Ra_f is the film Rayleigh number

$$\mathrm{Ra}_f = \frac{H^3 g(\rho_l - \rho_v)h_{fg}}{k_l \nu_l (T_s - T_c)} \tag{14}$$

and where the parameter B measures the degree of subcooling in the film

$$B = \frac{3}{8} c_p \frac{T_s - T_c}{h_{fg}} \tag{15}$$

Subscripts l and v stand for liquid and vapor phases, respectively, and h_{fg} is the latent heat of condensation. Solutions (10)–(12) satisfy the boundary conditions for the condensation side of the system

$$\begin{aligned} &v_* = 0,\ T = T_w(y) && \text{at } x_* = 0 \\ &\frac{\partial v_*}{\partial x_*} = 0,\ T = \tfrac{1}{2} && \text{at } x_* = -\delta \end{aligned} \tag{16}$$

The remaining condition which couples the two reservoirs is that the heat flux is continuous at the wall. In terms of dimensionless quantities this condition reads

$$A\left(\frac{\partial T}{\partial x_*}\right)_{x_* = 0^-} = \left(\frac{\partial T}{\partial x}\right)_{x = 0^+} \tag{17}$$

where

$$A = \frac{k_l}{k}\frac{\mathrm{Ra}^{-1/4}}{\mathrm{Ra}_f^{-1/4}} \tag{18}$$

Before closing this section it is worth clarifying that implicit in the formulation of the problem is the simplifying assumption that the thermal resistance of the wall separating the two reservoirs is negligible in the horizontal direction following [1, 4]. Hence, the temperature of the wall is independent of the horizontal coordinate.

3 Theoretical Solution

Since the expressions for the temperature distribution, the velocity, and the film thickness for the condensation space were obtained in the previous section, here we will focus on the Oseen-linearized solution for the open space. The Oseen method gives excellent results in natural convection problems [2–5, 9]. One obvious advantage of this method compared to classical integral solutions is that the velocity and the temperature profiles are not guessed but obtained by solving the linearized governing equations. In addition, the Oseen method contains all the attractive (for their simplicity) features of the integral methods.

According to the Oseen linearization method the horizontal velocity u and the temperature gradient in the vertical $\partial T/\partial y$ are assumed to be unknown functions of altitude, $\bar{u}(y)$ and $\bar{T}'(y)$ in the energy equation (3). Based on this assumption the energy equation becomes linear and can be solved theoretically. Omitting all the intermediate steps, for they can be found in [4], we report only the final expressions for the temperature and the velocity distributions

$$v = \frac{T_w + \tfrac{1}{2}}{2\lambda\xi} e^{-\lambda x}\sin(\xi x) \tag{19}$$

$$T = -\frac{T_w + \tfrac{1}{2}}{2\lambda\xi} e^{-\lambda x}[(\lambda^2 - \xi^2)\sin\xi x - 2\lambda\xi\cos\xi x] - \tfrac{1}{2} \tag{20}$$

To determine the unknowns $\lambda(y)$, $\xi(y)$ we require that equations (19) and (20) satisfy the energy equation (3) on the wall ($x = 0$) and after it is integrated over the boundary layer thickness (from $x = 0$ to $x \to \infty$). These operations yield two more equations for λ and ξ. Eliminating ξ in favor of λ the following expression is obtained

$$\frac{d}{dy}\left[\frac{(T_w + \tfrac{1}{2})^2}{16\lambda^3}\right] = \lambda(T_w + \tfrac{1}{2}) \tag{21}$$

In addition, combining the matching condition of equation (17) with equations (11) and (20) and eliminating ξ yields

$$A = \lambda\delta\frac{\tfrac{1}{2} + T_w}{\tfrac{1}{2} - T_w} \tag{22}$$

To proceed, equations (12), (21), and (22) are combined to yield the following two expressions containing two unknowns namely, $T_w(y)$ and $\delta(y)$

$$\frac{d\delta}{dT_w} = \frac{-2\delta(\tfrac{1}{2} + T_w)^4(2 - T_w)}{(2A)^4(\tfrac{1}{2} - T_w)^4[1 + B(\tfrac{1}{2} - T_w)] + 3(\tfrac{1}{2} + T_w)^5(\tfrac{1}{2} - T_w)^2} \tag{23}$$

$$\frac{dy}{dT_w} = \frac{2[1 + B(\tfrac{1}{2} - T_w)](\tfrac{1}{2} + T_w)^4\delta^4(2 - T_w)}{(2A)^4(\tfrac{1}{2} - T_w)^5[1 + B(\tfrac{1}{2} - T_w)] + 3(\tfrac{1}{2} + T_w)^5(\tfrac{1}{2} - T_w)^2} \tag{24}$$

The above differential equations (23) and (24) need to be integrated numerically to determine $T_w(y)$, $\delta(y)$. In the boundary layer regime ($H \gg \tilde{\delta}$) the system operates like a very long counterflow heat exchanger. Therefore, $T_w(y)$ assumes values between the two reservoir temperatures, $\tfrac{1}{2}$ and $-\tfrac{1}{2}$. The numerical integration was performed by using the Runge-Kutta method [10, 11]. To start the integration, initial values (at $y = 0$) for both y and δ are required. The initial value of y is known ($y = 0$). However, the value of the condensation thickness δ at $y = 0$ is not known. Hence, an interactive process is followed: The initial value of δ is guessed and the integration in T_w follows next by starting at $T_w = -\tfrac{1}{2}$ and by advancing in small steps in T_w until the other "extreme" of the T_w range, namely, $T_w = \tfrac{1}{2}$ is reached. The value of y at which $T_w = \tfrac{1}{2}$ is then checked. The process is repeated by adjusting the initial value of δ so that eventually $T_w = \tfrac{1}{2}$ takes place at $y = 1$. The step in T_w used was small enough so that reducing the step in T_w further had no effect on the results. The numerical procedure outlined above was repeated for a wide range of parameters A and B and the main results are reported in Table 1.

Table 1 Summary of numerical results

A	B	$\delta(y=0)$	$\mathrm{Nu}\,\mathrm{Ra}^{-1/4}$
0.01	1	1.183	0.0108
0.03	1	1.175	0.0309
0.1	1	1.152	0.0904
0.3	1	1.101	0.209
1	1	0.975	0.4005
3	1	0.785	0.538
10	1	0.559	0.597
20	1	0.449	0.606
1	0	1.056	0.391
1	0.1	1.046	0.392
1	10	0.727	0.4336
1	10^2	0.44	0.4874
1	10^3	0.2506	0.534

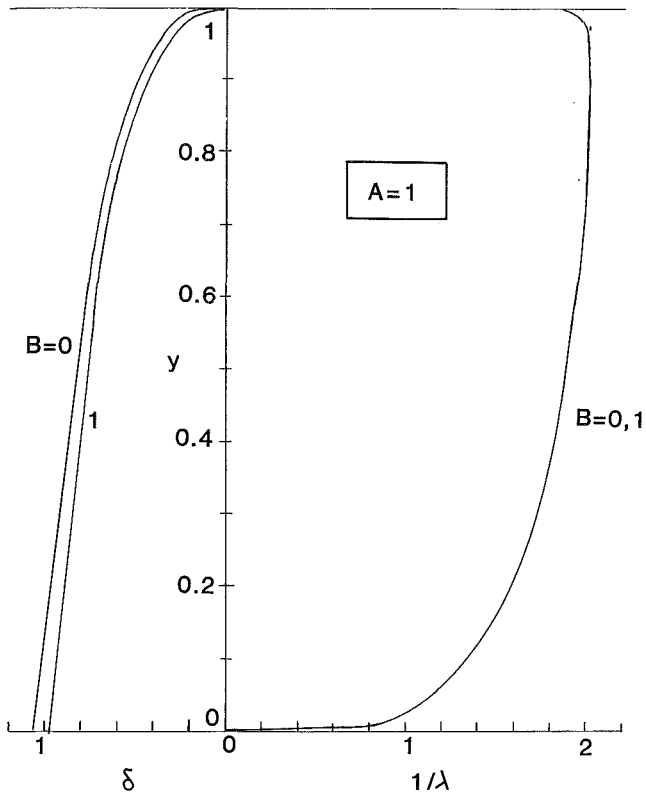

Fig. 2 The thickness of the condensation film (left) and the natural convection boundary layer (right) for $A = 1$ and representative values of B

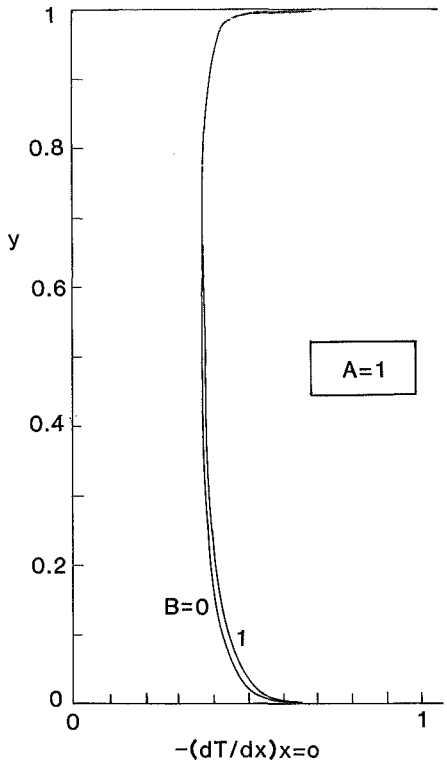

Fig. 4 The wall heat flux distribution for $A = 1$ and representative values of B

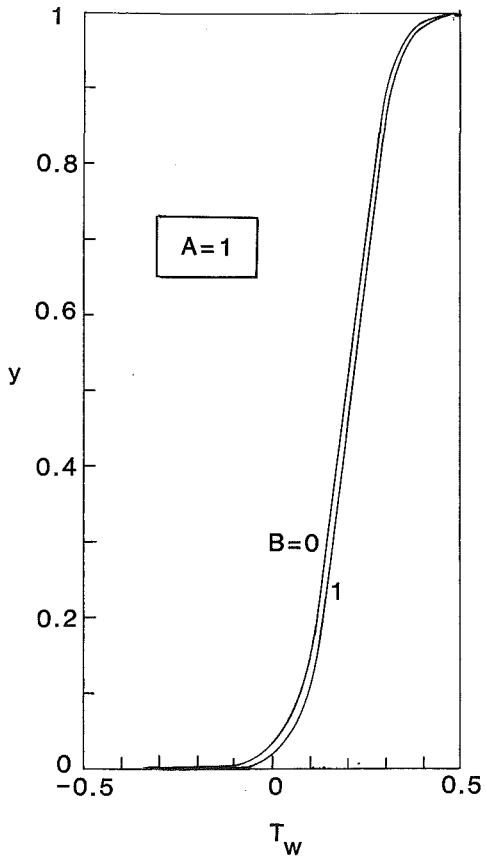

Fig. 3 The wall temperature distribution for $A = 1$ and representative values of B

4 Results and Discussion

At first, the numerical calculations were focused on determining the importance of the subcooling parameter B on the resulting flow structure and heat transfer. Figure 2 shows plots of the condensation film thickness (δ) and the natural convection boundary layer thickness ($1/\lambda$) versus the vertical coordinate y. The fact that the quantity $1/\lambda$ is the dimensionless boundary layer thickness results from the exponential term in equation (20) representing the decay of the temperature distribution with x [4, 5]. Both boundary layers increase in thickness in the flow direction with the exception of a thin region near $y = 1$ where the thickness of the natural convection boundary layer reduces rapidly to zero. Clearly, the effect of the subcooling parameter B is felt more on the condensation side than in the natural convection. In fact, in the scale of Fig. 2 the effect of B on the natural convection boundary layer thickness cannot be distinguished. Increasing B yields thinner boundary layers on both sides. This result makes sense physically since enhanced subcooling means enhanced heat transfer across the wall, hence sharper thermal boundary layers.

Figures 3 and 4 exemplify the wall temperature distribution and wall heat flux distribution, respectively. The wall temperature increases almost linearly with height. Near the two ends of the wall, where the present boundary layer approximations break down, the wall temperature departs from its linear distribution and assumes the values of the reservoir temperatures (Fig. 3). Increasing B yields a more uniform wall temperature distribution. The trend shown in Fig. 3 reveals that as B becomes increasingly large the wall will take on the saturation temperature of the condensation side. However, this will require extremely large values of B which, in turn, will yield very thin condensation films as indicated in Fig. 2 (note that the value $B = 1$ is already large from a practical standpoint). It is worth clarifying that the present analysis does not account for the phenomenon of rippling which may appear as the thickness of the condensation film diminishes ($B \to \infty$).

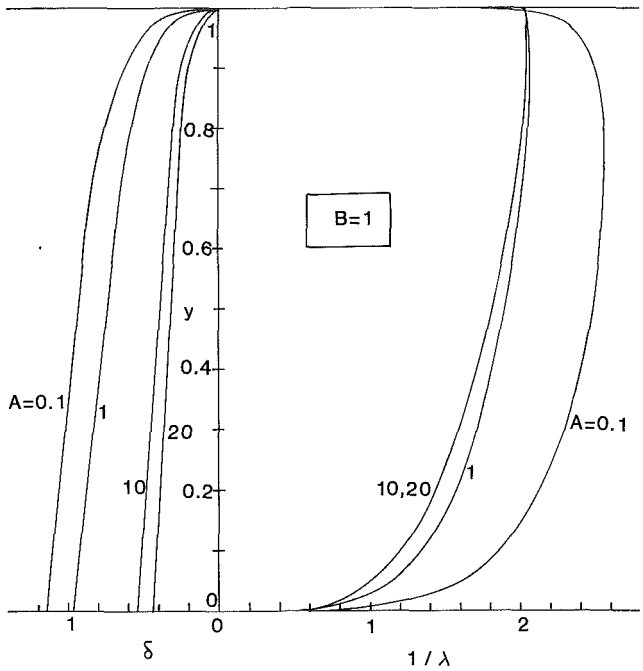

Fig. 5 The thickness of the condensation film (left) and the natural convection boundary layer (right) for $B = 1$ and representative values of A

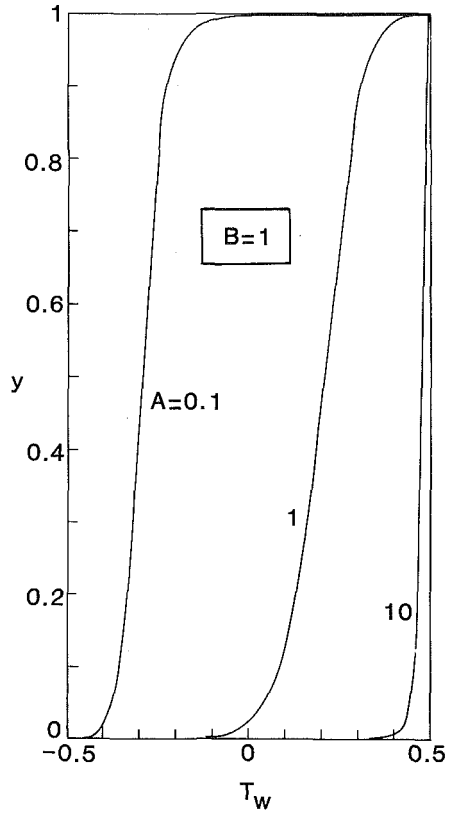

Fig. 6 The wall temperature distribution for $B = 1$ and representative values of A

Figure 4 shows that for small values of B the heat flux distribution is almost independent of altitude for most part of the wall. Near the two ends the heat flux blows up. Increasing B enhances the local heat flux. In addition, the heat flux distribution exhibits a stronger dependence on y as B increases.

Next, the effect of parameter A on the main characteristics of the problem of interest is examined. As illustrated in Figs. 5–7, in a qualitative sense, the effect of parameter A is similar to that of parameter B. However, examining Figs. 2–4 vis-à-vis Figs. 5–7 proves that the effect of "interaction" parameter A on the conjugate condensation–natural convection phenomenon is much more pronounced. Increasing A results in thinner layers on both sides (Fig. 5). In addition, very large values of A yield a uniform wall temperature distribution equal to the saturation temperature of the hot reservoir (Fig. 6). Examining the physical significance of parameter A indicates that this result is correct. Indeed, equation (18) implies that large values of A correspond to cases where the condensation phenomenon dominates over the

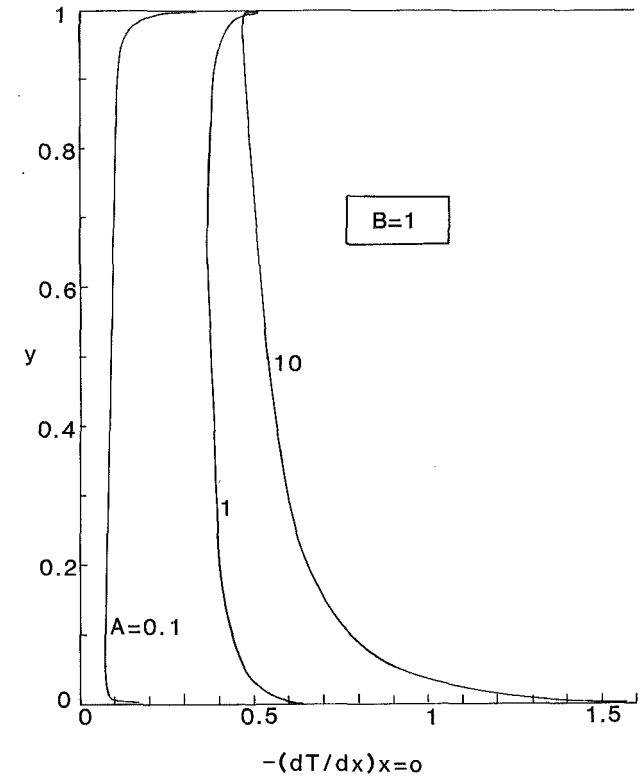

Fig. 7 The wall heat flux distribution for $B = 1$ and representative values of A

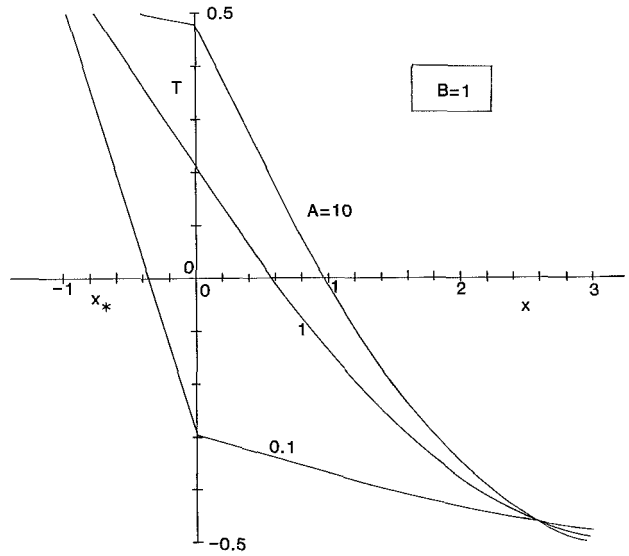

Fig. 8 Temperature profiles in the condensation film and the natural convection boundary layer at midheight for $B = 1$ and representative values of A

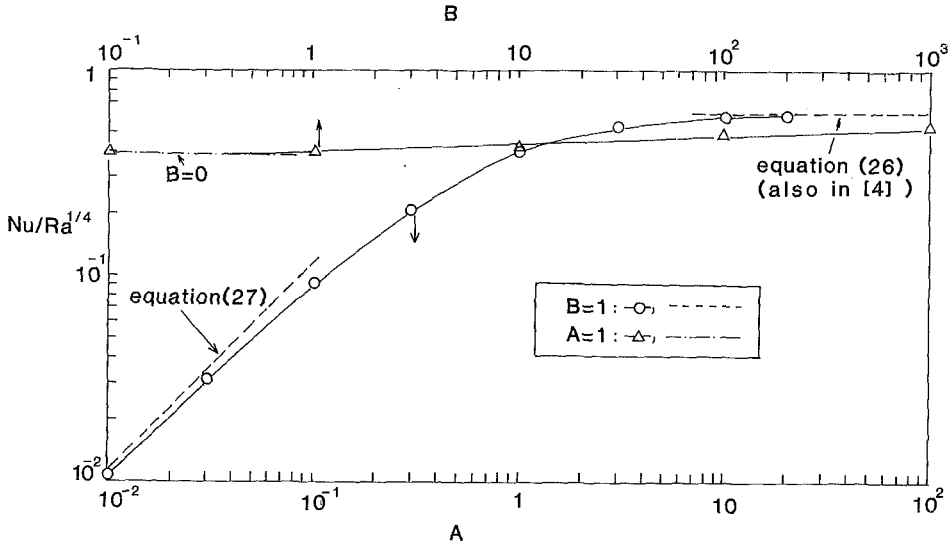

Fig. 9 Summary of heat transfer results documenting the effect of parameters A and B on the overall heat flux from the condensation side to the natural convection side

natural convection phenomenon. The effect of increasing A is to enhance the local heat flux on the wall (Fig. 7).

The temperature distribution within the condensation film and within the natural convection boundary layer at midheight is shown in Fig. 8. Clearly, parameter A has a dominant effect on the temperature distribution. Increasing A also increases the wall temperature at midheight. In addition, going from $A=0.1$ to $A=10$ in Fig. 8 alters the picture from one exhibiting an almost isothermal natural convection thermal boundary layer interacting with a significantly nonisothermal condensation film, to one exhibiting a nonisothermal natural convection thermal boundary layer coupled with an almost isothermal condensation film. Note that the temperature profiles in the left side of Fig. (8) extend between the wall and the edge of the respective condensation film. Outside the condensation film the temperature is constant and equal to that of the warm reservoir ($T=0.5$).

Finally, in Fig. 9 our attention is shifted to reporting heat transfer results of engineering importance. This task is performed with the help of a $Nu/Ra^{1/4}$ versus A graph. The Nusselt number is defined as follows

$$Nu=\frac{Q}{k(T_s-T_c)} \tag{25}$$

where k is the thermal conductivity of the fluid in the natural convection side, and Q is the total heat flux through the wall obtained by integrating numerically the local heat flux in the horizontal direction over the entire height of the wall. As explained in the discussion pertaining to Figs. 4 and 7 the local heat flux is singular at $y=0$ and 1. However, the total heat flux Q through the wall is finite. Similar behavior of the heat flux integral is reported in [1-5]. Increasing A while keeping B constant (Fig. 9) enhances heat transfer until a plateau is reached for large values of A. This plateau corresponds to the case where the wall has the temperature of the condensation reservoir ($T_w=1/2$). Focusing on the natural convection side and repeating the analysis reported in the previous section while keeping $T_w=1/2$ yields

$$Nu=0.621Ra^{1/4} \tag{26}$$

As Bejan and Anderson noted in [4] this asymptotic result agrees well (within 2.6 percent) with similarity solution results [8] for the constant wall temperature natural convection problem in the limit of large Pr.

An asymptotic expression for Nu can also be obtained in the limit of small A. In this case the wall temperature is $T_w=-1/2$. Working with the condensation side this time for $T_w=-1/2$ yields

$$Nu=\frac{4}{3}A\left(\frac{1+B}{4}\right)^{1/4}Ra^{1/4} \tag{27}$$

The validity of equation (27) is justified by the fact that in the extreme $B=0$ and for $k_l=k$, it becomes identical to the Nusselt number expression reported by Rohsenow [12] for the case of film condensation from a vertical wall at constant temperature ($Nu=0.943\,Ra_f^{1/4}$). Expression (27) is also plotted in Fig. 9 for $B=1$. The points denoted by circles bridging the gap between asymptotes (26) and (27) were obtained numerically. Clearly, for $A<0.1$ and $A>10$ expressions (27) and (26), respectively, constitute a good approximation for Nu.

The points denoted by triangular symbols correspond to the case $A=1$ and illustrate the effect of B on the overall heat transfer through the wall. Increasing B enhances the heat transfer from the condensation side to the natural convection side; however, this effect is considerably weaker than the effect of A on the overall heat transfer.

The fact that the impact of parameter B on the results is weak, as clearly illustrated in Figs. 2-4 and 9 and in Table 1, has a number of important implications which generalize the usability of Fig. 9 as a thermal design tool. First, we note that for water condensation the values of B are in the range $10^{-4}<B<10^{-2}$. In this range, the maximum change in $NuRa^{-1/4}$ induced by varying B is 0.26 percent (Fig. 9, Table 1). In fact, going from $B=0$ to $B=1$ increases $NuRa^{-1/4}$ by less than 2.4 percent. Therefore, the effect of B may be neglected for all practical purposes. Even using results for $B=1$ in cases where $B<10^{-2}$ constitutes an excellent approximation.

Based on the above observations, the following can be deduced regarding the use of Fig. 9 for values of A and B other than the ones investigated in the present study:

- Since varying B from $B=0$ to $B=1$ leaves the value of the group $NuRa^{-1/4}$ practically unchanged, the curve reported in Fig. 9 for $B=1$ provides an excellent estimate for all values of B in the above range.
- For similar reasons, a family of $A=$const curves can be

easily obtained in the range $B<1$ by drawing lines parallel to the line $B=0$, $A=1$, for different values of A.

5 Conclusion

This paper reported a theoretical study of conjugate film condensation and boundary layer natural convection coupled through a vertical wall. The natural convection side of the system was treated based on the Oseen-linearization method and the condensation side based on thin film analysis. The solution of the problem was made possible by matching the findings of the analyses for each side, on the wall. Representative results for the condensation film thickness, the natural convection boundary layer thickness, the wall temperature and the wall heat flux were presented in the course of the study. The temperature variation along the wall was approximately linear except in the regions near the two ends. Increasing the "interaction" parameter A or the subcooling parameter B yielded thinner layers on both sides and enhanced the local flux at the wall. The effect of A on the flow and heat transfer characteristics of the system was drastic relative to the effect of B.

Heat transfer results were reported in Table 1, and in Fig. 9 by means of a $Nu/Ra^{1/4}$ versus A plot. Asymptotic expressions for the overall heat transfer through the wall were also obtained in the limits of small A (equation (27)) and large A (equation (26)). These expressions agree very well with known results for the case of film condensation along a vertical wall at constant temperature [12] and for natural convection along a vertical wall at constant temperature [8].

Acknowledgments

I am grateful to NSF for providing financial support for this research through Grant ENG-8451144.

References

1 Lock, G. S. H., and Ko, R. S., "Coupling Through a Wall Between Two Free Convective Systems," *International Journal of Heat and Mass Transfer*, Vol. 16, 1973, pp. 2087–2096.

2 Anderson, R., and Bejan, A., "Natural Convection on Both Sides of a Vertical Wall Separating Fluids at Different Temperatures," ASME JOURNAL OF HEAT TRANSFER, Vol. 102, 1980, pp. 630–635.

3 Bejan, A., and Anderson, R., "Heat Transfer Across a Vertical Impermeable Partition Imbedded in Porous Medium," *International Journal of Heat and Mass Transfer*, Vol. 24, 1981, pp. 1237–1245.

4 Bejan, A., and Anderson, R., "Natural Convection at the Interface Between a Vertical Porous Layer and an Open Space," ASME JOURNAL OF HEAT TRANSFER, Vol. 105, 1983, pp. 124–129.

5 Gill, A. E., "The Boundary Layer Regime for Convection in a Rectangular Cavity," *Journal of Fluid Mechanics*, Vol. 26, 1966, pp. 515–536.

6 Sparrow, E. M., and Prakash, C., "Interaction Between Internal Natural Convection in an Enclosure and an External Natural Convection Boundary Layer Flow," *International Journal of Heat and Mass Transfer*, Vol. 24, 1981, pp. 875–907.

7 Sparrow, E. M., and Faghri, M., "Parallel Flow and Counterflow on an Internally Cooled Vertical Tube," *International Journal of Heat and Mass Transfer*, Vol. 23, 1980, pp. 559–562.

8 Rohsenow, W. M., Hartnett, J. P., and Ganic, E., eds., *Heat Transfer Fundamentals*, 2nd ed., McGraw-Hill, New York, 1985.

9 Bejan, A., *Convection Heat Transfer*, Wiley, New York, 1984.

10 Carnahan, B., Luther, L. A., and Wilkes, J. O., *Applied Numerical Methods*, Wiley, New York, 1969.

11 Ferziger, J. H., *Numerical Methods for Engineering Application*, Wiley, New York, 1981.

12 Rohsenow, W. M., "Heat Transfer and Temperature Distribution in Laminar Film Condensation," ASME JOURNAL OF HEAT TRANSFER, Vol. 78, 1956, pp. 1645–1648.

K. N. Agrawal
Lecturer.

H. K. Varma
Professor.

S. Lal
Professor.

Mechanical and Industrial Engineering Department, University of Roorkee, Roorkee-247 667, India

Heat Transfer During Forced Convection Boiling of R-12 Under Swirl Flow

This work is an experimental investigation of heat transfer augmentation in a horizontal R-12 evaporator, continuing an earlier study [1] *by the authors on swirl flow pressure drops. Twisted tapes were used to create swirl motion during the flow boiling inside an evaporator tube of 10 mm i.d. Average heat transfer coefficients have been determined for 60 runs corresponding to three heat fluxes, five mass velocities, and four twist ratios. Swirl flow heat transfer coefficients have been found, in general, to be greater than the corresponding plain flow values, but the degree of enhancement varies depending on the test conditions and the twist ratio of the inserted tape. An empirical correlation which predicts the average swirl flow heat transfer coefficients within ±30 percent of the experimentally observed values has been successfully developed.*

Introduction

It has always been the endeavor of the designers to achieve maximum heat transfer rates in heat exchangers and other such equipment. The idea of enhancing heat transfer rates by using "turbulence promoters" (also called "spiral generators," "swirl generators," or "vortex generators") in fluid flow passages is not new [2–4], but the literature in this area has grown larger and faster recently [5–8]. Several investigations carried out earlier in this direction have established that the swirl generators are promising devices for augmenting heat transfer rates in heat exchangers.

The spiral generators used for creating swirl/disturbance in the flow are of various shapes and sizes, and the performance of these turbulators has been investigated from time to time. A review of literature in this field indicates that although the swirl generators improve heat transfer rates, a clear generalized quantitative picture is not yet available. Most of the experiments carried out in this direction relate to single-phase swirl flow studies. Work on two-phase swirl flow boiling of liquids [5, 9–11] is comparatively less while data on swirl flow boiling of refrigerants have been scantily reported [11, 12]. The present work was taken up, therefore, with the possible aim of achieving better heat transfer results in a refrigerant evaporator by swirling the flow inside it. Refrigerant 12 was taken as the working fluid because of its wide application in refrigeration systems.

Experimental Setup and Operating Procedure

This study concerns the determination of heat transfer rates occurring during forced convection boiling of R-12 in a horizontal stainless steel evaporator under swirl flow conditions. The schematic diagram of the experimental setup used for this purpose is shown in Fig. 1. It was a closed circuit heat transfer test loop in which a condensing unit circulated R-12 through the rotameter, preheater, test section, and afterheater. Two manually operated expansion valves were connected in parallel in the circuit ahead of the preheater. One valve provided a coarse control of flow rate of refrigerant while the other one was a precision expansion valve. The refrigerant, after throttling in the expansion valves, entered the preheater where it could be supplied a predetermined quantity of heat to obtain a desired vapor quality at the test section inlet. The liquid-vapor mixture then passed through the test section where it was heated up electrically by passing alternative current through the tube wall with the help of a variable voltage transformer. A back-pressure regulating valve (not shown) installed downstream of the test section maintained constant pressure at the tube outlet. An afterheater was installed in the suction line to ensure that no liquid refrigerant entered the compressor.

Test Equipment. The test section consisted of a round stainless steel tube, 10 mm in internal diameter and 12.94 mm in outer diameter. It was 2.1 m long with copper buss connectors at both ends to supply electrical power to the tube. Two pressure taps were on the sides of the connector. Twenty-four S.W.G. copper-constantan thermocouples were spot welded at ten locations, equally spaced at regular intervals of 20 cm, one each at the top, side, and bottom of the tube. Mild steel flange couplings were brazed at the two ends of the tube so that the tube could be detached out of the test assembly for the insertion of twisted tapes. The stainless steel tube, along with the buss connectors and flange coupling, was electrically isolated from the rest of the assembly by nuprone tubing. The test section was placed inside a wooden box to insulate it thermally from the surroundings. A 6-mm-thick roll of glass wool was wrapped around the tube and the entire wooden box was filled with loose glass wool. The test-section assembly is shown in Fig. 2.

The twisted strips were made from 0.5-mm-thick stainless steel flats and fitted snugly inside the test section tube as described in [1]. Necessary controls and instruments were installed to control and measure the heating rates, flow rates,

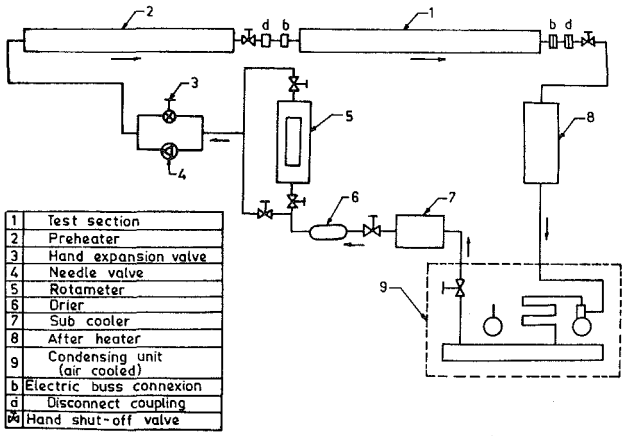

Fig. 1 Schematic diagram of experimental setup

Contributed by the Heat Transfer Division for publication in the JOURNAL OF HEAT TRANSFER. Manuscript received by the Heat Transfer Division August 9, 1983.

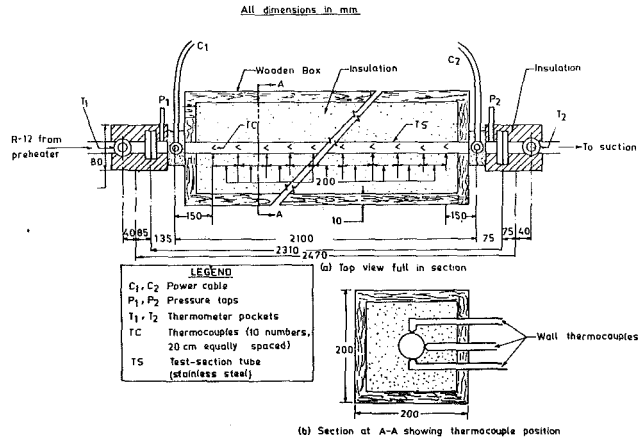

Fig. 2 Test-section assembly

and various pressures and temperatures at the desired locations.

Operating Procedure. First of all, the discharge valve of the compressor was opened and water from the mains was made to flow through the subcooler and the after-heater tank. The compressor motor was then started and the suction valve of the compressor was gradually opened. The receiver valve was opened next, and the liquid refrigerant was then allowed to flow in a small quantity to the test section through the rotameter and preheater by operating the two hand expansion valves. The power supply was then passed to the test section with the help of the stepdown transformer and the desired heat flux was obtained by regulating the transformer in such a way that the digital multimeter showed the required voltage across the test section. The desired refrigerant flow rate was obtained by adjusting the expansion valves again and observing the reading on the rotameter. The electric load required in the preheater in order to get a predetermined refrigerant quality at the test section inlet was supplied by regulating the voltage supplied to the preheater with the help of variable transformer. A constant gage pressure of 137.8 kPa (20 psig) was maintained at the test-section outlet in all the runs with the help of a back-pressure regulator (not shown in Fig. 1). In order to determine whether the system had attained the steady state, wall and refrigerant temperatures were observed frequently. The data were recorded when these values stabilized.

Experiments were conducted first with the bare tube; when the recording of a set of experimental data for this tube was over, the system was pumped down and the desired twisted tape was installed. The required data were recorded again for the tube now fitted with the tape.

Experimental Parameters. The pertinent dimensions of the test section and the range of operating parameters for this investigation were as follows:

(*i*) Tubing: stainless steel, round cross section
Roughness = 1.08 μm (average value)
Inside diameter = 10 mm
Outside diameter = 12.94 mm
Heated length = 2.1 m

(*ii*) Twisted tapes: stainless steel flats

Nomenclature

A = flow area, m^2
a = tape thickness, m
A_0, A_1, A_2 = coefficients
B, B_1, B_2 = coefficients
b = tape width, m
C = fluid velocity, m/s
C_p = specific heat at constant pressure, J/kg-K
D = inside tube diameter, m
F = dimensionless parameter
f = function of
G = mass velocity, kg/s-m^2
g = acceleration due to gravity, m/s^2
H = enthalpy, J/kg
h = heat transfer coefficient, W/m^2-K
J = mechanical equivalent of heat, used in equation (6)
k = thermal conductivity, W/m-K
L = heated length, m
M = mass flow rate, kg/s
m_1, m_2, n_1, n_2 = exponents
q = heat flux, W/m^2
R = radius of the tube, m
T_w = wall temperature inside tube, K
T_{sat} = saturation temperature, K
ΔT = wall to bulk fluid temperature difference, K
X_{tt} = Lockhart-Martinelli chi parameter,

$$= \left(\frac{1-x}{x}\right)^{0.9} \left(\frac{\rho_g}{\rho_l}\right)^{0.5} \left(\frac{\mu_l}{\mu_g}\right)^{0.1}$$

x = vapor quality
Δx = change in vapor quality
y = twist ratio (ratio of "half of the pitch of the helix" to the inside tube diameter)
Bo = boiling number = $q/(G H_{fg})$
Fr = Froude number = C_a^2/gD
Gr = Grashof number = $g\beta\Delta TD^3/\nu^2$
Pr = Prandtl number = $\mu C_p/k$
Re = Reynolds number = GD/μ
β = volumetric coefficient of expansion, K^{-1}
μ = absolute viscosity, kg/s-m
ν = kinematic viscosity, m^2/s
ρ = density, kg/m^3

Subscripts

a = axial component
b = bulk
B = bottom
BP = Bo Pierre equation (equation (6))
cc = centrifugal convection
f = film temperature
fg = latent heat
h = hydraulic
l = liquid
m = arithmetic mean value
np = nonboiling plain flow
ns = nonboiling swirl flow
p = plain flow boiling
pm = plain flow boiling—observed mean values
px = plain flow boiling—observed local values
s = swirl flow boiling
sm = swirl flow boiling—observed mean values
sp = swirl flow boiling—predicted mean values
sx = swirl flow boiling—observed local values
s = side
t = tangential component
T = top
x = local value
z = location number

Roughness = 0.267 μm (average value)
Thickness = 0.5 mm
y values = 3.76, 5.58, 7.37, 10.15

(*iii*) Test conditions: fluid R-12
Mass velocity = (7.0 to 14.0) $\times 10^5$ kg/hr-m^2
Heat flux = 8.0 to 13.6 kW/m^2
Vapor quality = 0.30–0.75
System pressure = 138 to 166 kPa

Data Reduction

In order to analyze the experimental data, it was necessary to reduce them into desired parameters. A computer program was written for this purpose and was run to calculate these parameters. As mentioned earlier, the test evaporator tube was heated electrically by passing an alternating current through it. Since the tape was snugly fitted inside the tube, a part of the total electric current was also flowing through it. In order to have an estimate of the amount of heating being done in the tape, the electrical resistances of the bare tube and the tube fitted with the four different twisted strips were measured. The resistance of the strips was found to be in the range of 7.415 to 7.566 times the bare tube resistance. The amount of heat generated in the strips was also calculated and it was found in the range of 11.67 to 11.88 percent of the total heat generated. The results of Lopina and Bergles [6] who conducted a similar experiment on single-phase swirl flow of water adopting d-c heating of the tube do not indicate any apparent effect of the heating of the tape on the heat transfer behavior for a similar situation. The amount of heating of the tape in the present investigation is expected not to affect the heat transfer mechanism significantly.

The heat flux q was calculated by dividing the product of the voltage applied to the test section and the total current by the inside surface area of the tube as was also done by Lopina and Bergles [6]. Equation (1) was used to calculate the heat transfer coefficients

$$h = \frac{q}{T_w - T_{\text{sat}}} \tag{1}$$

Since the outside wall temperatures at the top, side, and bottom points at a particular location were measured, the inside wall temperatures at respective points were found by subtracting temperature drop from these known values. The temperature drop in the wall of the tube was found by using the equation of internal heat generation given by McAdams [13]. The T_{sat} in equation (1) was taken as the saturation temperature corresponding to the pressure of the refrigerant at any section of the tube. The pressure at any section was calculated on the basis of measured pressures at the inlet and exit of the tube and by assuming a linear pressure drop along the test-evaporator length. Equation (1) was then applied to find the top, side, and bottom heat transfer coefficients h_T, h_S, and h_B, respectively, at any section.

The local heat transfer coefficient h_x at any location (section) x was found by using equation (2)

$$h_x = \frac{h_T + 2h_S + h_B}{4} \tag{2}$$

The temperatures at stations 1, 2, and 10 of the thermocouples showed in general a random behavior. This was apparently due to entrance and axial conduction effects. In order to calculate the average heat transfer coefficients therefore only seven values of h_x from the third to ninth location were taken. At each heat flux when the desired vapor quality did not occur at the exit of the tube in one run, heating was employed in the preheater so that the vapor quality at the inlet and hence at the exit of the tube increased. This ensured that the vapor quality at the tube outlet for all the test conditions was about 75 percent.

Results and Discussion

Overlapping of Data and Plain Flow Boiling Local Heat Transfer Coefficients. When the desired range of vapor quality during evaporation was achieved in two or more runs as described above, the heat transfer coefficients obtained in such runs were checked for continuity (overlapping). It was observed that the coefficients showed a continuous trend in the heat flux range of 8000 W/m^2 to 13,600 W/m^2. Furthermore, the plain flow boiling heat transfer coefficients were compared with the Lavin-Young [15] and Chaddock-Noerager [14] correlations, and were found to agree satisfactorily with them as shown later.

At the higher heat fluxes of 16,000 W/m^2 and 20,000 W/m^2, it was observed that the heat transfer coefficients both in plain flow and swirl flow boiling are reduced considerably when the vapor quality of the refrigerant at the test-section inlet is high, of the order of 0.5. An examination of the heat transfer coefficients for plain flow showed that they do not agree satisfactorily with the values predicted by correlations of Lavin and Young (equation (4)) and Chaddock and Noerager (equation (3)). However, the agreement was found to be quite satisfactory when the refrigerant either entered the test section directly from the expansion valve or had a low vapor quality of the order of 0.3 at the inlet. A study of experimental data obtained at these high heat fluxes and higher vapor qualities

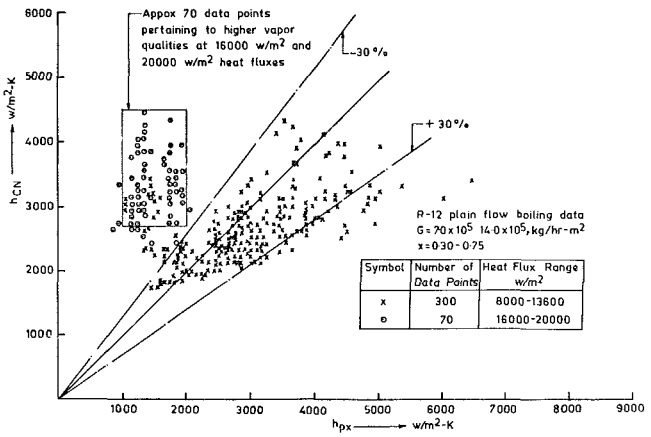

Fig. 3 Comparison of observed plain flow boiling local heat transfer coefficients with values predicted by the Chaddock—Noerager equation (3)

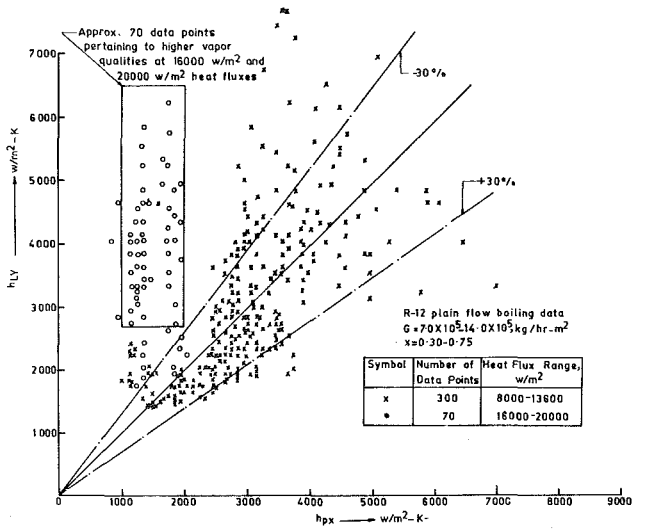

Fig. 4 Comparison of observed plain flow boiling local heat transfer coefficients with values predicted by the Lavin—Young equation (4)

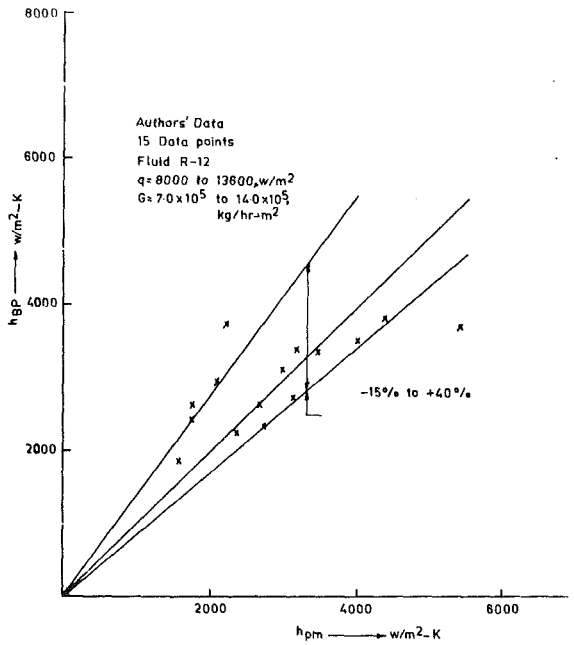

Fig. 5 Comparison of authors' plain flow boiling mean heat transfer coefficients with the values predicted by the Bo Pierre equation (6)

suggests that a highly unstabilized flow exists in the evaporator when the inlet vapor quality is high. This instability in flow, coupled with an increased rate of vapor formation at higher heat fluxes, appparently leads to an unstable liquid film at the wall. Thus an increase in the wall temperatures results, which consequently yields a lower heat transfer coefficient.

During plain flow boiling of liquids in a horizontal evaporator, equations (3) and (4), proposed by Chaddock and Noerager [14] and Lavin and Young [15], respectively, are widely accepted as standard correlations for predicting local heat transfer coefficents h_{px}

$$h_{CN} = (1.85)(h_{DB})\left[\mathrm{Bo}(10^4) + \left(\frac{1.0}{X_{tt}}\right)^{0.67}\right]^{0.6} \tag{3}$$

$$h_{LY} = (6.59)(h_{DB})(1-x)^{0.8}\left(\frac{1+x}{1-x}\right)^{1.16}(\mathrm{Bo})^{0.1} \tag{4}$$

where h_{DB} is the Dittus-Boelter heat transfer coefficient calculated by equation (5)

$$h_{DB} = 0.023\left(\frac{k_l}{D}\right)(\mathrm{Re})_l^{0.8}(\mathrm{Pr})_l^{0.4} \tag{5}$$

A comparison of the present experimentally observed plain flow boiling local heat transfer coefficients h_{px} with h_{CN} and h_{LY} is shown in Figs. 3 and 4, respectively. Approximately 370 data points in the heat flux range of 8000 to 20,000 W/m^2, with the refrigerant mass velocities varying from 7.0×10^5 to 14.0×10^5 kg/hr-m^2 in the vapor quality range of 0.30 to 0.75, have been plotted on these graphs. In this investigation lower values of the heat transfer coefficients were observed at heat fluxes of 16,000 W/m^2 and 20,000 W/m^2 when the inlet quality was increased with the help of the preheater (vapor quality approximately 0.50 to 0.75). It is seen in Figs. 3 and 4 that approximately 70 data points (shown in rectangle) which pertain to this condition do not agree well with h_{CN} and h_{LY}.

The remaining 300 data points correlate satisfactorily with h_{CN} and h_{LY} and it is also noticeable that h_{px} shows a better agreement with h_{CN} than with h_{LY}. Since a discontinuous change in heat transfer coefficients was observed at 16,000 W/m^2 and 20,000 W/m^2 heat fluxes, finding average h values and trying to develop a correlation including these data was not attempted. Average heat transfer coefficients were calculated for the heat flux range of 8000 W/m^2 to 13,600 W/m^2 only and these data were correlated.

Plain Flow Boiling Average Heat Transfer Coefficients. Equation (6) proposed by Bo Pierre [16] is a widely accepted standard correlation for predicting average heat transfer coefficients during plain flow boiling of a refrigerant in a horizontal evaporator

$$h_{BP} = \left(\frac{k_l}{D}\right)(\mathrm{B})\left[(\mathrm{Re})_l^2\left(\frac{J\,\Delta x\,H_{fg}}{L}\right)\right]^n \tag{6}$$

where $B = 0.0009$ and $n = 0.5$ for exit vapor qualities ≤ 0.9; $B = 0.0082$ and $n = 0.4$ for exit vapor qualities > 0.9 to 6K superheat.

A comparison of the average plain flow boiling heat transfer coefficients h_{pm} from the present investigation with h_{BP} is shown in Fig. 5. Fifteen data points corresponding to three heat fluxes of 8000, 10,700, and 13,600 W/m^2 and the five mass velocities have been plotted. It is seen in this figure that approximately 12 data points lie between the -15 percent and $+40$ percent lines. The tending of data toward the $+40$ percent line suggests that the Bo Pierre equation slightly overpredicts the experimental values. Overprediction from the Bo Pierre equation has also been reported by Singal et al. [17].

Behavior of Swirl Flow Heat Transfer Coefficients. Curves are plotted in Figs. 6 through 8 to study the effect of twist ratio, vapor quality, and heat flux on the heat transfer coefficients. These curves show that there are marked random variations in the heat transfer coefficients. Such fluctuations have been widely reported for plain flow boiling [18]. That there are similar large random fluctuations during swirl flow boiling is not surprising since flow boiling is known to be a highly unstable phenomenon. The reason that the lines of constant twist ratios cross each other, and sometimes the values of h_{sx}/h_{px} fall below 1.0 as seen in Figs. 6 to 8, may be this unstable nature of boiling. Figure 6 shows that except in the narrow vapor quality ranges of 0.29 to 0.32 and 0.50 to 0.55, the heat transfer coefficients for the lowest twist ratio are the highest. If Figs. 6, 7, and 8 are compared for the effect of twist ratio, it is observed, in general, that as the twist ratio increases, the heat transfer coefficient decreases.

It is also seen in Figs. 6 through 8 that not only the twist ratio, but also the vapor quality x and the heat flux q influence the ratio h_{sx}/h_{px} considerably. While at heat flux of 8000 W/m^2 (Fig. 5), h_{sx}/h_{px} has a maximum value of approximately 2, it shifts to approximately 2.6 and 3.2, respectively, at heat fluxes of 10,700 to 13,600 W/m^2. As can be observed in these figures, h_{sx}/h_{px} ratios also vary significantly with the change in vapor qualities at all three heat fluxes. Their values are different at different vapor qualities, and an optimum range of vapor quality which would give a maximum h_{sx}/h_{px} at all the twist ratios and heat flux is difficult to predict. However, in Figs. 7 and 8, which have been drawn for the two higher heat fluxes of 10,700 and 13,600 W/m^2, respectively, the vapor quality range of 48 to 60 percent appears to be favorable because in this range, the ratio h_{sx}/h_{px} is found to be uniformly high.

Development of an Empirical Correlation

The effect of twist ratio, heat flux, and mass velocity on the heat transfer coefficients has been discussed above, and it was found that the ratios h_s/h_p are mainly dependent on these three parameters. The dependence of h_s/h_p on these parameters thus suggests that the enhanced heat transfer coefficients in swirl flow are a function of both forced convection and swirl flow effects. On the basis of these observations, a model is proposed which considers that while the forced convection effects may be taken into account by two dimensionless parameters, the Boiling number Bo and the Reynolds number Re, the swirl flow effect may be represented by the

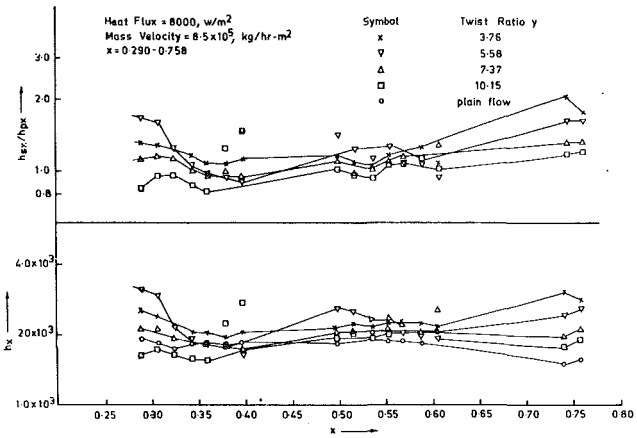

Fig. 6 Variation of local heat transfer coefficients h_x and h_{sx}/h_{px} ratios with vapor quality at different twist ratios, heat flux and mass velocity being constant

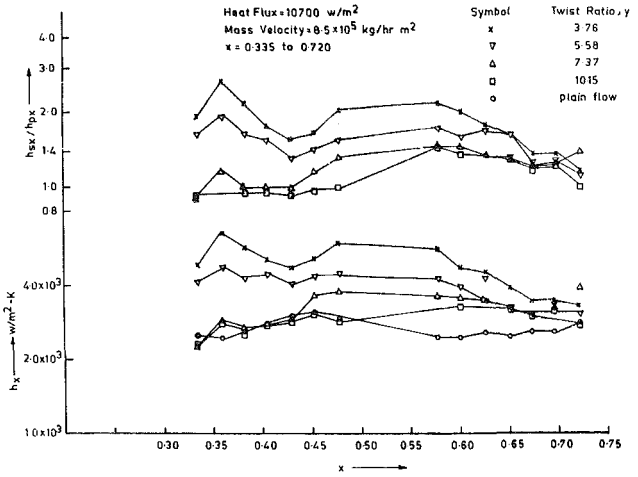

Fig. 7 Variation of local heat transfer coefficients h_x and h_{sx}/h_{px} ratios with vapor quality at different twist ratios, heat flux and mass velocity being constant

twist ratio y. The ratio h_s/h_p can therefore be written mathematically in terms of these nondimensional numbers by expression (7)

$$\frac{h_s}{h_p} = f[\text{Re, Bo, } y] \tag{7}$$

The present plain flow boiling heat transfer coefficients h_p were found in fair agreement with the Bo Pierre correlation given by equation (6). It was felt that replacing h_p by h_{BP} in expression (7) would yield a better form of the equation because of the readily available values of h_{BP} from equation (6). This leads to expression (8)

$$h_s/h_{\text{BP}} = f[\text{Re, Bo, } y] \tag{8}$$

A study of past literature [5, 6, 9, 10] suggests that the swirl flow effects, which have been accounted for empirically by the twist ratio y in equation (8), consist of two factors: one pertaining to increased fluid velocity at the tube wall, and the other to a centrifugal force field set up in the flow due to the tape. The former effect has been termed the "spiral convection effect," and the latter the "centrifugal convection effect," by Lopina and Bergles [6]. They have suggested an additive expression of the following form to predict the single-phase swirl flow heat transfer coefficients of water

$$h_{ns} = \left(\frac{k}{D_h}\right)(B_1)\left[[0.023(\alpha\ \text{Re}_h)^{0.8}(\text{Pr})^{0.4}] + B_2\left[\left(\frac{\text{Re}_h}{y}\right)^2\left(\frac{D_h}{D}\right)(\beta\Delta T\text{Pr})\right]^{1/3}\right] \tag{9}$$

where $\alpha = \sqrt{(\pi^2+4y^2)}/2y$. However, the experimental data of this investigation which are for the swirl flow boiling of R-12 did not agree with such an expression.

Since spiral and centrifugal convection effects are not independent, and a change in one factor affects the other also, an additive type of correlation to express equation (8) has not succeeded. A multiplication type of correlation given by equation (10) was, therefore, attempted

$$\frac{h_s}{h_{\text{BP}}} = A_1(\text{Re})^{a_1}(\text{Bo})^{b_1}(y)^{c_1} \tag{10}$$

A computer program was run to calculate the coefficient A_1 and exponents a_1, b_1, and c_1 of equation (10) by the method of least squares. Experimental average swirl flow heat transfer coefficients h_{sm} were taken for h_s in equation (10) for a total of 60 data points. This yielded the best fit equation (11) for predicting the swirl flow boiling heat transfer coefficients of the present investigation

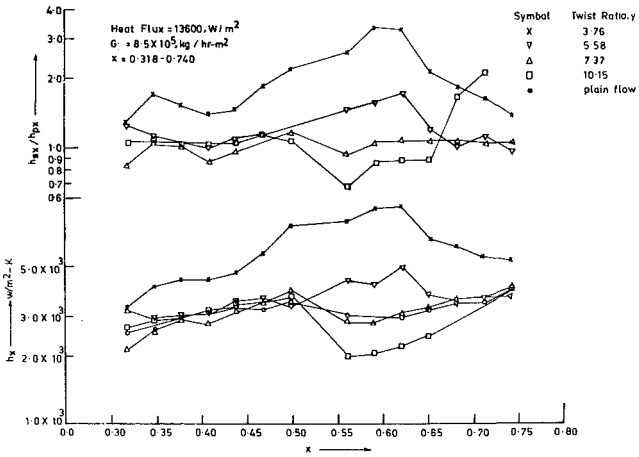

Fig. 8 Variation of local heat transfer coefficients h_x and h_{sx}/h_{px} ratios with vapor quality at different twist ratios, heat flux and mass velocity being constant

$$\frac{h_{sp}}{h_{\text{BP}}} = (0.2944)(10^{-2})(\text{Re})^{2.247}(\text{Bo})^{1.624}(y)^{-0.5219} \tag{11}$$

It should be noted that equation (11) has been developed for R-12 under the following experimental conditions

$$8 \le q \le 13.6\ \text{kW/m}^2$$
$$0.30 \le x \le 0.75$$
$$7\times10^5 \le G \le 14\times10^5\ \text{kg/hr-m}^2$$
$$3.76 \le y \le 10.15$$

The values of predicted swirl flow heat transfer coefficients h_{sp} given by equation (11) have been plotted against the experimentally observed values h_{sm} in Fig. 9. It is observed in this figure that most of the predicted values lie within ±30 percent of the experimental values. The above equation predicted the data with a mean deviation of −4.16 percent and a standard deviation of 28.16 percent.

A Physical Model. It may be recalled that the term y in equation (11), which is the twist ratio, accounts for the swirl effects of the tape in the heat transfer coefficient. As men-

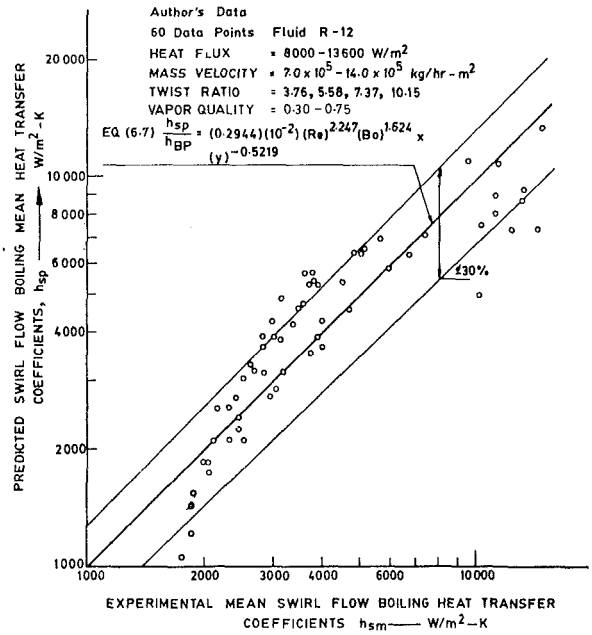

Fig. 9 Correlation of swirl flow boiling heat transfer data

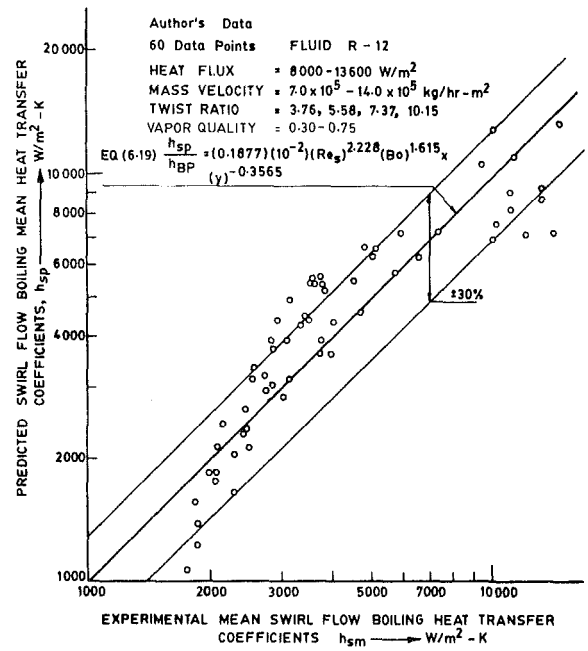

Fig. 10 Correlation of swirl flow boiling heat transfer data

tioned earlier, the swirl effect consists of two factors, namely, the spiral convection effect and the centrifugal convection effect. Lopina and Bergles [6] have shown that the spiral convection effect of tape insert can be accounted for if Re in equation (11) is substituted by a term called "swirl Reynolds number" Re_s given by equation (12)

$$\mathrm{Re}_s = \frac{C_s \cdot D}{\nu} \tag{12}$$

where

$$C_s = \sqrt{C_t^2 + C_a^2} \tag{13}$$

and

$$C_a = \frac{M}{\rho\left[\frac{\pi}{4}D^2 - aD\right]} \tag{14}$$

Table 1 Coefficients, exponents, mean deviation and standard deviation of equations (11) and (23)

Equation (11)	0.2944×10^{-2}	2.247	1.624	−0.5219	−4.16	28.16
Equation (23)	0.1877×10^{-2}	2.228	1.615	−0.3565	−4.20	28.17

$$C_t = C_a\left(\frac{\pi}{2y}\right) \tag{15}$$

from which

$$\mathrm{Re}_s = \mathrm{Re}\left[\frac{\sqrt{\pi^2 + 4y^2}}{2y}\right] \tag{16}$$

where

$$\mathrm{Re} = \frac{C_a \cdot D}{\nu} \tag{17}$$

Also, let the centrifugal convection effect be accounted for by a dimensionless parameter F_{cc} which is derived later. Equation (10) may then be written in the form of equation (18) which includes the spiral convection effect and centrifugal convection effect separately

$$\frac{h_s}{h_{\mathrm{BP}}} = A_2(\mathrm{Re}_s)^{a_2}(\mathrm{Bo})^{b_2}(F_{cc})^{c_2} \tag{18}$$

In order to determine the nature of the centrifugal convection function F_{cc} in equation (18), Tatom [19] has suggested that the effect of centrifugal convection can be accounted for if the Froude number, given by equation (19), is suitably modified

$$\mathrm{Fr} = \frac{C_a}{gD} \tag{19}$$

The Froude number Fr physically represents the ratio of inertial forces to gravitational forces in forced convection. In swirling flow, the tangential component of the fluid velocity creates a centrifugal force field, and at high fluid velocities the centrifugal acceleration at the tube wall may considerably exceed gravitational acceleration. This condition suggests the use of a modified Froude number, called the Swirl Froude number Fr_s given by equation (20) which represents F_{cc} of equation (18) appropriately

$$Fr_s = \frac{C_s^2}{\left(\frac{C_t^2}{R}\right)D} \tag{20}$$

Substituting the value of C_t from equation (15) in equation (20) it is seen that Fr_s is proportional to y^2. Fr_s has been called the centrifugal convection parameter F_{cc} of equation (18) and it may be expressed by equation (21)

$$F_{cc} = A_3(y)^{n_3} \tag{21}$$

Substituting F_{cc} from equation (21) into equation (18), equation (22) is obtained

$$\frac{h_s}{h_{\mathrm{BP}}} = A_4(\mathrm{Re}_s)^{a_3}(\mathrm{Bo})^{b_3}(y)^{c_3} \tag{22}$$

A best-fit correlation for the swirl flow data of the present investigation is obtained again in the form of equation (22) to give

$$\frac{h_{sp}}{h_{\mathrm{BP}}} = (0.1877)(10^{-2})(\mathrm{Re}_s)^{2.228}(\mathrm{Bo})^{1.615}(y)^{-0.3565} \tag{23}$$

For the same test conditions as in equation (11), the predicted values of the average heat transfer coefficients h_{sp} from equation (23) have been plotted against the experimentally observed values, h_{sm}, in Fig. 10. It is again found that equation (23), like equation (11), predicts the swirl flow heat transfer coefficients satisfactorily with a mean deviation of −4.20 percent and a standard deviation of 28.27 percent. Table 1 has been prepared to compare the coefficient, exponent, mean, and standard deviations of equations (11) and (23).

It is seen in Table 1 that both equations (11) and (23) predict data with aproximately the same accuracy. It may be recalled here that while equation (11) is a purely empirical one, equation (23) has been developed by considering a physical picture of the swirl flow phenomenon and by taking into account separately the spiral convection effect and centrifugal convection effect existing in such flows.

Conclusions

1 Heat flux, tape-twist ratio, and vapor quality, in addition to mass velocity, affect swirl flow boiling heat transfer coefficients to a great extent.

2 In general, a smaller twist ratio has been found to yield greater heat transfer coefficients.

3 The results of the present investigation suggest that the twisted-tape type of turbulence promoter may be usefully employed in a refrigerant-12 evaporator to obtain a better heat transfer rate.

4 Equations (11) and (23) predict swirl flow boiling heat transfer coefficients with fair accuracy.

References

1 Agrawal, K. N., Varma, H. K., and Lal, S., "Pressure Drop During Forced Convection Boiling of R-12 Under Swirl Flow," ASME JOURNAL OF HEAT TRANSFER, Vol. 104, 1982, pp. 758-762.

2 Royds, R., *Heat Transmission by Radiation, Conduction and Convection*, Constable and Co., London, 1921.

3 Colburn, A. P., and King, W. J., "Heat Transfer and Pressure Drop in Empty, Baffled and Packed Tubes,"' *Industrial and Engineering Chemistry*, Vol. 23, 1931, pp. 910-923.

4 Seigel. L. G., "The Effect of Turbulence Promoters on Heat Transfer Coefficients for Water Flowing in Horizontal Tubes," *Heating, Piping and Air-Conditioning*, Vol. 52, June 1946, p. 111-114.

5 Smithberg, E., and Landis, F., "Friction and Forced Convection Heat Transfer Characteristics in Tubes With Twisted Tape Swirl Generators," ASME JOURNAL OF HEAT TRANSFER, Vol. 86, 1964, pp. 39-49.

6 Lopina, R. P., and Bergles, A. E., "Heat Transfer and Pressure Drop in Tape Generated Swirl Flow of Single-Phase Water," ASME JOURNAL OF HEAT TRANSFER, Vol. 91, 1969, pp. 434-442.

7 Megerlin, F. E., Murphy, R. W., and Bergles, A. E., "Augmentation of Heat Transfer in Tubes by Use of Mesh and Brush Inserts," ASME JOURNAL OF HEAT TRANSFER, Vol. 96, 1974, pp. 145-151.

8 Marner, W. J., and Bergles, A. E., "Augmentation of Tubeside Laminar Flow Heat Transfer by Means of Twisted-Tape Inserts, Static-Mixer Inserts and Internally Finned Tubes," *Proceedings of the Sixth International Heat Transfer Conference*, Toronto, Canada, 1978, Vol. 2, pp. 583-588.

9 Kreith, F., and Margolis, D., "Heat Transfer and Friction in Swirling Turbulent Flow," Preprints of the Heat Transfer and Fluid Mechanics Institute, Stanford University Press, California, 1958.

10 Kreith, F., and Margolis, D., "Heat Transfer and Friction in Turbulent Vortex Flow," *Applied Scientific Research*, Section A, Vol. 8, 1959, pp. 457-473.

11 Blatt, T. A., and Adt, R. R., "The Effects of Twisted Tape Generators on the Heat Transfer Rates and Pressure Drop of Boiling Freon-11 and Water," ASME Paper No. 63-WA-42.

12 Bryan, W. L., and Seigel, L. G., "Heat Transfer Coefficients in Horizontal Tube Evaporators," *Refrigerating Engineering*, Vol. 63, May 1955, pp. 36-45.

13 McAdams, W. H., *Heat Transmission*, 3rd ed., McGraw-Hill, New York, 1954.

14 Chaddock, J. B., and Noerager, J. A., "Evaporation of Refrigerant-12 in a Horizontal Tube at Constant Wall Heat Flux," *ASHRAE Transactions*, Vol. 72, Part I, 1966, pp. 90-103.

15 Lavin, J. G., and Young, E. H., "Heat Transfer to Evaporating Refrigerants in Two Phase Flow," *AIChE Journal*, Vol. 11, No. 6, 1965, pp. 1124-1132.

16 Bo Pierre, "Flow Resistance With Boiling Refrigerants—Part I," *ASHRAE Journal*, Vol. 6, Sept. 1964, pp. 58-65, "Part II," Oct. 1964, pp. 73-77.

17 Singal, L. C., Sharma, C. P., and Varma, H. K., "Experimental Heat-Transfer Coefficient for Binary Refrigerant Mixtures of R-13 and R-12," *ASHRAE Transactions*, Vol. 89, Part I, 1983.

18 Mishra, M. P., "Heat Transfer to Boiling Binary Mixture of Pure Refrigerants Under Forced Convection," Ph.D. Thesis, University of Roorkee, Roorkee, India, 1979.

19 Tatom, F. B., "An Investigation of Heat Transfer and Pressure Drop With Local Boiling and Swirl Flow," MS Thesis, Auburn University, Alabama, 1962.

20 Seymour, E. V., "Fluid Flow Through Tubes Containing Twisted Tapes," *The Engineer*, Vol. 222, Oct. 28, 1966, pp. 634-642.

S. M. Morcos
Associate Professor.
Assoc. Mem. ASME

M. M. Hilal
Professor.

M. M. Kamel
Professor.

M. S. Soliman
Graduate Student.

Mechanical Engineering Department,
Cairo University,
Cairo, Egypt

Experimental Investigation of Mixed Laminar Convection in the Entrance Region of Inclined Rectangular Channels

The present experimental study considers the effect of combined forced and free laminar convection on the heat transfer in the entrance region of horizontal and inclined rectangular channels under uniform wall heat flux. The test facility includes electrically heated aluminum rectangular channels having aspect ratios AR = 2.667 and 0.375, with water as the working fluid. The experimental results included the circumferential wall temperature distribution and the axial variation of Nusselt number. Correlations of the experimental results of Nusselt number in the fully developed region were obtained in terms of Rayleigh number, Reynolds number, and inclination angle.

Introduction

Laminar flow heat transfer in rectangular channels is encountered in a wide variety of engineering applications, such as solar collectors and concentrators, as well as compact heat exchangers. However, in laminar flow, buoyancy effects can significantly enhance the convective heat transfer coefficent over the pure forced convection values [1, 2], thereby affecting the performance of the heat transfer surface. The essence of the phenomenon in horizontal and inclined channels is a double helix secondary flow resulting from the upward motion of the relatively warm fluid along the side walls and the downward motion of the cooler, and therefore denser fluid in the core.

Analytical solutions for the problem of combined forced and free laminar convection in rectangular channels have generally utilized the uniform wall heat flux boundary condition with a peripheral thermal conductivity of either zero or infinity. Numerical studies of fully developed laminar flow under the thermal boundary condition of axially uniform wall heat flux with peripherally uniform wall temperature include Cheng and Hwang [3] and Nakamura et al. [4] for horizontal rectangular channels, and Ou et al. [5] for inclined rectangular ducts.

However, the assumption of fully developed flow can only be established if the channel is very long. In spite of its practical importance, the only available numerical results for the entrance region of rectangular channels with significant buoyancy effects under the thermal boundary condition of uniform wall heat flux are those of Cheng et al. [6] for horizontal orientation with large Prandtl number fluids, and Abou-Ellail and Morcos [7, 8] for both horizontal and inclined rectangular ducts. Recently, Morcos and Abou-Ellail [9] presented a numerical solution for the problem of mixed laminar convection in the entrance region of an inclined multirectangular channel solar collector. The upper wall heat flux was taken to be uniform while the lower wall was assumed to be insulated. The heat flux distribution on the side wall of the rectangular channel was obtained by coupling a heat-conduction numerical procedure in the metallic region surrounding the channel to the main numerical procedure which solves the hydrodynamic and energy equations of the flow inside the channel.

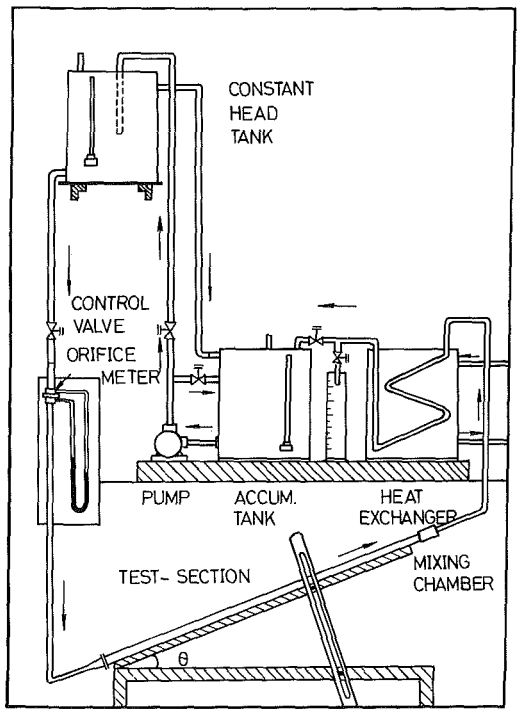

Fig. 1 Schematic layout of test loop

Experimental data for the case of mixed laminar convection in inclined rectangular channels are, to the knowledge of the present authors, nonexistent. The shortage of experimental data makes it hard to judge the validity of the foregoing numerical predictions.

The present investigation is, therefore, concerned with the experimental study of the problem of combined forced and free laminar convection in the entrance region of inclined rectangular channels. The experiments reported in this paper were performed with water as the working fluid and with two aluminum rectangular channels having aspect ratios AR = 2.667 and 0.375. The rectangular channels were electrically heated to approximate the uniform wall heat flux.

Experimental Apparatus

The test facility used in the present investigation was designed and constructed to allow maximum flexibility in testing

Contributed by the Heat Transfer Division for publication in the JOURNAL OF HEAT TRANSFER. Manuscript received by the Heat Transfer Division February 1, 1985.

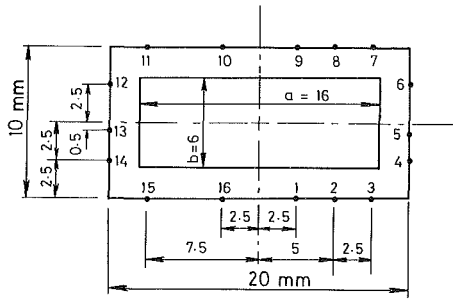

Fig. 2 Circumferential distribution of the wall thermocouple junctions

different test sections at various inclination angles. The test loop shown in Fig. 1 is a closed low-pressure system with all the piping made of 12.5-mm nominal diameter galvanized steel tube. Water is circulated through the loop by a small centrifugal pump. After the pump, the flow splits into a test-section line and a bypass line for flow control.

In the test-section line, water flows into an upper constant head tank fitted with an overflow path. The water then passes through a control needle valve, a calibrated orifice meter, the test section, and a heat exchanger before it returns to the accumulating tank where it merges with the bypass line. The differential head across the orifice meter was measured by a U-tube differential manometer. The flow rate was only observed with the orifice meter, but the mass flow rate was quantitatively determined by weighing a timed sample from the return line to the accumulating tank.

The test section is an aluminum rectangular channel having an outer dimension of 20 × 10 mm with a wall thickness of 2 mm and a total length of 2.25 m. This yields a value of the aspect ratio AR = 2.667 for the rectangular channel. At each end of the test section, an aluminum flange of 40 × 30 mm was fixed to the duct. Uniform electrical heating was applied to such a relatively thick wall channel with high thermal conductivity by a nickel–chrome wire wound around the duct. The wire strip has a cross section of 0.36 × 2.0 mm with a total resistance of 22 Ω. This wire was electrically insulated from the channel by a thin layer of mica tape, and was also covered on the outside with another layer of mica tape. The wire was fixed at its two terminals by two copper rings at both ends of the test section. Electrical power was provided by a 220 V a-c power supply through an adjustable autotransformer. An ammeter and a voltmeter were used to measure the electric power supplied. The test section was finally covered with three layers of asbestos chord having a total thickness of 30 mm for thermal insulation.

An inlet cone of 15 deg divergent angle was used to guide the flow from the 12.5-mm nominal diameter piping of the test loop to the rectangular cross section of the test section. The rectangular side of the inlet cone has exactly the same internal dimensions as the rectangular channel. A 3-mm rubber gasket was placed between the two flanges of the test-section channel and the inlet cone in order to minimize the axial heat loss through the channel wall. A mixing chamber was installed at the exit end of the rectangular channel. Another rubber gasket was placed between the exit flange of the test section and the mixing chamber. Both the inlet cone and the mixing chamber were also thermally insulated by three layers of asbestos chord. The rectangular channel was supported on an adjustable table to the desired inclination angle.

The fluid bulk and wall temperatures were measured by copper-constantan thermocouple wires of 0.25-mm diameter. Thermocouple potentials were measured with a precision manual potentiometer of 0.005 mV sensitivity. The inlet bulk fluid temperature was measured by a thermocouple probe installed directly in the fluid stream just prior to the inlet cone. The outlet bulk fluid temperature was measured by a thermocouple probe located after the mixing chamber.

The outside wall temperature were measured at six axial locations of 0.03, 0.07, 0.18, 0.40, 1.00, and 2.10 m downstream from the onset of heating. A guard heater of 30 mm was installed at the inlet end of the test-section channel. In order to measure the circumferential wall temperature distribution at each axial location, a number of 16 thermocouple junctions were welded to the rectangular channel as shown in Fig. 2. This distribution was selected in order to check the symmetry of the circumferential temperature profile around the meridional plane. Moreover, the above circumferential distribution of wall thermocouple junctions allows for the rotation of the test section by 90 deg about its axis so that a new value of the aspect ratio AR = 0.375 is obtained. The two bulk thermocouple junctions as well as the 96 wall thermocouple junctions were connected through two selector switches to the potentiometer and a common cold junction.

Experimental Procedure

The test loop was first filled completely with water from the upper constant head tank and air was bled from all high points of the system. Water was allowed to circulate in the test loop with the a-c power on for several hours, until it had been sufficiently deaerated. The apparatus was checked extensively at the beginning of the program to verify the accuracy of the instrumentation and the measuring techniques.

The testing generally proceeded by adjusting the mass flow rate through the test section depending on the value of the inlet bulk temperature in order to yield a specified value of the inlet Reynolds number Re_i. The power input to the test section was then adjusted in order to obtain the desired value of the mean Rayleigh number Ra_m. The equipment was allowed to operate for at least 30 min before recording the run data, so that steady-state conditons were established, and two successive readings, separated by 10 min, gave the same value. Once equilibrium was established, the test-section flow rate,

Nomenclature

a, b = width and height of the rectangular channel
AR = aspect ratio of the rectangular channel = a/b
D_e = equivalent hydraulic diameter = $2\,ab/(a+b)$
Gr = Grashof number = $g\beta\Delta T_e \cdot D_e^3/\nu^2$
g = gravitational acceleration
h = local heat transfer coefficient = $q_w/(\bar{T}_w - T_b)$
k = thermal conductivity
Nu = local Nusselt number = $h\,D_e/k$
Pr = Prandtl number = $c_p\,\mu/k$
q_w = uniform wall heat flux
Ra = Rayleigh number = Gr Pr
Re = Reynolds number = $W\,D_e/\nu$
T_b = fluid bulk temperature
T_w = wall temperature
W = mean inlet velocity
z = axial distance in the main flow direction
Z = dimensionless axial distance = $z/D_e\mathrm{Re}_m\mathrm{Pr}_m$
β = coefficient of thermal expansion
ΔT_e = equivalent temperature difference = $q_w\,D_e/k$
θ = inclination angle
θ_w = dimensionless wall temperature difference = $(T_w - T_{bi})/\Delta T_e$
μ = viscosity
ν = kinematic viscosity
ρ = density

Subscripts

i = inlet condition
m = mean condition

Superscripts

$\bar{}$ = average value

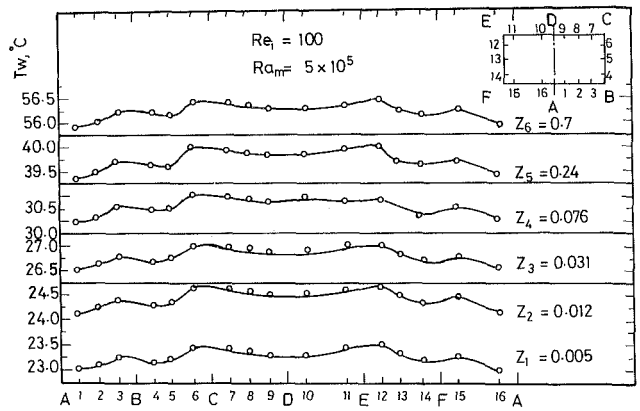

Fig. 3 Circumferential wall temperature distributions for AR = 2.667 and θ = 0 deg

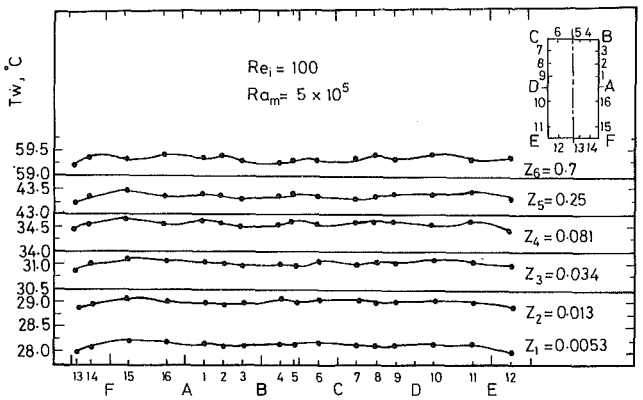

Fig. 4 Circumferential wall temperature distributions for AR = 0.375 and θ = 30 deg

inlet and outlet bulk temperatures, the circumferential outer wall temperatures, and the electric power input were recorded.

The above experimental procedure was carried out for various values of Re$_i$, Ra_m, and the channel inclination angle θ.

After proceeding with the above experimental runs for the rectangular channel having an aspect ratio AR = 2.667, the test section was turned 90 deg about its axis, so that a second value of the aspect ratio AR = 0.375 was obtained. The same previous experimental procedure was also repeated for the second aspect ratio.

Data Reduction

The heat input to the test section was based on the actual fluid enthalpy rise across the test section. The local bulk temperature T_b at each axial location was computed from inlet temperature, mass flow rate, and power input.

The inside channel wall temperatures were obtained from the outside wall temperature measurements and the actual heat input using the one-dimensional conduction equation for the channel wall. This simple one-dimensional method was used for data reduction as it gives essentially the same results as the two-dimensional solution of the conduction equation [1, 2]. With the present configuration, this temperature difference was always less than 0.5°C. The circumferential average wall temperature $\bar{T}_w$ was computed from the 16 inner wall temperatures by numerical integration.

The local heat transfer coefficient was calculated using the heat flux based on the inside channel surface area, the circumferential average wall temperature, and the calculated local bulk fluid temperature. Values of the thermodynamic and transport properties used in the dimensionless groups were based on the local bulk fluid temperature, unless otherwised noted.

Further details of the experimental apparatus, test procedure, and data reduction are given in [10].

Experimental Results and Discussion

The experimental results of the mixed laminar convection in the entrance region of inclined rectangular channels were carried out for the two aspect ratios AR = 2.667 and 0.375. These results were obtained for the channel inclination angle θ = 0, 15, 30, and 45 deg. At each inclination angle, the experimental runs were performed at three values of the inlet Reynolds number Re$_i$ = 100, 250, and 500, together with various constant values of the mean Rayleigh number ranging from Ra$_m$ = 5 × 10^4 to 10^6. The experimental results obtained from each run include the circumferential wall temperature distributions as well as the local heat transfer

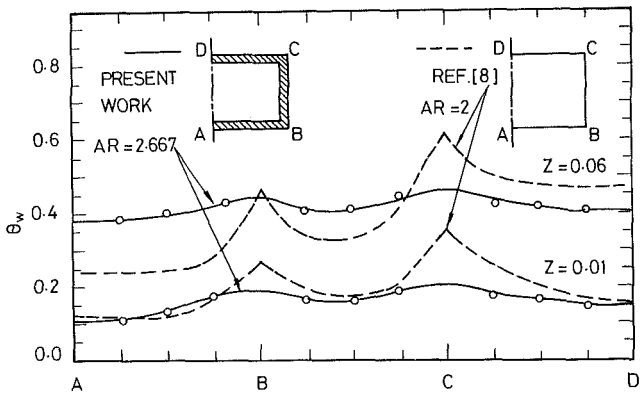

Fig. 5 Comparison between the present results and the available numerical predictions [8] of the circumferential wall temperature distributions for Re$_i$ = 100, Ra$_m$ = 10^5, and θ = 0 deg

coefficient at each of the six measuring planes along the channel axis.

Wall Temperature. Typical examples of the circumferential wall temperature distributions for Re$_i$ = 100 and Ra$_m$ = 5 × 10^5 are depicted in Figs. 3 and 4 for various values of the dimensionless axial distance Z. Figure 3 is plotted for AR = 2.667 with θ = 0 deg, while Fig. 4 is shown for AR = 0.375 with θ = 30 deg. Examination of Fig. 3 reveals that the upper wall temperatures are higher than the lower wall temperatures and the highest wall temperatures are located at the upper corners as a result of the secondary flow motion. However, the difference between the top and bottom wall temperatures is generally less than 1°C. Moreover, the results presented in Fig. 3 show, within the experimental accuracy, that the circumferential wall temperature distribution is symmetric around the vertical meridional plane AD.

As for the second aspect ratio AR = 0.375, Fig. 4 indicates that the circumferential wall temperature distributions tend to be more uniform with a relatively small difference between the top and bottom wall temperatures. This is mainly due to the decreasing effect of the secondary motion as a result of the longer height of the rectangular channel for this aspect ratio.

A comparison between the present experimental results of the circumferential wall temperature distributions for AR = 2.667, and the numerical results of Abou-Ellail and Morcos [8] for AR = 2 with axially and circumferentially uniform wall heat flux, is depicted in Fig. 5 for the two axial locations Z = 0.01 and 0.06. The results presented in Fig. 5 are for horizontal channels with Re$_i$ = 100 and Ra$_m$ = 5 × 10^5. The good agreement between the experimental results and the numerical predictions is clearly shown in Fig. 5, specially at Z = 0.01. However, the experimental results do not show sharp

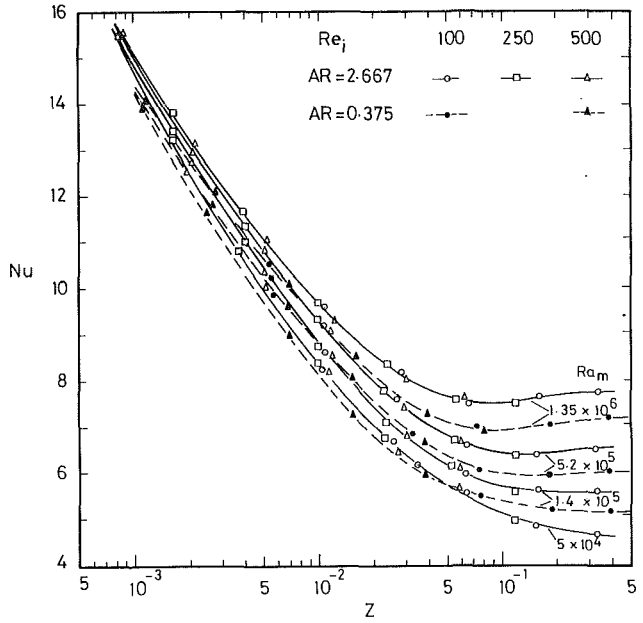

Fig. 6 Nusselt number variation in the entrance region of horizontal rectangular channels

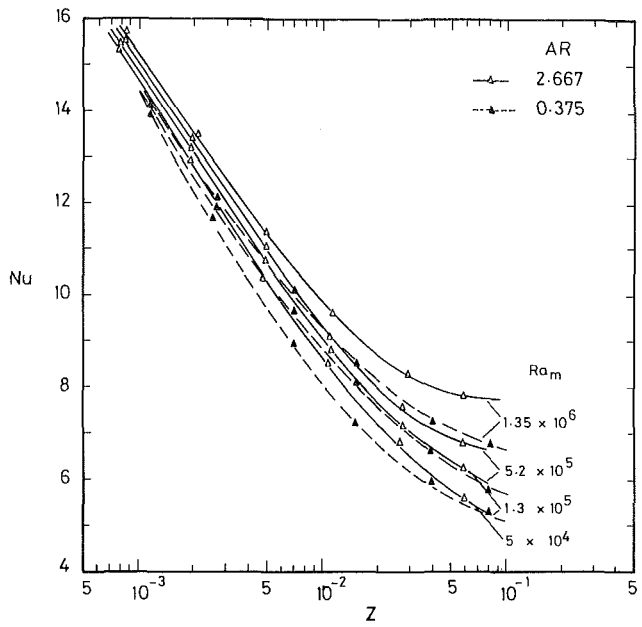

Fig. 8 Nusselt number variation in the entrance region of inclined rectangular channels with θ = 30 deg and Re$_i$ = 500

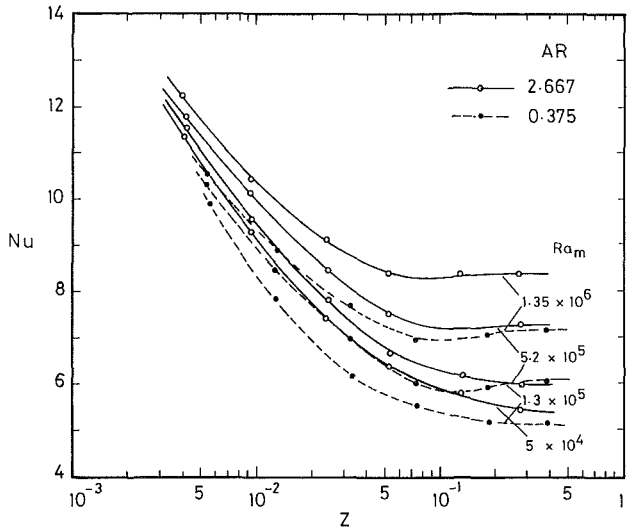

Fig. 7 Nusselt number variation in the entrance region of inclined rectangular channels with θ = 30 deg and Re$_i$ = 100

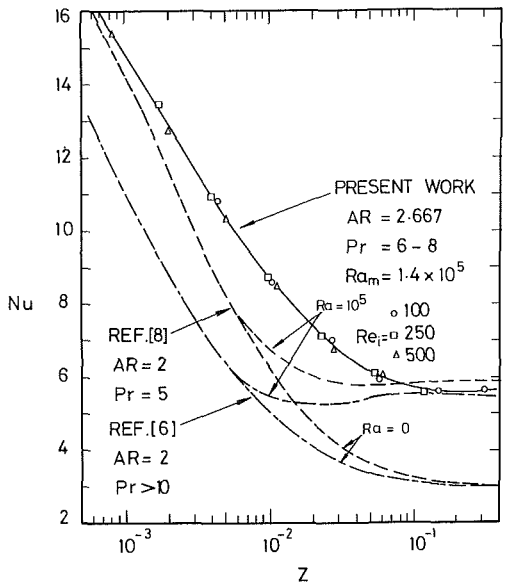

Fig. 9 Comparison between the present results and the available numerical predictions [6, 8] of Nu for a horizontal rectangular channel

temperature peaks at the corners of the rectangular channel as heat is conducted through the relatively thick wall of the aluminum channel from the top to the bottom walls resulting in the experimental data being lower on the top wall and higher on the bottom wall than the numerical predictions. This behavior is in good agreement with the numerical results of Morcos and Abou-Ellail [9] for the case of multirectangular channels where the effect of wall conduction was taken into consideration.

Nusselt Number. The experimental results of local Nusselt number Nu in the entrance region of the rectangular channel for the horizontal orientation are depicted in Fig. 6 for both AR = 2.667 and 0.375. The results presented in Fig. 6 are obtained for three values of the inlet Reynolds number Re$_i$ = 100, 250, and 500, together with various constant values of the mean Rayleigh number ranging from Ra$_m$ = 5 × 10^4 to 10^6. The variation of Nusselt number along the channel axis for a given value of Ra$_m$ showed that Nu decreases with the dimensionless axial distance Z, and after reaching a minimum value, Nu approaches a constant value corresponding to the fully developed conditions. Near the entrance, the initial decrease in Nu is due to the fact that conditions are dominant by forced convection. However, such decay is attenuated by the onset of the buoyancy-driven secondary flow, until a minimum is reached and Nu subsequently increases due to the increased importance of the secondary flow. The minimum in the Nusselt number distribution and the subsequent leveling out are typical of results obtained by other investigators [6–9]. The effect of increasing Ra$_m$ is seen to increase Nu and decrease the entrance length due to the strong influence of the buoyancy effects.

Examination of Fig. 6 shows that for the horizontal orientation and for both AR = 2.667 and 0.375, increasing Re$_i$ from 100 to 500 has a negligible effect on the value of Nu, which confirms the numerical findings of Abou-Ellail and Morcos [8]. However, a comparison between the experimental results of Nu shown in Fig. 6 for AR = 2.667 and 0.375 indicates that the effect of increasing the aspect ratio is to increase both the

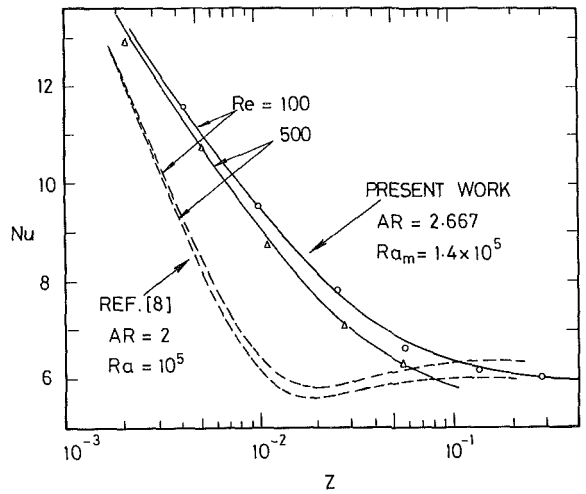

Fig. 10 *Comparison between the present results and the available numerical prediction [8] of Nu for an inclined rectangular channel with θ = 30 deg*

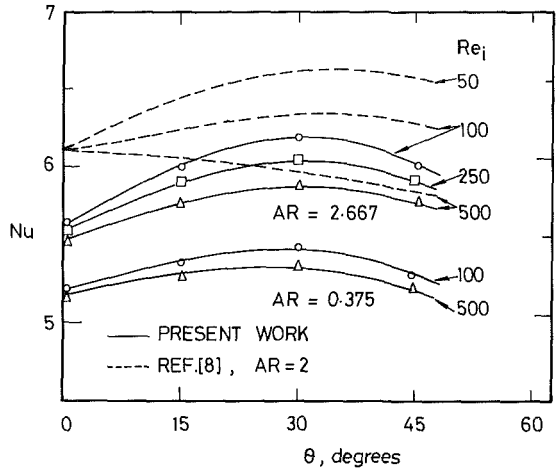

Fig. 11 Effect of inclination angle on the value of Nusselt number in the fully developed region with $Ra_m = 1.4 \times 10^5$

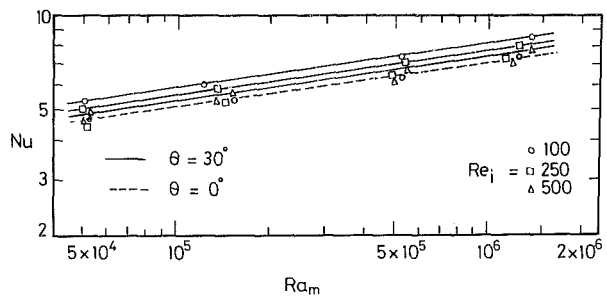

Fig. 12 *Variation of Nu in the fully developed region versus Ra_m for θ = 0 and 30 deg*

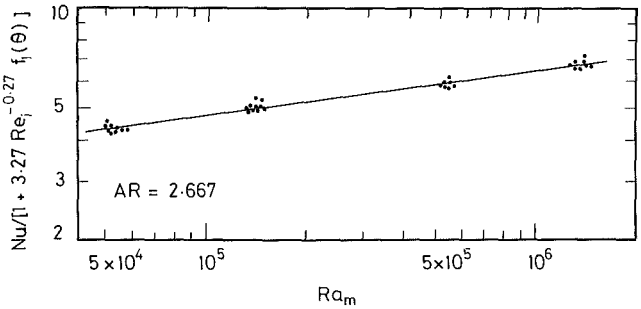

Fig. 13 Correlation of present results of Nu in the fully developed region for AR = 2.667

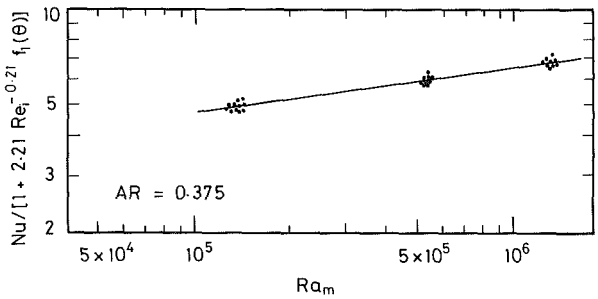

Fig. 14 *Correlation of present results of Nu in the fully developed region for AR = 0.375*

value of Nu and the entrance length for a given value of Ra_m which, again, agrees with the numerical results of Abou-Ellail and Morcos [7].

Similar results of the Nusselt number variations in the entrance region of the rectangular channel with an inclination angle θ = 30 deg are shown in Fig. 7 and 8 for Re_i = 100 and 500, respectively. The experimental results presented in these figures are similar to those shown in Fig 6. However, a quantitative comparison between the experimental results depicted in Figs. 7 and 8 indicates that the effect of increasing Re_i from 100 to 500 results in a slight decrease in both the values of Nu and the entrance length for given values of Ra_m and AR. This is mainly due to the fact that increasing Re_i tends to diminish the free convection effects which results in a lower value for Nu.

A direct comparison between the present experimental results of Nu in the entrance region of a horizontal rectangular channel with AR = 2.667 and $Ra_m = 1.4 \times 10^5$, and the available numerical results of Cheng et al. [6] and Abou-Ellail and Morcos [8] for AR = 2 and $Ra = 10^5$, is shown in Fig. 9. Also shown in Fig. 9 is the numerical prediction for pure forced convection flow with $Ra_m = 0$. Examination of Fig. 9 indicates that the present experimental results are in good agreement with the numerical predictions of Abou-Ellail and Morcos [8] in the first part of the rectangular channel where the effect of the property variation is very small. The deviation of the numerical results of Cheng et al. [6] from the present results is mainly due to the assumption of large Prandtl number effects used in the numerical solution. Moreover, the good agreement between the present results of Nu in the fully developed region and the two numerical predictions is also shown in Fig. 9. However, Fig. 9 indicates that the available numerical results deviate from the present experimental results in the transition region from the constant property solution to the fully developed region due to the effect of the heat conducted from the top to the bottom walls of the rectangular channel. This behavior was pointed out in the numerical results of Morcos and Abou-Ellail [9] where the value of Nu obtained taking into consideration the circumferential wall conduction was higher than that obtained with zero peripheral thermal conductivity. This is mainly due to the fact that the circumferential wall conduction increases the already established secondary flow which, in turn, enhances the value of Nu.

A similar comparison between the present results of Nu for AR = 2.667 with $Ra_m = 1.4 \times 10^5$ and the numerical prediction of Abou-Ellail and Morcos [8] for AR = 2 with $Ra_m = 10^5$ is shown in Fig. 10 for the inclination angle θ = 30 deg with Re_i = 100 and 500. Again, the good agreement between the experimental and numerical results in both the first part of the rectangular channel and in the fully developed region is clearly shown in Fig. 10. The effect of increasing Re_i from 100

to 500 is seen to decrease the value of Nu in both the present results and the numerical predictions of Abou-Ellail and Morcos [8]. However, these findings are contrary to the numerical results of Ou et al. [5] for inclined rectangular channels which were limited to relatively small Rayleigh numbers.

A composite plot showing the effect of the inclination angle on the value of Nu in the fully developed region for both AR = 2.667 and 0.375 is depicted in Fig. 11 for various values of Re_i with $Ra_m = 1.4 \times 10^5$. Figure 11 reveals that, within the experimental accuracy, Nu in the fully developed region is almost independent of Re_i for the horizontal orientation. However, the effect of Re_i is progressively more significant with higher values of the inclination angle. The optimum value of the inclination angle that yields the maximum value of Nu is seen from Fig. 11 to be 30 deg. Also shown in Fig. 11 is the numerical results of Abou-Ellail and Morcos [8] for AR = 2 with $Ra = 10^5$. Figure 11 indicates that the numerical results have the same trend as in the present results. Moreover, the above numerical predictions show an optimum inclination angle between 30 and 45 deg for $Re_i = 50$ and 100, which agrees with the present experimental results. However, the numerical results of Nu for $Re_i = 500$ do not show any optimum angle, which is contrary to the present results.

Correlation of Experimental Results

The experimental results of Nu in the fully developed region are correlated taking into consideration the effect of Ra_m, Re_i, and θ for each value of the channel aspect ratio.

Starting with AR = 2.667, typical representations of Nu versus Ra_m for $\theta = 0$ and 30 deg are shown in Fig. 12 for various values of Re_i. The resulting parallel straight lines shown in Fig. 12 of constant slope 0.135, which was also the case for other inclination angles, suggest that Nu could be correlated in the following form

$$Nu = 1.05\,[1 + f_1(\theta) f_2(Re_i)]\,Ra_m^{0.135} \quad (1)$$

where $f_1(\theta)$ is a function of θ and $f_2(Re_i)$ is a function of Re_i. As was shown in Fig. 11, the value of Nu at $\theta = 0$ deg is independent of Re_i, and Nu has a maximum value at $\theta = 30$ deg. Therefore, the best expression for $f_1(\theta)$ that has the same trend as the experimental results was found to be

$$f_1(\theta) = \sin\theta \cos(\theta + 30) \quad (2)$$

The expression for $f_2(Re_i)$ was obtained from a least-square fitting of all the experimental data. The final correlation of Nu for AR = 2.667 is given by

$$Nu = 1.05\,Ra_m^{0.135}[1 + 3.27\,Re_i^{-0.27} \sin\theta \cos(\theta + 30)] \quad (3)$$

In a similar manner, the correlation of the experimental results for Nu in the fully developed region for AR = 0.375 is given by

$$Nu = 0.95\,Ra_m^{0.135}\,[1 + 2.21\,Re_i^{-0.21} \sin\theta \cos(\theta + 30)] \quad (4)$$

Plots of the two correlations expressed by equations (3) and (4) together with the various experimental data are shown in Figs. 13 and 14 for AR = 2.667 and 0.375, respectively. Based on the range of parameter tested, the proposed correlation equations are expected to be valid for $5 \times 10^4 < Ra_m < 10^6$, $100 < Re_i < 500$, and $0 \text{ deg} < \theta < 45$ deg.

Conclusions

The circumferential wall temperature distributions indicated that the upper wall temperatures are higher than the lower wall temperatures and the highest wall temperatures are located at the upper corners as a result of the secondary flow motion. The circumferential wall temperature distributions for the aspect ratio AR = 0.375 tend to be more uniform than those for AR = 2.667 due to the decreasing effect of the secondary motion.

The variation of Nusselt number in the entrance region of a rectangular channel showed that Nusselt number decreases to a minimum value and then approaches a constant value corresponding to the fully developed conditions. The effect of increasing Rayleigh number is seen to increase Nusselt number and decrease the entrance length due to the strong influence of the buoyancy effects.

The experimental results reveal that Nusselt number is independent of Reynolds number for the horizontal orientation and the effect of Reynolds number is progressively more significant for higher values of inclination angle. The optimum value of the inclination angle that yields a maximum value of Nusselt number is $\theta = 30$ deg. The effect of increasing the aspect ratio is to increase both Nusselt number and the entrance length.

Comparison between the present experimental results and the available numerical predictions of Abou-Ellail and Morcos [7, 8] showed good agreement over the range of parameters considered. However, the effect of the peripheral wall conduction on the numerical results should be still further investigated.

The proposed correlations for the experimental results of Nusselt number in the fully developed region took into consideration the effect of Rayleigh number, Reynolds number, and inclination angle for each value of the aspect ratio.

References

1 Hong, S. W., Morcos, S. M., and Bergles, A. E., "Analytical and Experimental Results for Combined Forced and Free Laminar Convection in Horizontal Tubes," *Heat Transfer 1974*, Vol. 3, Paper No. NC 4.6, Tokyo, 1974.

2 Morcos, S. M., and Bergles, A. E., "Experimental Investigation of Combined Forced and Free Laminar Convection in Horizontal Tubes," ASME JOURNAL OF HEAT TRANSFER, Vol. 97, 1975, pp. 212–219.

3 Cheng, K. C., and Hwang, G. J., "Numerical Solution for Combined Free and Forced Laminar Convection in Horizontal Rectangular Channels," ASME JOURNAL OF HEAT TRANSFER, Vol. 91, 1969, pp. 59–66.

4 Nakamura, H., Matsura, A., Kiwaki, J., Hiraoka, S., and Yamada, I., "Numerical Solutions for Combined Free and Forced Laminar Convection in Horizontal Rectangular Ducts by Conjugate Gradient Method," *Journal of Chemical Engineering* , Vol. 11, 1978, pp. 354–360.

5 Ou, J. W., Cheng, K. C., and Lin, R. C., "Combined Free and Forced Laminar Convection in Inclined Rectangular Channels," *International Journal of Heat and Mass Transfer*, Vol. 19, 1976, pp. 277–283.

6 Cheng, K. C., Hong, S. W., and Hwang, G. J., "Buoyancy Effects on Laminar Heat Transfer in the Thermal Entrance Region of Horizontal Rectangular Channels With Uniform Wall Heat Flux for Large Prandtl Number Fluids," *International Journal of Heat and Mass Transfer*, Vol. 15, 1972, pp. 1819–1836.

7 Abou-Ellail, M. M. M., and Morcos, S. M., "Buoyancy Effects in the Entrance Region of Horizontal Rectangular Channels," ASME JOURNAL OF HEAT TRANSFER, Vol. 105, 1983, pp. 924–928.

8 Abou-Ellail, M. M. M., and Morcos, S. M., "Combined Forced and Free Laminar Convection in the Entrance Region of Inclined Rectangular Channels," *Numerical Methods for Non-Linear Problems*, Pineridge Press, Swansea, U.K., 1980, pp. 807–820.

9 Morcos, S. M., and Abou-Ellail, M. M. M., "Buoyancy Effects in the Entrance Region of an Inclined Multirectangular-Channel Solar Collector," ASME *Journal of Solar Energy Engineering*, Vol. 105, 1983, pp. 157–162.

10 Soliman, M. S., "Experimental Investigation of Combined Forced and Free Laminar Convection in Inclined Rectangular Channels," M.S. Thesis, Mechanical Engineering Department, Cairo University, Cairo, Egypt, 1982.

Effects of Microstructure on the Conjugated Mixed Forced and Free Convection-Conduction Analysis of Heat Transfer in a Vertical Plate Fin

Fue-Sang Lien
Graduate Student.

Cha'o-Kuang Chen
Professor.

Department of Mechanical Engineering,
National Cheng Kung University,
Tainan, Taiwan, Republic of China

A conjugated convection-conduction analysis has been made for a vertical plate fin which exchanges heat with its micropolar fluid environment by mixed forced and free convection. The analysis is based on a one-dimensional model for the plate fin whereby the heat conduction equation for the fin is solved simultaneously with the conservation equations for mass, momentum, angular momentum, and energy in the micropolar fluid boundary layer adjacent to the fin. The local heat transfer coefficient is not specified in advance but is one of the results of the numerical solutions. Numerical results of the overall heat transfer rate, the local heat transfer coefficient, the local heat flux, and the fin temperature distribution for $Pr = 5$ are presented for various values of Δ (dimensionless material parameter), N_c (conjugated convection-conduction parameter), and Ω (buoyancy parameter).

Introduction

In the conventional approach to determining the heat transfer characteristics of fins, the fin heat conduction equation is solved using a literature value of convective heat transfer coefficient that is assumed uniform all along the fin surface. However, the heat transfer coefficient can experience substantial variations along the fin surfaces [1, 2]. These variations may be caused by nonuniformities in both the velocity and temperature fields in the fluid adjacent to the fin. For a thin fin, the temperature changing along the streamwise direction can be considered to be much larger than those in the transverse direction. Therefore it is reasonable to assume one-dimensional model for the fin conduction equation.

The conjugated conduction-convection analysis for a vertical plate fin with a solution-determined nonmonotonically varying heat transfer coefficient is considered by Sparrow et al. [3, 4], who concluded that the conventional fin model based on a uniform input value of heat transfer coefficient yields very good predictions for the overall heat transfer rate of the fin, but the local predictions can be substantially in error for forced convection flow. Even for natural convection flow, the local heat transfer coefficients were found not to decrease monotonically in the flow direction, as is usual. Rather, the coefficient decreased at first, attained a minimum, and then increased with increasing downstream distance. This behavior was attributed to an enhanced buoyancy resulting from an increase in the wall-to-fluid temperature difference along the streamwise direction.

Latto and Shen [5] studied the effects of injecting dilute aqueous polymer solutions into a turbulent boundary layer formed on a flat plate. They found that polymer concentration and injection velocity reduce the friction drag. This phenomenon cannot be explained on the basis of classical continuum mechanics. The theory of micropolar fluids proposed by Eringen [6] is capable of explaining this phenomenon. In this theory, the local effects arising from microstructure and intrinsic motion of the fluid elements are taken into account. Physically micropolar fluid may present the non-Newtonian fluids consisting of dumbbell molecules or short rigid cylindrical elements, polymer fluids, fluid suspensions, animal blood, etc. Peddieson and Mcnitt [7] applied the micropolar boundary layer theory to the problems of steady stagnation point flow, steady flow over a semi-infinite plate, and impulsively started flow past an infinite flat plate. Besides, it may be possible to use the theories of fluids with microstructure such as Eringen's theory of simple microfluid [8] to model turbulent flow. In such an application the macromotion of the model would correspond to the mean motion of turbulent flow, the micromotion of the model would correspond to the fluctuating motion of the turbulent flow, and the microinertia coefficients would correspond to the characteristic dimensions of the eddies. Gorla [9] investigated the steady boundary layer flow of a micropolar fluid at a two-dimensional stagnation point on a moving wall and demonstrated that the micropolar fluid flow model is capable of predicting results which exhibit turbulent flow characteristics.

As cooling of the boundaries has considerable utility in several practical problems and as some authors [10–12] have shown that the microelements present in the fluid cool the boundary, an intensive study of the heat transfer characteristics of these fluids inside the boundary layer is required. The purpose of this paper is to study the heat transfer rate of a plate fin in mixed forced and free convective flow of micropolar fluid such as suspension flow. The fin temperature distributions are strongly affected by the heat transfer coefficient and the heat transfer coefficient is determined by the thermal coupling conditions between the plate fin and the thermal boundary layer of micropolar fluids. Therefore, the temperature distributions of the fin will be solved by utilizing an iterative procedure, which is more complicated.

The fin temperature distribution, which is not known a priori, served as a boundary condition for the boundary layer equations. The solution of the local heat transfer coefficient along the fin surface from the boundary layer equation is substituted into the known fin energy equation, and the new fin surface temperature is found. This new temperature distribution is then imposed as the thermal boundary condition for the boundary layer equation, the solution of which is used to evaluate an updated h and so on until the maximum

Contributed by the Heat Transfer Division for publication in the JOURNAL OF HEAT TRANSFER. Manuscript received by the Heat Transfer Division October 16, 1984.

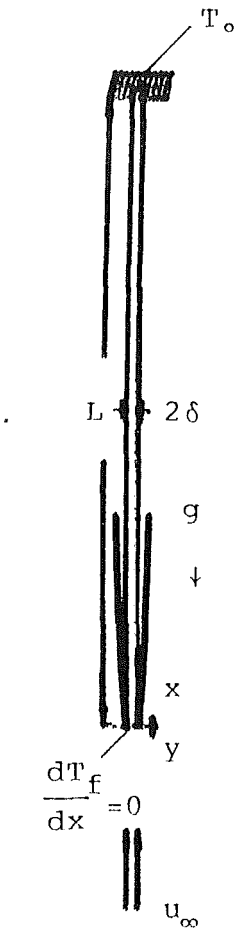

Fig. 1 Coordinate system

difference of temperature between successive cycles is less than 10^{-3}.

In the analysis, the conservation equations of the micropolar boundary layer and the fin energy equation are first transformed into a nondimensional form and their solutions are then simultaneously solved by an implicit finite difference scheme. Numerical results are presented for $\Pr = 5$ over a wide range of the conjugated convection-conduction parameter N_c, buoyancy parameter Ω, and dimensionless material parameter Δ.

Analysis

Consider a vertical plate fin of length L and thickness 2δ which is situated in a micropolar flow field with undisturbed oncoming free-stream velocity u_∞ and temperature T_∞ as shown in Fig. 1. Let the coordinates be chosen such that x measures the distance along the surface of the fin from the lower stagnation point and y measures the distance normal to the surface.

In the analysis, it will be assumed that the fluid properties are constant and the energy dissipation is negligible. Under usual Boussinesq approximation, the mixed forced and free convection boundary layer equations of micropolar fluid are expressed as follows:

Mass

$$\frac{\partial u}{\partial x}+\frac{\partial v}{\partial y}=0 \tag{1}$$

Momentum

$$u\frac{\partial u}{\partial x}+v\frac{\partial u}{\partial y}=\left(\nu+\frac{\hat{k}}{\rho}\right)\frac{\partial^2 u}{\partial y^2}+\frac{\hat{k}}{\rho}\frac{\partial \sigma}{\partial y}+\hat{g}\beta(T-T_\infty) \tag{2}$$

Angular momentum

$$u\frac{\partial \sigma}{\partial x}+v\frac{\partial \sigma}{\partial y}=-\frac{\hat{k}}{\rho j}\left(2\sigma+\frac{\partial u}{\partial y}\right)+\frac{\gamma\partial^2\sigma}{\rho j\partial y^2} \tag{3}$$

Energy

$$u\frac{\partial T}{\partial x}+v\frac{\partial T}{\partial y}=\alpha\frac{\partial^2 T}{\partial y^2} \tag{4}$$

The appropriate boundary conditions are

$$\text{at } y=0,\ u=v=0,\ \sigma=-\frac{1}{2}\frac{\partial u}{\partial y},\ T=T_w$$

$$\text{as } y\to\infty,\ u\to u_\infty,\ \sigma\to 0,\ T\to T_\infty \tag{5}$$

In the foregoing equation, γ is the spin gradient viscosity, $\hat{k}$ is the vortex viscosity, σ is the angular velocity of micropolar fluid, j is the micro-inertia, and the other standard symbols are defined in the nomenclature.

Equations (2)–(5) do not admit a similarity solution. The nonsimilarity arises from the surface temperature T_w which is undetermined. The pseudo-similarity variable η and the dimensionless streamwise coordinate ξ are introduced as follows:

$$\xi=\frac{x}{L},\ \eta=\frac{y\mathrm{Re}_L^{\frac{1}{2}}}{L\xi^{\frac{1}{2}}} \tag{6}$$

Nomenclature

f = reduced stream function
g = dimensionless microrotation
$\hat{g}$ = gravitational acceleration
Gr_L = Grashof number = $g\beta(T_0-T_\infty)L^3/\nu^2$
$h, \hat{h}$ = dimensional and dimensionless local heat transfer coefficient
k, k_f = fluid and fin thermal conductivity
$\hat{k}$ = vortex viscosity
L = fin length
N_c = conjugated convection-conduction parameter = $kL\mathrm{Re}_L^{\frac{1}{2}}/k_f\delta$
$\Pr$ = Prandtl number
Q = total heat transfer rate
q = local heat flux
Re_L = Reynolds number = $u_\infty L/\nu$
T, T_f = fluid and fin temperature
T_0 = root temperature
u_∞ = undisturbed oncoming free-stream velocity
u, v = velocity components in x and y direction, respectively
x, y = coordinate system
α = thermal diffusivity
β = thermal expansion coefficient
γ = spin gradient viscosity
δ = half-thickness of the fin
η = pseudo-similarity variable
θ, θ_f = dimensionless fluid and fin temperature
Δ, B, λ = dimensionless material parameters
μ = dynamic viscosity
ν = kinematic viscosity
ξ = dimensionless streamwise coordinate
ρ = density of fluid
σ = angular velocity of micropolar fluid
ψ = stream function
Ω = buoyancy parameter

Subscripts

w = condition at wall
∞ = condition in surrounding medium

in which Re_L is the Reynolds number, $\mathrm{Re}_L = u_\infty L/\nu$.

The dimensionless stream function $f(\xi, \eta)$, the dimensionless angular velocity $g(\xi, \eta)$, and the dimensionless temperature $\theta(\xi, \eta)$ are defined by

$$f(\xi, \eta) = \psi(x, y)/(u_\infty L \xi \nu)^{\frac{1}{2}} \tag{7}$$

$$g(\xi, \eta) = \sigma(x, y)/\left(\frac{\mathrm{Re}_L^{\frac{1}{2}} u_\infty}{L\xi^{\frac{1}{2}}}\right) \tag{8}$$

$$\theta(\xi, \eta) = (T(x, y) - T_\infty)/(T_0 - T_\infty) \tag{9}$$

where the stream function $\psi(x, y)$ satisfies the continuity equation (1) with

$$u = \partial\psi/\partial y, \quad v = -\partial\psi/\partial x \tag{10}$$

Introducing equations (6)–(9) into equations (2)–(5) gives

$$f'''(1+\Delta) + \frac{1}{2} ff'' + \Delta g' + \xi\Omega\theta = \xi\left(f' \frac{\partial f'}{\partial \xi} - f'' \frac{\partial f}{\partial \xi}\right) \tag{11}$$

$$\lambda g'' + \frac{1}{2}(f'g + fg') - \Delta B\xi(2g + f'') = \xi\left(f' \frac{\partial g}{\partial \xi} - g' \frac{\partial f}{\partial \xi}\right) \tag{12}$$

$$\mathrm{Pr}^{-1}\theta'' + \frac{1}{2} f\theta' = \xi\left(f' \frac{\partial \theta}{\partial \xi} - \theta' \frac{\partial f}{\partial \xi}\right) \tag{13}$$

$$f = f' = 0, \ \theta = (T_w(x) - T_\infty)/(T_0 - T_\infty),$$

$$g = -\frac{1}{2} f'', \text{ at } \eta = 0$$

$$f' = 1, \ \theta = 0, \ g = 0, \text{ as } \eta \to \infty \tag{14}$$

in which the primes stand for partial derivatives with respect to η; Pr is the Prandtl number; Δ, λ, B are the dimensionless material parameters, i.e.,

$$\Delta = \frac{\hat{k}}{\mu}, \ B = \frac{L\nu}{j u_\infty}, \ \lambda = \frac{\gamma}{\rho j \nu} \tag{15a}$$

and Ω is the buoyancy parameter, defined as

$$\Omega = \mathrm{Gr}_L/\mathrm{Re}_L^2$$

in which Gr_L is the Grashof number, $\mathrm{Gr}_L = g\beta(T_0 - T_\infty) \cdot L^3/\nu^2$.

Assuming a one-dimensional model the thin fin energy equation allows the temperature distribution along the longitudinal direction to be written as

$$\frac{d^2(T_f - T_\infty)}{dx^2} = \frac{h(x)}{k_f \delta}(T_f - T_\infty) \tag{16}$$

where k_f is the fin thermal conductivity, T_f is the fin temperature, and $h(x)$ is the local heat transfer coefficient which can not be regarded as known from the current boundary layer solution.

The associated boundary conditions are

$$T_f = T_0 \text{ at } x = L$$

$$\frac{dT_f}{dx} = 0 \text{ at } x = 0 \tag{17}$$

Of particular interest is the thermal coupling between the fin and the convective boundary layer of micropolar fluid. The basic coupling is expressed by the requirement that the fin and fluid temperatures and heat fluxes be continuous at the fin-fluid interface, at all x

$$\left.\begin{aligned} T_w(x) &= T_f(x) \\ h(T_f - T_\infty) &= -k\frac{\partial T_w}{\partial y} \end{aligned}\right\} \text{ at } y = 0, \ 0 \leqq x \leqq L \tag{18}$$

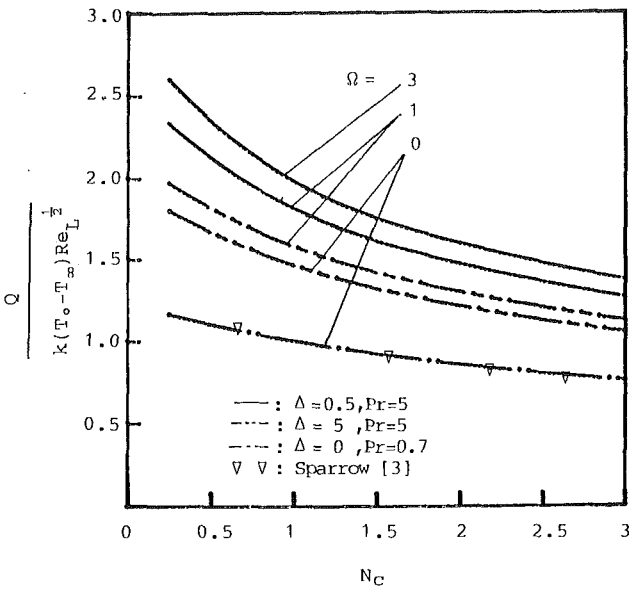

Fig. 2 Overall heat transfer rate of the fin for $\lambda = 5$ and $B = 0.1$

Equation (16) was recast in dimensionless form by substituting

$$\xi = \frac{x}{L}, \ \theta_f = \frac{T_f - T_\infty}{T_0 - T_\infty} \tag{19}$$

and combined with equations (18), so that

$$\frac{d^2\theta_f}{d\xi^2} = N_c \hat{h}\theta_f, \quad \text{and} \quad \left.\begin{aligned} \theta_w &= \theta_f \\ h &= k\mathrm{Re}_L^{1/2}\hat{h}/L \end{aligned}\right\} \text{at } \eta = 0 \tag{20}$$

where N_c is the conjugated convection-conduction parameter

$$N_c = \frac{kL\mathrm{Re}_L^{1/2}}{k_f \delta} \tag{21}$$

The quantity $\hat{h}$ is a dimensionless form of the local mixed convective heat transfer coefficient. The value of $\hat{h}$ is obtained by substituting equations (6) and (19) into equation (18)

$$\hat{h} = \left[-\frac{\partial\theta}{\partial\eta}/(\theta_f \xi^{1/2})\right]_{\eta=0} \tag{22}$$

Numerical Procedure

The solution begins by solving the mixed convective boundary layer flow of micropolar fluid for a vertical plate fin with guessed temperature along the fin surface. The dimensionless heat transfer coefficients $\hat{h}$ determined from equation (22) are then used as input to the fin heat conduction equation (20). With N_c prescribed, the differential equation (20) is then solved to yield θ_f. To begin the next cycle of the iterative procedure, the just-determined θ_f is imposed as the thermal boundary condition for the mixed convective boundary layer equations of micropolar fluid, the solution to which is used as input to the fin heat conduction equation. This procedure of alternately solving the boundary layer problem and the fin conduction problem was continued until convergence was attained.

The three systems of partial differential equations (11)–(13) are coupled. In the present study, these equations were solved by the accurate implicit finite-difference technique of Cebeci and Bradshaw [13]. To begin with, the partial differential equations (11)–(13) are first converted into a system of first-order equations which are then expressed in finite-difference form on the order of $(\Delta\xi)^2$ and $(\Delta\eta)^2$ by approximating the functions and their first derivatives in terms of centered difference and averaged at midpoints of the net segment in the (ξ,

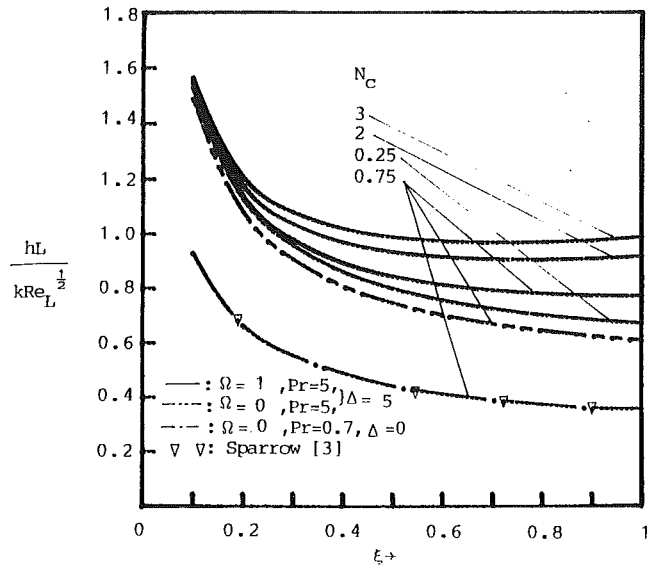

Fig. 3 The distributions of the local heat transfer coefficient for $\lambda = 5$ and $B = 0.1$

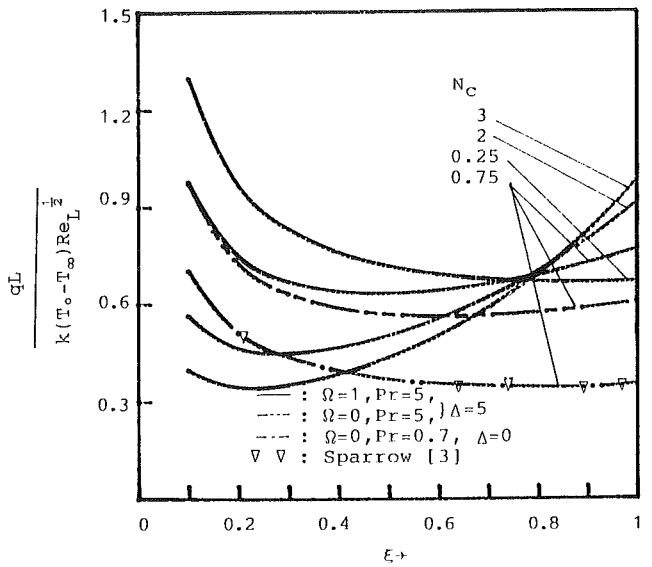

Fig. 5 The distributions of local heat flux for $\lambda = 5$, $B = 0.1$, and $Pr = 5$

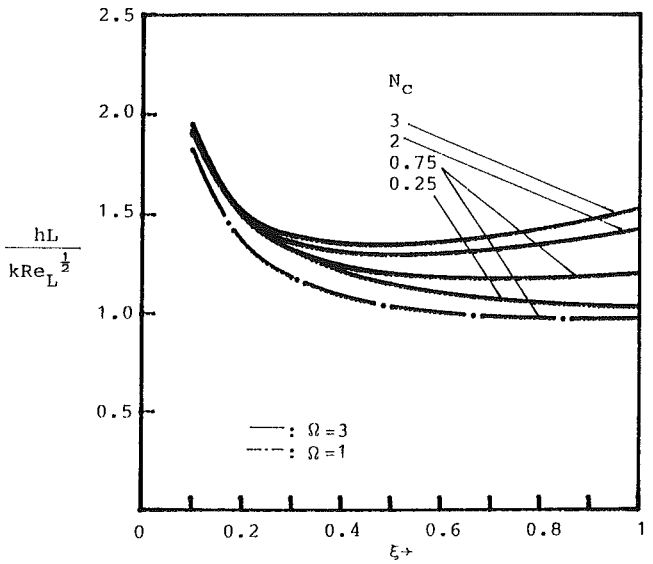

Fig. 4 The distributions of local heat transfer coefficient for $\Delta = 0.5$, $\lambda = 5$, $B = 0.1$, and $Pr = 5$

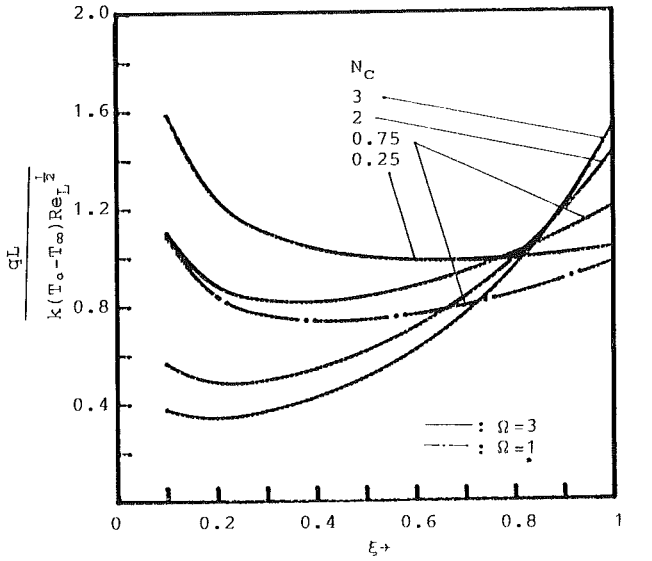

Fig. 6 The distributions of local heat flux for $\Delta = 0.5$, $\lambda = 5$, $B = 0.1$, and $Pr = 5$

η) coordinates. The resulting nonlinear finite-difference equations are then solved by Newton's iterative method.

The boundary layer solutions were obtained by a marching procedure, starting at the leading edge, and the grids were divided into 45 points in the streamwise direction and 61 grid points in the cross-stream direction. There was a denser concentration of points near the leading edge to accommodate the initial rapid growth of the boundary layer.

The fin conduction equation was solved by using the direct inverse matrix method. The fin equation was also divided into 45 grid points and expressed in finite-difference form. To ensure high accuracy, nonuniform grid points were employed. For small ξ, a finer ξ subdivision was needed for the boundary layer solution.

Results and Discussion

Numerical results were obtained for the cases of $Pr = 5$, $\lambda = 5$, $B = 0.1$ over a conjugated convection-conduction parameter of $N_c = 0.25$, 0.75, 2, and 3, buoyancy parameter of $\Omega = 0$ (forced convection), 1, and 3 (mixed convection), and dimensionless material parameter of $\Delta = 0.5$ and 5.

The overall rate of heat transfer Q from the fin can be obtained from the heat conducted from the wall into the fin base at $\xi = 1$ or from the integrating heat convection over the fin surface. The corresponding Q values of these two methods are found to be in agreement. They may be expressed in dimensionless form as

$$\frac{Q}{k(T_0 - T_\infty)\mathrm{Re}_L^{1/2}} = \frac{2}{N_c}\left.\frac{d\theta_f}{d\xi}\right|_{\xi=1} \tag{23}$$

or

$$\frac{Q}{k(T_0 - T_\infty)\mathrm{Re}_L^{1/2}} = 2\int_0^1 \left[-\frac{\partial\theta}{\partial\eta}/\xi^{1/2}\right]_{\eta=0} d\xi \tag{24}$$

The results of the overall heat transfer rate Q from the fin are shown in Fig. 2. The decrease of N_c indicates short fin length L, great fin conductance $k_f\delta$, and lower convection coefficient (low k and Re_L). Figure 2 illustrates that the overall heat transfer rate Q increases with increasing buoyancy parameter Ω. This figure also shows that an increase in the dimensionless material parameter Δ gives rise to a larger value in Q. This is because the effective viscosity, which is composed of the dynamic viscosity and the vortex viscosity of micropolar fluid,

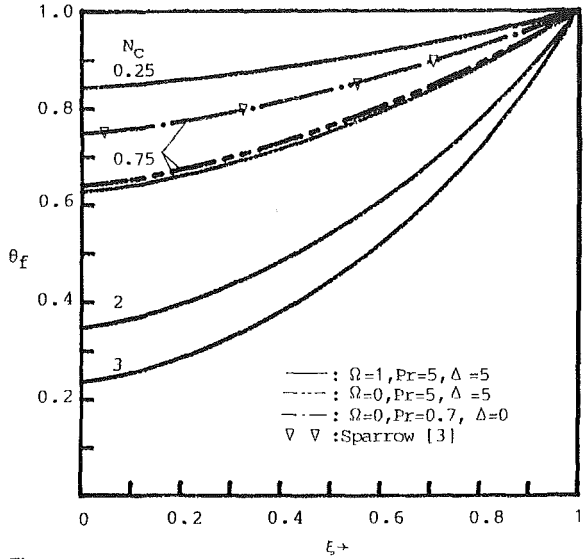

Fig. 7 The temperature distributions of fin for $\lambda = 5$ and $B = 0.1$

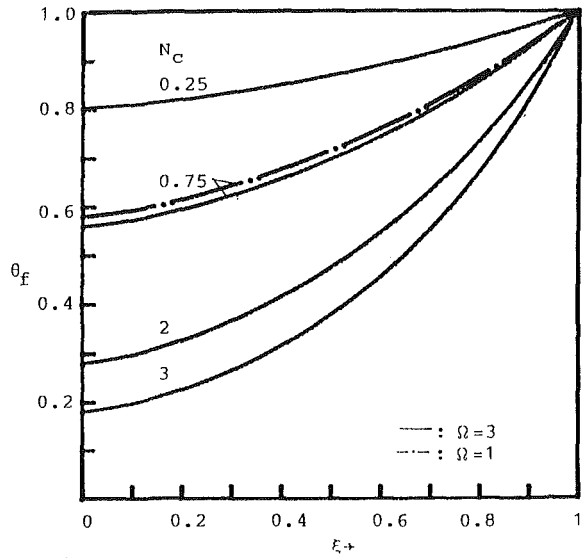

Fig. 8 The temperature distributions of fin for $\Delta = 0.5$, $\lambda = 5$, $B = 0.1$, and $Pr = 5$

is higher than that of the laminar Newtonian fluid. The agreement of the results for the special case ($\Delta = 0$, $Pr = 0.7$) with [3] is truly remarkable.

The distributions of the local heat transfer coefficient $\hat{h}$ for mixed convection along the surface with various values of N_c, Δ, and Ω are shown in Figs. 3 and 4. The local heat transfer coefficient can be taken as

$$\frac{hL}{k\mathrm{Re}_L^{1/2}} = \left[-\frac{\partial\theta}{\partial\eta}/(\theta_f\xi^{1/2})\right]_{\eta=0} \tag{25}$$

It is shown that larger values of the local heat transfer coefficient give rise to a larger streamwise variation of the fin surface temperature. From Figs. 3 and 4, we may find that the local heat transfer coefficients do not decrease monotonically in the flow direction for larger values of N_c and Ω. They decrease first to some minimum, and then increase steadily with ξ. This phenomenon is the same as the natural convective Newtonian flow over a vertical plate [4], and is attributed to enhanced buoyancy associated with an increase in the wall-to-fluid temperature difference along the streamwise direction.

The variations of the dimensionless local heat flux at the fin surface are presented in Figs. 5 and 6 as a function of N_c with various values of Δ and Ω. The local heat flux can be expressed as

$$\frac{qL}{k(T_0 - T_\infty)\mathrm{Re}_L^{1/2}} = -\left[\frac{\partial\theta}{\partial\eta}/\xi^{1/2}\right]_{\eta=0} \tag{26}$$

Figures 5 and 6 show that the local heat flux from the fin surface is increased as N_c decreased for most part of the fin surface except the small region near the base, which agrees with the predictions in Fig. 2.

It is observed from Figs. 3–6 that an increasing buoyancy parameter or a decreasing material parameter Δ gives rise to larger values in both of the local heat transfer coefficient and local heat flux when the other parameters are fixed.

Representative results for the fin temperature are presented in Figs. 7 and 8 for different Δ and Ω. Each case contains the fin temperature distributions as a function of N_c. Figures 7 and 8 show the expected trend whereby the fin temperature decreases monotonically from the root to tip. The two figures also confirm the assertions that larger values of N_c and Ω or smaller values of Δ give rise to larger fin temperature variations.

Conclusion

The present analysis has yielded the results of physical fin model for mixed forced and free convection flow of micropolar fluid. A comparison of our results for the special case of $Pr = 0.7$, $\Delta = 0$, and $\Omega = 0$ with [3] are found to be truly remarkable. In order to solve simultaneously the coupled fin conduction equation and the mixed convective boundary layer equations of micropolar fluid, an efficient implicit finite-difference technique is employed here. It is found from the results that the local heat transfer coefficient, local heat flux, and total heat transfer rate of the fin decrease with increasing dimensionless material parameter Δ. This behavior is attributed to an increasing effective viscosity (combined dynamic viscosity and vortex viscosity of micropolar fluid) associated with a decrease in the surface heat flux along the streamwise direction.

References

1 Sparrow, E. M., Baliga, B. R., and Patankar, S. V., "Forced Convection Heat Transfer From a Shrouded Fin Array With and Without Tip Clearance," ASME JOURNAL OF HEAT TRANSFER, Vol. 100, 1978, pp. 572–579.

2 Stachiewicz, J. W., "Effect of Variation of Local Film Coefficients on Fin Performance," ASME JOURNAL OF HEAT TRANSFER, Vol. 91, 1969, pp. 21–26.

3 Sparrow, E. M., and Chyu, M. K., "Conjugated Forced Convection-Conduction Analysis of Heat Transfer in a Plate Fin," ASME JOURNAL OF HEAT TRANSFER, Vol. 104, 1982, pp. 204–206.

4 Sparrow, E. M., and Acharya, S., "A Natural Convection Fin With a Solution-Determined Nonmonotonically Varying Heat Transfer Coefficient," ASME JOURNAL OF HEAT TRANSFER, Vol. 103, 1981, pp. 218–225.

5 Latto, B., and Chi-Hung Shen, *Proc. Turbulence Measurements in Liquids*, University of Missouri, 1969.

6 Eringen, A. C., *Contributions to Mechanics*, D. Abir, ed., Pergamon Press, 1970, pp. 23–40.

7 Peddieson, J., Jr., and McNitt, R. P., *Rec. Adv. Engng. Sci.*, Vol. 5, 1970, p. 405.

8 Eringen, A. C., *Int. J. Engng. Sci.*, Vol. 2, 1964, p. 205.

9 Gorla, R. S. R., *Int. J. Engng. Sci.*, Vol. 21, 1983, p. 25.

10 Sastry, V. U. K., Ph.D. Thesis, I. I. T. Kharapur, India, 1971.

11 Balaram, M., and Sastry, V. U. K., *Int. J. Heat Mass Transfer*, Vol. 16, 1973, p. 437.

12 Maiti, G., *ZAMM*, Vol. 55, 1975, p. 105.

13 Cebeci, T., and Bradshaw, P., "Momentum Transfer in Boundary Layers," Hemisphere, Washington, D.C., 1977.

Hybrid Analytical/Numerical Computation of Heat Transfer in a Gas-Driven Fracture

S. K. Griffiths
Sandia National Laboratories,
Livermore, CA 94550

R. H. Nilson
S-CUBED,
La Jolla, CA 92038
Assoc. Mem. ASME

F. A. Morrison, Jr.[1]
Lawrence Livermore National Laboratory,
Livermore, CA 94550
Mem. ASME

In gas-driven hydraulic fractures, as occur in rock blasting and underground nuclear testing, the high-temperature gases (1000 to 30,000 K) are radically cooled by heat transfer to the host material. This significantly reduces both the maximum extent and rate of fracture growth. The coupled processes of fluid flow, heat transfer, and rock deformation governing fracture growth are calculated here by a hybrid analytical/numerical procedure. The gas motion along a fracture of increasing length and aperture is described by a finite-difference form of the one-dimensional transport equations; fluid friction, advective heat transfer, and heat loss to the walls of the fracture are considered. Lateral heat losses are evaluated in a quasi-analytical fashion, based on an integral method that accounts for the convective film resistance between the fluid and fracture wall, as well as the conductive resistance within the surrounding medium. The calculations are performed on a difference grid that expands to maintain a fixed number of points uniformly distributed along the fracture. The present numerical results agree, within appropriate limits, with known similarity solutions. Beyond this, new nonsimilar solutions for early-time fracture growth are presented.

Introduction

Several applications motivate the study of gas-driven fracture propagation. In bench-blasting road cuts and quarries, the desired fragmentation results not only from stress waves, but also from gas penetration into the rock [1, 2]. In well shooting the primary objective is to create major fractures linking the borehole with adjacent oil-bearing or gas-bearing rock [3]; even multiple fractures of considerable extent can be produced by burning a military gun propellant within the well [4]. Also of current interest, the explosive fragmentation of oil shale [5] is a prerequisite to in-situ retorting, as recently demonstrated in the Colorado shale deposits. Again, gas-driven fractures play an important role in this fragmentation process. The primary motivation for the work reported here is a safety-related interest, aside from these mining and energy-related applications. Following an underground nuclear test, fluid-driven fractures may sometimes propagate from the explosively formed cavity, into the surrounding rock and toward the surface. Thus, an ability to predict the speed and extent of such fractures is helpful in assuring the containment of radioactive gases.

Previous numerical simulations of fluid-driven fracture propagation are based on an Eulerian approach in which the grid points are located at fixed points in space [6–9]. However, for most engineering problems the region of interest grows from the size of minute flaws, upward to tens or even hundreds of meters. This poses serious difficulties with computational gridding, both in accommodating fracture growth and in resolving thermal gradients within the surrounding rock. When employing the Eulerian approach, strict limits must be imposed on the permissible time step since there will always be large time derivatives of the pressure in the recently exposed regions of the grid near the tip. Moreover, nonphysical disturbances can be introduced as the tip jumps from one grid line to the next.

An alternative approach is used in the present numerical simulation of gas-driven fracture propagation. The calculations are performed on an expanding finite-difference grid, with a fixed number of grid points remaining uniformly distributed along the time-dependent length of the fracture. This approach alleviates all of the difficulties noted above, as demonstrated in a previous paper [10] concerning the idealized case of isothermal fluid flow. Although this grid-stretching approach is advantageous in treating the equations governing fracture mechanics, it presents some difficulties in treating the heat transfer outside the fracture.

The present paper describes a hybrid analytical/numerical procedure which couples a numerical treatment of the fracturing process with a quasi-analytical treatment of the heat transfer within the host rock. Heat fluxes from the driving fluid to the fracture wall are evaluated using a conventional convection correlation for laminar or turbulent channel flow. An analytical integral approach, described by Goodman [11], is used to model the conduction heat transfer within the wall. The resulting equations are all transformed into the expanding grid system and a method-of-lines numerical scheme is used to integrate them forward in time.

The hybrid analytical/numerical methods developed and tested here can also be applied to other engineering problems of similar character. For example, the linear Darcian seepage of fluid into the fracture walls can be treated in the same manner as the conductive heat transfer. Likewise, the method is applicable to any flow of fluid or heat along a preferred axial path which is depleted by lateral losses.

Mathematical Model

The geometry of a fracture can often be approximated by a planar (wedge-shaped) model, as indicated schematically in Fig. 1. Our discussion will be restricted to that planar configuration, with the understanding that axisymmetric (disk-shaped) fractures can be handled by analogous means. The extension to more general cases can be accomplished, for example, via the approach described by Cleary [12].

The aperture w of a planar fracture depends on the pressure p along the entire length. In accordance with linear/elastic fracture mechanics [13]

$$w(\theta, t) = \frac{4(1-\nu)L}{\pi G} \int_{\theta}^{1} \int_{0}^{\xi} \frac{[p(\zeta)-\sigma]d\zeta}{\sqrt{\xi^2-\zeta^2}} \frac{\xi d\xi}{\sqrt{\xi^2-\theta^2}} \tag{1}$$

[1] Deceased.

Contributed by the Heat Transfer Division for publication in the JOURNAL OF HEAT TRANSFER. Manuscript received by the Heat Transfer Division January 9, 1984. Paper No. 83-WA/HT-35.

where G and ν are the shear modulus and Poisson ratio, respectively, and σ is the in-situ compressive stress acting normal to the plane of the fracture. L is the length of the fracture, and

$$\theta = \frac{x}{L(t)} \tag{2}$$

is the normalized position along the fracture. This quasi-steady treatment of the solid mechanics is valid provided that the fracture speed is small compared to the wave speed in the solid; theoretical arguments [14] and laboratory experiments [15] suggest that this condition is usually satisfied.

Fracture propagation can occur only if the stress intensity at the tip is equal to or greater than a critical value K, which is a measurable property of the rock. In mobile equilibrium fracturing, the pressures exerted by the fluid are just sufficient to continuously maintain the critical stress intensity, as embodied by the following integral constraint [13, 16]

$$I = \int_0^1 \frac{[p(\theta) - \sigma]}{\sqrt{1-\theta^2}}\, d\theta = \frac{K}{\sqrt{2L}} \tag{3}$$

This condition ensures that the energy flow to the fracture tip is just sufficient to create the new free surface.

The fluid flow along the fracture is governed by conservation of mass, momentum, and energy, as expressed by the following one-dimensional transport equations [17]

$$\frac{\partial}{\partial t}(\rho w) + \frac{\partial}{\partial x}(\rho w u) = 0 \tag{4}$$

$$\frac{\partial}{\partial t}(\rho w u) + \frac{\partial}{\partial x}(\rho w u^2) = -\rho w \left[\frac{1}{\rho}\ \frac{\partial p}{\partial x} + \frac{\psi}{2}\ \frac{u^2}{w}\right] \tag{5}$$

$$\frac{\partial}{\partial t}(\rho w e) + \frac{\partial}{\partial x}\left[\rho w u\left(e + \frac{p}{\rho}\right)\right] = -p\ \frac{\partial w}{\partial t} - 2q \tag{6}$$

in which ρ is the density, u is the fluid speed, and e is the internal energy, each averaged over the cross section. The so-called friction factor ψ is approximated here by the simple analytical expression [10]

$$\psi = \frac{24}{\mathrm{Re}} + 2a\left[\frac{\epsilon}{w}\right]^b \tag{7}$$

which describes a smooth transition between the Poiseuille analysis for small Reynolds number ($\mathrm{Re} = \rho u w/\mu$) and Huitt's experimental data for high Reynolds number flow in fractures having roughness height ϵ [18]. The empirical constants a and b are typically about 0.1 and 0.5, respectively. Inertial effects are currently deleted from the left side of the momentum equation under the presumption of a low Mach number; this approximation can be verified after the fact for a given calculation.

The lateral heat flux q from the driving fluid to the wall of the fracture is evaluated as

$$q = h(T - T_s) \tag{8}$$

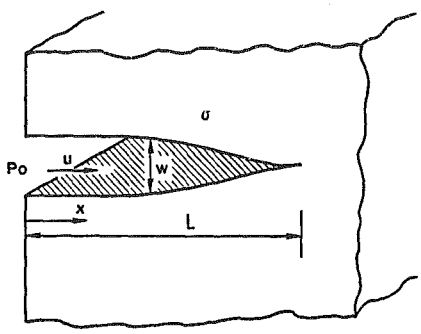

Fig. 1 Schematic of a hydraulically driven wedge-shaped fracture

where T and T_s are the bulk temperature of the fluid and the wall temperature at any axial location; h is the convection coefficient which depends on the local speed, density, and Reynolds number. By the Reynolds/Prandtl analogy to the fluid drag coefficient [19]

$$h = \frac{1}{8}\rho u c_p \psi \mathrm{Pr}^{-2/3} \tag{9}$$

Colburn's [20] experimental results suggest that this relationship is useful for fluids having a Prandtl number in the range 0.5 to 100. Radiative heat transfer could also be included in equation (8), but it is generally not important unless the emissivity of the gas is greatly increased by suspended particulate solids. Note that equations (8) and (9) can be used to calculate the gas-to-wall heat transfer only if the wall temperature is known, and this depends on the history of the heat flow within the rock.

Conduction heat transfer within the host rock is governed by the two-dimensional, time-dependent heat equation. However, rather than expending computational effort on a direct numerical treatment, we chose to apply a convenient analytical approximation [11]

$$T_s - T_\infty = \pm\frac{1}{k}\left[\frac{3}{2}\ \alpha h Q(T - T_s)\right]^{1/2} \tag{10}$$

This provides the wall temperature T_s as a function of the thermal conductivity k, diffusivity α, and ambient far-field temperature T_∞, as well as the instantaneous and integrated fluxes, q and Q.

$$Q(t) = \int_0^t q(t')dt' \tag{11}$$

Although the wall temperature appears on both sides of equation (10), an explicit form can be written by squaring both sides, and then applying the quadratic formula to obtain T_s as a function of h, T, T_∞, Q, and the thermal properties.

To solve the governing equations, with heat transfer and the integral constraint, only an equation of state for the driving fluid is yet needed. For all of the results shown here, an ideal-

Nomenclature

a = turbulent drag constant
b = exponent in turbulent drag relation
c_p = constant pressure specific heat
c_v = constant volume specific heat
e = specific internal energy
G = shear modulus
h = convective heat transfer coefficient
k = thermal conductivity
K = fracture toughness
L = fracture length
N = driving pressure ratio = p_0/σ
p = fluid pressure
p_0 = fluid pressure at inlet
Pr = Prandtl number = $\mu/\rho\alpha$
q = instantaneous wall flux
Q = integrated wall flux
Re = Reynolds number = $\rho u w/\mu$
t = time
T = fluid temperature
T_0 = fluid temperature at inlet
T_s = local wall temperature
T_∞ = far-field ambient temperature
u = fluid speed
w = local fracture aperture
x = spatial position
α = rock thermal diffusivity
γ = ratio of specific heats = c_p/c_v
ϵ = fracture surface roughness
θ = normalized position = x/L
μ = dynamic viscosity
ν = Poisson ratio
ρ = fluid density
σ = far-field confining stress
ψ = fluid friction factor

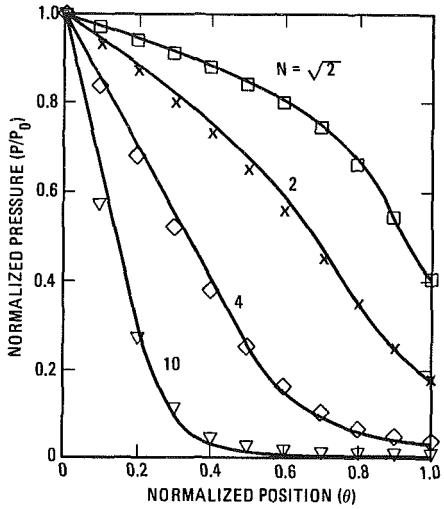

Fig. 2 Self-similar pressure distributions for turbulent flow with adiabatic fracture walls: comparison of analytical (curves) and numerical (symbols) results

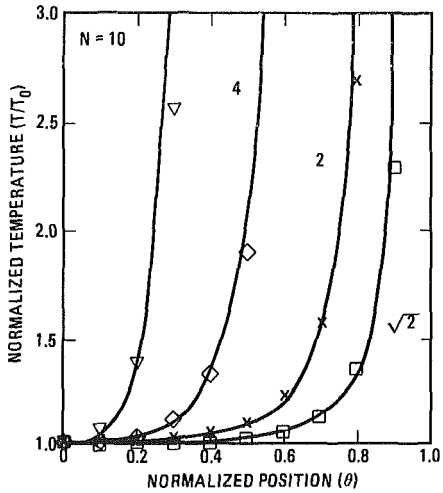

Fig. 3 Temperature distribution for adiabatic self-similar solutions; the analytical results (curves) and numerical results (symbols) are in close agreement

gas relation was used to determine the pressure and temperature from the energy and density. However, the computational scheme is not restricted to such simple fluids; our choice of energy and density as the dependent variables in the governing equations was to permit calculations involving multiphase driving fluids sometime in the future.

Numerical Method

To facilitate a numerical solution, the governing equations (4)–(6) are transformed into the straining coordinate system, $\theta = x/L(t)$. The transformed equations are then discretized on the interval $\theta = (0, 1)$ and the spatial derivatives, in terms of θ, are written as finite differences. By transforming the analytical conduction approximation along with the other governing equations, the problem of reconciling the straining coordinate system with the fixed rock surrounding the fracture is avoided. An overview of this computational approach is given in the next few paragraphs, with further details available in [10] and the Appendix.

In order to ensure that the integral constraint, equation (3), is always satisfied, we take its derivative with respect to time, set the resulting expression equal to zero, and integrate this equation along with those governing the fluid motion and lateral conduction. If the integral constraint is initially satisfied, this approach guarantees that it will remain so thereafter. This additional relation serves as an auxiliary equation which, together with the other governing equations, controls the fracture length.

As the aperture approaches zero near the fracture tip, the equations governing fluid motion become degenerate. To circumvent this difficulty, a mass and energy balance is written for a small triangular control volume that coincides with the tip portion of the fracture. The details of this, for the continuity equation, are described in a previous paper [10]. The energy equation introduced here is handled in an entirely analogous fashion.

Note that the fracture speed $\dot{L}$ will appear in each of the transformed governing equations. Since the fracture length is treated as a dependent variable, its derivative (the fracture speed) must be computed along with the time derivatives of the fluid density and energy; hence, the equations are implicitly coupled. Additionally, the time derivatives of the aperture w, arising in the continuity and energy equations, depend on the time derivatives of the pressure everywhere in the fracture, as well as the fracture length and speed. This further contributes to the implicit coupling of the equations. Finally, the pressures must each evolve in such a manner as to collectively satisfy the integral constraint at all times.

We address the implicit coupling of the transformed equations by writing the integral constraint (3) and the double integral for the local aperture (1) as sums over the difference intervals spanning the fracture; these sums are all linear in the pressures. Using thermodynamic relations, the pressure derivatives that appear are then written as derivatives of the density and energy, forming a nonsparse linear system. This system, as previously described for isothermal flows [10], can be inverted to yield explicit expressions for the local time derivatives of our four dependent variables: local density, energy and accumulated wall flux, and the fracture length. With these, the solutions are marched forward in time employing the well-known method of lines via a library ODE integrator. Often the differential equations are stiff, degenerating in some cases to algebraic equations, so we have generally relied on integrators such as DEBDF [21] based on backward difference algorithms.

Although this numerical scheme requires inverting a matrix for every derivative evaluation, the method is reasonably fast overall; we can typically calculate an order-of-magnitude increase in fracture length using 11 grid points (34 equations) in less than one CPU-minute on a CYBER-76/172 machine. Moreover, if the problem being analyzed possesses a similarity solution, the computational speed increases dramatically as the density, energy, and fracture wall temperature become stationary on the expanding grid.

Comparison of Numerical Results With Similarity Solutions

In some simplified cases, the gas-driven fracture problem has self-similar solutions for which the pressure and temperature are independent of time at fixed values of the normalized position. These solutions exist if the following conditions are met: (1) inlet pressure and temperature are constant in time, (2) fracture toughness K is negligible, and (3) the flow is fully turbulent everywhere along the fracture. Additionally, one of two thermal restrictions must be satisfied: (1) isothermal flow or (2) adiabatic flow. The case of isothermal flow does not involve the energy equation; it served as a test problem in the initial development of our basic numerical method [10]. The adiabatic case, however, provides a very stringent test of the numerical accuracy in solving the energy equation, since the fluid temperature along the fracture varies widely from the inlet value.

Table 1 Parameters, properties and conditions used in sample fracture calculations

Test Conditions	
Inlet fluid pressure, p_0	8.2 MPa
Inlet fluid temperature, T_0	1300 K
Ambient temperature, T_∞	300 K
Far-field confining stress, σ	2.5 MPa
Rock Properties	
Shear modulus, G	3 GPa
Poisson ratio, ν	0.3
Surface roughness, ϵ	400 μm
Thermal conductivity, k	0.2 and 2.0 W/m-K
Thermal diffusivity, α	4×10^{-6}m^2/s
Fracture toughness, K	0.5 MPa$\sqrt{\text{m}}$
Gas Properties (Air)	
Specific heat ratio, γ	1.4
Specific heat, c_p	1100 J/kg-K
Viscosity, μ	1.9×10^{-5}kg/m-s
Prandtl number, Pr	0.7
Computational Parameters	
Drag constant, a	0.1
Drag constant, b	0.5
Relative error tolerance	1.0×10^{-5}
Absolute error tolerance	1.0×10^{-5}

A comparison of pressure and temperature profiles is shown in Figs. 2 and 3, illustrating very good agreement between the present numerical results and the adiabatic similarity solutions previously derived [22]. The only parameters influencing the outcome are the specific heat ratio, $\gamma = c_p/c_v$, which is taken as 1.4, and the pressure ratio, $N = p_0/\sigma$, which is varied in the plots. These similarity solutions may be regarded as essentially exact. Our numerical results are generated by the marching procedure described above, starting with an arbitrary temperature profile and a pressure profile that satisfies the integral constraint, but is otherwise arbitrary. The calculations are continued until $p(\theta, t)$ and $T(\theta, t)$, or equivalently $\rho(\theta, t)$ and $e(\theta, t)$, are no longer changing in time; this usually occurs within a tenfold to hundredfold increase in fracture length.

As seen in Fig. 2, the gas need not penetrate to the tip of the fracture in order to drive it forward. It is only necessary that the collective action of the pressure forces be sufficient to maintain a slight tensile stress at the tip; the low-pressure region near the tip is held open by shear forces transmitted through the rock, not by the local gas pressure. In contrast to the isothermal cases previously studied [10, 23], the adiabatic flows do have a finite pressure at the fracture tip. This results from the very high temperatures generated by viscous heating in the absence of convective losses, which significantly reduce the density, and so reduce the turbulent friction and associated pressure gradient. Similar behavior can be seen in the related problems of adiabatic flow through a porous column [24].

The similarity solutions in Figs. 2 and 3 serve to validate the numerical method and to illustrate some qualitative features of the problem. However, those results are based on an assumption that the flow is adiabatic. In reality, heat is lost from the driving gas to the colder fracture walls, in accordance with the coupled processes of convection heat transfer in the gas and conduction heat transfer in the rock. This behavior is illustrated in the following nonsimilar calculations.

Nonsimilar Sample Calculations

To demonstrate the effect of heat transfer on fracture growth we have made sample calculations for a set of conditions (Table 1) which are typical of an underground nuclear explosion [6, 25]. Within about one tenth of a second after initiation of the device, the explosion-produced cavity reaches its full size ($R \sim 30$ m) and the internal pressure decreases to a level which is comparable to the overburden pressure of 50-100 bars (5-10 MPa). It is usually expected that the plastic deformation occurring during cavity growth and the subsequent elastic rebound of the surroundings will induce a residual compressive stress around the cavity which is sufficient to contain the cavity gases. In some cases, however, this stress cage may be degraded by decoupling of the explosion, low rock strength, or the presence of nearby lithologic interfaces. Under these circumstances the equilibrium cavity pressure at the end of the dynamic cavity-formation phase may be greater than the minimum compressive stress at the wall of the cavity. Under these conditions hydraulic fractures may pose a threat to successful containment of the radioactive gasses, so it is important to predict the speed and the probable extent of fracture growth.

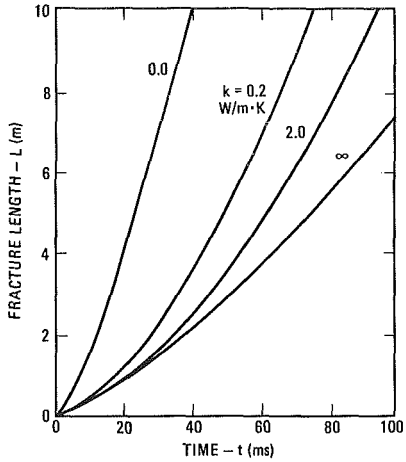

Fig. 4 Fracture length/time histories for sample calculations. The limiting cases ($k = 0$ and $k = \infty$) are roughly the local similarity results. At any time, the lengths span about a factor of five.

In the sample calculations presented here the driving pressure is held constant and the confining stress is uniform. The material properties, parameters, and initial conditions are given in Table 1. Properties shown for the rock are typical of those for bedded tuffs found at the Nevada Test Site. The fracture toughness has relatively little influence in this application since $K/L^{1/2} << P_0 - \sigma$ for $L > 0.1$ m, so there is no need to account for variations in K with temperature or fracture speed. Two values of the rock thermal conductivity are given: 2.0 and 0.2 W/m-K. These provide reasonable upper and lower bounds on expected values for a variety of loosely consolidated rock. Additionally, the lower value corresponds to the conductivity of plastics such as polymethyl methacrylate which are used in laboratory experiments [14, 15, 28].

Figure 4 shows the calculated fracture length/time history for our sample problem. The four curves are for four values of the rock thermal conductivity. The two limiting cases, $k = 0$ and $k = \infty$, correspond roughly to the local similarity solutions for an adiabatic and isothermal fracture wall, respectively. In these extremes, the convective heat transfer between the driving fluid and the host rock is not coupled with the far-field diffusion problem. In the first case ($k = 0$), the rock surface instantaneously reaches the fluid temperature, eliminating the temperature differences necessary to drive any energy exchange. In the second case ($k = \infty$), the conductivity of the rock is presumably high enough that the wall temperature remains constant at its initial condition over the time interval of interest. For intermediate values of rock conductivity, $k = 0.2$ and 2.0 W/m-K, the coupled heat transfer gradually raises the wall temperature, slowly reducing the convective losses from the fluid. All else being the same, the rate at which these losses diminish determines the fracture length/time history.

The most remarkable feature of Fig. 4 is the large effect heat transfer has on fracture length. At 10 ms, the calculated lengths range from 0.36 m to 1.6 m – spanning almost a factor

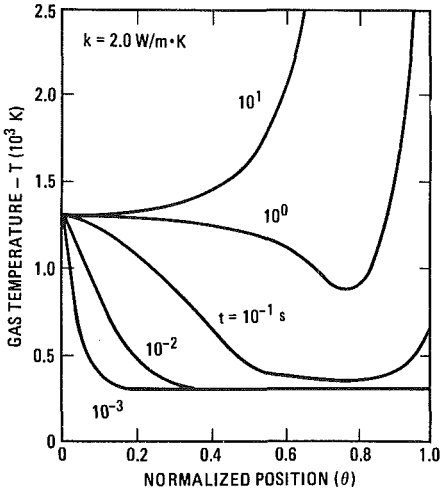

Fig. 5 Nonsimilar gas temperature profiles for one sample problem. The curves approach the adiabatic limit as the fracture wall temperature increases, reducing the overall heat transfer rate.

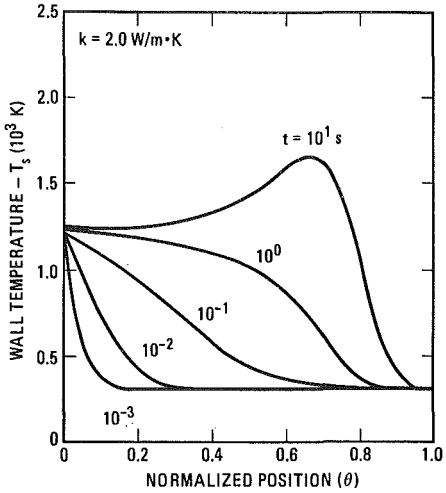

Fig. 6 Rock surface temperatures for the sample problem with $k = 2.0$ W/m-K; the instantaneous wall temperature is always below the fluid temperature at the same position

of five. By 100 ms, the lengths range from 7.5 m to 35. m, again varying by a factor of five or so between the isothermal-wall ($k = \infty$) and adiabatic-wall ($k = 0$) limits. When the coupled heat transfer is considered, the resulting length/time curves lie between these extremes. At 10 ms, the length predicted for a rock conductivity of 2.0 W/m-K is 0.38 m, very close to the isothermal case. Later, at 100 ms, the same conductivity gives a predicted length of 11. m, not quite a factor of two above the isothermal limit and a factor of about three below the adiabatic calculation. The results for a conductivity of 0.2 W/m-K show a similar trend, initially following the isothermal case and then departing toward the adiabatic limit, but the transition occurs much earlier due to a more rapid increase in the fracture wall temperature.

Figures 5 and 6 show the temperature profiles of the driving fluid and fracture wall at various times for the 2.0 W/m-K conductivity sample problem. We have extended these calculations beyond the normal period of interest to help show the gradual evolution of the temperature distributions. Initially, the wall temperature is uniformly at the far-field value, 300 K. The gas temperature, regardless of its initial conditions, almost immediately assumes the ambient value, due to the very large convective losses. By 1.0 ms the rock temperature near the inlet has increased to almost that of the driving fluid. For the next 100 ms the gas and wall temperatures near the inlet rise smoothly and at 100 ms the gas temperature at the tip just begins to climb. This continues through about 10 s, at which time the temperature profile of the gas is nearly the same as that for adiabatic fracture walls. The wall temperatures tend to follow the gas temperatures, except that near the tip they remain close to the far-field value. This is because the rock in the tip region is always just recently exposed to the hot gas and has not yet had time to heat.

Summary

We have developed and tested a fast numerical procedure for calculating the growth of hydraulically driven fractures. The continuity and energy equations governing fluid motion and an auxiliary constraint, related to the fracture toughness, are integrated on a finite-difference coordinate system that expands as the fracture grows.

To account for the energy exchange between the driving fluid and the host material, a hybrid analytical/numerical approach is used. The lateral convective transport is described by a usual heat transfer correlation. This appears in the energy equation for the driving fluid, which is solved numerically. The conductive lateral transport is governed by diffusion within the host material. Rather than solve this conduction problem numerically, however, we employ an analytical solution based on an integral method. This is coupled to the numerical portion of the analysis through the fracture wall temperature and so circumvents introducing numerous grid points outside the fracture. Only one dependent variable, either the accumulated lateral flux or the wall temperature, need be added to the governing equations.

Our present numerical results agree well with known similarity solutions. Since the largest errors occur where the densities are very small, the fracture lengths and speed are not seriously affected; the numerically determined speeds typically differ from the exact results by only a few percent. In light of the very large fluid temperatures that are sometimes generated by the viscous heating, the accuracy of the numerical scheme seems more than adequate.

Beyond reproducing the similarity solutions, new nonsimilar results have been obtained. This is demonstrated in sample calculations of fractures driven following a hypothetical nuclear test. For the sample problem, we find that convective losses from the driving fluid significantly diminish fracture growth; in a realistic case the speed and length are reduced by a factor of about three below the adiabatic limit when the coupled convective and conductive heat transfer are considered. These convective energy losses would have an even greater influence if the driving pressure decayed rapidly during growth, as is the case in most applications.

Overall, this hybrid analytical/numerical scheme is reasonably efficient. The work saved in using an analytical solution for the conduction within the host material permits rapid calculation of fracture growth. In most cases, we can compute a tenfold increase in fracture length, using 11 grid points, in a minute or so of CYBER-76/172 CPU time.

Acknowledgments

This work was performed at Sandia National Laboratories by the U.S. Department of Energy under Contract DE-AC04-76DP00789.

References

1 Kutter, H. K., and Fairhurst, C., "On the Fracture Process in Blasting," *Int. J. Rock Mech. Min. Sci.*, Vol. 8, 1971, pp. 181-202.

2 Coursen, D. L., "Cavities and Gas Penetrations From Blasts in Stressed Rock With Flooded Joints," *Acta Astronautica*, Vol. 6, 1979, pp. 341-363.

3 Howard, G. C., and Fast, C. R., *Hydraulic Fracturing*, Society of Petroleum Engineers of AIME, Dallas, TX, 1970.

4 Warpinski, N. R., Schmidt, R. A., Cooper, P. W., Walling, H. C., and Northrop, D. A., "High Energy Gas Frac: Multiple Fracturing in a Borehole," *Proc. 20th US Symp. on Rock Mech.*, Austin, TX, June 4-6, 1979, pp. 143-152.

5 Grady, D. E., and Kipp, M. E., "Continuum Modeling of Explosive Fracture in Oil Shale," *Int. J. Rock Mech. Min. Sci.*, Vol. 17, 1980, pp. 147-157.

6 Keller, C. E., Davis, A. H., and Stewart, J. N., "The Calculation of Steam Flow and Hydraulic Fracturing in a Porous Medium With the KRAK Code," Los Alamos Scientific Laboratories, LA-5602-MS, 1974.

7 Pitts, J. H., and Brandt, H., "Gas Flow in a Permeable Earth Formation Containing a Crack," *J. Appl. Mech.*, Vol. 44, 1977, pp. 553-558.

8 Palen, W. A., and Narasimhan, T. N., "The Roles of Pore Pressure and Fluid Flow in Hydraulic Fracturing," Lawrence Berkeley Laboratory, LBL-13049 (DE81-029886), June 1981.

9 Settari, A., "Simulation of Hydraulic Fracturing Processes," *Soc. Pet. Eng. J.*, Dec. 1980, pp. 487-499.

10 Nilson, R. H., and Griffiths, S. K., "Numerical Analysis of Hydraulically-Driven Fractures," *J. Computer Meth. Appl. Mech. Eng.*, Vol. 36, 1983, pp. 359-370.

11 Goodman, T. R., "Applications of Integral Methods to Transient Nonlinear Heat Transfer," *Adv. Heat Trans.*, Vol. 1, 1964, pp. 52-122.

12 Cleary, M. P., "Comprehensive Design Formulae for Hydraulic Fracturing," SPE Paper No. 9259, 55 Annual Fall Tech. Conf., Dallas, Sept. 21-24, 1980.

13 Sneddon, I. N., and Lowengrub, M., *Crack Problems in the Classical Theory of Elasticity*, Wiley, New York, 1969.

14 Erdogan, F., "Crack-Propagation Theories," in: *Fracture II*, Academic Press, New York, 1968.

15 Daly, J. W., Fourney, W. L., and Holloway, D. C., "Influence of Containment of the Borehole Pressure on Explosive Induced Fracture," *Int. J. Rock Mech. Min. Sci.*, Vol. 12, 1975, pp. 5-12.

16 Barenblatt, G. I., "The Mathematical Theory of Equilibrium Cracks in Brittle Materials," *Advances in Applied Mechanics*, Vol. 7, 1962, pp. 55-129.

17 Shapiro, A. H., *The Dynamics and Thermodynamics of Compressible Fluid Flow*, Vol. II, Ronald Press, New York, 1954.

18 Huitt, J. L., "Fluid Flow in Simulated Hydraulic Fractures," *AIChE Journal*, Vol. 2, No. 2, 1956, pp. 259-264.

19 Kreith, F., *Principles of Heat Transfer*, 3rd ed., Intext Educational Publishers, New York, 1973.

20 Colburn, A. P., "A Method of Correlating Forced Convection Heat Transfer Data and a Comparison With Fluid Friction," *Trans. AIChE*, Vol. 29, 1933, p. 174.

21 Haskell, K. H., Vandevender, W. H., and Walton, E. L., "The SLATEC Mathematical Subprogram Library: SNLA Implementation," SAND80-2792, Sandia National Laboratories, Albuquerque, NM, 1980.

22 Nilson, R. H., and Griffiths, S. K., "Self-Similar Fracture Propagation With Heat Transfer," *Int. J. Fracture*, in press.

23 Nilson, R. H., "Gas Driven Fracture Propagation," ASME *J. Appl. Mech.*, Vol. 48, 1981, pp. 757-762.

24 Morrison, F. A., Jr., "Transient Gas Flow in a Porous Column," *Ind. and Eng. Chem. Fund.*, Vol. 11, 1972, pp. 191-197.

25 Teller, E., Talley, W. K., Higgins, G. H., and Johnson, G. W., *The Constructive Uses of Nuclear Explosives*, McGraw-Hill, New York, 1968.

26 Griffiths, S. K., Smith, C. W., and Nilson, R. H., "Gas Fracturing: Numerical Calculations and Field Experiments," *Proc. 25th Symp. on Rock Mechanics*, Evanston, IL, June 25-27, 1984, Soc. Mining Engr., New York, pp. 157-164.

27 Griffiths, S. K., and Nilson, R. H., "Gas-Driven Fractures in Nuclear Test Containment," *Proc. 3rd Symposium on Containment of Underground Nuclear Explosions*, Idaho Falls, ID, Sept. 9-13, 1985.

28 Fourney, W. L., Barker, D. B., and Holloway, D. C., "Model Studies of Well Stimulation Using Propellant Charges," *Int. J. Rock Mech. Min. Sci.*, Vol. 20, No. 2, 1983, pp. 91-101.

APPENDIX

The governing transport equations (4)-(11) are strongly coupled through the fracture length $L(t)$ and aperture $w(\theta, t)$. A method for decoupling these equations was outlined in [10] for the continuity equation only. Here, that method is extended to the somewhat more complex equations which include energy transport.

Starting with equation (6), the first step is a transformation to the straining coordinate system, $\theta = x/L(t)$. For the energy equation, this gives

$$\frac{\partial}{\partial t}(\rho e w) - \theta \frac{\dot{L}}{L}\frac{\partial}{\partial \theta}(\rho e w) + \frac{1}{L}\frac{\partial}{\partial \theta}\left[\rho w u\left(e + \frac{p}{\rho}\right)\right] = -p\left[\frac{\partial w}{\partial t} - \theta \frac{\dot{L}}{L}\frac{\partial w}{\partial \theta}\right] - 2q \tag{A1}$$

where, as before, the local wall flux q is evaluated from equations (8)-(11). Now, since the aperture (and hence its time derivative) depend only on the pressure distribution and fracture length, we introduce the constant influence coefficients

$$\alpha_{ij} = \frac{1}{L}\frac{\partial w_i}{\partial P_j} \tag{A2}$$

and, following some rearrangements can write equation (A2) as

$$(ew\dot{\rho})_i + (\rho w \dot{e})_i + \left((2\rho e + p)_i w_i - \theta p_i \left.\frac{\partial w}{\partial \theta}\right|_i - \left.\frac{\partial}{\partial \theta}(\rho \theta w e)\right|_i\right)\frac{\dot{L}}{L} + L(\rho e + p)_i \sum_j \alpha_{ij}\left(\left.\frac{\partial p}{\partial \rho}\right|_j \dot{\rho}_j + \left.\frac{\partial p}{\partial e}\right|_j \dot{e}_j\right) = -\frac{1}{L}\frac{\partial}{\partial \theta}((\rho e + p)uw)\Big|_i - 2q_i \tag{A3}$$

where i and j denote the ith or jth node on an M node grid. The corresponding form of the continuity equation is [10]

$$w_i\dot{\rho}_i + \left(2\rho_i w_i - \left.\frac{\partial}{\partial \theta}(\rho \theta w)\right|_i\right)\frac{\dot{L}}{L} + L\rho_i \sum_j \alpha_{ij}\left(\left.\frac{\partial p}{\partial \rho}\right|_j \dot{\rho}_j + \left.\frac{\partial p}{\partial e}\right|_j \dot{e}_j\right) = -\frac{1}{L}\frac{\partial}{\partial \theta}(\rho u w)\Big|_i \tag{A4}$$

Some obvious simplifications have been omitted in order to show the exact form of the difference equations used in the numerical computation.

The spatial derivatives in equations (A3) and (A4) are all evaluated using central differencing; the only precaution is to ensure that there are no fluxes out of nodes in the evacuated region of the fracture tip. To avoid degenerancy of the governing equation, a triangular control volume is used in region just behind the tip. By integrating linear profiles over this volume, an expression involving the transport properties at the tip node M and one node back $M-1$ is obtained. In some applications it may be possible to simply prescribe the appropriate values of e_M and ρ_M, thus avoiding the need for any special near-tip equations.

An evolutionary equation for $\dot{L}$ is obtained by differentiating the integral constraint (3) with respect to time

$$\sum_j \beta_j\left(\frac{\partial p}{\partial \rho}\dot{\rho} + \frac{\partial p}{\partial e}\dot{e}\right)_j + \frac{K}{(2L)^{2/3}}\dot{L} = 0 \tag{A5}$$

where $\beta_j = \partial I/\partial p_j$ are constant influence coefficients calculated from equation (3).

The system of equations (A3)-(A5) can be cast in the implicit linear form

$$A(\dot{\rho}_1, \dot{\rho}_2, \ldots \dot{\rho}_M, \dot{e}_1, \dot{e}_2, \ldots \dot{e}_M, \dot{L})^T = b \tag{A6}$$

where A is an $M+1$ by $M+1$ matrix and b is a column vector containing the spatial differences. At each time step, equation (A6) is solved by LU decomposition to obtain time derivatives of the primary dependent variables, ρ_i, e_i, and L. Once $\dot{L}$ is available, it is easy to calculate the time derivative of the integrated heat flux into each grid interval using the formula

$$\dot{Q}_i = q_i + \theta_i \frac{\dot{L}}{L}\left.\frac{\partial Q}{\partial \theta}\right|_i \tag{A7}$$

where the spatial derivative is evaluated as a central difference, and instantaneous heat flux q_i is evaluated from equations (7)-(10). By this procedure we determine the time derivatives of all quantities, and these are then supplied to an ODE integrator which advances the solution in time.

Thermal Finite Element Formulation and Solution Versus Experimental Results for Thin-Plate GTA Welding

H. G. Kraus
Senior Engineering Specialist,
EG&G Idaho, Inc.,
Idaho Falls, ID 83415
Assoc. Member ASME

The problem of steady-state and transient heat transport associated with thin-plate welding is formulated and solved using the finite element method. Phase change is accurately accounted for through an element phase property averaging and quadratic/integral capacitance fitting technique. Three cases of quasi-steady welding of SS (stainless steel) 304 plates were simulated: input powers of 285, 405, and 588 W with corresponding velocities of 0.408 × 10^{-3}, 1.270 × 10^{-3}, and 2.540 × 10^{-3} m/s. Comparison to experimental results shows good agreement of weld pool size with a shape discrepancy developing as welder power and velocity increase. Arc heat flux and weld pool convection effects are discussed. A review of these results, combined with a survey of current literature, enabled possible causes of these weld pool shape differences to be identified and enabled recommendations for future research to be made.

Introduction

The theoretical prediction of temperature fields in welding processes continues to receive attention in efforts to move welding technology from an art to a science. The quasi-steady-state temperature fields and thermal transient history of welds are important to the study of the metallurgical aspects of welds, e.g., grain growth, size, and orientation, and solid-state phase transformations, which in turn lead to the understanding of associated mechanical properties, e.g., residual stress, distortion, ductility, and strength. The research described herein was undertaken in support of a program to acquire enough knowledge to ultimately develop automated control of the welding process for optimizing or controlling weld size and strength properties. The subject of this article concerns primarily the accurate numerical solution to the thermal physics of gas-tungsten arc (GTA) welding of two thin plates. However, experimental and theoretical modeling research of thick-plate welding will be conjointly discussed. This will aid in conveying the context of research reported herein, in relating thick and thin-plate welding phenomena, and in making recommendations for the direction of future research.

General Welding Modeling Review

The work of Kou et al. [1], Krutz and Segerlind [2], Friedman [3], Goldak et al. [4], Heiple et al. [5], Oreper et al. [6], Oreper and Szekley [7], and Karniadakis and Unkel [8] forms a representative cross section of the state of the art in welding modeling. Included collectively in these works are literature reviews of older research and recent advancements in detailed modeling such as: distributed arc heat fluxes; weld pool metal vaporization and condensation; Lorentz, plasma jet shear, buoyancy, and surface tension forces, and incident electric current flux distribution effects on the weld pool temperature distribution and thus shape. No work simultaneously includes all of these effects. Of the above list, only distributed arc heat fluxes have been studied in thin-plate welding. All known weld pool modeling to date has been for stationary thick-plate quasi-steady-state or transient weld pools. No weld pool convection models have been developed for thin-plate full penetration welding. In addition, there are a number of other factors that have been overlooked in past modeling. A couple of these factors, which are important in the modeling, are discussed below.

The emissivity for metals is temperature dependent, contrary to the model treatment by Kou et al. [1], Goldak et al. [4], and Karniadakis and Unkel [8], where a constant was used. There is also a large difference between solid and liquid metal emissivities. For example, steels have an emissivity of 0.7 to 0.9 as a solid near the melting temperature; on the liquid side the emissivity is near 0.3 [9, 10]. Additionally, the solidified weld material ends up coated with metallic oxides. Visual inspection of welds makes this readily apparent and enough experimental data are usually available that the surface oxide can be determined. The emissivity of such oxides is not the same as the base metal, nor is it temperature independent [11]. Such nonlinearities induced by temperature-dependent thermophysical properties do have significant effects in weld models which are overlooked when treating properties as constant.

Many researchers have used the parameters of their models as variables to fit models to experimental data. Arc efficiency (defined as the net energy received by the anode divided by the welder input energy) and weld pool conductivity (treated as a constant) were varied by Kou et al. [1] in the modeling of thin-plate aluminum alloy welds until the model results matched the experimental data. Various combinations of the magnitude of these parameters of 50–70 percent and two to three times the liquid conductivity, respectively, were predicted. However, since the work of Kuo et al., Smartt et al. [12] have experimentally measured the arc efficiency for an aluminum anode to be 80.2–83.2 percent with an average of 81.3 percent. Thus, it is difficult to make definite conclusions about the true magnitude of unknown parameters based on such a solution fitting scheme. These solutions may not be unique and/or physically important phenomena not present in the model may be responsible for the experimental model/data discrepancies.

Formulation and Thin-Plate GTA Welding Model

Two possible formulations to the energy transport problem of the welding of two thin plates are based on having the coordinate system fixed with respect to the plate or the welder. The

Contributed by the Heat Transfer Division for publication in the JOURNAL OF HEAT TRANSFER. Manuscript received by the Heat Transfer Division April 13, 1985.

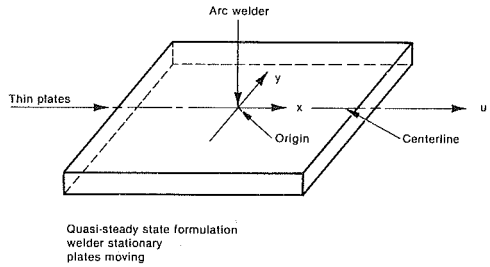

Fig. 1 Thin-plate quasi-steady-state welding model

latter was chosen for this formulation. For quasi-steady-state weld pool predictions, this results in having to solve a steady-state rather than transient differential equation, although advective terms corresponding to the motion of the plate relative to the welder are then needed.

Figure 1 illustrates the process and the associated coordinate system centered at the arc welder. Because the plates are thin, the temperature is lumped through the plate thickness. The energy equation/finite element formulation of this process is

$$\sum_{i=1}^{N} \iint_{A_i} \left[bk\frac{\partial W_j}{\partial x}\frac{\partial T}{\partial x} + bk\frac{\partial W_j}{\partial y}\frac{\partial T}{\partial y} + bW_j\rho C_p\frac{\partial T}{\partial t} + bW_j\rho C_p u\frac{\partial T}{\partial x}\right]_i dA_i = \sum_{i=1}^{N}\left\{\iint_{A_i}\left[W_j q_w + bQ - (h_t + h_b)(T-T_\infty)\right]_i dA_i + \oint_{S_i} W_j[k\nabla T\cdot n]_i dS_i\right\} \quad (1)$$

which makes use of the continuity equation

$$\frac{\partial \rho}{\partial t} + \frac{\partial}{\partial x}(\rho u) = 0 \quad (2)$$

and has associated boundary conditions

$$\frac{\partial T}{\partial x} = \frac{\partial T}{\partial y} = 0 \text{ on } S_1 \quad (3)$$

$$T = T_0 \text{ on } S_2 \quad (4)$$

$$u = u_0 \text{ on } S_2 \quad (5)$$

where x and y are the Cartesian coordinates, b is the plate thickness, k is the thermal conductivity, T is the temperature, $q_w = q_w(x, y)$ is the welder arc heat flux, Q is the welder energy deposition density, ρ is density, C_p is heat capacity, h_t and h_b the combined convective and radiative heat transfer coefficients for the top and bottom surfaces of the plate, respectively, T_∞ is the ambient temperature, $T_0 = T_\infty$, u_0 is the plate velocity (i.e., negative of welder velocity), S_1 is the side, centerline, and right domain boundaries, and S_2 is the left or inlet flow boundary.

The domain of equation (1) is divided into N bilinear quadrilateral isoparametric elements, W_j are the Galerkin weighting functions, A_i and S_i are the element cross-sectional and surface areas, respectively, and n is a unit vector normal to S_i. All terms on the left side of equation (1), except the transient term, were integrated exactly using Gaussian quadrature. The storage term was first-order finite differenced in time and all other terms were evaluated at the end of a time step resulting in a fully implicit algorithm. Adherence to the basic Galerkin-finite element method (GFEM) for treating the advective terms in the energy equation [13], coupled with physically realistic boundary conditions [14], resulted in superior stability and accuracy over finite difference, mass lumped finite element, and first-order upwind methods. However, the transient term is zero for this quasi-steady-state weld model. Simulating the startup and shutdown of this welding process would require the transient solution of this equation. While this capability has been developed, such simulation has not yet been performed.

System symmetry about the x axis of Fig. 1 allowed the solution domain of this weld model to be reduced to the positive rectangular region of the x–y plane. Since GTA welding is a low rather than high penetration process (such as electron beam or laser welding), Q of equation (1) is equal to zero. Natural convective heat loss from the top and bottom sides of the plates was accounted for using the simplified convection coefficient equations for air [15], where a characteristic length of 0.1 m was used. Radiation heat loss from the top and bottom sides of the workpiece was treated as radiation to a temperature sink at T_∞. A multiplication factor of 0.9 was used of the top side radiation heat loss boundary condition to approximate the presence of the welder. Emissivity was temperature dependent and was specified separately for three different regions: solid phase of the workpiece [11], liquid phase (weld pool) [10], and the solidified weld track which for SS 304 has a Cr_2O_3 surface oxide layer [11]. McCullough et al. [16] have described in detail the oxidation of SS 304.

All thermal properties of equation (1) were treated as temperature dependent based on the SS 304 data reported by Kim [17]. Properties were assumed constant throughout an element, being based on an average element temperature. The exception to this is the elements in which phase change is present, which is discussed in detail below.

Alloys typically do not pass through the solid-to-liquid phase transition at a single temperature, but rather over a temperature range from the solidus temperature T_S to the liq-

Nomenclature

A_i = element area
a_1, a_2, a_3 = quadratic polynomial coefficients
b = plate thickness
c_p = heat capacity at constant pressure
d, e, f = ellipse parameters
E = welder arc voltage
h_t, h_b = top and bottom side plate combined convection and radiation transport coefficients
H_{s1} = heat of fusion
i = element number (subscript)
I = welder arc current
k = thermal conductivity
N = number of elements in mesh
p = iteration number (superscript)
P = $\eta EI/0.95$ = net power transmitted to plate
q_w = welder arc heat flux distribution (area based)
Q = welder energy deposition distribution (volume based)
S_i = element surface area (laterally, not top and bottom)
S_1, S_2 = mesh domain surface boundaries
t = time
T = temperature
ΔT = temperature difference
T_L = liquidus temperature
T_P = phase interface temperature
T_S = solidus temperature
T_∞, T_0 = ambient temperature
u, u_0 = plate or welder velocity
W_j = Galerkin weighting functions
x, y = Cartesian coordinates
γ = relaxation parameter
η = welder arc efficiency
π = radians in a half circle
ρ = density

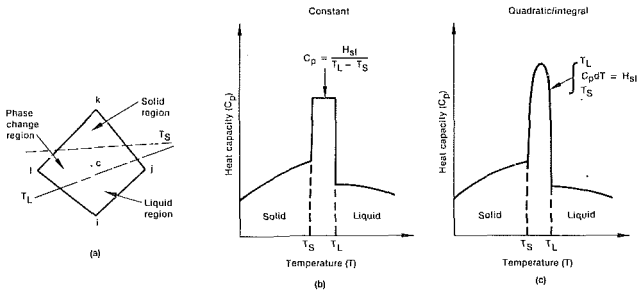

Fig. 2 Element phase property averaging and quadratic/integral capacitance fitting technique illustrations

uidus temperature T_L. For the purpose of locating the phase front, the solid/liquid interface was considered to occur at the pinch-off temperature defined as

$$T_P = T_S + 2/3(T_L - T_S) \tag{6}$$

T_P is commonly accepted as the temperature at which movement of the liquid due to convective motion ceases due to solid phase impediment. Initially, the integral phase change method by Lemmon [18] was used to calculate properties in elements experiencing phase change. This method does not work well for the quadrilateral isoparametric elements used herein, resulting in significant error in element property values and relative insensitivity to the location of the phase front inside an element (for this does not directly enter into the calculation scheme). As a result, indefinite solution oscillation occurred.

A phase change technique was developed in two parts which enables the solidus and liquidus fronts to be accurately located and results in smooth monotonic solution convergence. For the first part, consider the quadrilateral element of Fig. 2(*a*) through which the phase fronts pass. An area-weighted property average is taken based on the liquid, phase change, and solid regions. This allows accurate tracking and location sensitivity to the T_S and T_L phase fronts as they influence element average property values.

The second part of the phase change technique has to do with how the heat of fusion is spread over the T_S to T_L interval. Figure 2(*b*) shows the typical method of using a constant C_p over this temperature interval equal to $H_{sl}/\Delta T$ where H_{sl} is the heat of fusion and $\Delta T = T_L - T_S$. However, the step change in C_p at T_L and T_S prevents nonlinear iterative convergence as the solution at a node may oscillate indefinitely between values slightly greater and slightly smaller than T_L or T_S. To circumvent this problem and be physically realistic, a continuous quadratic function for C_p was defined as

$$C_p(T) = a_1 + a_2 T + a_3 T^2, \qquad T_S \le T \le T_L \tag{7}$$

for the C_p spread equivalent of H_{sl}. The constants a are determined based on the following conditions which must be satisfied:

1 $C_p(T)$ equals the solid phase C_p at T_S
2 $C_p(T)$ equals the liquid phase C_p at T_L
3 The following integration must hold true

$$\int_{T_S}^{T_L} C_p(T)\,dT = H_{sl} \tag{8}$$

With the constants determined, $C_p(T)$ appears as in Fig. 2(*c*) to account for the heat of fusion. There may also be discontinuities in other thermophysical property data through the phase change region. In this case, property values were linearly interpolated between T_S and T_L. Quick nonlinear convergence results when combining the two parts of the above phase change technique with this linear property bridging.

The workpiece incident arc heat flux distribution for GTA welding has been measured experimentally by Smartt et al. [19] for a stationary welder without a weld pool present. The

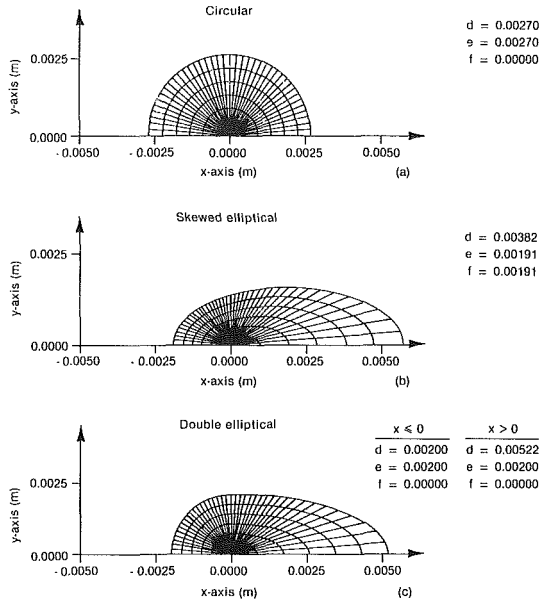

Fig. 3 Example meshes within circular, skewed elliptical, and double elliptical arc heat flux distributions

experimental data were found to fit a form of circular Gaussian distribution. Arc heat flux distribution has not been characterized in the case of a moving welder with a fully developed quasi-steady-state weld pool. However, in this case, visual and photographic observations were made which reveal a dragging or stretching of the plasma arc on the tailing side. Similar observations were made by Tsai [20]. The arc heat flux may also be skewed in a similar manner. In order that such effects be investigated theoretically, the welder arc heat flux, $q_w(x, y)$ of equation (1), was generalized so that circular, elliptical, skewed elliptical, or double elliptical (teardroplike) Gaussian distributions could be modeled. The associated relation is

$$q_w(x, y) = \frac{3P}{\pi de} e^{-3(x-f)^2/d^2} e^{-3y^2/e^2} \tag{9}$$

where q_w drops to ~ 5 percent of its peak value on the arc boundary defined by the associated ellipse equation

$$\frac{(x-f)^2}{d^2} + \frac{y^2}{e^2} = 1 \tag{10}$$

In equation (9), $P = \eta EI/0.95$, η is the arc efficiency, E and I are the voltage and the current of welder arc, respectively, and the denominator factor is necessary to account for the energy which would otherwise lie outside the ellipse boundaries of equation (10) in the tail of the Gaussian distribution. Other parameters in equations (9) and (10) include d and e, the ellipse half length and half width, respectively, and f, the x-coordinate distance that the center of the ellipse is displaced to produce a skewed distribution. The various distribution types can be produced with the appropriate choices of d, e, and f values.

A general finite element mesh generator was written which allowed generating meshes in an overall rectangular region with an internal shape such that element boundaries matched the arc heat flux elliptical boundary of equation (10). Three examples, showing only the mesh within the arc heat flux boundaries, are given in Fig. 3. The q_w term of equation (1) was integrated to five decimal place accuracy using a two-directional trapezoidal rule algorithm.

It is not sufficient for highly nonlinear problems, such as this welding model, simply to use fully implicit differencing in equation (1) to achieve a stable convergent scheme as is guaranteed in the case of linear analysis. A nonlinear under-

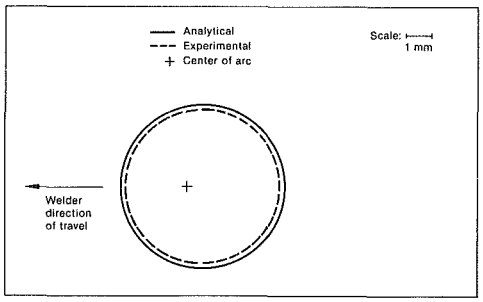

Fig. 4 Analytical versus experimental weld pool geometry, Case A/A-1

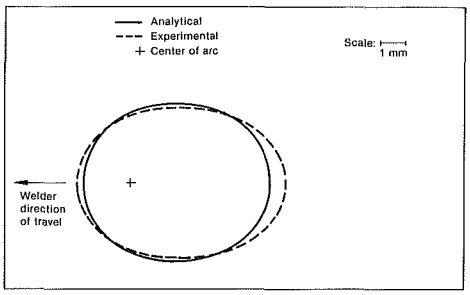

Fig. 5 Analytical versus experimental weld pool geometry, Case B/B-1

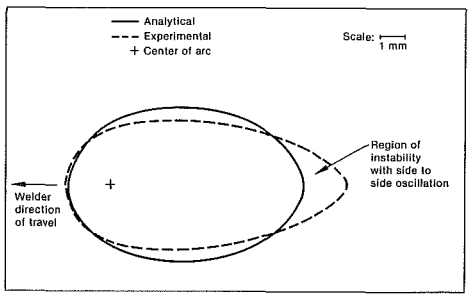

Fig. 6 Analytical versus experimental weld pool geometry, Case C/C-1

relaxation algorithm was developed to enable solution convergence. This is represented by

$$\{T\}^{p+1} = \gamma\{T\}^{p+1} + (1-\gamma)\{T\}^{p} \tag{11}$$

$$\gamma = (\Delta T_{max})^{-n}, \qquad \gamma \leq 1 \tag{12}$$

where T is the vector of unknown node temperatures, p and $p+1$ represent successive iterations, γ is the relaxation parameter, ΔT_{max} is the maximum change in node temperature from one iteration to the next, and n is the relaxation power exponent. Using $n = 0.90$ to 0.95 produced convergence in 12 to 24 iterations. A similar finite difference based model [1] using linear relaxation (i.e., $\gamma = \text{const}$) took 60 to 300 iterations to achieve convergence.

Results and Discussion

Table 1 lists the experimental and FEM model run conditions with the weld pool results for a 1.5×10^{-3} m thick SS 304 plate. Experimental results show that the weld pool is essentially the same size on the top as on the bottom of the plate, verifying the assumption that the plate may be lumped in temperature through its thickness. The model mesh consisted of 1200 elements and 1271 nodes. The length of the mesh was not as critical as the width. If was found that, with the welder centered at $x = y = 0.0$, a mesh bounded by $-0.050 \leq x \leq 0.150$ m, $0.000 \leq y \leq 0.050$ m was needed to validate the boundary conditions of equations (3)-(5). In other words, the boundary at $y = y_{max}$ must be far enough away from the welder

Table 1 Experimental and FEM model run conditions—weld pool results for SS 304

Case	Data	Molten Pool (1435°C Isotherm) Length (mm)	Width (mm)	Area (mm^2)	Welder Velocity, u (m/s)	Arc Parameters n (percent)	V (Volts)	I (Amps)
A	Experimental	5.9	5.7	26.4	0.408×10^{-3}	75-79	7.5	38
A-1	FEM Model	6.2	6.0	29.2	0.408×10^{-3}	77	7.5	38
B	Experimental	8.2	5.9	38.0	1.270×10^{-3}	75-79	8.1	50
B-1	FEM Model	7.2	6.2	35.1	1.270×10^{-3}	77	8.1	50
C	Experimental	11.3	5.0	44.4	2.540×10^{-3}	75-79	8.4	70
C-1	FEM Model	9.3	6.1	44.6	2.540×10^{-3}	77	8.4	70
C-2	FEM Model	7.5	5.5	32.4	2.540×10^{-3}	77	8.4	70
C-3	FEM Model	5.6	4.6	20.2	2.540×10^{-3}	77	8.4	70
C-4	FEM Model	10.1	5.5	43.6	2.540×10^{-3}	77	8.4	70
C-5	FEM Model	10.4	5.7	46.6	2.540×10^{-3}	77	8.4	70
C-6	FEM Model	9.2	6.1	44.1	2.540×10^{-3}	77	8.4	70
C-7	FEM Model	9.5	6.2	46.3	2.540×10^{-3}	77	8.4	70

so as not to restrict conductive heat flow; also, diffusive transport must not penetrate to the $x = x_{min}$ boundary. If these conditions are not met, the boundary conditions are inappropriate and the solution will be erroneous.

Cases A, B, and C define the experimental results which represent averages of several welds each. Cases A-1, B-1, and C-1 are the corresponding model predictions. For the model, an arc efficiency of 77 percent was used representing the average experimentally measured results for SS 304 by Smartt et al. [12], which ranged from 75 to 79 percent. The model arc heat fluxes were circular Gaussian distributions, having radii of 2.0×10^{-3}, 2.3×10^{-3}, and 2.7×10^{-3} m, respectively. The radius for Case A-1 was fixed at 2.0×10^{-3} m as a value larger than that which would be predicted by the McIlwain et al. [21] data, assuming that the arc cross-sectional area is proportional to current. This proportionality was also the basis for defining the other radii. Values larger than that which would be predicted based on the McIlwain et al. data were used because there was not an established weld pool under the arc in these measurements. When there is, metallic vapor will also be present which may broaden the arc as explained by Johnson and Pfender [22]. Figure 3(*a*) is typical of the arc heat flux geometry for these cases. Experimental and model results are compared in Figs. 4, 5, and 6. These results represent the basic predictions of this model, based on well-defined thermophysical properties and modeling parameters, without recourse to model/parameters semiempirical fitting procedures as discussed earlier. Good agreement is obtained at low power and low velocity. However, as power and velocity are increased, the model predicts too wide and too short a weld pool, although the overall weld pool area prediction remains accurate as Table 1 shows.

Effects of several parameters on weld pool shape were investigated via variations of Case C-1. To illustrate the effects of not using accurate emissivity properties, Case C-2 was run with the solid emissivity data for the entire weld plate. Emissivity temperature dependence was maintained. As shown by Table 1 molten pool data, this effect alone causes nearly a 30 percent error in weld pool area prediction.

Case C-3 was run to investigate the effect of weld pool convection assuming the result is uniform mixing. In this instance, a liquid effective thermal conductivity of twice that of the molten SS 304 was used. Table 1 data reveal the severe 55 percent undersized weld pool which results. Evidently, although weld pool convection is very likely present, its effect is not one of good mixing. It appears that no one has theoretically modeled the weld pool convection for a moving welder and

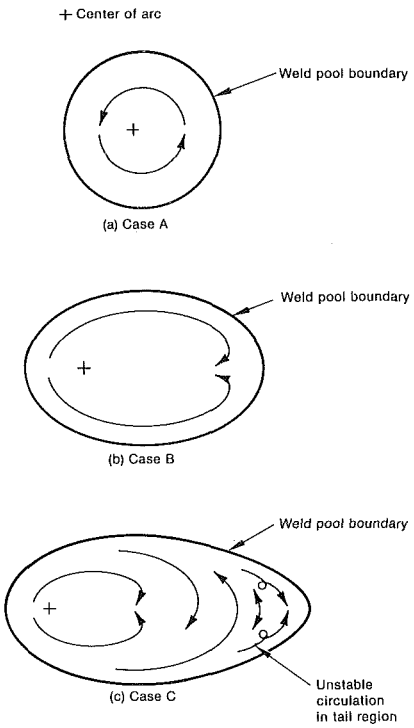

Fig. 7 Surface circulation patterns for Cases A, B, and C based on videotape observations of the welding process

thin plates, where there is a molten free surface on the upper and the lower surfaces. Videotape observations for the Case A, B, and C welding conditions show surface circulation patterns as illustrated in Fig. 7. The observation of weld pool circulation is not new and has been reported by Christensen et al. [23], Woods and Milner [24], and others. However, the specific qualitative data for SS 304 of Fig. 7 do represent a weld pool circulation pattern development with increasing welder power and velocity not previously presented. It is believed that the weld pool convection may be dominated by surface tension forces because of the doubling of molten metal surface area for full penetration welds. Electromagnetic force effects may also be significant whereas buoyancy forces, due to the thinness of the plate, may play only a minor role. Because of the recirculating patterns of Cases B and C as compared to Case A of Fig. 7, welder velocity is believed to play an important role also. In any case, weld pool convection does not appear to be significant in determining weld pool size, but may explain a portion of the experimental/model weld pool shape differences as welder power and velocity are increased.

Arc heat flux distribution and geometry represent another area of uncertainty. Cases C-4 and C-5 show the result if the arc dragging effect discussed earlier causes a skewed elliptical or a double elliptical distribution, respectively. Figures 3(*b*) and 3(*c*) show the corresponding arc heat flux geometries. Only the double elliptical (or teardroplike) shape resulted in a close fit to the experimental data of Fig. 6. Experimental confirmation of this arc heat flux shape is needed. Using a constant heat flux, rather than a Gaussian distribution, may closer represent reality as the Johnson and Pfender [22] analysis reveals. Even so, the Case C-6 data of Table 1 reveal little associated effect. The influence of arc radius was studied in Case C-7 where a radius of 3.6×10^{-3} m (1/3 increase) resulted in ~4 percent change in weld pool area with no change in shape.

Ganaha and Kerr [25] give experimental weld pool shapes for carbon steels. Therein, the elongated tail at higher welding velocities appears even more pronounced than for the present case of SS 304. This is the primary area of experimental/model weld pool shape discrepancy of this work as reinspection of Fig. 6 shows. Easterling [26] discusses fusion welds and points out that the solidification process is not simply the reverse of melting as modeled herein. It is shown qualitatively that the thermal history of the weld material can result in a phenomenon known as constitutional supercooling. Constitutional supercooling is greatest at higher welding speeds and at the weld centerline where element concentration pile-ups are the greatest. This is believed to be the source of experimental/model weld pool shape differences in the tail of the weld pool. Verification of such is needed. This effect has not been accounted for in any of the welding models known to date and most appear to possess similar deviations from experiment. It is estimated that a mean constitutional supercooling of ~140 K would allow this model to match experiment in the weld pool tail region of Fig. 6.

Summary

The GTA welding of two thin plates has been modeled using a finite element based solution method. Welder input powers from 285 to 588 W and welder velocities from 0.408×10^{-3} to 2.540×10^{-3} m/s were simulated. Results show good agreement of experimental and model weld pool areas. The details of weld pool shape are predicted well at low power and velocity. However, as welder power and velocity increase, differences in weld pool width and tail shape are revealed. Reference to results of this work and current literature forms the basis of the statements below which include recommendations for the direction of future research.

Using proper and accurate thermophysical property data is very important in welding modeling. Temperature dependencies, resulting in nonlinear defining equations, must be used. An example was given showing the importance of emissivity, not only with respect to temperature variation, but also with respect to the differences between the solid and liquid phases of the metal. No model of molten pool convection for thin-plate moving welders has been made. This does not appear to be important for modeling weld pool size but may influence shape. Results herein indicate that molten pool convection does not result in a well-mixed weld pool. Videotape weld pool surface observations for SS 304 thin plate welding reveal a developing recirculation and instability pattern as welding power and velocity are increased. Weld pool convection may explain the narrowing of the pool over theoretical predictions. For this relatively small gain in weld pool shape accuracy, a complex convective model, including the following, may be needed:

1 Arc plasma jet and cover gas surface shear forces
2 Cover gas/arc pressure
3 Well-characterized arc heat and electric current flux distributions
4 Electromagnetic or Lorentz forces
5 Buoyancy forces
6 Surface tension forces
7 Weld pool vaporization/condensation.

Arc drag due to welder motion/arc/anode interaction may alter the heat flux distribution on the surface of the plates. This may be largely responsible for narrowing and elongating the weld pool as observed experimentally at high welding velocities compared to the diffusion/advection model results given herein. The author is beginning experimental research to make such measurements.

Constitutional supercooling may be responsible for the elongated and pointed tail observed experimentally at high welding velocities. This may be more important to investigate than weld pool convective effects. The reason for this is based on the fact that metallurgical solidification models depend on the local phase front curvature as primary dendritic growth occurs with ~30 deg of normal to this front. It is in the weld pool tail region where the largest experimental/model phase

front curvature differences exist. An experiment to noninvasively measure pool surface temperature to investigate this possibility is presently being performed by the author.

Welding processes are indeed physically complex. No completely comprehensive welding models have yet been formulated. To model thin-plate weld pool convection will require a three-dimensional model, as will thick-plate weld pool convection simulations for moving welders. The above effects should be included and assessed.

Acknowledgments

The following individuals involved in the Idaho National Engineering Laboratory welding research programs were instrumental in bringing the author's knowledge to a point sufficient to write this article: H. B. Smartt, G. R. Smolik, C. J. Einerson, J. A. Stewart, M. E. McIlwain, and J. O. Bolstad. This work was funded by the U.S. Department of Energy, Office of Energy Research, Office of Basic Energy Sciences, under contract number DE-AC07-76ID01570.

References

1 Kou, S., Kanevsky, T., and Fyfitch, S., "Welding Thin Plates of Aluminum Alloys – A Quantitative Heat-Flow Analysis," 62nd AWS Annual Meeting, Cleveland, OH, Apr. 5–10, 1981.

2 Krutz, G. W., and Segerlind, L. J., *Welding J. Res. Suppl.*, Vol. 57, 1978, pp. 211–216s.

3 Friedman, E., "Thermomechanical Analysis of the Welding Process Using the Finite Element Method," ASME *J. Press. Ves. Tech.*, Vol. 97, 1975, pp. 206–213.

4 Goldak, J., Chakravarti, A., and Bibby, M., "A New Finite Element Model for Welding Heat Sources," *Metal. Trans. B*, Vol. 15, No. 2, 1984.

5 Heiple, C. R., et al., "Surface Active Element Effects on the Shape of GTA, Laser, and Electron Beam Welds," *Welding J.*, Mar. 1983, pp. 72–77s.

6 Oreper, G. M., Eager, T. M., and Szekley, J., "Convection in Arc Weld Pools," *Welding J.*, Nov. 1983, pp. 307–312S.

7 Oreper, G. M., and Szekley, J., "Heat- and Fluid-Flow Phenomena in Weld Pools," *J. Fluid Mech.*, to be published (1984).

8 Karniadakis, G. E., and Unkel, W., "Development and Experimental Validation of a Predictive Model for a GTA Weld Pool Geometry," *Int. J. Heat Mass Transfer*, submitted for publication (1984).

9 Touloukian, Y. S., and Dewitt, D. P., *Thermophysical Properties of Matter, Vol. 7 – Thermal Radiative Properties, Metallic Elements and Alloys*, Plenum Press, New York, 1970, pp. 1220–1227.

10 West, R. C., ed., *CRC Handbook of Chemistry and Physics*, 57th ed., CRC Press, Cleveland, OH, 1976, pp. E-229–E-230.

11 Touloukian, Y. S., and Dewitt, D. P., *Thermophysical Properties of Matter, Vol. 8 – Thermal Radiative Properties, Nonmetallic Solids*, Plenum Press, New York, 1972, p. 231.

12 Smartt, H. B., Stewart, J. A., and Einerson, C. J., "GTAW Arc Efficiency," presented at the 66th Annual AWS Convention, Las Vegas, NV, May 1, 1985.

13 Gresho, P., and Lee, R. L., "Don't Suppress the Wiggles – They're Telling You Something," *Finite Element Methods for Convection Dominated Flows*, AMD-Vol. 34, ASME, 1979.

14 Gartling, D. K., "Some Comments on the Paper by Heinrich, Huyakorn, Zienkiewicz, and Mitchell," *Int. J. Num. Meth. Eng.*, Vol. 12, 1978, pp. 187–190.

15 Holman, J. P., *Heat Transfer*, 4th ed., McGraw-Hill, New York, 1976.

16 McCullough, H. M., Fontana, M. G., and Beck, F. H., "Formation of Oxides on Some Stainless Steels at High Temperatures," *Trans. Amer. Soc. Metals*, Vol. 43, 1951, pp. 404–425.

17 Kim, C. S., "Thermophysical Properties of Stainless Steels," ANL-75-55, Argonne National Laboratory, Argonne, IL, Sept. 1975.

18 Lemmon, E. C., "Phase-Change Techniques for Finite Element Conduction Codes," *Numerical Methods in Thermal Problems*, R. W. Lewis and K. Morgan, eds., Redwood Burn Limited, Great Britain, 1979.

19 Smartt, H. B., Stewart, J. A., and Einerson, C. J., "GTA Heat Input Distribution Measurements," presented at the American Weld. Soc. 66th Annual Convention, Las Vegas, NV, May 1, 1985.

20 Tsai, N., "Heat Distribution and Weld Bead Geometry in Arc Welding," Ph.D. Dissertation, MIT, USA, Apr. 1983.

21 McIlwain, M. E., Smartt, H. B., Stewart, J. A., and Einerson, C. J., "Characterization of the Heat Source Distribution of a Typical GTAW Welding Arc," Int. Soc. of Opt. Engs., Thermal Sense 8th, Boston, MA, Nov. 5–8, 1984.

22 Johnson, D. C., and Pfender, E., "The Effects of Low-Ionization-Potential Contaminants on Thermal Plasmas," *Plasma Chemistry and Plasma Processing*, Vol. 3, No. 2, 1983, pp. 259–273.

23 Christensen, N., Davies, V. de L., and Gjermundsen, K., *British Welding J.*, Vol. 12, 1965, p. 54.

24 Woods, R. A., and Milner, D. R., "Motion in the Weld Pool in Arc Welding," *Welding J.*, Apr. 1971, pp. 163–173S.

25 Ganaha, T., and Kerr, H. W., "TIG Weld Solidification Structures in Carbon Sheet Steels," *Metals Tech.*, Feb. 1978, pp. 62–69.

26 Easterling, K. E., "Solidification Microstructure of Fusion Welds," *Mats. Sc. and Eng.*, Vol. 65, 1984, pp. 191–198.

M. F. Modest
Mem. ASME

H. Abakians
Student Mem. ASME

Department of Mechanical Engineering,
University of Southern California,
Los Angeles, CA 90089-1453

Heat Conduction in a Moving Semi-infinite Solid Subjected to Pulsed Laser Irradiation

Heat conduction in a moving semi-infinite medium subject to laser irradiation is considered. The body of knowledge of exact analytical solutions for Gaussian laser irradiation is expanded to include pulsed lasers, and laser beams that penetrate into the medium with exponential decay. For applications with complicated geometries (laser melting and evaporation), a simple integral method, based on one-dimensional diffusion, is presented, and its range of validity determined.

Introduction

Lasers have a variety of applications in modern day technology, primarily because of their ability to produce high-power beams. With such concentrated energy it is possible to heat, melt, or even vaporize any known material. Presently, laser applications include welding, drilling, cutting, machining of brittle or refractory materials, heat treatment of metals, fabrication of electronic components, medical surgery, and production of charged particles.

Most of the theoretical work on laser-treatment heat transfer to date has centered on the solution of the classical heat conduction equation for a stationary or moving semi-infinite solid. Cases with and without phase change and a variety of irradiation and source conditions have been studied. The simplest case without phase change arises when a semi-infinite half-space is heated uniformly over its entire boundary surface. This type of problem was first treated by Carslaw and Jaeger [1], while the case of a pulsed source was addressed by Carslaw and Jaeger [1], White [2, 3] and Rykalin, Uglov, and Makarov [4]. The more realistic case of a disk-shaped source (constant in time or pulsed) was first addressed by Paek and Gagliano [5]. Further refinement of the theory was achieved by assuming the laser beam to have a Gaussian distribution, i.e., the intensity decreases exponentially from the center of the beam with the square of radial distance; this type of problem has been addressed by Ready [6], Cline and Anthony [7], and Nissim et al. [8]. Some researchers, in particular Brugger [9] and Maydan [10, 11], have solved the stationary semi-infinite slab problem assuming that the intensity of the incident beam decays exponentially with distance into the material (internal absorption).

The problem is considerably more complicated when phase transition takes place. In the case of rapid material removal by melting and/or evaporating, most of the laser energy is used to cut (melt and evaporate) the solid, and only a small fraction is lost to heat conduction into the body. To date, most investigations have concentrated on solving the heat conduction problem accurately but made simplifying assumptions with respect to the phase change, e.g., Cline and Anthony [7]. In contrast, to predict the groove formation associated with laser cutting, it is more important to treat the mechanics of melting and evaporation accurately, while the relatively small conduction losses could be approximated.

The purpose of the present paper is twofold: (*i*) to expand the body of conduction solutions to include the cases of scanning CW and pulsed Gaussian lasers, whose energy penetrates into a semi-infinite body with exponential decay, and (*ii*) to develop and determine the conditions of validity of a simple approximate conduction model, which could be employed in the much more complicated case of laser-induced melting and evaporation.

Analysis

The heat conduction equation for a solid moving with velocity u in the positive x direction under a pulsed, penetrating, Gaussian laser source is [1]

$$\frac{1}{\alpha}\left(\frac{\partial T}{\partial t}+u\,\frac{\partial T}{\partial x}\right)=\nabla^2 T+\frac{F_0\beta}{k}\,g(t)e^{-(x^2+y^2)/R^2-\beta z}, \tag{1}$$

subject to the boundary conditions

$$t\to-\infty,\ x\to\pm\infty,\ y\to\pm\infty,\ z\to+\infty:\ T\to T_\infty;\ z=0:\ \frac{\partial T}{\partial z}=0. \tag{2}$$

Here F_0 is the time-averaged absorbed laser flux at the center of the beam, R is the effective laser radius, β is the extinction coefficient of the medium, and $g(t)$ is a periodic pulsing function with period P. From the definition for F_0 it follows that the pulsing function is normalized, i.e.

$$\frac{1}{P}\int_t^{t+P} g(t)\,dt=1. \tag{3}$$

The solution to equations (1) and (2) for a point source of strength $d^3Q = F(t)dxdydz$ located at $x=y=z=0$ is given by Carslaw and Jaeger [1] as

$$d^3(T-T_\infty)=\frac{dxdydz}{8\rho c(\pi\alpha)^{3/2}}\int_{-\infty}^{t} e^{-\{[x-u(t-t')]^2+y^2+z^2\}/4\alpha(t-t')}\times\frac{F(t')dt'}{(t-t')^{3/2}}. \tag{4}$$

Using equation (4) the solution to the present problem is readily found to be

$$T-T_\infty=\frac{F_0\beta}{8\rho c(\pi\alpha)^{3/2}}\int_{-\infty}^{\infty}\int_{-\infty}^{\infty}\int_{-\infty}^{\infty}\int_0^{\infty} g(t-\omega)\times e^{-[(x-x'-u\omega)^2+(y-y')^2+(z-z')^2]/4\alpha\omega}\,\frac{d\omega}{\omega^{3/2}}\times e^{-(x'^2+y'^2)/R^2-\beta|z'|}dx'dy'dz'. \tag{5}$$

Introducing the following nondimensional variables and parameters

$$\xi=x/R,\ \eta=y/R,\ \zeta=z/R,\ \tau=ut/R; \tag{6a}$$

$$\theta=\frac{T-T_\infty}{T_{\text{ref}}-T_\infty},\ N_k=\frac{k(T_{\text{ref}}-T_\infty)}{RF_0},\ U=\frac{uR}{\alpha},\ K=\beta R, \tag{6b}$$

and carrying out the space integration results in

Contributed by the Heat Transfer Division for publication in the JOURNAL OF HEAT TRANSFER. Manuscript received by the Heat Transfer Division July 19, 1985. Paper No. 85-WA/HT-61.

$$\theta(\xi,\ \eta,\ \zeta,\ \tau)=\frac{K}{2N_k}\int_0^{\infty} g(\tau-\omega)e^{-[(\xi-\omega)^2+\eta^2]U/(U+4\omega)-\zeta^2 U/4\omega}$$

$$\times\left\{\operatorname{erfn}\left(K\sqrt{\frac{\omega}{U}}+\frac{\zeta}{2}\sqrt{\frac{U}{\omega}}\right)\right.$$

$$\left.+\operatorname{erfn}\left(K\sqrt{\frac{\omega}{U}}-\frac{\zeta}{2}\sqrt{\frac{U}{\omega}}\right)\right\}\frac{d\omega}{U+4\omega}, \tag{7}$$

where

$$\operatorname{erfn}(x)=e^{x^2}\operatorname{erfc}(x). \tag{8}$$

It is assumed that the complementary error function of negative arguments is evaluated as

$$\operatorname{erfc}(-x)=1+\operatorname{erf}(x)=2-\operatorname{erfc}(x). \tag{9}$$

If the laser energy deposition is entirely on the surface ($K\to\infty$), the solution becomes, either by omitting the z' integration in equation (5) or by finding the limting value for equation (7),

$$\theta(\xi,\ \eta,\ \zeta,\ \tau)\,|_{K\to\infty}=\frac{1}{N_k}\sqrt{\frac{U}{\pi}}\int_0^{\infty} g(\tau-\omega)e^{-[(\xi-\omega)^2+\eta^2]U/(U+4\omega)}$$

$$\times e^{-\zeta^2 U/4\omega}\frac{d\omega}{(U+4\omega)\sqrt{\omega}}. \tag{10}$$

For the CW laser case ($g\equiv 1$), this solution has already been given by Cline and Anthony [7].

The laser pulse function has a nondimensional period $p=uP/R$ of which a part ϵ describes the laser-on time and $p-\epsilon$ is the laser-off time. By eliminating the laser-off time from the solution, equation (7) may be rewritten as

$$\theta(\xi,\ \eta,\ \zeta,\ \tau)=\frac{K}{2N_k}\sum_{n=-\infty}^{N}\int_{np}^{\min(np+\epsilon,\tau)} g(\tau'-np)$$

$$\times\left\{\operatorname{erfn}\left(K\sqrt{\frac{\tau-\tau'}{U}}+\frac{\zeta}{2}\sqrt{\frac{U}{\tau-\tau'}}\right)\right.$$

$$\left.+\operatorname{erfn}\left(K\sqrt{\frac{\tau-\tau'}{U}}-\frac{\zeta}{2}\sqrt{\frac{U}{\tau-\tau'}}\right)\right\}$$

$$\times e^{-[(\xi-\tau+\tau')^2+\eta^2]U/(U+4\tau-4\tau')-\zeta^2 U/4(\tau-\tau')}\times\frac{d\tau'}{U+4(\tau-\tau')}, \tag{11}$$

where N is the largest integer less than τ/p. The upper limit of the integral is always $np+\epsilon$, unless $n=N$ and τ is during the laser-on interval. If the laser-on time is very short, $\epsilon\ll 1$, the solution reduces to

$$\theta(\xi,\ \eta,\ \zeta,\ \tau)\,|_{\epsilon\to 0}=\frac{pK}{2N_k}\sum_{n=-\infty}^{N} e^{-[(\xi-\tau+np)^2+\eta^2]U/(U+4\tau-4np)}$$

$$\times\left\{\operatorname{erfn}\left(K\sqrt{\frac{\tau-np}{U}}+\frac{\zeta}{2}\sqrt{\frac{U}{\tau-np}}\right)\right.$$

$$\left.+\operatorname{erfn}\left(K\sqrt{\frac{\tau-np}{U}}-\frac{\zeta}{2}\sqrt{\frac{U}{\tau-np}}\right)\right\}$$

$$\times e^{-\zeta^2 U/4(\tau-np)}/[U+4\tau-4np]. \tag{12}$$

As noted by Rykalin et al. [4], as $p\to 0$ the solution reduces to the CW case.

The foregoing theory applies only to a body with a flat surface normal to the laser irradiation. If the irradiation is strong enough, the laser may be used as a cutting tool, either by melting the solid with continuous melt removal, or by evaporation. In either case the solid surface will have a complex shape in the vicinity of the laser, making accurate prediction of temperature field and conduction (and convection) losses extremely difficult and cumbersome. It is, therefore, desirable to find a simple approximate solution to equations (1) and (2) which is easily applied to the more complicated case. We start by investigating the relative importance of the different terms in equation (1). The unsteady term describes time-temperature variation due to the laser pulsing, and would not be present for a CW laser. Thus, the absorbed laser energy is partially carried away by the moving solid, and partially conducted away into all directions. If laser heat generation drops off more rapidly into the solid than radially along the surface ($K\gg 1$) and if the velocity of the solid is much larger than the speed of diffusion ($U\gg 1$), then the temperature gradient (and conduction) will be much greater in the direction normal to the surface than along it (as long as the temperature gradient is approximately constant). Under these conditions, which are quite reasonable for laser machining, sideways conduction may then be neglected. For the present case this leaves conduction in the z or ζ direction (the extension to the irregular surface case is straightforward and has been done by Modest and Abakians [12] for the case of a CW laser with surface energy deposition). Equations (1) and (2) become, for a stationary solid with moving laser source,

$$U\frac{\partial\theta}{\partial\tau}\simeq\frac{\partial^2\theta}{\partial\zeta^2}+G(\xi^*,\ \eta,\ \tau)\frac{K}{N_k}e^{-K\zeta}, \tag{13}$$

$$\tau\to-\infty,\ \zeta\to+\infty:\ \theta=0,\ \zeta=0:\ \frac{\partial\theta}{\partial\zeta}=0, \tag{14}$$

$$G(\xi^*,\ \eta,\ \tau)=g(\tau)e^{-(\xi^*+\tau)^2-\eta^2}, \tag{15}$$

where ξ^* is the ξ location on the stationary solid, $\xi^*=\xi-\tau$. Although an exact solution of equations (13)-(15) is possible,

Nomenclature

c = heat capacity
$\operatorname{erfn}(x)$ = normalized complementary error function
F_0 = absorbed laser flux
$g(t)$ = pulsing function
k = thermal conductivity
K = laser penetration depth = βR
N_k = conduction-to-irradiation parameter
p = nondimensional period = uP/R
P = laser pulse period
R = effective laser beam radius
t = time
T = temperature
T_{ref} = reference temperature
T_∞ = ambient temperature
u = laser scanning speed
U = laser-to-diffusion-speed parameter = uR/α
x, y, z = Cartesian coordinates
α = thermal diffusivity
β = extinction coefficient
δ = thermal penetration depth
ϵ = nondimensional laser pulse length
θ = nondimensional temperature
θ_w = nondimensional wall temperature
ρ = density
τ = nondimensional time = ut/R

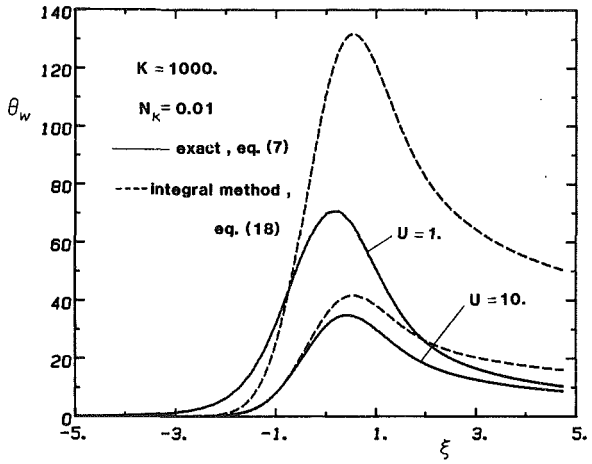

Fig. 1 Effect of laser-to-diffusion-speed parameter U on surface temperature

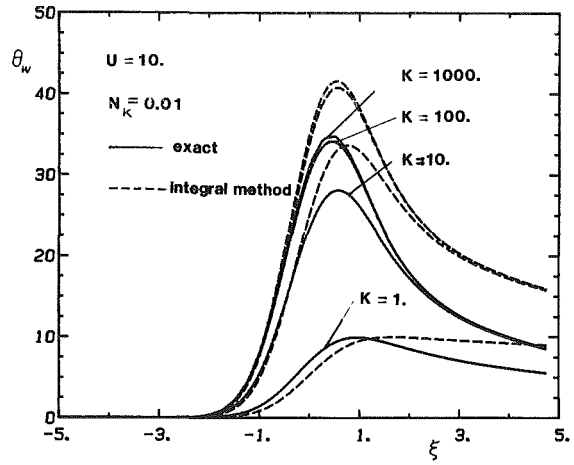

Fig. 2 Effect of laser penetration depth K on surface temperature

we prefer to keep the solution as simple as possible, using an integral method with a second-order-polynomial profile. In order to apply Duhamel's superposition integral, equations (13)–(15) are first solved for the dependent variable ϕ for the case of a uniform step source $G \equiv 1$ for $\tau > 0$; ϕ is found by making equation (13) homogeneous and by approximating the exponential term by a second-order polynomial. After some manipulation this results in

$$N_k \phi(\tau, \zeta) = \begin{cases} \frac{\delta}{2}\left(1-\frac{\zeta}{\delta}\right)^2 - \frac{\sqrt{6}}{2K}\left(1-\frac{K\zeta}{\sqrt{6}}\right)^2 & 0<\zeta<\frac{\sqrt{6}}{K}, \\ \frac{\delta}{2}\left(1-\frac{\zeta}{\delta}\right)^2 & \frac{\sqrt{6}}{K}<\zeta<\delta, \\ 0 & \delta<\zeta, \end{cases} \quad (16)$$

$$\delta(\tau) = \sqrt{6\left(\frac{\tau}{U}+\frac{1}{K^2}\right)}. \quad (17)$$

The approximation for $e^{-K\zeta}$ is chosen as to correctly predict the total energy release and to be compatible with the integral method, giving the correct initial value for $\phi(0, \zeta) = 0$. Applying Duhamel's integral finally gives the solution to equations (13)–(15) as

$$\theta(\xi^*, \eta, \zeta, \tau) \simeq -\frac{\sqrt{6}}{4N_k\sqrt{U}} \int_{-\infty}^{\min(\tau, \tau + U/K^2 - U\zeta^2/6)} g(\tau') \times e^{-(\xi^*+\tau')^2-\eta^2}\left[1-\frac{U\zeta^2}{6\left(\tau-\tau'+\frac{U}{K^2}\right)}\right]\frac{d\tau'}{\sqrt{\tau-\tau'+\frac{U}{K^2}}}. \quad (18)$$

Transforming back to the coordinate system fixed to the laser beam center, this may be rewritten as

$$\theta(\xi, \eta, \zeta, \tau) \simeq \frac{1}{2N_k\sqrt{U}} \sum_{n=-\infty}^{N_i(\zeta)} \int_{np}^{\min\left(np+\epsilon, \tau, \tau+U/K^2-U\zeta^2/6\right)} g(\tau'-np) e^{-(\xi-\tau+\tau')^2-\eta^2}\left[1-\frac{U\zeta^2}{6\left(\tau-\tau'+\frac{U}{K^2}\right)}\right] \cdot \frac{d\tau'}{\sqrt{\tau-\tau'+\frac{U}{K^2}}}, \quad (19)$$

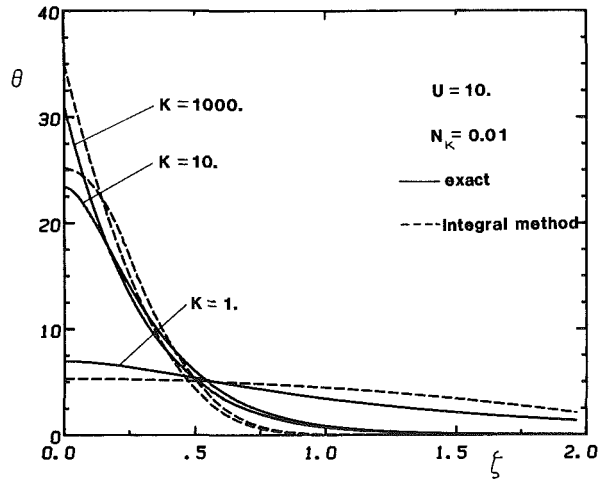

Fig. 3 Effect of laser penetration depth K on internal temperature

where N_i is governed by the upper limit of the integral; unlike in the case of the "exact" solution, the effect of the (latest) pulse is not immediately felt deep inside the medium ($\zeta > 0$). If the pulse length ϵ is short the equivalent to equation (12) is

$$\theta(\xi, \eta, \zeta, \tau) \simeq \frac{\sqrt{6p}}{4N_K\sqrt{U}} \sum_{n=-\infty}^{N_i(\zeta)} e^{-(\xi-\tau+np)^2-\eta^2} \cdot \left[1-\frac{U\zeta^2}{6(\tau+U/K^2-np)}\right] \Big/ \sqrt{\tau+U/K^2-np} \quad (20)$$

Illustrative Examples

In the following, a number of sample results are presented for the heating of a moving slab by laser irradiation, which is pulsed and/or penetrates into the medium. Figures 1–3 deal with the CW case and Figs. 4–6 with pulsed laser irradiation. In all cases the value of the parameter N_k (ratio of energy conducted through to irradiation) is taken to be 0.01. N_k merely acts as a multiplicative factor increasing (for small N_k) or decreasing (large N_k) the surface temperature. For simplicity of presentation all results are shown for the line of symmetry, $y = 0$, where temperatures are highest, and where the approximate integral method is most inaccurate.

Changes in the surface temperature for different values of the laser-to-diffusion speed parameter U are shown in Fig. 1. In this case the medium is assumed to be highly absorbing ($K = 1000$), i.e., all laser energy is deposited on the surface. As

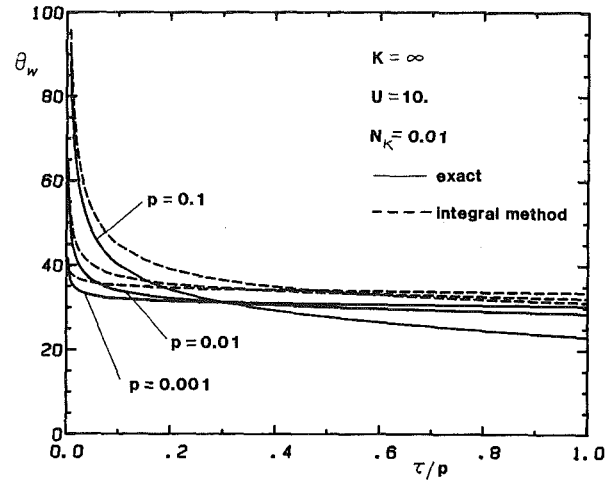

Fig. 4 Effect of laser pulse period p on temporal variations of the surface temperature ($\xi = 0$)

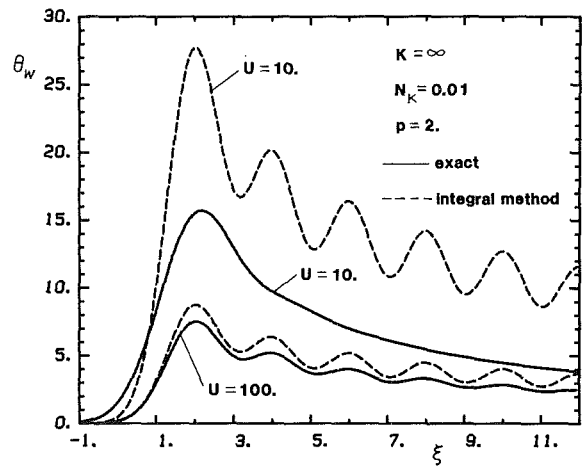

Fig. 5 Effect of laser-to-diffusion-speed U on surface temperature for a pulsating laser beam

U is increased, a lesser amount of incident energy per unit area is delivered to the medium resulting in a lower surface temperature. For large U, since relatively little energy is conducted away laterally, the integral method agrees well with the exact solution. However, the integral method becomes less accurate when the temperature growth is significantly lowered due to sideways conduction, as is seen for $U = 1$: Neglecting lateral conduction overpredicts the maximum surface temperature; moreover, neglecting conduction in the ξ direction results in a more abrupt temperature rise in this direction (the temperature profile for the integral method crosses the exact one). Nevertheless, it is seen that the integral method is good for $U > 10$ and $\xi < 0$ (warmup region).

Figure 2 shows the variation of the surface temperature with the laser penetration depth K. Here $U = 10$ has been chosen as representative, i.e., the smallest value for which the integral method is expected to be accurate. As long as the surface temperature is increasing rapidly, the conduction of heat in the lateral direction appears negligible, giving the integral method a high degree of accuracy even for relatively small K. As expected, the highest discrepancy between the integral and the exact method occurs where the temperature reaches a maximum (maximum lateral conduction). Beyond this point the agreement is good once again; however, due to the accumulated error the integral method merely follows the exact temperature decay staying almost parallel to it. For small K, the heat source decays slowly in the z direction, making the integral method less accurate.

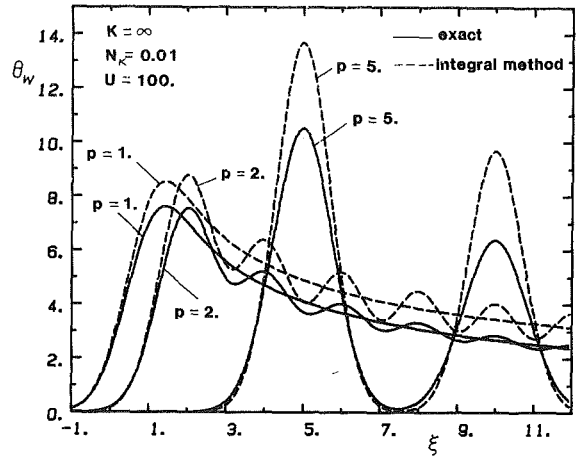

Fig. 6 Effect of laser pulse period p on surface temperature

The effect of the laser penetration depth K on the temperature variation inside the medium is depicted in Fig. 3 for the location $\xi = 0$ and for $U = 10$. For large values of K the surface temperature is higher while decaying rapidly into the medium. On the other hand a small K results in a lower surface temperature with a gradual decay in the z direction. The agreement between the exact solution and the integral method is good as long as K is not very small (a small K results in a slow decay of temperature in the z direction and thus increases the relative amount of sideways conduction). The accuracy of the integral method is even better for $\xi < 0$ and/or $U > 10$.

Figure 4 depicts the influence of a pulsating Gaussian source on the time variation of the surface temperature. To reduce the number of variables it is assumed that the laser on-time ϵ is approaching zero, and the penetration depth K is infinity (surface deposition). Again, $U = 10$ has been chosen as a representative laser-to-diffusion-speed ratio, and $\xi = 0$ as a representative location. Without loss of generality, it is sufficient to consider τ to vary between 0 and p, since the laser source function and, therefore, the temperature field are both periodic in time with period p. Moreover, since it is assumed that $\epsilon = 0$, the temperature at the surface must rise to infinity at $\tau = 0$ to accommodate the finite amount of energy delivered. To facilitate plotting, the time τ is nondimensionalized with the period p. Thus in actuality the $p = 0.001$ case will have 100 times more rapid pulses in the same time as $p = 0.1$. The curves, as expected, cross each other signifying that the total energy delivered is the same for different p. It is seen that for $p \ll 1$ the time variation flattens out more rapidly, thus approaching the CW case as indicated by Rykalin et al. [4].

The effect of the laser-to-diffusion-speed ratio U on surface temperature, for pulsed irradiation with surface deposition ($K \to \infty$), is shown in Fig. 5. In most applications one would expect $p < 1$, i.e., the medium travels less than the effective laser-beam radius between pulses. This results in relatively smooth surface temperature versus location behavior at any given time without local minima and maxima (not shown here), although the surface temperature undergoes significant temporal variations as demonstrated in Fig. 4. For very large p the body travels a good distance before the next pulse (with Gaussian decay along the surface), making local temperature minima and maxima a possibility. A large p also implies additional time between pulses for lateral conduction making the integral method inaccurate, unless U is also very large (small thermal diffusivity). Thus we must have $U \gg p$ as well as $U \gg 1$ if the integral method is to be accurate. In the case of $p = 2$ shown here, the exact solution is relatively smooth while the integral method shows much more distinct peaks and valleys because of the neglected lateral conduction.

Finally, the effect of a large laser pulse period p on the surface temperature is shown in Fig. 6 for $U=100$ and $K\to\infty$. It is observed that as long as the temperature is rising or decaying sharply, sideways conduction will be relatively minor and the integral method accurate. For large p, the peaks are sharper and higher (the high peaks occur at times when the laser pulse is turned on).

Conclusions

The purpose of the present paper was (*i*) to expand the body of conduction solutions to include the cases of CW and pulsed laser irradiation, whose energy penetrates into the medium, and (*ii*) to develop and determine the conditions of validity of a simple conduction model which would be applicable in the more complicated cases of laser-induced melting and evaporation. It is observed that for a continuous source the integral method agrees well with the exact solution for negative ξ (body-warmup region) as long as $U>10$. An additional condition arises for a pulsating source for which one must also have $U\gg p$ in order to neglect lateral conduction. For average values of K ($10<K<1000$) the accuracy of the integral method is undiminished as compared to the surface deposition case ($K\to\infty$).

For laser cutting applications one may expect rapid pulses, $p<0.1$. In addition, conduction in these applications is important only in the warmup region ($\xi<0$), and in the melting/evaporating region ($\theta_w=\text{const}$). Thus we feel that the integral method with one-dimensional conduction (normal to the surface) will be a viable model for laser cutting applications as long as $U>10$.

Acknowledgments

Support for this work under National Institute of Arthritis, Diabetes, Digestive and Kidney Diseases, Grant AM30240 is gratefully acknowledged.

References

1 Carslaw, H. S., and Jaeger, J. C., *Conduction of Heat in Solids*, 2nd ed., Oxford University Press, 1959.

2 White, R. M., "Elastic Wave Generation by Electron Bombardment or Electromagnetic Wave Absorption," *Journal of Applied Physics*, Vol. 34, 1963, pp. 2123–2124.

3 White, R. M., "Generation of Elastic Waves by Transient Surface Heating," *Journal of Applied Physics*, Vol. 34, 1963, pp. 3559–3567.

4 Rykalin, N. N., Uglov, A. A., and Makarov, N. I., "Effects of Peak Frequency in a Laser Pulse on the Heating of Metal Sheets," *Soviet Physics—Doklady*, Vol. 12, 1967, pp. 644–646.

5 Paek, U-C., and Gagliano, F. P., "Thermal Analysis of Laser Drilling Processes," *IEEE Journal of Quantum Electronics*, Vol. QE-8, 1972, pp. 112–119.

6 Ready, J. F., *Effects of High Power Laser Radiation*, Academic Press, New York, 1971.

7 Cline, H. E., and Anthony, T. R., "Heat Treating and Melting Material With a Scanning Laser or Electron Beam," *Journal of Applied Physics*, Vol. 48, 1977, pp. 3895–3900.

8 Nissim, Y. I., Lietoila, A., Gold, R. B., and Gibbons, J. F., "Temperature Distributions Produced in Semiconductors by a Scanning Elliptical or Circular CW Laser Beam," *Journal of Applied Physics*, Vol. 51, 1980, pp. 274–279.

9 Brugger, K., "Exact Solutions for the Temperature Rise in a Laser Heated Slab," *Journal of Applied Physics*, Vol. 43, 1972, pp. 577–583.

10 Maydan, D., "Fast Modulator for Extraction of Internal Laser Power," *Journal of Applied Physics*, Vol. 41, 1970, p. 1552–1559.

11 Maydan, D., "Micromachining and Image Recording on Thin Films by Laser Beams," *Bell System Technical Journal*, Vol. 50, 1971, pp. 1761–1789.

12 Modest, M. F., and Abakians, H., "Evaporative Cutting of a Semi-infinite Body With a Moving CW Laser," ASME JOURNAL OF HEAT TRANSFER, this issue, pp. 602–607.

Evaporative Cutting of a Semi-infinite Body With a Moving CW Laser

M. F. Modest
Mem. ASME

H. Abakians

University of Southern California,
Department of Mechanical Engineering,
Los Angeles, CA 90089-1453

The formation of a deep groove by evaporation on a moving semi-infinite solid is considered. Evaporative removal of material is achieved by focusing a high-power, highly concentrated Gaussian laser beam of constant wattage (CW laser) onto the surface of the solid. Assuming thermal losses due to conduction and convection to be relatively minor, these losses are treated in an approximate fashion using a simple integral method. The relevant nonlinear partial differential equations are solved numerically, and results for groove depth and shape are presented for a variety of laser and solid parameters.

Introduction

Lasers have a variety of applications in modern day technology, primarily because of their ability to produce high-power beams. With such concentrated energy it is possible to heat, melt, or even vaporize any known material. Presently, laser applications include welding, drilling, cutting, machining of brittle or refractory materials, heat treatment of metals, fabrication of electronic components, medical surgery, and production of charged particles.

Most of the theoretical work on laser-treatment heat transfer to date has centered on the solution of the classical heat conduction equation for a stationary or moving semi-infinite solid. Cases with and without phase change and a variety of irradiation or source conditions have been studied. The simplest case without phase change arises when a semi-infinite half space is heated uniformly over its entire boundary surface. This type of problem was first treated by Carslaw and Jaeger [1], while the case of a pulsed source was addressed by Carslaw and Jaeger [1], White [2, 3], and Rykalin et al. [4]. The more realistic case of a disk-shaped source (constant in time or pulsed) was first addressed by Paek and Gagliano [5], and a Gaussian distribution has been addressed by Ready [6].

A number of authors have considered laser heating of metals with temperature-dependent material properties (absorptivity, thermal conductivity, and volume heat capacity) [7–10]. Some researchers, in particular Brugger [11] and Maydan [12, 13], have solved the moving semi-infinite slab problem assuming that the intensity of the incident beam decays exponentially with distance into the material (internal absorption).

The problem is considerably more complicated when phase transition takes place. Cases studied include stationary or moving sources with a variety of source conditions. Soodak [14] was the first to address the problem of melting with complete removal of melt. He considered constant heating of the surface and numerically evaluated the steady-state melting rate. Landau [15] considered melting with complete removal of melt of a one-dimensional slab with one end subjected to time-varying heating and the other end insulated. Rogerson and Chayt [16] calculated the total melting time of a one-dimensional ablating slab subjected to constant heating (time and space) with complete removal of melt. Dabby and Paek [17], by considering laser penetration into the solid, solved for the temperature profile inside a stationary semi-infinite solid that is vaporizing on its free surface. Later von Allmen [18], by assuming reflection losses and vapor absorption to be negligible, considered drilling processes with material expulsion due to pressure gradients caused by evaporation; his theoretical results showed considerable agreement with experiments. A further complication of the problem arises if the irradiation source is moved across the surface (cutting rather than drilling). Gonsalves and Duley [19], by considering a uniform disk source and assuming no interaction between solid, melt, and vapor, found the melting isotherm for a given fraction of absorbed laser energy.

In the present work partial surface vaporization of a semi-infinite medium caused by a moving Gaussian laser irradiation (across the vaporization surface) is considered. Assuming relatively minor thermal losses due to convection, conduction, and radiation, a simple integral method is used for the evaluation of the temperature distribution. The relevant nonlinear partial differential equation is then solved numerically, and the results for the groove depth, width, and shape are presented for a variety of laser and solid parameters.

Theoretical Background

In order to obtain a realistic yet feasible description of the evaporation front on a moving solid irradiated by a concentrated laser beam, a number of simplifying assumptions will be made:

1 The solid moves at constant velocity u.

2 The solid is isotropic with constant properties, such as thermal conductivity k, specific heat c, and density ρ. Since, in cutting applications, conduction losses should be relatively small, temperature dependence of properties is expected to have only a minor effect on the results.

3 The material is opaque, i.e., the laser beam does not penetrate appreciably into the medium, with constant absorptivity (independent of direction and temperature). The assumption of opaqueness should be a good one for many solids: Absorption coefficients of several thousand cm^{-1} and beam radii of approximately 100 μm are common, resulting in total absorption within a zone which is a small fraction of the laser beam radius or the groove width. Assuming a constant absorptivity may not be very good. While easily relaxed this assumption is made here because little is known about the absorptivity behavior during evaporation.

4 Change of phase of the medium from solid to vapor occurs in one step at a single evaporation temperature T_{ev}. Real materials may show significantly different behavior, such as liquefaction followed by evaporation, decomposition into liquid and gas, gradual evaporation over a wide range of temperatures, outgassing followed by microexplosive removal of solid particles, etc. Assuming that the most important parameter is the total amount of energy required to remove material, the present model should do quite well. More accurate modeling would have to address specific materials.

Contributed by the Heat Transfer Division for publication in the JOURNAL OF HEAT TRANSFER. Manuscript received by the Heat Transfer Division May 7, 1985. Paper No. 85-HT-25.

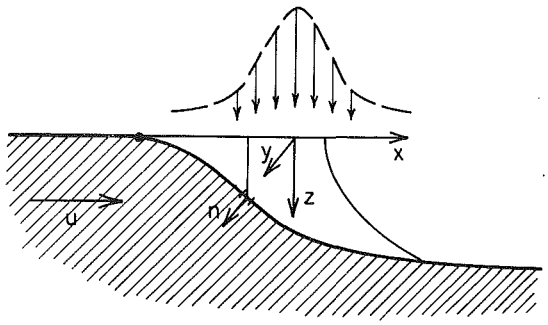

Fig. 1 Coordinate system for groove formation

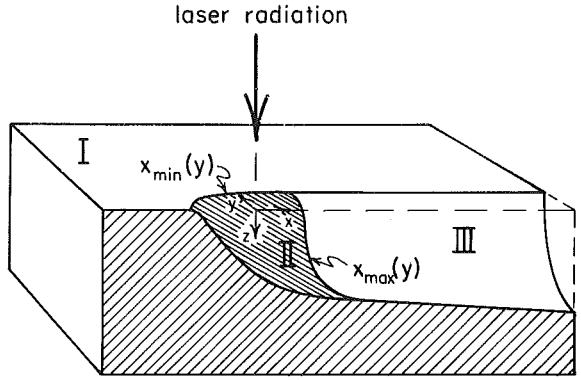

Fig. 2 Identification of different regions

5 The evaporated material does not interfere with the laser beam reaching the surface. This will be a good assumption if the material is evaporated completely (and the vapor has no absorption band at the laser wavelength), or if a strong jet assist is employed, which would blow particles out of the laser path.

6 Multiple reflections of laser radiation within the groove are neglected. This is a severe limitation which restricts the present model to materials with high absorptivities (even at grazing angles), e.g., if the evaporation surface is rough. This would most likely occur in nonhomogeneous materials with stepwise evaporation and/or microexplosive removal.

7 Heat losses to the outside can be approximated using a single, and constant, heat transfer coefficient for both convective and (linearized) radiative losses. Obviously, a constant heat transfer coefficient is very unrealistic. The assumption is made here to show that surface losses are nearly always negligible (e.g., Fig. 8).

Under the above conditions, the heat transfer problem is governed by (cf. Fig. 1)

$$\rho c u \frac{\partial T}{\partial x} = k \nabla^2 T \tag{1}$$

subject to the boundary conditions

$$x \to \pm\infty,\ y \to \pm\infty,\ z \to \infty:\ T \to T_\infty \tag{2}$$

The necessary boundary condition at the surface is obtained from an energy balance on a surface element on or away from the vaporization front (Fig. 1)

$$\alpha F_0 (\hat{n} \cdot \hat{k}) e^{-(x^2+y^2)/R^2} = h(T - T_\infty) - k(\hat{n} \cdot \nabla T) - \rho h_{ig} u (\hat{i} \cdot \hat{n}) \tag{3}$$

where $\hat{i}$ and $\hat{k}$ are unit vectors in the x and z directions, respectively, and $\hat{n}$ is the unit surface normal pointing into the medium. We distinguish between three different regimes on the surface of the medium (cf. Fig. 2): Regime I, the flat region, is that part of the surface that is still too far away to have reached evaporation temperature ($x << 0$), or too far away sideways to ever undergo evaporation ($y > y_{max}$, where y_{max} is the half-width of the final groove). In this regime $\hat{i} \cdot \hat{n} = 0$ so that the evaporation terms drops out of equation (3), and $\hat{n} = \hat{k}$, such that

$$\alpha F_0 e^{-(x^2+y^2)/R^2} = h(T - T_\infty) - k \frac{\partial T}{\partial z},\ x < x_{min}(y) \tag{3a}$$

Regime II, the evaporation zone, is that regime close to the laser center where evaporation takes place, i.e., where $\hat{i} \cdot \hat{n} < 0$. If the local depth of the groove is denoted by $s(x, y)$, the local surface normal may be evaluated in terms of s, and equation (3) becomes

$$\alpha F_0 e^{-(x^2+y^2)/R^2} = (h(T - T_\infty) - k\hat{n} \cdot \nabla T)\sqrt{1 + \left(\frac{\partial s}{\partial x}\right)^2 + \left(\frac{\partial s}{\partial y}\right)^2} + \rho h_{ig} u \frac{\partial s}{\partial x};$$

$$z = s(x, y),\ x_{min}(y) < x < x_{max}(y) \tag{3b}$$

For this regime equation (3b) is not really a boundary condition for equation (1), but rather the governing equation for the groove depth $s(x, y)$. The additional boundary condition needed for this regime is

$$T = T_{ev},\ z = s(x, y),\ x_{min}(y) < x < x_{min}(y) \tag{4}$$

Finally, Regime III, the established groove region, is that part of the surface where evaporation has taken place, but which has moved too far away from the laser beam, so that the surface temperature has dropped below T_{ev}. Here $\hat{i} \cdot \hat{n} = 0$ but $\hat{n} \cdot \hat{k} \neq 0$ and

$$\alpha F_0 e^{-(x^2+y^2)/R^2} = (h(T - T_\infty) - k\hat{n} \cdot \nabla T)\sqrt{1 + \left(\frac{\partial s_\infty}{\partial y}\right)^2};$$

$$z = s_\infty(y),\ x > x_{max}(y) \tag{3c}$$

where $s_\infty(y)$ is the depth of the fully established groove which is no longer a function of x.

Before attempting to solve the above set of equations, it is

Nomenclature

Bi = Biot number
c = specific heat
F_0 = laser flux at center of beam
h_{ig} = heat of sublimation
h = convective heat transfer coefficient
$\hat{i}, \hat{k}$ = unit vectors in x and z directions, respectively
k = thermal conductivity
$\hat{n}$ = unit vector normal to groove surface
N_e = evaporation-to-laser power parameter
N_k = conduction-to-laser power parameter
R = effective laser beam radius
s, S = groove depth
S_{max} = maximum groove depth
$S_\infty(\eta)$ = established groove cross section
T_{ev} = evaporation temperature
T_∞ = ambient temperature
u = laser scanning speed
U = laser speed-to-diffusion parameter
x, y, z = Cartesian coordinates
α = absorptivity
δ = thermal penetration depth
$\eta_{max}(\xi)$ = local half-width of the groove
θ = nondimensionalized temperature
θ_0 = nondimensionalized surface temperature
ξ, η, ζ = nondimensionalized x, y, z coordinates
ρ = density

advantageous to introduce a number of nondimensional variables and parameters, viz.

$$\xi = x/R,\ \eta = y/R,\ \zeta = z/R; \tag{5a}$$

$$S = s(x, y)/R,\ \theta = (T - T_\infty)/(T_{ev} - T_\infty); \tag{5b}$$

$$N_e = \frac{\rho u h_{ig}}{\alpha F_0},\ N_k = \frac{k(T_{ev} - T_\infty)}{R\alpha F_0},\ \mathrm{Bi} = \frac{hR}{k},\ U = \frac{\rho c u R}{k} \tag{5c}$$

Physically, N_e gives the ratio of power required to evaporate material normal to the irradiation, and absorbed laser flux. N_k approximates the ratio of conduction losses, again for a surface normal to irradiation, and absorbed laser flux. Finally, the Biot number indicates the ratio of convective-to-conductive losses, and U relates the speed of the medium to that of thermal diffusion into the medium. Note that a small N_e may mean large losses due to conduction and convection, or it may mean a very deep and steep groove. On the other hand, a small N_k does not ensure small conduction losses since, for a very steep groove, the ratio of conduction area to area normal to the laser becomes very large. Employing the definitions of equations (5), equations (1)–(4) may be rewritten as

$$U\frac{\partial\theta}{\partial\xi} = \frac{\partial^2\theta}{\partial\xi^2} + \frac{\partial^2\theta}{\partial\eta^2} + \frac{\partial\theta^2}{\partial\zeta^2};\ -\infty < \xi,\ \eta < +\infty,\ S \le \zeta < +\infty \tag{6}$$

subject to

$$\xi \to \pm\infty,\ \eta \to \pm\infty,\ \zeta \to +\infty:\ \theta \to 0 \tag{7}$$

and

$$\text{(I)}\ \zeta = 0:\ e^{-(\xi^2+\eta^2)} - N_k\left(\mathrm{Bi}\theta - \frac{\partial\theta}{\partial\zeta}\right) = 0;$$

$$-\infty < \xi < \xi_{\min}(\eta),\ -\infty < \eta < +\infty \tag{8a}$$

$$\text{(II)}\ \zeta = S(\xi, \eta):\ N_e\frac{\partial S}{\partial\xi} = e^{-(\xi^2+\eta^2)} - N_k\left(\mathrm{Bi} - \frac{\partial\theta}{\partial n}\right)\sqrt{1 + \left(\frac{\partial S}{\partial\xi}\right)^2 + \left(\frac{\partial S}{\partial\eta}\right)^2} \tag{8b}$$

$$\theta = 1;\ \xi_{\min}(\eta) \le \xi \le \xi_{\max}(\eta),\ -\eta_{\max} \le \eta \le +\eta_{\max} \tag{9}$$

$$\text{(III)}\ \zeta = S_\infty(\eta):\ e^{-(\xi^2+\eta^2)} - N_k\left(\mathrm{Bi}\theta - \frac{\partial\theta}{\partial\zeta}\right)\sqrt{1 + \left(\frac{\partial S}{\partial\eta}\right)^2} \tag{8c}$$

$$\xi_{\min}(\eta) < \xi < +\infty,\quad -\eta_{\max} \le \eta \le \eta_{\max}$$

Since for the vast majority of applications the depth, width, and general shape of the groove are desired, rather than accurate knowledge of the temperature field, and since N_k and, therefore, overall conduction losses are expected to be small, the emphasis of the solution will be given to the groove formation, i.e., to the solution of equation (8*b*). In order to solve equation (8*b*), it is necessary to find the boundaries of Regime II, i.e., $\xi_{\min}(\eta)$ and $\xi_{\max}(\eta)$, as well as the conduction loss $(-\partial\theta/\partial n)_{\zeta=S}$. The conduction loss will be estimated by making the following assumptions:

8 Since the temperature drop inside the medium will be strongest normal to the surface, the diffusion term may be replaced by one-dimensional diffusion in the normal direction, i.e., $\nabla^2\theta \simeq \partial^2\theta/\partial n^2$ where n is distance along the vector $\hat{n}$.

9 The conduction equation may be solved by the integral method, for which the temperature profile normal to the surface may be approximated by a quadratic polynomial, i.e., $\theta \simeq \theta_0\,[1 - n/\delta]^2$, where θ_0 is the nondimensional surface temperature, and δ is a penetration depth.

These simplifications have been shown to be accurate for many situations in a followup paper by the authors [20]. Thus one obtains for Regime I

$$\frac{\partial}{\partial\xi}(\theta_0\delta) = \frac{6\theta_0}{U\delta} \tag{10}$$

$$N_k\theta_0\left(\mathrm{Bi} + \frac{2}{\delta}\right) = e^{-(\xi^2+\eta^2)} \tag{11}$$

with $\theta_0(\xi \to -\infty) = 0$. These equations are valid up to $\xi = \xi_{\min}(\eta)$ where $\theta_0 = 1$ or, equivalently, where $\partial S/\partial\xi = \partial S/\partial\eta = 0$ in equation (8*b*).

In order to invoke assumption (7) for Regime II, i.e., when $\hat{n}$ is not parallel to $\hat{k}$, one may introduce a coordinate transformation $\xi = \xi,\ \eta = \eta,\ n = n(\xi, \eta, \zeta)$. Then

$$\frac{\partial\theta}{\partial\xi} = \frac{\partial\theta}{\partial\xi} + \frac{\partial\theta}{\partial n}\frac{\partial n}{\partial\xi} = \frac{\partial\theta}{\partial\xi} - \frac{\partial\theta}{\partial n}\frac{\partial S}{\partial\xi}\Bigg/\sqrt{1 + \left(\frac{\partial S}{\partial\xi}\right)^2 + \left(\frac{\partial S}{\partial\eta}\right)^2} \tag{12}$$

and, approximately,

$$\frac{\partial\theta}{\partial\xi} - \frac{\partial\theta}{\partial n}\frac{\partial S}{\partial\xi}\Bigg/\sqrt{1 + \left(\frac{\partial S}{\partial\xi}\right)^2 + \left(\frac{\partial S}{\partial\eta}\right)^2} \simeq \frac{1}{U}\frac{\partial^2\theta}{\partial n^2} \tag{13}$$

Thus, for Regime II

$$\frac{\partial\delta}{\partial\xi} = \frac{6}{U\delta} - \frac{3\partial S}{\partial\xi}\Bigg/\sqrt{1 + \left(\frac{\partial S}{\partial\xi}\right)^2 + \left(\frac{\partial S}{\partial\eta}\right)^2} \tag{14}$$

$$N_e\frac{\partial S}{\partial\xi} = e^{-(\xi^2+\eta^2)} - N_k\left(\mathrm{Bi} + \frac{2}{\delta}\right)\sqrt{1 + \left(\frac{\partial S}{\partial\xi}\right)^2 + \left(\frac{\partial S}{\partial\eta}\right)^2} \tag{15}$$

with $S = 0$ at $\xi = \xi_{\min}(\eta),\ -\eta_{\max} \le \eta \le \eta_{\max}$. Equation (12) holds also for regime III but with $\theta_0 \ne 1$. Thus

$$\frac{\partial}{\partial\xi}(\theta_0\delta) = \frac{6\theta_0}{U\delta} \tag{16}$$

$$N_k\theta_0\left(\mathrm{Bi} + \frac{2}{\delta}\right)\sqrt{1 + \left(\frac{\partial S}{\partial\eta}\right)^2} = e^{-(\xi^2+\eta^2)} \tag{17}$$

since $(\partial S/\partial\xi) = 0$ in this regime. The line of transition from Regime II to III, $\xi = \xi_{\max}(\eta)$, is determined from equations (14) and (15), viz., when S has reached its maximum value, or $\partial S/\partial\xi = 0$, since a negative $\partial S/\partial\xi$ would indicate negative evaporation.

Solution Approach

Despite the great simplifications introduced here, the problem requires the solution of two simultaneous nonlinear partial differential equations spanning three regimes, for which the separation lines need to be determined. While in general only the solution to Regime II is of interest, Regime I must be solved first in order to provide the boundary between I and II, $\xi_{\min}(\eta)$, and a beginning value for the conduction penetration depth $\delta(\xi_{\min})$.

The solution to Regime I is relatively easily found since equations (10) and (11) may be treated as first-order ordinary differential equations with η as parameter. Setting

$$\phi = N_k\mathrm{Bi}\theta_0 e^{\eta^2} \tag{18}$$

one gets

$$\frac{d\phi}{d\xi} = \frac{\frac{3\mathrm{Bi}^2}{2U}(e^{-\xi^2} - \phi)^3 - 2\xi e^{-\xi^2}\phi^2}{\phi(2e^{-\xi^2} - \phi)} \tag{19}$$

with $\phi(\xi \to -\infty) = 0$. Equation (19) is readily solved by a standard Runge–Kutta routine, except that the boundary condition is not easily applied (and may lead to the wrong

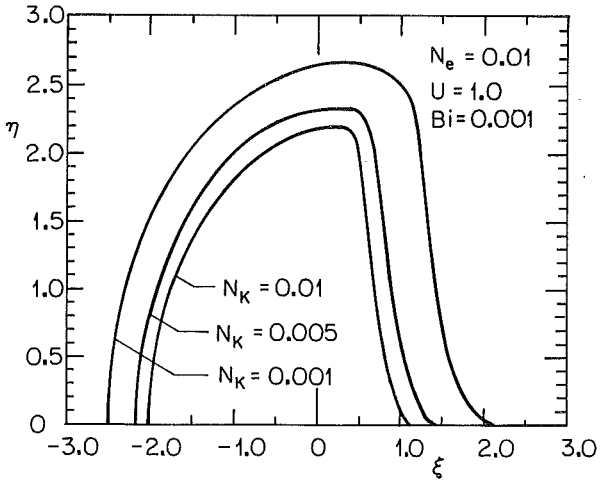

Fig. 3 Top view of evaporation region for different conduction-loss levels

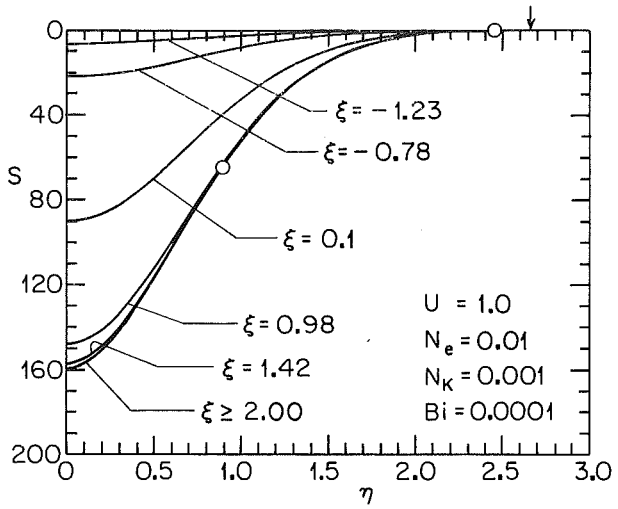

Fig. 4 Groove cross section at different ξ locations in evaporating region

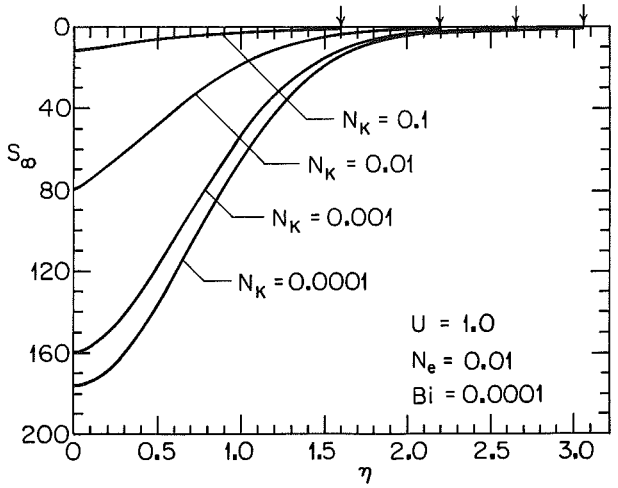

Fig. 5 Influence of conduction losses on groove depth and shape

parasitic solution $\phi = e^{-\xi^2}$). However, by careful examination of the limits one finds

$$\phi \to e^{-\xi^2} / \left(1 + \frac{2}{\mathrm{Bi}} \sqrt{-\frac{1}{3} U\xi}\right), \quad \xi << 0 \tag{20}$$

Then the Runge–Kutta solution may be started with some large negative ξ, say $\xi = -5$. In order to determine $\xi_{\min}(\eta)$ it is advantageous to invert equation (19) and solve for ξ as function of ϕ up to $\phi = N_k \mathrm{Bi} e^{\eta^2}$, i.e., to the point where $\theta_0 = 1$. Conversely, the local $\eta_{\max}(\xi)$ is found by integrating to the given ξ, so that $\eta_{\max}(\xi) = (\ln[\phi(\xi)/N_k \mathrm{Bi}])^{1/2}$. For some point $\xi > 0$ there is $d\phi/d\xi = 0$, indicating that the maximum groove width has been reached.

The determination of $S(\xi, \eta)$ requires the solution of equation (15), a nonlinear partial differential equation. This equation turns out to be very difficult to solve for all but the smallest values of N_k in a deep groove: $|\partial S/\partial \eta| >> 0$ for most values of η and $\xi > 0$, so that the nonlinear term dominates the equation. Since equation (15) is of first order it is hyperbolic in nature with a single set of characteristics. It is readily found that $\eta = 0$ is a characteristic line, and S may be discontinuous across that line. This is most easily seen by letting $N_e \to 0$ (zero laser velocity), for which equation (15) becomes

$$\left(\frac{\partial S}{\partial r}\right)^2 = e^{-2r^2}/N_k^2 \left(\mathrm{Bi} + \frac{2}{\delta}\right)^2 - 1, \quad r^2 = \xi^2 + \eta^2 \tag{21}$$

For this case, at steady-state conditions, the shaped surface will be steepest where laser flux is highest, in order to carry away the heat by convection and conduction, leading to a "trumpet-shaped" hole with a sharp apex at $r = \xi = \eta = 0$. For $N_e > 0$ one may expect a groove that resembles such a "trumpet shape" pushed through the medium. The groove described by equation (15) is most accurately solved by following characteristic lines from the boundary with Regime I until they intersect $\eta = 0$. This, however, causes problems because of the interrelationship with equation (14): Either interpolation is necessary if a rectangular grid is to be used for δ, or intersecting characteristics have to be used for the second-order equation resulting from combining equations (14) and (15); this in turn makes one lose control over nodal placement (it would also make it impossible to replace the present simple conduction model by a more sophisticated one should this prove desirable). Here we employed a simple explicit–implicit method which is unconditionally stable: In order to predict S and δ at a node (ξ_i, η_i), it is assumed that all S and δ are known for all nodes with $\xi < \xi_i$ and $\eta > \eta_i$. Therefore, the solution for a given ξ_i is started at $\eta = \eta_{\max}(\xi_i)$ (where $S = 0$ and δ has the value determined from the Regime I calculations), marching inward toward $\eta = 0$. To insure that the method converges to the correct solution, results were also obtained for constant conduction loss (δ = const) and compared with results found from the characteristics method.

Discussion of Results

Inspection of equation (3*c*) shows that in the absence of conduction losses, the evaporating region would be bounded by a semicircle for negative values of ξ, i.e., $\eta(\xi)$ will increase gradually for increasing ξ and reach its maximum value at $\xi = 0$. In the presence of conductive losses, $\eta_{\max}$ again increases to its maximum value not describing a semicircle, but rather an approximately elliptic shape (cf. Fig. 3); because of the diminishing conduction losses (increasing δ) along the periphery of the groove, the maximum width is attained at a ξ larger than zero. For larger positive values of ξ, $\eta_{\max}$ decreases sharply back to zero because the slope of the groove becomes so large that the conductive and convective heat losses use up most of the laser energy. However, evaporation still continues on a narrow strip along the ξ direction at small values of η, where the groove levels off somewhat.

Figure 4 shows how a typical groove develops along the ξ direction. For $\xi > 0.30$ (that location where the groove achieves its maximum width), no additional evaporation beyond a certain η will occur since that part of the groove has moved too far away from the laser center, i.e., the entire

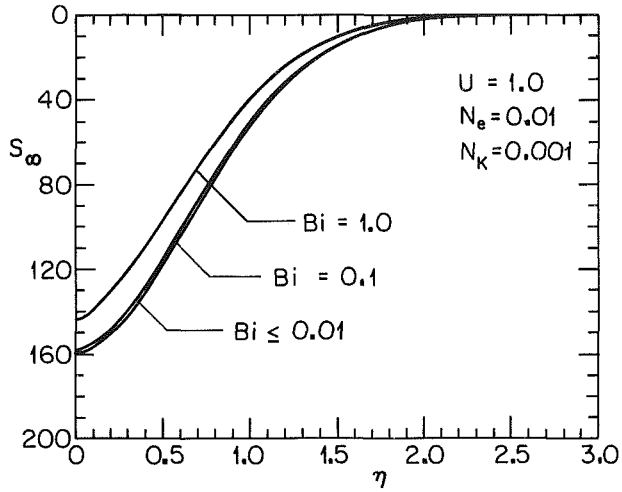

Fig. 6 Influence of convection losses on groove depth and shape

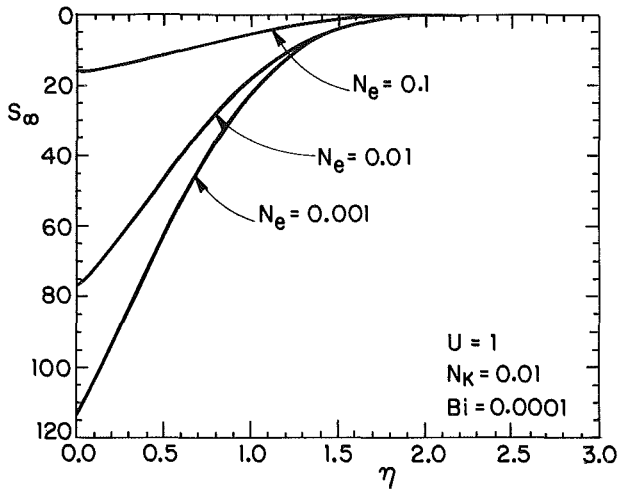

Fig. 7 Influence of latent heat-to-laser power N_e on groove depth and shape

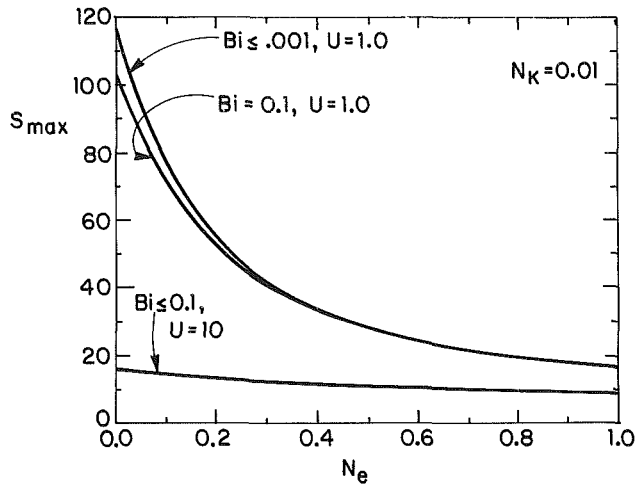

Fig. 8 Influence of scanning speed and convection losses on maximum groove depth

amount of local laser irradiation is lost to conduction and convection. For example, as depicted in Fig. 4, at $\xi = 0.98$ no more evaporation occurs beyond $\eta = 2.4$ (indicated by a circle). This point moves rapidly toward the center of the groove because of increasing heat losses (due to the steepness of the groove wall) and reaches $\eta = 0.9$ at $\xi = 1.42$ (cf. Fig. 3).

Changes in the groove shape and depth for different values of the conduction loss parameter N_k are shown in Fig. 5. For large values of N_k, the laser energy is mostly taken away by conductive losses (e.g., for $N_k = 0.1$, the groove has an average slope of about 10; thus nearly 100 percent of laser power is lost by conduction into the medium), explaining the shallow groove. Decreasing N_k will reduce conductive losses but this decrease will not be as rapid as the decrease in N_k, since, for a deep groove (small N_e), the ratio of the groove area to area normal to the laser beam becomes very small.

Figure 6 depicts the effect of convective losses on the groove shape and depth, which (for small conductive losses, $N_k \simeq 0.001$) are governed by the Biot number Bi. A large Biot number may be the result of a poorly focused beam, impinging on a poorly conducting medium with a high rate of blowing. This would produce a very shallow groove and is of no interest. A small Biot number, on the other hand, could occur with a focused beam, very little or no blowing over a highly conductive medium. In practical applications one may expect typical values for Bi of about 10^{-4} or less, and a maximum of about 0.1. Figure 6 shows that by taking Biot numbers of less than 0.1, no appreciable change in the groove occurs. This indicates that the effect of convection on groove shape is generally very small if not negligible.

The influence of the evaporation power-to-laser power parameter N_e on the groove shape and depth is shown in Fig. 7. Large values of N_e (i.e., $N_e \simeq 0.1$) generally mean shallow grooves and, therefore, relatively small heat losses (the ratio of groove surface to surface normal to the laser beam is relatively low due to the shallowness of the groove). A small N_e implies large laser power F_0, or a small heat of evaporation h_{ig}. Decreasing N_e will increase the groove depth and, because of the concurrent increase of groove surface area, conductive losses are increased even though N_k will remain unchanged.

Finally, Fig. 8 shows the effect of U (the ratio of laser scanning speed to that of heat diffusion into the medium) on the maximum groove depth S_{max}. By examining equation (16), one notices that for large values of U, the thermal penetration depth δ is small. This, in turn, increases the heat loss due to conduction and consequently the maximum groove depth is decreased. For such cases, convection losses are negligible even for relatively large Biot numbers, such as Bi = 0.1.

Summary

A fairly simple model has been developed to predict the shape of a groove formed by partially evaporating a semi-infinite body using a moving, Gaussian laser beam. The results clearly indicate that surface heat losses are nearly always negligible. It is seen that, for a Gaussian beam, the bottom of the groove may have a sharp apex. At this point the model is still fairly primitive, but it will be useful for predicting the ranges of values for which the nondimensional parameters N_e, N_k, and U will produce an efficient laser cut. The model will also be able to quantitatively predict groove depths accurately for a few idealized situations. For accurate quantitative results, however, a number of the simplifying assumptions need to be relaxed in future development, in particular assumptions (3) (constant absorptivity), (4) (evaporation mechanism), and (6) (beam guiding).

Acknowledgments

Support for this work under National Institute of Arthritis, Diabetes, Digestive and Kidney Diseases, Grant No. AM30240, is gratefully acknowledged.

References

1 Carslaw, H. S., and Jeager, J. C., *Conduction of Heat in Solids*, 2nd ed., Oxford University Press, 1959.

2 White, R. M., "Elastic Wave Generation by Electron Bombardment or Electromagnetic Wave Absorption," *Journal of Applied Physics*, Vol. 34, 1963, pp. 2123–2124.

3 White, R. M., "Generation of Elastic Waves by Transient Surface Heating," *Journal of Applied Physics*, Vol. 34, 1963, pp. 3559–3567.

4 Rykalin, N. N., Uglov, A. A., and Makarov, N. I., "Effects of Peak Frequency in a Laser Pulse on the Heating of Metal Sheets," *Soviet Physics—Doklady*, Vol. 12, 1967, pp. 644–646.

5 Paek, U.-C., and Gagliano, F. P., "Thermal Analysis of Laser Drilling Processes," *IEEE Journal of Quantum Electronics*, Vol. QE-8, 1972, pp. 112–119.

6 Ready, J. F., *Effects of High Power Laser Radiation*, Academic Press, New York, 1971.

7 Dobrovol'skii, I. P., and Uglov, A. A., "Analysis of the Heating of Solids by Laser Radiation Allowing for the Temperature Dependence of the Absorptivity," *Soviet Physics—Doklady*, Vol. 4, 1974, pp. 788–790.

8 Rykalin, N. N., Uglov, A. A., and Nizametdinov, M. M., "Calculation of the Heating of Materials by Laser Radiation Allowing for the Temperature Dependences of Thermal Properties," *Soviet Physics—Doklady*, Vol. 17, 1977, pp. 853–856.

9 Warren, R. E., and Sparks, M., "Laser Heating of a Slab Having Temperature-Dependent Surface Absorptance," *Journal of Applied Physics*, Vol. 50, 1979, pp. 7952–7957.

10 Rykalin, N. N., Uglov, A. A., and Smurov, I. Yu., "Nonlinearities of Laser Heating of Metals," *Soviet Physics—Doklady*, Vol. 27, 1982, pp. 970–972.

11 Brugger, K., "Exact Solutions for the Temperature Rise in a Laser Heated Slab," *Journal of Applied Physics*, Vol. 43, 1972, pp. 577–583.

12 Maydan, D., "Fast Modulator for Extraction of Internal Laser Power," *Journal of Applied Physics*, Vol. 41, 1970, pp. 1552–1559.

13 Maydan, D., "Micromachining and Image Recording on Thin Films by Laser Beams," *Bell System Technical Journal*, Vol. 50, 1971, pp. 1761–1789.

14 Soodak, H., "Effects of Heat Transfer Between Gases and Solids," Ph.D. Thesis, Duke University, Durham, NC, 1943.

15 Landau, H. G., "Heat Conduction in a Melting Solid," *Quarterly of Applied Mathematics*, Vol. 8, 1950, pp. 81–94.

16 Rogerson, J. E., and Chayt, G. A., "Total Melting Time in the Ablating Slab Problem," *Journal of Applied Physics*, Vol. 42, 1971, pp. 2711–2713.

17 Dabby, F. W., and Paek, U.-C., "High-Intensity Laser-Induced Vaporization and Explosion of Solid Material," *IEEE Journal of Quantum Electronics*, Vol. QE-8, 1972, pp. 106–111.

18 von Allmen, M., "Laser Drilling Velocity in Metals," *Journal of Applied Physics*, Vol. 47, 1976, pp. 5460–5463.

19 Gonsalves, J. N., and Duley, W. W., "Cutting Thin Metal Sheets With the CW CO_2 Laser," *Journal of Applied Physics*, Vol. 43, 1972, pp. 4684–4687.

20 Modest, M. F., and Abakians, H., "Heat Conduction in a Moving Semi-infinite Solid Subjected to Pulsed Laser Irradiation," ASME JOURNAL OF HEAT TRANSFER, this issue, pp. 597–601.

Radiative Transfer With Dependent Scattering by Particles: Part 1—Theoretical Investigation

J. D. Cartigny[1]
Graduate Student.

Y. Yamada[2]

C. L. Tien
Professor.
Fellow ASME

Department of Mechanical Engineering,
University of California,
Berkeley, CA 94720

Dependent radiation scattering for which the independent scattering theory fails to predict the scattering properties is important in analyzing radiative transfer in packed and fluidized beds. In this paper the dependent scattering properties have been derived assuming the Rayleigh–Debye scattering approximation for two cases: two identical spheres and a cloud of spherical particles. The two-sphere calculated results compare well with the exact solutions in the literature, giving confidence in the present analytical approach. The gas model and packed-sphere model have been employed to calculate dependent scattering properties for a cloud of particles of small and large particle volume fraction, respectively. The calculated dependent scattering efficiencies for a cloud of particles are smaller than the independent scattering efficiencies and decrease with increasing particle volume fraction. A regime map for independent and dependent scattering has been constructed and compared with existing empirical criteria.

Introduction

Chemical reactors, coal combustors, cryogenic insulation, and many other industrial systems often involve highly concentrated small particles in the form of packed and fluidized beds. In these small particle systems, scattering of radiant energy may play an important role, and the scattering properties are needed to formulate the radiative transfer.

It is well known that scattering by small spheres is well predicted by the Mie solution [1, 2] when a sphere is isolated or the distance between spheres in a cloud of particles is much greater than the particle diameter and the wavelength of the incident radiation. This means the interference between the scattering waves can be neglected. This condition can be described by the scattering of one isolated particle and is called independent single scattering. The intensity scattered by N identical particles is simply N times that from one isolated particle. When the distance between the particles in a cloud of particles is small compared with the particle dimension and wavelength, multiple scattering and the interference between the scattered waves cannot be neglected and the scattering is called dependent scattering.

Several experimental investigations [3–8] have been reported concerning the conditions that demarcate the dependent scattering regime from the independent scattering regime. In these papers, the particle volume fraction f_v, the ratio of center-to-center particle spacing to diameter δ/d, and the interparticle clearance measured in wavelength c/λ were suggested to be important parameters to characterize the limit of independent scattering. These criteria were obtained empirically, with limited experimental conditions for particle size parameter $x=\pi d/\lambda$ and particle volume fraction f_v. No theoretical work has been reported to determine the conditions under which dependent scattering would occur.

For the case of dependent scattering for two spheres, exact solutions of the Maxwell equations are available in the literature [9–12]. Jones [13] solved the case of dependent scattering by assemblies of particles and Purcell and Pennypacker [14] gave the results for agglomerates of about 100 particles. These studies, however, were accomplished by complicated time-consuming computations; they are neither adequate for obtaining the dependent scattering properties as functions of various parameters, nor for deriving generalized conditions for the demarcation of dependent scattering from independent scattering.

Phenomenologically, dependent scattering can be regarded as consisting of two effects: multiple scattering in which the scattered radiation by one particle is incident on another particle to be scattered again, and far-field interference between the waves scattered by the different particles with phase difference. In this work, only the latter effect of interference between the scattered waves is considered. By extending the concept of Rayleigh–Debye scattering, the dependent scattering properties will be obtained and the conditions for the delineation between dependent and independent scattering will be derived analytically by comparing the dependent scattering properties with the independent scattering properties.

Basic Formulation

Consider the far-field behavior of the waves scattered by small particles which are identical, uniform spheres homogeneously and isotropically distributed as shown in Fig. 1. The spheres are assumed to be nonabsorbing, and the following condition for Rayleigh–Debye scattering [1, 2] is satisfied:

$$2x(n-1)<<1 \tag{1}$$

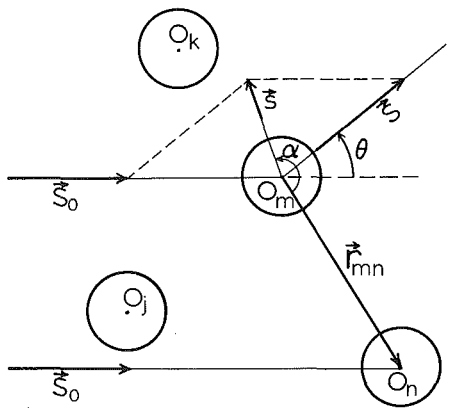

Fig. 1 A cloud of particles and definitions of vectors and angles

[1] Present address: Center of Energetics, Paris School of Mines, 60 Saint-Michael Blvd., 75006 Paris, France

[2] Visiting Scholar from Mechanical Engineering Laboratory, Agency of Industrial Science and Technology, Namiki 1-2, Tsukuba Science City, Ibaraki-ken, 305 Japan

Contributed by the Heat Transfer Division for publication in the JOURNAL OF HEAT TRANSFER. Manuscript received by the Heat Transfer Division January 2, 1985.

where n is the ratio of the refractive index of the particle to that of the matrix (both in vacuum). This condition, which is valid for a wide range of practical small-particle systems, allows one to neglect the effect of scattering by other particles on the incident wave as well as the scattered wave by each particle. Then all the particles have the same collimated incident radiation with the same intensity, and only the phase difference in the far field of the waves scattered by the different particles should be considered. Conventionally, the scatterers in Rayleigh–Debye scattering are the Rayleigh scatterers due to the additional condition of $x << 1$ [1, 2]. In this study the scattering properties of a single spherical particle are calculated by use of the Mie solution. In this sense, the approximation is called the extended Rayleigh–Debye scattering.

When N identical spheres with diameter d are distributed discretely with a particle volume fraction f_v, the phase difference Δ_{mn} between the wave scattered by the mth and nth scatterers, the centers of which are located at the positions O_m and O_n, respectively, as shown in Fig. 1, is expressed by [1, 2]

$$\Delta_{mn} = 2\pi \mathbf{r}_{mn}\mathbf{s} \tag{2}$$

where $\mathbf{r}_{mn}$ is the vector connecting the two points O_m and O_n, and $\mathbf{s}$ is the difference between the unit incident wave vector $\mathbf{S}_0$ and the unit scattered wave vector $\mathbf{S}$ in the direction θ, divided by the wavelength λ. Thus, $\mathbf{s} = (\mathbf{S} - \mathbf{S}_0)/\lambda$ and $s = |\mathbf{s}| = \sin(\theta/2)/\lambda$. Considering the phase difference of equation (2) and unpolarized incident radiation, the total intensity of the scattered radiation by N dependent identical spheres $I_D^{(N)}$ is described by

$$I_D^{(N)}(\theta) = NF(\theta) I_M(\theta) \tag{3}$$

where I_M is the intensity of Mie scattering for a single sphere and $F(\theta)$ is the form factor commonly used in x-ray optics [1, 15] and is given by

$$F(\theta) = \frac{1}{N} \sum_{m=1}^{N} \sum_{n=1}^{N} e^{-i\Delta_{mn}} \tag{4}$$

The double sum comes from the product of the amplitude and its complex conjugate to obtain the intensity after summing up all the amplitudes of the waves scattered by N particles. For independent scattering, the amplitudes of the scattered waves cannot be added, but the scattered intensities can, to give

$$I_I^{(N)}(\theta) = N I_M(\theta) \tag{5}$$

which means that the form factor $F(\theta)$ is unity.

The scattered intensity from a single sphere, given by the Mie solution $I_M(\theta)$, is expressed as follows by using Mie scattering efficiency Q_M and Mie scattering phase function $\phi_M(\theta)$

$$I_M(\theta) = Q_M \frac{\phi_M(\theta)}{4\pi} \frac{\pi a^2 I_0}{R^2} \tag{6}$$

where a is the radius of the sphere, I_0 the intensity of the incident beam, and R the distance from the center of the scattering sphere to the observer. The scattering efficiency is defined by

$$Q_M = \frac{\int_0^{4\pi} R^2 I_M(\theta) d\Omega}{\pi a^2 I_0} \tag{7}$$

where $d\Omega$ is the differential solid angle equal to $2\pi \sin\theta d\theta$. From equation (7), the dependent scattering efficiency $Q_D^{(N)}$ for N dependently scattering identical spheres can be defined as

$$Q_D^{(N)} = \frac{\int_0^{4\pi} R^2 I_D^{(N)}(\theta) d\Omega}{N\pi a^2 I_0} \tag{8}$$

where all N spheres have the same incident intensity I_0 according to the Rayleigh–Debye scattering approximation. Equations (3) and (6) reduce equation (8) to

$$Q_D^{(N)} = Q_M \int_0^{4\pi} F(\theta) \frac{\phi_M(\theta)}{4\pi} d\Omega \tag{9}$$

Similar to equation (6), there follows the dependent scattering phase function $\phi_D^{(N)}(\theta)$ for N particles

$$I_D^{(N)}(\theta) = Q_D^{(N)} \frac{\phi_D^{(N)}(\theta)}{4\pi} \frac{N\pi a^2 I_0}{R^2} \tag{10}$$

Combination of equations (3), (6), (9), and (10) gives

$$\phi_D^{(N)}(\theta) = \frac{Q_M}{Q_D^{(N)}} F(\theta) \phi_M(\theta) \tag{11}$$

An analytical expression for the dependent scattering efficiencies for smaller x, similar to the present study, was also given by Twersky [16]. Equations (9) and (11) describe the dependent scattering properties for N spheres assuming the extended Rayleigh–Debye scattering. Polarization effects neglected in the above analysis would be incorporated by considering the parallel and perpendicular components of scattered radiation separately.

Nomenclature

a = radius of sphere
C_D = floating constant less than unity
c = interparticle clearance
d = particle diameter
F = form factor
f_v = particle volume fraction
I = intensity of the scattered beam
I_0 = intensity of the incident beam
L = thickness of the scattering medium
N = number of particles
n = ratio of particle refractive index to that of the matrix (both in vacuum)
O_m = position of center of mth particle
Q = scattering efficiency
R = distance between scatterer and observer
r = coordinate for particle number density distribution
$\mathbf{r}_{mn}$ = vector connecting two position O_m and O_n
r_Q = ratio of dependent to independent scattering efficiences
$\mathbf{S}$ = unit vector in the direction of observation
$\mathbf{s}$ = vector defined as $(\mathbf{S} - \mathbf{S}_0)/\lambda$
s = absolute value of vector $\mathbf{s}$
x = particle size parameter $= \pi d/\lambda$
Y = $4y$
y = particle spacing parameter $= \pi\delta/\lambda$
α = angle between the vectors $\mathbf{s}$ and $\mathbf{r}_{mn}$
Δ = phase difference
δ = center-to-center particle spacing
θ = direction of observation
λ = wavelength measured in matrix
ρ = number density distribution function
τ = optical thickness
ϕ = scattering phase function
Ω = solid angle

Subscripts and Superscripts

0 = incident beam
a = average
B = backscattering
D, I = dependent, independent scattering
M = Mie solution
(N) = for N particles
R = Rayleigh scattering

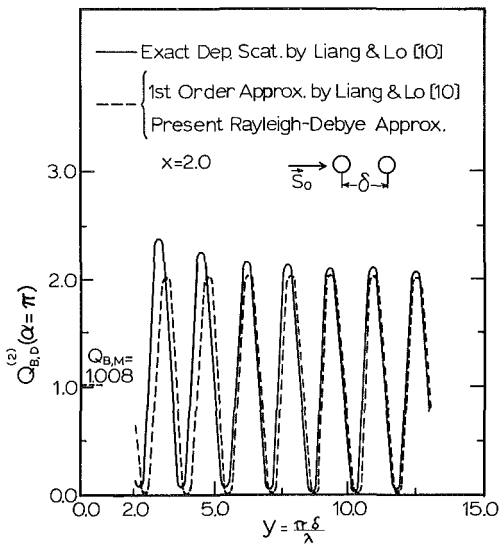

Fig. 2 Endfire backscattering efficiency for two spheres

Compared with equation (6), equation (10) can be regarded as describing the total intensity of the scattered waves by N independent spheres with the scattering efficiency of $Q_D^{(N)}$ and the phase function of $\phi_D^{(N)}(\theta)$. With this understanding, the dependent optical thickness of the scattering medium with thickness L containing N identical dependent scattering spheres with diameter d and volume fraction f_v can be expressed by [17]

$$\tau_D^{(N)} = 1.5 f_v Q_D^{(N)} L/d \tag{12}$$

The equation of transfer for a nonabsorbing scattering medium

$$\frac{dI}{d\tau} = -I + \frac{1}{4\pi}\int_0^{4\pi} I\phi(\theta)\,d\Omega \tag{13}$$

is applicable if the dependent optical thickness τ_D and the phase function $\phi_D(\theta)$ are employed. When solving the equation of radiative transfer in a dependently scattering medium, the near-field phase function may be preferable to the far-field phase function. However, obtaining the near-field phase function is far more difficult, and for engineering applications the far-field phase function gives satisfactory results for a dependently scattering medium. The problem of the equation of transfer for a scattering medium containing dependent scatterers will be studied in the following paper [24]. The following presents applications of the theoretical formulation to two specific problems: two spheres and a cloud of spherical particles.

Dependent Scattering by Two Identical Spheres

By setting $N=2$, the form factor $F(\theta)$ reduces to

$$F(\theta) = 1 + \cos\left(\frac{4\pi\delta}{\lambda}\cos\alpha\,\sin\frac{\theta}{2}\right) \tag{14}$$

where $\delta = r_{12}$ is the center-to-center particle spacing, and α is the angle between the two vectors $\mathbf{s}$ and $\mathbf{r}_{12}$. Substituting equation (14) into equations (9) and (11) gives $Q_D^{(2)}$ and $\phi_D^{(2)}(\theta)$, respectively. The problem of dependent scattering by two spheres was solved exactly for some cases [10–12]. Therefore, the results of this study assuming the extended Rayleigh–Debye scattering can be compared with these exact solutions to assess the validity of the present theoretical model.

Backscattering Efficiency. Backscattering efficiency for N spheres $Q_B^{(N)}$ can be defined by

$$Q_B^{(N)} = \frac{4\pi R^2 I^{(N)}(\theta=\pi)}{N\pi a^2 I_0} \tag{15}$$

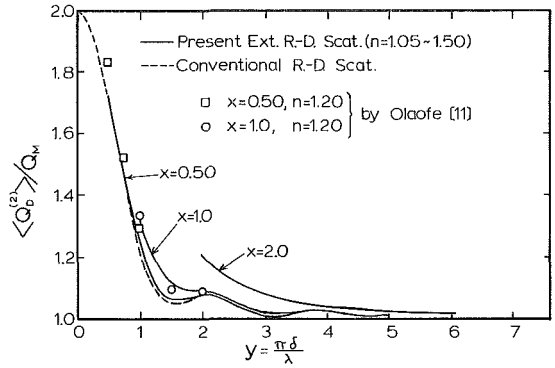

Fig. 3 Scattering efficiency for two spheres averaged over all incident angles

Following Liang and Lo [10], two cases of broadside incidence ($\alpha=\theta/2+\pi=3\pi/2$) and endfire incidence ($\alpha=\theta/2+\pi/2=\pi$) for perfect conductors are considered, and the dependent backscattering efficiencies $Q_{B,D}^{(2)}$ are related to the backscattering efficiency for single sphere $Q_{B,M}$ by

$$Q_{B,D}^{(2)}\left(\alpha=\frac{3}{2}\pi\right) = 2Q_{B,M} \tag{16}$$

$$Q_{B,D}^{(2)}\ (\alpha=\pi) = [1+\cos(4y)]Q_{B,M} \tag{17}$$

where $y=\pi\delta/\lambda$. For the perfect conductor with $x=2.0$, $Q_{B,M}$ is found to be 1.008 [19]. The result of equation (17) is compared with that of Liang and Lo in Fig. 2, which shows that equation (17) for endfire incidence agrees perfectly with their first-order approximation neglecting multiple scattering between two spheres. Equation (16) for broadside incidence is also identical with their first-order approximation for broadside incidence, although the curves are not shown here [20]. Equations (16) and (17) do not necessarily reflect their exact results, but the difference for endfire incidence is much smaller than that for broadside incidence.

Scattering Efficiency for Random Orientation of Two Spheres. Olaofe [11] gave the exact total scattering efficiencies averaged over incident angle α. When the direction of the line connecting two spheres is randomly oriented to the incident beam, the averaged scattering efficiency $\langle Q_D^{(2)}\rangle$ averaged over α is formulated as

$$\frac{\langle Q_D^{(2)}\rangle}{Q_M} = 1 + \frac{1}{4y}\int_0^{\pi}\phi_M(\theta)\,\sin\left(4y\,\sin\frac{\theta}{2}\right)\cos\frac{\theta}{2}d\theta \tag{18}$$

If the Rayleigh scattering phase function $\phi_R(\theta) = (3/4)(1+\cos^2\theta)$ is used as is usually done for Rayleigh–Debye scattering, equation (18) is easily integrated to yield

$$\frac{\langle Q_{D,R}^{(2)}\rangle}{Q_M} = 1 + \frac{3}{Y^2}\left[1 + \frac{4}{Y^2} + \frac{48}{Y^4} + \frac{4}{Y}\left(1 - \frac{12}{Y^2}\right)\sin Y - \left(1 - \frac{20}{Y^2} + \frac{48}{Y^4}\right)\cos Y\right] \tag{19}$$

where $Y=4y$. Figure 3 shows the curves calculated from equation (18) for the extended Rayleigh–Debye scattering for $x=0.5$, 1.0, and 2.0, the curve from equation (19) for the Rayleigh scattering limit, and the exact results of Olaofe [11]. The extended Rayleigh–Debye approximation gives better agreement with Olaofe's results than the conventional Rayleigh–Debye approximation.

Dependent Scattering by a Cloud of Particles

Dependent Scattering Properties. For a homogeneous and isotropic distribution of particles in a cloud of particles, the form factor is averaged over the angle α to give [15]

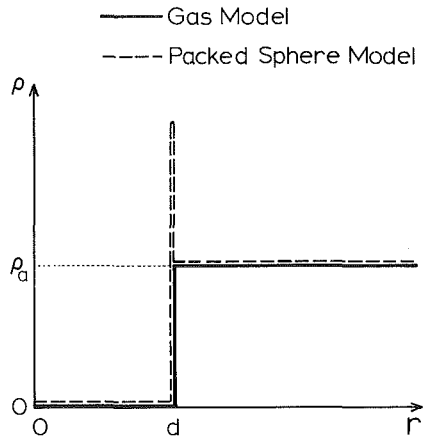

Fig. 4 Number density distribution for a cloud of particles

$$F(\theta)=\frac{1}{N}\sum_{m=1}^{N}\sum_{n=1}^{N}\frac{\sin(2\pi s r_{mn})}{2\pi s r_{mn}} \tag{20}$$

Under the assumption of a continuous and infinite distribution of the scatterers with the number density distribution of $\rho(r)$, the double sum in equation (20) can be replaced by an integral with respect to r, and is reduced to [15, 20]

$$F(\theta)=1+\int_0^{\infty}4\pi r^2[\rho(r)-\rho_a]\frac{\sin(2\pi s r)}{2\pi s r}dr \tag{21}$$

where ρ_a is the average number density.

Now, consider two models for $\rho(r)$ as shown in Fig. 4: the gas model following Debye [22], and the packed-sphere model following Gingrich, and Gingrich and Warren [21, 23]; more general expressions for $\rho(r)$ can be found in [26, 27]. In both models the other particles are prohibited to exist in the area $r<d$ $(\rho(r)=0)$, and the density is uniform with the average value for $r>d$ $(\rho(r)=\rho_a)$. The density at $r=d$ is given by

$$\lim_{\sigma\to 0}\rho(r=d-\sigma)=0,\quad \lim_{\sigma\to 0}\rho(r=d+\sigma)=\rho_a \tag{22a}$$

for the gas model, and

$$\lim_{\sigma\to 0}\int_{d-\sigma}^{d+\sigma}4\pi r^2\rho(r)dr=\left(1-\frac{3}{4\pi\sqrt{2}}\right)\frac{4}{3}\pi d^3\rho_a \tag{22b}$$

for the packed-sphere model. In the packed-sphere model some amount of mass is concentrated on the spherical shell with diameter d, which is the mass removed from the sphere within $r<d$ less one sphere at the center for face centered cubic arrangement. Using these two models, the form factors are calculated as

$$F(\theta)=1-8f_v G\left(4x\sin\frac{\theta}{2}\right) \tag{23a}$$

for the gas model, and

$$F(\theta)=1-8f_v\left[G\left(4x\sin\frac{\theta}{2}\right)-0.831\frac{\sin\left(4x\sin\frac{\theta}{2}\right)}{4x\sin\frac{\theta}{2}}\right] \tag{23b}$$

for the packed-sphere model, where

$$G(u)=\frac{3(\sin u-u\cos u)}{u^3},\quad f_v=\frac{4}{3}\pi\left(\frac{d}{2}\right)^3\rho_a$$

The gas model is applicable to the case of small f_v, and the packed-sphere model to that of large f_v.

For a few cases of large f_v and small θ, equation (23) gives negative values for $F(\theta)$, and this is corrected by setting $F(\theta)=0$. Figure 5 shows the dependent scattering efficiency Q_D (omitting superscript (N) for a cloud of particles) for both models with $n=1.21$ and $x=0.66$, 2.3, 5.9, and 9.9. Only the case with $x=0.66$ satisfies the condition of equation (1) for the Rayleigh–Debye approximation. The use of the above equations beyond the limit of the condition for that approximation will, of course, introduce errors in the results, but the calculated results are believed to give some insight to dependent scattering for the case of larger x. At $f_v=10^{-3}$, Q_D is identical with Q_M showing no dependent effect while Q_D decreases with increasing f_v. For $f_v<0.2$, the gas model gives smaller Q_D than the packed-sphere model does, and for $f_v>0.5$ with $x=2.3$, 5.9, and 9.9 the packed-sphere model gives smaller Q_D. In any case, Q_D becomes smaller and smaller with increasing f_v, thus indicating stronger dependent effect. This trend agrees with the existing experimental observations [7, 8, 24].

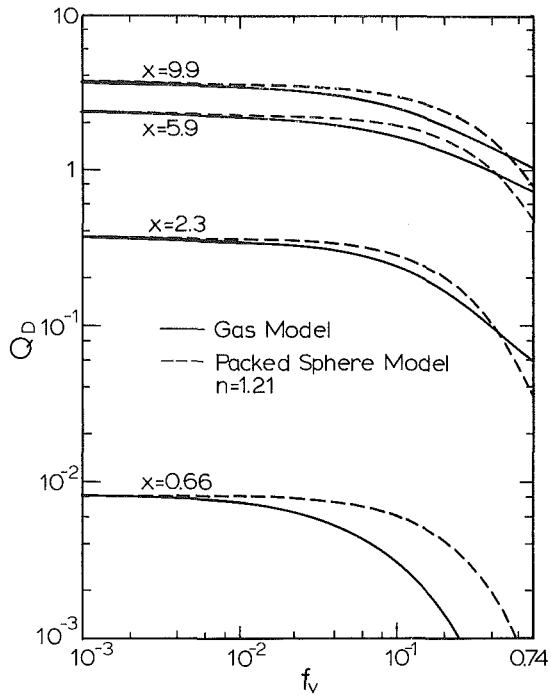

Fig. 5 Dependent scattering efficiency for a cloud of particles

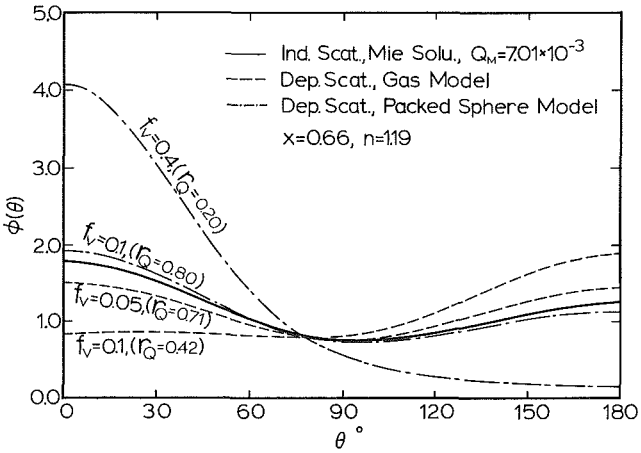

Fig. 6 Dependent scattering phase functions for a cloud of particles compared with independent scattering phase function

Figure 6 compares the dependent and independent phase function for $x=0.66$. In this case, the dependent phase function by the gas model shows stronger backward scattering than the independent Mie phase function, while the dependent phase function by the packed-sphere model shows slightly stronger forward scattering for the same particle volume fraction of $f_v=0.1$. The trend of the change given by the packed-sphere model is opposite to that by the gas model. It is difficult to tell which trend is correct without any experimental data for the phase function, although it should be noted that

the packed-sphere model does not necessarily reflect the real dependent effect for $f_v = 0.1$.

By using Rayleigh scattering phase function for $x << 1$, the dependent scattering efficiency is given by the following equation as a function of x by making use of the approximation of $G(u) \approx 1 - (u^2/10)$ and $\sin u/u \approx 1 - (u^2/6)$

$$\frac{Q_{D,R}}{Q_M} = 1 - 8f_v(1 - 0.8x^2) \quad \text{(gas model)} \tag{24a}$$

$$\frac{Q_{D,R}}{Q_M} = 1 - 8f_v(0.169 - 0.308x^2) \quad \text{(packed-sphere model)} \tag{24b}$$

The proposed model is useful for $x < 1$ and $f_v < 0.1$. A more general but also more complicated model for the number density function would extend the limit to larger f_v. One example is the solution to the Percus–Yevick integral equation satisfied by the pair distribution function [26, 27]. The limitation on x would not be improved by using a more general model as long as the Rayleigh–Debye approximation is employed.

Domain of Dependent Scattering. Brewster and Tien [8] reported that the dependent scattering domain is characterized by the condition $c/\lambda < 0.3$, while Hottel et al. [7] reported $c/\lambda < 0.5$ for $f_v < 0.3$. These criteria were obtained experimentally from their limited experimental data. Therefore, the criteria have not been verified in the areas of very small and very large x because of lack of experimental data in those areas. This study considers the demarcation of dependent scattering from independent scattering by making use of the dependent scattering efficiency for a cloud of particles Q_D. The basic idea for the criterion adopted here is that dependent scattering begins to be noticeable when Q_D becomes smaller than Q_M by some percentage. Therefore, for the case of small x which gives Q_M smaller than one, dependent scattering would occur when the ratio $r_Q = Q_D/Q_M$ is smaller than some constant less than but close to one.

In multiple scatter and dependent scatter environments when x is large enough for Q_M to exceed unity, due to either Fraunhofer or anomalous diffraction [1, 2], it is not only convenient but also desirable to eliminate the diffraction component when one tries to solve the equation of transfer to calculate the scattered intensity from a bolus of scatterers. The extremely large values of the exact phase function in the forward direction will cause erroneous results in the numerical solution of the equation of transfer if not removed. This is justifiable since the diffraction contribution to scattering is concentrated in the forward direction and can be treated as transmitted or unscattered radiation. Removal of diffraction from the scattering pattern is not at all straightforward in the case of anomalous diffraction but in the limit of very large phase shift, $2x(n-1)$, diffraction accounts for exactly half the total extinction of two, and thus $Q_M = 1$. For the purposes of this work the assumption $Q_M = 1$ was made for any Q_M calculated to be greater than one.

The following summarizes the criterion by use of floating constant C_D ($C_D < 1$)

$$r_Q = Q_D/Q_M < C_D \text{ for } Q_M < 1 \tag{25a}$$

and

$$Q_D < C_D \text{ for } Q_M > 1 \tag{25b}$$

Dependent scattering affects not only scattering efficiencies but also phase functions as shown in Fig. 6. However, the change of phase function appears to give little change in bidirectional transmittance and reflectance from a scattering medium [7, 24]. From an engineering point of view the change of phase function is ignored in the criterion for dependent scattering, although it is important in optics; a study is in progress.

Figure 7 shows the curves which demarcate the dependent scattering regime from the independent scattering regime for

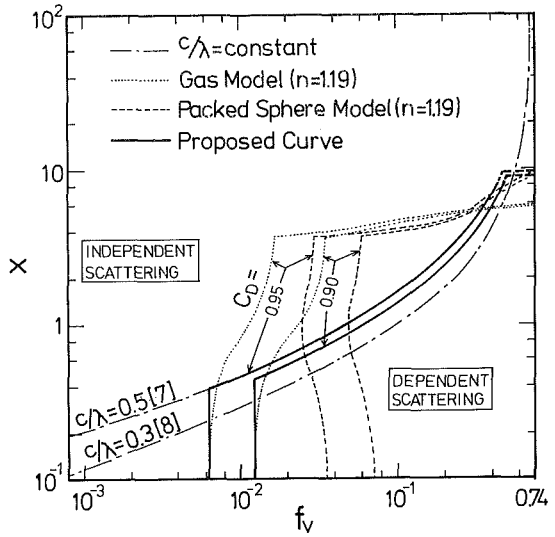

Fig. 7 Dependent and independent scattering regimes: x versus f_v

two values of $C_D = 0.95$ and 0.9, since it is not known what value of C_D clearly divides the two regimes and indeed the transition from one regime to the other should be somewhat gradual.

The discontinuities in the curves given by the gas model and the packed sphere model come from the change of criterion at $Q_M = 1.0$. The gas model applies at small f_v and the packed-sphere model at somewhat larger f_v. The packed-sphere model is not expected to describe the correct behavior of dependent scattering for x larger than unity, because the Rayleigh–Debye approximation holds only for small x. Figure 7 also includes curves of $c/\lambda = 0.5$ ($f_v < 0.3$) and $c/\lambda = 0.3$, the criteria previously suggested [7, 8]. The present curves are somewhat different from those in [7, 8]. The curves can be discussed in three different regions: small, intermediate, and large x.

1 Small x ($x < 0.5$). The vertical lines given by the present analysis are considered to be valid since the Rayleigh–Debye approximation is applicable for small x. The previously suggested criteria $c/\lambda = 0.5$ or 0.3 are merely the extension of the experimental results at intermediate x to small x where no experimental evidence is available.

2 Intermediate x ($0.5 < x < 10$). The present results are incorrect in this region, since the Rayleigh–Debye approximation is not applicable throughout. There are sufficient experimental data in this region [7, 8, 24]. $c/\lambda = 0.5$ corresponds to $C_D = 0.95$ and $c/\lambda = 0.3$ to $C_D = 0.90$, according to the correlation for Q_D/Q_M given by Hottel et al. [7].

3 Large x ($x > 10$). The Rayleigh–Debye approximation is not applicable in this region, but there is presently no established analysis and only limited experimental data are available. Among the publications, the experimental data of bidirectional transmittance and reflectance from slabs of scattering media with $x = 14$ to 79 and $f_v = 0.7$ [8, 24] agreed well with the numerical results of independent scattering, showing no observable dependent effects. On the other hand, Ishimaru and Kuga [25] experimentally determined that Q_D/Q_M for $x = 14$ to 83 increases slightly with increasing f_v, indicating Q_D is larger than two. In the case of multiple scattering by a slab, typical of many engineering applications, Q_D is set to unity in the course of solving the equation of transfer to calculate bidirectional properties as stated before. A slight increase in Q_D/Q_M with increasing f_v does not appear to affect the experimental and analytical results of bidirectional transmit-

tance and reflectance obtained in [8, 24], and therefore the results of these studies do not contradict those of [25]. The curves obtained by the present Rayleigh–Debye approximation are close to the demarcation curve given by the experimental results of [8, 24]. Horizontal broken lines are drawn in Fig. 7 near $x=10$ indicating the tenuous nature of this result. Clearly this result is controversial and requires further experimental evidence and refined analysis.

The above discussion leads to the following proposed demarcation curves using the floating constant C_D.

For $x<x_a$: $$f_v \geq (1-C_D)/8$$

For $x_a<x<10C_D$:

$$f_v > 0.741/[1+(0.502-0.356\ln(-\ln\ C_D))/x]^3 \tag{26}$$

For $x>10C_D$: no observable dependent effect

where $x_a=[0.502-0.356\ln(-\ln\ C_D)]/[1.81/(1-C_D)^{1/3}-1]$. The whole curve consists of a vertical line, a curve with constant c/λ and a horizontal line in the plot of x versus f_v. The demarcation curves for $C_D=0.95$ and 0.90 are shown in Fig. 7 by solid lines. For $x_a<x<10C_D$, Hottel's empirical correlation [7] has been used

$$\log_{10}\log_{10}(Q_M/Q_D)=0.25-3.83(c/\lambda) \tag{27}$$

For $x>10C_D$, no dependent scattering would be observed, although the value of $10C_D$ is somewhat arbitrary because the Rayleigh–Debye approximation is not valid for large x. More rigorous analysis, which would be most formidable indeed, may be able to determine the exact shape of the demarcation curve.

Conclusions

The dependent scattering properties have been derived by the extended Rayleigh–Debye scattering approximation and have been calculated for the problems of two spheres and of a cloud of spherical particles. For the two-sphere problem, the calculated dependent scattering efficiencies compare reasonably well with the existing exact results. For a cloud of particles, two number-density distribution models for small and large particle volume fraction have given the dependent scattering properties. Dependent scattering efficiencies, for particle size parameter small enough for the Rayleigh–Debye approximation to apply, have been shown to be less than the corresponding independent efficiencies. The dependent scattering regime for small size parameter has been determined analytically by comparing the dependent and independent scattering efficiencies. A new dependent scattering regime map has been proposed. It covers a wide range of particle size parameter and volume fraction and is based on both the present analysis and the existing experimental results, although there is still uncertainty at large particle size parameter ($x>10$).

References

1 van de Hulst, H. C., *Light Scattering by Small Particles*, Wiley, New York, 1957.

2 Kerker, M., *The Scattering of Light and Other Electromagnetic Radiation*, Academic Press, New York, 1969.

3 Churchill, S. W., Clark, G. C., and Sliepcevich, C. M., "Light Scattering by Very Dense Monodispersions of Latex Particles," *Discussions of the Faraday Society*, Vol. 30, 1960, pp. 192–197.

4 Hardin, R. H., Golding, B., and Morgen, R. A., "Optics of Light Scattering Films. Study of Effects of Pigment Size and Concentration," *Journal of Optical Society of America*, Vol. 50, 1960, pp. 446–455.

5 Blevin, W. R., and Brown, W. J., "Effects of Particle Separation on the Reflectance of the Semi-infinite Diffusers," *Journal of Optical Society of America*, Vol. 51, 1961, pp. 129–134.

6 Granatstein, V. L., Rhinewine, M., Levine, A. M., Feinstein, D. L., Mazurowski, M. J., and Piech, K. R., "Multiple Scattering of Laser Light From a Turbid Medium," *Applied Optics*, Vol. 11, 1972, pp. 1217–1224.

7 Hottel, H. C., Sarofim, A. F., Dalzell, W. H., and Vasalos, I. A., "Optical Properties of Coatings. Effect of Pigment Concentration," *AIAA Journal*, Vol. 9, 1971, pp. 1895–1898.

8 Brewster, M. Q., and Tien, C. L., "Radiative Transfer in Packed Fluidized Beds: Dependent Versus Independent Scattering," ASME JOURNAL OF HEAT TRANSFER, Vol. 104, 1982, pp. 573–579.

9 Trinks, W., "Zur Vielfachstreuung an Kleinen Kugeln," *Annalen der Physik*, Vol. 22, 1935, pp. 561–590.

10 Liang, C., and Lo, Y. T., "Scattering by Two Spheres," *Radio Science*, Vol. 2 (New Series), 1967, pp. 1481–1495.

11 Olaofe, G. O., "Scattering Cross-Section for Two Spheres," *Quarterly Journal of Mechanics and Applied Mathematics*, Vol. 27, 1974, pp. 403–422.

12 Hunka, J. F., and Mei, K. K., "Electromagnetic Scattering by Two Bodies of Revolution," *Electromagnetics*, Vol. 1, 1981, pp. 329–347.

13 Jones, A. R., "Electromagnetic Wave Scattering by Assemblies of Particles in the Rayleigh Approximation," *Proc. R. Soc. Lond.*, Vol. A.366, 1979, pp. 111–127.

14 Purcell, E. M., and Pennypacker, C. R., "Scattering and Absorption of Light by Nonspherical Dielectric Grains," *The Astrophysical Journal*, Vol. 186, 1973, pp. 705–714.

15 Guinier, A., *X-Ray Diffraction in Crystals, Imperfect Crystals, and Amorphous Bodies*, Freeman, San Francisco, 1963.

16 Twersky, V., "Coherent Scalar Field in Pair-Correlated Random Distributions of Aligned Scatterers," *J. Math. Phys.*, Vol. 18, 1977, pp. 2468–2486.

17 Siegel, R., and Howell, J. R., *Thermal Radiation Heat Transfer*, McGraw-Hill, New York, 1972.

18 Chandrasekhar, S., *Radiative Transfer*, Dover, New York, 1960.

19 Adler, S. B., and Johnson, R. S., "New Backscattering Computation and Tables for Dielectric and Metal Spheres," *Applied Optics*, Vol. 1, 1962, pp. 655–660.

20 Cartigny, J. D., "Radiative Transfer With Dependent Scattering of Particles," Ph.D. Dissertation, University of California, Berkeley, CA, 1984.

21 Gingrich, N. S., "The Diffractions of X-Rays by Liquid Elements," *Review of Modern Physics*, Vol. 15, 1943, pp. 90–110.

22 Debye, P., "Uber die Zerstreuung von Roentgensstrahlen an Amorphen Korpern," *Physikalische Zeitschrift*, Vol. 28, 1927, pp. 135–141.

23 Gingrich, N. S., and Warren, B. E., "The Interpretation of X-Ray Diffraction Patterns of a Fluid at Various Densities," *Physical Review*, Vol. 46, 1934, pp. 248–251.

24 Yamada, Y., Cartigny, J. D., and Tien, C. L., "Radiative Transfer With Dependent Scattering by Particles: Part 2–Experimental Investigation," ASME JOURNAL OF HEAT TRANSFER, this issue.

25 Ishimaru, A., and Kuga, Y., "Attenuation Constant of a Coherent Field in a Dense Distribution of Particles," *J. Opt. Soc. Am.*, Vol. 72, 1982, pp. 1317–1320.

26 Wertheimer, M. S., "Exact Solution of the Percus–Yevick Integral Equation for Hard Spheres," *Phys. Rev. Lett.*, Vol. 10, 1963, pp. 321–323.

27 Tsang, L., Kong, J. A., and Habashy, T., "Multiple Scattering of Acoustic Waves by Random Distribution of Discrete Spherical Scatterers With the Quasicrystalline and Percus–Yevick Approximation," *J. Acoust. Soc. Am.*, Vol. 71, 1982, pp. 552–558.

Radiative Transfer With Dependent Scattering by Particles: Part 2—Experimental Investigation

Y. Yamada
Visiting Scholar.

J. D. Cartigny
Graduate Student.

C. L. Tien
Professor.
Fellow ASME

Department of Mechanical Engineering,
University of California,
Berkeley, CA 94720

Dependent radiative scattering by particles is experimentally investigated using plane-parallel cells containing latex spheres of 11, 2, and 0.08 μm diameter dispersed in an air or water matrix. The dependent scattering efficiencies and the bidirectional transmittance and reflectance were measured and compared with analytical results. The close-packed 2-μm spheres, which were expected to show dependent scattering from the previous criterion, gave results identical to independent scattering. Measured dependent scattering efficiencies of the small particles tested decrease with increasing particle volume fraction and were compared with those predicted by the theoretical investigation. The bidirectional transmittance and reflectance of dependent scattering were compared with those of independent scattering with the same number of spheres within the test cells. Several different patterns of dependent transmittance and reflectance appeared depending on the optical thickness. Finally, a newly proposed regime map bounding independent and dependent scattering is compared with the present and previous experimental data.

Introduction

It has been mentioned previously [1, 2] that dependent scattering would appear when particles are packed close enough to each other. The theoretical investigation [2] enables analytical calculations of the dependent scattering properties for small spheres using the extended Rayleigh–Debye scattering approximation which assumes either a gas model or a packed-sphere model for the particle number-density distribution. The dependent scattering efficiencies and the dependent phase functions have been obtained as functions of particle volume fraction f_v and the Mie solution for independent scattering. The predicted dependent scattering efficiencies are consistently smaller than the independent scattering efficiency, and decrease with increasing f_v. In addition, the theoretical investigation has established the conditions that demarcate the dependent scattering regime from the independent on the plot of particle size parameter $x = \pi d/\lambda$ versus f_v. The proposed curve has different features from those suggested previously [1, 3].

The purpose of this experimental study is to obtain more dependent scattering data in addition to the previous works and to assess the validity of the dependent scattering properties and demarcation curve given by the theoretical investigation. Plane-parallel (slab) test cells were used to measure the scattering efficiencies and bidirectional transmittance and reflectance. The measured data were compared with the predicted results which were numerically calculated by integration of the equation of transfer. The effect of optical thickness on the appearance of dependent scattering bidirectional transmittance and reflectance has also been investigated. The newly proposed regime map for independent and dependent scattering [2] is shown to have the support of the present and previous experimental data.

Experiment and Data Reduction

Experimental Apparatus. The experimental apparatus was almost the same as that used by Brewster and Tien [1], and consisted of a laser, collimating lenses, a mirror, aperture stops, a test cell, attenuating filters, a photomultiplier, and a rotatable optical rail. The lasers used were Spectra-Physics type 155 He–Ne giving a randomly polarized 0.6328-μm beam and Liconix model 4050 He–Cd giving a linearly polarized 0.4416-μm beam. The 0.95-mW He–Ne laser was used for the 0.080-μm spheres, and the 45-mW He–Cd laser for the 2-μm and 11-μm spheres. Since the state of polarization of the incident beam has been shown to be unimportant by previous investigations [1, 3, 4] it was given little attention in the present study. The laser beam was first expanded and recollimated through a combination of convex lenses. Aperture stops were used so that only the central part of the recollimated beam was incident on the test cell to eliminate the Gaussian intensity distribution of the original laser beam. The consequent diameter of the incident beam was about 2 mm. The acceptance angle of the detector was about 0.33 deg, which was small enough to measure extinction for even the largest spheres according to Bohren and Huffman [10].

The spectrophotometer plane-parallel cells supplied by N.S.G. Precision Cells Inc. were used as the test cells. The type 20H quartz cells had about 1 cm × 5 cm cross-sectional area with 0.1, 0.5, 1.0, 5.0, and 10.0-mm thicknesses. The sides of the cells were painted black to eliminate the error caused by scattered radiation to the lateral directions.

Three kinds of nonabsorbing latex spheres manufactured by Dow Chemical Company were used as the scattering media, including polydivinylbenzene spheres with 11.15-μm diameter measured by Brewster and Tien [1], polyvinyltoluene spheres with 2.02-μm diameter measured by manufacturer, and polystyrene spheres with 0.080-μm diameter measured by the authors. The accuracy of the diameters of the larger spheres, 11 and 2-μm diameters, are unimportant for the comparison of the experimental data with the numerically calculated results since those spheres are large enough to show Fraunhofer diffraction giving a scattering efficiency near two. The accuracy of the small sphere diameter, 0.080 μm, affects the calculated results significantly because the scattering efficiency is proportional to the fourth power of the particle size parameter x in that range. The large discrepancy between the particle diameter measured in this work and that given by the manufacturer will be discussed in the following subsection.

Each sphere type was provided as an aqueous solution with the particle volume fraction $f_v = 0.1$. The large spheres with 11 and 2-μm diameters were closely packed in an air matrix by evaporation. The 0.080-μm sphere was used in water matrix

Contributed by the Heat Transfer Division for publication in the JOURNAL OF HEAT TRANSFER. Manuscript received by the Heat Transfer Division January 2, 1985.

with an f_v from 10^{-3} to 0.18 given by dilution with water or by evaporation, as required. The water used for dilution was double distilled and was filtered by Millipore Corporation GS filter to remove dusts.

A side-on type photomultiplier, RCA 1P28, and a Domer type photomultiplier, RCA 4526A, were used to detect the intensity of the beams.

Reduction of Data. The bidirectional transmittance T and reflectance R were calculated by the following equation

$$T(\theta), R(\theta) = \pi I(\theta)/I_0 \tag{1}$$

where I_0 is the intensity of the incident beam and $I(\theta)$ is the intensity of the scattered beam in the direction of angle θ from the incident.

The energy balance between the incident and the scattered beams is expressed by

$$1 = T_u + R_u + [T] + [R] \tag{2}$$

$$T_u = \frac{(1-\rho_0)^2 e^{-\tau}}{1-\rho_0^2 e^{-2\tau}}, \quad R_u = \rho_0(1 + T_u e^{-\tau}) \tag{3}$$

$$[T] = 2\int_0^1 T(\mu)\mu\, d\mu, \quad [R] = 2\int_0^{-1} R(\mu)\mu\, d\mu,$$

$$\mu = \cos\theta \tag{4}$$

where unity on the left-hand side of equation (2) represents the incident energy, T_u and R_u are the directly transmitted and reflected energy considering the reflection at the surfaces of the glass cell, and $[T]$ and $[R]$ are the integrated transmittance and reflectance, respectively. The reflectance of the normally incident beam on the glass cell ρ_0 is obtained as

$$\rho_0 = (\rho_1 + \rho_2 - 2\rho_1\rho_2)/(1 - \rho_1\rho_2) \tag{5}$$

where ρ_1 and ρ_2 are the interface reflectance between air and the glass cell, and that between the glass cell and the matrix, which are easily given by the Fresnel equations using the refractive indices of glass and water. The refractive index of the glass cell n_g was given as 1.55 and n_w is 1.332 for 0.6328 μm and 1.337 for 0.442 μm.

The optical thickness τ of the sample is calculated by

$$\tau = 1.5 Q f_v L/d \tag{6}$$

where Q is the scattering efficiency and L is the thickness of the test cell.

The values of the right-hand side of equation (2) were obtained from measurements of $[T]$, $[R]$, and T_u, since R_u was estimated from the measured T_u which gave the optical thickness τ with ρ_0 given. Because of scattering to the lateral directions, the right-hand side of equation (2) was measured to be less than unity. This was especially true when the cell thickness was large. Therefore, the measured $T(\theta)$ and $R(\theta)$ were corrected to give a good energy balance by compensating for the escape of the scattered energy to the lateral directions.

From equations (3) and (6), the measurement of T_u gave the value Q/d. Then, if scattering is independent with small f_v, Q can be calculated by the Mie solution as a function of d, the wavelength, and the refractive indices of the sphere and matrix. Thus we were able to determine the sphere diameter from the transmission measurement. The refractive index of the latex sphere is given in the literature [5] as 1.588 at 0.6328 μm and 1.615 at 0.4416 μm. The diameter of the small sphere, which was given as 0.091 μm with a standard deviation of 0.0058 μm by the manufacturer, was measured as 0.080 μm with an uncertainty of 0.001 μm using the Mie solution for $f_v = 10^{-3}$ which is considered to be within the independent scattering regime. The difference was as much as about 12 percent, so the existence of aggregates of the spheres was suspected [6]. In order to remove the aggregates both centrifuging and filtering were tried. Neither centrifuging nor filtering by Nuclepore Inc. 0.1-μm pore filter had considerable effect on the diameter although a slight increase in the diameter was observed after filtering. The diameter of 0.091 μm was reportedly measured by transmission electron microscopy [7]. This technique is sophisticated but has a tendency to overestimate the diameter due to the required coating procedures. Therefore 0.080 μm was used as the diameter of the small spheres for the numerical calculations to be compared with the experimental data.

By the same transmission measurement of T_u, the dependent scattering efficiencies Q_D were calculated and compared with the results of the theoretical investigation.

No attempt was made to determine the diameters of the large spheres with 2 and 11-μm diameter, because it was difficult to keep large particles distributed homogeneously in a water matrix for a sufficient time to measure transmission accurately. The large spheres settle to make sediment so rapidly that the particle volume fraction varied during measurement. Ishimaru and Kuga [8] employed the same technique, but their results showed some uncertainties concerning the measured diameters of 2.02 and 11.9-μm spheres. They also measured the diameter of the 0.091-μm sphere as 0.080 μm which is exactly the same as reported herein, showing the validity of the present technique. Independent scattering efficiencies are necessary in the calculation of bidirectional transmittance and reflectance to be compared with experimental measurements. The scattering efficiencies of small spheres are quite sensitive to diameter variation, but those of large spheres are much less sensitive. This is why accurate knowledge of the diameter of

Nomenclature

c = interparticle clearance
C_D = floating constant less than unity
d = particle diameter
f_v = particle volume fraction
I = intensity of the scattered beam
I_0 = intensity of the incident beam
L = thickness of the scattering medium
n = ratio of the refractive index of particle to that of matrix (both in vacuum); refractive index when accompanied by subscript
p = phase function for plane-parallel geometry
Q = scattering efficiency
R = bidirectional reflectance
$[R]$ = integrated bidirectional reflectance
R_u = dimensionless directly reflected energy
r_Q = ratio of dependent to independent scattering efficiencies = Q_D/Q_M
T = bidirectional transmittance
$[T]$ = integrated bidirectional transmittance
T_u = dimensionless directly transmitted energy
x = particle size parameter = $\pi d/\lambda$
y = coordinate in the cell along the direction of the incident beam
θ = scattering angle
λ = wavelength
μ = cosine of the scattering angle, $\cos\theta$
ρ_0 = reflectance of the normally incident beam on the glass cell
τ = optical thickness

Subscripts

D, I = dependent, independent scattering
g, p, w = glass, particle, water
M = Mie solution

the small spheres was necessary while the diameters of the large spheres were left somewhat uncertain.

Results and Discussion

Numerical Results. In order to compare with the experimental data, the equation of transfer for the nonabsorbing plane-parallel one-dimensional scattering medium is expressed by the following equation and was solved by the same procedure used by Brewster and Tien [1] to give the bidirectional transmittance and reflectance

$$\mu \frac{dI(y, \mu)}{d\tau} = -I(y, \mu) + \frac{1}{2}\int_{-1}^{1} I(y, \mu')p(\mu, \mu')d\mu' \tag{7}$$

where y is the coordinate along the direction of the incident beam and $p(\mu, \mu')$ is the scattering phase function modified to the plane-parallel geometry. As mentioned in the theoretical investigation equation (7) was derived for multiple scattering by independent scatterers but it can also be used for multiple scattering by dependent scatterers using the dependent scattering efficiency and phase function. The dependent scattering optical thickness τ_D was calculated by equation (6) using both measured and calculated values of the dependent scattering efficiency Q_D. The dependent phase function was given by the theoretical investigation using either the gas model or the packed sphere model. Numerical results so obtained are shown in Figs. 1–5 along with pertinent experimental data. The following contains a detailed discussion of the comparison between theoretical and experimental results.

Large Spheres. Figure 1 shows the bidirectional transmittance and reflectance for the spheres with $d = 11.15$ and 2.02 μm in an air matrix. Although the test cell of 0.10-mm thickness was used, only the product of f_v and L was measured by weighing the cell, and the thickness of the sample was not necessarily exactly 0.10 mm. The closely packed 2-μm spheres in the cell appeared to be loosely stuck to each other making control of the cell thickness difficult. The measurement of $f_v \cdot L$ was enough for the independent scattering calculation as can be seen from equation (6). However, f_v was needed to predict the dependent scattering properties from the analysis. A reasonable value of $f_v = 0.70$ was assumed.

The scattering efficiencies were set to unity when they were calculated larger than unity to remove diffraction effects from the Mie solution or from the dependent analysis using the packed-sphere model [2]. This is justifiable since diffraction is all in the forward direction and can be treated as unscattered radiation. The strong forward scattering components of the corresponding phase function were eliminated and the modified phase function was multiplied by some constant to keep energy conservation $\int_{4\pi} P(\theta)d\Omega = 4\pi$. The detailed procedure may be found in [9]. When this was done the numerical results of the bidirectional transmittance and reflectance gave almost the same results for dependent and independent scattering. These results also agreed very well with the experimental data. Thus both experimental and numerical results indicate that the approach is reasonable. The scatter of the experimental data in Fig. 1 mainly came from the undesirable layering of the particles which inevitably occurred during cell preparation by simple evaporation.

The case of $d = 11.15$ μm and $f_v = 0.70$ gave $c/\lambda = 0.48$ using the equation

$$x = \frac{\pi d}{\lambda} = \pi \frac{c}{\lambda} \frac{f_v^{1/3}}{0.9047 - f_v^{1/3}} \tag{8}$$

This was expected to give good agreement with the independent calculation since it was greater than the criterion ($c/\lambda < 0.3$) for dependent scattering given by Brewster and Tien [1]. The case of $d = 2.02$ μm, which gave $c/\lambda = 0.08$ assuming $f_v = 0.70$, was expected to show strong dependent scattering judging from that criterion. In this case, the independent and dependent scattering efficiencies are $Q_M = 2.58$ and $Q_D = 1.34$ according to the analysis using the packed-sphere model [2]. Therefore, the dependent scattering efficiency was set equal to unity for the numerical calculation which then yielded the same results as that of independent scattering. The same discussion holds for the case of $d = 11.15$ μm spheres which gave $Q_M = 2.17$ and $Q_D = 1.35$ for $f_v = 0.70$. The facts mentioned here for large spheres give the different demarcation curve from $c/\lambda = 0.3$ or 0.5 for the region of x greater than 10 as seen in Fig. 6 later on.

According to Ishimaru and Kuga [8], the scattering efficiencies of large spheres increase slightly with increasing volume fraction. This means that the scattering efficiencies were measured to be larger than two and that the forward scattering or diffraction component became stronger than that of independent scattering. However, when measuring bidirectional transmittance and reflectance from a slab of particles the diffraction component can be treated as unscattered radiation. In this case the scattering efficiency is reduced to one when the equation of transfer is solved as stated above. Thus in the present experiment, where multiple dependent scattering is studied, a slight increase in the scattering efficiency of large spheres does not yield different results than those gained from independent scattering. The present experiment did not directly measure the scattering efficiencies of large spheres. Therefore the present result is not contradictory to the results obtained by Ishimaru and Kuga. Further experimental evidence is welcome because only limited data are available for scattering efficiencies and bidirectional transmittance and reflectance in the case of large spheres.

Small Sphere. Figure 2 shows the experimental results for $r_Q = Q_D/Q_M$ together with the analytical results by use of the gas model and the packed-sphere model. The experimental value for Q_M was taken as that obtained for $f_v = 10^{-3}$ and $L = 10$ mm, and the uncertainties of f_v and r_Q were ± 5 percent. Figure 2 indicates that the packed-sphere model underestimates the dependent effects for all f_v and that the gas model slightly underestimates the dependent effect for $f_v < 0.1$ and overestimates for $f_v > 0.1$. The following empirical correlation given by Hottel et al. [3] and plotted in Fig. 2

$$\log_{10}\log_{10}(1/r_Q) = 0.25 - 3.83(c/\lambda) \tag{9}$$

agrees well with the present data for $f_v > 5 \times 10^{-2}$. The previous reports [1, 3] suggested either $c/\lambda < 0.3$ or 0.5 for the criterion of dependent scattering, but Fig. 2 shows that dependent scattering can be seen even for $c/\lambda > 0.5$ where r_Q is less than 1.0.

The experimental and numerical results of the bidirectional transmittance and reflectance are shown in Figs. 3 and 4. The dependent scattering results are compared with the independent scattering results for the same values of $f_v \cdot L$ in all three compartments of the two figures. Those values are $f_v \cdot L = 10^{-2}$, 5×10^{-2}, and 10^{-1} mm for Fig. 3 and $f_v \cdot L = 1.8 \times 10^{-2}$, 9.0×10^{-2}, and 1.8×10^{-1} mm for Fig. 4. A constant $f_v \cdot L$ with different cell thicknesses yields the same number of particles in the test cells with different interparticle clearances; in other words each test cell has the same optical thickness τ_I (determined by independent scattering).

In Fig. 3, the numerical results agree well with experiment except for the case of $L = 10$ mm and $f_v = 10^{-2}$. In that case the scattering to the lateral direction became significant and led to the failure of the one-dimensional assumption in the numerical calculation. Lateral losses, energy which went through the cell surfaces perpendicular to the incident beam, were negligible for the 0.1-mm-thick cell but were as much as 50 percent for the 10-mm-thick cell. The numerical calculation for dependent scattering used the gas model and predicted the experimental data for $f_v = 0.1$ reasonably well. Good agreement was expected because the predicted dependent scattering

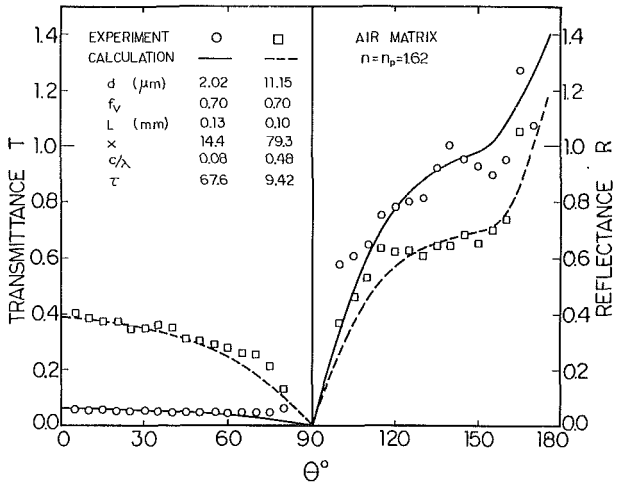

Fig. 1 Bidirectional transmittance and reflectance for the 11 and 2-μm spheres

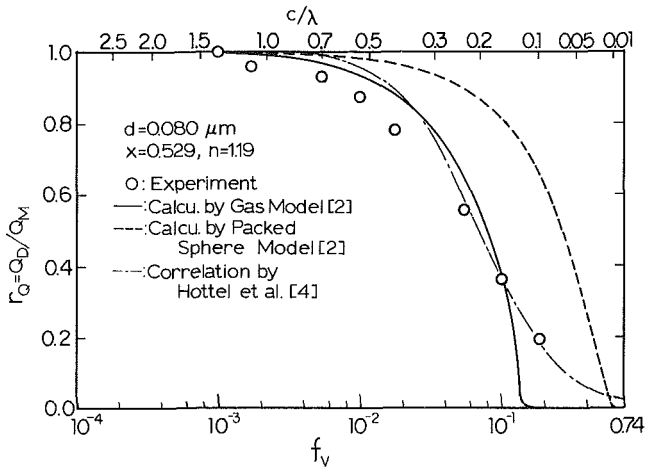

Fig. 2 Ratio of dependent to independent scattering efficiency as a function of the particle volume fraction for the 0.080-μm sphere

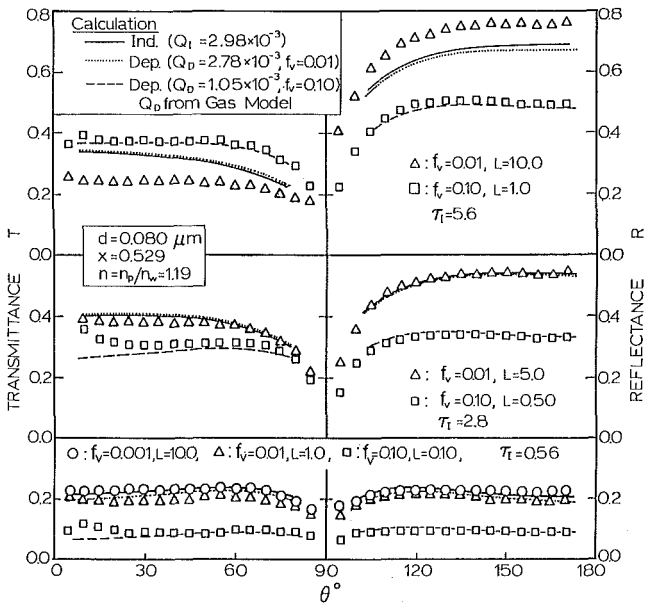

Fig. 3 Bidirectional transmittance and reflectance for the 0.080-μm sphere with $f_v = 10^{-3}$, 10^{-2}, and 10^{-1}

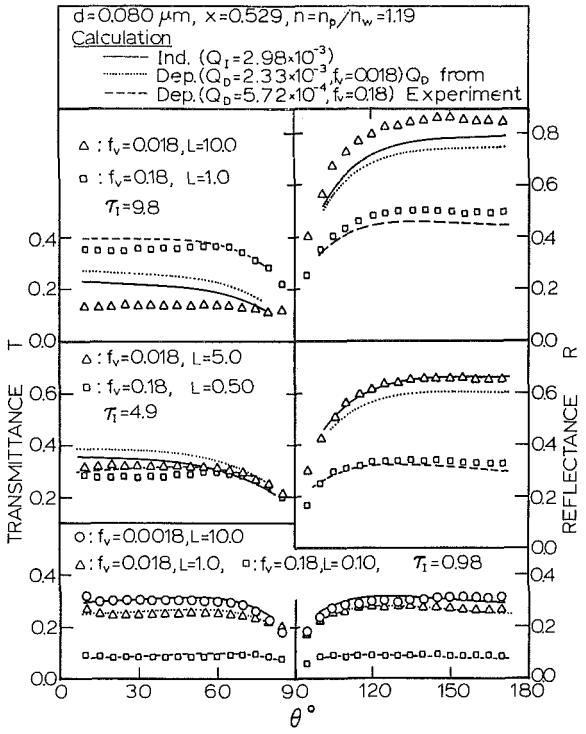

Fig. 4 Bidirectional transmittance and reflectance for the 0.080-μm sphere with $f_v = 1.8 \times 10^{-3}$, 1.8×10^{-2}, and 1.8×10^{-1}

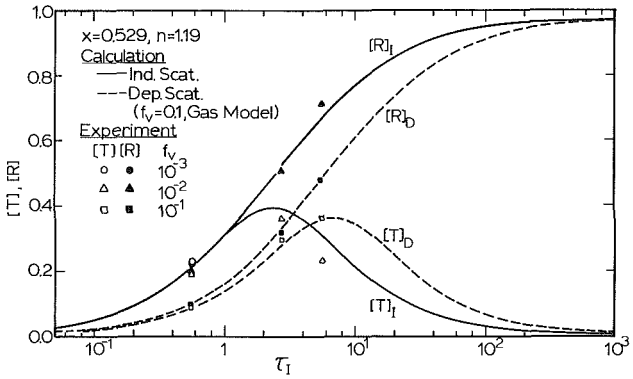

Fig. 5 Integrated bidirectional transmittance and reflectance for independent and dependent scattering

efficiency of 1.052×10^{-3} agreed well with the measured value of 1.03×10^{-3} as could be seen in Fig. 2. However, we cannot judge the correctness of the predicted dependent phase function because the phase function information was lost due to the plane-parallel geometry. Actually, the numerical calculation using the predicted dependent scattering efficiency and the independent scattering (Mie) phase function gave almost the same results for the bidirectional transmittance and reflectance as the dependent results in Fig. 3.

The numerical results for dependent scattering in Fig. 4 were obtained by use of the measured scattering efficiencies and the independent phase function because for $f_v = 0.18$ both the gas and packed-sphere models completely failed to predict the experimental data. The gas model gave a scattering efficiency which was too small while the packed-sphere model gave an efficiency which was too large as seen in Fig. 2. Both the gas and packed-sphere models were shown to be inadequate for f_v larger than 0.1.

Effect of Optical Thickness. Figures 3 and 4 indicate the variation of the dependent and independent bidirectional transmittance and reflectance as a function of the independent optical thickness τ_I. Figure 5 shows the independent and dependent integrated bidirectional transmittance and reflec-

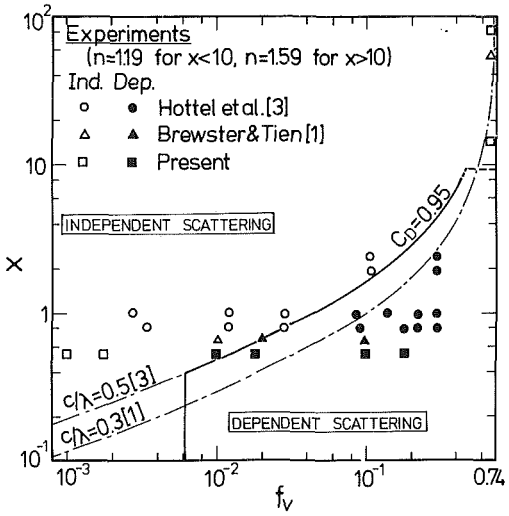

Fig. 6 Independent and dependent scattering regime: x versus f_v

tance, $[T]$ and $[R]$, as a function of τ_I for $d = 0.080$ μm spheres in a water matrix with $f_v = 0.1$ for dependent scattering using the gas model. Since the dependent scattering efficiency is smaller than the independent, the broken curves for dependent scattering $[T]_D$ and $[R]_D$ are almost identical to the solid curves for independent scattering $[T]_I$ and $[R]_I$ shifted to the right. As a result, $[R]_D$ is always smaller than $[R]_I$, $[T]_D$ is smaller than $[T]_I$ for $\tau_I < 4.5$ and $[T]_D$ is larger than $[T]_I$ for $\tau_I > 4.5$. The value of τ_I which divides the two regimes of $[T]_D < [T]_I$ and $[T]_D > [T]_I$ increases with increasing f_v. When τ_I is very small the directly transmitted energy T_u is very large resulting in a small difference between the dependent and independent integrated bidirectional transmittance and reflectance. On the other hand when τ_I is very large, both T_u and $[T]$ are very small which again results in small differences between dependent and independent integrated transmittance and reflectance. Therefore, the differences between dependent and independent scattering are more pronounced for the intermediate values of τ_I from about 0.2 to 50.

Regime Map. The present experimental data are shown in the regime map (Fig. 6) with the data by Hottel et al. [3] and Brewster and Tien [1]. Figure 6 also shows the proposed demarcation curve in the theoretical investigation [2] with $C_D = 0.95$, and two curves $c/\lambda = 0.5$ ($f_v < 0.3$) and $c/\lambda = 0.3$ proposed by Hottel et al. and Brewster and Tien, respectively. The present data cover the small and large size parameter ranges. The value of 0.95 was found to be adequate for C_D, and the criterion for dependent scattering is summarized as follows:

$$\begin{aligned} &\text{For } x \le 0.40, && f_v \ge 6.25 \times 10^{-3} \\ &\text{For } 0.40 < x \le 9.5, && f_v \ge 0.741/(1+1.56/x)^3 \\ &\text{For } x > 9.5, && \text{no observable dependent effect} \end{aligned} \tag{10}$$

The horizontal broken line at $x = 9.5$ shows that the region of large x is ambiguous as discussed in Part 1 [2]. In addition to the present demarcation curve, the optical thickness of the scattering medium should be considered, as mentioned above. If the optical thickness for independent scattering is less than 0.1 or larger than 100, the difference of the transmittance or reflectance between independent and dependent scattering will be too small to be observed.

Conclusion

Several sets of experimental data on dependent scattering were obtained by careful experimentation using latex spheres contained in plane-parallel test cells with various sphere diameters and particle volume fractions. These were compared with the independent scattering data. The predicted dependent scattering efficiencies derived from the extended Rayleigh-Debye scattering approximation have been compared with the experimental data. The numerical results of the dependent scattering bidirectional transmittance and reflectance for the plane-parallel geometry have been compared with the experimental data, and the following findings conclude this study:

1 For closely packed spheres with 11 and 2-μm diameters, the experimental bidirectional reflectance and transmittance results agreed well with the numerical results of independent scattering when the scattering efficiencies were set to unity by eliminating the Fraunhofer diffraction effect. Therefore, these closely packed spheres did not show dependent effects, as far as the bidirectional transmittance and reflectance are concerned, even for the case which was expected to show strong dependent scattering according to the previous criteria.

2 For the sphere with 0.080-μm diameter, the dependent scattering efficiency was experimentally found to decrease with increase of the particle volume fraction at least up to 0.18. The analytical results of the dependent scattering efficiency using the gas model have given slightly larger values than experimental data for the particle volume fraction smaller than 0.1, and have given much smaller values than the experimental data for the particle volume fraction larger than 0.1.

3 The numerical results of the dependent scattering bidirectional transmittance and reflectance for 0.080-μm spheres agreed well with the experimental data when the measured dependent scattering efficiencies were used in the calculation. The variation of the phase function caused by dependent scattering has been shown to have little effect on the numerical results.

4 It has been shown experimentally and numerically that the dependent integrated transmittance can be either larger or smaller than the corresponding independent transmittance depending on the optical thickness, while the dependent integrated reflectance is smaller than the independent reflectance regardless of the optical thickness.

Acknowledgments

Laser equipment used in this work was borrowed from San Francisco Laser Center, supported by the National Science Foundation, NSF Grant No. CHE79-16250, and the National Institute of Health, NIH Grant No. P41 PRO1613-02, awarded to the University of California at Berkeley in collaboration with Stanford University.

References

1 Brewster, M. Q., and Tien, C. L., "Radiative Transfer in Packed Fluidized Beds: Dependent Versus Independent Scattering," ASME JOURNAL OF HEAT TRANSFER, Vol. 104, 1982, pp. 573-579.

2 Cartigny, J. D., Yamada, Y., and Tien, C. L., "Radiative Transfer With Dependent Scattering by Particles: Part 1 – Theoretical Investigation," ASME JOURNAL OF HEAT TRANSFER, this issue.

3 Hottel, H. C., Sarofim, A. F., Dalzell, W. H., and Vasalos, I. A., "Optical Properties of Coatings. Effect of Pigment Concentration," *AIAA Journal*, Vol. 9, 1971, pp. 1895-1898.

4 Hottel, H. C., Sarofim, A. F., Vasalos, I. A., and Dalzell, W. H., "Multiple Scatter: Comparison of Theory With Experiment," ASME JOURNAL OF HEAT TRANSFER, Vol. 92, 1970, pp. 285-291.

5 Boundy, R. H., and Boyer, R. F., *STYRENE, Polymers and Copolymers and Derivatives*, Rheinholdt, New York, 1952.

6 Kratohvil, J. P., and Smart, C., "Calibration of Light-Scattering Instruments III. Absolute Angular Intensity Measurements on Mie Scatterer," *Journal of Colloid Science*, Vol. 20, 1965, pp. 875-892.

7 Bradford, E. B., and Vanderhoff, J. W., "Electron Microscopy of Monodisperse Latexes," *Journal of Applied Physics*, Vol. 26, 1955, pp. 864-871.

8 Ishimaru, A., and Kuga, Y., "Attenuation Constant of a Coherent Field in a Dense Distribution of Particles," *Opt. Soc. Am.*, Vol. 72, 1982, pp. 1317-1320.

9 Brewster, M. Q., "Radiative Transfer in Packed and Fluidized Beds," Ph.D. Dissertation, Department of Mechanical Engineering, University of California, Berkeley, 1981.

10 Bohren, C. F., and Huffman, D. R., *Absorption and Scattering of Light by Small Particles*, Wiley, New York, 1983, p. 111.

H. F. Nelson
Professor.
Mem. ASME

D. C. Look, Jr.
Professor.
Mem. ASME

A. L. Crosbie
Professor.
Mem. ASME

Thermal Radiative Transfer Group,
Department of Mechanical and Aerospace Engineering,
University of Missouri—Rolla,
Rolla, MO 65401

Two-Dimensional Radiative Back-Scattering From Optically Thick Media

The theoretical and experimental results of anisotropic back-scattering from an optically thick medium exposed to a laser beam are presented. The laser beam is incident normal to the upper surface of the scattering medium. Uniformly sized latex particles with diameters ranging from 0.046 to 0.35 μm are used for the scattering centers in a water solution. The results are discussed for back-scattered radiation as a function of optical radius from the laser beam and optical thickness of the scattering medium. It is shown that back-scattered radiation in optically thick media is very sensitive to small changes in albedo when the albedo is near unity. The sensitivity increases as the optical radius increases. Also, the isotropic scattering solution yields good agreement with the experimental data at large optical radii when one uses effective optical properties. The agreement between theory and experiment is improved when index of refraction effects at the interface are included.

Introduction

Prediction of two-dimensional radiation transfer in a multiple scattering medium is an important problem facing the heat transfer community [1, 2]. Two current applications in which multidimensional multiple scattering in the Mie Regime is significant are involved with radiative transfer in dust clouds and rocket plumes. Radiative reflection and transmission through dust clouds from near-surface nuclear bursts are important not only for military damage assessment but also for ascertaining climatic effects. Current emphasis on stealth technology has resulted in a concerted effort to study the effect of scattering by particles in rocket plumes on the plume infrared signature. This includes not only directional effects but also intensity magnitudes.

A two-dimensional problem that has received attention recently is the back-scattering of a laser beam by a multiple scattering medium when the incident laser beam is normal to the surface of the medium. Benchmark numerical results for this problem are available for a semi-infinite medium [3–5] and for a finite thick medium [6, 7]. The scattering phase function in these studies consisted of a spike in the forward direction superimposed on an isotropic [3, 6], linear [4, 7], or Rayleigh [5] phase function. Each of these studies was based on the assumption that the scattering occurred in a medium with a refractive index of unity.

The results of experiments in which well-defined scattering particles were used for multidimensional, multiple scattering radiative transfer are limited [8–11]. Look et al. [8] reported good agreement between theory and experiment for the back-scattering of a laser beam. The scattering medium was composed of uniformly sized latex particles with diameters ranging from 0.03 to 1.011 μm immersed in a water solution. The albedo was assumed to be unity. One minus the asymmetry factor was used to correlate the anisotropic scattering experimental results with isotropic scattering theory.

In [8] the back-scattering nondimensional intensity G varied with the optical distance from the beam τ_r^*. The behavior of G can be broken into three regions based on the optical distance from the beam: thin, intermediate, and thick. The optically thin region is close to the beam where G increases with optical radius, the intermediate region is where G reaches its maximum value, and the thick region is far from the beam where G decreases with increasing optical radius. Except for the 0.03-μm-dia particles, no results were presented for the thick region in [8]. However, the 0.03-μm data are questionable because of the difficulty in characterizing and handling the particles.

Preliminary investigations of the back-scattered radiation of a laser beam from a finite depth medium have been published [9, 10]. These investigations used 0.261-μm-dia latex particles for the scattering centers. In [9] the particles were suspended in two different liquids (distilled water and ethylene glycol) so that the influence of the refractive index of the liquid carrier on the back-scattering could be investigated. The effects of changing the laser wavelength and the liquid carrier were reported in [10]. In these experiments two laser wavelengths were used: 0.4414 and 0.6328 μm. Inspection of the results shows what appears to be an influence of the liquid carrier refractive index. At 0.6328 μm an increase in refractive index of the liquid reduced the back-scattered radiation, whereas at 0.4414 μm, an increase in the liquid refractive index produced an increase in the back-scattered radiation. This behavior was not explained by Look and Sundvold [9, 10].

The purpose of this paper is to extend the results obtained by Look et al. [8] to the optically thick radius region. This extension requires consideration of finite optical depth and absorption effects. In addition, the discrepancies in the 0.03-μm particle results obtained by Look et al. [8] and the index of refraction inconsistencies of Look and Sundvold [9, 10] are herein resolved.

The results of this paper are applicable to many realistic situations such as laser–material interaction, underwater radiation back-scattering, fog dissipation, and laser diagnostics of human skin and teeth (medical applications). There are many practical two-dimensional, multiple scattering problems and more of these problems will be encountered as laser applications are developed and refined.

Theoretical Analysis

The physical situation that was investigated for this research involved a laser beam incident on a scattering medium with finite depth as shown schematically in Fig. 1. The radiative transfer was multidimensional and involved multiple scattering. Thus the theoretical development was based on the following assumptions: steady state, coherent scattering, negligible interference and polarization effects, homogeneous

Contributed by the Heat Transfer Division and presented at the 23rd National Heat Transfer Conference, Denver, CO, August 1985. Manuscript received by the Heat Transfer Division June 6, 1985.

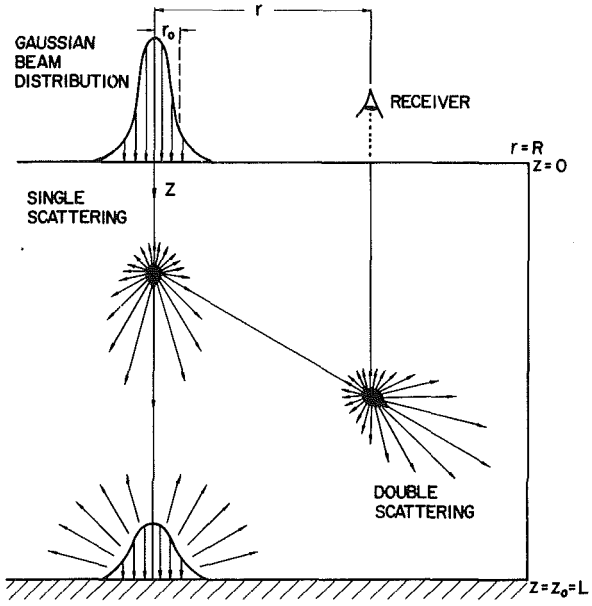

Fig. 1 Schematic of the two-dimensional, finite depth scattering situation

medium, no emission, refractive index of unity, and two-dimensional cylindrical geometry.

Incident Radiation. For this investigation the incident intensity was assumed to be a laser beam that was incident normal to the surface of the medium. The radial variation of the laser beam was Gaussian [12] so that the incident intensity was given by

$$I^+(\tau_r, \mu, \phi) = I_i \delta(\mu - 1)\delta(\phi)\exp[-\tau_r^2/\tau_{r_0}^2] \tag{1}$$

where

$$\tau_r = (NC_{sca} + \kappa)r,\ \tau_{r_0} = (NC_{sca} + \kappa)r_0 \tag{2}$$

The Dirac delta function product restricted the incident radiation to the normal direction. For this intensity distribution, the incident radiative flux was $I_i\exp(-r^2/r_0^2)$ and the magnitude of the incident flux at the center of the beam was equal to I_i.

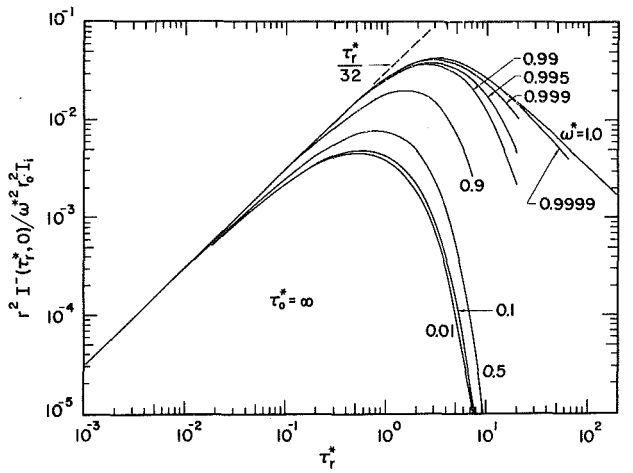

Fig. 2 Effect of absorption (ω^*) on the theoretical back-scattered intensity from a semi-infinite medium

Scattering Phase Function. When the wavelength of the radiation is small compared to the particle diameter, diffraction around the particles gives rise to a sharp forward peak in the scattering phase function. It was approximated as

$$P(\Theta) = 2g\delta(1 - \cos\Theta) + (1 - g) \tag{3}$$

where g is defined as

$$g = \frac{1}{2}\int_0^\pi \cos\Theta\, P(\Theta)\sin\Theta\, d\Theta \tag{4}$$

Van de Hulst [13] stressed that g is the fundamental phase function similarity parameter.

Solution of Transport Equation. Putting this phase function into the equation of transfer yields a modified transfer equation for isotropic scattering with the following modified optical coordinates and parameters [3]

$$\begin{aligned} \tau_r^* &= (1 - \omega g)\tau_r,\ \tau_{r_0}^* = (1 - \omega g)\tau_{r_0} \\ \tau_0^* &= (1 - \omega g)\tau_0,\ \omega^* = \omega(1 - g)/(1 - \omega g) \end{aligned} \tag{5}$$

in which

$$\tau_0 = (NC_{sca} + \kappa)L \text{ and } \omega = NC_{sca}/(NC_{sca} + \kappa)$$

Nomenclature

c = effective scattering coefficient $= 6\,C_{sca}/(\pi d^3)$
C_{sca} = scattering cross section
d = scattering particle diameter
g = asymmetry function
G = theoretical universal function $= r^2 I_N/(r_0^2 I_i)$
G_{exp} = experimental universal function $= r^2 I_{exp}/(r_0^2 I_i)$
I_i = magnitude of the incident intensity at $z = 0$
I_N = theoretical intensity leaving the medium normal to the surface
I^- = theoretical back-scattered intensity at any angle
I^+ = theoretical incident intensity
I_{exp} = measured intensity leaving the medium normal to the surface
$J_0(t)$ = Bessel function of order zero
L = depth of scattering medium
n = relative index of refraction of particle to water
n_m = refractive index of the liquid carrier medium
N = number density of scattering particles
P = scattering phase function
P_i = input power on the medium
Q_{sca} = scattering efficiency
r = radial distance from the center of the laser beam
r_0 = effective laser beam radius
R = function, see equation (6)
R_0 = detector probe aperture radius
V = voltage
x = particle size parameter $= n_m \cdot \pi d/\lambda_0$
z = distance into the scattering medium (normal to the surface)
β = spatial frequency
$\delta(t)$ = Dirac delta function
η = particle volume concentration
θ = polar angle of incident intensity
$\bar{\theta}$ = effective acceptance angle of detector
Θ = angle between incident and scattered ray
κ = absorption coefficient of scattering medium
λ_0 = wavelength in air
μ = cos θ
ρ_N = normal reflectance $= (n_m - 1)^2/(n_m + 1)^2$
τ_r = radial optical thickness
τ_0 = optical depth to bottom of scattering medium
τ_{r_0} = optical radius of incident laser beam
ω = single scattering albedo

Superscript

* = effective quantity which takes into account the effect of anisotropic scattering and albedo

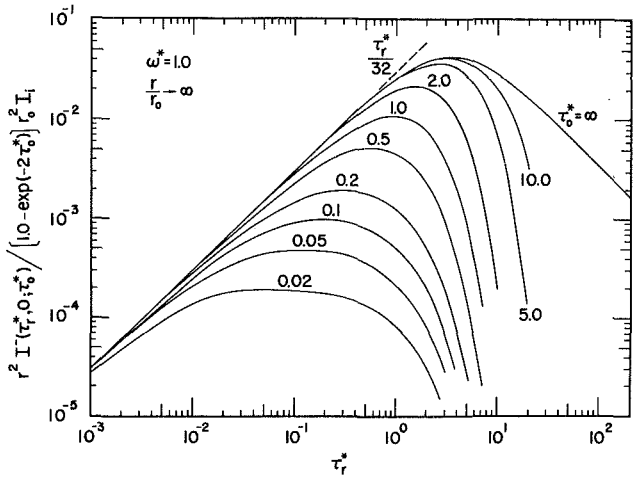

Fig. 3 Effect of finite optical thickness (τ_0^*) on the theoretical back-scattered intensity from a pure scattering medium

Thus, for anisotropic scattering with a peaked phase function as in equation (3), the isotropic solutions for the source function, flux, and intensity were used by adjusting the optical coordinates and the albedo according to equation (5) [3]. This type of approximation has been used in one-dimensional, multiple scattering, radiative transfer [14–17]. It is generally accepted in the treatment of anisotropic scattering. One of the main proponents of scaling is Van de Hulst [13]. The scaling procedure is easy to use and, therefore, it is appealing for industrial design applications of radiative scattering. There is a need to develop and incorporate more realistic models for anisotropic scattering; however, this is beyond the scope of the present paper.

The exact two-dimensional integral equation describing the source function for the modified transfer equation was solved by using separation of variables and superposition. The resulting back-scattered intensity normal to the surface could then be expressed as [3, 5]

$$I_N(\tau_r^*)=I^-(\tau_r^*,\,\mu=1,\,\phi)=\frac{\omega^* I_i}{8\pi}\left[\frac{r_0}{r}\right]^2$$

$$\int_0^\infty tJ_0(t)\exp\left\{-\frac{1}{4}\left(\frac{r_0}{r}\right)^2 t^2\right\}R\left\{\frac{t}{\tau_r^*};\,\omega^*,\,\tau_0^*\right\}dt \qquad (6)$$

The quantity $\omega^* J_0(\beta\tau_r^*)R(\beta;\,\omega^*,\,\tau_0^*)/4$ is the intensity leaving normal to medium when the medium is exposed to collimated radiation with a Bessel function radial variation $J_0(\beta\tau_r^*)\delta(\mu-1)\delta(\phi)$. The Bessel function boundary condition is used to separate variables. When $\beta=0$, the incident radiation is radially uniform, and the problem becomes one-dimensional. Equation (6) has been evaluated numerically for a wide range of parameters in [3, 5].

Large r/r_0 Case. When r/r_0 is large, the exponential term in equation (6) can be approximated by unity, and the intensity can be expressed as

$$I_N(\tau_r^*)=I_i\left(\frac{r_0}{r}\right)^2 G(\tau_r^*;\,\omega^*,\,\tau_0^*) \qquad (7)$$

where

$$G(\tau_r^*;\,\omega^*,\,\tau_0^*)=\frac{\omega^*}{8\pi}\int_0^\infty tJ_0(t)R\left\{\frac{t}{\tau_r^*};\,\omega^*,\,\tau_0^*\right\}dt \qquad (8)$$

For a pure scattering, semi-infinite medium, the solution is a function only of τ_r^* [3].

The influence of absorption on G is shown in Fig. 2 for a semi-infinite, isotropic scattering medium as a function of optical radius. At large optical radii a small amount of absorption can cause large variations in the back-scattered intensity.

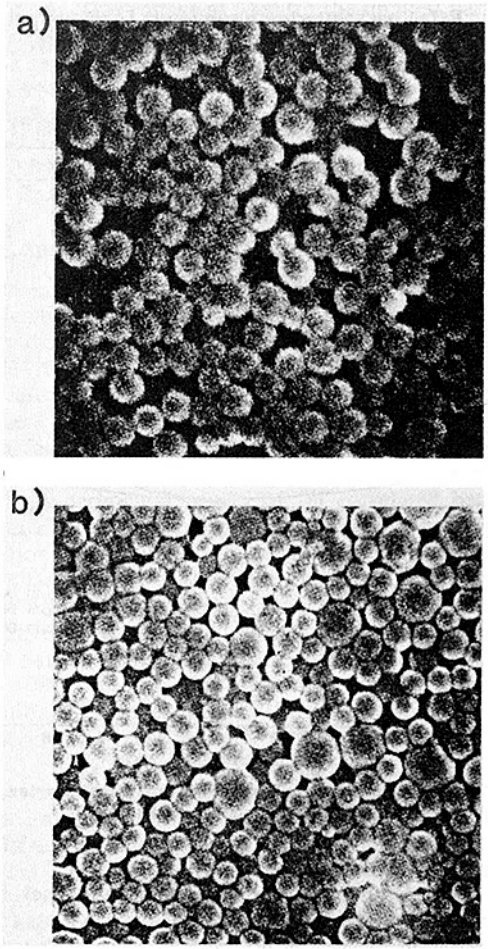

Fig. 4 Electron microscope pictures of spherical latex particles: (*a*) $d=0.18$ μm, magnification = 40,000; (*b*) $d=0.35$ μm, magnification = 13,000

For example, the results for $\omega^*=1.00$ and $\omega^*=0.99$ differ more than a factor of 2 for τ_r^* greater than 9.

The influence of finite optical thickness τ_0^* is illustrated in Fig. 3 for pure, isotropic scattering. Actually, the quantity $G/[1-\exp(-2\,\tau_0^*)]$ is presented because it collapses the curves at small optical radii. As might be expected, a pure scattering, semi-infinite medium case represents the upper bound on the back-scattered intensity.

The assumption of a refractive index of unity is questionable; however, it significantly reduces the numerical complexity. A single and double scattering analysis including the effects of refractive index shows that the back-scattered intensity should be reduced by $(1-\rho_N)^2/n_m^2$. This factor cannot be used over the entire optical radius range for a pure scattering, semi-infinite medium, because all the incident energy must be back-scattered. Consequently, a reduction in the reflected intensity at small optical radii dictates an increase in the intensity at large optical radii. An analysis including multiple scattering effects suggests shifting τ_r^* by $(1-\rho_N)^2/n_m^2$. This approximation for the pure scattering semi-infinite medium is strictly valid only for optical radii in the thin region.

The trends of this interface model are correct, even though it is a very simple model. Consideration of the interface greatly complicates the numerical solution, to the point that it becomes almost intractable, hence many authors have ignored interface effects. This is an area for future investigation.

Experimental Procedure

The experimental situation is shown schematically in Fig. 1. The experiment was designed to model a cylindrically sym-

Table 1 Effective scattering parameters for latex particles in water at a wavelength of 0.6328 μm and a relative index of refraction of 1.197

Dow polystyrene latex batch number	d (μm)	x	g	c (cm^{-1})	
				Theory	Exp[1]
XD-8859[2]	0.046	0.30	0.016	115	115
XD-8656	0.18	1.19	0.25	4850	5211
XD-7583	0.35	2.31	0.72	14,850	15,085

[1]From transmission measurements.
[2]Experiment data used to characterize these particles.

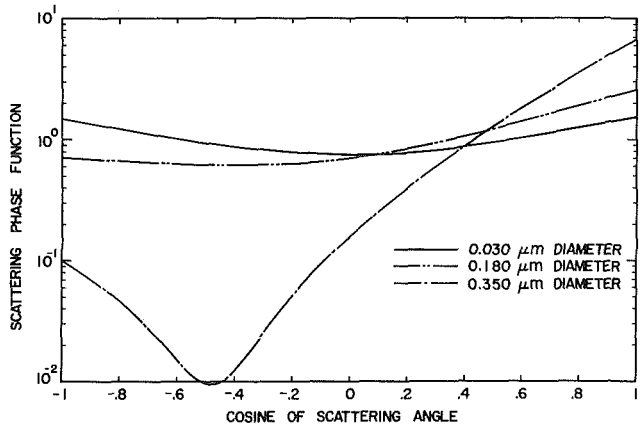

Fig. 5 Theoretical phase function versus cos θ for the latex particles used in the experiment ($n = 1.197$, and $\lambda_0 = 0.6328$ μm)

metric, finite depth scattering medium with a black bottom. The source was a He-Ne laser. A 26.6-cm-dia glass tank was used to contain the scattering medium. The tank was fitted with a bottom which was sprayed with a highly absorbing, diffusely reflecting black paint with a reflectance of less than 2 percent. For the experiments reported herein wall effects were negligible.

The scattering medium was composed of spherical latex particles immersed in distilled water. The amount of scattering was controlled by the concentration of latex particles. The laser beam was incident normal to the upper surface of the scattering medium, so that the scattered radiation in the medium was a function of r and z.

Data Reduction. The data analysis follows [8] quite closely; however, the magnitudes of some of the experimental parameters are different. The ratio of the reflected intensity to the incident laser beam intensity is

$$\frac{I_{\text{exp}}}{I_i} = \frac{1.53 \times 10^{-7}}{\pi} \left[\frac{r_0}{\bar{\theta} R_0}\right]^2 \frac{V}{P_i} \tag{9}$$

where $\bar{\theta}$ = 2.10 deg = 0.037 rad, R_0 = 0.169 cm, r_0 = 0.20 cm, V is in volts, and P_i is in watts. This equation is very sensitive to the values of $\bar{\theta}$, R_0, and r_0. The sensitivity to r_0 can be eliminated by rearranging equation (9) as follows

$$\frac{r^2 I_{\text{exp}}}{r_0^2 I_i} = G_{\text{exp}} = 0.001273 r^2 \frac{V}{P_i} \tag{10}$$

It is convenient to write the optical thickness in terms of the particle volume concentration

$$\eta = N\pi d^3/6 \tag{11}$$

From equation (2) the optical radius becomes

$$\tau_r = \left(\eta \frac{6C_{\text{sca}}}{\pi d^3} + \kappa\right) r = (\eta c + \kappa) r \tag{12}$$

The value of κ for distilled water was obtained from a table of values presented by Zuev [18], as 0.005 1/cm at λ_0. This value

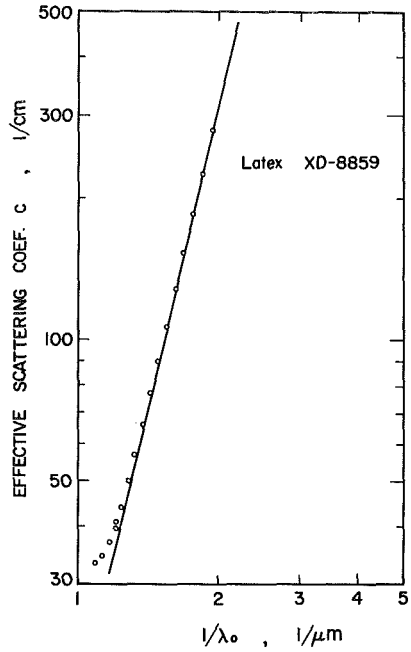

Fig. 6 The effective scattering coefficient for the XD-8859 latex particles as a function of $1/\lambda_0$; the circles are the experimental points

is somewhat questionable because of difficulties in making measurements when κ is small and difficulties in controlling water purity.

The data were correlated by using the effective optical coordinates and parameters. In other words, to compare the data to theory, the actual experimental optical radius for the anisotropic case τ_r was multiplied by $(1-\omega g)$ to yield the corresponding effective optical radius for the theoretical isotropic case τ_r^*. The $(1-\omega g)$ factor approximately transforms the anisotropic problem to an isotropic problem.

Particle Characterization. The latex particles that were used as scattering centers were donated by DOW CHEMICAL USA. Their mean diameters were listed as 0.03, 0.18, and 0.35 μm; however, their size distribution was not well characterized. The particles had approximately a neutral density in water (1.05 g/cc) and settling effects were not observed. Their refractive index was 1.593 (1.197 relative to water at λ_0). They were assumed to have a single scattering albedo of unity.

Electron microscope pictures of the 0.18 and 0.35-μm-dia particles were obtained as shown in Fig. 4. Clear electron microscope pictures of the 0.03-μm-dia particles could not be obtained.

The anisotropic character of the 0.18 and 0.35-μm particles in water at λ_0 is shown on Fig. 5. As expected the 0.35-μm particle phase function exhibits considerably more anisotropic character than that of the 0.18-μm particle. The scattering phase function of the 0.03-μm particles is also shown on Fig. 5. Its phase function has a Rayleigh distribution.

The particle size distribution was uncertain, so transmission measurements were made for each set of particles in the wavelength interval from 0.40 to 0.70 μm using a spectrophotometer. The experimental values of c at λ_0 are listed in Table 1. Mie theory was used to predict theoretical values for c. These are also given in Table 1. The experimental and theoretical values of c for the 0.18 and 0.35-μm particles agree quite well; however, the experimental value (115 1/cm) was much greater than the Mie theory value (32.5 1/cm) for the 0.03-μm particles. Therefore a theoretical approach was used to better characterize them. The nondimensional scattering cross section for Rayleigh scattering is

$$Q_{\text{sca}} = \frac{8x^4}{3} \left|\frac{n^2-1}{n^2+2}\right|^2 \tag{13}$$

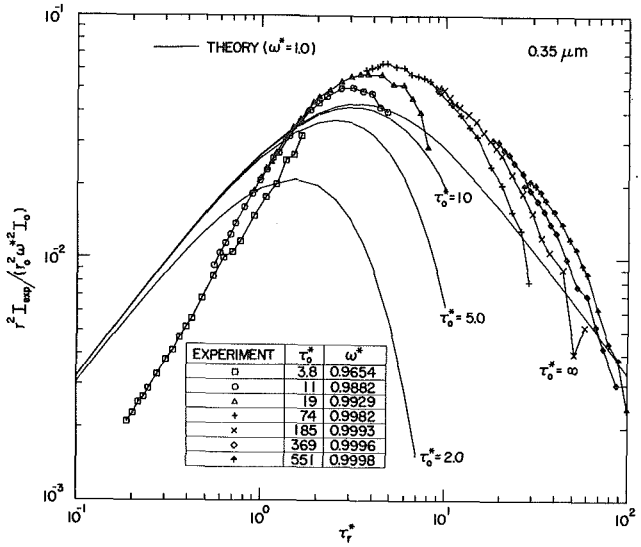

Fig. 7 Nondimensional back-scattered intensity from 0.35-μm-dia polystyrene latex particles in distilled water versus the effective optical radius

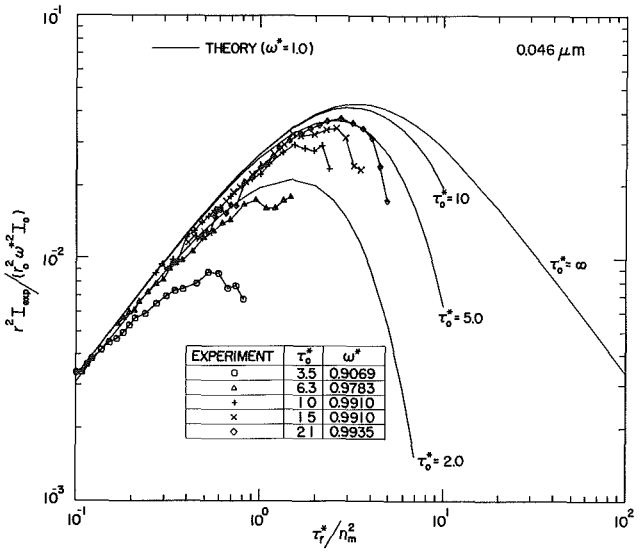

Fig. 8 Nondimensional back-scattered intensity from the XD-8859 latex particles versus τ_r^*/n_m^2

and c is related to Q_{sca} as

$$c=\frac{\pi d^2}{4} Q_{sca} \frac{6}{\pi d^3}=1.5Q_{sca}/d \tag{14}$$

so that

$$c=4\pi^4\frac{d^3 n_m^4}{\lambda_0^4}\left|\frac{n^2-1}{n^2+2}\right|^2 \tag{15}$$

This expression yields a value of c of 32.7 1/cm (for d = 0.03 μm, n_m = 1.331, λ_0 = 0.6328 μm, and n = 1.197), which is very close to the Mie scattering value of 32.5.

Figure 6 shows the values of c obtained from the transmission experiments as a function of $1/\lambda_0$. The slope of this curve is 4. Thus, even though the particle size distribution is not well known, one knows that the scattering is Rayleigh. The experimental magnitude of c (115 1/cm) at λ_0 = 0.6328 μm is considerably greater than the theoretical value for the 0.03-μm particles. This implies that large particles are present. However, the slope of the data indicates that even with these larger particles the scattering is still Rayleigh. The use of 115 1/cm for c in equation (15) gives an effective particle diameter of 0.0456 μm. This value was used for the smallest particle size instead of 0.03 μm.

In the presentation that follows, the experimental values were used for c. Theoretical values of x and g were used. They were obtained by assuming a uniform size distribution at the manufacturer's stated size for the 0.18 and 0.35-μm particles and at 0.0456 μm for the smallest particles. The values are given in Table 1.

Results and Discussion

The intent of this study was to investigate back-scattering in the optically thick radius region, account for finite thickness, consider the effects of absorption, and clarify the discrepancies in [8–10]. This required large quantities of latex particles. Hence, latex particles with a wider size distribution than those of [8] were used. The particles were characterized using electron microscope pictures, transmission data, and Rayleigh theory.

All the experimental results of [8] correlated better with theory as τ_r^* increased, except for the smallest particles. This observation was attributed to the 0.03-μm particles not being as well characterized as the other particles and the cross section not being as accurately known. Because of this, more small particles were obtained, and the data were retaken. The smallest particles used in [8] were obtained from MONSANTO CHEMICAL CO. and may have had a different size distribution than those used in the present study. However, the experimental cross sections were similar (115 versus 110 1/cm).

In the current study, a new procedure was used to analyze the data. In the old procedure [8], optical radius values were selected from lines of constant radius as the number density was varied. This procedure required experimental data from a large number of particle concentrations at each radius position and for each particle size. A single curve was fit through the data for each particle size to generate the results presented in [8]. There appeared to be no systematic variation between the data and the curve. Any variation was attributed to experimental error; hence, the effects of τ_0^* went unnoticed. In the new procedure, the number density was held constant and the radial distance was varied. The data show a definite dependence upon τ_0^*. This procedure was preferable because of its clarity in demonstrating optical thickness effects and was used for the data presentation that follows.

Figure 7 presents G_{exp}/ω^{*2} versus τ_r^* for the 0.35-μm-dia particles for values of τ_0^* from 3.8 to 551. The ω^{*2} in the ordinate partially accounts for absorption. The theoretical solution for isotropic scattering is also shown for $\omega^*=1$ at $\tau_0^*=2$, 5, 10, and infinity. The difference between the theory and experimental results shown on this figure is typical of all the current results and those of [8]. In the thin optical radius region, the experimental results are low compared to theory, whereas in the thick optical radius region, they are higher than the theory. The figure shows that use of the effective optical radius yields reasonable agreement with isotropic theory for anisotropic scattering from optically thick media. This same behavior was observed in [8]. However, herein the experimental data are presented to $\tau_r^*=100$ and $\tau_0^*=551$, which are considerably larger than their respective values for the data of [8].

In general the experimental and theoretical results have similar shapes. Each set of constant τ_0^* data (both experiment and theory) "peels off" at large effective optical radius values and is completely enclosed by the next higher τ_0^* data set. This behavior is due to the number of scattering events the radiation undergoes prior to leaving the scattering medium.

For low particle concentrations, most of the incident radiation strikes the bottom where it is strongly absorbed and diffusely reflected. The reflected radiation tends to either travel directly to top of the medium and escape or be internally reflected. Most of the radiation leaves the medium at small

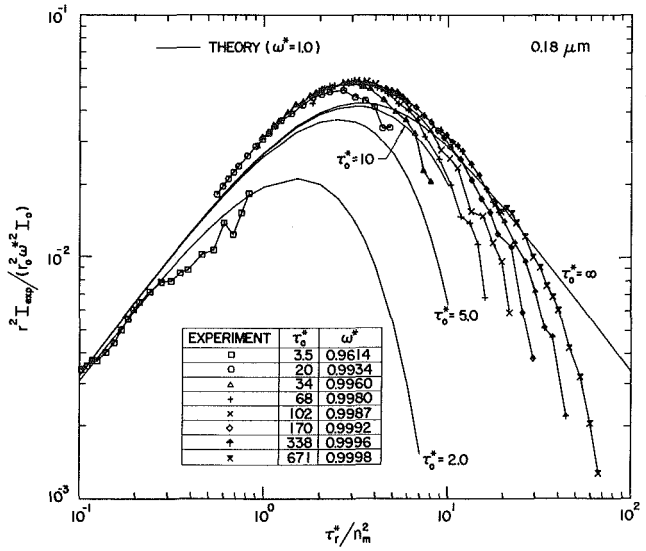

Fig. 9 Nondimensional back-scattered intensity from 0.18-μm-dia latex particles versus τ_r^*/n_m^2

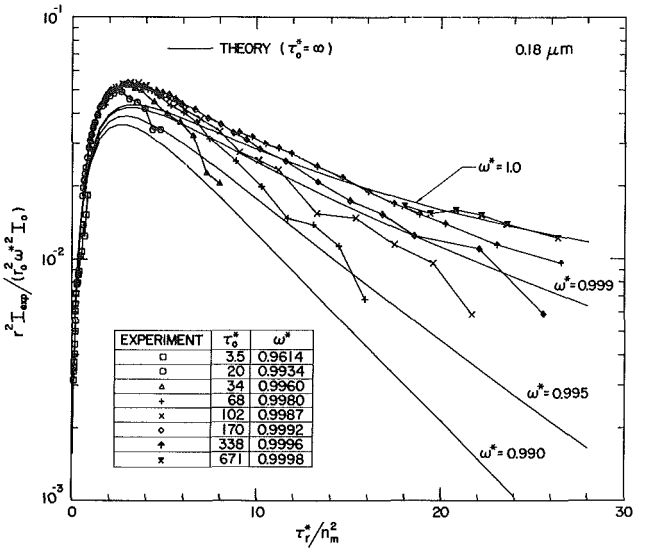

Fig. 11 Influence of τ_0^* and ω^* on the back-scattered intensity from 0.18-μm-dia latex particles versus τ_r^*/n_m^2

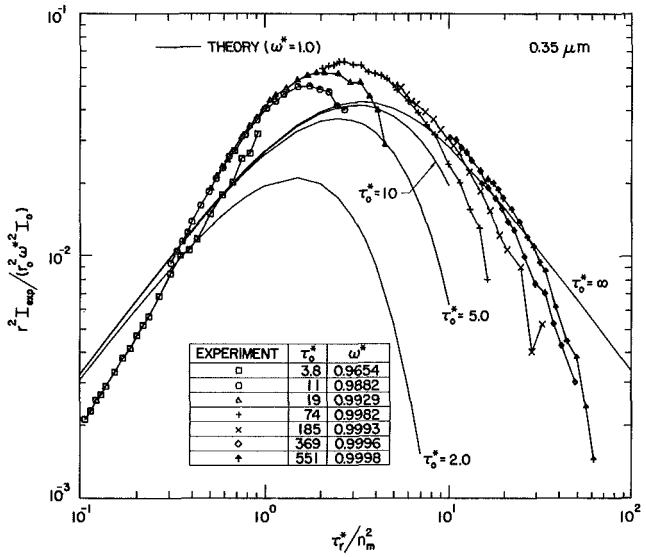

Fig. 10 Nondimensional back-scattered intensity from 0.35-μm-dia latex particles versus τ_r^*/n_m^2

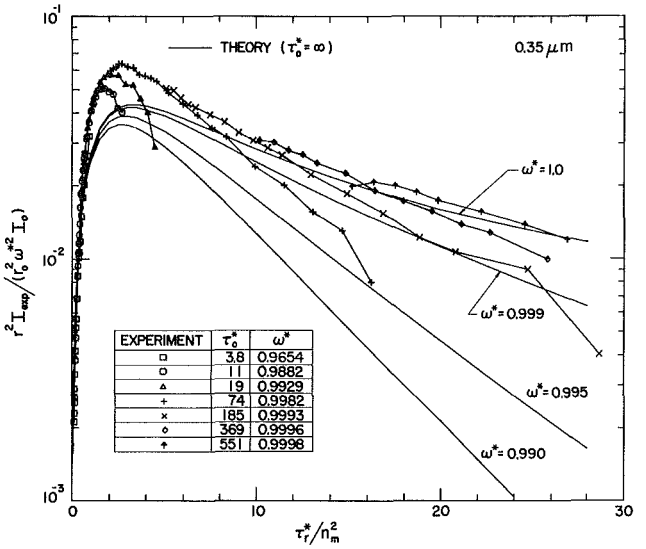

Fig. 12 Influence of τ_0^* and ω^* on the back-scattered intensity from 0.35-μm-dia particles versus τ_r^*/n_m^2

values of τ_r^* because not many scattering events occur. Consequently, side scattering is small. Also, the small scattering particle concentration makes τ_r^* small even at large radial positions. The larger τ_0^* becomes, the more scattering events the radiation undergoes before it escapes. This increases the probability of the radiation reaching a large τ_r^* position before it exits the medium, because (1) the larger number of scattering events increase the probability of side scattering so that the radiation has a higher probability of traveling in the radial direction before it escapes, and (2) the larger particle concentration increases the value of τ_r^* even if the physical distance r is small. When τ_0^* approaches infinity most of the radiation is back-scattered at very small radial values; however, the large particle concentration produces large values of τ_r^* even for very small radial positions. Thus, as τ_0^* increases the position for maximum G moves to higher τ_r^* positions. For τ_r^* values beyond the peak the value of G falls off rapidly. Consequently, both the experimental and theoretical nondimensional intensity curves as plotted in Fig. 7 peel off at large τ_r^* values and are bounded by the next higher τ_0^* data set. The infinite τ_0^* case is the envelope of the results.

The horizontal difference between the theoretical and experimental curves on Fig. 7 is roughly $1/n_m^2$. As discussed in the theory section, the τ_r^* axis should be τ_r^*/n_m^2 when τ_r^* is small and $\rho_N << 1$. Figures 8–10 show G_{exp}/ω^{*2} plotted versus τ_r^*/n_m^2 for the 0.046, 0.18, and 0.35-μm-dia particles, respectively. These particles exhibit progressively more forward scattering as is shown by their phase functions in Fig. 5 and their asymmetry factors in Table 1. In general, an increase in forward scattering tends to increase the maximum value of G and increase the slope of G at small τ_r^* values. The data of Figs. 7 and 10 are the same except for the shift of $1/n_m^2$. This shift improves the agreement between theory and experiment.

The τ_r^*/n_m^2 factor also improves the agreement between theory and experiment of the data shown in [8], Fig. 8, in the thin region for all the cases except the 0.03-μm-dia case. This case agrees well with theory when it is plotted against τ_r^*; however, it does not correlate with the other experimental data and at large τ_r^* values. Thus, the $1/n_m^2$ shift appears to be reasonable, because it improves all the current experimental data when compared to isotropic scattering theory as well as all the data of [8], except the 0.03-μm data.

The information in this paper also clarifies the discrepancies that occurred in [9, 10] where the water and ethylene glycol

liquid carrier data change relative positions in Fig. 3 of each paper. This situation occurred because the index of refraction used for ethylene glycol was incorrect. The value used was 1.47, and it should have been 1.43 [19]. This correction shifts the glycol data of Fig. 3 of [10] to the right by a factor of about 1.9 and the glycol data of Fig. 3 [9], to the right by a factor of 1.6. These shifts also increase the effective optical thickness value of the data by the same factors. These changes make the results of [9, 10] consistent with the $1/n_m^2$ shift used herein. This gives more justification for the shift.

Figures 11 and 12 show the same data as Figs. 9 and 10 except that they are plotted on a semilog scale to show the linear large τ_r^* behavior. These figures emphasize the efect of finite depth and absorption (τ_0^* and ω^*) on the anisotropic scattering. Theoretical results for albedos of 1.000, 0.999, 0.995, and 0.990 are included on the figures. The experimental data have the same general trends as the theory, but differ quantitatively. The albedos of the experiment are calculated and varied from 0.961 to 1.00. The results are very sensitive to small amounts of absorption and changes in τ_0^*. Note that for τ_r^* greater than 24, a change in ω^* from 1 to 0.990 results in more than an order of magnitude change in the nondimensional intensity. Unfortunately, at the present time it is not possible to discriminate between the effects of absorption and finite τ_0^*. It appears that ω^* is the more important parameter of the two for an effective optical thickness greater than about 50 and an effective optical radius value greater than about 10. For these conditions the scattering behavior should be very much like the semi-infinite theory curves shown in these figures.

Conclusions

This paper presents results that are roughly a factor of 10 greater in optical radius than those presented in our previous paper [8]. In addition it accounts for not only the influence of the scattering medium optical depth and albedo but also the index of refraction at the scattering medium boundaries.

The back-scattering measurement results presented herein are the only ones available in the literature for the thick optical radius region. In this region the influence of absorption and optical thickness of the medium are shown to be very important. The back-scattered radiation in optically thick media is very sensitive to small changes in the albedo when the albedo is near unity. The sensitivity increases as the optical radius increases.

For the optically thick radius region, it is shown herein that (1) anisotropic, multiple scattering results can be reduced to effective isotropic scattering results, and (2) the effect of the index of refraction is important and appears to be accounted for by the $1/n_m^2$ adjustment; however, all the thick experimental data peel off faster than the theory.

For the optically thin radius region, the influence of anisotropic scattering increases the slope of G/ω^{*2} and increases the maximum value of G/ω^{*2}. The influence of the index of refraction is accounted for by the $1/n_m^2$ shift.

In summary, the experimental results agree with theoretical analyses when the optical radii are large. The agreement is not as good for small to moderate optical radii, because the back-scattered radiation becomes sensitive to the shape of the scattering phase function. The increase in slope and maximum value of G/ω^{*2} in the thin and intermediate optical radius regions for anisotropic scattering need to be investigated further. Also, the effects of absorption and finite τ_0^* need to be studied in the thick optical radius region.

Acknowledgments

The authors acknowledge the partial support of the National Science Foundation (Grant No. NSF MEA 8121430 and Grant No. NSF CBT 8501099) for this research.

References

1 Viskanta, R., "Radiation Heat Transfer: Interaction With Conduction and Convection and Approximate Methods in Radiation," *Heat Transfer 1982—Proceedings of the Seventh International Heat Transfer Conference*, Vol. 1, Hemisphere, Washington, D.C., 1982, pp. 103–121.

2 Viskanta, R., "Radiative Heat Transfer," *Progress Chemical Engineering, Series A22*, 1984, pp. 51–81.

3 Crosbie, A. L., and Dougherty, R. L., "Two-Dimensional Isotropic Scattering in a Semi-infinite Cylindrical Medium," *Journal of Quantitative Spectroscopy and Radiative Transfer*, Vol. 20, No. 2, Aug. 1978, pp. 151–173.

4 Crosbie, A. L., and Dougherty, R. L., "Two-Dimensional Linear Anisotropic Scattering in a Semi-infinite Cylindrical Medium Exposed to a Laser Beam," *Journal of Quantitative Spectroscopy and Radiative Transfer*, Vol. 28, No. 2, Aug. 1982, pp. 233–264.

5 Crosbie, A. L., and Dougherty, R. L., "Two-Dimensional Rayleigh Scattering in a Semi-infinite Cylindrical Medium Exposed to a Laser Beam," *Journal of Quantitative Spectroscopy and Radiative Transfer*, Vol. 30, No. 3, Sept. 1983, pp. 255–280.

6 Crosbie, A. L., and Dougherty, R. L., "Two-Dimensional Isotropic Scattering in a Finite Thick Cylindrical Medium Exposed to a Laser Beam," *Journal of Quantitative Spectroscopy and Radiative Transfer*, Vol. 27, No. 2, Feb. 1982, pp. 149–183.

7 Crosbie, A. L., and Dougherty, R. L., "Two-Dimensional Linearly Anisotropic Scattering in a Finite Cylindrical Medium Exposed to a Laser Beam," *Journal of Quantitative Spectroscopy and Radiative Transfer*, Vol. 33, No. 5, May 1985, pp. 487–520.

8 Look, D. C., Nelson, H. F., and Crosbie, A. L., "Anisotropic Two-Dimensional Scattering, Comparison of Experiment With Theory," ASME JOURNAL OF HEAT TRANSFER, Vol. 103, Feb. 1981, pp. 127–134.

9 Look, D. C., and Sundvold, P. D., "Anisotropic Two-Dimensional Scattering, Part II: Finite Depth and Refractive Index Effects," *AIAA Journal*, Vol. 22, No. 4, Apr. 1984, pp. 571–573.

10 Look, D. C., and Sundvold, P. D., "Anisotropic 2-D Scattering 3: The Effects of Incident Laser Wavelength," *Applied Optics*, Vol. 23, No. 1, Jan. 1984, pp. 9–11.

11 Ishimaru, A., Kuga, Y., Cheung, R. L. T., and Shimizu, K., "Scattering and Diffusion of a Beam Wave in Randomly Distributed Scatters," *Journal of the Optical Society of America*, Vol. 73, No. 2, Feb. 1983, pp. 131–136.

12 Ready, J. T., *Effects of High-Power Laser Radiation*, Academic Press, New York, 1971.

13 Van de Hulst, H. C., *Multiple Light Scattering*, Vol. 2, Academic Press, New York, 1980, Chaps. 10 and 14.

14 Hansen, J. E., "Exact and Approximate Solutions for Multiple Scattering by Cloudy and Hazy Planetary Atmospheres," *Journal of Atmospheric Sciences*, Vol. 26, 1969, pp. 478–487.

15 Potter, J. F., "The Delta Function Approximation in Radiative Transfer Theory," *Journal of Atmospheric Sciences*, Vol. 27, 1970, pp. 943–949.

16 Wang, L., "Anisotropic Nonconservative Scattering in a Semi-infinite Medium," *The Astrophysical Journal*, Vol. 174, 1972, pp. 671–678.

17 Sobolev, V. V., *Light Scattering in Planetary Atmospheres*, Pergamon Press, New York, 1975, pp. 158–161.

18 Zuev, V. E., *Propagation of Visible and Infrared Radiation in the Atmosphere*, Wiley, New York, 1974, Appendix 2, p. 371.

19 *CRC Handbook of Chemistry and Physics*, 60th ed., 1979.

20 Brewster, M. Q., and Tien, C. L., "Radiative Transfer in Packed Fluidized Beds: Dependent Versus Independent Scattering," ASME JOURNAL OF HEAT TRANSFER, Vol. 104, 1982, pp. 573–579.

H. Lee
Department of Mechanical Engineering,
University of Minnesota,
Minneapolis, MN 55455
Assoc. Mem. ASME

R. O. Buckius
Department of Mechanical and
Industrial Engineering,
University of Illinois
at Urbana-Champaign,
Urbana, IL 61801
Mem. ASME

Combined Mode Heat Transfer Analysis Utilizing Radiation Scaling

Scaling laws have been formulated to predict the radiant heat flux in anisotropically scattering, one-dimensional planar media [1, 2]. The radiation portion of the problem is reduced to an equivalent nonscattering problem by the scaling. The same scaling laws are applied to problems when radiation is combined with other modes of heat transfer, requiring the solution of the energy equation for a temperature profile. The average incident intensity is accurately scaled by a multilayer approach. Results presented for radiation/conduction and the thermally developing Poiseuille flow problems show very good agreement between exact and scaled solutions for heat fluxes and temperature distributions.

1 Introduction

Although radiation may be the dominant mode of heat transfer in many high-temperature applications, there are important contributions from convection and conduction. The energy equation describes the interaction between the different heat transfer modes. A solution of the energy equation requires the solution of the equation of transfer to determine the contribution of the radiation component. Such solutions are complex even for a simple geometry like the one-dimensional planar, if the details of anisotropic scattering are to be included. Radiation scaling laws have been formulated which greatly simplify the radiation portion of the calculation by reducing a scattering problem to a nonscattering one [1, 2]. These radiation scaling laws and their incorporation into the energy equation are the basis for the present analysis.

The current effort focuses on two heat transfer problems: combined radiation/conduction in one-dimensional planar layers and combined radiation/convection in thermally developing Poiseuille flow. These problems are chosen because they encompass many engineering applications and reflect current research interests. Numerical results for combined radiation and conduction in one-dimensional, planar, isotropically scattering media are given by Viskanta [3]. Radiation/conduction through porous insulations which scatter anisotropically has been the subject of many recent analytical and experimental studies [4–6]. Yuen and Wong [7] present numerical results for heat transfer by radiation and conduction in isotropic and linear anisotropic scattering media as well as in media which do not scatter. Combined radiation/convection results in thermally developing Poiseuille flow for which only the laminar velocity distribution is assumed to be fully developed are given by Chawla and Chan [8] and Mengüc et al. [9]. Yener et al. [10] studied interaction with turbulent flow through a parallel plate channel. References [8–10] consider isotropically scattering media. Published research on similar problems or those concerning different geometries are not included in this brief review.

This work formulates and implements the radiation scaling laws into combined mode analysis to predict heat transfer and temperature distributions. The scaled heat transfer results are obtained by solving the finite differenced energy equation. In the energy equation the radiation contribution is represented by G, the average incident radiation. The scaled energy equation is then only as accurate as the G scaling. The accuracy of G scaling is tested and presented.

Contributed by the Heat Transfer Division and presented at the 23rd National Heat Transfer Conference, Denver, Colorado, August 1985. Manuscript received by the Heat Transfer Division April 29, 1985.

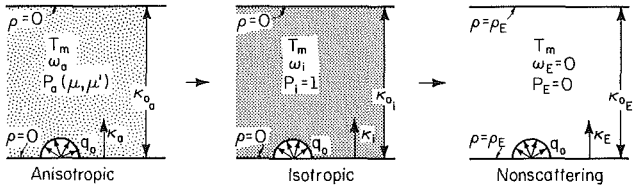

Fig. 1 The scaling diagram

It is the intent of this investigation to study problems in which radiation is an important feature. The presentation is therefore organized to first outline the radiation scaling already presented in [1, 2]. The multilayer solution technique is then discussed. The G scaling results and the radiation/conduction and the Poiseuille flow results from scaled energy equation follow.

2 Formulation

2.1 Radiation Scaling. Scaling is applied to a one-dimensional plane parallel medium between diffuse isothermal walls. The medium absorbs, emits and anisotropically scatters radiant energy. Assuming azimuthal symmetry, the radiant intensity is given by the following form of the equation of transfer

$$\mu\frac{\partial I(\kappa,\mu)}{\partial\kappa}+I(\kappa,\mu)=(1-\omega)I_b(T)+\frac{\omega}{2}\int_{-1}^{1}P(\mu,\mu')I(\kappa,\mu')d\mu' \tag{1}$$

$I(\kappa,\mu)$ is the intensity, κ is the optical depth, μ is the cosine of the polar angle, ω is the single scattering albedo, and $P(\mu,\mu')$ is the single scattering phase function. The medium extends from $\kappa=0$ to $\kappa=\kappa_0$. $I_b(T)$ is the Planck function at the medium temperature. The phase function is expanded into a series of Legendre polynomials

$$P(\mu,\mu')=\sum_{n=0}^{\infty}a_nP_n(\mu)P_n(\mu'),\qquad a_0=1 \tag{2}$$

The coefficients a_n are calculated to fit the Mie theory and $P_n(\mu)$ are the Legendre polynomials of order n. Once the intensity field is obtained with the appropriate boundary conditions, the average incident radiation is given by

$$G(\kappa)=2\pi\int_{-1}^{1}I(\kappa,\mu')d\mu' \tag{3}$$

The radiant heat flux is obtained from

$$q_r(\kappa)=2\pi\int_{-1}^{1}I(\kappa,\mu')\mu'd\mu'. \tag{4}$$

Figure 1 diagrams the reduction of an anisotropically scattering layer to a nonscattering layer in two steps: anisotropic to isotropic, and isotropic to nonscattering. Figure 1 shows an isothermal, anisotropically scattering system between black walls. The variables of an anisotropic scattering system are identified by the subscript a. The boundary at $\kappa=0$ emits a radiosity q_0 as a blackbody. The boundary at $\kappa=\kappa_0$ is cold and therefore does not contribute. Equations (1)–(4) apply directly to the anisotropic system. An anisotropic scattering problem is scaled to an isotropic scattering one by the following transformations [1]

$$\kappa_{0_i}=(1-\omega_a\langle\cos\theta\rangle)\kappa_{0_a} \tag{5a}$$

$$\omega_i=[\omega_a(1-\langle\cos\theta\rangle)]/[1-\omega_a\langle\cos\theta\rangle] \tag{5b}$$

The asymmetry factor $\langle\cos\theta\rangle$ is introduced to represent the anisotropy of the scattering phase function. For the phase function expanded as in equation (2), the asymmetry factor is equal to $a_1/3$. The scaled isotropic problem is shown in Fig. 1 with the subscript i. The medium temperature and the boundaries remain invariant by this scaling. The angular information necessary to describe the intensity field is lost by this scaling. Thus, only the integrated quantities of the intensity, the radiant heat flux, and the average incident radiation are scaled.

The scaling from isotropic to nonscattering takes two possible paths. The transformations are given below and the reduced system is shown in Fig. 1 with the subscript E [2].

Linear

$$\kappa_{0_E}=(1-\omega_i)\kappa_{0_i}:\rho_E=1-\frac{2}{\frac{3}{4}\kappa_{0_i}\omega_i+2} \tag{6}$$

Square root

$$\kappa_{0_E}=\sqrt{1-\omega_i}\kappa_{0_i}:\rho_E=\frac{2}{\omega_i}(1-\sqrt{1-\omega_i})-1 \tag{7}$$

The equivalent wall reflectivity ρ_E is introduced to retain the effect of backscattering in a physically different, nonscattering problem. The linear scaling is the more accurate one for small optical depths and high albedos ($\kappa_{0_i}<0.5$, $\omega_i>0.95$). For all other problems, square root is the proper scaling. See Fig. 5 of [2] for the detailed scaling regimes. As with the first scaling, additional details are lost and it is not possible to accurately scale the directional heat flux.

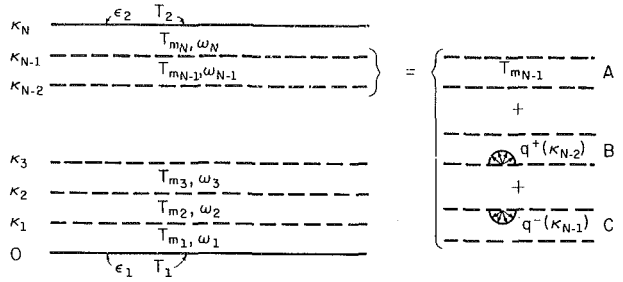

Fig. 2 The multilayer system

2.2 Multilayer Solution Technique. The scaling technique outlined in Section 2.1 is derived and tested for isothermal, homogeneous media. In general, the temperature profile predicted by the energy equation is not uniform, and the scattering particles are unevenly distributed. A multilayer solution technique is developed to solve general radiation problems.

A planar medium is divided into N isothermal and homogeneous sublayers. The layout of a multilayer system is shown in Fig. 2. The boundary at $\kappa=0$ is at temperature T_1 and has an emissivity of ϵ_1. The first layer extends from $\kappa=0$ to $\kappa=\kappa_1$ and is at a uniform temperature T_{m_1} and albedo ω_1. The next layers build on top of the first layer until the top boundary is reached. The boundary at $\kappa=\kappa_N$ is at temperature T_2 and its emissivity is ϵ_2.

Using the $(N-1)$th layer as an example, Fig. 2 also shows the principle of superposition which applies to radiative transfer. Because the equation of transfer (equation (1)) is linear in intensity, an isothermal layer solution is a superposition of three simpler problems: the two boundary incidence problems into a cold medium which are labeled B and C in the figure, and an isothermal emission problem without boundary effects which is labeled A. Depending on the position of a sublayer, the boundary incidences may either be the boundary wall radiosities or the sum of the energies from the adjoining layers. Radiation scaling is applied to each sublayer and the equivalent nonscattering heat flux distribution can be obtained. Thus, the radiative heat flux within the $(N-1)$th layer is composed of the three contributions

$$q_r(\kappa)=q^*_{A_{N-1}}(\kappa)\sigma T^4_{m_{N-1}}+q^*_{B_{N-1}}(\kappa)q^+(\kappa_{N-2})+q^*_{C_{N-1}}(\kappa)q^-(\kappa_{N-1}) \tag{8}$$

Nomenclature

a_n = coefficients of phase function expansion
$\langle\cos\theta\rangle$ = asymmetry factor
D_h = hydraulic diameter = $2L$
$E_n(\kappa)$ = exponential integral function of order n
$G(\kappa)$ = average incident radiation
I = radiant intensity
I_b = Planck function
k = thermal conductivity
L = channel width
N = number of sublayers
N_{cr} = conduction/radiation parameter
Nu = Nusselt number
$P(\mu,\mu')$ = scattering phase function
$P_n(\mu)$ = Legendre polynomial of order n
Pr = Prandtl number
$q(\kappa)$ = heat flux
q_0 = boundary incident radiosity
Re = Reynolds number
T = temperature
T^*_B = nondimensional bulk mean temperature
T_m = medium temperature
$u(\kappa)$ = velocity distribution
U = mean velocity
x = streamwise coordinate
y = transverse coordinate
α = thermal diffusivity
β = extinction coefficient
ϵ = wall emissivity
κ = optical depth = βy
κ_0 = total optical depth = βL
μ = cosine of the polar angle
ξ = dimensionless streamwise coordinate
ρ_E = equivalent reflectivity
σ = Stefan–Boltzmann constant
χ = forward-backward scattering parameter
ω = *single scattering albedo*

Superscripts

* = nondimensional variable
′ = integration variable
\+ = positive κ direction
− = negative κ direction

Subscripts

a = anisotropic scattering
A, B, C = superposition problems (Fig. 2)
c = convection variable
E = equivalent nonscattering
i = isotropic scattering
j = nodes in κ direction
m = medium variable
new = new iteration values
old = old iteration values
r = radiation variable
t = total combined variable

The notation A, B, and C follows the notation in Fig. 2. Superscript * denotes normalization with respect to the emissive power of a reference temperature. The $q^+(\kappa_{N-2})$ and the $q^-(\kappa_{N-2})$ are the interface radiosities directed in the positive and the negative κ direction. $T_{m_{N-1}}$ is the medium temperature. The subscript E is dropped in this and other equations in this section for clarity.

The unknown interface radiosities are obtained explicitly by applying the superposition principle to each layer. The fundamental quantity to conserve when building layers on top of another is the intensity in each direction. However, since the intensity field is no longer accurate, only the directional heat flux is conserved at the interfaces. It is further assumed that the interface radiosities are diffuse since this makes each sublayer consistent with the scaling. The interface radiosity equations for a multilayer system are given below

$$q^+(0) = \epsilon_1\sigma T_1^4 + (1-\epsilon_1)q_{A_1}^{-*}(0)\sigma T_{m_1}^4 + (1-\epsilon_1)q_{B_1}^{-*}(0)q^+(0) + (1-\epsilon_1)q_{C_1}^{-*}(0)q^-(\kappa_1)$$

$$q^-(\kappa_1) = q_{A_2}^{-*}(\kappa_1)\sigma T_{m_2}^4 + q_{B_2}^{-*}(\kappa_1)q^+(\kappa_1) + q_{C_2}^{-*}(\kappa_1)q^-(\kappa_2)$$

$$q^+(\kappa_1) = q_{A_1}^{+*}(\kappa_1)\sigma T_{m_1}^4 + q_{B_1}^{+*}(\kappa_1)q^+(0) + q_{C_1}^{+}(\kappa_1)q^-(\kappa_1)$$

$$q^-(\kappa_2) = q_{A_3}^{-*}(\kappa_2)\sigma T_{m_3}^4 + q_{B_3}^{-*}(\kappa_2)q^+(\kappa_2) + q_{C_3}^{-*}(\kappa_2)q^-(\kappa_3)$$

$$q^+(\kappa_2) = q_{A_2}^{+*}(\kappa_2)\sigma T_{m_2}^4 + q_{B_2}^{+*}(\kappa_2)q^+(\kappa_1) + q_{C_2}^{+*}(\kappa_2)q^-(\kappa_2)$$

$$q^-(\kappa_{N-1}) = q_{A_N}^{-*}(\kappa_{N-1})\sigma T_{m_N}^4 + q_{B_N}^{-*}(\kappa_{N-1})q^+(\kappa_{N-1}) + q_{C_N}^{-*}(\kappa_{N-1})q^-(\kappa_N)$$

$$q^+(\kappa_{N-1}) = q_{A_{N-1}}^{+*}(\kappa_{N-1})\sigma T_{m_{N-1}}^4 + q_{B_{N-1}}^{+*}(\kappa_{N-1})q^+(\kappa_{N-2}) + q_{C_{N-1}}^{+*}(\kappa_{N-1})q^-(\kappa_{N-1})$$

$$q^-(\kappa_N) = \epsilon_2\sigma T_2^2 + (1-\epsilon_2)q_{A_N}^{+*}(\kappa_N)\sigma T_{m_N}^4 + (1-\epsilon_2)q_{B_N}^{+*}(\kappa_N)q^+(\kappa_{N-1}) + (1-\epsilon_2)q_{C_N}^{+*}(\kappa_N)q^-(\kappa_N) \quad (9)$$

The directional radiative heat fluxes like q_A^+ need to be related to the equivalent heat fluxes by recalling that $q_r(\kappa) = q_r^+(\kappa) - q_r^-(\kappa)$. Once a temperature profile is given, the interface radiosities are the only unknowns in this linear system of equations. A banded matrix solver in the IMSL library called LEQT2B is used in computation.

3 G Scaling

Before considering the energy analysis, the basic ideas developed and presented in Section 2 are applied to the average incident radiation G. The average incident radiation is the zeroth moment of the intensity field (equation (3)) and is related to the slope of the radiant heat flux distribution

$$\frac{dq_r}{d\kappa} = (1-\omega)[4\sigma T^4(\kappa) - G(\kappa)] \quad (10)$$

The G scaling from anisotropic to isotropic is shown to be accurate in [1]. Judging from the radiant heat flux distribution comparisons between the exact isotropic and the equivalent nonscattering cases [2], it is inferred that the equivalent nonscattering G scaling is not as accurate.

Equivalent nonscattering G distribution is calculated by first applying the appropriate scaling from equations (6) and (7) to a scattering layer. Then the equation of transfer is solved for the resulting reduced system (Fig. 1)

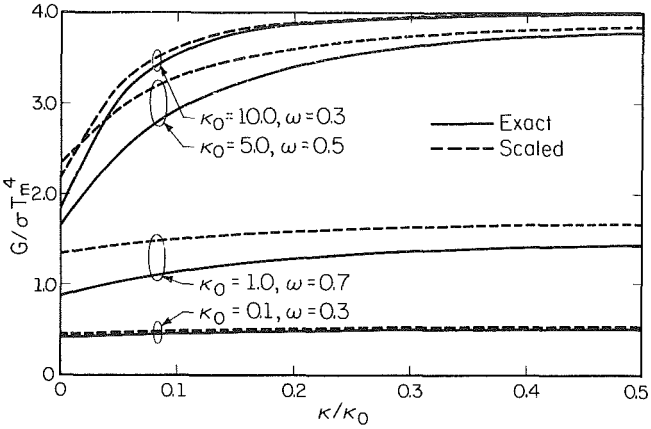

Fig. 3(*a*) Scaling: isothermal emission problem

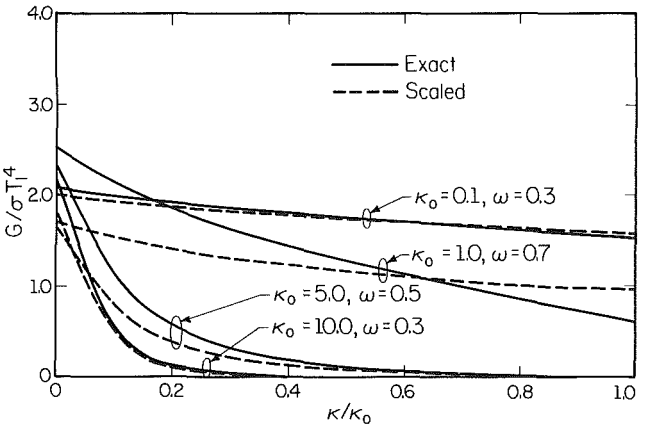

Fig. 3(*b*) G scaling: boundary incidence problem

$$G_E(\kappa_E) = 2\pi\{I^+(0)E_2(\kappa_E) + I^-(\kappa_{0_E})E_2(\kappa_{0_E} - \kappa_E) + I_b(T_m)[2 - E_2(\kappa_E) - E_2(\kappa_{0_E} - \kappa_E)]\} \quad (11)$$

where

$$I^+(0) = A/C \text{ and } I^-(\kappa_{0_E}) = B/C$$

with

$$A = (1-\rho_E)I_b(T_1) + 2\rho_E(1-\rho_E)E_3(\kappa_{0_E})I_b(T_2) + 2\rho_E[1+2\rho_E E_3(\kappa_{0_E})]\left[\frac{1}{2} - E_3(\kappa_{0_E})\right]I_b(T_m)$$

$$B = (1-\rho_E)I_b(T_2) + 2\rho_E(1-\rho_E)E_3(\kappa_{0_E})I_b(T_1) + 2\rho_E[1+2\rho_E E_3(\kappa_{0_E})]\left[\frac{1}{2} - E_3(\kappa_{0_E})\right]I_b(T_m)$$

and

$$C = 1 - 4\rho_E^2 E_3^2(\kappa_{0_E})$$

where $I^+(0)$ and $I^-(\kappa_{0_E})$ are the boundary incident intensities and $E_2(\kappa_E)$ and $E_3(\kappa_{0_E})$ are the exponential integral function of order 2 and 3. I_b represents the Planck function. T_m is again the uniform medium temperature. T_1 and T_2 are the boundary wall temperatures. The equivalent reflectivity is written as ρ_E. The successive substitution method is employed to obtain the isotropic solution [1].

Comparisons between the exact and the scaled G distributions, applying the above equations to the complete single layer, are shown in Fig. 3. In Fig. 3(*a*), a sample of the comparisons for an isothermal emission problem is presented. Results for boundary incidence into a cold medium are presented in Fig. 3(*b*). Both the linear and the square root scalings are utilized in the cases shown. From these and other comparisons, it is concluded that the G scaling is accurate for

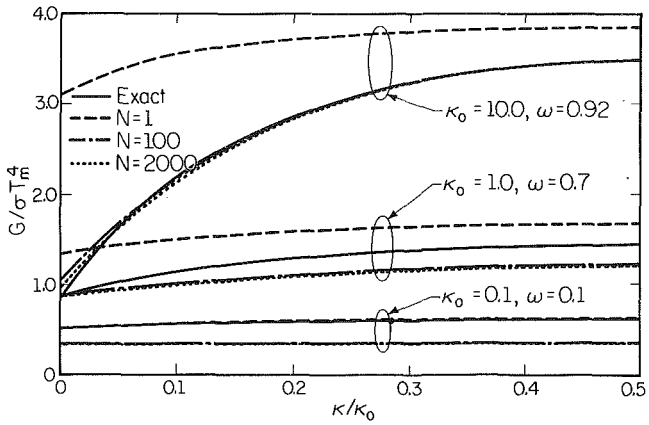

Fig. 4(*a*) Multilayer *G* scaling: isothermal emission problem

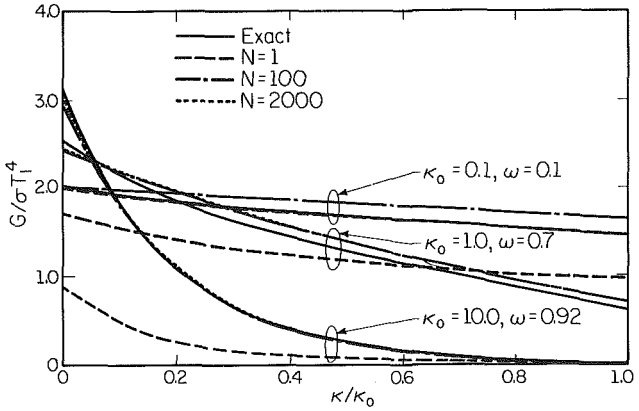

Fig. 4(*b*) Multilayer *G* scaling: boundary incidence problem

low-albedo and small optical depth problems. Large optical depth and low-albedo problems also scale well. The scaling accuracy becomes unacceptable as the albedo increases and scattering dominates the problem.

The effect of scattering is more accurately included by applying the scaling to a multilayer system. That is, the layer is divided into N sublayers and each layer is scaled. The formulation described in Section 2.2 is used to calculate the interface radiosities. The G distribution is then calculated by applying equation (11) within each layer. The results for the isothermal emission and the boundary incidence cases are shown in Fig. 4(*a*) and Fig. 4(*b*), respectively. Exact isotropic G distributions are shown compared with the multilayer scaled solutions where the number of sublayers range from $N=1$ to 2000. For $N=1$, the scaling regime dictates whether the linear or square root scaling is used. The scaling for each layer is linear for the larger N cases presented since the sublayer size is always in the linear regime.

It is evident that the scaling accuracy is greatly improved for the high-albedo cases, especially when the optical depth is large. For the other cases, the accuracy generally improves with larger N. A maximum N of 100 is sufficient to achieve good accuracy. For small optical depth, low-albedo problems, taking a larger number of divisions tended to decrease the scaling accuracy. Little improvement is expected for these cases for which the single layer scaling was already accurate. The phenomenon which is accentuated is the compounding of the error attributable to the assumption of diffuse interface radiosities to build the multilayer solution technique rather than using intensity. Notice, however, that this phenomenon does not dominate those problems for which scattering is important and that the error is bounded as N increases. The $N=2000$ results shown in the figures are virtually indistinguishable from the $N=100$ results. In general, the average incident radiation is accurately predicted by applying the scaling to a multilayer system.

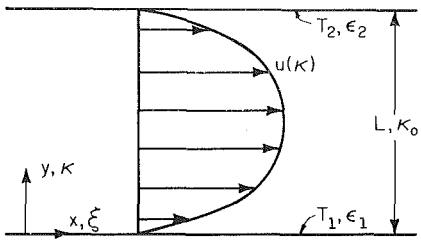

Fig. 5 Physical system for energy analysis

4 Energy Analysis

4.1 Scaled Energy Equation. The physical system of Fig. 5 shows the variables and the coordinates for the energy analysis. The energy equation for the channel flow is written in a nondimensional form

$$u^*(\kappa)\frac{\partial T^*}{\partial \xi}=\frac{\partial^2 T^*}{\partial \kappa^2}-\frac{1}{4N_{cr}}\frac{\partial q_r^*}{\partial \kappa} \tag{12}$$

where

$$u^*=u/U,\ T^*=T/T_1,\ \xi=\frac{x\alpha\beta^2}{U}=\frac{4\kappa_0^2(x/D_h)}{\mathrm{RePr}},$$

$$\kappa=\beta y,\ q_r^*=q_r/\sigma T_1^4,\ \text{and}\ N_{cr}=k\beta/4\sigma T_1^3$$

The medium properties are α, the thermal diffusivity; β, the extinction coefficient; and k, the thermal conductivity. D_h is the hydraulic diameter. The velocity profile is normalized with respect to the mean velocity U. The temperature is normalized to the boundary temperature T_1. ξ is the streamwise coordinate variable and includes the flow information as well as the optical depth. N_{cr} is the conduction/radiation parameter. The viscous dissipation and the streamwise conduction and radiation effects are neglected. The energy equation for radiation/conduction is the same as above with the left-hand side term set equal to zero.

Applying the scaling of equation (5) to equation (7) yields

$$u^*(\kappa_E)\frac{\partial T^*}{\partial \xi_E}=\frac{\partial^2 T^*}{\partial \kappa_E^2}-\frac{1}{4N_{cr_E}}\frac{\partial q_{r_E}^*}{\partial \kappa_E} \tag{13}$$

where

$$\xi_E=(1-\omega_a\langle\cos\theta\rangle)(1-\omega_i)\xi$$

$$\kappa_E=(1-\omega_a\langle\cos\theta\rangle)(1-\omega_i)\kappa$$

$$N_{cr_E}=(1-\omega_a\langle\cos\theta\rangle)(1-\omega_i)N_{cr}$$

The radiation contribution is expressed in terms of the average incident radiation (equation (10)). The albedo is equal to zero for the equivalent nonscattering problem and the scaled energy equation becomes

$$u^*(\kappa_E)\frac{\partial T^*}{\partial \xi_E}=\frac{\partial^2 T^*}{\partial \kappa_E^2}-\frac{1}{N_{cr_E}}\left[T^{*4}(\kappa_E)-\frac{1}{4}G_E^*(\kappa_E)\right] \tag{14}$$

where $G_E^*=G_E/\sigma T_1^4$. Again, equation (14) with $u^*=0$ is the scaled energy equation for conduction/radiation problem.

The multilayered approach developed for radiation in Section 2.2 is appropriate for a finite difference solution of the scaled energy equation. The sublayers for the radiation scaling are the control volumes for the differencing. The uniform layer temperature needed for the radiation calculation represents an energy averaged temperature of the cell. This temperature is assigned to a node point which is at the center of the sublayer. Although nonhomogeneous media can be handled, only homogeneous media are considered in subsequent sections where the scaled energy results are presented.

Table 1 Total heat flux for $\kappa_0 = 1.0$

			$\epsilon = 1.0$		$\epsilon = 0.1$	
N_{cr}	ω	χ	exact	scaled	exact	scaled
1.0	0.0		2.572	2.530	2.221	2.239
		1.0	2.594	2.580	2.157	2.167
	0.5	0.0	2.550	2.538	2.154	2.163
		−1.0	2.512	2.502	2.150	2.159
		1.0	2.602	2.625	2.048	2.048
	1.0	0.0	2.519	2.536	2.047	2.048
		−1.0	2.456	2.469	2.047	2.047
0.1	0.0		0.769	0.726	0.403	0.415
		1.0	0.793	0.779	0.349	0.357
	0.5	0.0	0.750	0.737	0.346	0.353
		−1.0	0.712	0.701	0.343	0.350
		1.0	0.802	0.825	0.248	0.248
	1.0	0.0	0.719	0.736	0.247	0.248
		−1.0	0.656	0.669	0.247	0.247
0.01	0.0		0.567	0.544	0.158	0.161
		1.0	0.600	0.583	0.131	0.134
	0.5	0.0	0.559	0.544	0.130	0.133
		−1.0	0.523	0.510	0.129	0.131
		1.0	0.622	0.645	0.068	0.068
	1.0	0.0	0.539	0.556	0.067	0.068
		−1.0	0.476	0.489	0.067	0.067

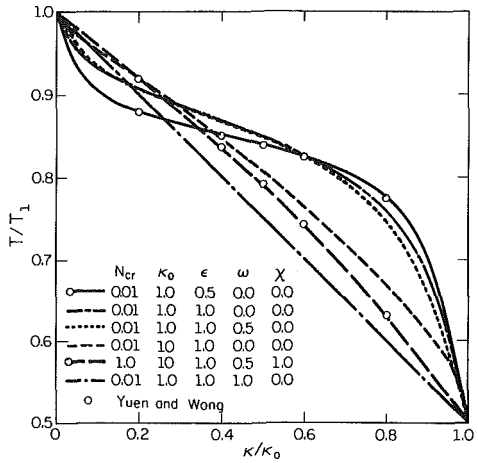

Fig. 6 Radiation/conduction temperature profiles

The scaled equation becomes invalid when $\omega = 1.0$ because conservative scattering uncouples the energy equation from the equation of transfer. The radiation scaling is then inappropriate for the energy equation although it still applies to the radiation solution. For this case, only the conduction or the convection problem, without radiation incorporated, needs to be solved in order to obtain the temperature profile. The scaling is applied to the radiation portion of the problem with the resulting temperature profile.

4.2 Radiation/Conduction Results. The scaled energy equation is discretized for the radiation/conduction in one-dimensional planar layer as

$$T^*_{j-1} - 2T^*_j + T^*_{j-1} - \frac{(\Delta\kappa_E)^2}{N_{cr_E}}[T^{*4}_j - \frac{1}{4}G^*_{Ej}] = 0 \qquad (15)$$

where j corresponds to the κ direction node subscript (see Fig. 5). The temperature and the average incident radiation are normalized with respect to T_1 and the emissive power at T_1, respectively. The discretization is derived from a control volume approach where the energies are balanced within each sublayer [11]. The solution is obtained by iterating from an old temperature distribution to a new one until the convergence criterion is met. An iterative solution is advantageous for a number of reasons. First, the discretized system is much easier to solve even with the required iteration. Second, it allows G_E to be calculated from the multilayer solution technique because the needed temperature distribution is available in the form of an old iteration result. The discretized energy equation (equation (15)) is similar to a conduction problem with a nonlinear source term from the radiation contribution. Rather than iterating with the entire source term from the previous iteration, the source term is linearized as

$$T^{*4}_j - \frac{1}{4}G^*_{Ej} \simeq 4T^{*3}_{j_{\text{old}}} T^*_{j_{\text{new}}} - 3T^{*4}_{j\,\text{old}} - \frac{1}{4}G^*_{Ej_{\text{old}}} \qquad (16)$$

This type of linearization results in a well-formulated and stable system of equations which includes a portion of the radiation contribution directly. With the linearized source term, equation (15) can be rewritten as

$$\left(2 + 4T^{*3}_{j_{\text{old}}}\frac{(\Delta\kappa_E)^2}{N_{cr_E}}\right)T^*_j = T^*_{j-1} + T^*_{j+1} + \frac{(\Delta\kappa_E)^2}{N_{cr_E}}\left\{3T^{*4}_{j_{\text{old}}} + \frac{1}{4}G^*_{Ej_{\text{old}}}\right\} \qquad (17)$$

The results are presented in Table 1 and Fig. 6 for the problem of diffuse, isothermal walls, $T^*_1 = 1.0$, $T^*_2 = 0.5$, $\epsilon_1 = \epsilon_2$. Nonscattering, isotropically scattering, and linear anisotropic media where χ is the forward and the backward scattering parameter are considered. The corresponding asymmetry factors are $\langle\cos\theta\rangle = 0.333$ for $\chi = 1.0$ and $\langle\cos\theta\rangle = -0.333$ for $\chi = -1.0$. The presented cases are compared with the solutions from Yuen and Wong [7]. An absolute temperature difference of less than 0.0001 is used as the convergence criterion. This criterion resulted in heat flux distributions which are uniform to within 0.005 except for the large optical depth of $\kappa_0 = 10.0$. The iteration is started from the conduction temperature profile. The total heat flux is given by

$$q^*_t = \left[-N_{cr}\frac{\partial T^*}{\partial\kappa} + q^*_r\right]_{\kappa=0} \qquad (18a)$$

and the scaled total heat flux is given by

$$q^*_{t_E} = \left[-N_{cr_E}\frac{\partial T^*}{\partial\kappa_E} + q^*_{r_E}\right]_{\kappa_E=0} \qquad (18b)$$

The scaled total heat flux results in Table 1 compare within 5 percent to the exact. The scaled solution is also able to predict the temperature profile accurately (see the comparison between the data points from [7] and the scaled temperatures for the two cases in Fig. 6). The overall accuracy is excellent.

The effect of radiation on the heat transfer and the temperature profile is discussed from the scaled solutions. Figure 6 shows the linear temperature profile for the $\omega = 1.0$ case, which is exactly the result for a pure conduction case

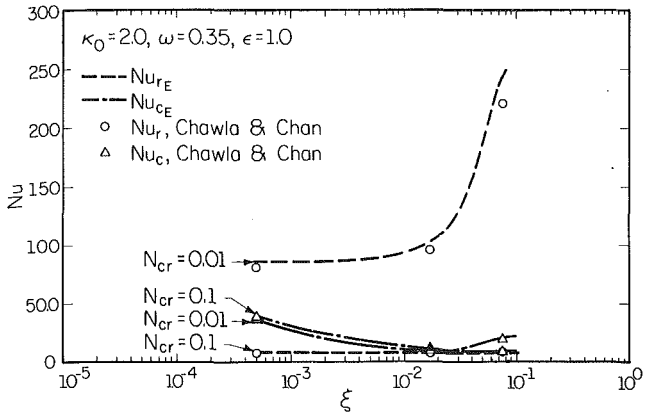

Fig. 7 Effect of radiation/conduction parameter on Nusselt number

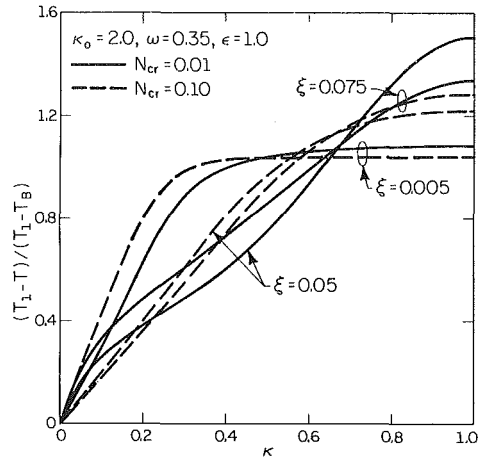

Fig. 8 Effect of radiation/conduction parameter on temperature profiles

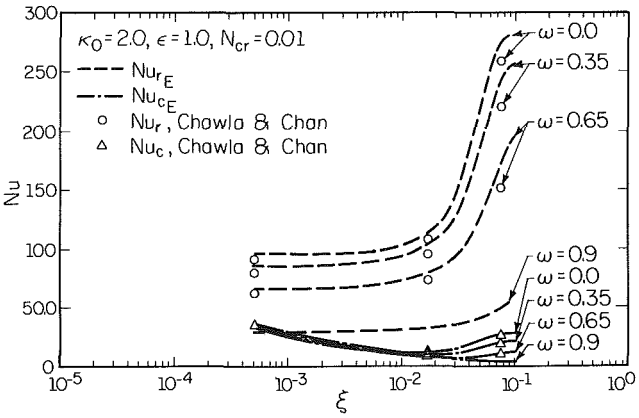

Fig. 9 Effect of albedo on Nusselt number

($N_{cr} \to \infty$). The two profiles for $\kappa_0 = 10.0$ show that the optically thick limiting problem for which the diffusion approximation is often applied is indeed similar to a conduction problem. Of these two, the profile for a smaller $N_{cr} = 0.01$ shows much more nonlinearity. Temperature profiles for small optical depth, the three cases of $\kappa_0 = 1.0$ at $N_{cr} = 0.01$, show pronounced nonlinearity. There is however no temperature slip at the walls with conduction. The effect of wall emissivity on the temperature profile is seen by comparing $\epsilon = 0.5$ and $\epsilon = 1.0$ cases for $\omega = 0.0$. The $\epsilon = 0.5$ shows steeper temperature gradients at the walls while becoming very flat for the middle part of the layer. The effect of albedo compares the $\omega = 0.0$ case with the $\omega = 0.5$ case. Only a small effect is noticed. It is hard to draw conclusions on the effect of anisotropy from the temperature profiles presented.

Table 1 shows that the anisotropy has a definite effect on the combined heat flux. Backward scattering always decreases the total heat flux. The effect of anisotropic scattering is more pronounced for the larger emissivity and also as the albedo increases. It is seen earlier that for smaller emissivity, the temperature profile shows larger gradients at the walls. However, the overall effect of a smaller emissivity is to reduce the total heat flux.

4.3 Radiation/Convection in Thermally Developing Poiseuille Flow. Results are presented for the thermally developing Poiseuille flow problem shown in Fig. 5. The fully developed laminar velocity profile is

$$u^* = u/U = 6\left[\frac{\kappa}{\kappa_0} - \left(\frac{\kappa}{\kappa_0}\right)^2\right] \tag{19}$$

The boundary conditions for solving the energy equation given in Section 4.1 are

$$T(0, \xi) = T(\kappa_0, \xi) = T_1 \text{ for } \xi > 0$$
$$T(\kappa, 0) = T_0 = 0 \text{ for } 0 < \kappa < \kappa_0$$

The walls are gray and diffuse reflecting with emissivities of $\epsilon_1 = \epsilon_2 = \epsilon$. Only isotropic scattering media are considered. Solving the energy equation yields the temperature profile. The Nusselt number is defined as

$$\mathrm{Nu}_t = \frac{\kappa_0}{2N_{cr}(T_1^* - T_B^*)}\left[-4N_{cr}\frac{\partial T^*}{\partial \kappa} + q_r^*\right]_{\kappa=0} = \mathrm{Nu}_c + \mathrm{Nu}_r \tag{20}$$

where the bulk mean temperature is defined as

$$T_B^* = \left[\int_0^L u(y)T(y)dy\right] \Big/ \left[T_1 \int_0^L u(y)dy\right] \tag{21}$$

The scaled energy equation (equation (14)) is solved with the velocity profile in the scaled equivalent domain as

$$u^*(\kappa_E) = 6[(\kappa_E/\kappa_{0_E}) - (\kappa_E/\kappa_{0_E})^2] \tag{22}$$

The boundary conditions become

$$T(0, \xi_E) = T(\kappa_{0_E}, \xi_E) = T_1 \text{ for } \xi_E > 0$$
$$T(\kappa_E, 0) = T_0 = 0 \text{ for } 0 < \kappa_E < \kappa_{0_E}$$

The equivalent Nusselt number is calculated by

$$\mathrm{Nu}_{t_E} = \frac{\kappa_{0_E}}{2N_{cr_E}(T_1^* - T_B^*)}\left[-4N_{cr_E}\frac{\partial T^*}{\partial \kappa_E} + q_{r_E}^*\right]_{\kappa_E = 0}$$
$$= \mathrm{Nu}_{c_E} + \mathrm{Nu}_{r_E} \tag{23}$$

Computationally, this radiation/convection problem builds on the radiation/conduction problem. Discretization in the κ_E direction across the channel is taken exactly the same way as in Section 4.2. Downstream differencing utilizes a first-order fully implicit scheme. Differencing in the ξ_E direction is not as accurate as in the κ_E direction but the scheme is stable. The source term from radiation is again linearized by equation (16). The iteration seed at a new ξ_E step is obtained by solving the convection only problem. This seems to be a logical choice because the energy equation neglects streamwise radiation effect.

The downstream marching technique by the iterative fully implicit method is time consuming and inaccurate, especially far downstream of this numerically stiff problem. But when small time steps are taken, the accuracy is good as compared with the numerical solution presented by Chawla and Chan [8] who use the method of collocation. As the Nusselt number and the temperature profiles are discussed, the accuracy of the scaled solutions is also shown.

The first effect to discuss is that of the radiation/conduction parameter N_{cr}. Figure 7 shows the comparison for Nu_r and Nu_c with the data points from [8]. It also shows that for $N_{cr} = 0.1$, the total Nusselt number follows the same trend

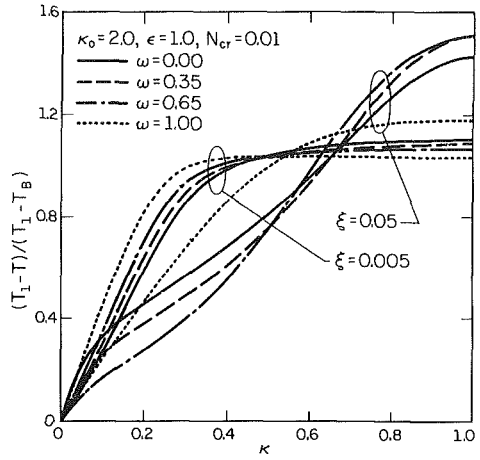

Fig. 10 Effect of albedo on temperature profiles

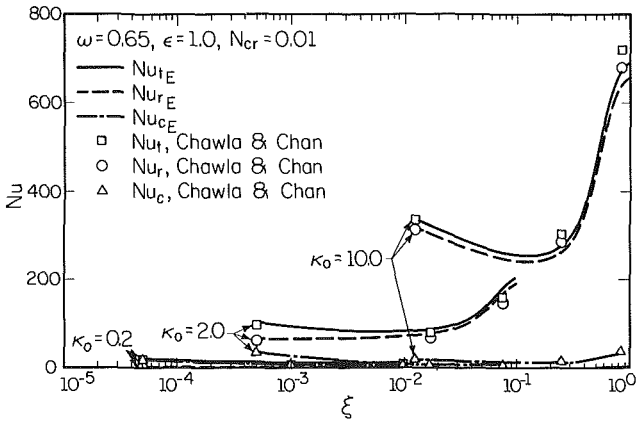

Fig. 11 Optical depth effect on Nusselt number

reported for the pure convection case, that is, it decreases downstream to an asymptotic value. Larger N_{cr} cases are not included in the figure because they are very similar to the $N_{cr}=0.1$ case. For the radiation dominant problem of $N_{cr}=0.01$, not only is the radiation an overwhelming contributor to the total Nusselt number, but Nu_t decreases at first to a minimum but then increases beyond this point. This behavior is pointed out not only by [8, 9], but also by [12] for circular tube flow problems. The effect of radiation for $N_{cr}=0.01$ is further illustrated in Fig. 8. The temperature profiles are in general agreement with Chawla and Chan [8] who present the same results for $\omega=0.0$. It is seen that for $N_{cr}=0.1$, the profiles do appear to be reaching a similar asymptotic profile when the temperature is normalized with respect to the bulk mean temperature. No such similarity is observed for the $N_{cr}=0.01$ case.

It is concluded that the radiation dominant case is the most interesting and pertinent for studying the effect of radiation in this problem. The effect of albedo is shown for $N_{cr}=0.01$ in Fig. 9. The Nu_r and Nu_c for the albedos of 0., 0.35, and 0.65 are compared with Chawla and Chan's numerical results. The case of $\omega=0.9$ is shown to illustrate the effect of high albedo even though [8] does not present results with which to compare. The scaled Nu results consistently overpredict Nu_r. As albedo increases Nu_r drops drastically, reducing the total heat flux. Together with the convective Nu_c, the total Nu_t does go through a minimum and then increases further downstream. But this effect is diminished for higher albedos. In fact, for $\omega=1.0$ the total Nu is close to the shown Nu_c of $\omega=0.9$ and it is precisely the Nu for pure convection. The albedo effect of the developing temperature profile is shown in Fig. 10 for the same cases as in Fig. 9. The figure presents the positions $\xi=0.005$ and $\xi=0.05$. The $\omega=1.0$ profile is same as the pure convection profile. The effect of increasing the albedo is to initially raise the temperature near the walls while flattening the profile at the center. Further downstream, the profiles become steeper as albedo increases. Although not indicated in the figure, the $\omega=0.0$ cases were compared against those shown by Chawla and Chan and the comparisons are very favorable.

Lastly, the effect of transverse optical depth is shown in Fig. 11. For $N_{cr}=0.01$, $\kappa_0=0.2$, 2.0, and 10.0 are shown. The radiation contribution for the small optical depth is negligible. The convective contribution remains roughly the same order of magnitude as the optical depth increases. The radiation Nu_r increases noticeably as κ_0 increases. The peculiar phenomenon of increasing total Nusselt number downstream is more pronounced for $\kappa_0=10.0$.

5 Conclusions

Radiation scaling is applied to the energy equation, which is solved by a finite difference technique. This allows for the use of the multilayer solution technique developed for radiation. The multilayer technique is important because it improves the G scaling accuracy. The scaled results for radiation/conduction are presented for one-dimensional planar layer problems. Heat flux and the temperature distributions are predicted accurately. The results for the thermally developing Poiseuille flow are also shown to follow the trends previously shown by other workers.

Acknowledgments

This work was supported in part by the National Science Foundation under Grant No. MEA 81-09250.

References

1 Lee, H., and Buckius, R. O., "Scaling Anisotropic Scattering in Radiation Heat Transfer for a Planar Medium," ASME JOURNAL OF HEAT TRANSFER, Vol. 104, 1982, pp. 68–75.

2 Lee, H., and Buckius, R. O., "Reducing Scattering to Nonscattering Problems in Radiation Heat Transfer," *Int. J. Heat Mass Transfer*, Vol. 26, No. 7, 1983, pp. 1055–1062.

3 Viskanta, R., "Heat Transfer by Conduction and Radiation in Absorbing and Scattering Materials," ASME JOURNAL OF HEAT TRANSFER, Vol. 87, Feb. 1965, pp. 143–150.

4 Kinoshita, I., Kamiuto, K., and Hasegawa, S., "Study of Simultaneous Conductive and Radiative Heat Transfer," *Proc. 7th Int. Heat Transfer Conf.*, Munich, West Germany, Paper No. R9, Sept. 1982.

5 Kinoshita, I., Miyoshi, Y., Kamiuto, K., and Hasegawa, S., "Fundamental Study of Multilayer Insulation Systems for High Temperatures," *Proc. ASME-JSME Thermal Engineering Joint Conf.*, Honolulu, HI, Mar. 1983.

6 Houston, R. L., and Korpela, S. A., "Heat Transfer Through Fiberglass Insulation," *Proc. 7th Int. Heat Transfer Conf.*, Munich, West Germany, Paper No. R8, Sept. 1982.

7 Yuen, W. W., and Wong, L. W., "Heat Transfer by Conduction and Radiation in a One-Dimensional Absorbing, Emitting and Anisotropically-Scattering Medium," ASME JOURNAL OF HEAT TRANSFER, Vol. 102, May 1980, pp. 303–307.

8 Chawla, T. C., and Chan, S. H., "Combined Radiation Convection in Thermally Developing Poiseuille Flow With Scattering," ASME JOURNAL OF HEAT TRANSFER, Vol. 102, 1980, pp. 297–302.

9 Mengüc, M. P., Yener, Y., and Özisik, M. N., "Interaction of Radiation and Convection in Thermally Developing Laminar Flow in a Parallel-Plate Channel," ASME Paper No. 83-HT-35.

10 Yener, Y., Shahidi-Zandi, B., and Özisik, M. N., "Simultaneous Radiation and Forced Convection in Thermally Developing Turbulent Flow Through a Parallel-Plate Channel," in: *Fundamentals of Thermal Radiation Heat Transfer*, (HTD-Vol. 40), T. C. Min and J. L. S. Chen, eds., ASME Winter Annual Meeting, 1984.

11 Patankar, S. V., *Numerical Heat Transfer and Fluid Flow*, McGraw-Hill, New York, 1980.

12 Azad, F. H., and Modest, M. F., "Combined Radiation and Convection in Absorbing, Emitting and Anisotropically Scattering Gas-Particulate Tube Flow," *Int. J. Heat Mass Transfer*, Vol. 24, No. 10, 1981, pp. 1681–1698.

The Formulation of Spray Combustion Models: Resolution Compared to Droplet Spacing

W. A. Sirignano
Department of Mechanical Engineering,
University of California,
Irvine, CA 92717
Mem. ASME

Formulations of the governing equations for burning air/fuel spray mixtures are discussed. The subsystem of equations describing liquid properties is formulated in three ways: Eulerian description, Lagrangian description, and probabilistic or distribution function description. The relationships among these approaches and the relative advantages and disadvantages are discussed. The reduction of numerical error, the ability to resolve multivalued solutions, and the ability to achieve resolution a scale smaller than droplet spacing lead to a preference of the Lagrangian method over the Eulerian method. However, when resolution is desired on a scale smaller than the average droplet spacing, the location of each droplet is known only in a statistical manner. The advantages of a probabilistic formulation in this case are evaluated.

I Introduction

The problem of spray combustion is of vital importance to practical combustors. It is mandatory to have reliable models of the relevant mechanical, physical, and chemical systems in order to achieve the predictive capability desired by the practicing combustion engineer and to acquire the understanding and insights sought by the combustion scientist.

In any review paper on the subject of spray combustion, complete coverage of the contributions cannot be presented on account of the limitations of times and expertise of any author. In this paper, which was an invited review at the 1984 ASME Winter Annual Meeting, the author does not even attempt to cover all material of interest to him since he has recently published an extensive review [1] on fuel droplet vaporization and spray combustion. Herein, the emphasis will be placed on the two-phase flow models that form the basis for computation.

An important factor for spray combustion calculations is the vaporization rate of individual droplets. Most of the existing work does not completely account for the effect of neighboring droplets on the rates of heat and mass transport and vaporization for any given droplet. There are two major ways in which these rates are affected. Firstly, the ambient gas properties just outside the film or boundary layer surrounding each droplet are affected by neighboring droplets since the gas exchanges mass, momentum, and energy with those droplets. Secondly, the Nusselt number or Sherwood number (or equivalently the characteristic length scales) is affected by the presence of the other droplets. The former phenomenon has been considered widely but the latter phenomenon has received limited attention [1–7]. The results of the spray calculations can be strongly related to the details of the vaporization model [8–15]. This is especially true in typical combustion situations where the ambient gas temperature is high and the vaporization rate is so high that droplet lifetimes and droplet heating times are of the same order of magnitude. It is noteworthy therefore that one should be very suspect of empirical spray vaporization based upon experimental data obtained in lower temperature ranges. The issues related to the vaporization rate of individual droplets will not be further discussed here.

In this paper, we shall discuss various approaches to formulating the system of differential equations that governs the spray and gas behavior in a coupled manner. Some comments will also be made about numerical methods of solution. The concept of treating the droplet properties as if they were continuous in the same domain as the gaseous properties will be discussed. This conceptual approach is useful when we are interested in resolving gas and liquid properties on a scale that is large compared to the average spacing between droplets. Here a droplet property at a point in space and time represents the average value over many droplets in a neighborhood of that point. An alternative approach is to track individual droplets and to calculate the properties for each droplet in the domain of interest. Obviously, this approach is useful when we are interested in resolution on a scale smaller than the average distance between droplets.

Several examples of such situations, where resolution must be finer than the droplet spacing, can be cited. Firstly, in the ignition of sprays by sources which are hot bodies or jets of hot gases, a thermal layer develops with time at the edge of the spray bordering the ignition source. Typically, the thermal layer reaches a thickness of a few millimeters at the end of the ignition time delay for a hydrocarbon fuel spray at atmospheric and near-stoichiometric conditions. For droplets of the order of 50–100 μm in diameter and near-stoichiometric mixtures, that thermal layer thickness is only a very few droplet spacings. A second example concerns a laminar flame propagation through a spray. For reasonably volatile fuels or for small droplets, the fuel vapor content in the mixture ahead of the flame can be sufficiently great to sustain a flame which would be a few millimeters in thickness. The droplets passing through this flame will heat and vaporize rapidly augmenting the combustion of the prevaporized fuel. Again, the thickness of the prevaporized fuel flame is a few droplet spacings so that fine-scale resolution with inherent unsteadiness is required. Another example involves group combustion of spray as defined by Chiu and co-workers [16–18]. In the limiting case of group combustion, a case of external sheath combustion results where only the droplets in a thin sheath or layer at the edge of a group of droplets are vaporizing. This layer regresses toward the interior of the sheath. Under proper conditions, this layer is only a few droplet spacings thick.

In each of the above examples, the results depend upon the initial conditions of the droplets including location, velocity, diameter, temperature, and composition. In a real spray these conditions will not be known exactly; only a distribution or probability function can be assigned. However, once we know the initial conditions for the droplets we can proceed to solve the problem in a deterministic fashion.

In Section II, we shall consider a two-continuum formulation wherein the gas properties and the droplet properties are

Contributed by the Heat Transfer Division for publication in the JOURNAL OF HEAT TRANSFER. Manuscript received by the Heat Transfer Division April 29, 1985. Paper No. 84-WA/HT-26.

each described by equations in the Eulerian form. This Eulerian–Eulerian form is not useful when resolution is desired on a scale as small as or smaller than the average distance between droplets. In Section III, we examine an Eulerian–Lagrangian approach wherein the gas properties are formulated in an Eulerian manner and the droplet properties are given in a Lagrangian formulation. We shall see that such a formulation is useful over a wide range of resolution. However, when resolution over a very fine scale compared to average droplet spacing is required, the practical problem becomes probabilistic rather than deterministic since we do not know exactly where each droplet is at each instant of time. In Section IV, a probabilistic formulation and its relationships with other formulations are discussed. This method also allows for a wide range of resolution since the probability density function (pdf) can be considered to give the number of droplets found in the smallest volume of resolution when the scale of resolution is very large compared to the average distance between droplets. When the resolution scale is very fine, the pdf shall be considered as the probability of finding one droplet in that smallest volume. Usually, the pdf approach has been used as a basis for analysis which yields other formulations that are employed for final solution of the spray behavior. In Section V, we discuss direct solution using the probabilistic formulation in cases where resolution on a very fine scale is desired. Concluding remarks are given in Section VI.

II Eulerian–Eulerian Formulation

The describing equations for a vaporizing and reacting spray can be obtained by a standard control volume approach which accounts for the fluxes of mass, momentum, and energy for the gas phase and also for the liquid phase through entering and exiting the control volume. Unsteady storage terms in the volume, exchanges of mass, momentum, and energy between the phases, and effects of chemical reaction are considered in order to balance the equations. Species conservation equations are written for each of the gas-phase species via the same control volume approach. Under the assumption that coalescence and breakup of droplets are insignificant after the initial atomization period, droplet numbers are conserved and the control volume method yields a droplet number continuity equation. The continuity equations for droplet number density and for droplet distribution function in this paper are formulated such that droplets are counted even after the radius becomes negligible or zero. If compared to experimental data, renormalization is therefore necessary since only droplets of certain minimum radii can be counted experimentally.

The equations may be derived in one, two, or three space dimensions in a steady or unsteady form. The gas-phase and the droplet properties are considered to be continuous in space and time. This implies that the properties at any point are the average values over some neighborhood of that point. The size of that neighborhood is much larger than the average spacing between droplets. This averaging method allows for the superposition of a continuous gas field and a continuous liquid droplet field. The initial conditions could be specified in a locally monodisperse fashion. This means that at each point in space one initial droplet size is specified. Since the equations do not allow for multivalued solutions, the spray will remain locally monodisperse. If desired, a polydisperse spray may be represented by the superposition of several monodisperse sprays. This is equivalent to approximating a continuous size distribution function by several delta functions. When this is done, we must formulate equations for the conservation of mass, momentum, energy, and droplet number for each distinct class of droplet as determined by the initial size.

In our formulation, we shall examine a multidimensional, unsteady situation for a dilute spray. In this spray, the volume of liquid contained in a volume of the smallest resolution is very small compared to that volume. Realize that in a combustion situation the mass of air required is at least one order of magnitude larger than the mass of fuel required. Furthermore, except for near-critical or supercritical situations, the liquid density is one to three orders of magnitude greater than the gas density. We will not use a void fraction in the equations for this reason.

The droplet continuity equation becomes

$$\frac{\partial n^{(k)}}{\partial t}+\frac{\partial (n^{(k)} u_{l_j}{}^{(k)})}{\partial x_j}=0 \tag{1}$$

where $n^{(k)}$, $u^{(k)}{}_{lj}$, t, and x_j are the droplet number density, the droplet velocity component in the j direction, the time coordinate, and the spatial coordinate in the j direction, respectively. The superscript k represents the integer index for the class of droplets as determined by the initial size. For a monodisperse spray $k=1$ while for a polydisperse spray $k=1,2,\ldots,N$ where N is chosen to give a reasonable fit to the distribution.

After some manipulation, the other conservation equations for the droplet properties will yield a droplet size equation, a droplet drag equation, and a droplet energy equation. The droplet size equation is

$$\frac{\partial R^{(k)}}{\partial t}+u^{(k)}{}_{l_j}\frac{\partial R^{(k)}}{\partial x_j}=\frac{-\dot{m}_j{}^{(k)}}{4\pi (R^{(k)})^2 \rho_l} \tag{2}$$

where $R^{(k)}$ is the instantaneous droplet radius, ρ_l is the liquid density, and $\dot{m}_j{}^{(k)}$ is the mass vaporization rate of a droplet. This rate is determined by some algorithm based upon a physical model of the behavior of the field in the liquid droplet and in the surrounding gas film. See [1, 8–15].

The droplet drag equations are given as

$$\frac{\partial u_{l_i}{}^{(k)}}{\partial t}+u_{l_j}{}^{(k)}\frac{\partial u_{l_i}{}^{(k)}}{\partial x_j}=F_i{}^{(k)} \tag{3}$$

where $F_i{}^{(k)}$ is the ith component of drag force on the droplet per unit mass of droplet. This drag can be modeled based upon some empirical evidence in the literature. (See [1].)

The liquid-phase energy equation may be formulated as

$$\rho_l \frac{\partial e_l{}^{(k)}}{\partial t}+\rho_l u^{(k)}{}_{l_j}\frac{\partial e_l{}^{(k)}}{\partial x_j}=\frac{3}{R^{(k)}}\lambda_l \frac{\partial T_l{}^{(k)}}{\partial r}\Big)_s \tag{4}$$

where $e_l{}^{(k)}$ is the average thermal energy per unit mass in the liquid. (Note that temperature gradients will exist in the liquid and the temperature variation can be determined by a solution of the heat diffusion in the liquid phase.) λ_l is a liquid thermal conductivity, $T_l{}^{(k)}$ is a liquid temperature, r is radial position in the droplet, and s is an index indicating a value at the droplet surface. The heat flux term should be taken as an average value over the surface.

The gas-phase continuity equation states that

$$\frac{\partial \rho}{\partial t}+\frac{\partial}{\partial x_j}(\rho u_j)=\sum_{k=1}^{N} n^{(k)} \dot{m}_v{}^{(k)} \tag{5}$$

where ρ and u_j are the gas density and gas velocity component in the j direction. The species continuity equations are written as

$$\frac{\partial}{\partial t}(\rho Y^{(l)})+\frac{\partial}{\partial x_j}(\rho u_j Y^{(l)})-\frac{\partial}{\partial x_j}\Big(\rho D \frac{\partial Y^{(l)}}{\partial x_j}\Big)$$
$$=\sum_{k=1}^{N} n^{(k)} \dot{m}_v{}^{(k,l)}+\dot{w}^{(l)} \tag{6}$$

Here $Y^{(l)}$ is the mass fraction of species l, D is a mass diffusivity (which is assumed to be the same for all species), $\dot{m}_v^{(k,l)}$ is the mass vaporization rate for the lth species (which is zero if that species is not one of the components of the fuel blend), and $\dot{w}^{(l)}$ is the mass chemical reaction rate for the lth species

(which is nonzero if that species is a reactant or a product). Note that

$$\dot{m}_v^{(k)} = \sum_{l=1}^{\hat{N}} \dot{m}_v^{(k,l)} \tag{7}$$

where $\hat{N}$ is the number of different species present. The $\hat{N}$ species equations can be summed to yield the continuity equation; therefore, only $N-1$ of the equations are independent.

The gas momentum equation can be formulated as:

$$\rho \frac{\partial u_i}{\partial t} + \rho u \frac{\partial u_i}{\partial xj} + \frac{\partial p}{\partial x_i} - \frac{\partial \tau_u}{\partial x} = \sum_{k=1}^{N} n^{(k)} \dot{m}_v^{(k)} [u_{l_i}^{(k)} - u_i]$$

$$- \sum_{k=1}^{N} \frac{4\pi}{3} \rho_l [R^{(k)}]^3 n^{(k)} F_i^{(k)} \tag{8}$$

Here p is the pressure and τ_{ij} is the viscous stress tensor.

The gas energy equation may be written as follows:

$$\rho c_p \frac{\partial T}{\partial t} + \rho u_j c_p \frac{\partial T}{\partial x_j} - \frac{\partial}{\partial x_j}\left(\lambda \frac{\partial T}{\partial x_j}\right) - \frac{\partial p}{\partial t}$$

$$= \sum_{k=1}^{N} \dot{w}^{(l)} Q^{(l)} - \sum_{k=1}^{N} n^{(k)} \dot{m}_v^{(k)} [h - h_s + L^{(k)}_{\text{eff}}] \tag{9}$$

where T, c_p, λ, and h are the gas temperature, specific heat, thermal conductivity, and enthalpy outside of the gas films surrounding droplets. h_s is the gas enthalpy at the droplet surface; $Q^{(l)}$ is the energy released in combustion of the lth component (if that component is not a fuel, $Q^{(l)}$ is zero); and $L^{(k)}_{\text{eff}}$ is an effective latent heat of vaporization which accounts for the heat conducted into the surface of the droplet. This form of the energy equation is based upon a neglect of kinetic energy, viscous dissipation, radiation, and transport of energy via mass diffusion of species with different specific heats. Part of this heat is necessary for vaporization and the remainder is stored in the liquid interior.

It can be shown that

$$L^{(k)}_{\text{eff}} = L^{(k)} + 4\pi\lambda_l \frac{\partial T_l^{(k)}}{\partial r}\Big)_s (R^{(k)})^2 / \dot{m}_v^{(k)} \tag{10}$$

where $L^{(k)}$ is a latent heat of vaporization for the fuel. For a single-component fuel, $L^{(k)}$ may be regarded as a constant independent of droplet size while for a multicomponent fuel, it depends upon the relative vaporization rates and the latent heat of each component. In that case, it implicitly can be time and size dependent. For proper evaluation of that heat flux, a droplet heating and vaporization model is required. See [1, 8–15].

An ideal gas law may be written as

$$p = \rho R T \tag{11}$$

where the gas "constant" R depends upon the local mixture composition.

The above-described model is based upon diffusion governed by Fick's Law and laminar flows. Generalizations for other situations have been presented in the literature. The chemical rate terms may be modeled here via single-step or multistep kinetics as preferred. The formulation also assumes that the time for energy and mass transport across the gas film surrounding a droplet is negligible.

Equations (1) through (4) represent $4N$ equations governing the liquid properties $n^{(k)}$, $R^{(k)}$, $u_{l_i}^{(k)}$, and $e_l^{(k)}$. Of course, since equation (3) is a vector equation, we really have $6N$ scalar equations. Equation (4) is, however, never actually employed in the form presented. In the special case where droplet temperature is assumed to be uniform in the droplet, we consider that $e_l^{(k)}$ is directly proportional to $T_l^{(k)}$ and that the heat flux term on the right-hand side of equation (4) is not represented in terms of a temperature gradient at the surface but rather as the difference between the heat flux coming from the gas to the surface and the rate of energy conversion associated with the vaporization process. In general, for combustion applications where heating rates are rapid, the uniform temperature model is not recommended. In the case where temperature gradients in the droplet are taken into account, it is not useful to evaluate $e_l^{(k)}$ which is the average liquid thermal energy per unit mass. Therefore, equation (4) is not employed. Rather, the equations governing energy transport in the film surrounding the droplet and in the liquid interior are solved as discussed in [1, 8–15].

Equations (5), (6), (8), and (9) represent a subsystem of $5 + (\hat{N}-1)$ partial differential equations governing scalar gaseous properties. They can be solved numerically via finite difference schemes on an Eulerian mesh by explicit, implicit, block implicit, or split operator techniques. In general, the problem has many time and space scales and it is difficult to give a general preferred method for integration. Note that in the one-dimensional case with low flow Mach number, the momentum equation (8) may be replaced by a uniform pressure assumption. In confined flows, the pressure may still be time varying. An example of this type of calculation is given in [19].

The subsystem of equations governing the droplet properties is also solved numerically by finite difference schemes on an Eulerian mesh. The numerical scheme might introduce artificial diffusion into the results. Although the same effect may be present with the gas properties, it is less severe there since it is superimposed upon real diffusion effects. Since no physical diffusion of liquid properties occurs (the behavior is totally hyperbolic), artificial or numerical diffusion is more bothersome there. An example of a troublesome situation is one where a sharp boundary exists between a region where fuel spray and gas occur and a region where only gas exists. Numerical errors could lead to a diffusion of liquid properties across these boundaries.

In this two-continuum approach, droplet properties represent averages in neighborhoods so that only single-valued solutions should be allowed. In practice, however, multivalued solutions are possible and interesting. This occurs when we have two or more clouds of droplets (all in the same class as determined by initial size), with each cloud following different paths which cross in space and time. Realize that, since the droplets are small in size compared to the average spacing between droplets, the droplet clouds may cross paths with each other with no or negligible collisions. In general, the droplets in different clouds will have different properties such as size and temperature, even if initially they were of the same size and same temperature. Therefore, the two or more clouds on intersecting paths should have different temperatures, different diameters, and different velocities. Such physically meaningful multivalued solutions are lost due to a combination of the averaging of properties and the large numerical diffusion which occurs when the two clouds approach each other creating large gradients of the averaged properties. Note that most finite difference schemes are designed to provide unique solutions to partial differential equations and would automatically suppress multivalued evolutions.

The two-continuum approach is not able to resolve phenomena on the scale of the droplet spacing since averaging occurs over a distance that is large compared to that spacing.

On account of these problems with an Eulerian–Eulerian formulation, the approach of the next section becomes worthy of attention.

III Eulerian–Lagrangian Formulation

An alternative approach [20–22] has received attention in recent years. The gas-phase subsystem of equations (5)–(11) remains the same as in the previous section. The droplet prop-

erties are no longer governed by equations (1)–(4), however. Instead, ordinary differential equations are written which describe the change in droplet properties along the droplet path.

We have the choice of following every individual droplet which is representative of a fixed number of droplets in a neighborhood. It is assumed here that initial conditions are continuous so that any droplet which begins in the neighborhood of some given droplet remains in the neighborhood of that droplet as they both move. On account of this type of calculation which involves a fixed number of droplets, there is no need to develop an equation for the conservation of droplet numbers; droplet numbers are automatically conserved.

It is necessary to track the droplets as they move. The trajectory is given by

$$\frac{dx_{li}^{(k)}}{dt} = u_{li}^{(k)} \tag{12}$$

where $x_{li}^{(k)}$ is the position of the center of the droplet in the kth size class. In general, the paths will not pass through mesh points for the Eulerian calculation of the gas-phase properties.

The droplet radius is governed by

$$\frac{dR^{(k)}}{dt} = \frac{-\dot{m}_v^{(k)}}{4\pi(R^{(k)})^2 \rho_l} \tag{13}$$

This is essentially equivalent to equation (2) except that a Lagrangian time derivative is taken.

The droplet velocity is given by the relationship

$$\frac{du_{li}^{(k)}}{dt} = F_i^{(k)} \tag{14}$$

while the droplet thermal energy can be calculated via

$$\rho_l \frac{de_l^{(k)}}{dt} = \frac{3}{R^{(k)}} \lambda_l \frac{\partial T_l^{(k)}}{\partial r}\Big)_s \tag{15}$$

Note that equation (12) not only gives the droplet path but it also describes the characteristic direction for the first-order hyperbolic partial differential equations (2), (3), and (4). We may view equations (12)–(15) as describing a method of characteristics whereby integration occurs along the characteristic paths.

The integration of these ordinary differential equations along the trajectories or characteristic lines avoids numerical diffusion which would result from upwind differencing of the spatial derivatives in the hyperbolic equations (1)–(4). One must be careful, however, in interpolation between the Lagrangian mesh and the Eulerian mesh. This interpolation is necessary because the droplet equations and the gas equations are strongly coupled due to the exchange of mass, momentum, and energy and the characteristic paths, in general, pass between rather than through the Eulerian mesh points. The interpolation scheme should be second order accurate in order to avoid errors of the same magnitude as the numerical diffusion which has been eliminated [21].

When resolution is desired on a scale large compared to the spacing between droplets, each characteristic is representative of many droplets. The characteristics along which droplet calculations are made should be chosen so as to be separated by a distance of the same order of magnitude as the Eulerian mesh size for the gas property calculations. In this case, characteristics may cross, implying multivalued solutions, without significant collisions between droplets.

In the case where resolution is desired on a scale small compared to the spacing between droplets, a calculation of equations (12)–(15) is performed for each droplet. Obviously, a limited number of droplets can be considered in accordance with computer resources. The Eulerian mesh size for the gas property calculations is taken to be small compared to the droplet spacing. The approximation is made that the droplets provide point monopole sources of mass, momentum, and energy so droplet diameter and varying vaporization rate over the droplet surface are not taken into account. Typically, no more than one droplet center and usually none exists in any cell defined by the Eulerian mesh points. The source terms are distributed via linear interpolation at the two, four, or eight rectangular mesh points (for one, two, or three dimensional calculations) that define the edge of the cell containing a droplet. Realize that if two droplet paths cross in these calculations, a collision is implied (unless the mesh size is much larger than a droplet diameter).

The Eulerian–Lagrangian approach can be used either in a case where the droplet properties are viewed as a second continuum superimposed upon the gas field or in a case where droplets are considered as discrete particles which are individually tracked. In the former case, the Lagrangian calculations are a method of characteristics and resolution is expected on a scale that is large compared to the droplet spacing. In the latter case, resolution is expected on a scale that is small compared to droplet spacing. In the intermediate case where mesh size and average droplet spacing are of the same order of magnitude, the droplet properties cannot be viewed as continuous but the error associated with discrete particle calculation is large; for example, the crossing of droplet paths does not necessarily imply collision since resolution has been lost in the calculation.

IV Probabilistic Formulation

It is sometimes convenient to define a droplet number distribution function or, in other words, a droplet number probability density function. This function $f(x, t, R, v, e_l)$ depends upon spatial position x, time t, droplet radius R, droplet velocity v, and droplet thermal energy e_l. f is a function of time plus eight scalar properties; we consider an infinitesimal eight-dimensional volume as $dV = dx\, dv\, dR\, de_l$, and $f\, dV$ is the number of droplets in the infinitesimal volume located at x, v, R, and e_l at the instant of time t.

When the desired resolution of the liquid and gas properties is sufficiently coarse so that the volume of a cell in a numerical mesh would contain very many droplets, we can view the droplet properties as continuous. At the other extreme where very fine resolution is required, most cells will not contain a droplet at some particular instant of time. The exact location of the individual droplets will not be known in a practical spray situation. The function f should be viewed as the probability of finding a droplet in a unit volume of eight-dimensional space.

When resolution is required on a large scale, averaging over many droplets is useful. Among other things, this averaging eliminates unsteadiness on the scale of the spacing between droplets; if no large-scale unsteadiness is present, the average properties will behave in a steady fashion. However, when fine-scale resolution is required, averaging is not useful and the unsteadiness on the scale of droplet spacing is inherent. For example, the motion of droplets through the gas is unsteady on the fine scale since at one instant of time a droplet may be at some position and at a later instant, the droplet has moved and gas exists at the same position. With averaging on the coarse scale, both droplet properties and gas properties will exist at any point at any time and this type of unsteadiness is not resolved.

If we assume conservation of droplet numbers and consider a sufficiently dilute spray so that droplet collisions are negligible, the following evolution equation may be derived

$$\frac{\partial f}{\partial t} + \frac{\partial (v_j f)}{\partial x_j} + \frac{\partial (F_j f)}{\partial v_j} + \frac{\partial (\dot{R} f)}{\partial R} + \frac{\partial (\dot{e}_l f)}{\partial e_l} = 0 \tag{16}$$

where the superscript dot denotes a time derivative. If we relate the divergence term to the rate of change of a small volume ΔV in eight-dimensional space, we have

$$\frac{1}{\Delta V}\frac{d(\Delta V)}{dt}=\frac{\partial v_j}{\partial x_j}+\frac{\partial F_j}{\partial v_j}+\frac{\partial \dot{R}}{\partial R}+\frac{\partial \dot{e}_l}{\partial e_l}$$

and therefore by combination with equation (16), we find

$$\frac{d}{dt}(f\Delta V)\equiv\left(\frac{\partial}{\partial t}+v_j\frac{\partial}{\partial x_j}+F_j\frac{\partial}{\partial v_j}+\dot{R}\frac{\partial}{\partial R}+\dot{e}_l\frac{\partial}{\partial e_l}\right)f\Delta V=0 \tag{17}$$

This equation states that the number of droplets $f\Delta V$ remains constant along the trajectory in eight-dimensional space.

Integration of equation (16) and its moments will lead to equations (1)–(4). It is useful to define the droplet number density

$$n^{(k)}=\iiint f^{(k)}dv\,dR\,de_l \tag{18}$$

Here and later, integration with respect to the three velocity components and the thermal energy is performed over the infinite ranges of values. Note that we have a different distribution function $f^{(k)}$ for each class of droplet; the kth class of droplets is the set of all droplets with initial radius between $\zeta^{(k-1)}$ and $\zeta^{(k)}$ where $\zeta^{(0)}$, $\zeta^{(1)}$, etc., is a monotonically increasing sequence. The average initial radius for the kth class will lie between the values of $\zeta^{(k-1)}$ and $\zeta^{(k)}$. The vaporization will lead to droplet radius of the kth class decreasing below $\zeta^{(k-1)}$ toward zero; the limits of integration with respect to radius are zero and $\zeta^{(k)}$ for the kth class of droplets.

We also define the average droplet velocity

$$\langle u_{l_i}{}^k\rangle=\frac{\iiint v_i f^{(k)}dv dR\,de_l}{n} \tag{19}$$

where $\langle\ \rangle$ implies an average over a large number of droplets. Similarly, we define

$$\langle F_i^{(k)}\rangle=\frac{\iiint F_i f^{(k)}dv\,dR\,de_l}{n} \tag{20}$$

$$\langle \dot{R}^{(k)}\rangle=\frac{\iiint \dot{R} f^{(k)}dv\,dR\,de_l}{n} \tag{21}$$

$$\langle R^{(k)}\rangle=\frac{\iiint R\,f^{(k)}dv\,dR\,de_l}{n} \tag{22}$$

$$\langle \dot{e}_l^{(k)}\rangle=\frac{\iiint \dot{e}_l f^{(k)}dv\,dR\,de_l}{n} \tag{23}$$

$$\langle e_l^{(k)}\rangle=\frac{\iiint e_l f^{(k)}dv\,dR\,de_l}{n} \tag{24}$$

We can interpret equation (16) as governing $f^{(k)}$ for each value of k. Integration of (16) with use of the definitions (18) and (19) leads to an equation governing droplet number density for each value of k

$$\frac{\partial n^{(k)}}{\partial t}+\frac{\partial}{\partial x_j}(n^{(k)}\langle u_{lj}^{(k)}\rangle)=0 \tag{25}$$

This equation is essentially identical to equation (1). They are strictly identical when the variations of f^k with respect to initial values of R, v_i, and e_l are represented by delta functions. If the ranges $\Delta\zeta=\zeta^{(k)}-\zeta^{(k-1)}$ are sufficiently narrow, and if at any x position at the initial time both e_l and v_i correlate well with R, the distinction has no practical significance. By a good correlation we mean that each narrow initial size has a narrow range of e_l values and a narrow range of v_i values associated with it. For our purposes, we disregard the differences, eliminate the use of the averaging symbol $\langle\ \rangle$, and regard the two equations as identical.

Now, if we multiply equation (16) by v_i and integrate the resulting moment equation, we find an equation essentially equivalent to equation (3). In addition to the neglect of differences such as mentioned above, we neglect effects of the order of the dot product of $v_i-u_{li}^{(k)}$ with itself. This error is insignificant if droplets in the same initial size range do not vary widely in their initial velocity; a correlation of initial size and initial velocity is implied.

Multiplication of equation (16) by R and integration leads to an equation approximately equivalent to equation (2). If the initial droplet diameter and the initial droplet velocity are not widely varying and do correlate well, the approximation is good; in the limit where the distribution function becomes a delta function, the two equations are exact. Similarly, e_l is multiplied by equation (16) and the resulting equation can be integrated to yield an equation approximately equivalent to equation (4). These two equations become identical as the distribution function becomes a delta function.

The characteristics for equation (17) are

$$\frac{dx_i^{(k)}}{dt}=v_i^{(k)} \tag{26}$$

$$\frac{dv_i^{(k)}}{dt}=F_i^{(k)} \tag{27}$$

$$\frac{dR^{(k)}}{dt}=\dot{R}^{(k)}=-\frac{\dot{m}^{(k)}}{4\pi(R^{(k)})^2\rho_l} \tag{28}$$

$$\frac{de_l^{(k)}}{dt}=\dot{e}_l^{(k)}=4\pi(R^{(k)})^2\lambda_l\left(\frac{\partial T_l^{(k)}}{\partial r}\right)_s \tag{29}$$

Realize that averaging of these equations via integration over many droplets yields equations similar to equations (12)–(15). As the distribution function $f^{(k)}$ goes to a delta function, the two sets of equations become exactly identical. Otherwise, the two sets have important differences that are self-evident.

In the case where resolution is desired on a scale smaller than the droplet spacing, integration of equations (26)–(29) describes the path along which some probable number of droplets will move through eight-dimensional space. Note that equation (16) or equivalently the system of equations (26)–(29) is deterministic in nature with no randomization effect present. The initial conditions for those equations will be random in practical situations but once conditions are specified, the droplets will behave in a deterministic fashion. Equation (16) is different, therefore, from the Boltzmann equation for the kinetic behavior of gases where the collision term provides a randomizing effect that usually makes the solutions independent of the detailed initial conditions. In the droplet case, the solution to (16) is strongly dependent on initial conditions. Randomization effects may occur with sprays in special situations that we shall not consider. One example is the case where turbulent fluctuations in the gas cause a dispersion of the droplets. Another special situation is the case of very small droplets where Brownian motion is important.

The distribution function that has been formulated here is somewhat more general than what exists in the literature. In particular, the dependence on the droplet thermal energy has been included. Since droplet heating strongly affects vaporization rate which affects droplet size and, in turn, influences droplet drag and trajectory since trajectory and heating are related via a varying gas environment, we see that a strong coupling exists. While the inclusion of thermal energy is important, the present approach is limited. The extension to a more exact description is obvious.

Whenever droplet heating is sufficiently rapid tempertaure gradients will occur in the droplet interior. It is then necessary to solve a heat diffusion equation in the liquid. Although the partial differential equation is linear, the boundary condition at the regressing droplet surface causes the problem to be nonlinear. Numerical integration of the diffusion equation has been performed but a more efficient approximate method is recommended [14, 19, 27, 28]. A Green's function is

developed via eigenfunction expansion; then the partial differential equation in the droplet interior is transformed to an integral equation for the droplet surface temperature. The coefficients multiplying the eigenfunction in the expansion are time-varying and from the integral formulation, a system of ordinary differential equations governing these coefficients is developed. In the solution of these first-order ordinary differential equations, marching with Lagrangian time occurs along the droplet trajectory. e_l would be now eliminated as a dependent variable. It would be replaced by the number of coefficients in the eigenfunction expansion required for convergence of that expansion.

The use of such coefficients would increase the number of terms in equation (16). In principle, an infinite number of terms is required in an eigenfunction expansion but, in practice, a finite number will suffice. Likewise equation (29) would be replaced by a set of ordinary differential equations governing the coefficients along the characteristic paths. Note that the extension of variables to account for droplet temperature would also imply that equations (4) and (15) would each be replaced by a set of equations governing the coefficients.

Another generalization of the distribution function and of equation (16) can be made for the case of multicomponent fuels. Here the composition of the droplets becomes relevant; the composition varies spatially as well as temporally. It is necessary to solve an equation for mass diffusion in the liquid phase. An eigenfunction approach can also be made for this effect with an extension of the number of the independent variables for the distribution function and of the number of characteristic equations.

V Droplet Spacing and Probabilistic Behavior

An equation governing the droplet number distribution function, such as equation (16), has typically been used via integration of moments to obtain other equations governing average liquid properties; it generally is not employed directly to solve for the distribution function. However, in an emerging set of problems, there is an interest in dealing with phenomena that must be resolved on a scale as small as or smaller than the average spacing between them. It is useless and, in fact, counterproductive to seek average properties by integrating over a scale large compared to the droplet spacing. Rather, we must treat directly equation (16), or equivalently, equations (26)–(29).

A need is seen, therefore, for a theoretical/computational approach to this probabilistic problem. There are two general approaches that might be developed. At this point, the more straightforward approach is to solve a large number of deterministic problems where different sets of initial conditions are employed in each calculation. The probability density function associated with each set of initial conditions provides a weighting factor on the results of all the calculations. With this weighting factor, the statistical results can be developed.

A second approach would involve direct solution of equation (16) coupled with the solution of equations (5)–(11) governing the gas phase. Since the droplet properties have a probabilistic character, the source terms in equations (5), (6), (8), and (9) related to droplet vaporization and drag will also have a probabilistic character. Therefore, the gas properties which are solutions to these equations will have a probabilistic character and will depend upon an extended set of independent variables in the same fashion as the droplet distribution function depends upon these variables. It is felt that it is better to proceed with the former approach and to accept the tradeoff in favor of lower dimensionality at the expense of more but less extensive calculations.

Suppose, as an example, we were interested in the ignition of a monodisperse fuel spray which at the initial time is stagnant and is placed in contact on one side with a hot planar surface. A one-dimensional unsteady analysis of this situation has been performed [23]. It has been found that the ignition delay and the minimum ignition energy are very sensitive to the initial distance from the hot wall of the droplet nearest to the wall. This is the result of many deterministic calculations for different initial droplet locations x_0. As a result of this set of deterministic calculations, we can deduce the ignition delay time

$$\tau_{ig} = \tau_{ig}(x_0)$$

Now, say we also know that the probability of having the initial condition between the values of x_0 and of $x_0 + dx_0$ is $f(x_0)dx_0$. Then the probability for the ignition delay to have a value between τ_{ig} and $\tau_{ig} + d\tau_{ig}$ is given by

$$P(\tau_{ig})d\tau_{ig} = \Sigma f(x_0(\tau_{ig}))dx_0$$

where a summation is taken since more than one value of x_0 may exist for a given value of τ_{ig}. It follows that the probability function for ignition delay can be related to the probability function for location of the nearest droplet to the ignition source by the formula

$$P(\tau_{ig}) = \Sigma f(x_0(\tau_{ig})) \frac{dx_0}{d\tau_{ig}} (\tau_{ig})$$

Obviously, it is convenient to invert the function $\tau_{ig}(x_0)$ to obtain $x_0(\tau_{ig})$. This method exemplifies the first approach described above.

The interesting result is that the ignition delay and also the minimum ignition energy will not have precise values for a given mixture ratio as they do for a gaseous mixture. Rather, ranges of values exist and we can represent the ignition delay and the minimum ignition energy in a statistical manner for a spray. Therefore, the statistical results are of practical engineering value.

More work is required in order to apply these concepts to a wider range of problems. Also, in addition to the statistical variation in droplet location, the variations in droplet size, velocity, and temperature can be taken into account in future studies.

VI Concluding Remarks

The three formulations of equations describing the liquid properties have been presented and the relationships among them with relative advantages and disadvantages have been discussed.

In situations where resolution is desired only on a scale that is large compared to the average spacing between droplets, the Lagrangian formulation of the droplet equation is superior to the Eulerian formulation. The advantages are that numerical error is more easily reduced and the ability to resolve multivalued solutions is maintained in the Lagrangian method. The probabilistic formulation is not directly useful on this scale but serves as a basis for developing other formulations. Examples of cases with coarse resolutions where deterministic Lagrangian or Eulerian calculations have been useful are presented in [19–25].

In other situations where the droplet spacing is as large as or larger than the resolution scale, the Eulerian formulation governing average droplet properties is not useful. The Lagrangian formulation only remains useful when applied to individual droplets rather than to the average droplet in some cluster of droplets. That is, on this scale, the Lagrangian method should be used as a method of characteristics for the hyperbolic equation (16) which governs the probability density function rather than as a method of characteristics for the hyperbolic system of equations (1)–(4) which govern the average droplet properties. At this point, it seems more convenient to solve equation (16) indirectly by a method of characteristics, as represented by equations (26)–(29), than to solve it directly. If some randomizing effect such as turbulent motion entered equation (16) this last conclusion might change.

An interesting approach that employs a gas concentration pdf for spray analyses can be found in [26]. The pdf discussed in that paper is different from the pdf discussed herein, however, in that we are dealing with liquid properties in this paper.

The equations presented herein could be generalized to account for temperature and composition gradients in the liquid droplet interior. The major conclusions above are not expected to change under those conditions but the system of equations will become more complex.

The errors associated with the formulation of the equations (Eulerian or Lagrangian) governing average droplet properties become greater as the correlation between initial droplet diameter and other droplet properties decreases. That is, the averaged equations are most accurate when the droplets in some narrow range of initial droplet size and spatial location also have narrow ranges of initial velocity and thermal energy.

Acknowledgments

This effort was supported by AFOSR and ARO grants to Carnegie-Mellon University and by a DOE Office of Basic Energy Sciences grant to Sandia National Laboratories where the author served as Consultant and Visiting Research Scientist at the Combustion Research Facility during the writing of this paper.

References

1 Sirignano, W. A., "Fuel Droplet Vaporization and Spray Combustion," *Progress Energy Combustion Science*, Vol. 9, 1983, pp. 291–322.

2 Twardus, E. M., and Brzustowski, T. A., "The Interaction Between Two Burning Fuel Droplets," *Archiwum Processor Spalania*, Vol. 8, 1977, pp. 347–358.

3 Labowsky, M., "A Formalism for Calculating the Evaporation Rates of Rapidly Evaporating Interacting Particles," *Combustion Science and Technology*, Vol. 18, 1978, pp. 145–151.

4 Tal, R., and Sirignano, W. A., "Cylindrical Cell Model for the Hydrodynamics of Particle Assemblages at Intermediate Reynolds Numbers," *AIChE Journal*, Vol. 28, 1982, pp. 233–237.

5 Tal. R., Lee, D. N., and Sirignano, W. A., "Hydrodynamics and Heat Transfer in Sphere Assemblages – Cylindrical Cell Models," *Int. J. Heat Mass Transfer*, Vol. 26, No. 9, 1983, pp. 1265–1273.

6 Tal, R., Lee, D. N., and Sirignano, W. A., "Periodic Solutions of Heat Transfer for Flow Through a Periodic Assemblage of Spheres," *Int. J. of Heat Mass Transfer*, Vol. 27, No. 8, 1984, pp. 1414–1417.

7 Tal, R., Lee, D. N., and Sirignano, W. A., "Heat and Momentum Transfer Around a Pair of Spheres in Viscous Flow," *Int. J. Heat Mass Transfer*, Vol. 27, No. 11, 1984, pp. 1953–1962.

8 Prakash, S., and Sirignano, W. A., "Liquid Fuel Droplet Heating With Internal Circulation," *Int. J. Heat Mass Transfer*, Vol. 23, 1978, pp. 885–895.

9 Prakash, S., and Sirignano, W. A., "Theory of Convective Droplet Vaporization With Unsteady Heat Transfer in the Circulating Liquid Phase," *Int. J. Heat Mass Transfer*, Vol. 23, 1980, pp. 253–268.

10 Law, C. K., and Sirignano, W. A., "Unsteady Droplet Combustion With Droplet Heating – II: Conduction Limit," *Combustion and Flame*, Vol. 28, 1977, pp. 175–186.

11 Lara-Urbaneja, P., and Sirignano, W. A., "Theory of Transient Multicomponent Droplet Vaporization in a Convective Field," *Proc. Eighteenth Symposium (Intl.) on Combustion*, Combustion Institute, 1981, pp. 1365–1374.

12 Law, C. K., "Unsteady Droplet Combustion With Droplet Heating," *Combustion and Flame*, Vol. 26, 1976, pp. 17–22.

13 Tong, A. Y., and Sirignano, W. A., "Transient Thermal Boundary Layer in Heating of Droplet With Internal Circulation: Evaluation of Assumptions," *Combustion Science and Technology*, Vol. 11, 1982.

14 Tong, A. Y., and Sirignano, W. A., "Analysis of Vaporizing Droplet With Slip, Internal Circulation, and Unsteady Liquid-Phase and Quasi-Steady Gas-Phase Heat Transfer," presented at ASME–JSME Thermal Joint Engineering Conference, Mar. 1983, Honolulu, Hawaii.

15 Aggarwal, S. K., Tong, A. T., and Sirignano, W. A., "A Comparison of Vaporization Models in Spray Calculations," *AIAA Journal*, Vol. 22, No. 10, 1984, pp. 1448–1457.

16 Suzaki, T., and Chiu, H. H., "Multi Droplet Combustion on Liquid Propellants," *Proc. Ninth International Symposium on Space Technology and Science*, AGNE Publishing Co., Tokyo, Japan, 1971, pp. 145–154.

17 Chiu, H. H., and Liu, T. M., "Group Combustion of Liquid Droplets," *Combustion Science and Technology*, Vol. 17, 1971, p. 127–131.

18 Chiu, H. H., Kim, H. Y., and Croke, E. J., "Internal Group Combustion of Liquid Droplets," *Proceedings Nineteenth Symposium (International) on Combustion*, Combustion Institute, 1983, pp. 971–980.

19 Seth, B., Aggarwal, S. K., and Sirignano, W. A., "Flame Propagation Through an Air-Fuel Spray With Transient Droplet Vaporization," *Combustion and Flame*, Vol. 32, 1978, pp. 257–270.

20 Dukowicz, J. K., "A Particle-Fluid Numerical Model for Liquid Sprays," *Journal of Computational Physics*, Vol. 35, 1980, pp. 229–253.

21 Aggarwal, S. K., Lee, D. N., Fix, G. J. and Sirignano, W. A., "Numerical Optimization Studies of Axisymmetric Unsteady Sprays," *Journal of Computational Physics*, Vol. 50, No. 1, 1983, pp. 101–115.

22 Aggarwal, S. K., Lee, D. N., Fix, G. J., and Sirignano, W. A., "Numerical Computation of Fuel Air Mixing in a Two-Phase Axisymmetric Coaxial Free Jet Flow," *Proceedings Fourth IMACS Intl. Symposium on Computer Methods for Partial Differential Equations*, IMACS, 1981.

23 Aggarwal, S. K., and Sirignano, W. A., "Ignition of Fuel Sprays: Deterministic Calculations for Idealized Droplet Arrays," *Proceedings of Twentieth Symposium (International) on Combustion*, Combustion Institute, 1985, pp. 1773–1780.

24 Aggarwal, S. K., and Sirignano, W. A., "Unsteady Flame Propagation in a Closed Volume," *Combustion and Flame*, Vol. 62, 1985, pp. 69–84.

25 Aggarwal, S. K., and Sirignano, W. A., "An Ignition Study of Polydisperse Sprays," presented at the 23rd Aerospace Sciences Meeting, Reno, NV, Jan. 1985, AIAA Preprint No. 85-0320.

26 Kerstein, A. R., "Prediction of the Concentration PDF for Evaporating Sprays," *Int. J. Heat Mass Transfer*, Vol. 27, No. 8, 1984, pp. 1291–1309.

27 Tong, A. Y., and Sirignano, W. A., "Multicomponent Droplet Vaporization in a High Temperature Gas," presented at the ASME Winter Annual Meeting, New Orleans, LA, Dec. 1984, ASME Paper No. 84-WA/HT-17.

28 Tong, A. Y., and Sirignano, W. A., "Multicomponent Transient Droplet Vaporization With Internal Circulation: Integral Equation Formulation and Approximate Solution," submitted for publication, 1985.

K. Saito

F. A. Williams

Department of Mechanical and Aerospace Engineering,
Princeton University,
Princeton, NJ 08544

A. S. Gordon

Department of Applied Mechanics and Engineering Sciences,
University of California, San Diego,
La Jolla, CA 92093

Structure of Laminar Coflow Methane-Air Diffusion Flames

Measured temperature and composition profiles are reported for a number of flames. Implications concerning flame structure are deduced, with emphasis on soot formation and on correlations involving conserved scalars.

Introduction

Structures of laminar diffusion flames are of current interest for a number of reasons. In addition to fundamental curiosity about effects of chemical kinetics in laboratory flames, there is practical concern about chemical nonequilibrium, soot production, and radiant energy emissions in turbulent diffusion flames.

A promising approach to the analysis of turbulent flames is to introduce conserved scalars so that data on laminar flames can be used [1]. Correlations of laminar-flame structures on the basis of mixture fractions can enable turbulent-flame properties of interest to be calculated relatively simply. There are indications that the correlations can be applied approximately, even for chemical species that are known to be out of chemical equilibrium [2]. Although there have been a number of experimental and analytical studies of structures of laminar diffusion flames [3, 4] there is still need for further testing of mixture-fraction correlations for flames in different configurations with varying overall residence times. An objective of the present work is to increase the extent of testing by providing new data on flame structures and by analyzing other data available in the literature.

Another objective of the study is to obtain information relevant to processes of soot formation in methane-air diffusion flames. Soot production is of interest in connection with pollutant escape and also because of its correlation with radiant energy emissions.

To better understand sooting processes, over a one-year period beginning in 1982 measurements were made on four different flames in the same, highly overventilated, coflow burner; a small blue flame at a low fuel flow rate, a blue flame with a small yellow region at a higher flow rate, a blue flame with a larger yellow region and a small orange region, as described earlier [5], at a still higher fuel flow rate, and a largely yellow-orange flame at the highest flow rate tested. The configuration, results for which are reported here, is most similar to that of Mitchell et al. [6], although the fuel exit velocities and flame heights are smaller here. Comparisons of results for different flow rates and with widely different amounts of soot production helps to clarify kinetic processes and mechanisms of sooting.

Apparatus and Procedure

The apparatus employed and the measurement methods were essentially the same as those described previously [5, 7] for measurement of temperature and composition profiles and are illustrated schematically in Fig. 1. The methane-air diffusion flames to be studied were stabilized on a burner in highly overventilated conditions to eliminate small fluctuations in the flame. The range of the average fuel flow rates in the annular region was 0.54 cm/s to 2.2 cm/s and the air flow rate was always fixed at 9.3 cm/s. The quartz burner of diameter 1.6 cm was enclosed by a Pyrex chimney of 7 cm diameter and 38 cm height. A slit was cut into the side of the chimney for inser-

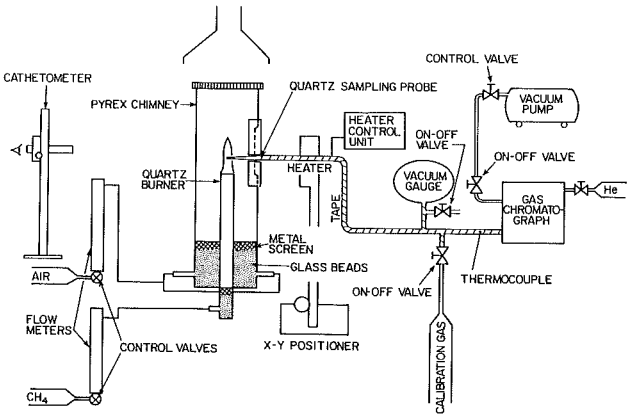

Fig. 1 Schematic diagram of the apparatus

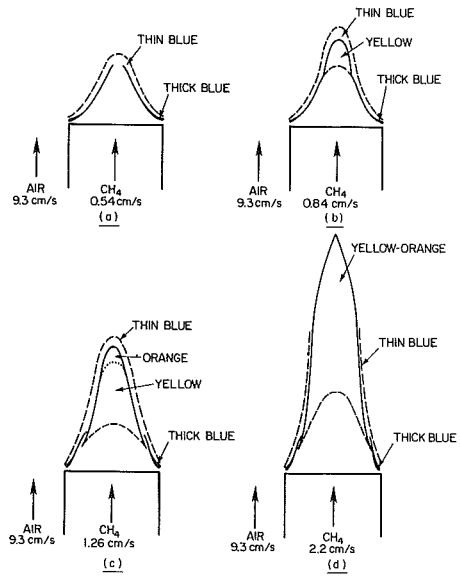

Fig. 2 Illustration of the four flames probed; burner diameter 1.6 cm in all cases

Contributed by the Heat Transfer Division and presented at the 23rd National Heat Transfer Conference, Denver, Colorado, August 1985. Manuscript received by the Heat Transfer Division May 24, 1985.

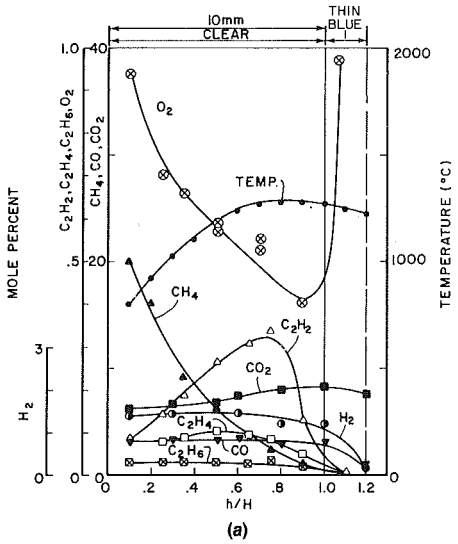

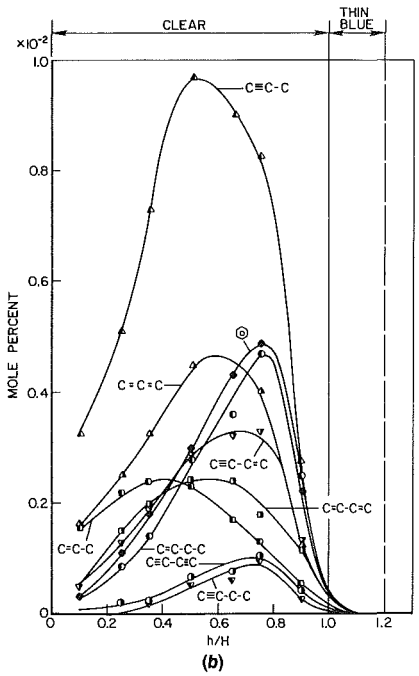

Fig. 3 Axial profiles of concentrations and temperature along the centerline for flame (*a*): (*a*) temperature and concentrations of species containing fewer than three carbon atoms; (*b*) concentrations of species containing three or more carbon atoms

tion of a sampling probe and a thermocouple. A layer of fine glass beads at the bottom of both the burner and the chimney served to produce a uniform upward flow of the fuel and air.

The quartz microsampling probe employed was a standard type as described by Fristrom and Westernberg [8] and was mounted on an x–y positioner to fix the probe at the proper location. The inner diameter of the probe tip was about 0.10 mm. The procedure involved continuous sampling and gas chromatographic analysis. The species H_2, O_2, N_2, CH_4, CO, CO_2, C_2H_2 + C_2H_4, C_2H_6, and H_2O were measured by use of a gas chromatograph that employed molecular sieve and Porapak Q columns with a thermal conductivity detector. The heavy hydrocarbons were separated by use of an SP-1000 column at a column temperature of $-25°C$ in a batch-sampling system that employed a flame-ionization detector. Agreement of results with the two different systems was established by duplicate measurements for CH_4 and C_2H_6. A cathetometer having reading accuracy within ± 0.05 mm was used to check the location of the thermocouple bead and the sampling-probe tip.

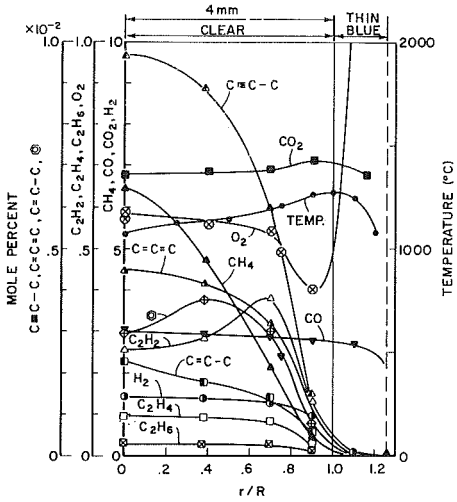

Fig. 4 Radial profiles of concentrations and temperature at half the flame height for flame (*a*)

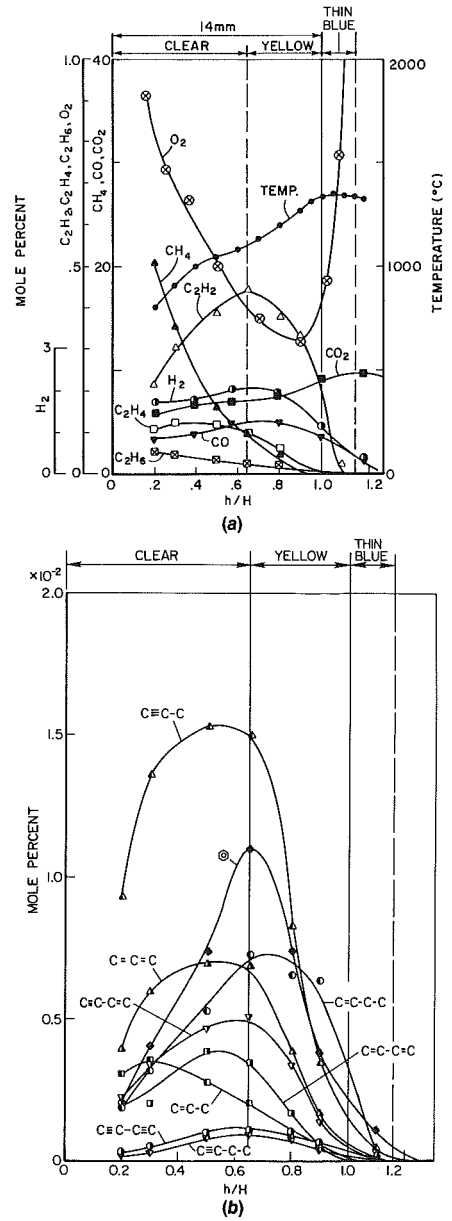

Fig. 5 Axial profiles along the centerline for flame (*b*): (*a*) temperature and concentrations of species containing fewer than three carbon atoms; (*b*) concentrations of species containing three or more carbon atoms

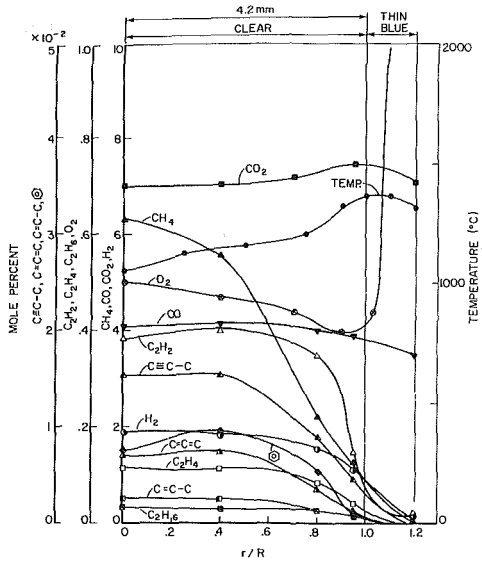

Fig. 6 Radial profiles of concentrations and temperature at half the flame height for flame (*b*)

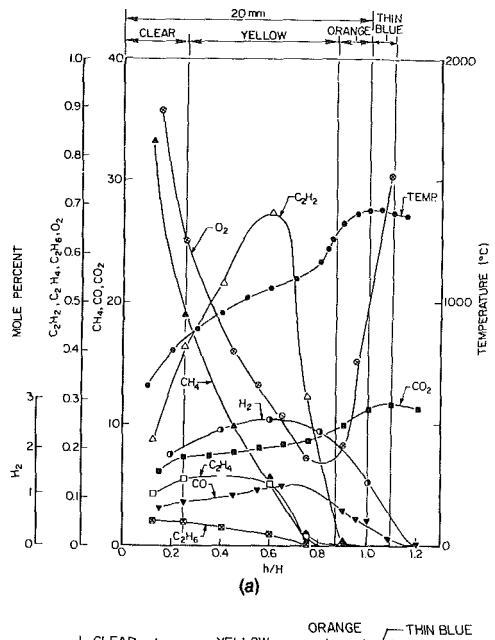

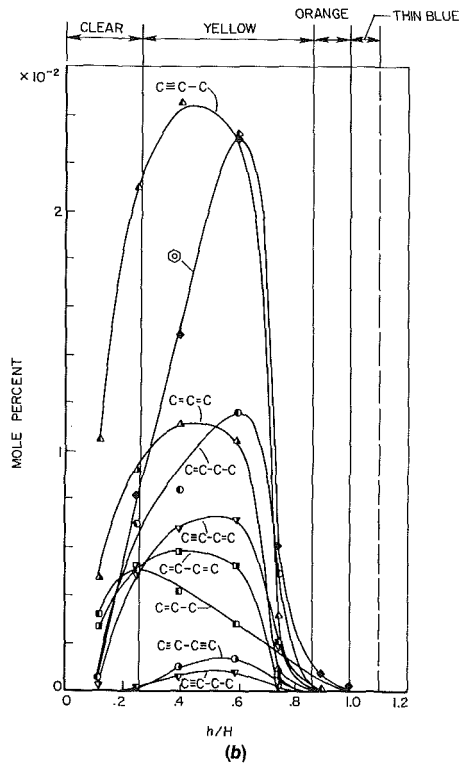

Fig. 7 Axial profiles along the centerline for flame (*c*): (*a*) temperature and concentrations of species containing fewer than three carbon atoms; (*b*) concentrations of species containing three or more carbon atoms

The local flame temperatures were measured with a silica-coated 0.05-mm-dia Pt-6 percent Rh versus Pt-30 percent Rh thermocouple. The coated thermocouple wire and bead diameters are about 0.1 mm and 0.15 mm, respectively. It should be mentioned here that in the yellow region (but not in the orange or blue region) soot coated the thermocouple quickly and necessitated extrapolation of the reading back to the time of insertion to obtain correct results [5]. Corrections for radiation and conduction effects are straightforward but were not employed since different investigators prefer different correction procedures. The reported temperatures include errors that are due to these effects and that range from negligible values at temperatures below 800°C to about 300°C at the highest temperature. The general trends for the temperature profiles reported are the same as the trends obtained when the above-mentioned corrections are included.

Experimental Results

The four flames whose structures were probed in the 1.6 cm diameter burner are shown in Fig. 2. At the lowest fuel flow rate (*a*, 0.54 cm/s), the flame height is about 1 cm and the flame is entirely blue, with the two distinct shades shown in the figure. As the flow rate of the fuel is increased the flame height increases, and at a critical rate a yellow spot appears inside the blue. At the second condition selected for measurement (*b*, 0.84 cm/s), the flame height is about 1.6 cm, and there is a small region of yellow. When the fuel flow is increased sufficiently further a small orange region appears just above the yellow, as described by Saito et al. [5]. The third condition selected (*c*, 1.26 cm/s) has a flame height of about 2 cm and clearly distinguishable yellow and orange regions inside the blue. With further increase in the fuel flow velocity the yellow and orange regions gradually merge and become indistinguishable, and the outer blue region becomes indiscernible in the upper part of the flame [5]. At the fourth condition selected for measurement (*d*, 2.2 cm/s), the flame height is about 3.8 cm, and the yellow and orange regions have merged.

It seems likely that the radiation from the inner, lower, thick blue region in each of these four flames is predominantly chemiluminescence from radicals (e.g., CH*) formed in hydrocarbon oxidation, while the outer, thin blue is radiation from CO_2^*, associated with CO oxidation. The yellow and orange are characteristic of radiation from soot particles, as discussed by Saito et al. [5]. These interpretations are consistent with the measured profiles of temperature and species concentrations, shown in Figs. 3–10. Since measurement of H_2O necessitated heating of the sampling line and accelerated deterioration of chromatographic columns, H_2O profiles were measured only for the largest flame (*d*); all mole fractions for the other three flames are reported on a dry basis. To protect the columns during the dry-basis measurements, a water condenser (a stainless-steel tubing coil soaked in an ice-water bath) was placed in the sampling line to remove moisture from the sample. Results on a dry basis are sufficient for drawing the general conclusions needed here.

In Figs. 3–10, h denotes the height above the burner port, H the flame height, r the radial distance from the axis of symmetry, and $R(h)$ the flame radius at the measurement height h. Figures 3 and 4 concern flame (*a*) of Fig. 2; Figs. 5 and 6,

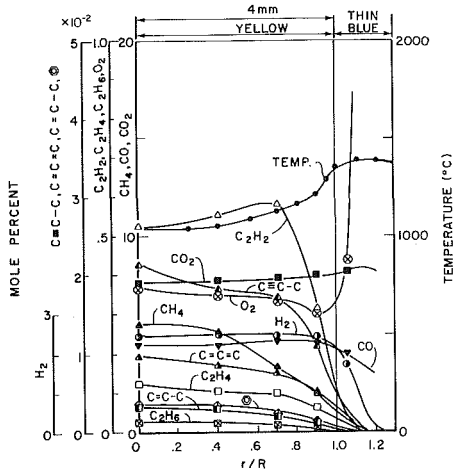

Fig. 8 Radial profiles of concentrations and temperature at half the flame height for flame (c)

flame (*b*); Figs. 7 and 8, flame (*c*); and Figs. 9 and 10, flame (*d*). For each flame the first of the figures gives axial profiles and the second radial profiles. The species measured include hydrocarbons through C_4 and benzene, ⬡. For brevity of notation the hydrogens are not shown on the C_3 and C_4 hydrocarbons in the figures.

Discussion of Experimental Results

The general profile shapes for N_2, CH_4, O_2, H_2, CO, and products are similar to those of earlier studies [6, 9] and are readily understandable; since they have been discussed by Mitchell et al. [6], for example, no further comments about them are needed here. That the scaled profiles of major species are not very dependent on burner diameter is illustrated by the data shown in Fig. 11; thus, the results to be discussed here are representative of a range of burner diameters.

We are unaware of any previously reported data on C_2, C_3, and C_4 hydrocarbons and benzene for coflow methane diffusion flames. The most striking aspect of our concentration profiles is the large number of unsaturated hydrocarbons found inside the flame envelope. The only saturated compounds detected are methane and ethane. The hydrocarbons present in highest concentrations are methane, acetylene, ethene, and ethane in decreasing order. The C_3 and C_4 hydrocarbons and benzene are present at one-tenth or less of the mole fraction of acetylene. The concentrations of the unsaturated hydrocarbons increase with increasing height, reach maximum values and then decrease to zero. There seems to be a tendency for the peak concentrations of unsaturates to occur at greater heights for species with greater numbers of double or triple CC bonds and for species with greater numbers of C atoms, as expected for pyrolysis and recombination processes that produce increasingly large molecules. So many unsaturates are observed that one particular key species leading to soot is not readily identifiable.

By comparing the profiles for the four different flames it is seen that the peak concentrations of acetylene and of higher unsaturates increase with increasing flame height (i.e., fuel flow rate), as does the highest flame temperature. Nevertheless, the same species are present in all four flames. Thus, even the purely blue flames contain soot precursors, but these molecules are oxidized in the blue flame external to the pyrolysis cone before they produce soot. The peak concentrations of the olefinic and aromatic precursors increase as the extent of yellow emission increases (as expected, since their polymerization produces soot).

It might be thought that an essential element to understanding of yellow emissions would be the effect of oxygen on

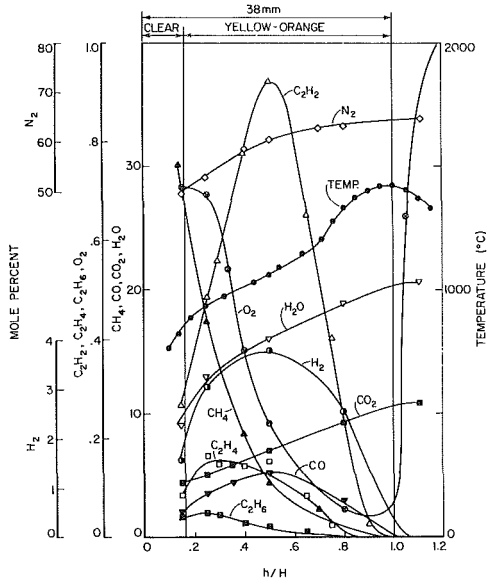

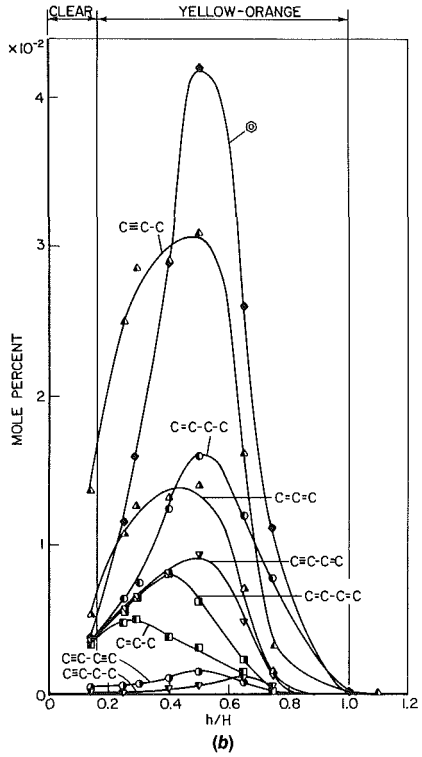

Fig. 9 Axial profiles along the centerline for flame (*d*): (*a*) temperature and concentrations of species containing fewer than three carbon atoms; (*b*) concentrations of species containing three or more carbon atoms

pyrolysis rates. As the fuel exit velocity varies, the height of the quench zone at the burner tip changes, and the extent to which oxygen diffuses inward is modified. If oxygen were to influence pyrolysis then a consequent variation in yellow emissions with flow rate would be expected. However, Saito et al. [10] have shown by addition of small amounts of oxygen to the fuel that effects of oxygen are negligible. Therefore, the oxygen can be ignored in the core of the methane flame for purposes of explaining color changes.

Buoyancy and burner-tip heat transfer are essential to explanations of variations of the yellow color indicative of soot. The heat transfer between the burner tip and the gas varies with the fuel exit velocity. As explained by Saito et al. [5], in-

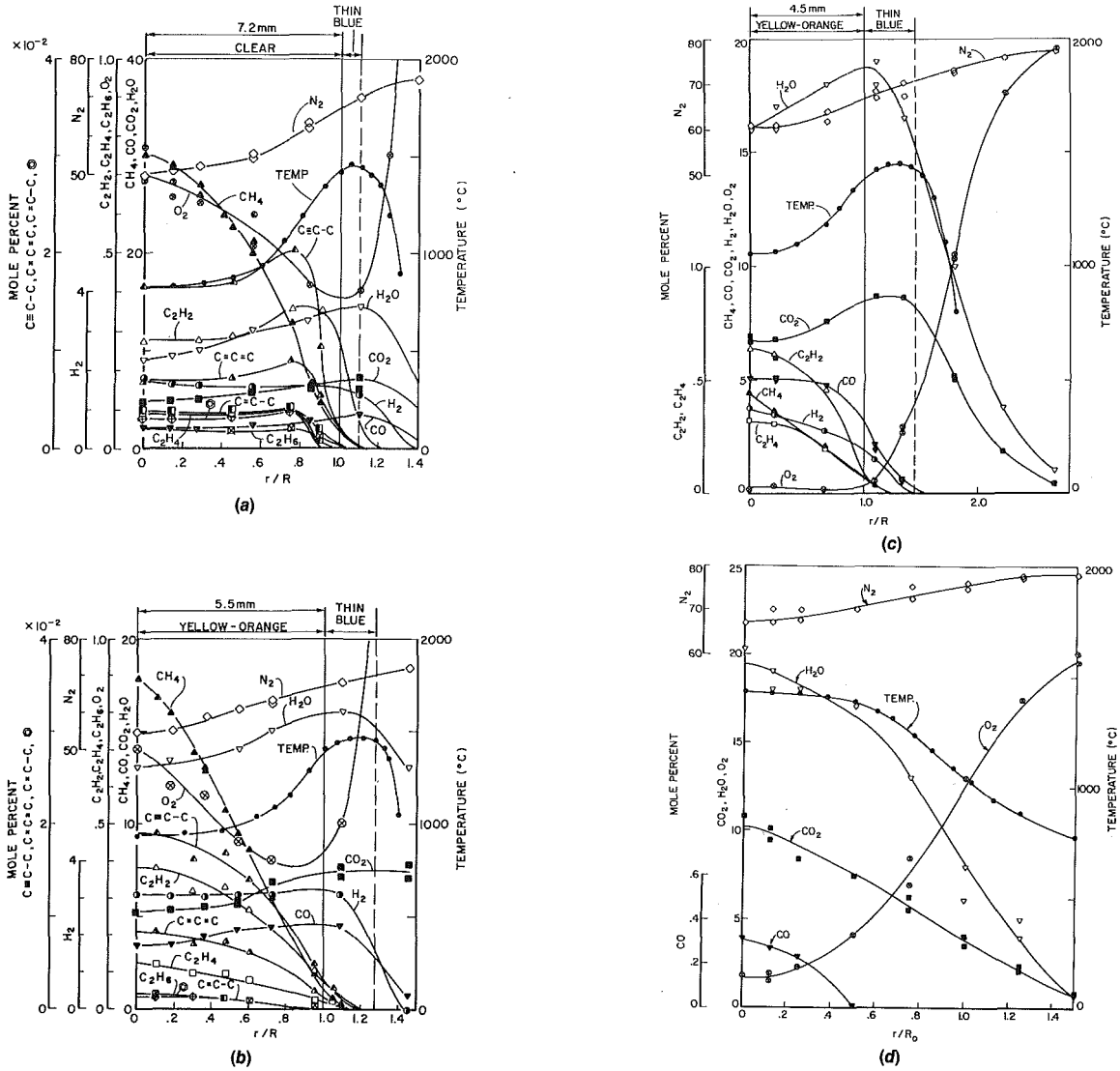

Fig. 10 Radial profile of concentrations and temperature at four different heights for flame (*d*): (*a*) $h/H = 0.14$; (*b*) $h/H = 0.25$; (*c*) $h/H = 0.50$; (*d*) $h/H = 1.1$

creasing the fuel exit velocity increases the rate of heat transfer from the burner tip to the fuel and thereby increases the peak fuel temperature, as is readily seen by the comparisons collected in Fig. 12, where the flame tip occurs approximately at the position of maximum temperature. The strong influence of temperature on pyrolysis rates then leads to the variations in yellow emissions with fuel exit velocity. The buoyancy is of significance in influencing residence times of fuel elements in any given temperature range [10–13].

If buoyancy were negligible then the time for a fuel element to reach the flame tip would be independent of the exit velocity, and the time to reach any given height h would vary inversely with the exit velocity. In fact this last relationship applies only very near the exit, and throughout the region of interest times are buoyancy-dominated. The time to reach a height h therefore is approximately proportional to $\sqrt{h/g}$, where g is the acceleration of gravity; this time is independent of the exit velocity. Since the flame height H increases in proportion to the exit velocity, the time to reach the flame tip ($\sim\sqrt{H/g}$) is approximately proportional to the square root of the exit velocity. The total residence time in the interior of a large flame thus in fact is larger. Roper [11] showed how this result remains consistent with the classical flame-height correlations [14] for round burners.

If variations in burner-tip heat transfer were negligible, then

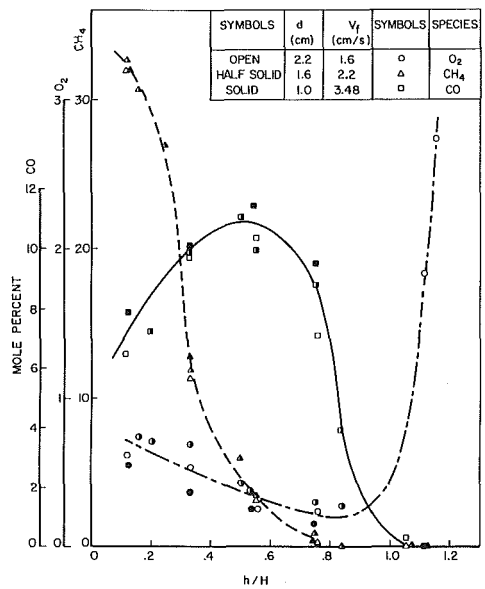

Fig. 11 Axial profiles of concentrations of CH_4, O_2, and CO along the centerline for flames on burners of three different diameters

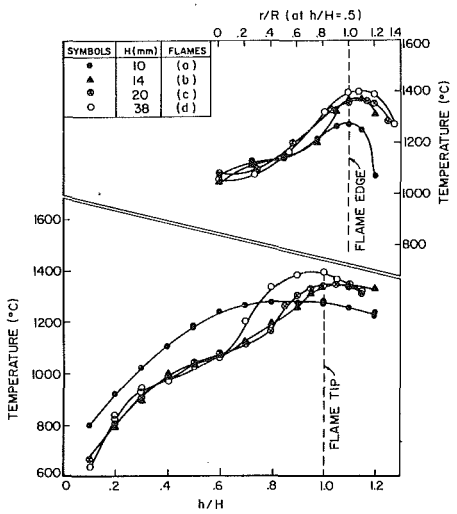

Fig. 12 Comparisons of measured, uncorrected temperature profiles, radial at $h/H = 0.5$ and axial along the centerline, for flames (*a*), (*b*), (*c*), and (*d*)

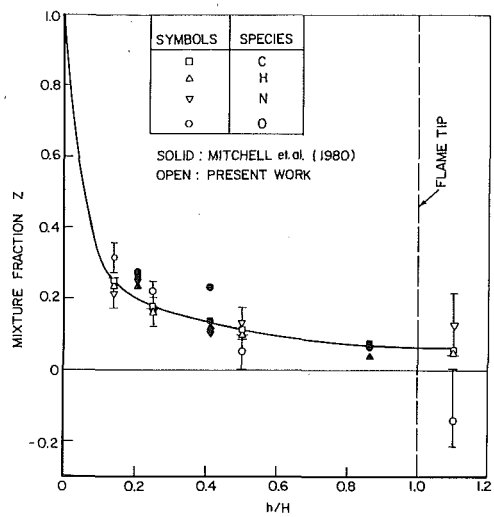

Fig. 13 Axial profiles of mixture fraction along the centerline, separately based on C, H, O and N, for flame (*d*) and for the flame of Mitchell et al. [6]

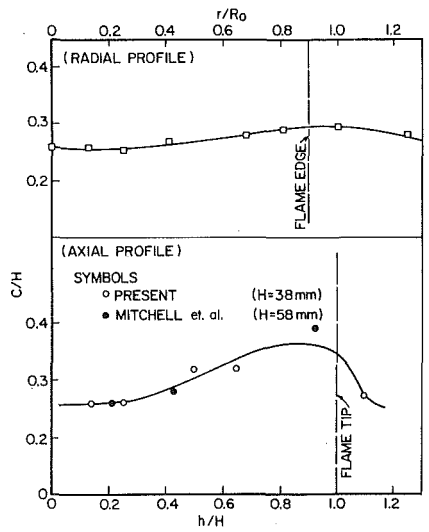

Fig. 14 Profiles of the total carbon-to-hydrogen atom ratio (C/H), axial along the centerline for flame (*d*) and for the flame of Mitchell et al. [6], and radial for flame (*d*) at $h/H = 0.14$

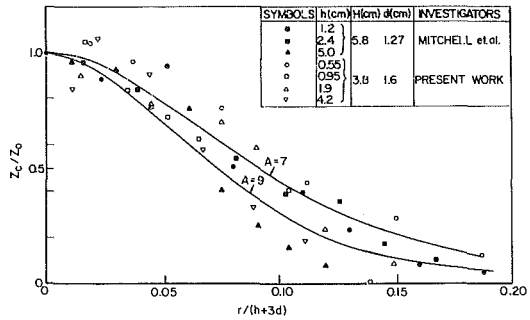

Fig. 15 Radial profiles of nondimensional mixture fraction based on C for flame (*d*) and for the flame of Mitchell et al. [6]

the increase in residence time with flame height would give rise to a critical flame height above which yellow emissions occur because the high-temperature fuel-rich residence time becomes sufficient for pyrolysis to proceed to soot. Further increases in exit velocity would cause yellow emissions to begin at a larger value of h (because of the lower centerline temperature at fixed h) but at a smaller value of h/H, so that the size of the yellow region grows. The variation in burner-tip heat transfer with exit velocity enhances this growth and lessens the tendency for h at yellow onset to increase with increasing exit velocity. Thus, the observed variations in yellow emissions are qualitatively consistent with expectations based on variations in rates of fuel pyrolysis with temperature–time histories.

Mixture-Fraction Correlations

As indicated in the introduction, there is interest in investigating the possibility of correlating compositions with mixture fractions[1] for diffusion flames in various configurations. Bilger [2] found good correlations for a counterflow heptane–air flame. Here we consider methane flames, employing data of Mitchell et al. [6], of Tsuji and Yamaoka [15], and of our four different flames. Although H_2O concentrations were not measured for the flames (*a*), (*b*), and (*c*), an assumption that the atom ratio $C/H = 0.28$[2] was used to calculate Y_{H_2O} for these three flames, following a suggestion by Bilger [16]. The tests will serve to compare our coflow axisymmetric flame (*d*) and that of Mitchell et al. [6] with the counterflow flame of Tsuji and Yamaoka [15], as well as to investigate the influence of flow rate in our flames (on the basis of a reasonable C/H approximation).

We define the mixture fraction Z to be unity in the fuel stream and zero in the air stream [1]. Four different mixture fractions can be calculated from measured concentrations, depending on whether the atom C, H, O, or N is selected in defining Z. Any linear, homogeneous combination of these with coefficients summing to unity also could be used and although some authors prefer to introduce a linear combination that enforces agreement at stoichiometry, we choose not to employ such artifices. Figure 13 shows axial profiles of Z along the centerline for the axisymmetric flames, calculated from the data according to each of the four definitions. The profiles are seen to appear to depend substantially on the definition. However, there are uncertainties in the calculated profiles, stemming from inaccuracies in measured concentrations on the order of ±7.5 percent. These inaccuracies produce uncertainties of this same order of magnitude in the pro-

[1] Mixture fractions for the two-feed system considered here are defined as: $Z \equiv (Y_i - Y_{i2})/(Y_{i1} - Y_{i2})$, where Y_i is mass fraction of element i and the subscripts 1 and 2 refer to the composition in the two feeds.

[2] This value is used instead of the formal value 0.25 to account approximately for the higher diffusion coefficients of the H-containing species; the difference in results is small.

files based on C and H but much larger percentage uncertainties in the profiles based on O and N because the calculation using either of these atoms involves subtraction of two numbers that are nearly equal. Error estimation was made for species O and N based only on uncertainties of measured H_2O concentrations and is indicated by error bars in Fig. 13.

It is seen from Fig. 13 that although the profiles with large uncertainty differ appreciably, the more accurate profiles (based on C and H) are in reasonably good agreement, as found earlier [2] for the counterflow flame. Therefore, henceforth we restrict attention to mixture fractions based on C and H. It is seen in Fig. 13 that these two mixture-fraction profiles agree well for flame (*d*) and also for the flame of Mitchell et al. [6], but there are noticeable (although not large) differences between the profiles for the two flames. These differences may be associated with the different burner diameters and exit velocities of the two experiments. Thus, profiles in scaled spatial dimensions may be expected to differ not only for different configurations but also somewhat for different fluid-mechanical feed-flow values in any given configuration; Mitchell et al. [6] employed plug flow in fuel and air passages, while fully developed parabolic flow was used in the present experiments.

The general agreement in the axial Z profiles based on C and H motivates a closer look at differences that may arise in the use of one or the other of these atoms for defining the mixture fraction. Profiles of the C/H ratio, as shown in Fig. 14, provide an indication of the differences to be expected. If the two mixture fractions were the same then C/H would remain constant at its value (0.25) for the fuel molecule. It is seen in Fig. 14 that variations on the order of 50 percent in the ratio may occur, with a peak roughly just inside the outer exothermic reaction-zone location. The behavior is consistent with the relatively hydrogen-rich products (H_2, H_2O, . . .), generated near the flame, having higher molecular diffusivities on the average than the carbon-containing products, since lower H concentrations and higher C concentrations would then be observed near the reaction zone. This same effect was found previously by Seshadri and Williams [17] for diffusion flames of liquid fuels. It implies that local differences in Z values on the order of 50 percent occur in some regions, depending on whether C or H is selected. With this in mind, and in view of the relative inaccuracy of H_2O measurement, we select C for defining Z,[3] as in earlier work [2].

The radial Z profile (based on C or H) for flame (*d*) and also for the flame of Mitchell et al. [6] can be correlated approximately on the basis of similarity theory for laminar jets [18]. Since Z has no chemical source term it should spread by diffusion approximately like a passive scalar. According to incompressible similarity theory, we then find

$$Z/Z_0 = \{1 + [Ar/(h+H_0)]^2\}^{-2}$$

where Z_0 is the centerline value, H_0 is the vertical distance of the virtual origin below the exit plane, and A is a measure of the exit Reynolds number. The data shown in Fig. 15 test this formula. The approximation $H_0 \simeq 3d$ has been introduced here, and the curves shown for $A=7$ and $A=9$ suggest that $A \simeq 8$ gives the best correlation. In view of the strong density variations and buoyancy effects not taken into account by the formula, the degree of agreement of the data with the similarity formula seems reasonable.

Having established smooth profiles of Z based on C atoms, we employ this Z to investigate correlations of species concentrations with mixture fraction, in the manner of Bilger [2], who reported results only for counterflow flames. Results for

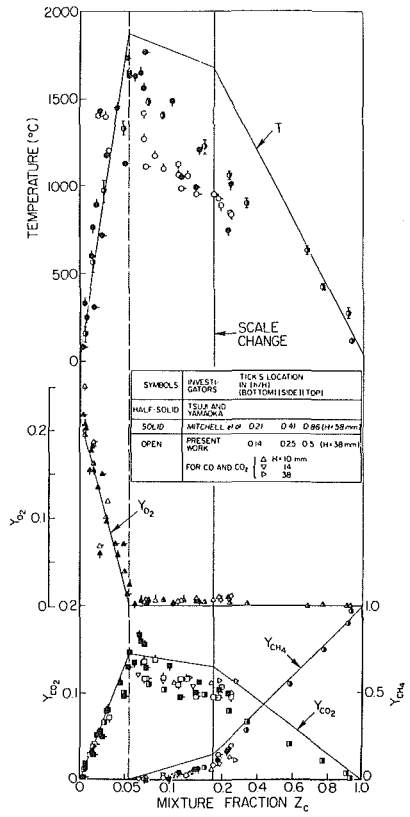

Fig. 16 Profiles of temperature and of mass fraction of CH_4, CO_2, and O_2 plotted against mixture fraction based on C for four different flames (*a*, *b*, *c*, *d*), for the flame of Mitchell et al. [6], and for the flame of Tsuji and Yamaoka [15]

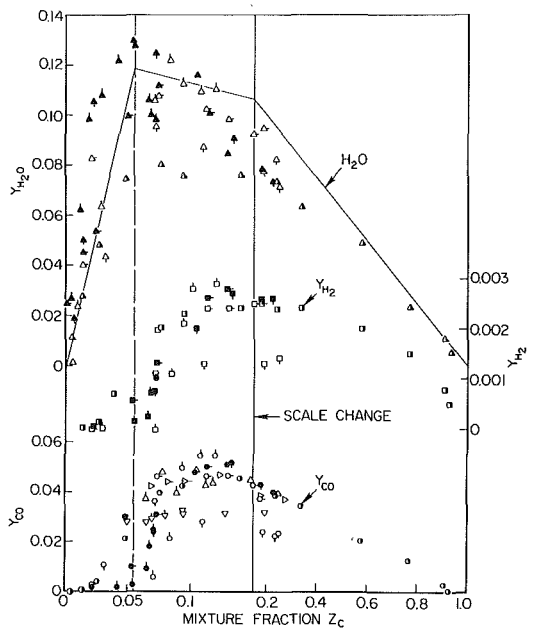

Fig. 17 Profiles of mass fraction of CO, H_2, and H_2O plotted against mixture fraction based on C for four different flames (*a*, *b*, *c*, *d*), for the flame of Mitchell et al. [6], and for the flame of Tsuji and Yamaoka [15]

temperature and major species are shown in Figs. 16 and 17 for the six flames identified at the beginning of this section. For purposes of comparison in these figures solid lines are drawn that represent an ideal condition of complete combustion without dissociation. Since the counterflow data reported [15] for O_2 include argon, a calculation was made here to subtract argon by using the measured N_2 concentrations and

[3] Errors introduced in the Z calculations by not measuring higher hydrocarbons and soot would tend to reduce the observed C/H ratio below 0.25. No such reduction was found in any of the measurements.

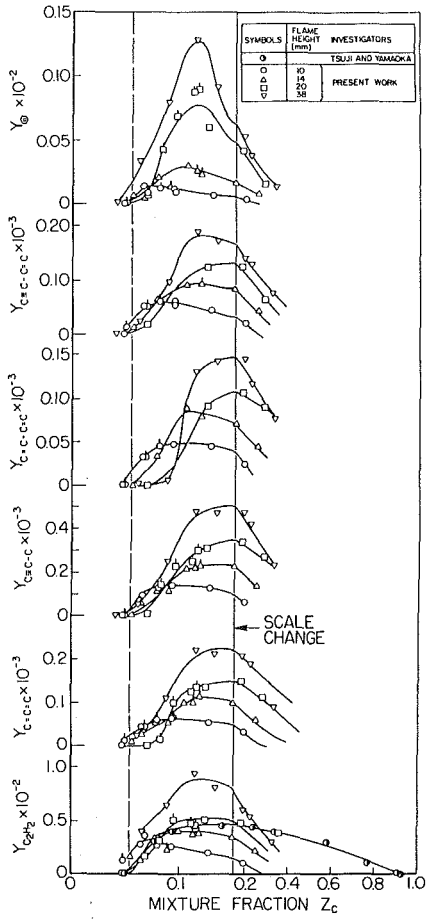

Fig. 18 Profiles of mass fraction of acetylene, allene, methyl acetylene, 1,3-butadiene, vinylacetylene, and benzene plotted against mixture fraction based on C for four different flames (*a*, *b*, *c*, *d*), with half-open symbols for acetylene giving data of Tsuji and Yamaoka [15]

assuming equal molecular diffusivities of N_2 and argon. The error bars shown on the counterflow temperature data represent extremes of the scatter reported [15]. The counterflow temperatures, like those for the present work, are uncorrected, while the temperatures of Mitchell et al. [6] contain thermocouple corrections.

With reasonable thermocouple corrections [5], temperature curves for both sets of coflow experiments agree within the scatter of the data. On the air side (values of Z below the stoichiometric value) these temperatures also are in reasonable agreement with counterflow temperatures and with ideal equilibrium temperatures, but on the fuel side differences occur that are well beyond experimental uncertainty. The fuel-side counterflow temperatures exceed the coflow temperatures but are appreciably below the ideal temperature. The departure from ideality can be attributed to increased heat capacities of pyrolysis products of the fuel, and the difference between coflow and counterflow results can be ascribed to the greater extent of pyrolysis in the coflow experiments, caused by their relatively longer fuel-side residence times. The comparisons indicated that if temperatures are to be correlated with Z in fuel-rich regions of elevated temperature, then an appropriate residence time must be identified in constructing the correlation.

The O_2, CH_4, CO_2, H_2O, and H_2 profiles correlate reasonably well for the three experiments. Moreover, the major features of these correlations follow the trends of the ideal equilibrium curves within the accuracy of the data for O_2, CH_4, CO_2, and H_2O. The departures from ideality, e.g., the small amounts of oxygen on the fuel side and the reduced fuel-side CO_2 concentrations in the region where CO concentrations are appreciable, all are comprehensible from knowledge of diffusion-flame structure. Closer study, however, reveals certain systematic differences. The air-side CO concentrations for the counterflow experiments seem to be somewhat higher at the larger values of Z than those of the coflow measurements; this is consistent with the shorter counterflow residence times, so that CO burnup extends to smaller values of Z in the counterflow experiments. Near-stoichiometric fuel-side CO concentrations in Fig. 17 for coflow experiments appear to exhibit large scatter but in fact reflect systematically increasing CO concentrations with increasing height in the fuel-rich portion of the flame as a consequence of the flow configuration. Certain good correlations observed are likely to be fortuitious; for example, the O_2 concentrations on the fuel side are mainly from leakage through the flame in the counterflow experiments but from diffusion through the quench zone at the burner port in the coflow tests. Thus, a number of potential sources of breakdown of the correlations can be identified. Evolving flames such as those of coflow experiments possess a greater number of phenomena capable of destroying the correlations.

Sharper tests of mixture-fraction correlations may be expected to be provided by concentrations of the higher hydrocarbons that are soot precursors. Results from our four different flames for acetylene, allene, methylacetylene, 1, 3-butadiene, vinylacetylene, and benzene are shown in Fig. 18. Data for acetylene from the counterflow experiment [15] also are shown; no results for the other hydrocarbons are available from other investigators for comparison. The evolving character of the coflow flame enables tests of correlations to be performed by comparing data with those of our four different flames: (*a*), (*b*), (*c*), and (*d*). All six hydrocarbon species plotted show systematic differences of species buildup processes – the taller the flame height is, the greater is the maximum concentration of these heavy species. This trend is entirely expected from the explanation for the buoyancy-dominated coflow flames, given in the previous section – that is, the taller flame has the longer resident time and the larger effect of heat transfer from the burner port as well; therefore pyrolysis proceeds farther to form soot. All species in Fig. 18 except benzene showed nearly the same fractional increase in peak concentration with increasing H; since the buoyancy-dominated residence time is proportional to $\sqrt{H}$, if the production rates of these relatively light precursors are approximately independent of time then about 50 percent of the observed increase of a factor of 3 or 4 may be attributed to the increased residence time, with the remaining increase accounted for by the effect of heat transfer from the burner port. Since benzene concentrations are seen to exhibit greater variations than the other hydrocarbons, mixture-fraction correlations for the soot concentration seem likely to be appreciably poorer even than for benzene – the greater the influence of chemical kinetics, the poorer the correlation is expected to be.

Conclusions

From the measurements reported here, and from earlier measurements by other investigators, it is concluded that chemical kinetics of fuel pyrolysis processes are of significance in the production of soot in methane–air diffusion flames. Concentrations of major species can be correlated well with the mixture fraction based on carbon atoms. The same correlations can be used for coflow and counterflow flames over a wide range of residence times. However, temperatures in fuel-rich zones of elevated temperature and CO concentrations in near-stoichiometric and fuel-lean regions do not correlate very well. Mixture-fraction correlations are very poor for benzene and other species comparably far along the chain to soot formation. If mixture-fraction correlations are employed in turbulent-flame analyses for temperature, CO, higher hydrocarbons, or soot concentrations, then careful at-

tention should be paid to identifying representative microscale residence times as a basis for selection of the most reasonable correlation. An expanded data base is needed to aid in this selection.

Acknowledgments

We would like to thank I. Glassman and A. Gomez for their interests in this work and for a series of invaluable discussions. Helpful comments by R. Bilger also were greatly appreciated. Thanks are also due to K. Brezinsky, R. Yetter, and E. Burke for help with the gas-chromatographic analysis and to H. Olson for his professional work with fabrication of glasses.

References

1 Bilger, R. W., "Turbulent Jet Diffusion Flames," *Progress in Energy and Combustion Science*, Vol. 1, 1976, pp. 87–109.

2 Bilger, R. W., "Reaction Rates in Duffision Flames," *Combustion and Flame*, Vol. 30, 1977, pp. 227–284.

3 Tsuji, H., "Counterflow Diffusion Flames," *Progress in Energy and Combustion Science*, Vol. 8, 1982, pp. 93–119.

4 Dixon-Lewis, G., et al., "Calculation of the Structure and Extinction Limit of a Methane-Air Counterflow Diffusion Flame in the Forward Stagnation Region of a Porous Cylinder," *Twentieth Symposium (International) on Combustion*, The Combustion Institute, 1984, pp. 1893–1904.

5 Saito, K., Gordon, A. S., and Williams, F. A., "Origin of Orange Region for Small Hydrocarbon Diffusion Flames," to be submitted to *Combustion Science and Technology*.

6 Mitchell, R. E., Sarofim, A. F., and Clomburg, L. A., "Experimental and Numerical Investigation of Confined Laminar Diffusion Flames," *Combustion and Flame*, Vol. 37, 1980, pp. 227–234.

7 Saito, K., Gordon, A. S., and Williams, F. A., "Anomalous Quenching of Hydrogen Diffusion Flames in Coflow Configurations," *Combustion Science and Technology*, Vol. 36, 1984, pp. 285–299.

8 Fristrom, R. M., and Westernberg, A. A., *Flame Structure*, McGraw-Hill, New York, 1965.

9 Smith, S. R., and Gordon, A. S., "Studies of Diffusion Flames. I. The Methane Diffusion Flame," *Journal of Physical Chemistry*, Vol. 60, 1956, p. 759.

10 Saito, K., Gordon, A. S., and Williams, F. A., "Effect of Oxygen on Soot Formation in Methane Diffusion Flames," *Combustion Science and Technology*, 1986 (in press).

11 Roper, F. G., "The Prediction of Laminar Jet Diffusion Flame Sizes: Part I. Theoretical Model," *Combustion and Flame*, Vol. 29, 1977, pp. 219–226.

12 Roper, F. G., Smith, C., and Cunningham, A. C., "The Prediction of Laminar Jet Diffusion Flame Sizes: Part II. Experimental Verification," *Combustion and Flame*, Vol. 29, 1977, pp. 227–234.

13 Kent, J., and Wagner, H. G., "Why Do Diffusion Flames Emit Smoke?" *Combustion Science and Technology*, Vol. 41, 1984, pp. 245–269.

14 Burke, S. P., and Schumann, T. E. W., "Diffusion Flames," *Proceedings of the First Symposium on Combustion* (reprinted in *Industrial and Engineering Chemistry* in 1965), 1928, pp. 2–11.

15 Tsuji, H., and Yamaoka, I., "Structure Analysis of Counterflow Diffusion Flames in the Forward Stagnation Region of a Porous Cylinder," *Thirteenth Symposium (International) on Combustion*, The Combustion Institute, 1970, pp. 723–731.

16 Bilger, R. W., personal communication, 1985.

17 Seshadri, K., and Williams, F. A., "Effect of CF_3Br on Counterflow Combustion of Liquid Fuel With Diluted Oxygen," in: *Halogenated Fire Suppressants*, R. G. Gann, ed., ACS Series No. 16, American Chemical Society, Washington, 1975, pp. 149–182.

18 Schlichting, H., *Boundary Layer Theory*, 4th ed., McGraw-Hill, New York, 1960, p. 181.

Correlation of Melting Results for Both Pure Substances and Impure Substances

E. M. Sparrow

G. A. Gurtcheff

T. A. Myrum

Department of Mechanical Engineering,
University of Minnesota,
Minneapolis, MN 55455

Melting experiments were performed encompassing both pure and impure substances. The pure substances included n-*octadecane paraffin and* n-*eicosane paraffin, while the impure substances were mixtures synthesized from the pure paraffins. The experiments were carried out in a closed vertical tube whose wall was subjected to a step-change increase in temperature to initiate the melting. For each impure substance, supplementary measurements were made of two characteristic temperatures: the temperature* T^{**} *at which melting of the solid phase first begins and the lowest temperature* T^{*} *at which the melting can go to completion. For a pure substance,* $T^{**} = T^{*}$. *The time-dependent melting results for all the investigated substances, both pure and impure, were well correlated as a function of* $FoSte^{**}(Gr^{**})^{1/8}$ *alone, where the* ** *signifies the presence of* T^{**} *in the temperature difference which appears in Ste and Gr. This correlation enables melting rates for impure substances to be determined from melting rates for pure substances. The* T^{**} *values needed for the implementation of the correlation can be obtained from simple experiments, obviating the need for the complete equilibrium phase diagram.*

Introduction

The recent experimental work on the heat transfer characteristics of melting has, in the main, been performed using phase-change media which have a well-defined melting temperature, i.e., either pure substances or eutectics [1, 2]. While such media have proven to be excellent vehicles for research, they are too costly to be used in most applications, for instance, for phase-change thermal storage. Impure substances melt over a range of temperatures and, when used in melting experiments, have yielded substance-specific heat transfer results (e.g., [3]). Nevertheless, impure substances are of practical interest because they are generally less costly than pure substances.

The present research is concerned with the melting of both pure and impure phase-change media and with the unification and generalization of their heat transfer characteristics. To this end, melting experiments were performed using two pure substances and two impure substances, with each impure substance being synthesized as a mixture of the pure substances. The two pure substances were *n*-octadecane paraffin ($C_{18}H_{38}$) and *n*-eicosane paraffin ($C_{20}H_{42}$), each 99 percent pure, with respective melting temperatures of 28.2°C and 36.4°C. The synthesized mixtures were 50 percent *n*-octadecane, 50 percent *n*-eicosane (by mass) and 25 percent *n*-octadecane, 75 percent *n*-eicosane (by mass). Use of synthesized paraffin mixtures, rather than of a commercially available impure paraffin (as in [3]), enabled the thermophysical properties needed in the correlation work to be computed from the properties of the parent pure substances.

As is true for most impure substances, an equilibrium phase diagram (temperature versus concentration) was not available for mixtures of *n*-octadecane and *n*-eicosane. Because of this, supplementary experiments were performed to determine the phase equilibrium information needed for the correlation of the melting heat transfer data. The supplementary experiments involved the measurement of two temperatures for each mixture. One of these is the temperature T^{**} at which the solid phase of the particular mixture just begins to melt. The other is the minimum temperature T^{*} at which melting can go to completion. Note that for a pure substance, $T^{**} = T^{*}$.

The melting experiments were performed with the phase-change medium situated in a closed vertical tube. In the experiments, the tube, initially containing the solid phase of the phase-change medium, was subjected to a step change of temperature at its cylindrical surface, and the ensuing increase of the melted mass with time was measured. The experiments were performed for various tube wall temperatures.

In the correlation effort, consideration was first given to the two pure substances since, seemingly, the time-dependent melting results for different pure substances have not heretofore been correlated. With guidance from the pure-substance correlation but with suitable modifications to account for the difference between T^{**} and T^{*} for impure substances, the melting results for both pure and impure substances were brought together. It may be noted that melting-related natural convection heat transfer coefficients for several pure substances have been correlated in [4].

Experiments

Apparatus. The apparatus for the melting experiments consisted mainly of a containment tube for the phase-change medium and two temperature-controlled water baths. The containment tube, a slightly modified version of that of [5], was a composite structure of which the main component was a vertically oriented, thin-walled copper sleeve (inner radius = 2.54 cm, wall thickness = 0.15 cm). At the top and bottom, the sleeve was closed by cylindrical plugs made of plastic-covered, closed-pore polystyrene insulation (Styrofoam). The cylindrical volume between the insulation plugs was 27.5 cm in height, and the height of the solid which occupied this volume prior to a melting experiment was 22.5 cm – leaving a 5 cm clearance at the top. What with the insulation plugs and the air space, heat transfer from the ends of the tube to the phase-change medium was effectively suppressed.

One of the constant-temperature water baths served to bring the containment tube and its charge of solid phase-change material to a preselected uniform temperature prior to the initiation of a melting run. The second bath was used to impose

Contributed by the Heat Transfer Division for publication in the JOURNAL OF HEAT TRANSFER. Manuscript received by the Heat Transfer Division September 10, 1985.

a step change of temperature at the wall of the tube at the initiation of the melting and to maintain that temperature during the entire melting period. The second bath was highly agitated to ensure high values of the convective heat transfer coefficient at the outside surface of the containment tube. The suspension arrangements in the baths were such that the water enveloped the containment tube to a height at least 5 cm above the level of the phase-change medium in the tube.

Measurements of the mass of the solid phase-change medium before and after the melting period were made with a triple-beam balance having a resolution of 0.1 g and a capacity of 2610 g. The shape of the solid which remained unmelted at the end of the melting period was measured with a dial-gage-equipped caliper having a resolution of 0.001 in.

Experimental Procedure. For a given thermal operating condition defined by the initial temperature of the solid and the step-change temperature increase imposed on the tube wall by the water bath, the timewise increase of the melted mass was measured in a succession of independent data runs of preselected duration. The aforementioned succession of data runs for each of the synthesized impure substances (50/50 and 25/75 octadecane/eicosane) had to be carried out with special care to avoid inadvertent changes in the octadecane-to-eicosane mass ratio. The objective of the precautions was to eliminate mass losses during the post-run cleaning of the containment tube and in the pre-run preparatory steps related to the charging of the tube with the solid phase-change medium. To verify the constancy of the octadecane-to-eicosane ratio, data runs corresponding to a given duration of the melting period were repeated periodically. These repeated runs always agreed to within 1–2 percent, establishing the effectiveness of the procedures used to maintain the constancy of the mass ratio.

The steps followed in the execution of a data run are similar to those of [5] and need not be elaborated here. For most of the data runs, the solid test specimen which participated in the melting process was prepared by placing the liquid-filled containment tube in an ice bath. However, for selected runs, an alternate, less-rapid freezing procedure was employed, the key feature of which was the immersion of the tube in running 15°C tap water for about 60 min. Of the 14 cases in which the alternate freezing procedure was used, the melting results for 12 were indistinguishable from those corresponding to the normal freezing procedure, and in only two runs were there modest deviations. On this basis, it may be concluded that the results were not materially influenced by the specifics of the freezing procedure.

Determination of T^{**} and T^{*}. A small, closed plexiglass container, 2.54 cm in diameter and 10.8 cm in length, was used for the determination of T^{**} and T^{*} for each of the two synthesized impure substances. After the container was filled approximately half full with the liquid phase of the substance, it was sealed and placed in an ice bath. When freezing of the liquid was completed, the container was transferred to the temperature-controlled equilibration bath.

The bath temperature was first set at a value about 1°C below the approximate value of T^{**} that had been identified in a preliminary experiment. Then, the bath temperature was raised by 0.05–0.1°C and held fixed for about 24 hr, at which time the phase-change substance was carefully inspected. If no melting was observed, the temperature was again increased by 0.05–0.1°C and a new observation made after 24 hr. This procedure was continued until the onset of melting was encountered, thereby providing the value of T^{**}.

Beyond T^{**}, a succession of small temperature increases punctuated by waiting periods of 24 hr or longer were made. Periodic observations were performed during each waiting period to monitor the progress of the melting. At all temperatures below a certain value, the melting would not go to completion regardless of the duration of the waiting period. The lowest temperature at which complete melting occurred was identified as T^{*}.

Data Reduction

The quantity on which attention will be focused in the correlation effort is the timewise variation of the melted mass, with the amount of mass liquefied between the onset of melting ($t=0$) and any time t being denoted by M_L. For a dimensionless presentation, M_L will be ratioed with the total mass M_T of the phase-change medium in the containment tube that is available for melting, so that M_L/M_T varies from 0 to 1 during the melting period. M_L and M_T were evaluated from the mass measurements made before and after the melting period in each experiment.

The basic data will be displayed in the form M_L/M_T versus time in order to call attention to the very considerable differences in the melting rates of the various media under investigation. Subsequently, the correlation of the melting results will be explored using candidate independent variables which are combinations of dimensionless groups, instead of time alone. In one of the candidate independent variables, the participating groups are

$$\mathrm{Fo}=\alpha t/R^2, \qquad \mathrm{Ste}^{*}=c(T_\infty-T^{*})/\lambda, \qquad \mathrm{Gr}^{*}=g\beta(T_\infty-T^{*})R^3/\nu^2 \tag{1}$$

while a second candidate independent variable involves the groups

$$\mathrm{Fo}=\alpha t/R^2, \qquad \mathrm{Ste}^{**}=c(T_\infty-T^{**})/\lambda, \qquad \mathrm{Gr}^{**}=g\beta(T_\infty-T^{**})R^3/\nu^2 \tag{2}$$

where Fo, Ste, and Gr, respectively, denote the Fourier, Stefan, and Grashof numbers. In addition to its involvement

Nomenclature

c = specific heat
Fo = Fourier number $=\alpha t/R^2$
Gr^{*} = Grashof number $=g\beta(T_\infty-T^{*})R^3/\nu^2$
Gr^{**} = Grashof number $=g\beta(T_\infty-T^{**})R^3/\nu^2$
g = acceleration of gravity
k = thermal conductivity
M = molecular weight
M_L = mass liquefied from $t=0$ to $t=t$
M_T = total mass available for melting
m = mass
R = inner radius of containment tube
Ste^{*} = Stefan number $=c(T_\infty-T^{*})/\lambda$
Ste^{**} = Stefan number $=c(T_\infty-T^{**})/\lambda$
T_i = initial temperature of solid
T_∞ = temperature of melting environment bath
T^{*} = lowest temperature at which melting can go to completion
T^{**} = temperature at which solid begins to melt
t = time
W = mass fraction
X = mole fraction
α = thermal diffusivity
β = thermal expansion coefficient
λ = latent heat of melting
μ = viscosity
ν = kinematic viscosity
ρ = density

Subscripts

e = n-eicosane
o = n-octadecane
mix = mixture

Table 1 Values of T^* and T^{**} for synthesized substances (°C)

Mix *o/e*	T^{**}	T^* experimental	T^* equation (11)
50/50	29.1	31.1	32.1
25/75	32.7	33.4	34.2

with Fo and Gr to form a correlation parameter, Ste will also serve as a dimensionless representation of the characteristic temperature differences $(T_\infty - T^*)$ and $(T_\infty - T^{**})$.

The temperatures T^* and T^{**} have already been defined, while T_∞ is the temperature of the melting environment bath. In view of the high values of the convective heat transfer coefficient at the external surface of the containment tube, T_∞ is very nearly equal to the tube wall temperature. The thermophysical properties appearing in equations (1) and (2) are those of the liquid melt, and their evaluation will be discussed shortly. The tube inner radius R was chosen as the characteristic dimension in both Fo and Gr. This choice was made because R is much smaller than the other candidate characteristic dimension – the height.

The only difference between Ste* and Ste** and between Gr* and Gr** is the respective presences of T^* and T^{**}. Since $T^{**} = T^*$ for a pure substance, the dimensionless groups of equations (1) and (2) merge into a single set for such substances.

The thermophysical properties of *n*-octadecane and *n*-eicosane were taken from [6]. These properties were evaluated at the respective melting temperatures T^* of the substances. This choice of temperature was made because the thermal resistance at the melting front (where the temperature is T^*) is the main resistance of the system, since its surface area is always smaller than that at the wall of the containment tube.

The equations used for the evaluation of the thermophysical properties of the synthesized substances will now be detailed. In these equations, subscripts *mix*, *o*, and *e* will be used to respectively identify properties of the mixture, *n*-octadecane, and *n*-eicosane. The mass fractions W and the mol fractions X needed in the specification of the mixture rules are given by

$$W_o = m_o/(m_o + m_e), \qquad W_e = 1 - W_o \tag{3}$$

$$X_o = (m_o/M_o)/[(m_o/M_o) + (m_e/M_e)], \qquad X_e = 1 - X_o \tag{4}$$

where m and M, respectively, denote mass and molecular weight.

The relevant properties are:

Thermal conductivity ([7], p. 532)

$$(k_{mix} - k_o)/(k_e - k_o) = 0.28 W_e + 0.72 W_e^2 \tag{5}$$

Specific heat ([7], p. 171)

$$c_{mix} = X_o c_o + X_e c_e \tag{6}$$

Density

$$\rho_{mix} = [(W_o/\rho_o) + (W_e/\rho_e)]^{-1} \tag{7}$$

Latent heat

$$\lambda_{mix} = W_o \lambda_o + W_e \lambda_e \tag{8}$$

Expansion coefficient

$$\beta_{mix} = (\rho_{mix}/\rho_o) W_o \beta_o + (\rho_{mix}/\rho_e) W_e \beta_e \tag{9}$$

Viscosity ([7], p. 462)

$$\ln \mu_{mix} = X_o \ln \mu_o + X_e \ln \mu_e \tag{10}$$

As will be seen shortly, the melting correlation is not very sensitive to the mixture rule for μ, since μ appears to the ¼ power. From the foregoing, α_{mix} was evaluated as $(k/\rho c)_{mix}$ and ν_{mix} as $(\mu/\rho)_{mix}$.

A simple rule for estimating T^* for binary mixtures has been suggested by Dwyer [8] as

$$T^*_{mix} = T^*_o + X_e (T^*_e - T^*_o) \tag{11}$$

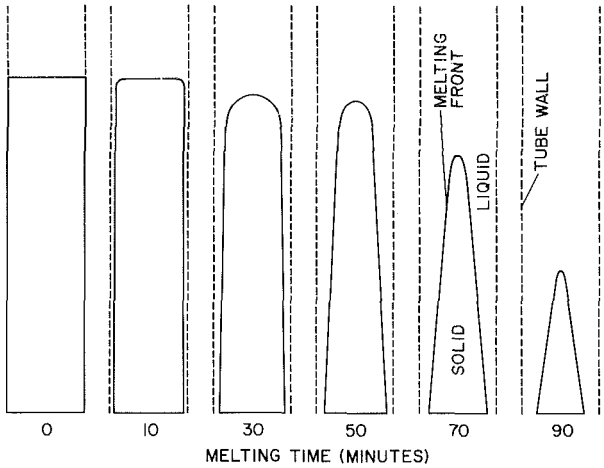

Fig. 1 Representative time history of the melting process

The T^* values predicted by equation (11) are compared in Table 1 with those measured as described earlier, and satisfactory agreement is seen to prevail. The deviations may be due, in part, to the fact that the "pure" *n*-octadecane and *n*-eicosane paraffins necessarily contained small amounts of impurities. According to [9], even among 99-percent-pure paraffins, there is a range of up to 1.3°C in the stated values of T^*, depending on the supplier of the material and on the composition of the impurities.

Results and Discussion

Melting Front Position and Shape. A history of the progress of the melting process can be assembled from the measured shapes of the solids which remained unmelted at the ends of the successive data runs. One such representative history is presented in Fig. 1, where longitudinal cross sections of the unmelted solid are shown at six instants of time. The unmelted solid, the liquid melt, the melting front, and the tube wall are identified in the figure. The specific results conveyed in Fig. 1 correspond to a 50/50 mixture of *n*-octadecane and *n*-eicosane and to a Stefan number Ste* = 0.056. The main point conveyed by Fig. 1 emerges from comparisons with Figs. 1–3 of [5], which show melting patterns for a pure paraffin. Such comparisons show no differences between the shapes of the melting solids for the impure and pure substances.

Timewise Increase of Melted Mass. The basic melting data collected during the course of the experiments are, for the most part, presented in Figs. 2 and 3 in terms of the M_L/M_T ratio. As indicated in the legend, each figure conveys data for *n*-octadecane, *n*-eicosane, and the two synthesized mixtures. By its inherent nature, M_L increases with time. All of the melted mass versus time results of Fig. 2 correspond to a given thermal operating condition. In particular, all of the melting runs were initiated with the solid at a temperature T_i just below the 28.2°C melting temperature of *n*-octadecane, while the temperature T_∞ of the melting environment bath was fixed at 38.2°C. Therefore, $(T_\infty - T_i) \cong 10$°C for all cases in Fig. 2. For Fig. 3, the initial temperature T_i of the solid was as in Fig. 2, but $T_\infty = 58.2$°C. Consequently, for all cases in Fig. 3, $(T_\infty - T_i) \cong 30$°C. Because of the higher thermal driving force in Fig. 3, the range of time on the abscissa is smaller than that for Fig. 2, reflecting the more rapid melting.

The objective of Figs. 2 and 3 is to display the differences in the melting rates of the various media and, thereby, to define the task of bringing the data together. In general, for a given thermal operating condition, melting becomes progressively slower for the sequence: *n*-octadecane, 50 percent octadecane and 50 percent eicosane, 25 percent octadecane and 75 percent

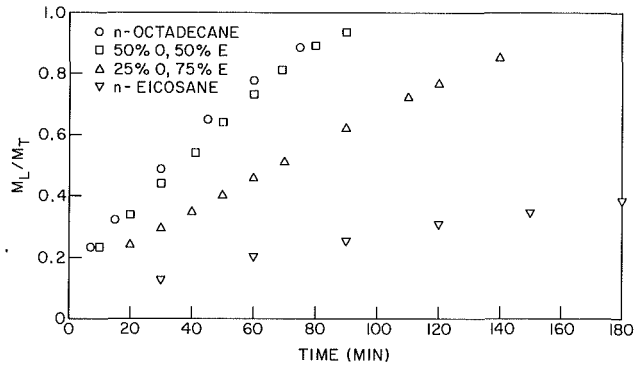

Fig. 2 Basic melting data for pure and impure substances, $(T_\infty - T_i) \cong 10°C$

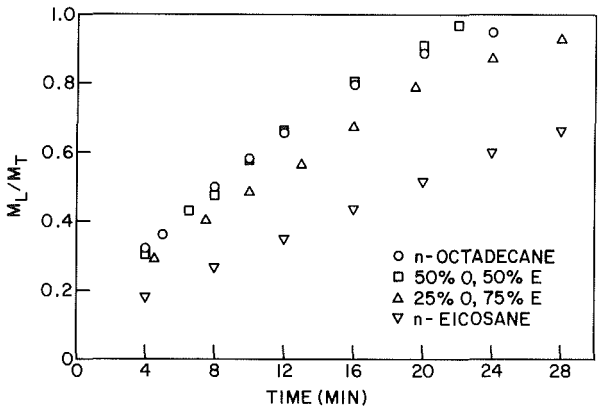

Fig. 3 Basic melting data for pure and impure substances, $(T_\infty - T_i) \cong 30°C$

eicosane, *n*-eicosane. This ordering reflects the different degrees of initial subcooling $(T^{**} - T_i)$ of the solid phases of the various substances, namely, 0, 0.9, 4.5, and 8.2°C (recall that $T^{**} = T^*$ for the pure substances). The subcooled solid absorbs energy which would otherwise cause melting, and the subcooling may even bring about a delay in the onset of melting (note that time = 0 in Figs. 2 and 3 corresponds to the moment that the tube is exposed to the step change of temperature).

Comparison of Figs. 2 and 3 indicates that greater differences among the melting rates of the various substances are in evidence for the former. This is as it should be, since subcooling should have a greater effect on melting at smaller values of the overall temperature difference $(T_\infty - T_i)$. Furthermore, in each figure, the melting rates of *n*-octadecane and the 50/50 octadecane/eicosane mixture are hardly different, reflecting the fact that both substances are similarly subcooled ($\cong 0$). The near-coincidence of the melting rates for these substances obviated the need for considering the 75 percent octadecane, 25 percent eicosane mixture.

In addition to the cases for which results are presented in Figs. 2 and 3, melting experiments were also performed for *n*-octadecane at a temperature difference $(T_\infty - T_i) = 5°C$. These results were obtained to provide additional inputs to the upcoming correlation of pure substance melting.

Correlation of Pure Substance Melting. The first step in the development of a melting correlation is to work with the pure substances (*n*-octadecane and *n*-eicosane), with the melting initiated without subcooling of the solid. This is the simplest of the investigated situations and is, therefore, an appropriate starting point for the correlation effort. The non-subcooled *n*-eicosane results used in the correlation were measured here with the same batch of paraffin as for the

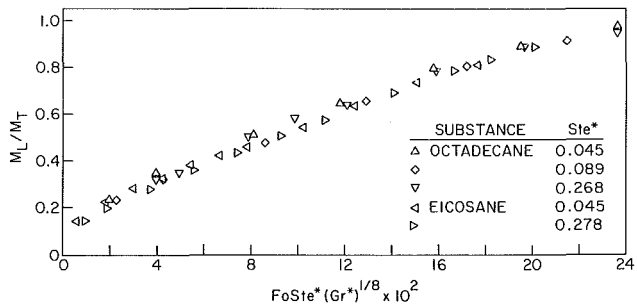

Fig. 4 Correlation of melting results for pure substances

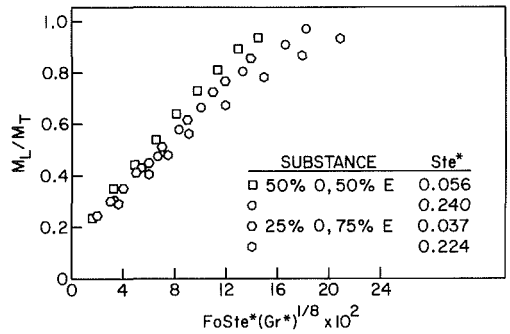

Fig. 5 Exploratory use of FoSte*(Gr*)$^{1/8}$ as a correlation parameter for melting of impure substances

various eicosane-involved substances of Figs. 2 and 3. This was deemed preferable to using the results of [5] which were obtained with a different batch of eicosane.

The first correlation parameter to be considered is the FoSte* product. This group is suggested by a one-dimensional melting model in which conduction is the only mechanism for transferring heat from the tube wall to the liquid-solid interface. The conduction-based solution indicates that aside from a weak dependence on Ste* (for the Ste* range of interest here), M_L/M_T should be a unique function of FoSte*. When the M_L/M_T data for *n*-octadecane and *n*-eicosane were plotted against FoSte*, good correlation was achieved at small FoSte* but not at larger FoSte*. This outcome is to be expected since, as previously noted, heat conduction is the dominant mode of heat transfer only at small times (small FoSte*) while natural convection dominates at larger times (larger FoSte*).

To account for the effect of natural convection, it is appropriate to include the Grashof number Gr* in the correlation parameter. To this end, the already-established form FoSte*(Gr*)^n was considered, and n was varied parametrically. The best representation of the data was achieved for $n = 1/8$. This representation is displayed in Fig. 4, where the M_L/M_T data for *n*-octadecane and *n*-eicosane, both without initial subcooling, are plotted as a function of FoSte*(Gr*)$^{1/8}$. Aside from minimal scatter, it is seen that the data for the two substances and for the various Ste* have been brought together – signaling the attainment of a correlation for pure substance melting.

Correlation of Impure and Pure Substance Melting. A correlation which encompasses both the melting of pure substances and the melting of impure substances will now be sought. In view of Fig. 4, the correlation parameter must reduce to FoSte*(Gr*)$^{1/8}$ for pure substances. Since $T^{**} = T^*$ for pure substances, it follows that both

$$\text{FoSte}^{**}(\text{Gr}^{**})^{1/8} \text{ and } \text{FoSte}^{*}(\text{Gr}^{*})^{1/8} \qquad (12)$$

are candidate parameters for correlating the pure substance and impure substance results.

The efficacy of FoSte*(Gr*)$^{1/8}$ will be examined first, and

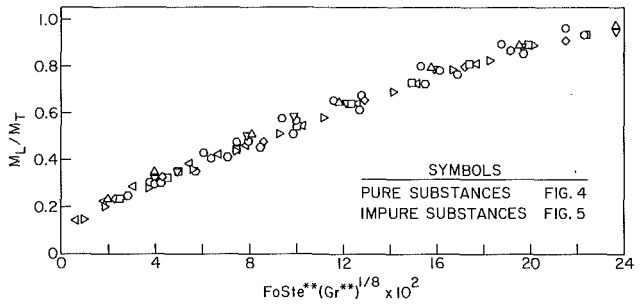

Fig. 6 Correlation of melting results for both pure substances and impure substances

Fig. 5 has been prepared to this end. This figure presents the melting results for the two synthesized mixtures, plotted in the form M_L/M_T versus FoSte*(Gr*)$^{1/8}$. Examination of the figure shows that a correlation as tight as that of Fig. 4 has not been achieved. This outcome prompts consideration of FoSte**(Gr**)$^{1/8}$ as the correlating parameter.

The M_L/M_T results for both the pure substances and the synthesized impure substances have been brought together and plotted in Fig. 6 as a function of FoSte**(Gr**)$^{1/8}$. These substances include nonsubcooled *n*-octadecane and *n*-eicosane, for which data symbols are listed in Fig. 4, and the 50/50 and 25/75 octadecane/eicosane mixtures, with data symbols given in Fig. 5.

From an examination of Fig. 6, it is seen that the melting data for the various pure and impure substances are very well correlated as a function of FoSte**(Gr**)$^{1/8}$, thereby signaling the fulfillment of the objective of the research. From the standpoint of practice, the existence of a correlation such as that of Fig. 6 means that the melting characteristics of impure substances can be obtained from the melting characteristics of related pure substances.

Concluding Remarks

The objective of the investigation reported here was to seek a means for correlating melting results for pure and impure substances. To this end, melting experiments were performed for two nominally pure paraffins, *n*-octadecane and *n*-eicosane, and for two synthesized impure substances – mixtures of the octadecane and the eicosane. The melting occurred in a closed vertical tube whose wall was subjected to a step-change increase in temperature.

Supplementary experiments were also carried out to measure two characteristic temperatures for each mixture. One of these, T^{**}, is the temperature at which melting of the solid phase begins. The other, T^*, is the lowest temperature at which melting can go to completion. For a pure substance, $T^{**} = T^*$.

The melting results for all of the investigated substances, both pure and impure, were successfully correlated as a function of FoSte**(Gr**)$^{1/8}$. [Note that FoSte**(Gr**)$^{1/8}$ reduces to FoSte*(Gr*)$^{1/8}$ for a pure substance]. Use of this correlation enables melting rates for impure substances to be determined from melting rates for pure substances. The evaluation of the impure substance melting rate requires that T^{**} be known, the value of which is readily measured in a simple experiment of the type used here for the synthesized mixtures. Note that it is not necessary to have information about the entire phase equilibrium diagram nor is there a need to know about possible variations of the temperature at the solid-liquid interface during the melting process.

The research performed here was concerned with impure substances which are binary mixtures of pure substances. It remains to investigate whether the present correlation method is applicable to more complex impure substances.

References

1 Viskanta, R., "Phase-Change Heat Transfer," *Solar Heat Storage: Latent Heat Materials*, G. A. Lane, ed., CRC Press, Boca Raton, FL, 1983.

2 Viskanta, R., Bathelt, A. G., and Hale, N. W., Jr., "Latent Heat-of-Fusion Energy Storage: Experiments on Heat Transfer During Solid-Liquid Phase Change," *Alternative Energy Sources III. Solar Energy 1*, T. N. Veziroglu, ed., Hemisphere Publishing, Washington, D.C., 1983, Vol. 1, pp. 279–304.

3 Mujumdar, A. S., Ashraf, F. A., Menon, A. S., and Weber, M. E., "PCM Thermal Storage in Cylindrical Containers of Various Configurations," *Proceedings, Second International Conference on Alternative Energy Sources*, Miami, FL, Dec. 1979.

4 Bareiss, M., and Beer, H., "Experimental Investigation of Melting Heat Transfer With Regard to Different Geometric Arrangements," *International Communications in Heat and Mass Transfer*, Vol. 11, 1984, pp. 323–333.

5 Sparrow, E. M., and Broadbent, J. A., "Inward Melting in a Vertical Tube Which Allows Free Expansion of the Phase-Change Medium," ASME JOURNAL OF HEAT TRANSFER, Vol. 104, 1982, pp. 309–315.

6 Humphries, W. R., and Griggs, E. I., "A Design Handbook for Phase Change Thermal Control and Energy Storage Devices," NASA Technical Paper 1074, 1977.

7 Reid, R. C., Prausnitz, J. M., and Sherwood, T. K., *The Properties of Gases and Liquids*, McGraw-Hill, New York, 1977.

8 Dwyer, L. R., Harrison Radiator Division, General Motors Corporation, Lockport, NY, personal correspondence, November 17, 1983.

9 Bailey, J. A., "Thermal Capacitor Design Rationale, Part 1: Thermal and Mechanical Property Data for Selected Materials Potentially Useful in Thermal Capacitor Design and Construction," NTIS Paper No. N75-18326, 1975.

Freezing of Liquid-Saturated Porous Media

J. A. Weaver

R. Viskanta
Fellow ASME

Heat Transfer Laboratory,
School of Mechanical Engineering,
Purdue University,
West Lafayette, IN 47907

The paper reports on an experimental and analytical study of freezing of a liquid-saturated porous medium. Experiments have been performed in a cylindrical capsule cooled from the outside and oriented vertically and horizontally to obtain quantitative temperature distribution and fusion front motion and shape data. Different-size glass and aluminum spherical beads were used for the porous medium, and distilled water was used as the phase-change material. A mathematical model, based on a one-dimensional analysis which considered heat conduction as the only mode of heat transfer in both the solid and liquid regions, has been developed and sensitivity studies have been carried out. Comparison of experimental data with predictions of the solid–liquid interface position and temperature distribution shows good agreement and thus confirms the mathematical model for a system of glass beads and water. However, for a system of aluminum beads and water the thermophysical property model is inadequate, and agreement between predictions and data is relatively poor.

Introduction

Solid–liquid phase-change heat transfer occurring in saturated porous media is of interest to problems in geophysics and numerous technologies. Some applications include latent heat-of-fusion energy storage [1], artificial and natural soil freezing and thawing [2], and food processing. Little attention has been given to the problem because of the inherent complexity encountered when dealing with porous media combined with the motion of the solid–liquid interface. Properties such as density, specific heat, and thermal conductivity intimately depend on the characteristics of the porous media (e.g., porosity and permeability). Natural convection, ground water seepage, and other types of fluid flow in the liquid further complicate the phase-change problem.

Artificial freezing of the ground is frequently used for construction and mining purposes. The frozen soil is employed as structural support and as a water barrier in large-scale excavations and tunnel or shaft construction. A review paper by Sanger [3] examines the applications and other aspects of artificial soil freezing arising in construction. Natural freezing of the soil is important in determining the heat loads of underground buildings. Performance of ground-based heat pumps could be affected by the freezing and thawing of the soil around the heat exchanger pipes in the ground [4, 5].

A large part of the available literature has been aimed toward practical design applications used for construction. Hashemi and Sliepcevich [6] numerically modeled freezing around a row of pipes in the presence of a groundwater flow normal to the pipe centerline using a finite element method. The same energy equation is used to describe the temperature fields in both the solid and liquid, and the latent heat effects are accounted for in the temperature-dependent specific heat over a suitable temperature range. Frivik and Comini [7] used an analysis similar to that of Hashemi and Sliepcevich [6]. In addition, they performed experiments using sand as the porous medium and measured both flow rates and temperature fields. Good agreement for both mass flow rates and temperature fields was found between experimental data and predicted results for the single test presented. Using advanced mathematical solution techniques, Goldstein and Reid [8] have studied freezing or melting in a water-saturated porous medium in the presence of seepage flow. The energy equation in the unfrozen region was solved without knowing the shape of the frozen region. The nonlinear interfacial energy balance was transformed into a nonlinear integral equation which was linearized by solving the equation over short time increments.

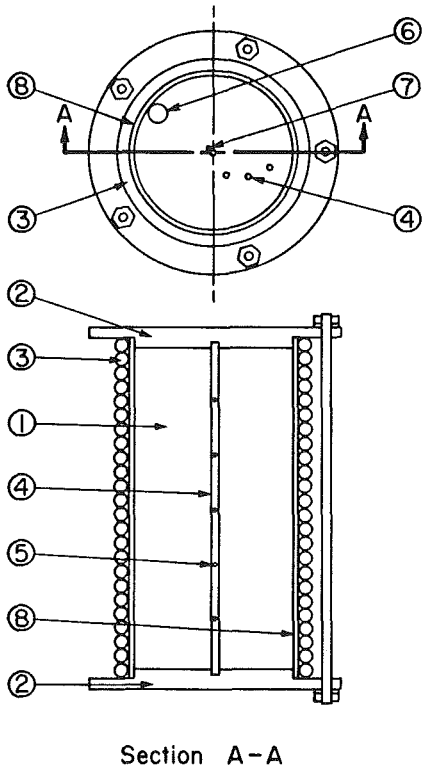

Fig. 1 Schematic of test cell: (1) test section; (2) acrylic end caps; (3) copper heat exchanger; (4) thermocouple rake; (5) thermocouple position on rakes; (6) fill tube; (7) overflow tube; (8) cylindrical brass tube

Only a very limited amount of analytical and experimental work on phase-change heat transfer in liquid saturated porous media has been reported, and understanding of the phenomenon is incomplete. This paper reports on an analytical and experimental study of solidification of a liquid-saturated porous medium contained in a cylindrical capsule. Results of numerical calculations and comparison of experimental data with predictions based on a pure heat conduction model are reported.

Contributed by the Heat Transfer Division and presented at the 23rd National Heat Transfer Conference, Denver, Colorado, August 1985. Manuscript received by the Heat Transfer Division May 15, 1985.

Experiments

Experimental Apparatus. Experiments of solid–liquid phase-change heat transfer in saturated porous media were performed in the cylindrical capsule shown in Fig. 1. The capsule consists of a brass cylinder (73.0 mm i.d., 1.07 mm wall thickness, and 158.8 mm long) with a bottom and top cap made of acrylic plastic. The thermal conductivity of acrylic is less than the thermal conductivity of the PCM and porous medium which helps in reducing the end effects. The heat source/sink consisted of two copper tubes (6.35 mm o.d., 4.76 mm i.d.) wrapped and soldered around the outside of the brass cylinder with the two tube inlets each at opposite ends of the cylinder. In this manner, the double-wrapped tubing acts like a counterflow heat exchanger to give a uniform wall temperature. The copper tubing does not cover the surface of the brass cylinder well at the ends. Therefore, a portion of the cap fits down inside of the brass cylinder to ensure that the inside test section had the same wall temperature everywhere. A tight seal was obtained using thin rubber gaskets made from surgical gloves and threaded rod to clamp the caps to the cylinder. An extra, hard rubber washer was used on one end to allow for some expansion of the test section if needed without breaking the test cell. Two tubes placed in the top cap enable excess water to be removed from the capsule as the water freezes (at the center of the cap) and the test section to be filled with the porous medium and PCM (near the inside wall of the cylinder). The test cell was insulated using Styrofoam fitted around the heat exchanger and caps (5.09 cm thick radially).

Measurement of the temperature distribution and wall temperature was made by four thermocouple rakes and five thermocouples placed on the outside of the brass cylinder using thermal epoxy. Radial and azimuthal positions of the rakes are shown in Fig. 1. This rake arrangement allows temperature measurements to be affected little by a rake at a larger radius. The copper-constantan thermocouples had a wire diameter of 0.13 mm. They were placed through holes in the plexiglass rakes, ran down the back of the rake and out the bottom cap. The thermocouple bead was placed approximately 0.5 mm away from the rake and directed radially outward.

Test Materials. Aluminum and glass spherical beads were used as the porous media. The beads were of soda-lime glass with diameters of 1.59, 2.89, and 6.0 mm. The properties used were for a soda-lime glass with a chemical composition as close as could be obtained to the chemical composition of the glass beads used in this study. The aluminum was commercially pure (Type 1100) with a bead diameter of 3.18 mm. Again, the properties were for aluminum of chemical composition as close as possible to the aluminum bead used in this study. The phase-change material was once-distilled, degasified water.

The porosity (volume of voids over the total volume) was determined in two ways using a separate cylindrical container. The porosity of the aluminum bead was 0.39; for the largest glass bead size it was 0.38 and for the smaller sizes 0.36. The porosity for all sizes of spherical beads should be equal assuming the same packing arrangement. The discrepancy is due to the roundness of the beads and increase in porosity near the wall of the container which is more significant for the larger bead size [9].

Test Procedure and Data Reduction. In preparing for an experiment, the test cell was first filled with the porous medium. The balls were settled to obtain approximately the same conditions for each run. After degasification, the water was carefully siphoned into the test cell to ensure that no air was trapped in the matrix or to prevent air from mixing with the water. A mixture of alcohol and water was circulated through the heat exchanger from two constant-temperature baths. After initial conditions were established, solidification of the water was initiated by circulating cooling fluid through the coils on the outside test cell wall at the desired wall temperature (below the fusion temperature). The difference between the wall and cooling fluid temperature was taken into account in the data reduction procedure.

The thermocouple output was read at a given interval of time using a data logger. From these temperatures, the temperature distributions and solid–liquid interface position as a function of time were determined. The time at which the interface reaches an arbitrary thermocouple, i.e., radial position, is determined as the time when the temperature difference between two consecutive temperature readings can be detected (second reading is below the fusion temperature for an initial liquid superheat or second reading is below the temperature of the subcooled water when it is initially at the fusion temperature). Since the temperature readings are taken at finite intervals, this introduces some error in the experimental determination of the solid–liquid interface motion and position.

Analysis

Assumptions and Model Equations. The physical system modeled for freezing consists of a cylinder, closed at the ends, filled uniformly with spheres (porous media) and liquid. Initially, the system is at a uniform temperature greater than or equal to the fusion temperature $T_i \geq T_f$. At time $t \geq 0$, a uniform temperature is imposed on the inside of the cylinder wall which is less than the fusion temperature, $T_w < T_f$. This initiates the freezing process with the fusion front moving radially inward.

The following assumptions are made in the analysis:

1 The porous medium is isotropic and homogeneous.
2 Physical properties are independent of temperature but are different for each phase.
3 Overall volume change due to phase change is negligible.
4 Heat conduction is the only mode of heat transfer in both the solid and the liquid, i.e., natural convection is assumed to be absent.
5 The solid–liquid interface is clearly defined, i.e., the PCM has a well-defined fusion temperature.

Nomenclature

c = specific heat
Fo = Fourier number $= \alpha_{sm} t/R^2$
Δh_f = latent heat of fusion
k = thermal conductivity
q^* = dimensionless heat flux $= -qR/k_{sm}(T_f - T_w)$
r = radius
r_I = radial interface position
R = inside radius of test section
S = solid thickness
Ste = Stefan number for freezing $= c_s(T_f - T_w)/\Delta h_f$
t = time
T = temperature
α = thermal diffusivity $= k/\rho c$
δ = dimensionless interface position $= r_I/R$
θ = dimensionless temperature for freezing $= (T - T_w)/(T_f - T_w)$
λ = dimensionless solid thickness $= S/R$
ξ = dimensionless radius $= r/R$
ρ = density
τ = dimensionless time $=$ Fo•Ste
ϕ = porosity

Subscripts

f = fusion
I = interface
i = initial
l = liquid phase
lm = effective liquid
m = porous medium
s = solid phase
sm = effective solid
w = wall

6 The local temperatures of the phase in the voids and porous medium are the same.
7 Porosity is uniform.

With the preceding assumptions, the resulting dimensionless energy equations for the solid and liquid are, respectively,

$$\text{Ste}\,\frac{\partial\theta_{sm}}{\partial\tau}=\frac{1}{\xi}\frac{\partial}{\partial\xi}\left(\xi\frac{\partial\theta_{sm}}{\partial\xi}\right) \tag{1}$$

$$\text{Ste}\left(\frac{\alpha_{sm}}{\alpha_{lm}}\right)\frac{\partial\theta_{lm}}{\partial\tau}=\frac{1}{\xi}\frac{\partial}{\partial\xi}\left(\xi\frac{\partial\theta_{lm}}{\partial\xi}\right) \tag{2}$$

The initial, boundary, and interface conditions for freezing are:

$$\theta_{lm}=\theta_i \quad \text{for } \tau\le 0 \tag{3a}$$

$$\theta_{sm}=\theta_w=0 \text{ at } \xi=1 \tag{3b}$$

$$\theta_{sm}=\theta_{lm}=1 \text{ at } \xi=\delta \tag{3c}$$

$$\phi\frac{(\rho c)_s}{(\rho c)_{sm}}\frac{\partial\delta}{\partial\tau}=\frac{\partial\theta_{sm}}{\partial\xi}-\left(\frac{k_{lm}}{k_{sm}}\right)\frac{\partial\theta_{lm}}{\partial\xi} \text{ at } \xi=\delta \tag{3d}$$

$$\frac{\partial\theta_{lm}}{\partial\xi}=0 \text{ at } \xi=0 \tag{3e}$$

The difference in density of the solid and liquid PCM is accounted for in the interfacial energy balance, but is neglected in the energy equation (i.e., convection is absent).

Before the model equations can be solved, a viable means of determining the thermophysical properties of the porous media is needed. Effective or average properties are used which are based on the fraction of each constituent. Specifically, the effective thermal capacitance (density times specific heat) is needed, which results in the following equation for the solid [10]

$$(\rho c)_{sm}=(\rho c)_m(1-\phi)+(\rho c)_s\phi \tag{5}$$

where *sm*, *m*, and *s*, respectively, refer to the solid influenced by the porous medium, the porous medium, and the solid phase. The equation for the liquid is determined by simply replacing *sm* and *s* by *lm* and *l*, respectively.

The thermal conductivity is more complex, because it depends on the geometry, heat flux direction, and volume fraction of each constituent. Methods for calculating the thermal conductivity of saturated and unsaturated soils have been evaluated [11], and a number of effective thermal conductivity models for porous medium have been discussed [10]. Of these, the series and parallel models are the simplest ones. Veinberg [12] has derived an equation which is claimed to be universally applicable for randomly distributed spherical inclusions in a medium. The equations for the series and Veinberg models, which are used in this work are, respectively,

$$\frac{1}{k_{sm}}=\frac{(1-\phi)}{k_m}+\frac{\phi}{k_s} \tag{6}$$

$$k_{sm}+\phi\left(\frac{k_m-k_s}{k_s^{1/3}}\right)k_{sm}^{1/3}-k_m=0 \tag{7}$$

Method of Solution. When solving a moving boundary heat transfer problem numerically, complications arise due to the motion of the solid–liquid interface with time. As such, the position of the interface is not known a priori and the domains over which the energy equations are solved vary. Furthermore, there exists a discontinuity in the temperature gradient at the fusion front.

Briefly, the method of solution uses a fixed grid system [13] coupled with an implicit time scheme. A node is specified at the interface, and the interface position must be determined as it progresses through the nodal system. To eliminate the inaccuracy introduced by the interpolation or extrapolation [13], unequal spacing in the computational grid on both sides of the interface (which changes with time) is employed. To handle this unequal spacing, the energy equation for the solid and liquid phases are finite differenced by first multiplying by the radius ξ and then integrating over a unit control volume in space [14].

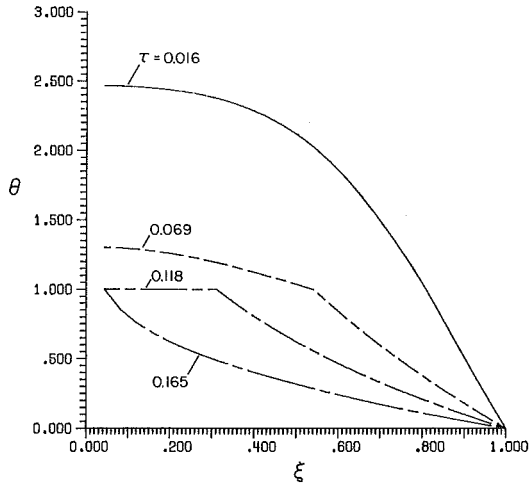

Fig. 2 Temperature distribution at various times; Ste = 0.1, ϕ = 0.5, θ_i = 2.5

Finite differencing of the interfacial energy balance requires an accurate approximation for the first derivative of temperature using the unequal spacing at the interface. By twice differentiating a second-order polynomial and solving for the first derivative (e.g., solid side of the interface), a suitable formula was derived which uses the interface node and two adjacent nodes on the solid side of the interface.

Initially ($t<0$) there is no solid phase present. Assuming that the fusion front velocity is proportional to the amount of energy removed at the cylinder wall, a dimensionless energy balance at the wall derived similar to the preceding interfacial energy balance yields

$$\phi\frac{(\rho c)_s}{(\rho c)_{sm}}\frac{\partial\delta}{\partial\tau}=\left(\frac{k_{lm}}{k_{sm}}\right)\frac{\partial\theta_{lm}}{\partial\xi} \tag{8}$$

This energy balance was used in the numerical solution to determine an initial fusion front velocity (i.e., solid thickness) for the first time step only. The purpose of the wall energy balance is to initiate the numerical solution. After the solid phase is established, the interfacial energy balance was used.

The independence of the solution on the grid was established by performing calculations for different grids. The model equations were also solved for the limiting case of a homogeneous medium (no porous media, $\phi=1.0$). The numerical results obtained for the interface position were found to be in excellent agreement with numerical predictions reported in the literature for freezing [15] and established confidence in the numerical algorithm employed.

Results and Discussion

Parametric Calculations. To gain insight into the effect of various parameters during the phase-change process (in the absence of natural convection in the melt), a parametric study was made [16]. These results are obtained using the series model for the effective thermal conductivity. Only some sample results for glass as the porous medium and water as the PCM are included here. Much more extensive results of parametric calculations are available elsewhere [16].

A typical temperature distribution during freezing of a superheated liquid is shown in Fig. 2. The solid region is represented by the portion of the temperature distribution between the fusion temperature ($\theta=1.0$) and the wall temperature ($\theta=0$). When the liquid is initially superheated, the liquid region is represented by the portion of the

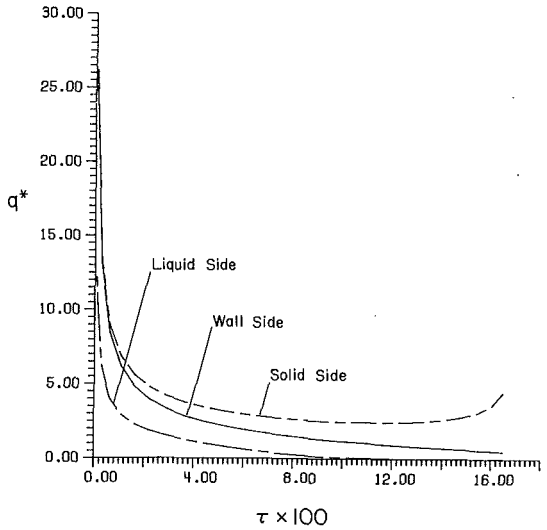

Fig. 3 Variation of heat flux at the wall and solid and liquid sides of the interface with time; Ste = 0.1, $\phi = 0.5$, $\theta_i = 2.5$

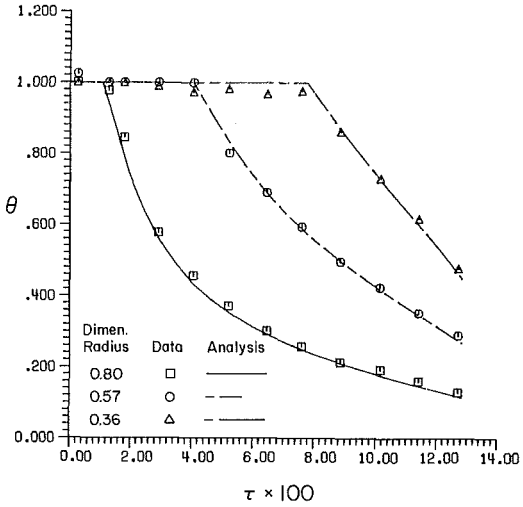

Fig. 5 Comparison of predicted and measured temperatures for freezing of water: glass beads 2.89 mm in diameter, $\theta_i = 1.0$

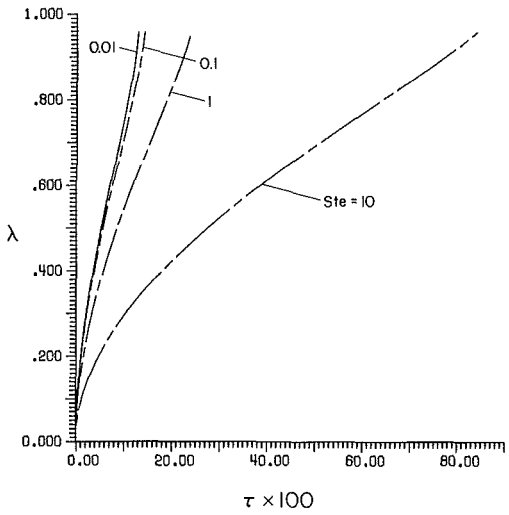

Fig. 4 Variation of solid thickness with time for different Stefan numbers; $\phi = 0.5$, $\theta_i = 1.0$

temperature distribution above the fusion temperature ($\theta = 1.0$). In the absence of a superheat, the liquid temperature would be uniform and would equal the fusion temperature.

Initially, the temperature distribution in the solid is practically linear due to the rapid growth of the solid phase. As the solid thickness increases, the rate of solidification decreases due to the increasing thermal resistance to heat flow. At later times, the temperature distribution becomes curved downward. This is due to the fact that the temperature at the outside wall (wall temperature, $\theta = 0$) is less than the temperature at the solid–liquid interface (fusion temperature, $\theta = 1.0$). Therefore, the heat transfer is in the direction of increasing radius. For a unit control volume, the area normal to the radial direction increases with increasing radius. This results in the temperature distribution being curved downward.

Figure 3 shows the typical variation of the dimensionless heat flux q^*. Initially, the heat flux at the wall and solid side of the fusion front are very high due to the small solid thickness. The wall heat flux decreases continuously due to the growth of the solid phase. In contrast, the heat flux at the solid side of the interface starts to increase just before complete solidification. This occurs because the area of the interface decreases more quickly than the temperature gradient on the solid side of the interface, which increases the heat flux on the solid side of the interface. Moreover, in Fig. 3 the initial superheat has been dissipated when the temperature gradient on the liquid side of the interface vanishes. An initial superheat in the liquid results in a heat flux to the interface (on the liquid side) along with a heat flux away from the interface (on the solid side). Therefore, the net energy removed at the interface (representing the rate at which the liquid is solidified) is smaller, resulting in increased time for complete solidification.

For a given PCM and other parameters defining the porous medium, decreasing the wall temperature is equivalent to increasing the Stefan number. This decreases the actual time for complete solidification (Fig. 4). Note, the dimensionless time τ is a function of various parameters (including the Stefan number) and therefore does not always exhibit the same trends as does the actual time.

Effects of using different phase change materials have been investigated, and it has been found that the rate of solidification is not very sensitive to the PCM [16]. The temperature distribution depends strongly on the effective thermal diffusivity, but the effective thermal conductivity is the most important parameter of the porous medium. It determines the heat flux at the interface which controls the rate of solidification. The effect of changing the porous medium (like the PCM) is manifested through its effective properties and influences the rate of solidification for otherwise identical thermal conditions imposed on the system [16].

Effects of the initial temperature or amount of initial superheat on the interface velocity are not illustrated for the sake of brevity. As previously discussed, the superheat in the liquid reduces the net heat flux at the interface [see equation (3*d*)]. Therefore, the actual time for solidification is increased as the amount of initial superheat of the liquid is increased.

Comparison of Predictions With Data. In comparing predictions of the numerical model with experimental data, the variation of the wall temperature with time resulting from the finite heat capacity of the test capsule walls must be accounted for. Only for very large heat fluxes would there be an appreciable difference in the outside and inside wall temperatures of the brass cylinder. Therefore, the measured outside wall temperatures were used in the numerical calculations. It is important to note that the dimensionless temperature is a function of the instantaneous wall temperature. Furthermore, the Stefan number and dimensionless time are functions of the wall temperature. Therefore, for any given time, the wall temperature must be known to determine the other model variables.

A sensitivity study was performed [16] using various effec-

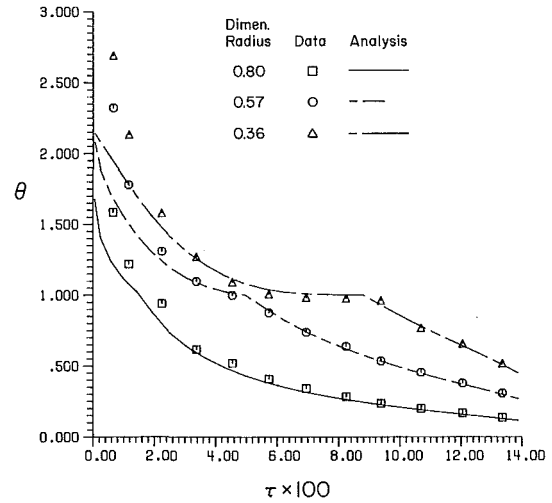

Fig. 6 Comparison of predicted and measured temperatures for freezing of water: glass beads 2.89 mm in diameter, $\theta_i = 2.145$

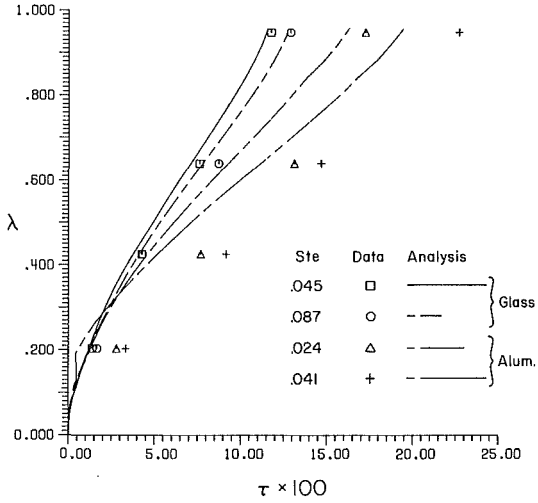

Fig. 8 Effect of Stefan number on the solid layer thickness for freezing of water; glass beads 2.89 mm in diameter, aluminum beads 3.18 mm in diameter, $\theta_i = 1.0$

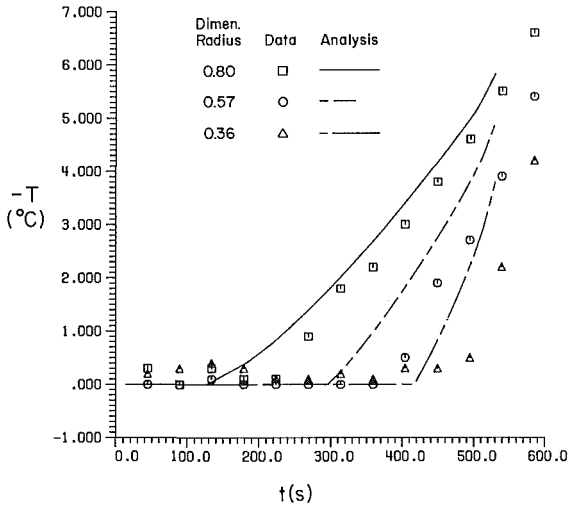

Fig. 7 Comparison of predicted and measured temperatures for freezing of water: aluminum beads 3.18 mm in diameter, $\theta_i = 1.0$

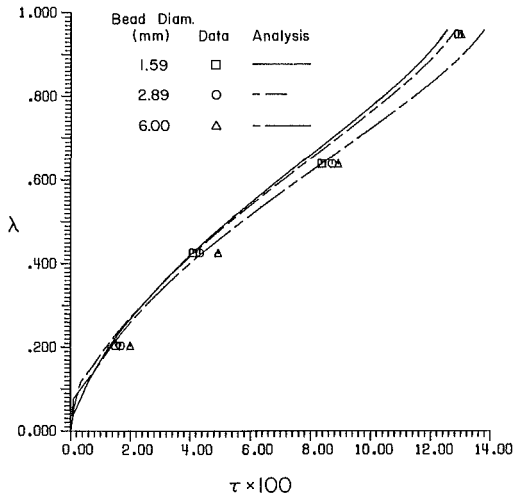

Fig. 9 Effect of bead diameter on the solid layer thickness for freezing of water, $\theta_i = 1.0$

tive thermal conductivity models to determine which best represents the system of spherical beads and water (or ice). By examining the temperature distribution and solid–liquid interface position, the Veinberg [12] model was found to give the best agreement for a water–glass bead system. For a water–aluminum bead system, the Veinberg model also gave the best agreement, but the discrepancy was larger. All of the results given are at the midheight of the test section.

Different glass bead diameters (6.0, 2.89, and 1.59 mm) had little effect on the agreement between data and predictions of the temperature distribution. Agreement is good for all three bead sizes. This was expected since the properties of the porous media and phase change material are similar and no natural convection was present ($\theta_i = 1.0$). Figure 5 illustrates the temperature variation with time for a glass bead diameter of 2.89 mm.

Figure 6 shows the temperature distribution with time for $\theta_i = 2.145$. Because the initial superheat is represented with some initial liquid temperature and the dimensionless temperature is defined using the wall temperature which varies with time until steady-state conditions are reached, the question arises as to what value of the wall temperature should be used to define the initial superheat. It was represented with the wall temperature averaged only over the time the liquid was superheated. Therefore, the discrepancy between the data and predictions at early times is due to this approximation. The overall agreement is, however, quite good. The temperature distribution confirmed the absence of natural convection during inward freezing of water in both vertically and horizontally oriented cylindrical capsules. Because of the good agreement, nothing further can be shown by examining the temperature distributions for the other experiments using glass beads; therefore, no additional comparisons will be given for the sake of brevity, but they can be found elsewhere [16].

Comparison of measured and predicted temperature distributions with time for a water–aluminum bead system is shown in Fig. 7. The results are presented in terms of dimensional parameters because when represented in dimensionless form, the data trends become exaggerated and therefore not representative. There are significant discrepancies for both the slope and magnitude of the temperature data compared with predictions. These results are partially attributed to the Veinberg model overpredicting the effective thermal conductivity. In addition, the assumption that the phase change material and porous media are in local temperature equilibrium becomes invalid when the difference between the properties of the porous media and the PCM is quite large. As a consequence, there may be a preferential direction for heat flow, because the aluminum beads have a much higher thermal conductivity than the PCM. Furthermore, the interface

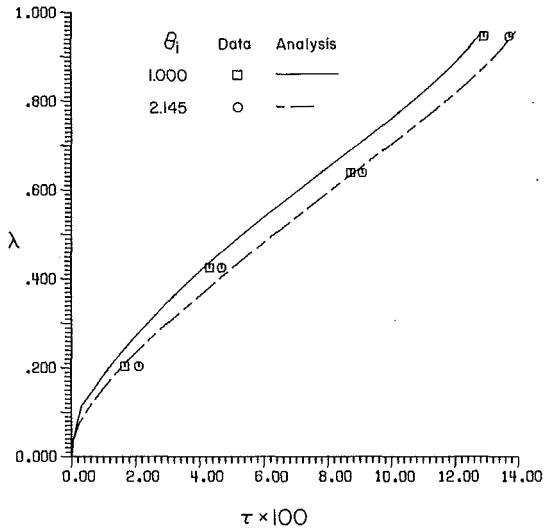

Fig. 10 Effect of the initial temperature on the solid layer thickness for freezing of water; glass beads 2.89 mm in diameter

does not progress smoothly through the porous media because the cross-sectional area of the pore varies.

Figure 8 shows the variation of the solid thickness with time for glass (Ste = 0.045 and 0.087) and aluminum (Ste = 0.024 and 0.041) beads as the porous media. Note that the slope between the last two data points for a water–glass bead system is larger than predicted (i.e., the system solidifies more quickly near completion). Since there is approximately a 10 percent decrease in the density of ice over that of water, 10 percent of the original mass of the phase-change material is removed from the test cell during freezing. This is not accounted for in the model. Therefore, the data show quicker freezing near complete solidification due to the loss of mass from the capsule. This occurred for every experiment except the test with aluminum beads and a Stefan number of 0.041. The four data points show practically a linear variation with time. This finding is attributed to rapid growth of the solid layer coupled with the uncertainty in the measurements.

Variation of the Stefan number resulted in the same trends as predicted by the parametric study (Fig. 4). The Stefan number in Fig. 8 refers to the parameter at complete solidification, since it varies with time. The good agreement for solidification with glass beads and the fact that there is considerable discrepancy between data and predictions for freezing with aluminum beads should be noted. The smaller Stefan number gives slightly better agreement for solidification with aluminum beads. This is believed to be due to a slower solidification rate. Therefore, the system is closer to temperature equilibrium between the porous medium and phase change material (which is assumed in the analytical model).

Different bead diameters had little effect on the solidification rate and agreement between data and predictions is within experimental error (Fig. 9). This was expected since the initial temperature is equal to the fusion temperature. There is slightly more discrepancy for the 6.0-mm bead size due to the increase in porosity near the wall and thermocouple rakes as mentioned earlier.

The presence of an initial superheat increases the time for complete solidification (Fig. 10). This confirms the findings of the parametric study, but the magnitude of the difference is smaller for the predictions. This result is attributed to the variation of the wall temperature with time for the experiment in contrast to a step change in wall temperature for the parametric study (Figs. 2, 3 and 4). As a result, the portion of the solid thickness on which the superheat has an effect is smaller for the experiment. Also, there is greater discrepancy between the data and predictions when the liquid is initially superheated. This is due to the approximation of the initial superheat used in the model as mentioned in discussing the temperature distribution. Furthermore, it was established that within experimental error the orientation of the test cell has no effect on the solidification rate as expected in the absence of initial superheat in the liquid.

Conclusions

The one-dimensional model for solid–liquid phase change heat transfer in porous media predicted reasonably well the temperature distribution and solid thickness with time for freezing. Comparison was slightly worse for the larger glass beads due to the noticeable increase in porosity near the wall and thermocouple rakes, and because the effective properties become less adequate as the system becomes more nonhomogeneous.

The results show that the effective thermal conductivity model of Veinberg is adequate only for a system in which the porous media and the PCM have similar values. The model overpredicts the effective conductivity when there is a very large difference in the thermal conductivities between the porous medium and the PCM. Furthermore, the assumption that the PCM and porous medium are in local temperature equilibrium becomes invalid.

Acknowledgments

The work was supported, in part, by the National Science Foundation Heat Transfer Program under Grant CBT-8313573. The authors are indebted to Professor W. Leidenfrost for many helpful discussions.

References

1 ME Staff, "Seasonal Thermal Energy Storage," *Mechanical Engineering*, Vol. 105, No. 3, 1983, pp. 28–34.

2 Lunardini, V. J., *Heat Transfer in Cold Climates*, Van Nostrand Reinhold Co., New York, 1981.

3 Sanger, F. J., "Ground Freezing in Construction," *ASCE Mechanics and Foundations Division*, Vol. 94, 1968, pp. 131–158.

4 Metz, P. D., "A Simple Computer Program to Model Three-Dimensional Underground Heat Flow With Realistic Boundary Conditions," ASME *Journal of Solar Energy Engineering*, Vol. 105, 1983, pp. 42–49.

5 Svec, O., Goodrich, L. E., and Planar, J. H. L., "Heat Transfer Characteristics of In-Ground Heat Exchangers," *Journal of Energy Research*, Vol. 7, 1983, pp. 263–278.

6 Hashemi, H. T., and Sliepcevich, C. M., "Effect of Seepage Stream on Artificial Soil Freezing," *ASCE Mechanics and Foundations Division*, Vol. 99, No. 1, 1973, pp. 267–289.

7 Frivik, P. E., and Comini, G., "Seepage and Heat Flow in Soil Freezing," ASME JOURNAL OF HEAT TRANSFER, Vol. 104, 1982, pp. 323–328.

8 Goldstein, M. E., and Reid, R. L., "Effect of Fluid on Freezing and Thawing of Saturated Porous Media," *Proceedings of the Royal Society of London*, Series A, Vol. 364, 1978, pp. 45–73.

9 Chandrasekhara, B. C., and Vortmetyer, D., "Flow Model for Velocity Distribution in Fixed Porous Beds Under Isothermal Conditions," *Wärme- und Stoffübertragung*, Vol. 12, 1979, pp. 105–111.

10 Combarnous, M. A., and Bories, S. A., "Hydrothermal Convection in Saturated Porous Media," *Advances in Hydroscience*, Vol. 10, Academic Press, New York, 1975, pp. 231–307.

11 Farouki, O., "Evaluation of Methods for Calculating Soil Thermal Conductivity," Cold-Regions Research and Engineering Laboratory Report 82-8, Mar. 1982.

12 Veinberg, A. K., "Permeability, Electrical Conductivity, Dielectric Constant and Thermal Conductivity of a Medium With Spherical and Ellipsoidal Inclusions," *Soviet Physics–Doklady*, Vol. 11, No. 7, 1967, pp. 593–595.

13 Murray, W. D., and Landis, F., "Numerical and Machine Solutions of Transient Heat Conduction Problems Involving Melting or Freezing," ASME JOURNAL OF HEAT TRANSFER, Vol. 81, 1959, pp. 106–112.

14 Patankar, S. V., *Numerical Heat Transfer and Fluid Flow*, McGraw-Hill, New York, 1980.

15 Sparrow, E. M., and Broadbent, J. A., "Freezing in a Vertical Tube," ASME JOURNAL OF HEAT TRANSFER, Vol. 105, 1983, pp. 217–225.

16 Weaver, J. A., "Solid–Liquid Phase Change Heat Transfer in Porous Media," MSME Thesis, Purdue University, May 1985.

Natural Convection Experiments in a Stratified Liquid-Saturated Porous Medium

D. C. Reda
Fluid and Thermal Sciences Department,
Sandia National Laboratories,
Albuquerque, NM 87185
Mem. ASME

Natural convection heat transfer from a constant-flux cylinder, immersed vertically through a stratified (two-layer) liquid-saturated porous medium, was investigated experimentally. Measured radial temperature profiles and heat transfer rates agreed well with numerical predictions based on the work of Hickox and Gartling. The 1:6 permeability-ratio interface existing between the two layers was found to effectively trap buoyancy-driven fluid motion within the high-permeability region, beneath the interface. Within this high-permeability region, Nusselt number versus Rayleigh number data were found to correlate with previously measured results, obtained for the same basic geometry, but with a fully permeable upper-surface hydrodynamic boundary condition. In both cases, the vertical and radial extent of the region under study were large compared to the radius of the heat source. Combined results indicate that, for a given Rayleigh number in the Darcy-flow regime, heat transfer rates from cylinders immersed vertically in uniform liquid-saturated porous media of large vertical and radial extent potentially approach limiting values. Variable-porosity effects which occur in unconsolidated porous media adjacent to solid boundaries were investigated numerically for cases where the particle-to-heater diameter ratio was small ($\approx 10^{-2}$). Results showed variable-porosity effects to have a negligible influence on the thermal field adjacent to such boundaries under conditions of Darcy flow.

Introduction

The subject of this paper is the study of nonisothermal buoyancy-driven flows in a liquid-saturated porous medium consisting of two horizontal layers of different permeability. Interest in this topic has increased in recent years due primarily to its impact on various engineering problems. Two notable examples include nuclear-waste isolation in geologic repositories [1] and geothermal energy extraction [2].

Convective flows in layered porous media have been studied numerically by McKibbin [3–6], Rana [2], Poulikakos and Bejan [7], and Gartling [8], in the latter case using the finite-element code MARIAH [9]. Ribando [10, 11] has done related numerical work on natural convection in liquid-saturated porous media wherein permeability varies with depth.

Experimental results for forced flows through layered porous media have been reported in the chemical engineering literature, e.g., Moranville [12]. However, no experimental results for natural convection in stratified liquid-saturated porous media were found during an extensive search of the literature.

The objective of the present research was, therefore, to generate an experimental data base aimed at identifying important aspects of the phenomenology encountered in such flows and which could also be used to validate the physics and numerics incorporated in any of the above-noted models. Special emphasis was placed herein on the MARIAH code [9] because of its application to nuclear-waste isolation problems.

Experimental Approach

Figure 1 shows a schematic of the experimental apparatus. The vertical annular region containing the liquid-saturated porous media had a radial gap width $\Delta r = 20.96$ cm, and was bounded by an inner cylinder of radius $r_i = 0.95$ cm and a concentric outer cylinder of radius $r_o = 21.91$ cm. The nondimensionalized vertical coordinate $Z/\Delta r$ was measured from a zero position at the bottom of the test region.

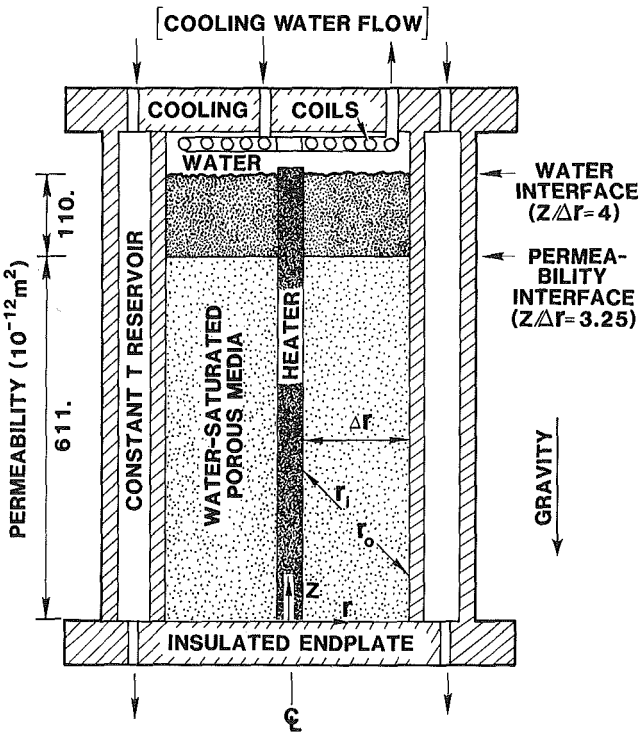

Fig. 1 Schematic of experimental apparatus

The inner cylinder was a resistance heater comprised of six coiled resistors wired in parallel, packed in magnesium oxide powder, and encased in a thick-wall stainless-steel shell. X-ray photography showed these resistors to be separated from one another by vertical spacings of $Z/\Delta r = 0.1$. (Note: Axial conduction along the heater, and effects of minor axial variations in an otherwise uniform power-dissipation rate, were both accounted for in the finite-element modeling.) Power input to the heater was measured by an electronic wattmeter and maintained constant for each experiment via a feedback loop incorporating a microcomputer and stepping-motor-controlled

Contributed by the Heat Transfer Division and presented at the 23rd National Heat Transfer Conference, Denver, Colorado, August 1985. Manuscript received by the Heat Transfer Division April 10, 1985.

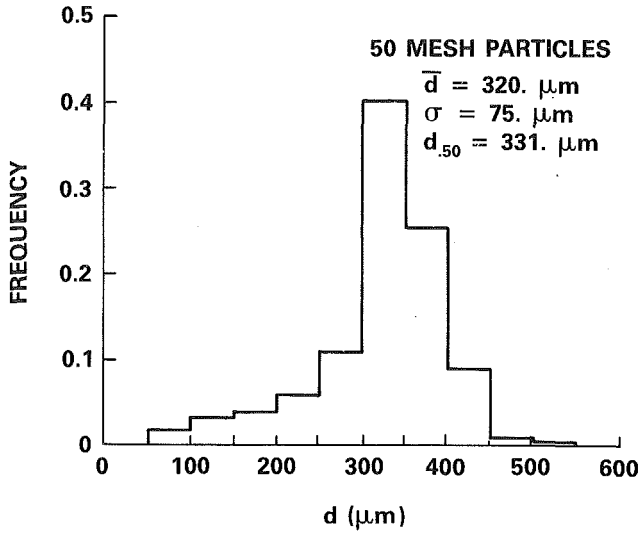

Fig. 2 Particle diameter distribution, 50 mesh

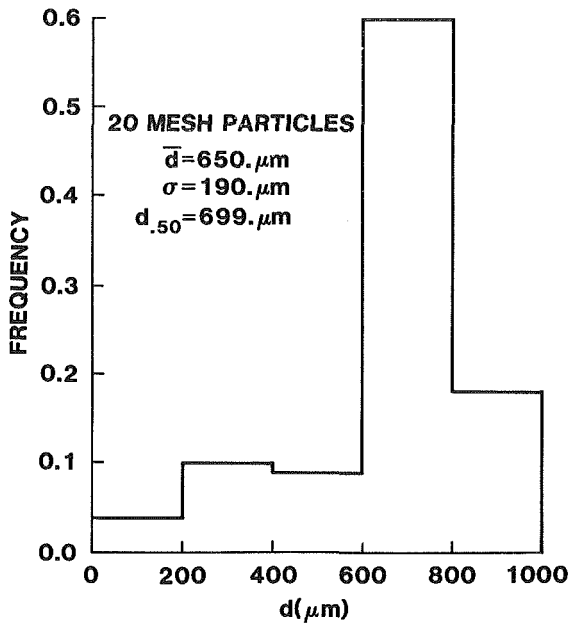

Fig. 3 Particle diameter distribution, 20 mesh

variac. Four separate power-per-unit-length values P of 34.5, 69.1, 103.6, and 138.1 W/m were utilized in the present investigation.

The porous media were comprised of solid glass beads, essentially spherical, with diameter distributions shown in Figs. 2 and 3. All properties of these media were measured: porosity, $\phi = 0.34$; effective (liquid-saturated) thermal conductivity, $K_e = 0.87$ W/m-°C; and permeabilities, $k = 110$ and 611×10^{-12} m^2. Distilled, deaerated water was used as the working fluid.

A permeability interface was established at $Z/\Delta r = 3.25$ by positioning the 50 mesh particles above the 20 mesh particles. Mixing of these two media was minimized due to the approximate 1:2 ratio of their average particle diameters.

A liquid/porous-medium interface was located at $Z/\Delta r = 4$, providing a constant-pressure, permeable-surface boundary condition across the top of the 50 mesh particles. The overlying liquid layer was maintained isothermal at 22.5°C through use of an immersed cooling coil linked to a constant-temperature bath.

The entire outer circumference of the test vessel was surrounded by a separate annulus. Temperatures along the r_o boundary were measured and maintained constant at 22.5°C by the continual recirculation of cooling water from this annulus through a second constant-temperature bath. Temperature measurements across the thickness of the lower end plate showed this boundary to be adiabatic.

Temperatures along the inner cylinder were measured via miniature surface-mounted thermocouples, while temperature distributions across the annulus were measured via radial thermocouple-probe arrays. Exposed-bead probes were utilized in the steep-temperature-gradient regions nearest the heater surface, while sheathed-thermocouple probes were utilized elsewhere. Probe calibration tests showed that this deployment would keep maximum probe conduction errors to within ≈ -1°C. More detailed discussions of the instrumentation and data-acquisition system are given in [13].

Physical Modeling and Numerical Results

The mathematical formulation and the computational approach utilized in the MARIAH code have been previously published [9]. Two aspects of the physical modeling, however, are discussed here: (1) utilization of Darcy's law as the momentum equation, and (2) flow channeling near impermeable boundaries.

In the present mathematical formulation, utilization of

Nomenclature

C_p = specific heat at constant pressure, kJ/kg-°C
d = particle diameter, μm
$\bar{d}$ = average particle diameter, μm
g = gravitational constant = 9.792 m/s^2
K_e = effective thermal conductivity of the liquid-bead mixture, W/m-°C
k = permeability, m^2
Nu = Nusselt number; see equation (4)
P = heater power per unit length, W/m
Ra = Rayleigh number; see equation (5)
r = radial coordinate, measured from centerline, m
Δr = annular gap width = $r_o - r_i$, m
T = temperature, °C
$\bar{T}_i$ = average heater surface temperature, °C; see equation (2)
ΔT = average temperature drop across Δr, °C; see equation (3)
$\bar{T}$ = average temperature for property evaluation, °C; see equation (7)
Z = vertical coordinate, measured from bottom of test region, m
α_e = effective thermal diffusivity, m^2/s; see equation (6)
β = volumetric expansion coefficient, 1/°C
λ = multiplier of permeability near a solid surface
μ = viscosity, kg/m-s
ρ = density, kg/m^3
σ = standard deviation
ϕ = porosity

Subscripts

f = of fluid phase
i = at the innermost radial location (r_i) of the annular test region
M = measured
max = maximum
o = at the outermost radial location (r_o) of the annular test region
P = predicted
0.50 = fifty percentile value
∞c = infinite cylinder

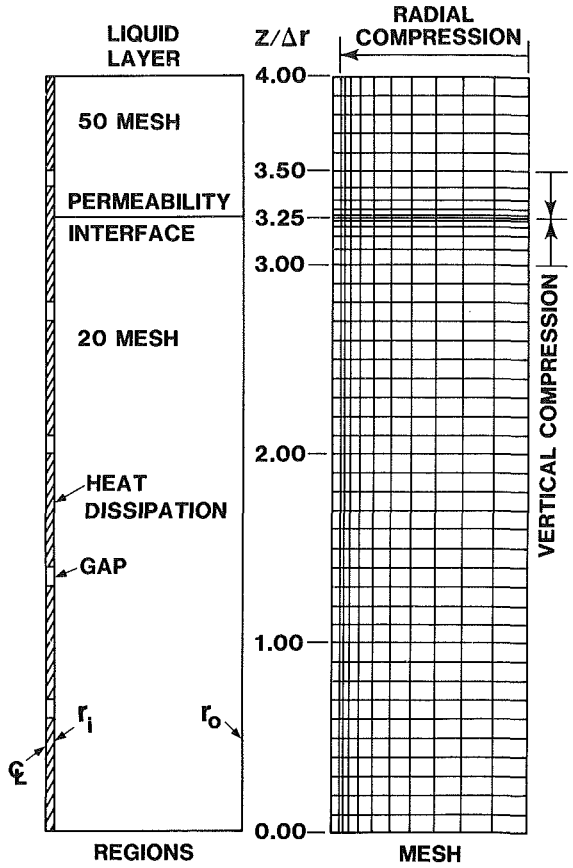

Fig. 4 Regions and finite-element mesh

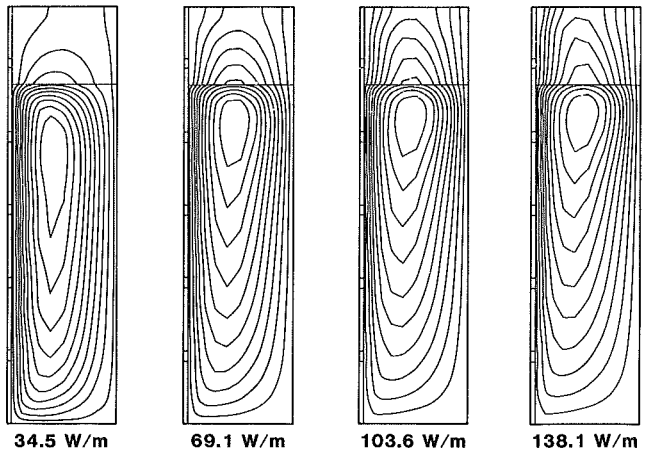

Fig. 5 Predicted streamlines

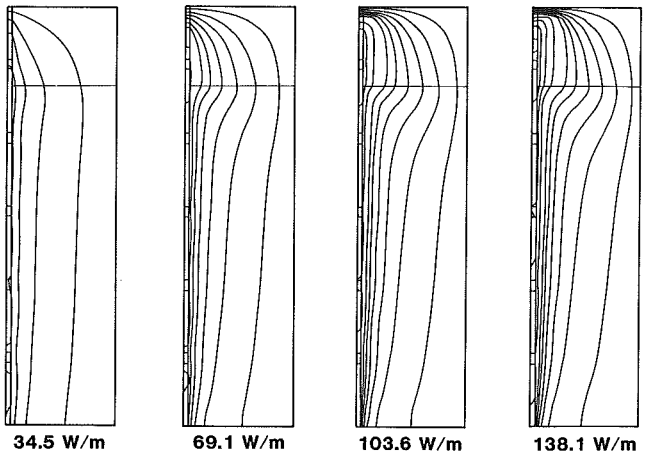

Fig. 6 Predicted isotherms

Darcy's law as the momentum equation dictates that the no-slip hydrodynamic boundary condition at impermeable surfaces cannot be applied. Maximum velocities parallel to such surfaces are thus predicted to occur at the surface. Application of mathematically more complex momentum equations, e.g., the Brinkman model [14], would result in a no-slip condition at impermeable boundaries, with predicted maximum velocities parallel to such surfaces occurring immediately adjacent to the surface. The attainment of the no-slip hydrodynamic boundary condition via Brinkman's model, however, forces the introduction of another parameter, the so-called "effective viscosity," the value of which is not strictly defined. Recent papers by Nield [15] and Haber [16] discuss the controversy which exists surrounding this issue.

Another near-surface phenomenon which could conceivably influence the thermal and velocity fields immediately adjacent to solid boundaries is "flow channeling." This effect arises due to porosity variations (increases) which occur in the packing of unconsolidated particles against solid surfaces. For perfect spheres, only point contacts with the solid boundary could exist, and the porosity of the medium would approach a limiting value of unity at the boundary.

Ranganathan [17] addressed this problem numerically for the case of *mixed* convection about a heated vertical surface in a liquid-saturated porous medium wherein the superimposed flow aided the buoyancy-induced motion. Brinkman's model was applied with the effective viscosity set equal to the fluid viscosity. Inertial effects were also modeled using the Ergun equation [18]. Results showed that, ". . . taking into account the variation of wall porosity within the medium influenced the temperature profiles by less than 1 percent. This was valid for a range of wall porosities between 0.8 and 1.0. It is believed that since the variation in the porosity is confined to a very small region near the boundary, its influence on the temperature field within the boundary layer is negligible." It was further noted in [17], "that variation of porosity had a slightly greater influence (~8 percent) on the velocity profiles near the boundary. Hence, from a heat transfer standpoint, it can be concluded that the variation of porosity near the boundary can be neglected."

Vafai [19] applied a Brinkman/Ergun extension of Darcy's law to the problem of *forced*-convection (inertially influenced) flows in fluid-saturated porous media; specific attention was given to flows in packed beds in the vicinity of an impermeable boundary. Vafai concluded that, "The variable-porosity effects are shown to be important and significant for most (forced-convection) cases. For calculating the heat flux at the boundary, for some cases, Darcy's law provides a better approximation for accounting the variable-porosity effects than the modified Darcy's law."

Therefore, based on the combined results of [17] and [19], it would be expected that variable-porosity (flow-channeling) effects are negligible in cases wherein the Reynolds number, based on pore velocity and particle size, is less than order one (i.e., in the Darcy-flow regime). An attempt was made to substantiate this assumption in the present research.

Flow-channeling effects were modeled herein by specifying a spatially dependent permeability, which linearly increased from its far-field value (k) to any prescribed value (λk), where $\lambda \geq 1$, as r decreased over the radial extent of the innermost finite element, a distance equal to 4.6 $\bar{d}$ for the 20 mesh particles and 9.3 $\bar{d}$ for the 50 mesh particles. Two points regarding this model warrant discussion. First, the ratios of particle diameters to heater diameter were 0.017 for the 50 mesh beads and 0.034 for the 20 mesh beads, both very small values. Ex-

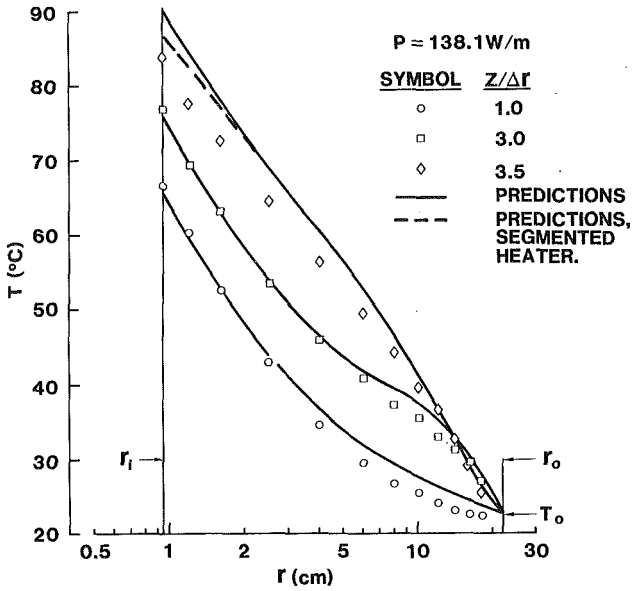

Fig. 7 Radial temperature profiles, $P = 138.1$ W/m

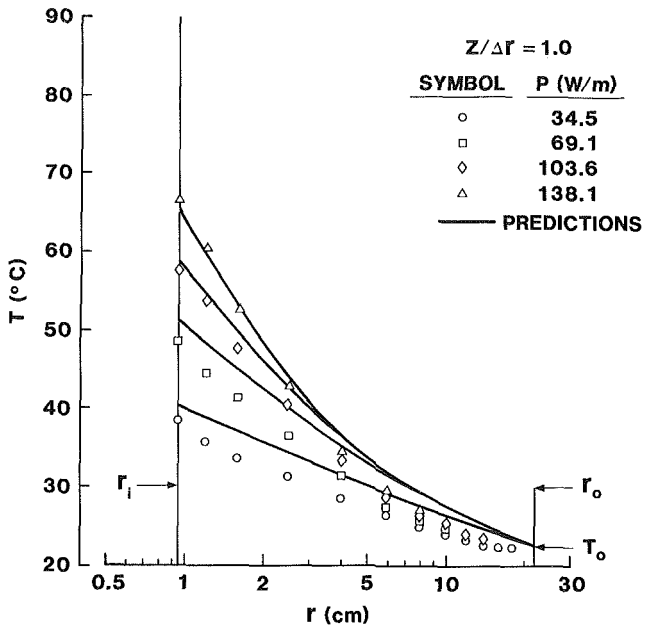

Fig. 8 Radial temperature profiles, $Z/\Delta r = 1$

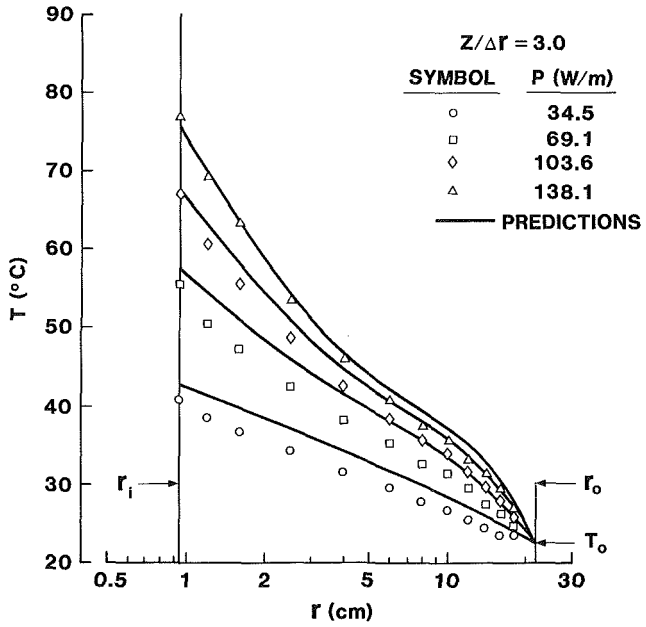

Fig. 9 Radial temperature profiles, $Z/\Delta r = 3$

tensions of the present findings to cases where the particle-to-heater diameter ratio becomes large may not be justified. Second, this flow-channeling model was applied solely along the r_i boundary, in the region of heat input, i.e, where the driving force for the fluid motion was applied. This fact, coupled with the annular geometry of the problem, dictated that maximum fluid velocities always occurred in the immediate vicinity of the r_i boundary. Flow-channeling effects, if found to be unimportant in this maximum-velocity region, would surely be negligible along all other boundaries of the problem.

A numerical sensitivity study was conducted, wherein λ was systematically varied from 1 to 8 while P was held constant at 138.1 W/m. Comparisons of predicted and measured surface temperatures along the inner heated boundary were used to quantify the influence of flow channeling on the thermal field. Results showed predicted T_i values to linearly decrease with increasing λ, consistent with the increased convective cooling of a constant-flux surface, but the overall influence was quite weak; an eightfold increase in near-surface permeability caused only a $\approx 6°C$ reduction in T_i levels. More importantly, λ values in the range 1 to 2 yielded best overall agreement with measured surface temperatures. (Note: Both of these observations are consistent with those of [13] wherein a doubling of near-wall permeability was found to affect predicted surface temperatures by less than 1°C.) Since uncertainties in this "free parameter" λ, in the range $1 \leq \lambda \leq 2$, corresponded to changes in predicted surface temperatures of only $\approx 1°C$, its inclusion in present analyses was concluded to be unjustified and unnecessary. In summary, flow-channeling effects adjacent to impermeable surfaces, within the Darcy-flow regime, were found to have a negligible influence on the predicted thermal field. Analyses reported herein were thus conducted without the utilization of any free parameters.

Figure 4 presents an outline of the physical regions encountered in the present problem, as well as the finite-element mesh used to compute the fluid flow and heat transfer throughout these regions. The finite-element mesh was comprised of 495 elements. Element dimensions were compressed in both the radial and vertical directions in order to more accurately compute the large temperature and velocity gradients which occurred in the immediate vicinity of both the heated surface and the permeability interface.

Measured boundary conditions, physical properties for pure water (including viscosity, thermal conductivity, and volumetric expansion coefficient as functions of temperature) and physical properties of the matrix material (including measured values for porosity, permeability, and effective thermal conductivity) were input to the code for each power level tested. Computations were done on a CRAY-1 computer; run times required to obtain steady-state solutions ranged from 85 to 200 s as P was increased from the minimum to the maximum value.

Figures 5 and 6 show predicted steady-state streamlines and isotherms for each of the four power levels tested. (Note: The ten predicted streamlines, for each power level, are plotted such that an equal mass flux occurs between any two adjacent contours; predicted isotherms are plotted in 5°C increments, for temperatures from 25°C to 50°C, then in 10°C increments for the temperature range 50°C to 90°C.) For each power level, the presence of buoyancy-driven fluid motion was more pronounced within the high-permeability region beneath the

Table 1 Comparison of measured and predicted results

P (w/m)	$\frac{Z}{\Delta r}$	$\lvert T_M - T_P \rvert_{MAX}$ (°C)	$\Delta T_{\infty C}$ (°C)	$\frac{\lvert T_M - T_P \rvert_{MAX}}{\Delta T_{\infty C}}$	$[T_i - T_o]_M$ (°C)	$\frac{\lvert T_M - T_P \rvert_{MAX}}{[T_i - T_o]_M}$
34.5	1.0	3.5	19.8	0.177	15.6	0.224
	3.0	3.0		0.152	18.4	0.163
	*3.5	1.5		0.076	17.5	0.086
69.1	1.0	4.0	39.6	0.101	26.2	0.153
	3.0	4.0		0.101	32.9	0.122
	*3.5	4.0		0.101	35.9	0.111
103.6	1.0	2.5	59.4	0.042	35.1	0.071
	3.0	2.5		0.042	44.3	0.056
	*3.5	5.5		0.093	49.3	0.112
138.1	1.0	2.5	79.2	0.032	44.0	0.057
	3.0	2.0		0.025	54.4	0.037
	*3.5	5.0		0.063	61.1	0.082
				AVG. = 0.084		AVG. = 0.106

*PREDICTIONS ASSUMING SEGMENTED HEATER

permeability interface, as expected. The upper layer of reduced permeability was seen to trap a major portion of the mass flux flowing vertically upward along the inner boundary, forcing it to turn and flow radially outward beneath the permeability interface. Outflow and inflow across the interface between the low-permeability medium and the overlying liquid layer were also seen. Quantitative comparisons between measured and predicted radial temperature profiles, and between measured and predicted heat transfer rates, are presented in the next section.

Experimental Results in Comparison With Numerical Predictions

Figure 7 shows radial temperature profiles (for a constant power level of 138.1 W/m) at three vertical locations, two beneath the permeability interface and one above. Several observations were made from these results. Surface and near-surface temperatures beneath the permeability interface were seen to increase with increasing vertical distance, indicating the presence of a strong buoyancy-driven upflow along the inner, heated boundary. By contrast, the radial temperature profile through the low-permeability layer showed higher absolute temperatures and an approximate linear relationship in T versus $\ln(r)$ coordinates, both facts indicating heat transfer within the conduction-dominated regime. A comparison of temperature profiles measured immediately below and above the permeability interface (i.e., at $Z/\Delta r = 3.0$ and 3.5) showed a crossover at large radial distance ($r > 15$ cm) with slightly higher temperatures occurring *below* the permeability interface near the outer boundary. These results indicate that the buoyancy-driven upflow along the inner cylinder (originating beneath the permeability interface) failed to penetrate the overlying low-permeability region to any significant extent, and was thus forced to turn outward, flowing radially beneath this interface toward the outer boundary.

Numerical predictions were found to be in good agreement with measured results for all power levels tested (see Figs. 8, 9, and 10). The existence of short unheated lengths along the inner boundary was found to affect the thermal field only within very localized volumes immediately adjacent to each such unheated length. Of the three data planes shown in Figs. 7 through 10, this minor experimental limitation influenced predicted results only on the $Z/\Delta r = 3.5$ plane. As can be seen in Fig. 10, modeling this effect resulted in improved agreement between predictions and measurements for radial locations within one heater radius of the r_i boundary.

Table 1 quantifies the comparisons of Figs. 7 through 10 in terms of maximum relative differences between predicted and measured radial temperature profiles using each of two distinct bases for nondimensionalization. In the first case, maximum observed differences between measured (T_M) and predicted (T_P) temperatures along each radial temperature

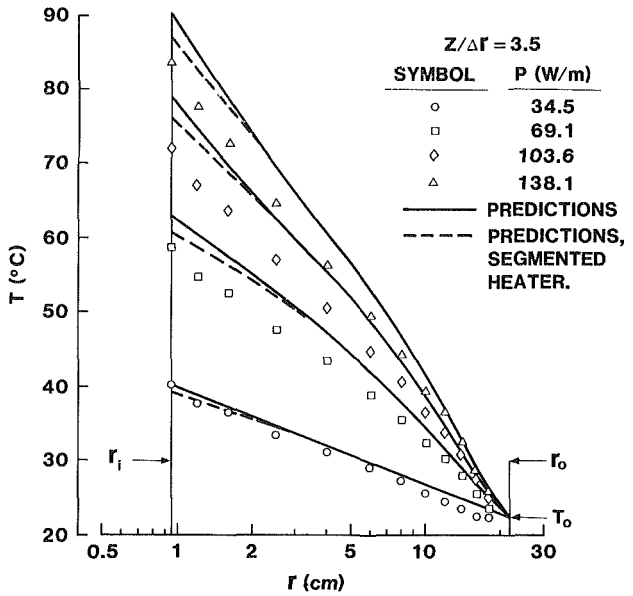

Fig. 10 Radial temperature profiles, $Z/\Delta r = 3.5$

distribution were divided by the limiting annular temperature drop dictated by the infinite-cylinder conduction solution

$$\Delta T_{\infty c} = \frac{P}{2\pi K_e} \ln\left(\frac{r_o}{r_i}\right) \tag{1}$$

The rationale for this basis is the fact that all numerical solutions, and/or experimental states, involving convective energy transport can be quantified by their "departure" from the conduction limit. Using this reference, numerically predicted temperatures were found, on the average, to be within ≈ 8 percent of measured values. Alternatively, the measured temperature drop across the annulus, $[T_i - T_o]_M$, on each $Z/\Delta r$ plane under study, was also utilized as a basis of comparison. Using this reference, numerically predicted temperatures were found, on the average, to be within ≈ 10 percent of measured values.

Figures 11 and 12 complete the present analysis by showing comparisons of measured and predicted results in terms of parameters which quantify heat transfer rates. Attention is focused here on the region below the permeability interface, treating the interface between this region and the overlying low-permeability layer as a *semi-permeable* hydrodynamic boundary condition. (Semi-permeable implies that mass can cross the permeability interface at any point, dependent solely on local vertical versus horizontal pressure, and thus velocity, gradients; recall the predicted streamline patterns of Fig. 5.)

Figure 11 shows a plot of temperature drop across the annulus as a function of the linear power dissipation rate. Equation (1) was used to calculate the theoretical curve for conduction heat transfer from an infinite cylinder (the limiting case for this problem).

In the presence of convection, both the measurements and the predictions showed that T_i increases with Z due to the buoyancy-driven upflow along the heater surface. Hence, in order to represent such cases in the present plot, average T_i and ΔT values were introduced

$$\bar{T}_i \equiv \frac{T_{i,z/\Delta r=1} + T_{i,z/\Delta r=3}}{2} \tag{2}$$

$$\Delta T \equiv (\bar{T}_i - T_o) \tag{3}$$

Measured and predicted results are plotted as symbols in Fig. 11, with "bars" above and below them to represent the magnitude of the vertical temperature difference along the heated surface. As can be seen, the magnitude of the average

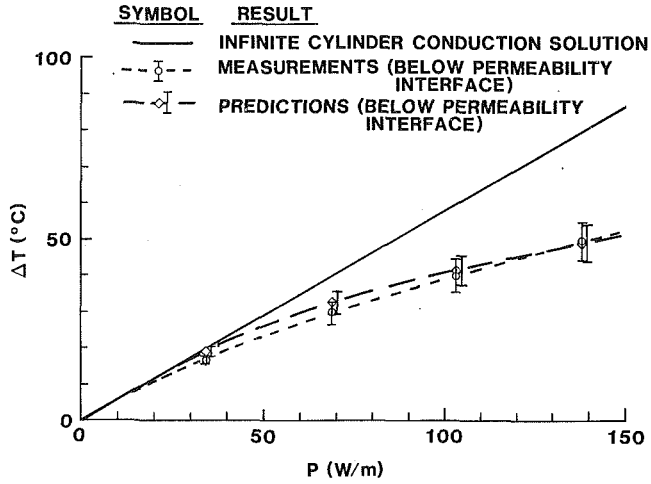

Fig. 11 Average radial temperature drop versus power input

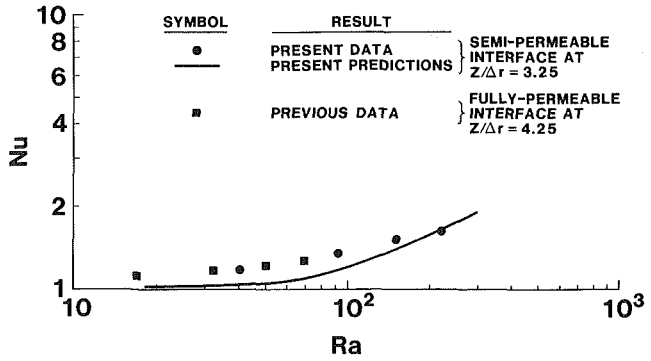

Fig. 12 Nusselt number versus Rayleigh number

radial temperature drop (ΔT), and the magnitude of the vertical temperature difference along the heater, both increased with increasing power input. These natural-convection results were at or below the infinite-cylinder conduction curve for all power levels, the extent of the departure increasing with increasing power. Measured and predicted values were found to be in good agreement.

These results can be interpreted in the classic Nusselt-number versus Rayleigh-number framework by defining the dependent variable (i.e., the Nusselt number) as the ratio of the actual power per unit length transferred away from the heater to the power per unit length which would be transferred away by conduction only *at the measured, or predicted,* ΔT

$$\mathrm{Nu} \equiv \frac{P}{\left[\dfrac{2\pi K_e \Delta T}{\ln(r_o/r_i)}\right]} \tag{4}$$

The independent variable in this correlating approach is the Rayleigh number, defined here by

$$\mathrm{Ra} \equiv \left[\frac{\rho_f g \beta_f \Delta T k \Delta r}{\mu_f \alpha_e}\right] \tag{5}$$

where

$$\alpha_e = \frac{K_e}{\rho_f C_{pf}} \tag{6}$$

Since, at this point, we are dealing with the region below the permeability interface, k in the definition of Ra is the permeability of the 20 mesh particles. Results of this correlating approach are shown in Fig. 12, where all fluid properties in equations (5) and (6) were evaluated at an average temperature $\bar{T}$ given by

$$\bar{T} = \left[\frac{\bar{T}_i + T_o}{2}\right] \tag{7}$$

Present results are shown here in comparison with results from [13] for natural convection in a liquid-saturated porous medium with an overlying *fully permeable* hydrodynamic boundary condition.

First, consider present results. The numerically predicted curve of Nu versus Ra showed initial (observable) departure from the conduction-dominated regime (Nu = 1.0) at Rayleigh numbers of ≈ 40, while experimental results indicated some convective-energy transport at this condition. (Due to the vertical orientation of the heat source, the theoretical limiting Rayleigh number for the absence of buoyancy-induced fluid motion is, of course, zero.) Predicted Nusselt numbers were seen to be ≈ 10 percent below measured values for low Rayleigh numbers, followed by an increased level of agreement at higher Rayleigh numbers.

Present and previous [13] measurements, obtained for the same basic geometry, but with different upper-surface hydrodynamic boundary conditions, were found to collapse to a single curve. In both cases, flow was vertically upward along the heat source, the upper surface hydrodynamic boundary condition allowing the heated fluid to either exit from the porous medium [13], or to be directed away from the heat source toward the outer boundary (the present case). Further, in both cases, the heat source was a long, slender cylinder immersed vertically in a uniform porous medium of large vertical and radial extent. (Note: Large is used in the context of geometric ratios. In terms of the heated cylinder radius, the location of the upper-surface hydrodynamic boundary condition was $Z/r_i = 93.5$ in [13], and 71.5 here, while the outer boundary was at $r_o/r_i = 23.0$ for both.) Therefore, these combined results indicate that, for a given Rayleigh number in the Darcy-flow regime, heat transfer rates from heated cylinders immersed vertically in uniform liquid-saturated porous media of large vertical and radial extent potentially approach limiting values.

No claim is made as to the universality of the experimental results shown in Fig. 12. Systematic variations in the locations of the outer boundaries relative to the heat source would have to be made before limiting conditions for total insensitivity to these boundary conditions could be determined. This was not an objective of the present research.

Summary

Based on present measurements, and on comparisons of these measured results with previous measurements and with numerical predictions, the following observations were made:

(1) The 1:6 permeability-ratio interface was found to effectively trap buoyancy-driven fluid motion within the high-permeability region, beneath the interface.

(2) Numerically predicted thermal fields, generated with the finite-element code of [9], were found to be within ≈ 8 percent of measured results, using the infinite-cylinder conduction solution as a reference for both.

(3) Nusselt number versus Rayleigh number data, measured for both a fully permeable and a semi-permeable upper-surface hydrodynamic boundary condition, were found to collapse to a single curve. (Fully permeable refers to the presence of a liquid layer overlying the porous region under study, while semi-permeable refers to the presence of a lower-permeability medium overlying the porous region under study.) In both cases, the ratio of the vertical extent of the porous medium to the heater radius was large (≈ 70 to ≈ 95); similarly, the ratio of the radial extent of the porous medium to the heater radius was large (23 in both cases). Therefore,

these combined results indicate that, for a given Rayleigh number in the Darcy-flow regime, heat transfer rates from heated cylinders immersed vertically in uniform liquid-saturated porous media of large vertical and radial extent potentially approach limiting values.

(4) Variable-porosity effects which occur in unconsolidated porous media adjacent to solid boundaries were investigated numerically for cases where the particle-to-heater diameter ratio was small (order 0.01 to 0.03). Results showed variable-porosity effects to have a negligible influence on the thermal field adjacent to such boundaries under conditions of Darcy flow.

Acknowledgments

This work was performed at Sandia National Laboratories supported by the U.S. Department of Energy under contract number DE-AC04-76DP00789.

References

1 Hickox, C. E., Gartling, D. K., McVey, D. F., Russo, A. J., and Nuttall, H. E., "Analysis of Heat and Mass Transfer in Subseabed Disposal of Nuclear Waste," *Marine Geotechnology*, Vol. 5, 1984, pp. 335–360.

2 Rana, R., Horne, R. N., and Cheng, P., "Natural Convection in a Multi-Layered Geothermal Reservoir," ASME JOURNAL OF HEAT TRANSFER, Vol. 101, 1979, pp. 411–416.

3 McKibbin, R., and O'Sullivan, M. J., "Onset of Convection in a Layered Porous Medium Heated From Below," *J. Fluid Mechanics*, Vol. 96, 1980, pp. 375–393.

4 McKibbin, R., and O'Sullivan, M. J., "Heat Transfer in a Layered Porous Medium Heated From Below," *J. Fluid Mechanics*, Vol. 111, 1981, pp. 141–173.

5 McKibbin, R., and Tyvand, P. A., "Anisotropic Modelling of Thermal Convection in Multilayered Porous Media," *J. Fluid Mechanics*, Vol. 118, 1982, pp. 315–339.

6 McKibbin, R., and Tyvand, P. A., "Thermal Convection in a Porous Medium Composed of Alternating Thick and Thin Layers," *Int. J. Heat and Mass Transfer*, Vol. 26, 1983, pp. 761–780.

7 Poulikakos, D., and Bejan, A., "Natural Convection in Vertically and Horizontally Layered Porous Media Heated From the Side," *Int. J. Heat and Mass Transfer*, Vol. 26, 1983, pp. 1805–1814.

8 Gartling, D. K., "Finite Element Analysis of Thermal Convection in Deep Ocean Sediments," *Advances in Water Resources*, Vol. 5, 1982, pp. 136–141.

9 Hickox, C. E., and Gartling, D. K., "A Numerical Study of Natural Convection in a Horizontal Porous Layer Subjected to an End-to-End Temperature Difference," ASME JOURNAL OF HEAT TRANSFER, Vol. 103, 1981, pp. 797–802.

10 Ribando, R. J., and Torrance, K. E., "Natural Convection in a Porous Medium: Effects of Confinement, Variable Permeability, and Thermal Boundary Conditions," ASME JOURNAL OF HEAT TRANSFER, Vol. 98, 1976, pp. 42–48.

11 Ribando, R. J., Torrance, K. E., and Turcotte, D. L., "Numerical Models for Hydrothermal Circulation in the Oceanic Crust," *J. Geophysical Research*, Vol. 81, 1976, pp. 3007–3012.

12 Moranville, M. B., Kessler, D. P., and Greenkorn, R. A., "Dispersion in Layered Porous Media," *AIChE J.*, Vol. 23, 1977, pp. 786–794.

13 Reda, D. C., "Natural Convection Experiments in a Liquid-Saturated Porous Medium Bounded by Vertical Coaxial Cylinders," ASME JOURNAL OF HEAT TRANSFER, Vol. 105, 1983, pp. 795–802.

14 Brinkman, H. C., "A Calculation of the Viscous Force Exerted by a Flowing Fluid on a Dense Swarm of Particles," *Appl. Sci. Res.*, Vol. A1, 1947, pp. 27–34.

15 Nield, D. A., "The Boundary Correction for the Rayleigh-Darcy Problem: Limitations of the Brinkman Equation," *J. Fluid Mechanics*, Vol. 128, 1983, pp. 37–46.

16 Haber, S., and Mauri, R., "Boundary Conditions for Darcy's Flow Through Porous Media," *Int. J. Multiphase Flow*, Vol. 9, 1983, pp. 561–574.

17 Ranganathan, P., and Viskanta, R., "Mixed Convection Boundary-Layer Flow Along a Vertical Surface in a Porous Medium," *Numerical Heat Transfer*, Vol. 7, 1984, pp. 305–317.

18 Ergun, S., "Fluid Flow Through Packed Columns," *Chem. Eng. Prog.*, Vol. 48, 1952, pp. 89–94.

19 Vafai, K., "Convective Flow and Heat Transfer in Variable-Porosity Media," *J. Fluid Mechanics*, Vol. 147, 1984, pp. 233–259.

Condensation Effects in a Fibrous Insulation Slab

K. Vafai
Mem. ASME

S. Sarkar

Department of Mechanical Engineering,
The Ohio State University,
Columbus, OH 43210

This paper analyzes the moisture accumulation and the increase in the effective thermal conductivity of a fibrous insulation slab due to moisture migration. The problem is modeled as a transient, multiphase flow, with variable properties, in a porous slab with impermeable, adiabatic horizontal boundaries and permeable vertical boundaries. A detailed investigation of the interaction between condensation rate, temperature, liquid content, and vapor density fields is presented. The influences of different humidity levels at the boundaries of the insulation slab are investigated in detail and the importance of the Peclet and Lewis numbers on the condensation process is demonstrated. The analysis shows that condensation, and the resulting augmentation of heat transfer, is a serious problem at large Peclet numbers ($Pe > 1$). Furthermore, the increase in the Nusselt number for fibrous insulation due to condensation is found to be minimized by designing an insulation slab which has a low Lewis number.

1 Introduction

Heat and mass transfer in porous media have been the subject of extensive investigations because of the applicability of such studies to a variety of problems including geothermal engineering, soil hydrology, energy conservation, drying technology, and nuclear waste disposal. An important topic in the area of energy conservation is the condensation effects on the performance of highly porous fibrous insulation.

Fibrous insulation consists of a solid matrix in a gas phase consisting of a mixture of air and water vapor and a very small amount of adsorbed liquid water. In many applications the fibrous insulation is part of an envelope separating the warm, humid air from a colder environment. Condensation may occur in the interior of the insulation if the heat losses decrease the vapor temperature to its saturation value. This results in augmented heat transfer as a result of the liberated latent heat of evaporation. Condensation also leads to an increase in the apparent thermal conductivity of an insulation slab as the thermal conductivity of water is approximately 24 times that of air.

Energy transfer in the fibrous insulation involves several different transport mechanisms. There is heat conduction in all three phases. Vapor diffusion and convection occur in the gas phase due to density variations induced by temperature and vapor concentration gradients. Infiltration occurs as a result of the pressure drop across the insulation walls. In addition, phase changes can lead to condensation or evaporation. The general aspects of transport mechanisms in porous media are utilized [1-9] to gain an understanding of the physics of the condensation process and its effects in a fibrous insulation.

When the temperature and vapor density gradients are moderate, the liquid accumulation by phase change is small [7] and therefore the condensate is usually present in a discontinuous and pendular state. In the pendular state, the liquid is practically immobile [8]. Hence vapor transfer, and not liquid transfer, is the dominant mode of moisture transport. Furthermore, moderate temperature gradients and the large aspect ratio of a typical fibrous insulation greatly reduce the free convection heat transfer process. However, the bulk convection due to air infiltration is usually very important.

In the present work the transient and spatial variations of liquid and gaseous content and the augmented heat transfer by the phase change are analyzed. For the first time the interface between the dry and wet zones is found directly from the solution of the transient governing equations, accounting for the gas density variations as well as the variable properties. The condensation regions are found to be significantly affected, both qualitatively and quantitatively, when the full transient problem and the variations of all thermophysical properties are considered. For example, the assumption of constant gas density leads to significant errors not only in the magnitude of the condensation rate but also in predicting the dry and wet interface regions. Likewise, an assumption such as nonzero condensation rates at steady state leads to significant errors. These results are very important since they have not been considered in any of the previous investigations.

The results in this paper present a detailed investigation of the interaction between condensation rate, temperature, liquid content, and vapor density fields. The condensation problem is formulated rigorously using a local volume-averaging technique. The assumptions used in analyzing the problem are explicitly stated. The importance of the Peclet and Lewis numbers on the condensation process is demonstrated. The influences of different humidity levels at the boundaries of an insulation slab are investigated in detail. It is shown that the heat transfer augmentation due to condensation is a serious problem for large Peclet numbers.

2 Analysis

The formulation of this problem is based on the local volume-averaging technique for mass, momentum, and energy equations for each phase to come up with the governing equations for the condensation process in the fibrous insulation. This is done by associating with every point in the porous medium a small volume V bounded by a closed spatial surface A. Let V_f be that portion of V containing the fluid. The average of a quantity Φ associated with the fluid is then defined as:

$$\langle \Phi \rangle = \frac{1}{V} \int_{V_f} \Phi dV \tag{1}$$

The derivation of the governing equations for heat and mass transfer in a fibrous insulation is based on Whitaker's work on drying [1]. Several simplifying assumptions are made to arrive at the governing equations:

1 The insulation matrix has a large aspect ratio and a small modified Rayleigh number.

2 The bulk velocity in the gas phase is due to infiltration.

3 The liquid accumulation is small; therefore it exists in the pendular form.

4 The fibrous insulation is homogeneous and isotropic.

Contributed by the Heat Transfer Division for publication in the JOURNAL OF HEAT TRANSFER. Manuscript received by the Heat Transfer Division January 10, 1985.

5 The porous system is assumed to be in local thermal equilibrium.

After some algebraic manipulations the following nondimensional governing equations are obtained

Liquid phase continuity equation:

$$\frac{\partial \epsilon_\beta}{\partial t} + \frac{\langle \dot{m} \rangle}{P_1 P_6} = 0 \tag{2}$$

Gas phase continuity equation:

$$\frac{\partial (\epsilon_\gamma \langle \rho_\gamma \rangle^\gamma)}{\partial t} + \mathrm{Pe} \frac{\partial \langle \rho_\gamma \rangle^\gamma}{\partial x} - \frac{\langle \dot{m} \rangle}{P_4 P_6} = 0 \tag{3}$$

Gas phase diffusion equation:

$$\frac{\partial (\epsilon_\gamma \langle \rho_v \rangle^\gamma)}{\partial t} + \mathrm{Pe} \frac{\partial \langle \rho_v \rangle^\gamma}{\partial x} - \frac{\langle \dot{m} \rangle}{P_4 P_6 P_{11}} = \frac{1}{\mathrm{Le}} \frac{\partial}{\partial x} \left[\langle \rho_\gamma \rangle^\gamma \frac{\partial}{\partial x} \left(\frac{\langle \rho_v \rangle^\gamma}{\langle \rho_\gamma \rangle^\gamma} \right) \right] \tag{4}$$

Energy equation:

$$\frac{\partial \langle T \rangle}{\partial t} + \frac{P_{18} P_3 P_4 \mathrm{Pe}}{P_{19}} \langle \rho_\gamma \rangle^\gamma \frac{\partial \langle T \rangle}{\partial x} + \frac{P_{18}}{P_{19}} \langle \dot{m} \rangle = P_{18} \frac{\partial^2 \langle T \rangle}{\partial x^2} + \frac{P_{18}}{P_{19}} \left(\frac{\partial K_{\mathrm{eff}}}{\partial x} \right) \frac{\partial \langle T \rangle}{\partial x} \tag{5}$$

Volumetric constraint:

$$\epsilon_\beta (x, t) + \epsilon_\gamma (x, t) + \epsilon_\sigma = 1 \tag{6}$$

Thermodynamic relations:

$$\langle \rho_v \rangle^\gamma = \frac{1}{P_9 \langle T \rangle} \exp \left\{ - \frac{P_{16}}{\langle T \rangle} + \frac{P_{16}}{T_0} \right\} \tag{7}$$

$$\langle \rho_\gamma \rangle^\gamma = P_{11} \langle \rho_v \rangle^\gamma + P_{12} \langle \rho_a \rangle^\gamma \tag{8}$$

where $\langle \rho_v \rangle^\gamma$ and $\langle \rho_\gamma \rangle^\gamma$ are the intrinsic phase averages for ρ_v and ρ_γ in the gaseous phase. These are defined as

$$\langle \rho_v \rangle^\gamma = \frac{1}{V_\gamma (t)} \int_{V_\gamma (t)} \rho_v dV \tag{9}$$

$$\langle \rho_a \rangle^\gamma = \frac{1}{V_\gamma (t)} \int_{V_\gamma (t)} \rho_a dV \tag{10}$$

The variable volume-averaged properties in the porous medium are

$$\bar{\rho} = \epsilon_\sigma \bar{\rho}_\sigma + \epsilon_\beta \bar{\rho}_\beta + \epsilon_\gamma (\langle \bar{\rho}_v \rangle^\gamma + \langle \bar{\rho}_a \rangle^\gamma) \tag{11}$$

$$\bar{C}_p = \frac{\epsilon_\sigma \bar{\rho}_\sigma \bar{c}_\sigma + \epsilon_\beta \bar{\rho}_\beta \bar{c}_\beta + \epsilon_\gamma (\bar{c}_v \langle \bar{\rho}_v \rangle^\gamma + \bar{c}_a \langle \bar{\rho}_a \rangle^\gamma)}{\bar{\rho}} \tag{12}$$

$$\bar{K}_{\mathrm{eff}} \cong \epsilon_\sigma \bar{k}_\sigma + \epsilon_\beta \bar{k}_\beta + \epsilon_\gamma \frac{(\bar{k}_v \langle \bar{\rho}_v \rangle^\gamma + \bar{k}_a \langle \bar{\rho}_a \rangle^\gamma)}{\langle \bar{\rho}_v \rangle^\gamma + \langle \bar{\rho}_a \rangle^\gamma} \tag{13}$$

$$\bar{\alpha}_{\mathrm{eff}} = \frac{\bar{K}_{\mathrm{eff}}}{\bar{\rho} \bar{C}_p} \tag{14}$$

and the controlling parameters are

$$P_1 = \frac{\bar{\rho}_\beta}{\bar{\rho}_0}, \quad P_3 = \frac{\langle \bar{c}_\gamma \rangle^\gamma}{\bar{c}_0}, \quad P_4 = \frac{\bar{\rho}_{\gamma,0}}{\bar{\rho}_0} \tag{15}$$

$$P_6 = \frac{\Delta \bar{h}_{\mathrm{vap}}}{\bar{c}_0 \Delta \bar{T}}, \quad \mathrm{Pe} = \frac{\bar{V}_0 \bar{L}}{\bar{\alpha}_{0,\mathrm{eff}}}, \quad \mathrm{Le} = \frac{\bar{\alpha}_{0,\mathrm{eff}}}{\bar{D}_{v,\mathrm{eff}}} \tag{16}$$

$$P_9 = \frac{\Delta \bar{T}}{\bar{T}_0}, \quad P_{11} = \frac{\bar{\rho}_{v,0}}{\bar{\rho}_{\gamma,0}}, \quad P_{12} = \frac{\bar{\rho}_{a,0}}{\bar{\rho}_{\gamma,0}} \tag{17}$$

$$P_{16} = \frac{\Delta \bar{h}_{\mathrm{vap}}}{\bar{R}_v \Delta \bar{T}}, \quad P_{18} = \frac{\bar{\alpha}_{\mathrm{eff}}}{\bar{\alpha}_{0,\mathrm{eff}}}, \quad P_{19} = \frac{K_{\mathrm{eff}}}{\bar{K}_{0,\mathrm{eff}}} \tag{18}$$

and the nondimensional variables are

$$x_i = \frac{\bar{x}_i}{\bar{L}}, \quad T = \frac{\bar{T}}{\Delta \bar{T}}, \quad \rho_\gamma = \frac{\langle \bar{\rho}_\gamma \rangle^\gamma}{\bar{\rho}_{\gamma,0}}, \quad t = \frac{\bar{t}}{(\bar{L}^2 / \bar{\alpha}_{0,\mathrm{eff}})} \tag{19}$$

$$\langle \rho_v \rangle^\gamma = \frac{\langle \bar{\rho}_v \rangle^\gamma}{\bar{\rho}_{v,0}}, \quad \langle \rho_a \rangle^\gamma = \frac{\langle \bar{\rho}_a \rangle^\gamma}{\bar{\rho}_{a,0}},$$

$$\dot{m} = \frac{\dot{\bar{m}}}{(\bar{\rho}_0 \bar{c}_0 \bar{\alpha}_{0,\mathrm{eff}} \Delta \bar{T} / \bar{L}^2 \Delta \bar{h}_{\mathrm{vap}})} \tag{20}$$

Here, T is the dimensionless temperature, t the dimen-

Nomenclature

$\bar{C}_p$ = average heat capacity, Ws/kgK
$\bar{c}$ = heat capacity at constant pressure, Ws/kgK
$\bar{D}_{v,\mathrm{eff}}$ = effective vapor diffusivity coefficient, m^2/s
Fo = Fourier number $= \bar{\alpha}_{0,\mathrm{eff}} \bar{t} / \bar{L}^2$
$\Delta \bar{h}_{\mathrm{vap}}$ = enthalpy of vaporization per unit mass, Ws/kg
$\bar{k}$ = thermal conductivity, W/mK
K_{eff} = dimensionless effective thermal conductivity $= \bar{K}_{\mathrm{eff}} / \bar{K}_{0,\mathrm{eff}}$
$\bar{K}_\beta$ = liquid phase permeability, m^2
$\bar{L}$ = characteristic length of the insulation, m
Le = Lewis number $= \bar{\alpha}_{0,\mathrm{eff}} / \bar{D}_{v,\mathrm{eff}}$
$\dot{m}$ = dimensionless rate of phase change (negative for condensation and positive for evaporation) $= \dot{\bar{m}} / (\bar{\rho}_0 \bar{c}_0 \Delta \bar{T} \cdot \bar{\alpha}_{0,\mathrm{eff}} / \bar{L}^2 \Delta \bar{h}_{\mathrm{vap}})$
Pe = Peclet number $= \bar{V}_0 \bar{L} / \bar{\alpha}_{0,\mathrm{eff}}$
$\bar{R}_v$ = vapor gas constant, Nm/kgK
t = dimensionless time $= \bar{t} / (\bar{L}^2 / \bar{\alpha}_{0,\mathrm{eff}})$
T = dimensionless temperature $= \bar{T} / \Delta \bar{T}$
$\bar{T}_h$ = reference temperature for the hot side of the insulation, K
$\bar{T}_c$ = reference temperature for the cold side of the insulation, K
$\bar{V}_0$ = infiltration velocity, m/s
$\bar{\alpha}_{0,\mathrm{eff}}$ = effective reference thermal diffusivity $= \bar{K}_{0,\mathrm{eff}} / \bar{\rho}_0 \bar{c}_0$, m^2/s
$\Delta \bar{T}$ = reference temperature difference, K
ϵ = volume fraction
ρ = dimensionless total density $= \bar{\rho} / \bar{\rho}_0$
ρ_v = dimensionless vapor density $= \bar{\rho}_v / \bar{\rho}_{v,0}$
$\rho_{v,s}$ = dimensionless saturated vapor density
$\bar{\rho}$ = density, kg/m^3
ω = relative humidity $= \bar{\rho}_v / \bar{\rho}_{v,s}$

Subscripts

a = air phase
c = cold boundary
eff = effective properties
h = hot boundary
ideal = ideal conditions defined in Section 4
0 = reference quantities
s = saturated vapor
v = vapor phase
β = liquid phase
γ = gas phase which consists of air and water vapor
σ = solid phase

Superscripts

$\bar{}$ = dimensional quantities
γ = intrinsic phase averages in the gaseous phase

Other

$\langle \rangle$ = "local volume average" of a quantity

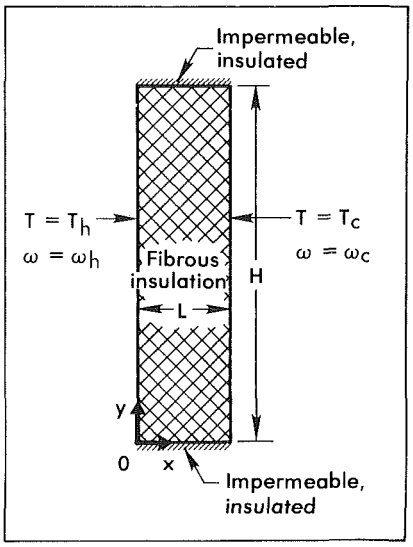

Fig. 1 The insulation slab with impermeable, adiabatic horizontal boundaries and permeable vertical boundaries

sionless time, ρ_v the vapor density, ϵ_β the liquid volume fraction, ϵ_γ the gaseous volume fraction, K_{eff} the effective thermal conductivity, ρ_γ the gas phase density, ρ the total density, C_p the average heat capacity, $\dot{m}$ the condensation rate, $D_{v,\text{eff}}$ the effective vapor diffusivity coefficient, $\alpha_{0,\text{eff}}$ the effective reference thermal diffusivity, and Δh_{vap} is the enthalpy of vaporization. The quantities with subscript 0 refer to the reference quantities, and the variables with a bar on top refer to dimensional quantities. The Peclet number Pe characterizes the relative importance of the convective and diffusive heat transfer process. The Lewis number Le characterizes the relative importance of the heat and mass transport mechanisms. Both the Peclet and Lewis numbers are independent of space and time.

To show the significance of the condensation process the above equations are solved subject to a different set of boundary and initial conditions. These boundary conditions are discussed in the next section. Among the controlling parameters, P_3, P_{18}, and P_{19} vary with transient and spatial variations of the thermophysical properties. On the other hand, P_1, P_4, P_6, P_9, P_{11}, P_{12}, and P_{16} are constants which are fixed once the reference properties are chosen.

3 Procedure and the Computational Scheme

The problem is modeled as an insulation slab with impermeable, adiabatic horizontal boundaries and permeable, isothermal vertical boundaries as shown in Fig. 1. The boundary and initial conditions on the temperature and the relative humidity ω are specified in nondimensional form as

$$\begin{aligned} T(x=0,\,t) &= 15.65 \\ T(x=1,\,t) &= 15.0 \\ T(x,\,t=0) &= 15.0 \end{aligned} \tag{21}$$

and

$$\begin{aligned} 0 < \omega(x=0,\,t) < 1 \\ \omega(x=1,\,t) &= 1 \\ \omega(x,\,t=0) &= 1 \end{aligned} \tag{22}$$

The above boundary conditions correspond to a hot and variable humidity environment on one side and a colder environment on the other side. As seen in equation (22) the humidity at the hot boundary was varied between zero and one to analyze the effects of different humidity levels on the condensation process.

The Lewis number (related to the thermophysical properties of the constituent phases) and the Peclet number (related to the infiltration velocity) were found to have a profound effect on the physics of the condensation process. To investigate the effects of these numbers on the condensation process, the numerical results were analyzed for the following range of these parameters

$$\begin{aligned} 0 < \text{Le} < 10 \\ 0 < \text{Pe} < 10 \end{aligned} \tag{23}$$

To measure the increase in heat transfer across the fibrous insulation slab, a Nusselt number based on phase change is introduced. This Nusselt number is defined at the colder surface with respect to the energy transfer when there is no phase change (ideal case), as follows

$$\text{Nu}_c = \frac{\text{Energy transfer across the colder surface accounting for the phase change}}{\text{Energy transfer across the colder surface neglecting the phase change}} \tag{24}$$

or

$$\text{Nu}_c = \frac{\left[\dfrac{\partial \langle T \rangle}{\partial x} - \text{Pe}_r \langle T \rangle\right]_{c,\text{actual}}}{\left[\dfrac{\partial \langle T \rangle}{\partial x} - \text{Pe}_r \langle T \rangle\right]_{c,\text{ideal}}} \tag{25}$$

where Pe_r is the reduced Peclet number defined as:

$$\text{Pe}_r = \text{Pe}\frac{\langle \bar{c}_\gamma \rangle^\gamma \langle \bar{\rho}_\gamma \rangle^\gamma}{\bar{C}_p \bar{\rho}} \tag{26}$$

The numerical scheme was based on the finite difference form of equations (2) through (8). The space derivatives were approximated by the central-difference form except for the convective terms which were approximated by using an upwind differencing scheme. The accuracy of the numerical solution was tested by decreasing the spatial and time increments and comparing the corresponding values of the pertinent variables in both cases. When there was no change in the values of T and $\langle \dot{m} \rangle$, up to five significant figures, steady-state conditions were assumed to have been reached.

In solving equations (2) to (8), depending on the magnitude of ϵ_β, two different approaches were pursued. Based on the experimental results of Langlais et al. [7], values of $\epsilon_\beta < 10^{-6}$ were considered to be part of the adsorbed water. It should be noted that the number 10^{-6} is an approximation obtained from the data in [7]. Therefore, when ϵ_β was less than 10^{-6}, the condensation rate was set equal to zero at that location in the slab. This is because vapor can no longer be considered as being in the saturated state when $\epsilon_\beta < 10^{-6}$; therefore bulk condensation is not possible. This way, for $\epsilon_\beta < 10^{-6}$ equation (7) was not used in the numerical solution. For regions where $\epsilon_\beta \geq 10^{-6}$, equations (2) through (8) were solved to obtain all the pertinent variables.

Initially, it was assumed that there is no water condensate inside the insulation slab. However, the solution scheme allowed the presence of some initial adsorbed water inside the slab. Although the nonhomogeneity near the insulation boundaries could be considered by letting ϵ_σ be a function of position, in the present analysis ϵ_σ was considered to be constant.

In analyzing the condensation process in a fibrous insulation slab the following physical data were used in the numerical calculations:

$\bar{L} = 0.12$ m, $\epsilon_\sigma = 0.03$, $\bar{T}_h = 313$K, $\bar{T}_c = 300$K,

$\bar{\rho}_0 = 31 \dfrac{\text{kg}}{\text{m}^3}$, $\bar{c}_0 = 842 \dfrac{\text{J}}{\text{kg-K}}$, $\bar{K}_{0,\text{eff}} = 0.026$ W/m-K,

$\bar{\rho}_\sigma = 1000$ kg/m^3, $\bar{c}_\sigma = 835$ J/kg-K, $\bar{k}_\sigma = 0.043$ W/m-K,

$\bar{\rho}_\beta = 1000$ kg/m^3, $\bar{c}_\beta = 4182$ J/kg-K, $\bar{k}_\beta = 0.603$ W/m-K,

$\bar{\rho}_{v,0} = 0.05$ kg/m^3, $\bar{c}_v = 1866$ J/kg-K,

$\bar{k}_v = 0.0191$ W/m-K, $\bar{\rho}_{a,0} = 1.045$ kg/m^3,

$\bar{c}_a = 1000$ J/kg-K, $\bar{k}_a = 0.0262$ W/m-K, $\bar{\rho}_{\gamma,0} = 1.16$ kg/m^3, $\bar{T}_0 = 313$ K,

$\Delta\bar{T} = 20$ K,

$\Delta\bar{h}_{\text{vap}} = 2442.5$ kJ/kg, $\bar{R}_v = 462.0$ J/kg-K.

4 Results and Discussion

The condensation process was found to be significantly affected by the thermophysical properties of the fibrous insulation, the infiltration velocity, and different humidity levels. In order to study these effects, the condensation process was analyzed for three cases. These were:

I Purely Diffusive Case, i.e., Pe = 0 and Le = 0(1). This case was analyzed for different humidity levels and different Lewis numbers. In this case convective vapor transport is negligible relative to diffusive vapor transport, as can be seen in equation (4), since $\text{Pe} << 1/\text{Le}$. Furthermore, convective heat transport is negligible relative to diffusive heat transport because in equation (5)

$$\frac{P_{18}P_3P_4\text{Pe}}{P_{19}} << P_{18} \quad \text{or} \quad \frac{P_{18}}{P_{19}}$$

II Convective Case, i.e., Le → ∞ and 1 ≤ Pe ≤ 10. The effects of different humidity levels and different Peclet numbers were analyzed. In this case Le → ∞ implies that Le is sufficiently large so that when Peclet number varies in the range of $1 \le \text{Pe} \le 10$, we may assume that $\text{Pe} >> 1/\text{Le}$ and thereby neglect diffusive vapor transport with respect to convective vapor transport in equation (4). However, diffusive heat transport is not negligible relative to convective heat transport because, in equation (5), and for the fibrous insulation properties

$$0(P_{18}) = 0\left(\frac{P_{18}}{P_{19}}\right) = 0(1)$$

while

$$0\left(\frac{P_{18}P_3P_4\text{Pe}}{P_{19}}\right) = 0(P_3P_4\text{Pe}) = 0.04\text{Pe}$$

Therefore, when $1 \le \text{Pe} \le 10$, diffusive heat transport is not negligible relative to convective heat transport.

III Combined Convective and Diffusive Case. In this case both convective and diffusive modes of transport are important during the heat and mass transfer process.

The condensation process was analyzed for different humidity levels in both the purely diffusive and the purely convective cases by varying $\omega(x=0)$ while keeping the other boundary conditions fixed. The changes in the condensation process caused by varying the humidity boundary condition are better understood by comparing the "ideal" vapor density field ($\rho_{v,\text{ideal}}$) with the ideal saturated vapor density field [$\rho_{v,s}(T_{\text{ideal}})$] for different values of $\omega(x=0)$. An ideal solution of a field variable is defined as the steady-state solution obtained after completely neglecting the phase change process in equations (2) to (8). It is shown later that in some cases such an ideal solution may not be physically viable.

Purely Diffusive Case (Pe = 0). For the purely diffusive case, the ideal profiles for the temperature and vapor density are linear. For ideal case $\langle\rho_\gamma\rangle^\gamma$ is constant, because there is no condensation at any time. Figure 2(*a*) shows three different linear profiles of $\rho_{v,\text{ideal}}$ obtained for three different values of $\omega(x=0)$, when the other boundary conditions are kept constant. Note that the profile of $\rho_{v,s}$ (T_{ideal}) which depends on $T(x=0)$ and $T(x=1)$ is not altered by a change in $\omega(x=0)$. The three different humidity levels in Fig. 2(*a*) represent three types of boundary conditions on $\omega(x=0)$. These three boundary conditions are chosen because they induce significant differences in the corresponding condensation and temperature solutions. These boundary conditions are classified as:

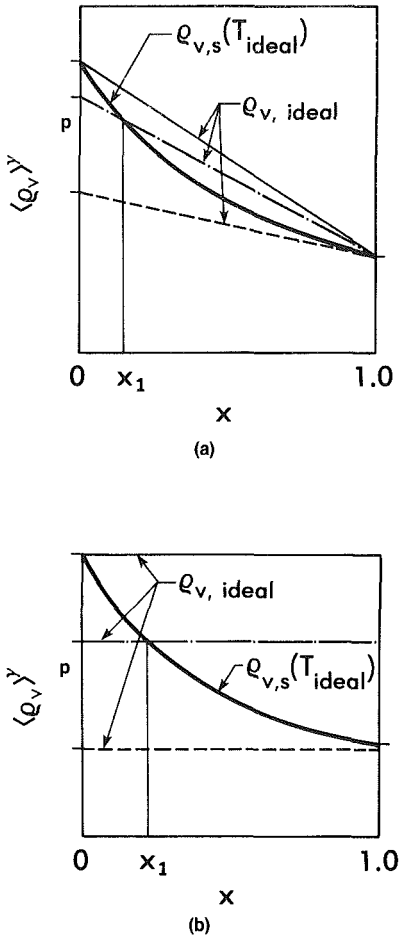

Fig. 2 The three possible boundary conditions obtained by varying humidity levels in the purely diffusive case (*a*), and in the purely convective case (*b*)

(*i*) Boundary conditions of type one

$$\omega(x=0) = 1.0$$

(*ii*) Boundary conditions of type two

$$\omega_p \le \omega(x=0) < 1.0$$

where ω_p is the relative humidity corresponding to point p in Fig. 2(*a*)

(*iii*) Boundary conditions of type three

$$\omega(x=0) < \omega_p$$

The above boundary conditions are analyzed for different Lewis numbers.

Boundary Conditions of Type One. At steady state, an ideal solution without phase change is not feasible in this case because the vapor density at any location cannot be greater than the saturation vapor density at the same location. Therefore, condensation would occur during the transient development of temperature and vapor density fields to reduce the vapor density to the saturated vapor density field. It was observed that the transient condensation process depended strongly on the Lewis number. However, at steady state, the gas density and the liquid content profiles do not vary with the Lewis number. The reason for this can be seen by examining equation (4). At steady state the condensation rate becomes zero and, for small liquid contents, the temperature distribu-

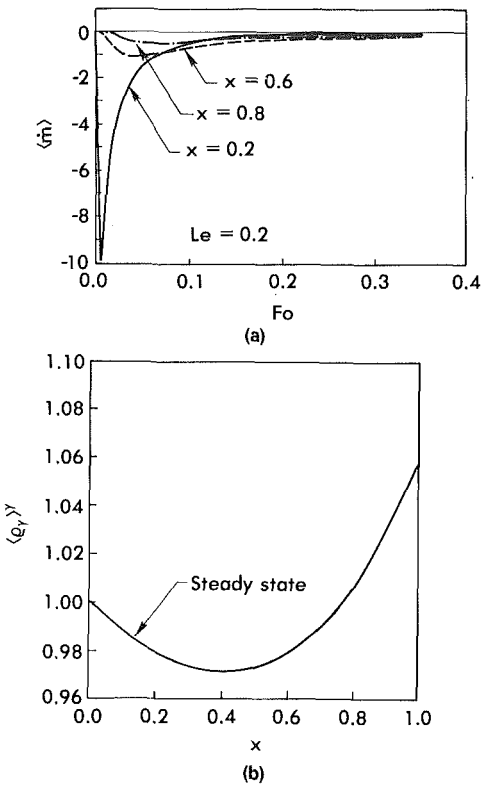

Fig. 3 Transient variations of the condensation rate (*a*) and the steady-state profile of the gas density for Pe = 0, and $\omega(x=0)=1$ (*b*)

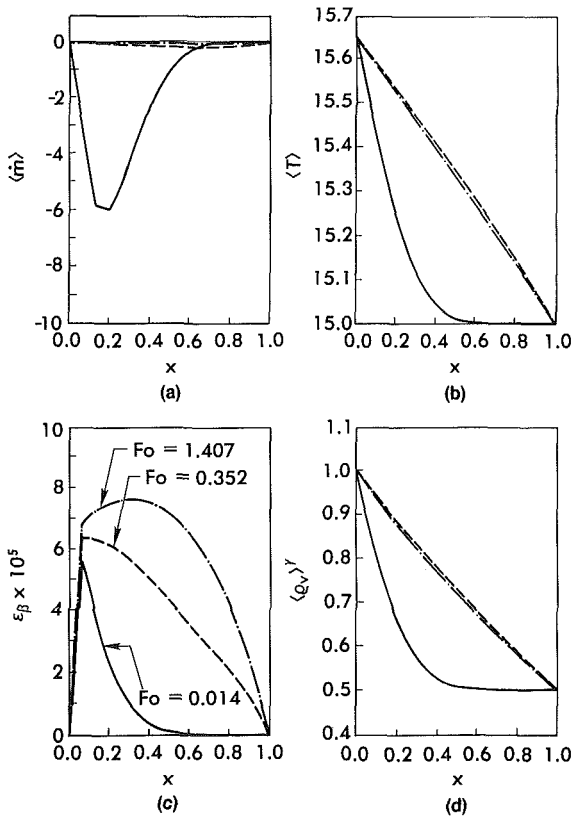

Fig. 4 The transient variations of the pertinent variables for Pe = 0, $\omega(x=0)=1$ and a small Lewis number (Le = 0.2)

tion approaches the ideal profile. Furthermore, the vapor content and the vapor density become invariant with time. Therefore equation (4) reduces to

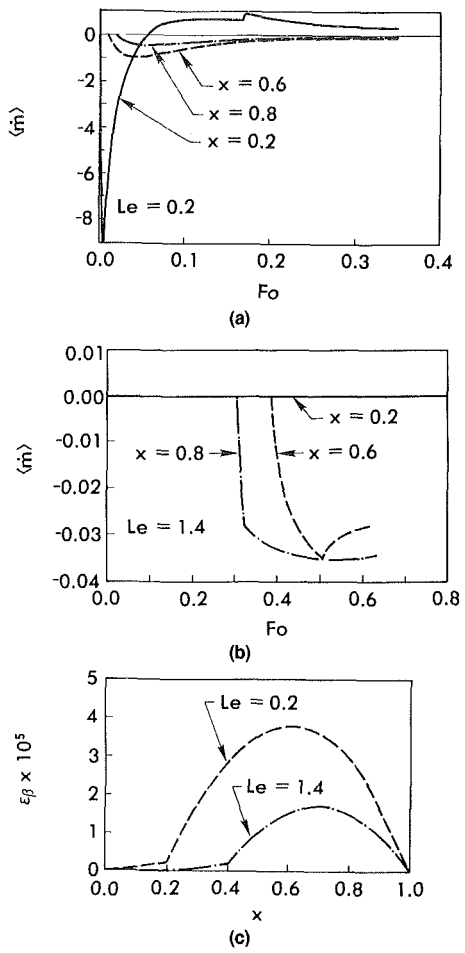

Fig. 5 The effects of the boundary conditions of type two, $\omega(x=0)=0.9$, on the condensation rate (*a*, *b*) and the liquid content at steady state (*c*) inside the insulation slab for the purely diffusive case

$$\frac{\partial}{\partial x}\left[\langle\rho_\gamma\rangle^\gamma \frac{\partial}{\partial x}\left(\frac{\rho_{v,s}}{\langle\rho_\gamma\rangle^\gamma}\right)\right]=0 \tag{27}$$

The above equation along with the two boundary conditions on the gas density uniquely specifies $\langle\rho_\gamma\rangle^\gamma$. Since there is no Lewis number dependency in equation (27) or the boundary conditions, the gas density will be independent of the Lewis number. The transient rate of phase change inside the insulation slab is shown in Fig. 3(*a*). The rate of phase change $\langle\dot{m}\rangle$ is negative for condensation and positive for evaporation. The steady-state gas density profile is shown in Fig. 3(*b*).

The transient response for the spatial condensation rate, temperature, liquid content, and the vapor density for a small Lewis number (Le = 0.2) are shown in Fig. 4. As seen in Figs. 3(*a*) and 4(*a*), at small Lewis numbers condensation starts immediately near the hot boundary and proceeds inward as the information from the left boundary reaches the inner regions. The condensation rate initially increases with time and later it decreases and converges to zero. The condensation acts as a heat source inducing the temperatures to rise above their ideal values. However, at steady state the condensation rate becomes zero and the temperature profile becomes almost linear. However, it should be noted that the vapor density profile at the steady state, as expected, is not linear. For a larger Lewis number (Le = 1.4), in contrast to the smaller Lewis numbers, initially there was no condensation. However, the condensation did occur after some time lag. This was because at smaller Lewis numbers the vapor density penetrates inward much faster than at larger Lewis numbers. Also, the condensation rate was significantly decreased and the temperature overshoot was smaller for the larger Lewis number. In addition, it

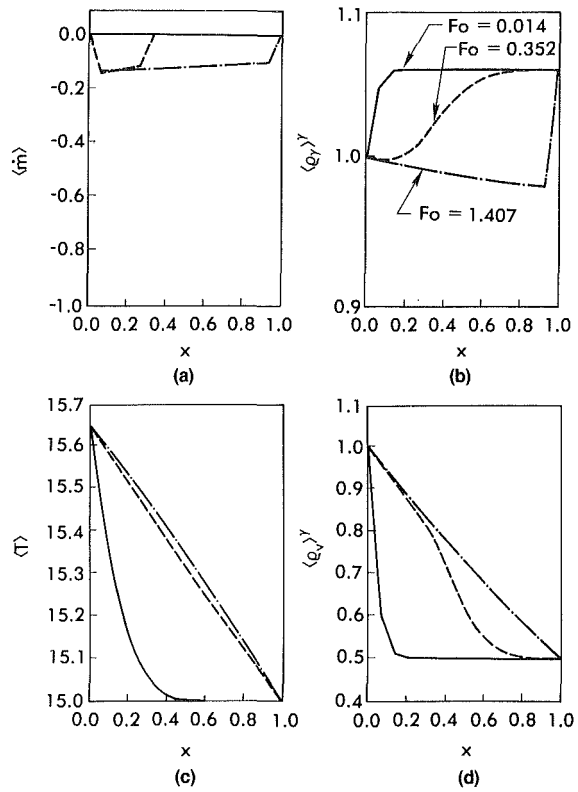

Fig. 6 The variations of the pertinent variables for the purely convective case, small Peclet numbers (Pe = 1), and the boundary conditions of type one ($\omega(x=0)=1$)

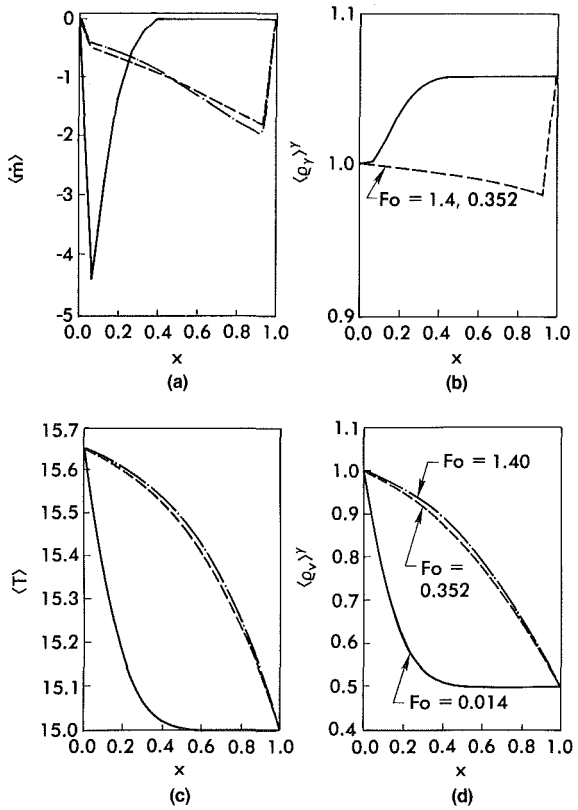

Fig. 7 The effects of larger Peclet numbers (Pe = 10) on the variables presented in Fig. 6

took longer to achieve steady-state conditions for larger Lewis numbers. It should be mentioned that in Fig. 4 as well as Figs. 6 to 10 the largest Fourier number profiles correspond to steady-state conditions.

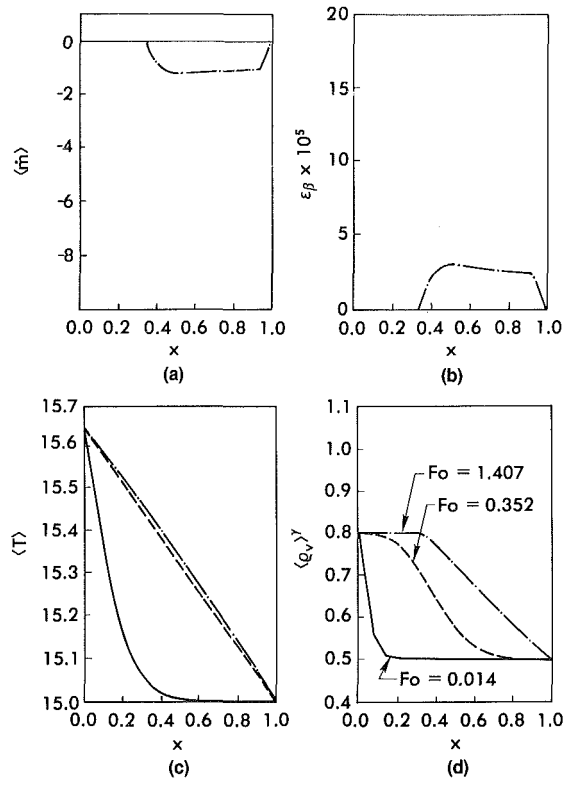

Fig. 8 The variations of the pertinent variables for the purely convective case, small Peclet numbers (Pe = 1) and boundary conditions of type two ($\omega(x=0)=0.8$)

The abrupt changes in some of field variables, shown in Figs. 3 and 4, are believed to be the result of the complex interaction of the temperature and moisture fields. This complex interaction, along with the application of a step change in the boundary conditions, does not allow for a smooth evolution of field variables. The spatial as well as the temporal grid steps were doubled to check the effect of the grid sizes on these abrupt changes. It was found that in general the curves become smoother, however, the very abrupt changes, and the qualitative behavior of the curves, were not affected by the increase in the grid sizes. This was found to be true for all of the figures presented in this paper.

Boundary Conditions of Type Two. In this case the ideal vapor density profile intersects the saturated vapor density field somewhere in the interior of the slab. Again, at steady state an ideal solution without phase change is not feasible because the vapor density at any location cannot be greater than the saturation vapor density at the same location. As seen in Fig. 5(*a*) the condensation rate initially increases and then decreases toward zero. As in type one, the temperature profile increases above the ideal profile and then converges back to the ideal profile. However, a dry zone is formed adjacent to the left boundary. Also, in contrast with type one, at steady state the gas density and liquid content were dependent on the Lewis number. The reason for this dependence can be seen by examining equation (4) for the dry zone. At steady state equation (4) reduces to

$$\frac{\partial}{\partial x}\left[\langle\rho_\gamma\rangle^\gamma \frac{\partial}{\partial x}\left(\frac{\langle\rho_v\rangle^\gamma}{\langle\rho_\gamma\rangle^\gamma}\right)\right]=0 \tag{28}$$

In the dry zone, $\langle\rho_v\rangle^\gamma$ is a function of not only the temperature but also the relative humidity of the vapor. Therefore, even though the steady-state temperature is independent of the Lewis number, the vapor density is dependent on the Lewis number. This in turn causes the gas density to be dependent on the Lewis number.

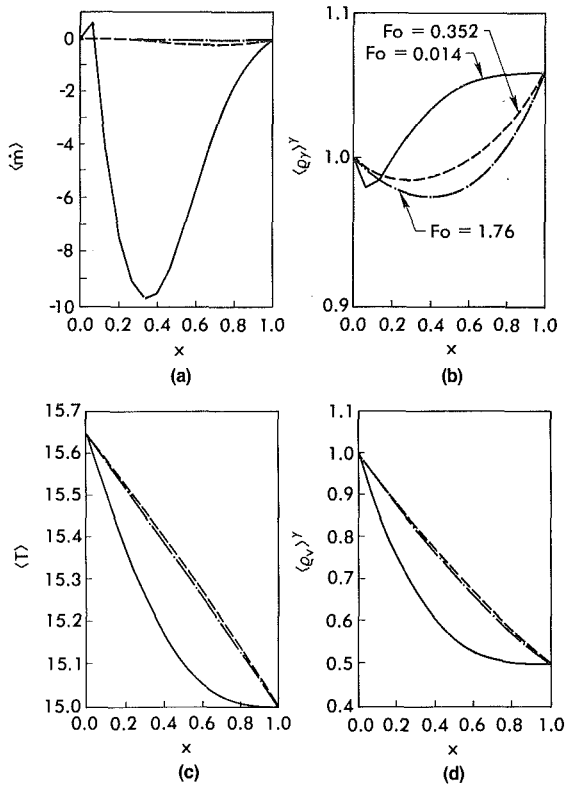

Fig. 9 Combined convective and diffusive case for Le = 0.05, Pe = 0.05, and $\omega(x=0)=1$

At a larger Lewis number (Le = 1.4), as seen in Fig. 5(*b*), the condensation process started only after a time lag and there was no condensation at any time at $x=0.2$. The steady-state liquid content distributions for the cases shown in Figs. 5(*a*) and 5(*b*) are shown in Fig. 5(*c*). From Fig. 5(*c*) it becomes clear that the length of the dry zone increases with an increase in the Lewis number. In addition, for larger Lewis numbers, the temperature overshoot decreases and the time required to reach the steady-state conditions increases. Note that, for Le = 1.4, the condensation rate profiles approach zero for larger Fourier numbers.

Boundary Conditions of Type Three. Type three boundary condition is possible at steady state since the ideal vapor density does not exceed the saturation vapor density. Again, at steady state the condensation rate for this case converges to zero and the temperature field converges to the ideal profile. For a given Lewis number this type of boundary condition produced a smaller temperature overshoot and a smaller condensation rate. Due to the presence of a dry zone, the steady-state profiles for the gas density and the liquid content are again functions of the Lewis number (see equation (28)).

For small Lewis numbers (Le = 0.2) condensation was found to occur initially due to the fast penetration of the vapor density. The condensation process was then followed by drying throughout the slab during the later stages of the temperature development. For a larger Lewis number (Le = 1.4) there was no phase change at all and the temperature and vapor density fields were completely uncoupled during their transient development. The possibility of condensation during the transient response of the slab could be neglected only for large Lewis numbers and type three boundary conditions.

Convective Case ($\mathrm{Le}\to\infty$ and $1\le\mathrm{Pe}\le 10$). For this case, Fig. 2(*b*) shows three different humidity levels based on a comparison with the saturation vapor density. These correspond to the same kinds of boundary condition which were discussed for the purely diffusive case. For the pure convective case the condensation process occurs immediately for large Peclet numbers while for small Peclet numbers there is either no condensation at all or the condensation process starts after some time lag.

The results for boundary conditions of the first and second types are shown in Figs. 6 to 8. At steady state, the colder boundary at $x=1$ had a significantly smaller effect on the gas density profile. This was because the gas phase continuity equation was purely a convective equation with a uniformly positive velocity field. Figures 6 and 7 show that increasing the Peclet number increases the overall condensation rates (Figs. 6*a* and 7*a*) and the overall temperature inside the slab (Figs. 6*c* and 7*c*). Also, as seen in Figs. 6(*a*) and 7(*a*), increasing the Peclet number shifts the maximum steady-state condensation rate location toward the downstream boundary. As seen in Figs. 6(*a*) and 8(*a*), lowering the humidity levels at the upstream boundary created a dry zone near the left boundary followed by a wet zone in the remaining portion of the slab. This behavior was similar to the purely diffusive case.

As seen in Fig. 8(*d*), at steady state the vapor density in the dry zone was uniformly constant and equal to its value at the hot boundary. This can be seen by examining equation (4). At steady state, in the dry zone, equation (4) reduces to

$$\mathrm{Pe}\frac{d\langle\rho_v\rangle^\gamma}{dx}=0 \text{ or } \langle\rho_v\rangle^\gamma=\text{const} \tag{29}$$

Furthermore, for the case presented in Fig. 8 an increase in the Peclet number was found to increase the extent of the dry zone. Based on very extensive numerical results, the main differences between the diffusive and convective cases were as follows:

1 At steady state, the condensation rate is zero for the purely diffusive case. For the purely convective case, at steady state the condensation rate is invariant with time but not zero. Consequently, at steady state, heat transfer augmentation occurs only for the purely convective case.

2 In the purely diffusive case, at steady state, the liquid content becomes invariant with time. For the purely convective case, the liquid is initially immobile during the transient development of the field variables. However, at steady state, the liquid content increases with time. Eventually, the liquid content becomes large enough to make the liquid phase mobile. Therefore, for the purely convective case, the initial transient phase is followed by a second phase where the liquid movement has to be taken into account. This second phase, where the liquid movement cannot be neglected, is not considered in this study.

3 For the purely convective case, the temperature increases monotonically to its steady-state distribution. However, for some diffusive cases, the temperature distribution overshoots and then it decreases to its steady-state value.

4 For the purely convective case, at steady state the gas density decreases monotonically inside the slab with a discontinuity at the downstream boundary. For the purely diffusive case, the steady-state gas density profile is concave upward.

5 For boundary conditions of type three, for the purely convective case, there is no possibility of condensation for either large or small Peclet numbers. For the purely diffusive case, condensation does not occur for large Lewis numbers, but it could occur for small Lewis numbers.

The reason that the condensation rate, at steady state, is always zero for the purely diffusive case can be seen by examining equations (2), (3), and (6). At steady-state conditions these equations can be combined to give

$$\mathrm{Pe}\frac{d\langle\rho_\gamma\rangle^\gamma}{dx}-\frac{\langle\dot m\rangle}{P_1P_4P_6}(P_1-P_4\langle\rho_\gamma\rangle^\gamma)=0 \tag{30}$$

For the purely diffusive case, the Peclet number is zero; therefore $\langle\dot m\rangle=0$. For the purely convective case, or as long as $\mathrm{Pe}\neq 0$, it is possible to have a nonzero condensation term.

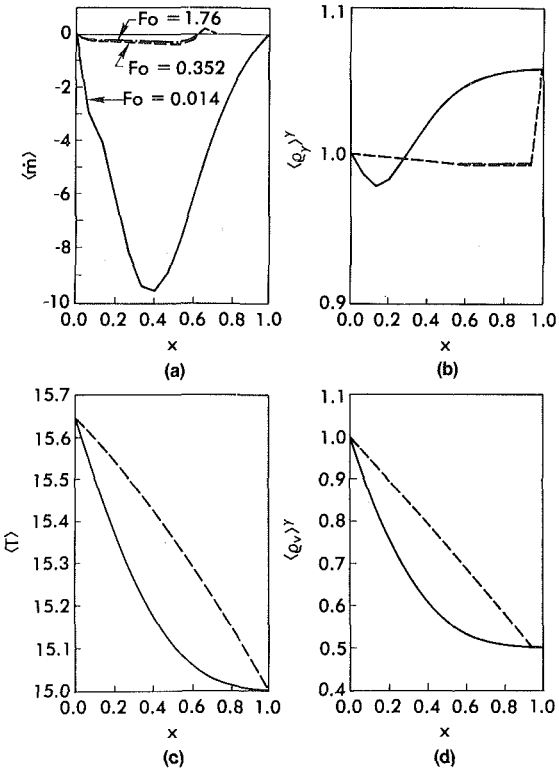

Fig. 10 Combined convective and diffusive case for Le = 0.05, Pe = 5, and $\omega(x=0)=1$

Combined Convective and Diffusive Case. For intermediate values of the Peclet and Lewis numbers, this case had the combined properties of the previous two cases. Based on the numerical results, this case reduces to the purely diffusive case for very small Peclet numbers and to the purely convective case for very large Lewis numbers. Figure 9 presents the results for the combined convective and diffusive cases when the Peclet number is very small. As seen in Fig. 9, at steady state the condensation rate converged to zero throughout the slab. This is due to the very small value of the Peclet number which makes the condensation process behave like the diffusive case. Also, as seen in Fig. 9, the gas density, temperature, and the vapor density all converge to typical diffusive type profiles at steady state.

The effect of an increase in the Peclet number is shown in Fig. 10. As seen in Fig. 10, at steady state the condensation rate was not zero in the left portion of the slab while it converged to zero in the right portion of the slab. As expected, for high Peclet numbers, the gas density and the temperature profiles displayed convective-dominated behavior. However, for the same type of boundary condition as in Fig. 10 there was no dry zone at steady state for the purely convective case. Furthermore, for this combined case, an increase in the Lewis number produces an increase in the steady-state condensation rate.

The results of the present work on the thermal performance of fibrous insulation are summarized in Fig. 11. This figure shows the dependence of Nu on Pe and Le for an insulation slab subject to the following temperature and humidity boundary conditions: $\bar{T}(x=0,\ t)=40°C$, $\bar{T}(x=1,\ t)=27°C$, $\omega(x=0,\ t)=1$, and $\omega(x=1,\ t)=1$. The Nusselt number as defined in equation (25) includes the convective contribution both in the numerator and the denominator, and therefore measures only the heat transfer increase owing to the phase change. The present analysis shows that condensation has a significant effect on the steady-state heat transfer through a fibrous insulation only when the convective vapor transport dominates over the diffusive vapor transport. In the present problem which considers 0.12-m-thick insulation, with a moderate temperature difference across the insulation slab, such a convection-dominated regime was found to occur for $Pe>1$ and $Le\neq 0$.

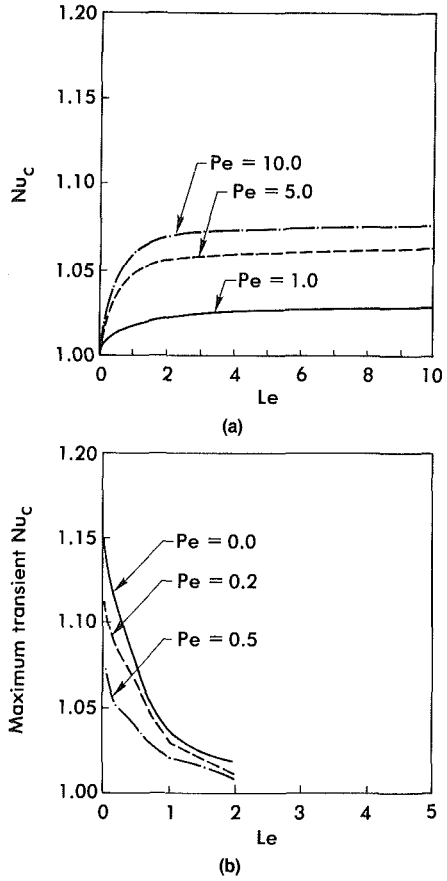

Fig. 11 Nusselt number dependence on the Lewis number: (*a*) steady-state results for convection-dominated regime; (*b*) transient results for diffusion-dominated regime

Figure 11(*a*) shows the variation of the steady-state Nusselt number Nu_c as a function of Le, with Pe as the parameter in the convection-dominated regime. For a fixed Pe, as Le increases the influence of diffusive vapor transport diminishes, and Nu_c asymptotically approaches the value corresponding to the purely convective case. For $Pe=10$, the maximum augmentation in the Nusselt number is seen to be about 7 percent (Fig. 11*a*). It is interesting to note that in the convection-dominated regime, for a fixed Peclet number, increasing the effective vapor diffusivity while holding the effective thermal diffusivity constant decreases the steady-state Nusselt number.

For a diffusion-dominated regime, which occurs for $Pe<1$, the Nusselt number is always observed to approach unity at steady state. However, the Nusselt number varies significantly during the transient evolution of the temperature field. Figure 11(*b*) shows the maximum value of the Nusselt number during the transient development in the diffusion-dominated regime. For a given Pe, as the effective vapor diffusivity increases (i.e., the Lewis number decreases), the transient condensation increases and correspondingly the maximum transient Nusselt number also increases. However, the time for which the Nusselt number remains above unity by a significant amount (e.g., 2 percent) is not large. Therefore, condensation does not seem to be a serious problem for $Pe<1$.

In thermal insulation applications, a Peclet number of the order of 10 may be caused by air infiltration through cracks and pinholes in the insulation boundaries. Therefore, condensation effects should be taken into account during the design of thermal insulation systems. The present analysis indicates that the augmentation of heat transfer induced by air infiltration through the insulation can be controlled by using low

Lewis number insulation. A low Le can be achieved by designing an open-structured, high-porosity insulation so that the effective vapor diffusivity approaches its upper bound of 3×10^{-5} m^2/s (which corresponds to vapor diffusion through air). Alternatively, using fibrous insulation composed of solid fibers with very low conductivity would also decrease the Lewis number.

5 Conclusions

The effects of the condensation process on the heat losses from a fibrous insulation slab were presented. This was accomplished by analyzing the problem as a multiphase flow heat and mass transfer in a porous slab with impermeable, adiabatic horizontal boundaries and permeable isothermal vertical boundaries. A detailed investigation of the interaction between condensation rate, temperature, liquid content, and vapor density fields was presented. The importance of the Peclet number, Lewis number, and different humidity levels on the condensation process is demonstrated. The results indicate that condensation and the resulting augmentation of heat transfer is a serious problem for large Peclet numbers ($Pe > 1$). Furthermore, it is shown that the condensation effects in increasing the Nusselt number can be controlled by designing a low Lewis number insulation slab.

References

1 Whitaker, S., "Simultaneous Heat, Mass and Momentum Transfer in Porous Media: A Theory of Drying," *Advances in Heat Transfer*, Vol. 13, Academic Press, New York, 1977.

2 Whitaker, S., "Advances in Theory of Fluid Motion in Porous Media," *Ind. Eng. Chem.*, Vol. 61, 1969, pp. 14–28.

3 Luikov, A. V., *Heat and Mass Transfer in Capillary-Porous Bodies*, Pergamon, Oxford, 1966.

4 Eckert, E. R. G., and Faghri, M., "Moisture Migration in an Unsaturated Porous Medium," *Int. J. Heat Mass Transfer*, Vol. 23, 1980, pp. 1613–1623.

5 Vafai, K., "Convective Flow and Heat Transfer in Variable Porosity Media," *J. Fluid Mechanics*, Vol. 147, 1984, pp. 233–259.

6 Vafai, K., and Tien, C. L., "Boundary and Inertia Effects on Convective Mass Transfer in Porous Media," *Int. J. Heat Mass Transfer*, Vol. 25, 1982, pp. 1183–1190.

7 Langlais, C., Hyrien, M., and Karlsfeld, S., "Moisture Migration in Fibrous Insulating Material Under the Influence of a Thermal Gradient," *Moisture Migration in Buildings*, ASTM STP 779, 1982, pp. 191–206.

8 Ceaglske, N. M., and Hougen, O. A., "Drying Granular Solids," *Ind. Eng. Chem.*, Vol. 29, 1937, pp. 805–813.

9 Ogniewicz, Y., and Tien, C. L., "Analysis of Condensation in Porous Insulation," *Int. J. Heat Mass Transfer*, Vol. 24, 1981, pp. 421–429.

Characteristics of a Simple Energy Absorption Transducer

B. T. Beck
Associate Professor of Mechanical Engineering, Kansas State University, Manhattan, KS
Assoc. Mem. ASME

G. L. Wedekind
Professor of Engineering, Oakland University, Rochester, MI
Mem. ASME

This paper presents the results of an investigation into a simple technique developed primarily for evaluating surface coating effectiveness for the absorption of a nonuniform laser radiation heat flux. Analysis suggests that if the transducer sensor is designed appropriately, and the experimental data analyzed in a particular manner, the temperature–time history of the transducer need be measured at only a single arbitrary location. These conclusions are also supported by experimental measurements of laser radiation absorption at a wavelength of 10.6 μm for polished copper, polished steel, and for a manganese-phosphate coating on a steel substrate. The absorptivities measured for the polished copper and steel agree well with other experimental data in the literature. Limitations of the measurement technique, resulting from the temperature dependence of the transducer material properties, radiation absorptivity, and combined convective and radiative heat flux, are also investigated theoretically and experimentally.

1 Introduction

A continuing interest exists in the utilization of high-energy gas lasers for various industrial applications involving machining, welding, and heat treating. Since many of these applications are associated with metals, whose untreated surfaces are generally highly reflective, there is a need to investigate the influence of surface coatings on the enhancement of the radiation absorption process. The impetus for such investigations exists not only from the standpoint of process control, but also in view of energy conservation and safety standards.

1.1 Requirements for Measurement Technique. The experimental measurement of absorbed radiation from high-energy gas lasers can impose complications which are normally not encountered in the typical measurement of surface heat fluxes. Not only is the radiation energy density of a gas laser often nonuniform across the laser beam, but in many applications, the cross-sectional area of the laser beam is smaller than that of the sensing surface of the flux transducer upon which it is impinging. Both of these conditions give rise to a very nonuniform or even discontinuous transducer heat flux.

An additional experimental complication is related to the type of surface coatings often used in the subject application. Many of the coatings of interest are deposited on the metal substrate by means of a chemical conversion process, making the coating an integral part of its metal substrate. Therefore, the absorption effectiveness of this type of coating must be measured with the particular metal substrate remaining an integral part of the experimental measurement.

1.2 Heat Flux Measurement. Historically, the development of heat flux transducers has always been directed toward some particular application [1]. Two of the basic measurement techniques which have evolved are thin-film surface thermometry and thick-film calorimetry [2]. A third type of thin-film heat flux transducer, frequently used for measuring radiative heat fluxes, is referred to as a Gardon-type transducer because of the early work of Gardon [3]. The Gardon-type transducer has received considerable attention such as that by Malone [4], Ash [5], and Keltner and Wildin [6].

Heat flux transducers are obviously based upon approximate models. For some applications, it is justifiable to assume that the transducer is isothermal at any instant of time, while other applications require that the temperature of the transducer be considered one dimensional. However, most, if not all, of the existing models for heat flux transducers assume that the heat flux is uniform over the sensing surface of the transducer; or, if the flux is not uniform, the nonuniformity is assumed not to have an effect on the transducer's performance. One exception is a study by Cunningham and Laughlin [7], where the surface absorption of unpainted alloys was measured for high-energy CO_2 laser radiation. In this study, a two-dimensional model was discussed (but not presented) which was apparently capable of taking into consideration a variable surface heat flux. However, the model was apparently restricted to radially symmetric flux distributions.

Because of the nonuniform and often discontinuous heat fluxes associated with laser applications, as well as the requirements dictated by the type of coatings involved, to the best knowledge of the authors, no compatible device nor proven experimental technique was available at the time this research was carried out, thus providing the impetus for the technique presented in this paper.

2 Description of Measurement Technique

The basic experimental technique is transient, where the absorbed laser energy is deduced from the temperature–time history of the transducer sensor. The difficulty encountered with a nonuniform surface heat flux is that the transducer sensor temperature at any instant of time is also nonuniform. This presents the problem of knowing at which, or at how many, positions on the sensor the temperature should be measured. Results of an analysis of the transducer sensor suggest that if the energy absorption sensor is designed appropriately, and the experimental data analyzed in a particular manner, the temperature–time history of the sensor need be measured at only a *single arbitrary* location. This important result was first suggested by a simplified double-lumped model of the transducer sensor [8, 9]. The purpose of the present paper is to place the conclusions apparent from the double-lumped model on a more firm analytical foundation, using a more general two-dimensional model for the transducer. In addition, some of the limitations of the measurement technique will also be investigated both analytically and experimentally. Finally, it should be noted that the proposed technique need not be restricted to laser power absorption, but should be applicable to other types of energy absorption as well.

Contributed by the Heat Transfer Division for publication in the JOURNAL OF HEAT TRANSFER. Manuscript received by the Heat Transfer Division August 24, 1984.

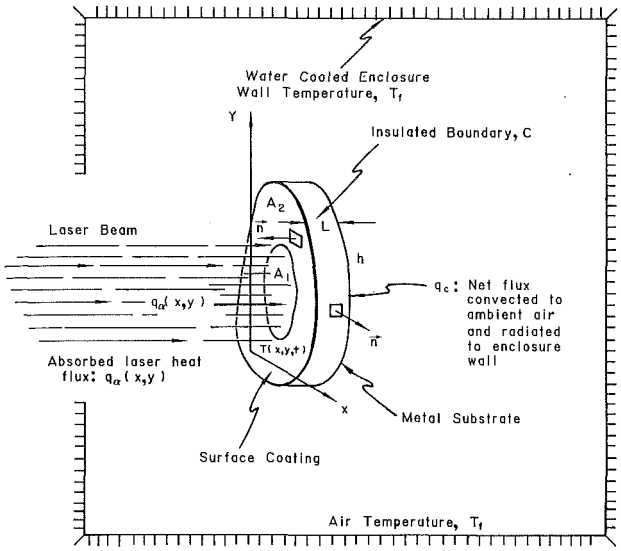

Fig. 1 General schematic of energy absorption transducer

2.1 Analysis of Transducer Sensor. A schematic of the laser energy absorption transducer is shown in Fig. 1. The absorbed heat flux is assumed to have an arbitrary spatial distribution $q_\alpha(x, y)$ over the sensing area. The transducer is assumed to be thin and flat, but with an arbitrarily shaped sensing area bounded by the curved surface C. The thickness of the transducer is assumed to be sufficiently small such that the temperature distribution is two dimensional[1] $T(x, y, t)$. The sensor is enclosed in an isothermal enclosure of temperature T_f.

[1]The Biot number for transducer targets was on the order of $\mathrm{Bi} \sim 10^{-5} << 1$.

The edges of the transducer, being negligible in area, are assumed to constitute for all practical purposes an insulated boundary. For other than the edges, heat losses are characterized by a uniform and constant combined convective and radiative heat transfer coefficient h on both sides of the transducer. If h were unequal on each side of the transducer, such as might be the case for coated targets with coating on one side only, then h may be thought of as an average of the front and back surface heat transfer coefficients.

Formulation of Differential Equations. Application of the conservation of energy principle in differential form to the transducer system depicted in Fig. 1 yields[2]

$$\tau \frac{\partial T}{\partial t} = \frac{1}{2h} q_\alpha(x, y) - (T - T_f) + \nu\tau \nabla^2 T \tag{1}$$

where $\nabla^2 T$ is the standard two-dimensional Laplacian operator applied to the temperature distribution, ν is the thermal diffusivity of the transducer material, and τ is a characteristic time parameter defined by

$$\tau \equiv \left(\frac{\rho c_v L}{2h}\right) \tag{2}$$

Physically, the left-hand side of equation (1) results from the instantaneous rate of thermal energy storage within the transducer per unit area. The right-hand side results from the instantaneous absorbed laser heat flux, the heat flux loss from the transducer by convection and radiation, and the heat transfer rate by conduction per unit area, respectively.

[2]It should be pointed out that for very fast transients the hyperbolic non-Fourier heat conduction equation, which allows for a finite speed of heat propagation, is sometimes necessary. Kao [12] discussed the influence of the hyperbolic heat conduction equation for thin surface layers. However, this phenomenon will not have an influence on the technique proposed in this paper, because measurements are actually not made until after the initial diffusion transient is complete.

Nomenclature

a = length and width of square transducer sensing area, cm
a_0 = zeroth-order least-square polynominal coefficient, °C
a_1 = first-order least-square polynomial coefficient, °C/s
a_2 = second-order least-square polynomial coefficient, °C/s²
A = $A_1 + A_2$ = total sensing area of transducer, cm²
A_1, A_2 = sensor areas beneath and outside of beam, respectively, cm²
Bi = $hL/(2k)$ = Biot number for transducer sensor
c_v = specific heat at constant volume of transducer sensor material, J/gm-°C
h = combined average effective convective and radiative heat transfer coefficient, W/m²-°C
k = thermal conductivity of transducer material, W/m-°C
L = thickness of transducer sensor, mm
n = coordinate normal to transducer edge boundary, cm
$\mathbf{n}$ = unit normal to transducer edge boundary, cm
P = laser power, W
P_α = absorbed power, W
q_c = convective heat flux to ambient air, W/cm²
q_0 = uniform heat flux absorbed beneath energy beam, W/cm²
q_α = absorbed heat flux, W/cm²
r = radial space coordinate, cm
r_1 = radius of laser beam and of subsystem No. 1, cm
r_2 = radius of transducer, cm
t = time, s
t_0 = particular time beyond initial diffusion transient, s
T = local transducer temperature, °C
T_f = ambient air temperature and environmental wall temperature, °C
ΔT = local temperature offset, °C
ΔT_m = maximum temperature variation across transducer, °C
x = position coordinate, cm
y = position coordinate, cm
α = effective absorptivity of transducer $\equiv P_\alpha/P$
β = total influence coefficient
γ = beam to transducer diameter ratio = r_1/r_2
∇^2 = two-dimensional Laplacian operator
∇ = gradient operator
θ = local steady-state temperature offset, °C
λ = wavelength of laser radiation, μm
ν = thermal difusivity of transducer material, cm²/s
ρ = density of transducer material, g/cm³
τ = time constant for lumped system, s
τ_D' = upper bound for time constant associated with initial diffusion effects, s
ϕ = transient function associated with initial diffusion effects, °C

Subscripts and Superscripts

C = insulated boundary of transducer
$\bar{}$ = spatial averages over entire sensing area of transducer
1, 2 = arbitrary locations on the transducer
$*$ = steady state

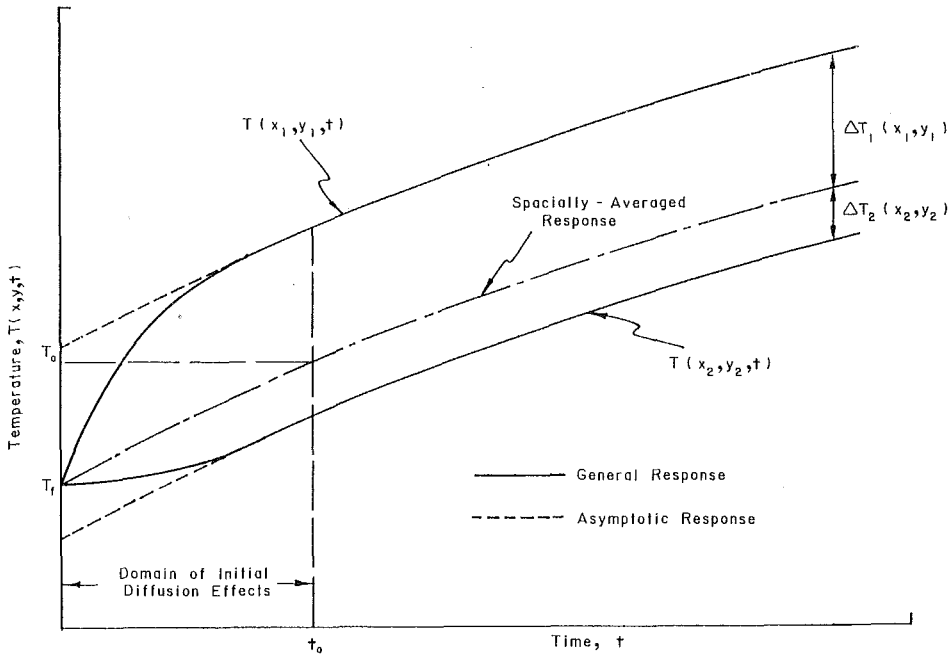

Fig. 2 Transient response of energy absorption transducer

The above differential equation is subject to the following boundary and initial conditions

$$(\nabla T \cdot \mathbf{n})_C = \left(\frac{\partial T}{\partial n}\right)_C = 0 \tag{3}$$

$$T(x, y, t)_{t=0} = T_f \tag{4}$$

Equation (3) follows directly from the assumption of insulated transducer edges, and equation (4) implies that the sensor is initially in equilibrium with the enclosure and ambient air, prior to heat flux application.

General Solution to Transducer Temperature Response. The general solution to equation (1) subject to the conditions given above may be constructed by superposition as follows

$$T(x, y, t) = \theta(x, y) - \phi(x, y, t)e^{-t/\tau} + \bar{T}(t) \tag{5}$$

where $\theta(x, y)$, $\phi(x, y, t)$ and $\bar{T}(t)$ are to be defined below. The basic form of the above construction was suggested by the simple double-lumped model for the transducer [10]. Verification of the above construction follows immediately by direct substitution into equations (1), (3), and (4), in conjunction with the definitions given below.

Spatially Averaged Transducer Temperature. The spatially averaged transducer temperature $\bar{T}(t)$ is defined by

$$\bar{T}(t) \equiv \frac{1}{A}\int_A T(x, y, t)dA \tag{6}$$

It is given as the solution to the following ordinary differential equation, which results from spatially averaging equation (1) and using the Gauss divergence theorem in conjunction with equation (3)

$$\tau \frac{d\bar{T}}{dt} + (\bar{T} - T_f) = \bar{q}_\alpha/(2h) \tag{7}$$

where

$$\bar{q}_\alpha \equiv \frac{1}{A}\int_A q_\alpha(x, y)dA \tag{8}$$

is the spatially averaged absorbed heat flux. The required initial condition follows from the spatially averaged form of equation (4), yielding

$$\bar{T}(0) = T_f \tag{9}$$

The solution to equation (7) subject to the given initial condition is

$$\bar{T}(t) = T_f + \left(\frac{\bar{q}_\alpha}{2h}\right)(1 - e^{-t/\tau}) \tag{10}$$

Note that equation (10) represents the response of the transducer if it behaved as a simple lumped system, with τ representing the corresponding lumped system time constant.

Steady-State Temperature Offset. The function $\theta(x, y)$ represents a steady-state temperature offset from the mean transducer temperature defined by

$$\theta(x, y) = T^* - \bar{T}^* \tag{11}$$

where $T^*(x, y)$ is the steady-state transducer temperature distribution, and $\bar{T}^*$ is its corresponding spatial average given by

$$\bar{T}^* = T_f + \bar{q}_\alpha/(2h) \tag{12}$$

which follows from equation (10) in steady state. This offset is given as the solution to the following

$$\nu\tau \nabla^2\theta - \theta = \frac{1}{2h}[\bar{q}_\alpha - q_\alpha(x, y)] \tag{13}$$

subject to the boundary condition

$$\left(\frac{\partial \theta}{\partial n}\right)_C = 0 \tag{14}$$

Initial Diffusion Transient Function. The function $\phi(x, y, t)$ characterizes the initial transient diffusion process and is given as the solution to the standard diffusion equation

$$\nabla^2\phi = \frac{1}{\nu}\left(\frac{\partial \phi}{\partial t}\right) \tag{15}$$

subject to

$$\left(\frac{\partial \phi}{\partial n}\right)_C = 0 \tag{16}$$

and

$$\phi(x, y, t)_{t=0} = \theta(x, y) \tag{17}$$

Determination of Asymptotic Response. As mentioned

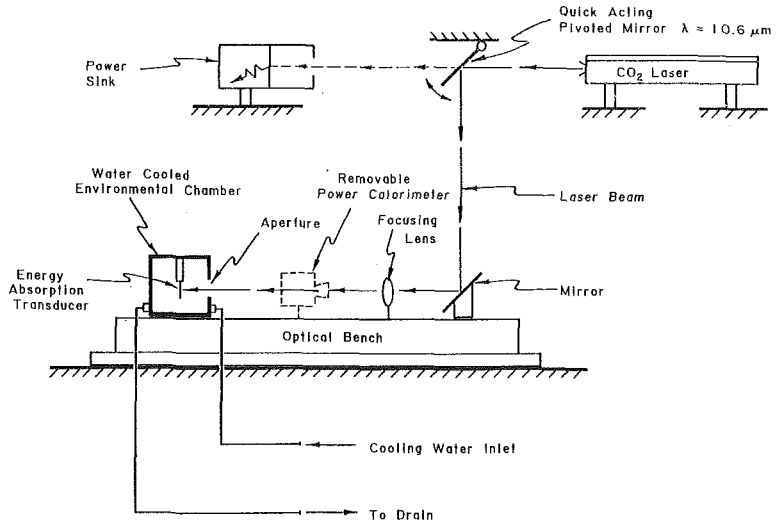

Fig. 3 Schematic of experimental apparatus

above, the function $\phi(x, y, t)$ characterizes the initial diffusion process during which the overall shape of the temperature distribution, or temperature offset, is established. This is shown graphically in Fig. 2 for two arbitrary locations on the transducer. Beyond the domain of initial diffusion effects the local temperature response tracks the response of the spatially averaged transducer temperature $\bar{T}(t)$ shifted by an amount equal to the local temperature offset $\theta(x, y)$.

Now, the above set of equations for $\phi(x, y, t)$ is analogous to that for an insulated container with a specified initial temperature distribution equal to the steady-state temperature offset $\theta(x, y)$. The function $\phi(x, y, t)$ therefore vanishes in the limit as $t \to \infty$, since

$$\lim_{t\to\infty} \phi(x, y, t) = \lim_{t\to\infty} \bar{\phi}(t) = \bar{\phi}(0) = \bar{\theta} \equiv 0 \tag{18}$$

The rate at which $\phi(x, y, t)$ vanishes depends upon the thermal diffusivity ν of the transducer material, its geometry, and the spatial distribution of the absorbed heat flux $q_\alpha(x, y)$.

The *largest time constant* from the infinite set of eigenfunctions necessary for a generalized Fourier series solution to equations (15), (16), and (17) may be used to characterize an upper bound on the time required for the initial diffusion transient.

For a square transducer sensing surface, of side a, an upper limit time constant τ_D' may be shown to take the following form

$$\tau_D' = \frac{1}{4\pi^2}\left(\frac{a^2}{\nu}\right) \tag{19}$$

If the time for the initial diffusion process is such that $\tau_D' << \tau$, then the general solution given by equation (5) may be replaced by an asymptotic response $T(x, y, t)_{t\geq t_0}$ valid after a sufficient period of time[3] t_0 as suggested in Fig. 2. Let

$$\Delta T(x, y) \equiv \theta(x, y) \tag{20}$$

represent the local temperature offset, analogous to the offsets resulting from the double-lumped transducer model [8, 9]. Then, substitution of equations (10) and (20) into equation (5), subject to the above constraints, yields the following asymptotic solution [11] to the transducer response

$$T(x, y, t) = T_f + \Delta T(x, y) + \left(\frac{\bar{q}_\alpha}{2h}\right)(1 - e^{-t/\tau}), \qquad t \geq t_0 \tag{21}$$

where $t_0 = 4\tau_D'$ represents the time required for about 98 percent of the initial diffusion process, associated with the vanishing of $\phi(x, y, t)$, to be complete.

The asymptotic solution given in equation (21) is identical in form with that obtained using a simple double-lumped model [8, 9]. The only difference is that the temperature offset $\Delta T(x, y)$ is now a *local* quantity which will in general vary from point to point on the transducer surface. Furthermore, as a direct consequence of this similarity, the average absorbed heat flux $\bar{q}_\alpha$ may be obtained from the local temperature response measurements by the same method as developed from the simple double-lumped transducer model [8, 9].

2.2 Method of Deducing Absorbed Energy. The purpose of this section is to briefly explain the technique used for indirectly deducing the absorbed laser energy from the direct experimental measurement of the transient temperature of the transducer sensor. This is accomplished by using a Taylor series approximation of equation (21), truncated as a second-order polynomial; thus

$$T(t) = a_0 + a_1(t - t_0) + a_2(t - t_0)^2 \tag{22}$$

It can be shown that the approximation will be accurate to within 5 percent if

$$\frac{1}{\tau}(t - t_0) \leq 0.5 \tag{23}$$

The absorbed laser radiation can now be deduced from the measured temperature response of the transducer. This is accomplished by first fitting, via the method of least squares, a second-order polynomial of the form of equation (22) to the measured temperature–time history at some point (x, y) for time greater than the initial diffusion time t_0, where $t_0 \geq 4\tau_D'$. The average absorbed heat flux $\bar{q}_\alpha$ can now be expressed in terms of the empirically measured coefficients as follows[4]

$$\bar{q}_\alpha = (\rho c_v L) a_1 \exp\left\{-2\left(\frac{a_2}{a_1}\right) t_0\right\} \tag{24}$$

In reference to the appendix, note that equation (24) does not require specific knowledge of the coefficient a_0, and hence the unknown local offset ΔT also need not be determined. Furthermore, the coefficients a_1 and a_2 are not position dependent and hence, using equation (24), the average absorbed flux $\bar{q}_\alpha$ may be determined from the temperature–time history at any *single arbitrary* location.

[3] A time $t_0 \geq 2$ s was sufficient for virtually all experimental tests.

[4] A more detailed derivation of equation (24) is given in the appendix.

If the total laser power striking the surface is represented by the sumbol P and the absorbed power by the symbol P_α, then the radiation absorptivity α can also be expressed by

$$\alpha = P_\alpha / P = \bar{q}_\alpha A / P \tag{25}$$

3 Laser Power Absorption

3.1 Description of Experimental Apparatus. A schematic of the experimental apparatus used for the results presented in this section is shown in Fig. 3. The apparatus consisted of an energy absorption sensor which was suspended and completely enclosed within a water-cooled environmental chamber. A small aperture in the chamber wall allowed the incoming laser beam to impinge upon the transducer sensor area. The chamber was mounted on an optical bench for ease in alignment of the sensor with the incoming beam. The spot size of the beam was varied by means of a water-cooled focusing lens, and was measured by obtaining a "burn pattern" before or after each test. The transducer sensors of square geometry were 1.27 cm on a side, and ranged in thickness from 0.25 mm to 0.51 mm. Circular targets were 0.594 cm in diameter and had a thickness of 0.38 mm. As a means of minimizing conduction losses, the square transducers were held in place by means of four ceramic-tipped nylon screws which achieved essentially point contact with the transducer corners. The circular transducers were suspended in place by means of four 36-gauge iron wires. Transducer temperatures were measured with 36-gauge chromel–alumel thermocouple junctions spot welded on the back side of the transducer. A thermocouple amplifier and strip chart recorder combination completed the transient temperature measurement capability. The environmental chamber and corresponding air temperature were also monitored during the tests. The time required for data collection was typically on the order of $\tau/3$, where τ was on the order of 30 s for the steel targets. The range of transducer temperature encountered during the tests was approximately 25–50°C.

Just prior to the start of a given test, the energy absorption transducer was allowed to come to thermal equilibrium with the air in the environmental chamber. By means of the quick-acting pivoted mirror shown in Fig. 3, at time $t=0$ the laser beam was deflected from the power sink onto the transducer sensor. The CO_2, 10.6 μm wavelength, laser power was measured both before and after each test by means of a commercially available laser power meter, which in turn was calibrated against an integrating sphere power calorimeter.

3.2 Laser Power Absorption

Polished Steel. A series of tests was performed on polished AISI-1085 steel, where the absorbed heat flux was measured as a function of laser power. Several different samples were tested where the laser power ranged from 20 to 135 W. A plot of the absorbed power P_α versus the laser power P was very linear, as shown in Fig. 4. Therefore, the slope of the best fit straight line through the data yields the absorptivity, which has a value of 0.055 for the 1095 steel. As a means of comparison, this value of spectral absorptivity at a wavelength of 10.6 μm is shown in Fig. 5 to fall between the normal spectral absorptivity of about 0.045 for polished iron as reported by Touloukian and DeWitt [13], and about 0.065 for polished steel (type unspecified) as reported by Eckert and Drake [14]. As radiation surface property measurements go, these results are quite good.

Polished Copper. In a similar manner, the absorptivity of polished pure copper was measured. Two different samples were tested for a range of laser power from 40 to 150 W. The linearity of the data for copper is also shown in Fig. 4. These data yielded an absorptivity of 0.010. Again as a means of comparison, this value of spectral absorptivity at a wavelength of 10.6 μm is shown in Fig. 5 to fall in the center of data reported by Touloukian and DeWitt [13], with data ranging from 0.0075 and 0.015. Again, as radiation surface properties go, these results are quite good. Since polished copper is considered somewhat of a standard, these results lend considerable credibility to the measurement technique.

Manganese-Phosphate Coating. One of the primary motivations for the development of this particular technique for the measurement of laser power absorption was to be able to evaluate the effectiveness of surface coatings on absorptivity enhancement. The particular coating–substrate combination under consideration in this section is a manganese-phosphate coating on an AISI-1095 steel substrate. For a range of laser power from 0–13 W, the measured absorptivity was 0.898. This implies a coating effectiveness of approximately 16.3 times that of the uncoated 1095 steel. The beam diameter for all of the tests ranged from 2 to 4 mm.

4 Limitations of Measurement Technique

From the analysis presented above it was concluded that the average absorbed power could be deduced from the measured temperature-time history of the transducer at a single ar-

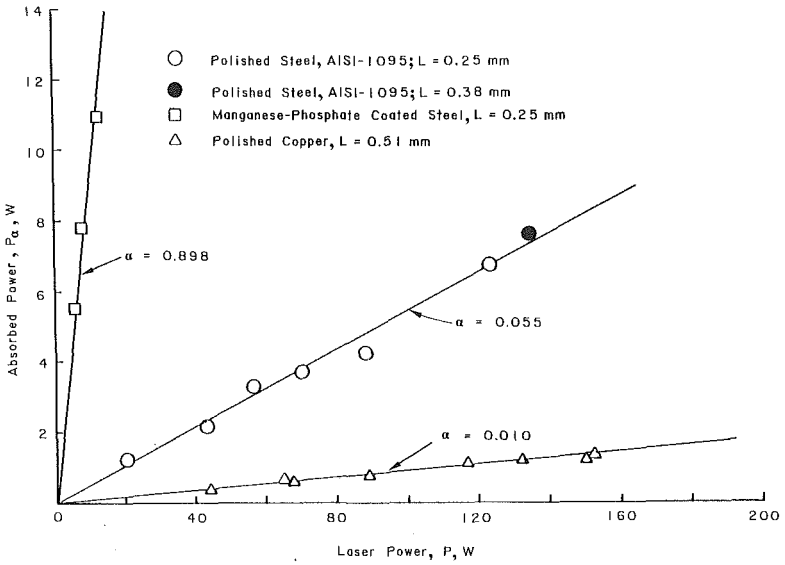

Fig. 4 Laser power absorptivity measurements

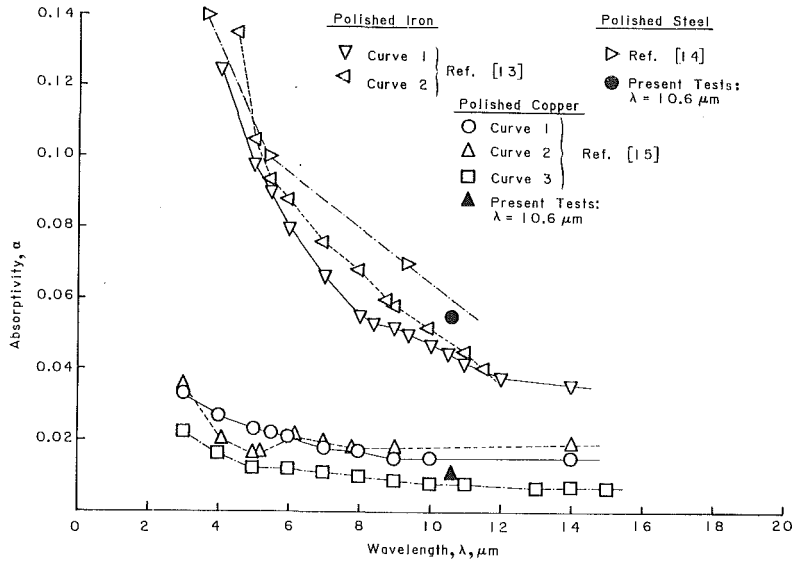

Fig. 5 Monochromatic absorptivity

bitrary location. This conclusion was seen to be independent of the spatial distribution of the absorbed heat flux, the resulting temperature distribution, and the shape of the transducer sensing surface. Furthermore, although the experimental results presented in the previous section generally support this conclusion, some variation in the measured absorbed power has been observed as a consequence of the location on the transducer where the temperature was measured. The present section will investigate both analytically and experimentally the cause for this variation. An attempt will be made to identify the major sources of the uncertainty in absorbed power and to provide an estimate of its magnitude.

4.1 Influencing Parameters. The variations in measured absorbed power were observed by comparing results obtained from the measured temperature–time history at the center and outer edge of the transducer. These locations represented the extremes in temperature variation across the transducer. Typically, after about 2.0 s had elapsed and the initial diffusion effects were essentially complete, a slow spreading of the two temperature responses was observed. This results in a variation in the measured absorbed power, in contrast with the model predictions depicted earlier in Fig. 2. Such spreading gives rise to a maximum variation in measured absorbed power on the order of 10 percent.

Various potential sources for the observed spreading of the two temperature–time histories have been investigated in connection with effects not incorporated in the transducer model. These include: (1) temperature dependence of specific heat, density, thermal conductivity, heat transfer coefficient and surface absorptivity; (2) spatial dependence of heat transfer coefficient; (3) temperature variation across thickness of transducer; (4) edge heat losses and conduction along transducer supports; and (5) thermocouple measurement error. The primary cause for the phenomena appears to be related to the temperature dependence of both the thermal conductivity of the transducer material and the absorptivity of the transducer sensing surface.

4.2 Quasi-Steady Analysis. A theoretical model has been developed for the purpose of estimating the relative uncertainty in the heat flux or absorptivity measurement as a result of measuring the temperature–time history at any arbitrary location on the transducer. For simplicity, the transducer was assumed to be circular with radially symmetric absorbed heat flux and temperature distribution. The model includes the effects of the important parameters involved, including the laser

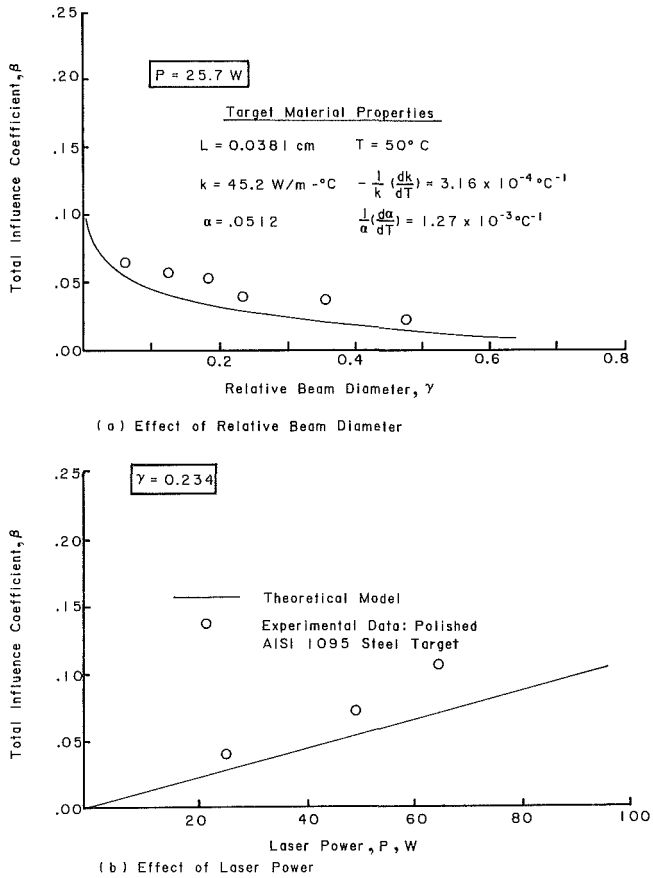

Fig. 6 Estimated absorptivity measurement error

beam-to-transducer diameter ratio. The absorbed heat flux distribution is assumed to take the following form:

$$q_\alpha(r) = q_0, \quad 0 \le r \le r_1$$
$$q_\alpha(r) = 0, \quad r_1 < r \le r_2 \tag{26}$$

For the radially symmetric geometry, equations (1), (3), and (4) become

$$\rho c_v L r\left(\frac{\partial T}{\partial t}\right) = r q_\alpha(r) + kL\,\frac{\partial}{\partial r}\left(r\,\frac{\partial T}{\partial r}\right) - 2hr(T - T_f) \tag{27}$$

subject to

$$\left(\frac{\partial T}{\partial r}\right)_{r=r_2} = 0 \tag{28}$$

$$T(r, t)_{t=0} = T_f \tag{29}$$

Now, according to the general asymptotic response given in equation (21) and shown in Fig. 2, the shape of the transducer temperature distribution reaches its steady-state form (as determined by the spatial function $\Delta T(x, y)$) very rapidly – much faster than the time associated with the response of the average transducer temperature. Hence, after sufficient time t_0, the temperature difference between any two arbitrary points on the transducer, $T(x_1, y_1, t) - T(x_2, y_2, t)$, would be independent of time (if properties were constant). This temperature difference is also dependent on various temperature dependent physical parameters; in particular, thermal conductivity k and absorptivity α. Hence, a slow drift in either k or α will cause a correspondingly slow drift in temperature difference across the transducer. Since this drift is so much slower than the initial diffusion time, a simple quasi-steady analysis of the extreme temperature difference across the transducer should yield a good representation of the slow drift.

Using the above approach, in steady state equation (27) becomes

$$\frac{kL}{r}\frac{d}{dr}\left(r\frac{dT^*}{dr}\right) + q_\alpha(r) = 2h(T^* - T_f) \tag{30}$$

Spatially averaging equation (30), and making use of equation (26), yields

$$\bar{q}_\alpha = 2h(\bar{T}^* - T_f) = \left(\frac{r_1}{r_2}\right)^2 q_0 \tag{31}$$

Furthermore, for typical conditions, it can be shown that in steady state the temperature variation across the transducer surface will be small compared to $\bar{T}^* - T_f$. Hence, the right-hand side of equation (30) may be replaced by equation (31) yielding after rearrangement

$$\frac{d}{dr}\left(r\frac{dT^*}{dr}\right) = -\frac{r}{kL}\{q_\alpha(r) - \bar{q}_\alpha\} \tag{32}$$

Differential Equation Solution. The solution to equation (32) may be expressed in piecewise form as follows

$$T^*(r) = T_1(r), \qquad 0 \le r \le r_1$$

$$T^*(r) = T_2(r), \qquad r_1 < r \le r_2 \tag{33}$$

where $T_1(r)$ and $T_2(r)$ are subject to the following boundary conditions

$$\left(\frac{dT_1}{dr}\right)_{r=0} = \left(\frac{dT_2}{dr}\right)_{r=r_2} = 0 \tag{34}$$

$$T_1(r)_{r=r_1} = T_2(r)_{r=r_1} \tag{35}$$

$$\left(\frac{dT_1}{dr}\right)_{r=r_1} = \left(\frac{dT_2}{dr}\right)_{r=r_1} \tag{36}$$

Solving equation (32) subject to equations (34), (35), and (36) yields

$$T_1(r) = \frac{q_0 r_1^2}{4kL}(1 - 2\ln r_1) - \frac{(q_0 - \bar{q}_\alpha)r^2}{4kL} + C \tag{37}$$

$$T_2(r) = \left(\frac{\bar{q}_\alpha}{4kL}\right)r^2 - \left(\frac{q_0 r_1^2}{4kL}\right)\ln r + C \tag{38}$$

where C is some constant. From equations (37) and (38) the maximum temperature variation across the transducer ΔT_m can now be expressed as follows

$$\Delta T_m \equiv T_1(0) - T_2(r_2) = \frac{P\alpha}{2\pi kL}\ln(1/\gamma) \tag{39}$$

where γ represents the relative beam diameter defined by

$$\gamma \equiv r_1/r_2 \tag{40}$$

Now, consistent with the assumed quasi-steady analysis, slow drift in ΔT_m can be seen to result from the temperature dependence of α and k.

Estimate of Absorptivity Error. From equations (24) and (25), it is readily recognized that the experimental measurement technique relies heavily upon the slope a_1 of the temperature–time history. Therefore, it is convenient to define an influence coefficient β which is a measure of the maximum variation in slopes between the two temperatures; thus

$$\beta \equiv \frac{d(\Delta Tm)}{dt} \Big/ \frac{d\bar{T}}{dt} \tag{41}$$

Assuming that the variation of both α and k in equation (39) is tied to the mean transducer temperature $\bar{T}$ yields

$$\beta = \frac{P\alpha}{2\pi kL}\left\{\frac{1}{\alpha}\left(\frac{d\alpha}{dT}\right) - \frac{1}{k}\left(\frac{dk}{dT}\right)\right\}\ln\left(\frac{r_2}{r_1}\right) \tag{42}$$

It can also be shown [15] that β provides an estimate of the relative error in measurement of absorptivity.

4.3 Experimental Results. Using the experimental apparatus described earlier, the influence coefficient β was measured as a function of both relative beam diameter γ and laser power P. The tests were performed on a circular, polished AISI-1095 steel disc transducer, having a diameter of 0.594 cm. Temperature measurements were made at the center and outer edge of the transducer. The laser beam was directed at the center of the transducer, where the diameter of the beam was varied as a means of controlling the beam-to-transducer diameter ratio γ. The spot size of the beam was varied by means of water-cooled focusing lens, and was measured by obtaining a "burn pattern" before or after each test.

Effect of Beam-to-Transducer Diameter Ratio. These experiments were performed at a laser power $P = 25.7$ W, and for a range of beam-to-transducer diameter ratios $0.05 < \gamma < 0.5$. The experimentally measured influence coefficient β is presented in Fig. 6(*a*), along with the model prediction of equation (42). The agreement between the experimental data and the theoretical model is quite reasonable, especially in light of the complexity of the phenomena involved, the relative simplicity of the model, and the potential uncertainty in both the experimental measurements and various material properties involved. For this particular measurement situation, the total influencing coefficient β ranged from $0.02 < \beta < 0.1$, as γ ranged from $0.5 > \gamma > 0.05$. It becomes clear, therefore, that any uncertainties in the experimental measurement technique, associated with the particular location on the transducer of the temperature measurement, can be minimized by keeping the beam-to-transducer diameter ratio γ as high as is practical; such uncertainties are below 2 percent for $\gamma \ge 0.5$.

Effect of Laser Power. These experiments were performed at a relative beam diameter of $\gamma = 0.234$, and a laser power which ranged from $25 < P < 65$ W. The experimental results, along with the theoretical predictions of equation (42), are plotted in Fig. 6(*b*) as a function of laser power P. Again the agreement is quite satisfactory, indicating that the model appears to have taken into account the dominant mechanisms involved.

5 Summary and Conclusions

The basic principle behind the experimental measurement technique described in this paper is to indirectly measure absorbed power by accounting for all thermal energy transfers, including thermal energy storage, during a particular span of

time that a distributed energy beam impinges on the transducer sensor. The technique was developed primarily to measure absorbed laser radiation, for the purpose of evaluating the absorption effectiveness of surface coatings deposited on a metal substrate; however, the technique should also be applicable to other types of energy absorption.

The results of this study place the tentative conclusions, developed earlier in conjunction with a much simpler double-lumped analysis of the transducer, on a firm analytical and experimental foundation. It can be concluded that if the energy absorption transducer is designed appropriately, and if the experimental data are obtained and analyzed in the particular manner described, the absorbed power may be deduced from the temperature-time history of the transducer at but a single arbitrary location. This conclusion appears to be valid regardless of the spatial distribution of the absorbed heat flux, its consequential nonuniform temperature distribution, or the geometry of the transducer sensing area.

Experimental evidence presented in this paper generally supports the above-mentioned conclusions; however, it is important to note that some measurement inaccuracy (on the order of less than 10 percent) has been observed associated with the location on the transducer where the temperature was measured. The primary cause for the measurement deviation is related to the temperature dependence of both the absorptivity of the transducer sensing area and the thermal conductivity of the transducer material. Furthermore, a theoretical model has been developed which is capable of estimating the relative uncertainty in the absorbed power or absorptivity measurement as a result of measuring the temperature-time history at any arbitrary location on the transducer. The model includes the effects of the important parameters involved, including the beam-to-transducer diameter ratio. As suggested by experiments using a laser beam, ratios greater than 0.5 seem to be the most desirable, when practical, because the uncertainty is minimized in this range.

Acknowledgments

The authors would like to acknowledge General Motors Technical Center, Manufacturing Development, Metals Engineering Department for their financial support of this research, and with respect to laboratory facilities. Specific thanks are due Dr. Victor Gregson, former Senior Research Engineer and Technical Leader in Industrial Lasers, for his helpful support and encouragement.

References

1 Scott, C. J., "Transient Experimental Techniques for Surface Heat Flux Rates," in: *Measurement Techniques in Heat Transfer*, E. R. G. Eckert and R. J. Goldstein, eds., Technivision Services, NATO Series, 1970, pp. 309-328.

2 Hall, J. G., and Hertzberg, A., "Recent Advances in Transient Surface Temperature Thermometry," *Jet Propulsion Journal*, Vol. 28, 1958, pp. 719-722.

3 Gardon, R., "An Instrument for the Direct Measurement of Intense Thermal Radiation," *Review of Scientific Instrumentation*, Vol. 24, 1953, pp. 366-370.

4 Malone, E. W., "Design and Calibration of Thin Foil Heat-Flux Sensors," Paper No. P6-2PHYMM1D-67, Instrument Society of America, 22nd Annual Conference, Chicago, Sept. 1967.

5 Ash, R. L., "Response Characteristics of Thin Foil Heat Flux Sensors," *AIIA Journal*, Vol. 7, 1969, pp. 2332-2335.

6 Keltner, H. R., and Wildin, M. W., "Transient Response of Circular Foil Heat-Flux Gauges to Radiative Fluxes," *Review of Scientific Instrumentation*, Vol. 46, 1975, pp. 1161-1166.

7 Cunningham, S. S., and Laughlin, W. T., "The Surface Absorption of Unpainted Alloys at 10.6 Microns," ASME Paper No. 75-WA/HT-66, 1975.

8 Wedekind, G. L., and Beck, B. T., "A Technique for Measuring Energy Absorption From High Energy Laser Radiation," *Proceedings of the 7th International Heat Transfer Conference*, Munich, Federal Republic of Germany, Sept. 6-10, 1982.

9 Wedekind, G. L., and Beck, B. T., "Laser Power Absorption Enhancement; A Technique for the Experimental Measurement of Absorbed Laser Radiation," Research Report submitted to General Motors Technical Center, Manufacturing Development, Metals Engineering Department, Dec. 1975.

10 Wedekind, G. L., Beck, B. T., and Bhatt, B. L., "Laser Power Absorption Enhancement; A Continuation in the Development of a Technique for the Experimental Measurement of Absorbed Laser Radiation," Research report submitted to General Motors Technical Center, Manufacturing Development, Metals Engineering Department, Aug. 1976.

11 Berg, P. W., and McGregor, J. L., *Elementary Partial Differential Equations*, Holden-Day, 1966, pp. 99-101.

12 Kao, T., "Non-Fourier Heat Conduction in Thin Surface Layer," ASME JOURNAL OF HEAT TRANSFER, Vol. 99, 1977, pp. 343-345.

13 Touloukian, Y. S., and DeWitt, D. P., "Thermal Radiative Properties, Metallic Elements and Alloys," in: *Thermo-physical Properties of Matter*, Vol. 7, IFI/Plenum, 1970, pp. 329.

14 Eckert, E. R. G., and Drake, R. M., *Analysis of Heat and Mass Transfer*, McGraw-Hill, 1972, p. 789.

15 Touloukian, p. 185.

16 Wedekind, G. L., Beck, B. T., and Bhatt, B. L., "An Investigation into the Limitations of a Technique Developed for the Experimental Measurement of Absorbed Laser Radiation," Research Report submitted to General Motors Technical Center, Manufacturing Development, Metals Engineering Department, July 1977.

APPENDIX

Equation (21) may be rearranged as follows

$$T(x, y, t) = T_0 + \left[\frac{\tilde{q}_\alpha}{2h} - (T_0 - T_f) + \Delta T\right][1 - e^{-(t-t_0)/\tau}] \quad \text{(A1)}$$

where t_0 is any arbitrary time greater than the initial diffusion time and $T_0 = T(x, y, t_0)$.

Expanding the exponential term in a Taylor series, truncated to a second-order polynomial, yields

$$T(x, y, t) = a_0 + a_1(t - t_0) + a_2(t - t_0)^2 \quad \text{(A2)}$$

where

$$a_0 = T_0 = T_f + \Delta T + \frac{\tilde{q}_\alpha}{2h}\,[1 - e^{-t_0/\tau}] \quad \text{(A3)}$$

$$a_1 = \left(\frac{\tilde{q}_\alpha}{2h\tau}\right) e^{-t_0/\tau} \quad \text{(A4)}$$

$$a_2 = -\left(\frac{\tilde{q}_\alpha}{4h\tau^2}\right) e^{-t_0/\tau} \quad \text{(A5)}$$

Now, solving equation (A4) for $\tilde{q}_\alpha$, and using the definition for τ from equation (2), yields

$$\tilde{q}_\alpha = 2h\tau a_1 e^{+t_0/\tau} = \rho c_v L a_1 e^{+t_0/\tau} \quad \text{(A6)}$$

Dividing equation (A4) by (A5) and solving for τ gives

$$\tau = -\frac{1}{2}(a_1/a_2) \quad \text{(A7)}$$

Substitution of equation (A7) into (A6) then yields

$$\tilde{q}_\alpha = (\rho c_v L) a_1 \exp\left[-2\left(\frac{a_2}{a_1}\right) t_0\right] \quad \text{(A8)}$$

The Use of Dehumidifiers in Desiccant Cooling and Dehumidification Systems

E. Van den Bulck

J. W. Mitchell
Mem. ASME

S. A. Klein
Assoc. Mem. ASME

University of Wisconsin
Solar Energy Laboratory,
Madison, WI 53706

The use of rotary dehumidifiers in gas-fired open-cycle desiccant cooling systems is investigated by analyzing the performance of the rotary heat exchanger–rotary dehumidifier subsystem. For a given cooling load, the required regeneration heat supply can be minimized by choosing appropriate values for the regeneration air mass flow rate and the wheel rotation speed. A map is presented showing optimal values for rotational speed and regeneration flow rate as functions of the regeneration air inlet temperature and the process air inlet humidity ratio. This regeneration temperature is further optimized as a function of the process humidity ratio. In the analysis, the control strategy adjusts the process air mass flow rate to provide the required cooling load. Additional control options are considered and the sensitivity of the regeneration heat required to the wheel speed, regeneration air mass flow rate, and inlet temperature is discussed. Experimental data reported in the literature are compared with the analytical results and indicate good agreement.

Introduction

Desiccant air conditioning and industrial drying systems using a rotary dehumidifier have been proposed as an alternative to conventional vapor compression units. Various systems for commercial and residential applications have been studied with respect to energy consumption and system performance [1–12, 14, 15]. Prototype units have been built and tested by AiResearch Manufacturing Company [9, 23], the Institute of Gas Technology [10], and Exxon. Currently, both DOE and the Gas Research Institute are supporting further development of these systems.

In desiccant air conditioning systems, air is dried by passing it over the desiccant and the heat of sorption is removed by sensible cooling. The air is further cooled by adiabatic humidification and is directed into the residence as cool dry air. The component configurations and psychrometric processes of the ventilation and recirculation cycles are illustrated in Figs. 1 and 2. An overview of the various proposed and tested cycles is given in [1, 3].

Parameters influencing system performance are regeneration air inlet temperature, wheel revolution speed, desiccant mass, and the ratio of regeneration air to process air mass flow rates. An optimal choice of these parameters will reduce the regeneration heat required for a given cooling load. Minimizing both air stream mass flow rates may also reduce the electrical fan power. Jurinak [3] numerically investigated the influence of regeneration air inlet temperature, wheel revolution speed and mass flow rate ratio on the performance of entire open cycle solid desiccant cooling systems. Values for the capacitance rate parameters Γ_1 and Γ_1/Γ_2 as defined by equation (1) of 0.15 and 0.60, respectively, for the recirculation mode, and values of 0.15 and 0.80, respectively, for the ventilation cycle are recommended. The COP based on thermal energy input shows a maximum between 65°C and 85°C regeneration temperature, while the COP based on electrical energy input, which includes parasitic power, is maximal at 105°C. Ingram and Vliet [17] present performance charts for a solid desiccant rotary dryer. These charts show the process outlet state of the dehumidifier as a function of the inlet conditions for a set of optimal design parameters, including a dimensionless wheel period and number of transfer units. The optimization was performed only with respect to minimal outlet humidity ratio of the process air stream, and did not consider regeneration energy.

In this paper, the optimization of dehumidifier operation for minimum energy use is determined, and the sensitivity of performance to deviations from optimum operation is evaluated. Results of the optimization analysis are compared to available experimental data and are in good agreement.

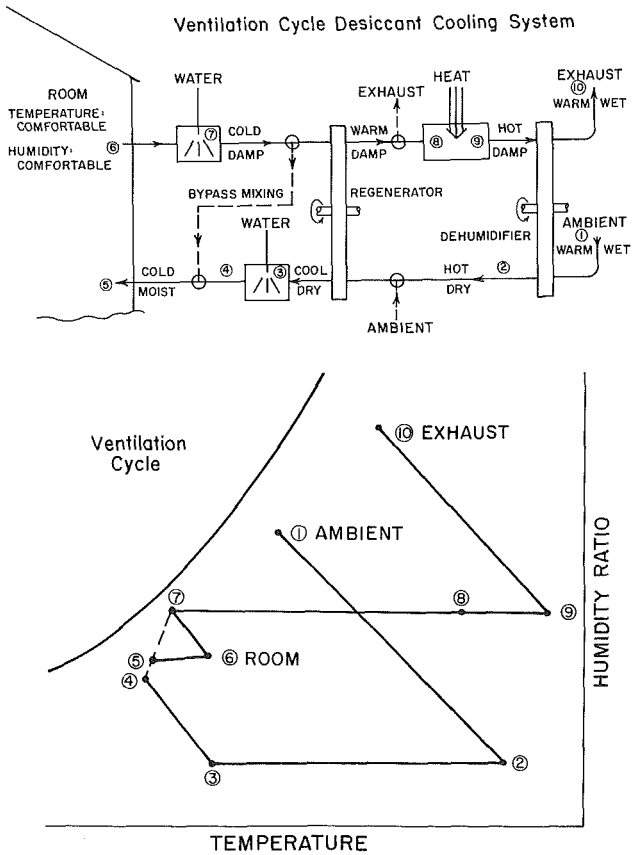

Fig. 1 Schematic and psychrometric diagram of a ventilation cycle desiccant cooling system (from [3])

Contributed by the Heat Transfer Division for publication in the JOURNAL OF HEAT TRANSFER. Manuscript received by the Heat Transfer Division August 30, 1985. Paper No. 84-HT-32.

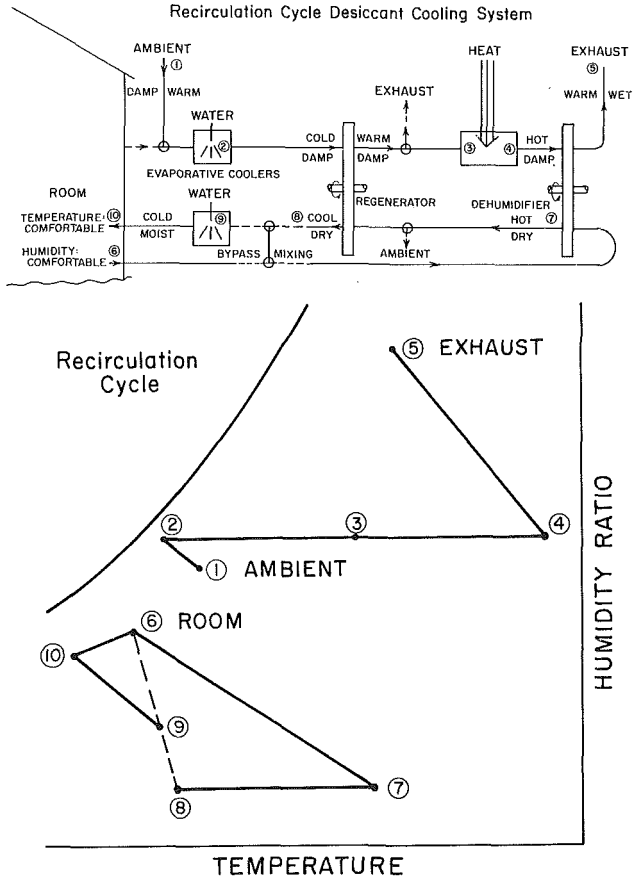

Fig. 2 Schematic and psychrometric diagram of a recirculation cycle desiccant cooling system (from [3])

Rotary Dehumidifier Model

Analytical models for the flow of moist air through packed beds of desiccant material have been developed based on the governing equations for heat and mass. Comparisons have been made between analytical solutions and experimentally obtained breakthrough curves [16, 24–26, 29, 30]. The agreement between theory and experiment is satisfactory. Rotary dehumidifiers have been modeled analytically [13, 18, 19, 20], and numerically [9, 13, 24]. Model predictions are compared to experimental data by Ball et al. [27], Pla Barby [24], and Rousseau [23]. It is found that the various models are satisfactory and allow acceptable accuracy in making dehumidifier performance predictions.

The analogy theory, introduced by Banks et al. [13, 18, 19], relates the performance of a rotary heat and mass exchanger to a superposition of two analogous thermal regenerators. Breakthrough curves based on this theory are given by Close [29, 30], and are compared to experimental data obtained by Close [29], and Bullock et al. [31]. The analogy method gives good agreement compared to tests on a silica gel bed which is subjected to step changes in the entering fluid state. Ball et al. [27] compared experimental data for a silica gel rotary dehumidifier to predictions by Nelson's model [28], which is also based on the analogy theory. Typical differences between experimental and model predicted values of the process exit temperature are less than 2°C, and humidity ratio exit differences are less than 0.001 kg/kg. Later, Maclaine-cross developed MOSHMX [13], a computer code that numerically solves the heat and mass equations for modeling rotary dehumidifiers. The code is superior in accuracy to the analogy-theory based models, but is obtained at high computational effort. Recently, Van den Bulck et al. [20] developed an effectiveness approach following that for regenerators which has accuracy similar to MOSHMX, but involves far less computation. This model is used for the

Nomenclature

A_j = total heat transfer area of the dehumidifier matrix in period j, m^2
COP = coefficient of performance
c_p = moist air specific heat, J/kg dry air•K
h = heat transfer coefficient, W/m^2K
h_w = mass transfer coefficient, kg dry air/m^2s
i = moist air enthalpy, J/kg dry air
i_{fg} = heat of vaporization, J/kg
i_{wv} = water vapor enthalpy, J/kg
I = desiccant matrix enthalpy, J/kg dry desiccant
L = axial flow length through the matrix, m
Le = NTU_t/NTU_w, overall Lewis number
$\dot{m}$ = moist air mass flow rate, kg dry air/s
M_d = mass of desiccant in the dehumidifier matrix, kg dry desiccant
M_f = mass of air in the dehumidifier matrix, kg dry air
NTU_t = $hA/\dot{m}c_p$, overall number of transfer units for heat transfer
NTU_w = $h_wA/\dot{m}$, overall number of transfer units for mass transfer
$\dot{Q}$ = thermal energy supply rate, W
RPM = dehumidifier wheel revolution speed, s^{-1}
t = temperature, °C
T = time required for a complete rotation of the matrix, s
w = moist air humidity ratio, kg/kg dry air
W = matrix water content, kg/kg dry desiccant
x = axial coordinate measured from period entrance
z = axial displacement through matrix measured from period entrance, m
Γ_j = jth operating parameter of the rotary dehumidifier defined in equation (1)
Δ = difference
ϵ_h = enthalpy effectiveness of the rotary dehumidifier
ϵ_w = humidity ratio effectiveness
θ = time, s
θ_j = duration of period j, s
τ = time coordinate
τ_{dj} = dwell time of a fluid particle in period j, s

Subscripts

d = desiccant
f = evaluated at fluid state
id = ideal outlet state
j = period index
load = load
m = evaluated at, or in equilibrium with, the matrix state
min = minimum
opt = optimal
reg = regeneration
room = evaluated at room air state
sys = system
t = heat transfer or temperature
w = mass transfer or moisture
wv = water vapor
11 = process air inlet state of the dehumidifier
12 = process air outlet state of the dehumidifier
21 = regeneration air inlet state of the dehumidifier
22 = regeneration air outlet state of the dehumidifier

Superscripts

$\dot{}$ = rate
$\bar{}$ = average value for a period

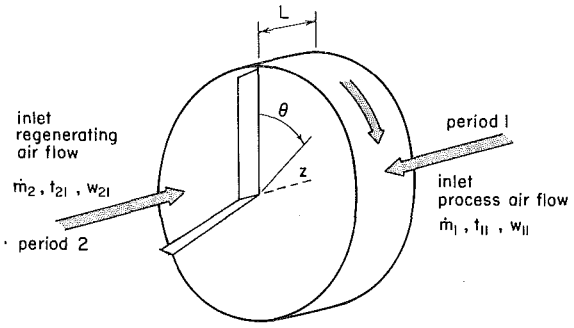

Fig. 3 Nomenclature and coordinate system for the rotary dehumidifier

analysis presented in this paper, and its concepts are briefly outlined below.

The nomenclature and coordinate system for the rotary dehumidifier are illustrated in Fig. 3. The adsorbent matrix is arranged as a rotating cylindrical wheel of length L and has a total mass of dry desiccant M_d. Two air streams are passed in counterflow through the regenerator. The process air stream has a low temperature and high relative humidity while the regeneration air stream has a high temperature and low relative humidity. For each period, the axial coordinate z is defined as positive in the fluid flow direction, while the rotary position is indicated by the time coordinate θ.

The model which describes the exchange of heat and mass between the moist air and the desiccant matrix is based on the following conventional assumptions for this situation [3, 13]:

1 The matrix is modeled as being of parallel passage form, consisting of a homogeneous solid with constant matrix characteristics and porosity, through which an air-water vapor mixture flows with constant velocity. Pressure drop effects through the bed are small with respect to absolute pressure [23], and are neglected.

2 The state properties of the air streams are spatially uniform at the inlet of each period.

3 The thermal and moisture capacities of the air entrained in the matrix are negligible compared to the matrix capacities.

4 The mixing or carryover of process and regeneration air streams is neglected. Banks [33] has numerically investigated the effect of fluid carryover on the performance of rotary heat exchangers and showed that the regenerator effectiveness increases linearly with the ratio of fluid dwell time τ_{dj} to period duration θ_j. The proportionality constant was defined as the carryover effect and is a function of the overall number of transfer units and the heat capacity rate ratio. For well-designed rotary dehumidifiers, the fluid dwell time is $\sim$ 0.2 s, the period duration is $\sim$ 360 s, the overall number of transfer units is $\sim$ 10, and the equivalent heat capacity rate ratio ranges from 2 to 5. Following Banks [33], the carryover effect is 0.05. The increase in dehumidifier effectiveness is then (0.05) (0.2)/(360) = 3×10^{-5}, which shows that the effect of carryover on dehumidifier performance may be neglected.

5 A transient one-dimensional approach is applied. There is no radial variation of fluid or matrix states, and diffusion fluxes of heat and mass due to tangential gradients of matrix and air state properties are neglected.

6 The axial heat conduction and water vapor diffusion flux are negligible in both the matrix and the air streams.

7 Transport of water vapor within the matrix occurs only through ordinary diffusion and transport of heat occurs only through ordinary heat conduction. Flux coupling is neglected.

8 The heat and mass transfer processes between the desiccant matrix and the air stream can be described by lumped transfer coefficients.

9 The periodic steady-state performance of the dehumidifier is considered.

The capacitance rate parameters Γ_1 and Γ_2 are defined as the ratio of matrix to fluid mass capacity rate

$$\Gamma_j=\frac{M_{dj}\tau_{dj}}{\theta_j M_{fj}}=\frac{M_d}{T\dot{m}_j} \qquad j=1,\ 2 \tag{1}$$

The regeneration air flow rate will in general be less than the process air flow rate for well-designed dehumidifiers. To account for unbalanced flow, the dehumidifier may be designed with an unequal partition of the wheel face area (Fig. 3). Flow unbalance and unequal area split are described by the ratio of the capacitance rate parameters. The following dimensionless coordinates are introduced

$$\begin{aligned} x&=\frac{z}{L}; & 0\le x\le 1\\ \tau&=\frac{\theta}{\tau_{dj}}\frac{M_{fj}}{M_{dj}}=\frac{\theta}{\theta_j}\frac{1}{\Gamma_j}; & 0\le\tau\le\frac{1}{\Gamma_j}\end{aligned} \tag{2}$$

Under the assumptions 1 to 9, the conservation and transfer rate equations for period j of the heat and mass regenerator have been written as [13]

$$\begin{aligned} \frac{\partial w_f}{\partial x}&+\frac{\partial W_m}{\partial\tau}=0\\ \frac{\partial w_f}{\partial x}&=\mathrm{NTU}_{w,j}(w_m-w_f)\\ \frac{\partial i_f}{\partial x}&+\frac{\partial I_m}{\partial\tau}=0\\ \frac{\partial i_f}{\partial x}&=\mathrm{NTU}_{t,j}\frac{\partial i_f}{\partial t_f}(t_m-t_f)+i_{wv}\mathrm{NTU}_{w,j}(w_m-w_f)\end{aligned} \tag{3}$$

Equations (3) are coupled through the thermodynamic property relationships for the desiccant-air-water vapor mixture. Property relations for silica gel are obtained from the literature [3]

$$\begin{aligned} w_m&=w_m(W_m,\ t_m)\\ i_m&=i_m(w_m,\ t_m)\\ I_m&=I_m(W_m,\ t_m)\end{aligned} \tag{4}$$

The initial conditions for this system of equations are

$$\begin{aligned} w_f(x=0,\ \tau)&=w_{j1}\\ i_f(x=0,\ \tau)&=i_{j1}\end{aligned} \qquad 0\le\tau\le\frac{1}{\Gamma_j};\ j=1,\ 2 \tag{5}$$

The periodic equilibrium boundary conditions for the matrix state properties are

for $0\le x\le 1$:

$$\begin{aligned} \lim_{\tau_1\to(1/\Gamma_1)^-}W_m(x,\tau_1)&=\lim_{\tau_2\to0^+}W_m(1-x,\tau_2)\\ \lim_{\tau_1\to(1/\Gamma_1)^-}I_m(x,\tau_1)&=\lim_{\tau_2\to0^+}I_m(1-x,\tau_2)\\ \lim_{\tau_1\to0^+}W_m(x,\tau_1)&=\lim_{\tau_2\to(1/\Gamma_2)^-}W_m(1-x,\tau_2)\\ \lim_{\tau_1\to0^+}I_m(x,\tau_1)&=\lim_{\tau_2\to(1/\Gamma_2)^-}I_m(1-x,\tau_2)\end{aligned} \tag{6}$$

Numerical solutions have been obtained for these equations by a number of authors [9, 13, 24]. There are no methods available for correlating these results in terms of nondimensional parameters. Such a method is presented in the next section.

The ϵ-NTU Method for Rotary Dehumidifiers

Two state properties of the moist air are required to fully characterize the process outlet state of a dehumidifier. These properties may be obtained by using a conventional effectiveness approach, in which the dehumidifier is compared to a

corresponding dehumidifier with infinite transfer coefficients. Two effectiveness factors for the process outlet state are needed. The effectiveness for humidity ratio is defined as

$$\epsilon_w = \frac{w_{11} - \bar{w}_{12}}{w_{11} - (\bar{w}_{12})_{id}} \tag{7a}$$

and for enthalpy

$$\epsilon_h = \frac{\bar{i}_{12} - i_{11}}{(\bar{i}_{12})_{id} - i_{11}} \tag{7b}$$

where the subscript *id* indicates the outlet state of a dehumidifier operating at the same inlet conditions, the same Γ_j parameters, and with infinite overall transfer coefficients for mass and heat. Equations (3), (5), and (6) show that the effectivenesses are functions of inlet temperature and humidity ratio, capacitance rate parameters Γ_j, transfer parameters $\mathrm{NTU}_{t,j}$, and the Lewis number Le. Effectiveness expressions for a nominal silica gel rotary dehumidifer are presented in [20]. These expressions are obtained by combining the solutions for the ideal dehumidifier with values from a numerical analysis of a dehumidifier with finite transfer coefficients [13].

The Ideal Rotary Dehumidifier

In the ideal dehumidifier, the overall heat and mass transfer coefficients are infinite. Thus at all times, each differential desiccant-moist air subsystem is in complete thermodynamic equilibrium (i.e., thermal and vapor pressure equilibrium). The conservation equations (3) may then be expressed as

$$\begin{aligned} \frac{\partial w_m}{\partial x} + \frac{\partial W_m}{\partial \tau} &= 0 \\ \frac{\partial i_m}{\partial x} + \frac{\partial I_m}{\partial \tau} &= 0 \end{aligned} \tag{8}$$

Equations (8), combined with the property relationships (4) and the initial and boundary conditions (5), (6), form a system of two coupled conservation laws. Each is a hyperbolic partial differential equation, and is nonlinear because of the nonlinear property relationships. Solutions may be obtained by the method of characteristics and the shock wave method [21]. These methods provide a set of analytical equations that allow prediction of the performance of an ideal dehumidifier for the entire range of operating parameters Γ_j, and for any inlet conditions. The functional form of the equations is presented in [20].

Design Parameter Optimization for Dehumidifiers in Desiccant Cooling Systems

The analysis will focus on the dehumidifier–regenerator subsystem that is common to both ventilation and recirculation cycles, and is shown schematically in Fig. 4. The independent variables are the dehumidifier inlet conditions t_{j1}, w_{j1}, the mass flow rates in both periods, and the wheel rotational speed RPM. The desiccant is silica gel.

The heat source is a gas furnace with adjustable thermal energy output $\dot{Q}_{reg}$ to provide the specified regeneration temperature t_{21}. For solar-fired systems, the energy output from the collectors decreases with increasing regeneration temperature and the analysis should take the performance characteristics of the collectors into account. The following analysis considers gas-fired systems only. The regeneration heat supply rate is obtained from an energy balance on the heat source

$$\dot{Q}_{reg} = \dot{m}_{reg} c_p (t_{21} - t) \tag{9}$$

Introducing Δt as the temperature difference between the air leaving and entering the regenerator, t may be expressed as

$$t = t_{12} - \Delta t \tag{10}$$

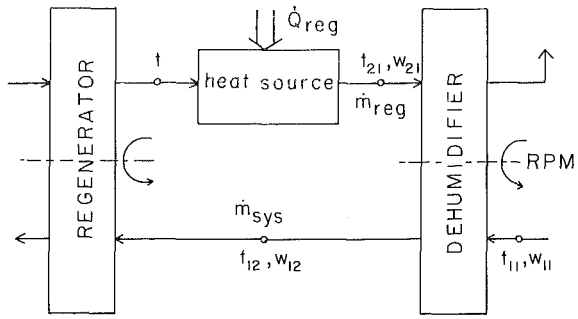

Fig. 4 Dehumidifer-regenerator subsystem of a desiccant cooling system

In these cycles, the variation of Δt with inlet conditions and mass flow rates through the heat exchanger is small compared to the temperature increase provided by the heat source. It is assumed that the temperature difference Δt is a constant equal to 4°C, which corresponds to a heat exchanger effectiveness of 90 percent for typical operating conditions. This effectiveness is typical of high-performance rotary regenerators which have large matrix to fluid heat capacity rate ratio [32]. The process air stream entering the heat exchanger has a nonuniform angular distribution of temperature (and humidity ratio). It has been shown by Brandemuehl and Banks [34] that nonuniformities in inlet fluid temperatures have little effect on the periodic steady-state performance of high-effectiveness regenerators at large matrix to fluid heat capacity rate ratio.

Using the parameters Γ_1 and Γ_2, the regeneration flow rate can be expressed in terms of the process mass flow rate

$$\dot{m}_{reg} = \frac{\Gamma_1}{\Gamma_2} \dot{m}_{sys} \tag{11}$$

Applying an energy balance on the conditioned space yields the process flow rate required to meet the load as

$$\dot{m}_{sys} = \frac{\dot{Q}_{load}}{\Delta i} \tag{12}$$

where Δi is the difference in enthalpy between the processed air entering the room and the room air. The temperature of the process air at the exhaust of the heat exchanger is assumed to be equal to the room temperature (see Figs. 1 and 2). Tests on experimental open-cycle desiccant cooling systems have shown this to be a very good approximation for both the ventilation cycle [9], and the recirculation cycle [23]. Equation (12) may thus be written as

$$\dot{m}_{sys} = \frac{\dot{Q}_{load}}{i_{fg} (w_{room} - w_{12})} \tag{13}$$

Substituting equations (10), (11), and (13) into (9), the regeneration heat supply may be expressed as

$$\dot{Q}_{reg} = \frac{c_p}{i_{fg}} \frac{\Gamma_1}{\Gamma_2} \frac{(t_{21} - t_{12} + \Delta t)}{(w_{room} - w_{12})} \dot{Q}_{load} \tag{14}$$

The dehumidifier transfer parameters are taken to be a $\mathrm{NTU}_{t,1}$ of 15 which is typical of a high-performance regenerator [32], and a Lewis number of unity. The regeneration period NTU is given by

$$\mathrm{NTU}_{t,2} = \mathrm{NTU}_{t,1} \frac{\Gamma_2}{\Gamma_1} \tag{15}$$

These values of transfer coefficients imply that the resistances for heat and mass transfer between the air stream and the surface of the desiccant particles dominate the overall transfer process and that the flow of the air through the matrix is laminar. The actual Lewis number for packed bed silica gel dehumidifiers is of the order of 2 [35]. It has been shown by Van den Bulck et al. [20], that the effect of the Lewis number on the performance of regenerative dehumidifiers is small for high overall NTU and Lewis numbers less than 2.

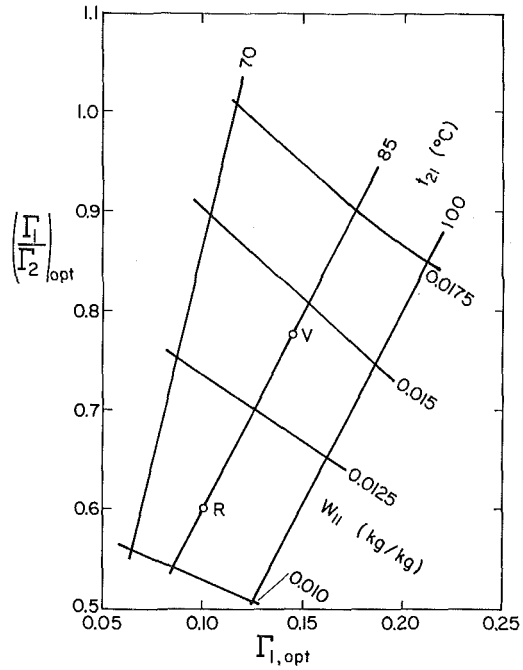

Fig. 5 Regeneration temperature and process humidity in a $\Gamma_{1,opt} - (\Gamma_1/\Gamma_2)_{opt}$ chart

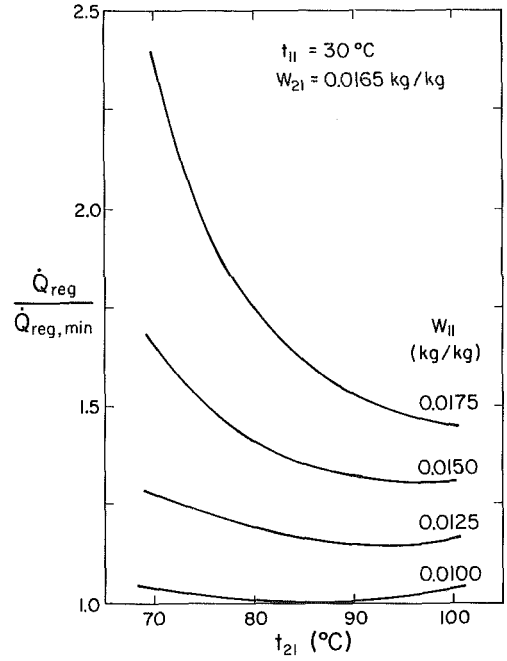

Fig. 6 Normalized regeneration heat required as a function of regeneration temperature for a tuned dehumdifier

Equation (14) gives the regeneration heat supply rate as a function of the cooling load, the room air humidity, the ratio of the capacitance rate parameters, the regeneration temperature, and the process air outlet state. In this equation, the process outlet state is a function of both process and regeneration air inlet states and capacitance rate parameters. Optimum system performance is achieved when the regeneration energy is minimum for a specified cooling load. In this analysis, the cooling load is held constant and w_{room} is set equal to the ARI standard room air humidity of 0.0111 kg/kg. Parameters for the optimization study are the process air temperature and humidity and the regeneration air humidity. The variables which can then be used to minimize $\dot{Q}_{reg}$ are the regeneration temperature and capacitance rate parameters Γ_1 and Γ_2. In the subsequent analysis, the optimization is carried out in two steps. First, values for Γ_1 and Γ_2 which minimize $\dot{Q}_{reg}$ are determined as functions of process and regeneration air inlet states. In a second step, the regeneration temperature that minimizes $\dot{Q}_{reg}$ for a "tuned" dehumidifier (i.e., optimal Γ_1 and Γ_2) is determined as a function of process temperature and humidity and regeneration humidity.

The results of an analysis based on this model [36] show that the regeneration heat required is less sensitive to Γ_1 than to Γ_1/Γ_2. These results also show that the effect of process temperature t_{11} and regeneration humidity w_{21} on the optimal value of Γ_1/Γ_2 is of second order compared to the effect of process humidity w_{11} and regeneration temperature t_{21}. The optimal values of Γ_1 and Γ_1/Γ_2 may therefore be averaged with respect to t_{11} and w_{21} and correlated as a function only of w_{11} and t_{21}. These averaged optimal values are shown in Fig. 5 for specified process air inlet humidity ratio and regeneration air inlet temperature. This figure establishes the optimum operating conditions Γ_1, Γ_2 for given process humidity and regeneration temperature.

The results in Fig. 5 demonstrate that an increase in process humidity w_{11} for a given regeneration temperature causes both $\Gamma_{1,opt}$ and $(\Gamma_1/\Gamma_2)_{opt}$ to increase. To extract more moisture from the process air stream as w_{11} increases, the matrix should be operated at a higher regeneration mass flow rate, contain more desiccant material, and/or rotate at a higher speed. Increasing the regeneration temperature t_{21} for a given process humidity ratio causes $\Gamma_{1,opt}$ to increase but $(\Gamma_1/\Gamma_2)_{opt}$ decreases. The process outlet humidity ratio will decrease and hence also the process mass flow rate. Therefore, a lower regeneration flow rate is required. The optimal amount of adsorbent in the dehumidifier or its rotational speed might increase or decrease depending on the inlet conditions.

Points marked with *V* and *R* in Fig. 5 show typical states for the ventilation and recirculation cycles, respectively. The values for $(\Gamma_1/\Gamma_2)_{opt}$ for these points agree with the values reported by Jurinak [3], which were obtained by a complete detailed analysis of the complete system, not just the rotary dehumidifier-regenerator subsystem.

If the dehumidifier is operated at the optimal values of Γ_1 and Γ_2 for the given inlet conditions, the outlet humidity ratio of the process air stream equals the minimum obtainable value for these inlet conditions [36]. Also, the regeneration mass flow rate is the minimum flow rate that can still regenerate the matrix without decreasing the cooling capacity of the system. Minimizing the regeneration heat supply for fixed inlet conditions corresponds to minimizing the regeneration mass flow rate. Hence, choosing the right values for Γ_1 and Γ_2 yields another advantage, it minimizes both mass flow rates and therefore the electrical fan power while producing maximum dehumidification.

For a "tuned" dehumidifier, which has optimal values for Γ_1 and Γ_2, the regeneration heat supply is a function of process and regeneration air inlet states. Figure 6 gives $\dot{Q}_{reg}$ as a function of the regeneration temperature and process humidity ratio for given process temperature and regeneration humidity ratio. $\dot{Q}_{reg}$ is normalized with respect to the minimum regeneration heat required for a process humidity of 0.010 kg/kg and a regeneration temperature of 85°C. If the dehumidifier is used in the recirculation cycle mode, the value of w_{11} is in the range 0.010–0.013 kg/kg. Figure 6 shows that the regeneration heat supply is only a weak function of the regeneration temperature in this humidity range. Thus, the COP of the recirculation cycle mode based on thermal energy input is not sensitive to an optimal choice of the regeneration temperature for optimal choices for Γ_1 and Γ_2. However, if the dehumidifier is used in the ventilation cycle mode, higher process humidity ratios (0.015 – 0.0175) result and a high regeneration temperature is recommended. Previous analytical studies have shown the COP based on thermal

Table 1 Dehumidifier parameters for sensitivity analysis

Ventilation cycle	Recirculation cycle
$t_{11} = 35.0°C$	$t_{11} = 26.7°C$
$w_{11} = 0.0142$ kg/kg	$w_{11} = 0.0111$ kg/kg
$t_{21} = 85.0°C$	$t_{21} = 85.0°C$
$w_{21} = 0.0140$ kg/kg	$w_{21} = 0.0190$ kg/kg
$\Gamma_{1,opt} = 0.170$	$\Gamma_{1,opt} = 0.093$
$\left(\frac{\Gamma_1}{\Gamma_2}\right)_{opt} = 0.823$	$\left(\frac{\Gamma_1}{\Gamma_2}\right)_{opt} = 0.600$

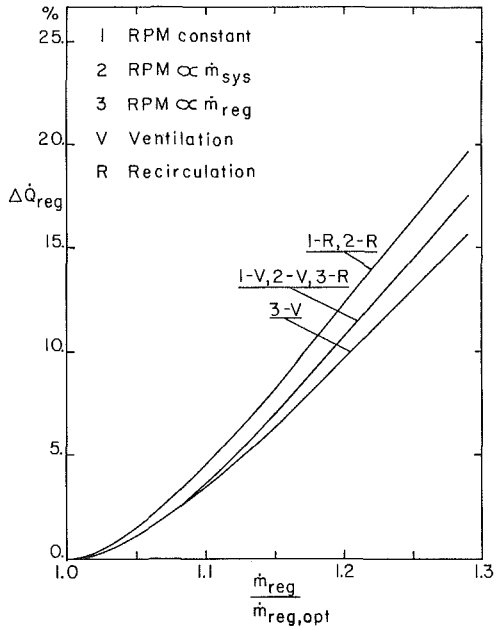

Fig. 7 Effect of regeneration flow rate on regeneration energy required

energy input to be maximal for t_{21} between 65°C and 85°C, but these studies were performed assuming either balanced flow [16], or fixed values for Γ_1 and Γ_2 [3]. Also, these studies do not presume a fixed total cooling load, as is done here, but instead presume a fixed process mass flow rate.

Increasing the regeneration temperature will lower the required process mass flow rate because the minimum obtainable process outlet humidity ratio decreases. Increasing this temperature also allows the dehumidifier to be operated at a lower value of $(\Gamma_1/\Gamma_2)_{opt}$, which decreases the regeneration mass flow rate even further. The parasitic power of desiccant cooling systems therefore decreases with increasing regeneration temperature [3, 16]. Thus, to maximize system performance, the regeneration temperature should be high. All experimental prototype air conditioning systems using a silica gel dehumidifier operate at regeneration temperatures between 80°C and 100°C [7, 9, 10]. The selected operation temperatures were arrived at experimentally, and are consistent with the analysis presented here.

Sensitivity Analysis

The optimal values for the regeneration temperature, regeneration mass flow rate, and wheel speed are presented in Figs. 5 and 6. If in operation the values for these parameters are different from their respective optimal values, the required regeneration heat supply will increase. This increase will be a function of the extent of the deviation, and also the strategy employed to control the dehumidifier system. Control options on the wheel speed might be to hold the speed constant, or vary the speed linearly with the process mass flow rate or the regeneration mass flow rate. Control options on the regeneration mass flow rate might be to hold this flow rate constant, or vary the regeneration flow rate linearly with the process mass flow rate. In the control strategy, the regeneration temperature is kept constant unless mentioned otherwise.

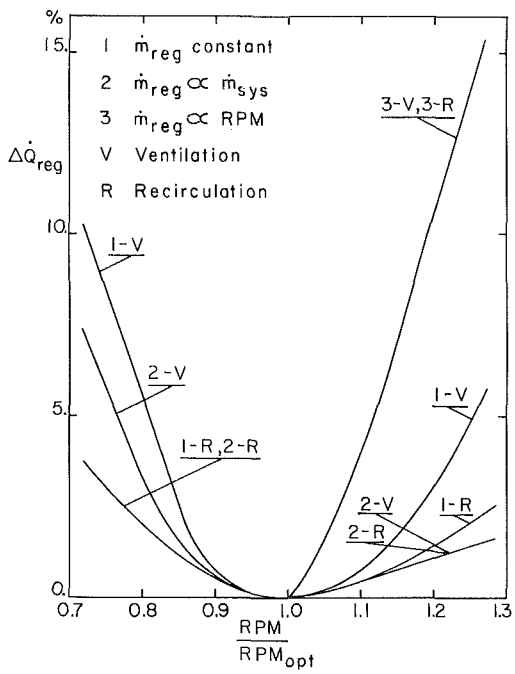

Fig. 8 Effect of wheel rotational speed on regeneration energy required

A sensitivity analysis was carried out for two typical dehumidifier parameter sets, reflecting the use of the dehumidifier in a ventilation and recirculation cycle system [36]. The parameters listed in Table 1 are based on the ARI standard room and ambient states of (26.7°C, 0.0111 kg/kg) and (35.0°C, 0.0142 kg/kg), as specified by the Solar Energy Research Institute for testing desiccant air conditioners [22]. The results are summarized in Table 1.

1 Effect of Regeneration Air Mass Flow Rate. If the regeneration mass flow rate is increased above the minimal value required to provide the given cooling load, the regeneration heat supply has to increase. Figure 7 shows the relative increase of $\dot{Q}_{reg}$ as a function of the relative increase of the regeneration flow rate for the recirculation and ventilation cycle, and for various control strategies.

The results in Fig. 7 show only minor differences between the ventilation and recirculation cycle systems. The effect of the different control strategy options is small. Increasing the regeneration flow rate to 20 percent above the minimal value required causes an increase of about 10 percent in required regeneration heat supply for the same cooling load. Hence, considerable energy savings may be accomplished by tuning the regeneration mass flow rate to the minimal value required for the given cooling load and inlet conditions.

2 Wheel Revolution Speed. The sensitivity of the dehumidifier performance to deviations of the wheel rotation speed from its optimal value is presented in Fig. 8. Various control strategies for the regeneration mass flow rates are examined for constant regeneration temperature. The results show that by keeping the regeneration mass flow rate proportional to the process mass flow rate (2-V and 2-R), the regeneration heat supply is the least influenced by wheel speed perturbations. In this case, the wheel speed may vary from -20 percent to $+30$ percent without significantly affecting

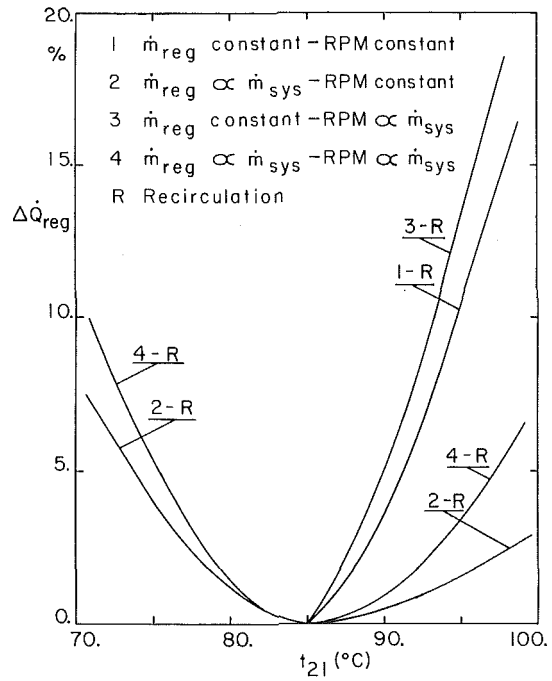

Fig. 9 Effect of regeneration temperature on regeneration energy required

$\dot{Q}_{reg}$. Positive wheel speed deviations are less influential than negative deviations. The dehumidifier performance is, in general, slightly more sensitive to the wheel revolution speed for the ventilation cycle than for the recirculation cycle.

3 Effect of Regeneration Air Inlet Temperature. In Fig. 5 it is shown that $\Gamma_{1,opt}$ and $\Gamma_{2,opt}$ are primarily a function of the regeneration temperature for a given process humidity ratio. Moreover it is shown in Fig. 6 that if Γ_1 and Γ_2 are controlled in response to the regeneration temperature, the required regeneration heat supply varies only slightly with the regeneration temperature provided that this temperature is chosen properly. However, this assumption requires a rather complex control strategy in which the regeneration mass flow rate and wheel speed are tied to both the regeneration temperature and process mass flow rate. Figure 9 shows the relative variation of the required regeneration heat supply with regeneration temperature for four other simple control options for the recirculation cycle. Curves for the ventilation cycle show the same trends. The results show that the regeneration heat supply is the least affected by the regeneration temperature for control option 2 in which the wheel speed is constant and the regeneration mass flow rate is varied in proportion to the process mass flow rate. In this case the regeneration temperature may vary from 75°C to 100°C without significantly increasing $\dot{Q}_{reg}$. Options in which the regeneration mass flow rate is kept constant are to be avoided, while it is preferable to keep the matrix rotating at a constant speed.

Comparison With Experimental Results

Desiccant cooling systems are under development and only limited experimental data are available. AiResearch Manufacturing Company has developed a prototype unit of an open-cycle solid desiccant air conditioner [9, 23]. Their data are described here in the context of the present analysis. The dehumidifier and the regenerator are packed beds and arranged as two coaxial cylinders rotating around parallel axes. The heater is mounted between the dryer and the heat exchanger. The desiccant is silica gel.

Table 2 Experimental data for the AiResearch test facility [23]

$t_{11} = 28.6°C$	$\dot{m}_{reg} = 0.34$ kg/s
$\dot{w}_{11} = 0.0128$ kg/kg	$NTU_{t,1}^{a} = 10$
$t_{21} = 83.3°C$	$M_d = 45.4$ kg
$\dot{w}_{21} = 0.0190$ kg/kg	$\tau = 720$ s

[a]Estimated value

AiResearch set up a system with the prototype unit and two humidifiers arranged in a recirculation type cycle [23]. They conducted experiments on the system to determine values for the design parameters that maximize the COP, defined as the ratio of cooling capacity to thermal heat input. The sensitivity of the COP to process and regeneration air mass flow rate and wheel speed were also investigated. The cooling capacity of the system at design conditions was rated at 4.7 kW.

Representative test data of the system are listed in Table 2. For these specified data, the variation of system COP with process air mass flow rate was determined experimentally and it was found that a flow rate of 0.50 kg/s yielded the maximum COP. From these measurements, values of the capacitance rate parameters that provided the optimum system performance can be calculated using equation (1)

$$\Gamma_1 = \frac{(45.4)}{(720)(0.50)} = 0.126 \tag{16a}$$

$$\frac{\Gamma_1}{\Gamma_2} = \frac{[(45.4)/(720)(0.50)]}{[(45.4)/(720)(0.34)]} = 0.68 \tag{16b}$$

These experimental values can be compared with values that are predicted by the model for this specific case as follows. Figure 5 shows analytically determined optimal values for the capacitance rate parameters as functions of regeneration temperature and process humidity. With the specified inlet conditions of Table 2 as entries in Fig. 5, the following values are obtained

$$\Gamma_{1,opt} = 0.125 \tag{17a}$$

$$\left(\frac{\Gamma_1}{\Gamma_2}\right)_{opt} = 0.71 \tag{17b}$$

This comparison establishes that the experimentally determined optimal values of the capacitance rate parameters agree with this analysis. The good agreement supports the approximation made with respect to the heat exchanger–dehumidifier subsystem.

AiResearch [23] conducted its experiments for a regeneration temperature of 83°C. The optimal regeneration temperature for the inlet process humidity as specified in Table 2 can be determined from Fig. 6 and is predicted to be ~ 92°C. Figure 6 also shows, however, that the optimum regeneration temperature is not well defined for low process humidities which are encountered in recirculation type systems.

The sensitivity of the regeneration heat supply to wheel speed was experimentally determined by AiResearch [23]. Process and regeneration air mass flow rate were kept constant. Measurements were taken for runs at wheel speed differing +10 percent and −10 percent from the optimal value. The reported results indicate no measurable effect on cooling capacity and COP of the system. This result is in agreement with the analytical results illustrated in Fig. 8, which shows sensitivity to wheel speed about the optimum.

The sensitivity of the COP to process and regeneration air mass flow rate was investigated experimentally. Since the cooling capacity of the system varied with flow rates, no comparison between the reported data and the model can be made. However, the experiments indicate the same effect on the COP as shown in Fig. 7. These results substantiate the analysis presented here.

Control Strategies for Desiccant Dehumidifier Cooling Systems

The optimal strategy for controlling a dehumidifier cooling system will provide the given cooling load with the least possible regeneration heat supply. This control strategy will not only maximize the COP based on thermal energy input but also minimize electrical energy input. An ideal controller would therefore sense room state and ambient conditions and adjust the process and regeneration mass flow rate, the wheel rotational speed and the regeneration temperature to optimal values. Such tasks can only be accomplished by a direct digital control system. Since this might not pay off for small-scale applications, simpler control strategies are needed.

The sensitivity analysis allows one to examine the influence of different control strategy options. If it is assumed that the process mass flow rate is adjusted to provide the given cooling load, the following control options are recommended.

1 The regeneration mass flow rate should vary in proportion to the process mass flow rate. At the optimal point, the outlet humidity ratio of the process air stream is minimal. Hence, any deviation from this optimal point will increase the process mass flow rate. If, however, the regeneration mass flow is increased, the drying capacity of the matrix increases. This will in turn lower the process outlet humidity ratio and hence, the process mass flow rate will drop. Thus, this control strategy is inherently stable, and will always provide the least possible flow rates for the following set of given parameters: ratio of regeneration mass flow rate to process mass flow rate, wheel revolution speed, regeneration temperature, room state, cooling load, and ambient conditions. It is important to choose and maintain a proper value for the ratio of regeneration mass flow rate to process mass flow rate.

2 The wheel speed may be kept constant. As has been shown, the influence of wheel speed control on the regeneration energy demand is of second order. Since the dehumidifier wheel rotates at a very low speed, it is practical that this speed may be set constant. The choice of the speed is not critical. Deviations of -20 percent to $+30$ percent of the optimal speed do not significantly decrease the COP of the system, provided that condition 1 has been met.

3 The regeneration heat supply is minimized by high regeneration temperatures. For gas-fired desiccant cooling systems at specified cooling load, the thermal regeneration energy input and electric power required to drive the air fans are minimized by regeneration temperatures ranging from 85 to 100°C. The COP based on thermal energy input is only weakly affected by the regeneration temperature in this range. Once the regeneration temperature has been chosen, the wheel speed and the ratio of regeneration to process air mass flow rate can be determined according to Fig. 5.

Conclusions

The performance of solid desiccant cooling and drying systems depends on the operating parameters of the dehumidifier. For a given cooling load, the required regeneration heat supply may be minimized by choosing proper values for these parameters, while also the dehumidifier control strategies influence system performance. This analysis presents a method for choosing optimal values for gas-fired systems, and is substantiated by available experimental results.

Substantial energy savings can be achieved by reducing the regeneration mass flow rate from balanced flow to between 60 percent and 80 percent of the process mass flow rate, depending on the regeneration temperature and process humidity ratio. The ratio of matrix mass capacity rate to process air mass flow rate should vary between 0.10 and 0.18. To reduce required mass flow rates, high regeneration temperatures of 85°C to 100°C are recommended.

The optimal control strategy will let the regeneration mass flow rate vary in proportion to the process mass flow rate. The wheel rotational speed may be kept constant and fine tuning of this speed is not important.

Acknowledgments

This project was supported by the Solar Heating and Cooling Research and Development Branch, Office of Conservation and Solar Applications, U.S. Department of Energy.

References

1 Jurinak, J. J., Mitchell, J. W., and Beckman, W. A., "Open Cycle Desiccant Air Conditioning as an Alternative to Vapor Compression Cooling in Residential Applications," ASME *Journal of Solar Energy Engineering*, Vol. 106, 1984, pp. 252–260.

2 Dunkle, R. V., "A Method of Solar Air Conditioning," *Mech. Chem. Engng. Trans. Inst. Engrs. Aust.*, Vol. 1, 1965, pp. 73–78.

3 Jurinak, J., "Open Cycle Solid Desiccant Cooling—Component Models and Systems Simulations," PhD thesis, University of Wisconsin—Madison, 1982.

4 *Proceedings of the 1981 Annual DOE Active Heating and Cooling Contractor's Review Meeting*, U.S. Department of Energy, Washington, D.C., 1981.

5 Sheridan, J. C., and Mitchell, J. W., "Hybrid Solar Desiccant Cooling Systems," *Progr. Sol. Energy*, Vol. 5, 1982, pp. 579–584.

6 Macdonald, N. J., "Utilization of Condensor Heat for Desiccant Dehumidifiers in Supermarket Applications," *Trans. Am. Soc. Heat. Refrig. Air-Condit. Engrs.*, Vol. 89, Part 2A, 1983, pp. 225–235.

7 Monnier, J. B., Worek, W. M., and Lavan, Z., "Performance of a Cross-Cooled Solar-Powered Desiccant Cooling System," Rep. No. DES-81-1, Illinois Institute of Technology, Chicago, 1982.

8 Shultz, K. J., and Mitchell, J. W., "The Performance of Solar-Desiccant Systems Using Cooled Desiccant Beds," *Progr. Sol. Energy*, Vol. 5, 1982, pp. 585–590.

9 Rousseau, J., "Development of a Solar Desiccant Dehumidifier: Phase II Technical Progress Report," Rep. No. 81-18436, AiResearch Manufacturing Company, Los Angeles, 1981.

10 Wurm, J., et al., "SOLAR-MEC Development Program: Semiannual Progress Report," Rep. No. C00-4495-23, Institute of Gas Technology, Chicago, 1979.

11 Collier, R. K., Barlow, R. S., and Arnold, F. H., "An Overview of Open-Cycle Desiccant-Cooling Systems and Materials," ASME *Journal of Solar Energy Engineering*, Vol. 104, 1982, pp. 28–34.

12 Jurinak, J. J., and Mitchell, J. W., "Recirculation of Purged Flow in an Adiabatic Counterflow Rotary Dehumidifier," ASME JOURNAL OF HEAT TRANSFER, Vol. 106, 1984, pp. 369–375.

13 Maclaine-cross, I. L., "A Theory of Combined Heat and Mass Transfer in Regenerators," PhD thesis, Monash University, Australia, 1974.

14 Lunde, P., "Solar Desiccant Air Conditioning With Silica Gel," *Proc. 2nd Workshop on the Use of Solar Energy for Cooling of Buildings*, SAN/1122-76/2, 1976, p. 280.

15 Burns, P. R., Mitchell, J. W., and Beckman, W. A., "Hybrid Desiccant Cooling Systems in Supermarket Applications," *Trans. Am. Soc. Heat. Refrig. Air-Condit. Engrs.*, Vol. 91, Part 1, 1985.

16 Schlepp, D., "A High Performance Dehumidifier for Solar Desiccant Cooling Systems," Rep. No. SERI/TP-252-1979, Solar Energy Research Institute, Denver, 1983.

17 Ingram, J. B., and Vliet, G. C., "Solid Desiccant Rotary Dryer Performance Charts," *Progr. Sol. Energy*, Vol. 5, 1982, pp. 603–608.

18 Maclaine-cross, I. L., and Banks, P. J., "Coupled Heat and Mass Transfer in Regenerators—Prediction Using an Analogy With Heat Transfer," *Int. J. Heat Mass Transfer*, Vol. 15, 1972, pp. 1225–1242.

19 Banks, P. J., "Prediction of Heat and Mass Regenerator Performance Using Nonlinear Analogy Method," ASME JOURNAL OF HEAT TRANSFER, Vol. 107, 1985, pp. 222–238.

20 Van den Bulck, E., Mitchell, J. W., and Klein, S. A., "Design Theory for Rotary Heat and Mass Exchangers," *Int. J. Heat Mass Transfer*, Vol. 28, 1985, pp. 1575–1595.

21 Lax, P., *Hyperbolic Systems of Conservation Laws and the Mathematical Theory of Shockwaves*, SIAM, Philadelphia, 1973.

22 Schlepp, D., "SERI Test Standard: Methods of Testing for Rating Solar Assisted Desiccant Cooling Systems," Solar Energy Research Institute, Denver, 1979.

23 Rousseau, J., "Development of a Solar Desiccant Dehumidifier: Phase I Final Summary Report," Rep. No. 80-17481, AiResearch Manufacturing Company, Los Angeles, 1980.

24 Pla Barby, F., "Solid Desiccant Air Conditioning With Silica Gel Using Solar Energy," PhD thesis, The University of Texas, Austin, 1978.
25 Pesaran, A. A., "Moisture Transport in Silica Gel Particle Beds," PhD thesis, University of California, Los Angeles, 1983.
26 Yoshida, H., and Ruthven, D. M., "Dynamic Behaviour of an Adiabatic Adsorption Column I," *Chem. Engng. Sci.*, Vol. 38, 1983, pp. 877–884.
27 Ball, H. D., Anath, G. P., and Singer, R. J., "The Dehumidification of Air Using Solar Regenerated Beds of Silica Gel," ASME Paper No. 83-WA-SOL-2.
28 Nelson, J. S., "An Investigation of Solar Powered Open Cycle Air Conditioners," MS thesis, University of Wisconsin—Madison, 1976.
29 Close, D. J., "Combined Heat and Mass Transfer in Porous Media—The Further Development of an Analogy With Heat Transfer," PhD thesis, Monash University, Australia, 1974.
30 Close, D. J., and Banks, P. J., "Coupled Equilibrium Heat and Single Adsorbate Transfer in Fluid Flow Through Porous Medium—II," *Chem. Engng. Sci.*, Vol. 27, 1972, pp. 1157–1168.
31 Bullock, C. E., and Threlkeld, J. L., "Dehumidification of Moist Air by Adiabatic Adsorption," *Trans. Am. Soc. Heat Refrig. Air-Condit. Engrs.*, Vol. 72, Part 1, 1966, pp. 301–313.
32 Shah, R. K., "Thermal Design Theory for Regenerators," in: *Heat Exchangers: Thermal Hydraulic Fundamentals and Design*, S. Kakao, A. E. Bergles, and F. Mayinger, eds., Hemisphere Publishing Corp., New York, 1981, pp. 721–763.
33 Banks, P. J., "Effect of Fluid Carry Over on Regenerator Performance," ASME JOURNAL OF HEAT TRANSFER, Vol. 104, 1982, pp. 215–217.
34 Brandemuehl, M. J., and Banks, P. J., "Rotary Heat Exchangers With Time Varying or Nonuniform Inlet Temperatures," ASME JOURNAL OF HEAT TRANSFER, Vol. 106, 1984, pp. 750–758.
35 Allander, C. G., "Untersuchung des Adsorptionsvorganges in Adsorbentenschichten mit linearer Adsorptionsisotherme," *Kungl. Tekniska Hoegskolans handlingar*, Vol. 70, 1953, pp. 1–160.
36 Van den Bulck, E., "Analysis of Solid Desiccant Rotary Dehumidifiers," MS thesis, University of Wisconsin—Madison, 1983.

Journal of Heat Transfer

Technical Notes

This section contains shorter technical papers. These shorter papers will be subjected to the same review process as that for full papers.

Analysis of Laminar Fully Developed Flow in Plate-Fin Passages: Effect of Fin Shape

C. Prakash[1] and R. Lounsbury[2]

Nomenclature

A = cross-sectional area of the computational domain, m^2
c_p = specific heat of the fluid, J/kg°C
f = friction factor, equation (1)
h = fin height, Fig. 1, m
h_T = heat transfer coefficient, equation (5), $W/m^2°C$
k = thermal conductivity of the fluid, W/m°C
L = axial length of the heat exchanger, m
$\dot{m}$ = mass flow rate through the computational domain, kg/s
Nu = Nusselt number, equation (6)
p = pressure, N/m^2
P = heated or wetted perimeter of the computational domain, m
$\mathcal{P}$ = pumping power for flow through the computational domain, W
q = average heat flux based on the base area, equation (4), W/m^2
Q' = heat transferred per unit axial length in the computational domain, W/m
Q = heat transferred by an exchanger of axial length L for each computational domain, equation (9), W
Re = Reynolds number, equation (2)
s = spacing between adjacent plates or adjacent fins, m
t = half of the fin base thickness, Fig. 1, m
T = temperature of the fluid, °C
T_b = bulk temperature of the fluid, °C
T_{bi} = bulk temperature of the fluid at some starting or inlet location, °C
T_w = uniform temperature of the plates and the fins, °C
w = axial velocity, m/s
$\bar{w}$ = average axial velocity, m/s
x, y = cross-stream coordinates, Fig. 1, m
z = axial coordinate, Fig. 1, m
δ = grid spacing, equation (7), m
μ = viscosity of the fluid, kg/ms
ρ = density of the fluid, kg/m^3

Introduction

Finned surfaces find application in a variety of practical heat exchange devices, such as radiators, air conditioners, heaters, etc. [1, 2]. Fins are also employed in cooling (heat "sink") assemblies such as those found in electrical/electronic cooling passages.

For heat transfer augmentation purposes, fins are generally kept very thin. However, there are occasions, especially in heat sink configurations, where the thickness of the fin is not negligible. Such finite thickness leads to a geometrically complex flow domain of which the heat transfer behavior can be quite different as compared to a thin-fin passage. The present study has been motivated by a desire to examine the effect of the shape of thick fins on their flow and heat transfer performance.

Laminar flow studies in finned passages have been reviewed in detail by Shah and London [1]. The particular configuration considered in this paper has not been studied before. The only work that comes close is from Sparrow et al. [3], corresponding to the rectangular fin case.

Problem Statement

The problem being analyzed is schematically sketched in Fig. 1. It concerns the prediction of laminar fully developed flow in finned parallel plate passage of plate spacing s. Thick fins are affixed on each plate, and the flow is parallel to the axis of the fins, i.e., the surface of the plates. A number of cross-sectional shapes of the fin are to be considered. In Fig. 1, fins of triangular cross-sectional shapes are drawn. The fins are of height h and spaced a distance s apart. Thus the fin pitch is identical to the plate spacing (s). This assumption is

[1]Adjunct Professor, Department of Mechanical Engineering, Aeronautical Engineering & Mechanics, Rensselaer Polytechnic Institute, Troy, New York 12181; Assoc. Mem. ASME; to whom all correspondence may be addressed at: CHAM of North America, Inc., 1525-A Sparkman Drive, Huntsville, Alabama 35805.

[2]Graduate Student, Department of Mechanical Engineering, Aeronautical Engineering & Mechanics, Rensselaer Polytechnic Institute, Troy, New York 12181. Current address: Aircraft Engine Group, General Electric Corporation, Cincinnati, Ohio 45215.

Contributed by the Heat Transfer Division for publication in the JOURNAL OF HEAT TRANSFER. Manuscript received by the Heat Transfer Division July 16, 1984.

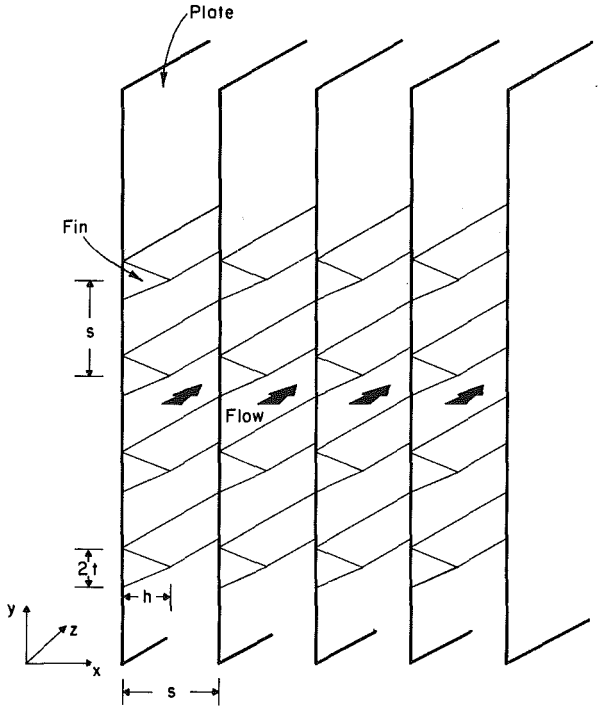

Fig. 1 A finned parallel plate assembly

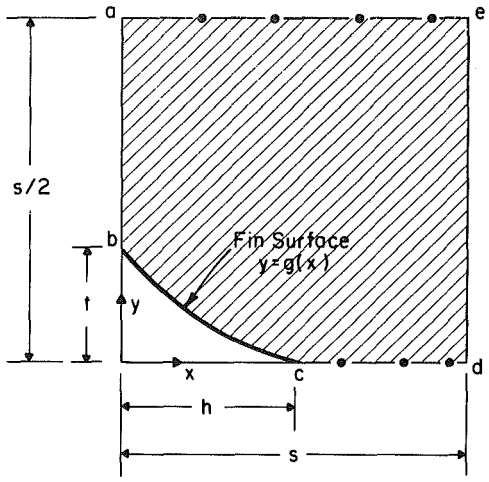

Fig. 2 The computational domain

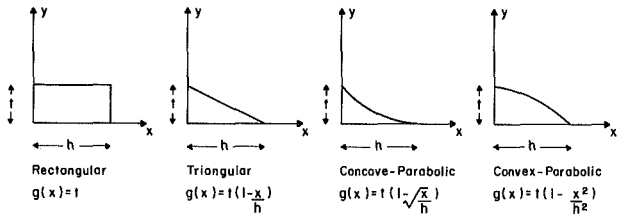

Fig. 3 Different fin shapes

just to reduce the number of parameters of the problem; the present study can, of course, be extended to cases where this is not so. Finally, the thickness of the fin at the base is equal to $2t$.

Because of the symmetry in the problem, we only need to consider the computational domain shown as the shaded region *a-b-c-d-e-a* in Fig. 2. The segment *b-c* represents the fin surface and is represented by a general equation $y = g(x)$ in the range $0 \le x \le h$. Four different fin shapes were considered which are described in Fig. 3. The corresponding equations are

$g(x) = t$: rectangular fins

$$= t\left(1 - \frac{x}{h}\right)\text{: triangular fins}$$

$$= t\left(1 - \sqrt{\frac{x}{h}}\right)\text{: concave-parabolic}$$

$$= t\left(1 - \frac{x^2}{h^2}\right)\text{: convex-parabolic}$$

A variety of thermal boundary conditions are possible as has been discussed by Shah and London [1]. For the present analysis we assume that the entire assembly, fins as well as the base plates, is isothermal with uniform temperature T_w everywhere. This is the so-called (T) boundary condition of Shah and London [1] and has applications in condensers, evaporators, etc. Such a treatment implicitly assumes that the base plates and the fins are made of a highly conducting material and that the fins are 100 percent efficient.

The fluid is assumed to be incompressible, and all fluid properties are assumed to be constant. Viscous dissipation, compression work, and radiation effects are to be neglected in the energy equation.

Analysis

The analysis of fully developed duct flows has been discussed at length in a number of heat transfer texts (see, e.g., Kays and Crawford [4]). Hence, details will be omitted, and only the main points will be highlighted. Recall the computational domain shown in Fig. 2. Let z be the coordinate normal to the plane of Fig. 2, and let w represent the velocity component along z. For fully developed conditions, there is no cross-stream flow and w is the only nonzero velocity component. Further, w is itself independent of z. The pressure p is a function of z only and dp/dz is uniform, i.e., independent of z. The axial velocity w satisfies a Poisson equation in which dp/dz appears as a source term. The main hydrodynamic quantity of interest is the friction factor f which may be defined as

$$f = (-dp/dz)s/[\rho \bar{w}^2/2] \tag{1}$$

Here ρ represents the density of the fluid, and $\bar{w}$ is the average velocity. Define the Reynolds number Re as

$$\mathrm{Re} = \rho \bar{w} s/\mu \tag{2}$$

where μ is the viscosity of the fluid. For fully developed flow, the friction factor f is inversely proportional to the Reynolds number Re, i.e.,

$$f\mathrm{Re} = \text{const} \tag{3}$$

where the constant on the right hand side is a function only of the fin shape and the geometric quantities h/s and t/s.

For thermally fully developed flow, the temperature also obeys a Poisson equation. For the chosen boundary condition of isothermal plates and fins, the problem leads to an eigenvalue formulation [4]. The main quantity of interest is the Nusselt number which may be defined in the following manner. Consider the computational domain shown in Fig. 2. Let

Q' = heat transfer per unit axial length z in the domain shown in Fig. 2

An average heat flux q can be defined using the base area s which would occur in the absence of any fins. That is

$$q = \frac{Q'}{s} \tag{4}$$

The heat transfer coefficient h_T can be defined as

$$h_T = \frac{q}{(T_w - T_b)} \tag{5}$$

where T_w and T_b are the plate (and fin) and the bulk

Table 1 Variation of the friction factor-Reynolds number product, $f \cdot Re$. Here, f and Re are based on the average velocity $\bar{w}$ and the interplate (or interfin) spacing s.

t/s	h/s	Rectangular	Triangular	Concave Parabolic	Convex Parabolic
1/6	1/3	43.86	34.16	33.44	35.54
1/3	1/3	54.94	36.37	34.36	39.62
1/2	1/3	54.0	39.13	35.83	43.10
1/6	2/3	87.42	57.44	54.37	62.42
1/3	2/3	194.8	67.56	58.80	82.92
1/2	2/3	216.0	80.33	65.13	102.4
1/6	1	91.93	70.19	63.79	79.25
1/3	1	273.3	96.44	74.79	138.1
1/2	1	-	139.5	91.64	243.8

Table 2 Variation of the Nusselt number $Nu = h_T s/k$, where $h_T = q/(T_w - T_b)$. Here, the average heat flux q is defined on the basis of plate surface area alone (i.e., excluding the fin surface area).

t/s	h/s	Rectangular	Triangular	Concave Parabolic	Convex Parabolic
1/6	1/3	5.373	4.705	4.664	4.789
1/3	1/3	5.700	4.810	4.712	4.978
1/2	1/3	5.655	4.916	4.768	5.094
1/6	2/3	7.156	6.127	6.049	6.297
1/3	2/3	12.36	6.368	6.129	6.796
1/2	2/3	11.31	6.520	6.240	6.993
1/6	1	6.511	6.102	5.990	6.306
1/3	1	10.55	6.497	6.139	7.156
1/2	1	-	6.509	6.282	6.744

Table 3 Variation of $Nu/(P/s)$, where P represents the total heated/wetted perimeter. This quantity represents a Nusselt number in which the average heat flux is obtained using the total (plate + fin) surface area.

t/s	h/s	Rectangular	Triangular	Concave Parabolic	Convex Parabolic
1/6	1/3	4.031	3.901	3.820	3.938
1/3	1/3	4.276	4.227	4.062	4.291
1/2	1/3	5.655	4.469	4.246	4.516
1/6	2/3	4.293	4.028	3.943	4.124
1/3	2/3	7.415	4.510	4.253	4.746
1/2	2/3	11.31	4.891	4.548	5.119
1/6	1	3.906	3.304	3.222	3.405
1/3	1	7.914	3.775	3.508	4.122
1/2	1	-	4.023	3.780	4.092

temperatures, respectively. The Nusselt number Nu can be defined as

$$\mathrm{Nu} = \frac{h_T s}{k} \tag{6}$$

Under the assumed fully developed conditions, Nu is independent of z and is a function only of the fin shape and the geometric quantities t/s and h/s.

Computational Procedure

As already mentioned, the task here is to solve the Poisson equations for the axial velocity w and the temperature T. Since the geometric shape of the computational domain is quite complex, a finite element method is an appropriate solution candidate. The control volume based finite element method of Baliga and Patankar [5] was employed in the present study. The method uses three node triangular elements, and for a Poisson equation, it employs linear shape functions.

The domain was triangulated as follows. First, N equally spaced vertical lines are drawn which run from the curve *b-c-d* to the top line *a-e*. Then, on each of these lines, N equally spaced grid points are placed. By joining the corresponding points on the vertical lines, the domain is divided into $(N-1) \times (N-1)$ quadrilaterals. The quadrilaterals are then triangulated by alternately joining the left bottom-right top and left top-right bottom grid points. The domain, thus, has an $N \times N$ grid, and a characteristic grid spacing of

$$\delta = s/(N-1) \tag{7}$$

The goal of this study, as already stated, is to examine the effect of the fin shape. Since such an effect can be small, it is necessary that the numerical results be extrapolated to zero grid size. This was indeed done, and the Richardson extrapolation formula

$$a = a_0 + b\delta^c \tag{8}$$

was employed for this purpose. Here a is any quantity of interest, a_0 is the value of a corresponding to zero grid size (which is supposedly the exact solution), c is the order of convergence of the method, and b is a constant. If the value of a is computed for three different values of δ, then a_0, b, and c can be determined. Of these, we need only a_0.

Both fRe and Nu values were extrapolated using the above procedure. The three δ's used correspond to $N = 10$ ($\delta = s/9$), $N = 19$ ($\delta = s/18$), and $N = 28$ ($\delta = s/27$). Consider the case of a rectangular fin with $h/s = 1$. This corresponds, really, to flow through a rectangular duct. Similarly, a triangular fin with $t/s = 1/2$ and $h/s = 1$ corresponds to flow through an isosceles triangular duct. For these limiting cases, the fRe and Nu of the present computations (the zero grid size extrapolated values) agree with those reported by Shah and London (Tables 42, 56, and 57 of [1]) to within 1 percent. This agreement was used as a check on the computational procedure.

The Baseline Friction Factor and Nusselt Number Results

The basic friction factor results are presented in Table 1. As can be seen, for a fixed plate spacing s and average velocity $\bar{w}$ (i.e., a fixed Re), the friction factor f (and hence the pressure drop dp/dz) increases with both t/s and h/s. Everything else remaining the same, rectangular fins have the maximum pressure drop followed in decreasing order, by convex-parabolic, triangular, and the concave-parabolic fins.

The Nusselt number values are listed in Table 2. It may be recalled that this Nusselt number is based on the heat flux calculated using the base heat transfer area s which would occur when there is no fin. Hence, the Nusselt number listed in Table 2 has built into it the effect of increased heat transfer area when the fins are present. All else remaining fixed, the Nusselt number is highest for the rectangular fins followed, in decreasing order, by convex-parabolic, triangular, and concave-parabolic fins. For any fin shape, the Nusselt number shows a mixed dependence on h/s and t/s, but generally, it increases with both. An increase in t/s or h/s affects the total heat transfer area (Table 4) and, due to the no-slip condition, the velocity distribution. The mixed dependence of the Nusselt number on t/s and h/s is due to these competing effects.

Using the friction factor and the Nusselt number values reported in Tables 1 and 2, other results of engineering interest can easily be calculated. Some examples of this will now be presented.

Table 4 P/s, where P is the wetted/heated perimeter of the computational domain

t/s	h/s	Rectangular	Triangular	Concave Parabolic	Convex Parabolic
1/6	1/3	1.333	1.206	1.221	1.216
1/3	1/3	1.333	1.138	1.160	1.160
1/2	1/3	1.000	1.100	1.123	1.128
1/6	2/3	1.667	1.521	1.534	1.527
1/3	2/3	1.667	1.412	1.441	1.432
1/2	2/3	1.000	1.333	1.372	1.366
1/6	1	1.667	1.847	1.859	1.852
1/3	1	1.333	1.721	1.750	1.736
1/2	1	-	1.618	1.662	1.648

Table 5 Variation of $\mathcal{P}/(\dot{m}^2 \mu L/\rho^2 s^4))$ where $\mathcal{P}$ represents the pumping power required to maintain a mass flow rate $\dot{m}$ through the computational domain of axial length L

t/s	h/s	Rectangular	Triangular	Concave Parabolic	Convex Parabolic
1/6	1/3	49.35	36.17	34.72	38.38
1/3	1/3	70.64	40.92	37.11	46.51
1/2	1/3	81.00	46.95	40.31	55.41
1/6	2/3	112.4	64.62	58.71	73.28
1/3	2/3	350.6	86.86	69.03	117.8
1/2	2/3	647.9	120.5	83.74	184.3
1/6	1	137.9	84.22	71.77	101.9
1/3	1	819.7	144.7	96.16	248.6
1/2	1	-	279	137.5	731.3

Heat Transfer Results on per Unit Heat Transfer Area Basis

As already mentioned, the Nusselt number presented in Table 2 is based on a heat flux Q'/s. A true average heat flux should be Q'/P, where P represents the actual heated (or wetted) perimeter of the computational domain. Thus P = length of $(a-b) + (b-c) + (d-e)$.[3] The Nusselt number using the heat flux Q'/P would be $\mathrm{Nu}/(P/s)$, and this would be more representative of the heat transfer on a per unit heat transfer area basis. Table 3 has been prepared for this purpose. It shows the variation of $\mathrm{Nu}/(P/s)$ with t/s and h/s. Accompanying Table 3 is Table 4 in which the values of the perimeter P have been listed. From Table 3 it is found that even on a per unit heat transfer area basis, a rectangular fin yields the highest heat transfer, followed in decreasing order, by convex-parabolic, triangular, and the concave-parabolic fins. The same behavior, it may be recalled, is displayed by the Nusselt number results of Table 2. The effect of increasing t/s, as may be noted from Table 3, is to increase the heat transfer per unit area for all fin shapes. With h/s, the heat transfer increases at first and then decreases.

Evaluation of the Total Heat Transfer by an Exchanger of Length L

Consider an exchanger of length L. Let Q be the heat transferred by each computational domain in the axial distance L. Assuming fully developed conditions all through, Q is given by

$$\frac{Q}{\dot{m}c_p(T_w - T_{bi})} = 1 - \exp\left(-\frac{\mathrm{Nu}kL}{\dot{m}c_p}\right) \tag{9}$$

[3] For a rectangular fin $P = s/2 + h + s/2$.

Table 6 A/s^2, where A is the flow area in the computational domain

t/s	h/s	Rectangular	Triangular	Concave Parabolic	Convex Parabolic
1/6	1/3	0.4444	0.4722	0.4815	0.4630
1/3	1/3	0.3889	0.4444	0.4630	0.4259
1/2	1/3	0.3333	0.4167	0.4444	0.3889
1/6	2/3	0.3889	0.4444	0.4630	0.4259
1/3	2/3	0.2778	0.3889	0.4259	0.3519
1/2	2/3	0.1667	0.3333	0.3889	0.2778
1/6	1	0.3333	0.4167	0.4444	0.3889
1/3	1	0.1667	0.3333	0.3889	0.2778
1/2	1	-	0.2500	0.3333	0.1667

where $\dot{m}$ is the total mass flow rate through the computational domain, k and c_p are the thermal conductivity and the specific heat of the fluid, and T_{bi} is the bulk temperature at the inlet. Clearly, the greater the value of Nu, the greater is the amount of heat transferred. Thus, everything else remaining fixed, the rectangular fins will transfer the maximum amount of heat followed, in decreasing order, by convex-parabolic, triangular, and concave-parabolic fins. If the heat duty Q and the exchanger length L are fixed, then the rectangular fins will need the smallest mass flow rate followed, in increasing order, by the convex-parabolic, triangular, and concave-parabolic fins. Similarly, if Q and $\dot{m}$ are fixed, then the length L will be maximum for an exchanger with concave-parabolic fins followed by the triangular, convex-parabolic, and rectangular fins.

Pumping Power Considerations

From an engineering standpoint, the important hydrodynamic quantity of interest is the pumping power $\mathcal{P}$ necessary to make the fluid flow through the exchanger. For an exchanger of length L, the power $\mathcal{P}$ required for the computational domain is given by

$$\mathcal{P} = (-dp/dz)L(\dot{m}/\rho) \tag{10}$$

In dimensionless form, the pumping power can be expressed as

$$\frac{\mathcal{P}}{\left(\frac{\dot{m}^2\mu L}{\rho^2 s^4}\right)} = \left(\frac{f\mathrm{Re}}{2}\right)\frac{1}{(A/s^2)} \tag{11}$$

where A is the cross-sectional area of the computational domain.

The pumping power results are presented in Table 5. In the accompanying Table 6, the values of A/s^2 have been listed. Everything else including the mass flow rate $\dot{m}$ remaining fixed, it is clear from Table 5 that the rectangular fins require the maximum pumping power followed in decreasing order by the convex-parabolic, triangular, and concave-parabolic fins. All else remaining constant, the pumping power increases with t and h.

From Tables 2 and 5 we note that both the Nusselt number Nu and the pumping power increase as one goes from concave-parabolic, to triangular, to convex-parabolic, to the rectangular fins. However, the factor by which the Nusselt number increases is much less than the factor by which the pumping power changes. Hence if the mass flow rate $\dot{m}$, the heat duty Q [recall equation (9)] and all other quantities are fixed except the exchanger length L, then L will be smallest for rectangular fins followed in increasing order by convex-parabolic, triangular, and concave-parabolic fins; however, the pumping power will be highest for rectangular fins followed, in decreasing order, by the convex-parabolic, triangular, and concave-parabolic fins. By the same token, if $\dot{m}$, the

pumping power $\mathcal{P}$, and all other quantities are kept fixed, then the exchanger length L and the heat transferred Q will be smallest for rectangular fins followed, in increasing order, by convex-parabolic, triangular, and concave-parabolic fins.

Many other design decisions of this nature can be concluded from the tabulated friction factor and Nusselt number data. Often, design considerations are based on the fin volume or fin weight. For such calculation, Table 6 would be useful since $(1/2 - A/s^2)$ is the dimensionless fin area (volume per unit axial length) in the computational domain.

Conclusions

Laminar fully developed flow in a finned parallel plate passage has been numerically analyzed. The goal of the study has been to examine the effect of the fin shape. Fins of rectangular, triangular, concave-parabolic, and convex-parabolic shapes have been considered. Baseline data for the friction factor and Nusselt number have been tabulated which can be used for a variety of design/optimization analyses. Everything else remaining the same, the rectangular fins are found to provide the maximum heat transfer followed, in decreasing order, by the convex-parabolic, triangular, and concave-parabolic fins. The pumping power also follows the same order, with the proportional change in the pumping power being greater. Thus, if pumping power is not a constraint, as in many special-purpose compact heat exchange devices, the rectangular fins are the best followed by convex-parabolic, triangular, and concave-parabolic fins.

Acknowledgments

The authors are grateful to the Department of Mechanical Engineering, Aeronautical Engineering and Mechanics of Rensselaer Polytechnic Institute for supporting this work under the auspices of this institute's BUILD program.

References

1 Shah, R. K., and London, A. L., *Laminar Flow Forced Convection in Ducts*, Advances in Heat Transfer, Academic Press, New York, 1978.

2 Bergles, A. E., "Survey and Evaluation of Techniques to Augment Convective Heat and Mass Transfer," in: *Progress in Heat and Mass Transfer*, Pergamon Press, Oxford, Vol. 1, 1969, pp. 331–424.

3 Sparrow, E. M., Baliga, B. R., and Patankar, S. V., "Forced Convection Heat Transfer From a Shrouded Fin Array With and Without Tip Clearance," ASME JOURNAL OF HEAT TRANSFER, Vol. 100, 1978, pp. 572–579.

4 Kays, W. M., and Crawford, M. E., *Convective Heat and Mass Transfer*, McGraw-Hill, New York, 1980.

5 Baliga, B. R., and Patankar, S. V., "A New Finite Element Formulation for Convection-Diffusion Problems," *Numerical Heat Transfer*, Vol. 3, 1980, pp. 393–409.

Crossflow Heat Transfer in Tube Bundles at Low Reynolds Numbers

T. H. Hwang[1] and S. C. Yao[2]

Introduction

Extensive studies [1–11] have been conducted for the heat transfer in tube bundles at crossflow in response to the wide applications of shell-and-tube exchangers. Some empirical heat transfer correlations for bundles with specific pitch-to-diameter ratios were presented in [8–11]. A large quantity of data was also compiled in [7] for heat transfer over smooth tube bundles at high Reynolds numbers, but no significant amount of data were available for the flow at low Reynolds numbers. More detailed heat transfer information in tube bundles were presented in [1]. The empirical correlations for different bundles geometries were proposed for wide range of Reynolds numbers. However, the empirical correlations fail to predict well the data, especially for the data of staggered bundle at low Reynolds number, say $\mathrm{Re}_d < 100$, where the Reynolds number is based upon the tube diameter and the flow velocity at minimum cross section in the bundles. The maximum error of the predictions for the staggered bundles data was as high as 240 percent.

When the Reynolds number is very low ($\mathrm{Re}_d < 1$), the flow field can be characterized by the creeping flow approximation. At this condition, the flow streamlines are symmetric with respect to a plane which passes through the tube and normal to the incoming stream. Various investigations [13, 14] of creeping flow through packed beds and fluidized beds have been conducted using a "free surface model." This model reduces the complex problem of the multiparticle assemblage by considering an equivalent concentric spherical cell around a particle. The interaction of a particular sphere with its neighbors is represented by this spherical cell. In actual package beds, these fluid envelopes will be distorted, but it is assumed that the cell can still be taken to be spherical. The hypothetical fluid cell is assumed to have zero shear stress at its outer surface. The fluid-to-particle volume ratio in the entire assemblage is preserved in this cell. In tube bundles, the creeping flow fluid mechanics has been studied in [13] using this free surface model. However, no analysis on heat transfer has been performed. In the following sections, the heat transfer information will be provided for bundles of various configurations.

Model

Figure 1 shows the typical staggered array and inline array tube bundle with the flow normal to the tubes, where X_L and X_T are the longitudinal pitch and transverse pitch in the bundles, respectively. The fluid flow and heat convection are analyzed under the following assumptions.

1 The flow is steady with constant fluid properties.

2 The fluid is at creeping flow ($\mathrm{Re}_d < 1$) with negligible energy dissipation.

3 The bundles are infinite in extent with negligible entry and exit effects and no wall effects.

4 The free surface model is applicable to a tube in bundles of any geometry. This assumption will be justified by the comparison of the results of the analysis to experimental data.

With the use of the free surface model, the hydrodynamics in bundles can be analyzed on a cylinder which has a radius a surrounded by a cylindrical cell of fluid with a free surface at radius b as shown in Fig. 2(*a*). The fluid envelope is assumed to move with respect to the tube at a constant velocity U, which is the velocity at the minimum cross section in the tube

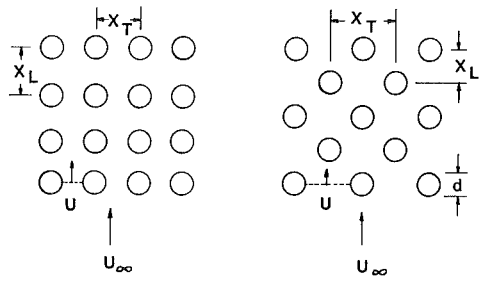

(a) Inline (b) Staggered

Fig. 1 Typical layout of tube bundles

[1]Research Associate, Department of Mechanical Engineering, Carnegie-Mellon University, Pittsburgh, PA 15213; Assoc. Mem. ASME

[2]Professor, Department of Mechanical Engineering, Carnegie-Mellon University, Pittsburgh, PA 15213; Mem. ASME

Contributed by the Heat Transfer Division for publication in the JOURNAL OF HEAT TRANSFER. Manuscript received by the Heat Transfer Division November 5, 1984.

pumping power $\mathcal{P}$, and all other quantities are kept fixed, then the exchanger length L and the heat transferred Q will be smallest for rectangular fins followed, in increasing order, by convex-parabolic, triangular, and concave-parabolic fins.

Many other design decisions of this nature can be concluded from the tabulated friction factor and Nusselt number data. Often, design considerations are based on the fin volume or fin weight. For such calculation, Table 6 would be useful since $(1/2 - A/s^2)$ is the dimensionless fin area (volume per unit axial length) in the computational domain.

Conclusions

Laminar fully developed flow in a finned parallel plate passage has been numerically analyzed. The goal of the study has been to examine the effect of the fin shape. Fins of rectangular, triangular, concave-parabolic, and convex-parabolic shapes have been considered. Baseline data for the friction factor and Nusselt number have been tabulated which can be used for a variety of design/optimization analyses. Everything else remaining the same, the rectangular fins are found to provide the maximum heat transfer followed, in decreasing order, by the convex-parabolic, triangular, and concave-parabolic fins. The pumping power also follows the same order, with the proportional change in the pumping power being greater. Thus, if pumping power is not a constraint, as in many special-purpose compact heat exchange devices, the rectangular fins are the best followed by convex-parabolic, triangular, and concave-parabolic fins.

Acknowledgments

The authors are grateful to the Department of Mechanical Engineering, Aeronautical Engineering and Mechanics of Rensselaer Polytechnic Institute for supporting this work under the auspices of this institute's BUILD program.

References

1 Shah, R. K., and London, A. L., *Laminar Flow Forced Convection in Ducts*, Advances in Heat Transfer, Academic Press, New York, 1978.

2 Bergles, A. E., "Survey and Evaluation of Techniques to Augment Convective Heat and Mass Transfer," in: *Progress in Heat and Mass Transfer*, Pergamon Press, Oxford, Vol. 1, 1969, pp. 331–424.

3 Sparrow, E. M., Baliga, B. R., and Patankar, S. V., "Forced Convection Heat Transfer From a Shrouded Fin Array With and Without Tip Clearance," ASME JOURNAL OF HEAT TRANSFER, Vol. 100, 1978, pp. 572–579.

4 Kays, W. M., and Crawford, M. E., *Convective Heat and Mass Transfer*, McGraw-Hill, New York, 1980.

5 Baliga, B. R., and Patankar, S. V., "A New Finite Element Formulation for Convection-Diffusion Problems," *Numerical Heat Transfer*, Vol. 3, 1980, pp. 393–409.

Crossflow Heat Transfer in Tube Bundles at Low Reynolds Numbers

T. H. Hwang[1] and S. C. Yao[2]

Introduction

Extensive studies [1–11] have been conducted for the heat transfer in tube bundles at crossflow in response to the wide applications of shell-and-tube exchangers. Some empirical heat transfer correlations for bundles with specific pitch-to-diameter ratios were presented in [8–11]. A large quantity of data was also compiled in [7] for heat transfer over smooth tube bundles at high Reynolds numbers, but no significant amount of data were available for the flow at low Reynolds numbers. More detailed heat transfer information in tube bundles were presented in [1]. The empirical correlations for different bundles geometries were proposed for wide range of Reynolds numbers. However, the empirical correlations fail to predict well the data, especially for the data of staggered bundle at low Reynolds number, say $\mathrm{Re}_d < 100$, where the Reynolds number is based upon the tube diameter and the flow velocity at minimum cross section in the bundles. The maximum error of the predictions for the staggered bundles data was as high as 240 percent.

When the Reynolds number is very low ($\mathrm{Re}_d < 1$), the flow field can be characterized by the creeping flow approximation. At this condition, the flow streamlines are symmetric with respect to a plane which passes through the tube and normal to the incoming stream. Various investigations [13, 14] of creeping flow through packed beds and fluidized beds have been conducted using a "free surface model." This model reduces the complex problem of the multiparticle assemblage by considering an equivalent concentric spherical cell around a particle. The interaction of a particular sphere with its neighbors is represented by this spherical cell. In actual package beds, these fluid envelopes will be distorted, but it is assumed that the cell can still be taken to be spherical. The hypothetical fluid cell is assumed to have zero shear stress at its outer surface. The fluid-to-particle volume ratio in the entire assemblage is preserved in this cell. In tube bundles, the creeping flow fluid mechanics has been studied in [13] using this free surface model. However, no analysis on heat transfer has been performed. In the following sections, the heat transfer information will be provided for bundles of various configurations.

Model

Figure 1 shows the typical staggered array and inline array tube bundle with the flow normal to the tubes, where X_L and X_T are the longitudinal pitch and transverse pitch in the bundles, respectively. The fluid flow and heat convection are analyzed under the following assumptions.

1 The flow is steady with constant fluid properties.

2 The fluid is at creeping flow ($\mathrm{Re}_d < 1$) with negligible energy dissipation.

3 The bundles are infinite in extent with negligible entry and exit effects and no wall effects.

4 The free surface model is applicable to a tube in bundles of any geometry. This assumption will be justified by the comparison of the results of the analysis to experimental data.

With the use of the free surface model, the hydrodynamics in bundles can be analyzed on a cylinder which has a radius a surrounded by a cylindrical cell of fluid with a free surface at radius b as shown in Fig. 2(*a*). The fluid envelope is assumed to move with respect to the tube at a constant velocity U, which is the velocity at the minimum cross section in the tube

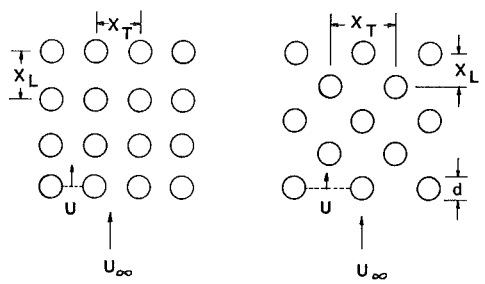

(a) Inline (b) Staggered

Fig. 1 Typical layout of tube bundles

[1]Research Associate, Department of Mechanical Engineering, Carnegie-Mellon University, Pittsburgh, PA 15213; Assoc. Mem. ASME

[2]Professor, Department of Mechanical Engineering, Carnegie-Mellon University, Pittsburgh, PA 15213; Mem. ASME

Contributed by the Heat Transfer Division for publication in the JOURNAL OF HEAT TRANSFER. Manuscript received by the Heat Transfer Division November 5, 1984.

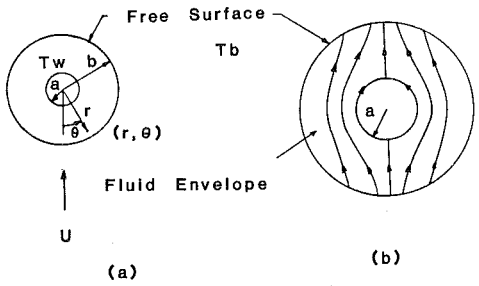

Fig. 2 Schematic of free surface model

bundle. The typical streamlines in the cell are shown in Fig. 2(*b*). The unit cell radius b in the free surface model is related to the tube pitches X_T and X_L as

$$b=\left(\frac{X_T X_L}{\pi}\right)^{1/2} \tag{1}$$

The voidage of a tube bundle can be also related to the tube pitches as

$$\epsilon=\frac{X_T X_L-\pi d^2/4}{X_T X_L} \tag{2}$$

The ratio of the cell radius to the tube radius, β, can be related to the voidage ϵ of the bundle as

$$\beta=\left(\frac{1}{1-\epsilon}\right)^{1/2} \tag{3}$$

It is noteworthy that the solidity of a bundle is simply $1/\beta^2$. With those notations, the stream function can be rewritten as [13]

$$\psi=\frac{\lambda U r \sin\theta}{(\beta^4-1)}\left(\frac{r^2}{a^2}+2(1+\beta^4)\ \ln(a/r)-(1-\beta^4)-\frac{\beta^4 a^2}{r^2}\right) \tag{4}$$

where

$$\lambda=\frac{(\beta^4-1)}{[(1+\beta^4)\ \ln\beta^2+(1-\beta^4)]}$$

is a parameter of the bundles geometry.

Formulation. Although the present analysis of fluid flow is restricted to creeping flow, at large Peclet number ($\mathrm{Pe}_d >> 1$) the thermal boundary layer will be thin and stays close to the surface of the heated tube. Therefore, the heat transfer can be evaluated from thermal boundary layer analysis. In a thin thermal boundary layer, $r \cong a$, the stream function in equation (4) can be expanded by using a Taylor series and reduced to

$$\psi \cong \frac{-2\lambda U \sin\theta (r-a)^2}{a} \tag{5}$$

Thus, the corresponding flow velocity components can also be obtained

$$V_r=\frac{\partial\psi}{r\partial\theta}\ ;\quad V_\theta=-\frac{\partial\psi}{\partial r} \tag{6}$$

Neglecting the viscous dissipation, the energy equation in the unit cell becomes

$$V_r\frac{\partial T}{\partial r}+V_\theta\frac{\partial T}{r\partial\theta}=\alpha\left(\frac{\partial^2 T}{\partial r^2}+\frac{1}{r}\frac{\partial T}{\partial r}\right) \tag{7}$$

with constant temperature boundary conditions

$$T=T_w \quad \text{at} \quad r=a \tag{8}$$

$$T=T_b \quad \text{at} \quad r=b \tag{9}$$

The energy equation can be transformed to a nondimensional form by introducing the dimensionless quantities

$$\eta=\frac{\psi}{Ua\lambda} \tag{10}$$

and

$$t=\frac{T-T_w}{T_b-T_w} \tag{11}$$

Due to the thin thermal boundary layer, $\partial^2 T/\partial r^2$ is much greater than $\partial T/r\partial r$. Thus, the second term on the right-hand side of equation (7) can be neglected. The steady-state convective-diffusion equation becomes

$$\frac{\partial t}{\partial\theta}=\frac{4(2\sin\theta)^{1/2}}{\mathrm{Pe}_d\lambda}\frac{\partial}{\partial\eta}\left((-\eta)^{1/2}\frac{\partial t}{\partial\eta}\right) \tag{12}$$

where $\mathrm{Pe}_d = 2Ua/\alpha$ is the Peclet number. Using the new variable

$$\epsilon=\frac{4(2)^{1/2}}{\mathrm{Pe}_d\lambda}\int_0^\theta(\sin\theta)^{1/2}d\theta \tag{13}$$

and the similarity variable Z [15]

$$Z=\frac{(-\eta)^{1/2}}{\xi^{1/3}} \tag{14}$$

the governing equation can be transformed into an ordinary differential equation

$$\frac{d^2 t}{dZ^2}+\frac{4}{3}Z^2\frac{dt}{dZ}=0 \tag{15}$$

Equation (15) can be integrated twice to obtain

$$t(Z)=c_3+c_2\int_0^Z e^{-\frac{4}{9}Z^3}dZ \tag{16}$$

where the constants c_2 and c_3 are evaluated from the boundary conditions

$$t=0 \quad \text{at} \quad r=a \tag{17}$$

$$t=1 \quad \text{at} \quad r=b\ (\eta\sim\infty, Z\sim\infty) \tag{18}$$

Therefore

$$c_3=0 \tag{19}$$

$$c_2=\left(\int_0^\infty e^{-\frac{4}{9}Z^3}dZ\right)^{-1} \tag{20}$$

The second boundary condition has been rewritten so that the stream function at the outer surface of the unit cell approaches infinity. This is reasonable because the quantity $(b-a)$ is always much greater than the thickness of the thermal boundary layer at high Peclet number conditions. Finally, the solution of the temperature profile is

$$t=\frac{T-T_w}{T_b-T_w}=\frac{\int_0^Z e^{-(4/9)Z^3}dZ}{(9/4)^{1/3}\Gamma(4/3)} \tag{21}$$

It is interesting to notice that the temperature profile in equation (21) is dependent upon β instead of the details of bundle geometry. This, in fact, originated from the application of the free surface model to the bundle as shown in Fig. 2.

Nusselt Number. The local Nusselt number which is based on the tube diameter can be used to describe the heat transfer

$$\mathrm{Nu}_d=\frac{hd}{k}=\frac{-k(\partial T/\partial r)\,|_{r=a}}{(k/d)(T_w-T_b)} \tag{22}$$

Substituting equation (21) into equation (22) yields

$$\mathrm{Nu}_d=\frac{(16\mathrm{Pe}_d\lambda)^{1/3}(\sin\theta)^{1/2}}{\Gamma(4/3)}\left(9\int_0^\theta(\sin\theta)^{1/2}d\theta\right)^{-1/3} \tag{23}$$

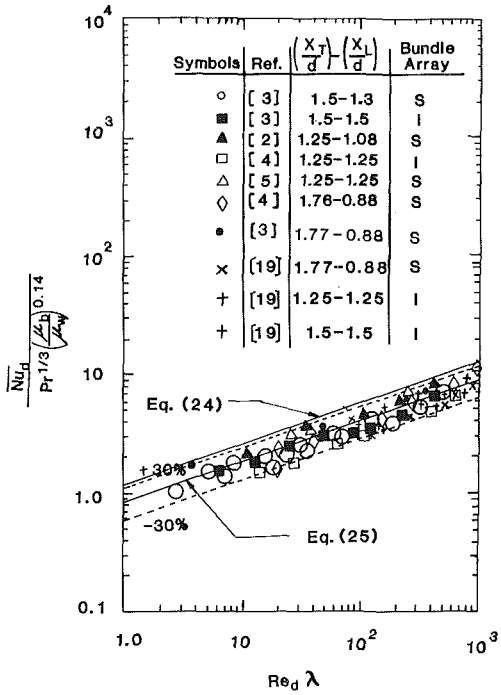

Fig. 3 Heat transfer in tube bundles at low Reynolds numbers and high Peclet numbers

The average Nusselt number $\overline{\mathrm{Nu}}_d$ can be evaluated by integrating the local Nusselt number around the tube. That gives

$$\overline{\mathrm{Nu}}_d = 1.185\mathrm{Re}_d^{1/3}\lambda^{1/3}\mathrm{Pr}^{1/3}\left(\frac{\mu_b}{\mu_w}\right)^{0.14} \tag{24}$$

The correction factor $(\mu_b/\mu_w)^{0.14}$ is applied here, similar to [2], to account for the effects of variable viscosity. Hence, equation (24) gives an analytical relationship between the average heat transfer coefficient and Reynolds number for the tube bundles of any regular pattern of tube layout with the solidity $(1/\beta^2)$ of the bundle as a parameter.

Discussion

The present heat transfer solution is restricted to the conditions of low Reynolds number ($\mathrm{Re}_d < 1$) and high Peclet number ($\mathrm{Pe}_d >> 1$). Figure 3 shows the comparison between the extrapolation of equation (24) and the data for bundles of various tube arrangements for Re_d less than 200. The data sets in which the natural convection is significant [16, 17] are excluded in present comparison. It is noticed that the free surface model can not distinguish between inline and staggered tube bundles with the same solidity (S); however, the model is expected to be more appropriate for staggered bundles than for inline bundles as shown in Fig. 3. Equation (24) generally overpredicts the data because the Reynolds numbers of the data base are higher than the Reynolds numbers of creeping flow. The flow streams are likely to be asymmetric with respect to a plane which passes through the tube but is normal to the incoming streams. The analysis, based upon creeping flow and high Peclet number assumptions, gives symmetric streamlines and a thin thermal boundary layer, therefore, overpredicts the heat transfer.

In order to fit the data base in this Reynolds number range, the constant in equation (24) is reduced. That gives

$$\overline{\mathrm{Nu}}_d = 0.83\mathrm{Re}_d^{1/3}\mathrm{Pr}^{1/3}\lambda^{1/3}\left(\frac{\mu_b}{\mu_w}\right)^{0.14} \tag{25}$$

for $\mathrm{Re}_d < 200$ and $p/d < 2.0$, where p represents the longitudinal pitch or transverse pitch regardless of inline or staggered array. As shown in Fig. 3, this semi-empirical correlation fits all the data within ± 30 percent. The solidity

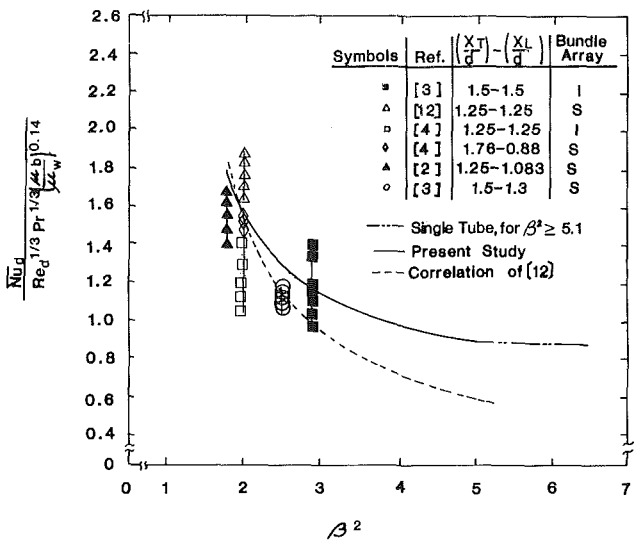

Fig. 4 Comparison of present analysis with Whitaker's heat transfer correlation

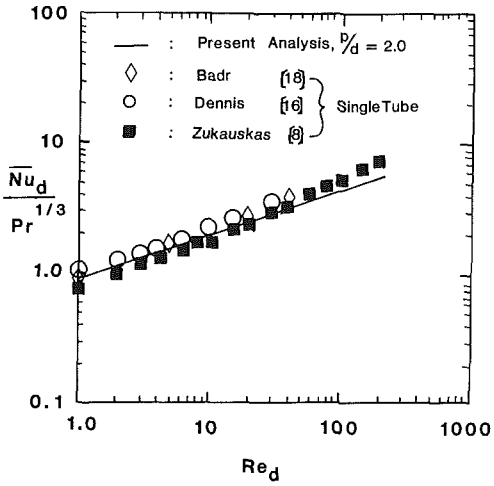

Fig. 5 Comparison of present analysis with the single tubes heat transfer data

$(1/\beta^2)$ of the bundle plays an important role in the heat transfer performance at low Reynolds number and high Peclet number conditions. Increasing the tube spacing or decreasing $1/\beta^2$ results in a lower heat transfer coefficient.

In order to compare on a common basis, Whitaker's empirical correlation [12] was converted to a form similar to equation (25)

$$\overline{\mathrm{Nu}}_d = 1.526\mathrm{Re}_d^{1/3}(\beta^2-1)^{-2/3}\mathrm{Pr}^{1/3}\left(\frac{\mu_b}{\mu_w}\right)^{0.14} \tag{26}$$

Equations (26) and (25) are compared with experimental data in Fig. 4 for the effects of β^2. Both equations show the tendency of decreasing heat transfer coefficient with decreasing solidity ($S = 1/\beta^2$) of the bundles. The present semi-empirical correlation, equation (25), is comparable with the empirical correlation of Whitaker's. However, the present analysis provides a theoretical foundation to the application of these formulations.

Equation (25) has also been compared with the correlation in [1]. Present semi-empirical correlation appears to be able to predict the bundles data at low Reynolds numbers ($\mathrm{Re}_d <$ 200) better than [1].

It should be mentioned here that the free surface model was successfully used for predicting pressure drop and heat

transfer in packed beds only in the range of voidage of 0.25 to 0.8 and at low Reynolds numbers [13, 14]. Similar restrictions may also be applicable to the tube bundles at crossflow. When the voidage is higher than 0.8 the prediction of creeping flow will deviate from the real situation seriously at $1 < \mathrm{Re}_d < 200$. The miscounted inertial effects in the wide opened space between tubes becomes significant. To illustrate this restriction, the heat transfer data of single tubes [8, 16, 18] are plotted in Fig. 5. The prediction of the present correlation in equation (25) gives good agreement when the pitch-to-diameter ratio is set at 2.0. When p/d is 2.0, the voidage is 0.8 in the bundle, and the fluid flow and heat transfer are very close to those of a single tube in infinite space. Therefore, as shown in Fig. 4, the present prediction will be suitable for $\beta^2 < 5.1$ (or $p/d < 2.0$). Beyond this, the prediction will come from setting $\beta^2 = 5.1$ in equation (25). Thus

$$\overline{\mathrm{Nu}}_d = 0.91 \mathrm{Re}_d^{0.6} \mathrm{Pr}^{1/3} (\mu_b/\mu_w)^{0.14} \tag{27}$$

for $\mathrm{Re}_d < 200$ and $p/d > 2.0$. This equation fits the data of single tubes within ± 30 percent.

Conclusions

At very low Reynolds numbers, the flow field can be approximated by the free surface model, together with a creeping flow approximation. Under conditions of high Peclet number, the average Nusselt number on a tube in a bundle is derived. Compared with the existing heat transfer data in the range of $\mathrm{Re}_d < 200$ and pitch-to-diameter ratios less than 2.0, a slightly modified correlation as shown in equation (25) is proposed which fits the data within ± 30 percent. For bundles with $p/d > 2.0$ and at $\mathrm{Re}_d < 200$, the heat transfer on a tube in a bundle is similar to the heat transfer of a single tube in an infinite pool. Therefore, the correlation in equation (27) is proposed which also fits the data within ± 30 percent.

References

1 Gnielinski, V., Zukauskas, A., and Skrinska, A., "Banks of Plain and Finned Tubes," in: *Heat Exchanger Design Handbook*, E. U. Schlunder, editor-in-chief, Section 2.5.3, Hemisphere, Washington, D.C., 1983.

2 Omohundro, G. A., Bergelin, O. P., and Colburn, A. P., "Heat Transfer and Fluid Friction During Viscous Flow Across Banks of Tubes," *Trans. ASME*, Vol. 71, 1949, pp. 27–34.

3 Bergelin, O. P., Colburn, A. P., and Hull, H. C., "Heat Transfer and Fluid Friction During Flow Across Banks of Tubes," University of Delaware, Engineering Experiment Station Bulletin No. 2, 1950.

4 Bergelin, O. P., Davis, E. S., and Hull, H. C., "A Study of Three Tube Arrangements in Unbaffled Tubular Heat Exchangers," *Trans. ASME*, Vol. 71, 1949, pp. 367–374.

5 Pierson, O. L., "Experimental Investigation of the Influence of Tube Arrangement on Convection Heat Transfer and Flow Resistance in Cross Flow of Gases Over Tube Banks," *Trans. ASME*, Vol. 59, 1937, pp. 563–572.

6 Bergelin, O. P., Brown, G. A., Hull, H. C., and Sullivan, F. W., "Heat Transfer and Fluid Friction During Viscous Flow Across Banks of Tubes," *Trans. ASME*, Vol. 72, 1950, pp. 881–888.

7 Kays, W., and London, A. L., *Compact Heat Exchanger*, 3rd ed., McGraw-Hill, New York, 1984.

8 Zukauskas, A., "Heat Transfer From Tubes in Crossflow," *Advances in Heat Transfer*, J. P. Hartnett and T. F. Irvine, Jr., eds., Academic Press, New York, 1972, Vol. 8, pp. 93–160.

9 Polley, G. T., Ralston, T., and Grand, J. D. R., "Forced Crossflow Boiling in an In-Line Tube Bundle," ASME Paper No. 80-HT-46.

10 Snyder, N. W., "Heat Transfer in Air from a Single Tube in a Staggered Tube Bank," *AIChE Symposium Series*, Vol. 49, No. 5, 1953, pp. 11–20.

11 McAdams, W. H., *Heat Transmission*, 3rd ed., McGraw-Hill, New York, 1954.

12 Whitaker, S., "Forced Convection Heat Transfer Correlation for Flow in Pipes, Past Flat Plates, Single Cylinders, Single Spheres, and Flow in Packed Beds and Tube Bundles," *AIChE Journal*, Vol. 18, 1972, pp. 361–371.

13 Happel, J., "Viscous Flow Relative to Arrays of Cylinders," *AIChE Journal*, Vol. 5, 1959, pp. 174–177.

14 Pfeffer, R., "Heat and Mass Transfer in Multiparticle System," *Industrial and Engineering Chemistry Fundamentals*, Vol. 3, 1964, pp. 380–383.

15 Hansen, A. G., "Generalized Similarity Analysis of Partial Differential Equations," *Nonlinear Partial Differential Equations*, W. F. Ames, ed., Academic Press, New York, 1967, pp. 1–17.

16 Dennis, S. C. R., Hudson, J. D., and Smith, N., "Steady Laminar Forced Convection From a Cylinder at Low Reynolds Numbers," *Physics of Fluids*, Vol. 11, 1968, pp. 933–940.

17 Collis, D. C., and Williams, M. J., "Two-Dimensional Convection From Heated Wires at Low Reynolds Numbers," *Journal of Fluid Mechanics*, Vol. 6, 1959, pp. 357–384.

18 Bader, H. M., "A Theoretical Study of Laminar Mixed Convection From a Horizontal Cylinder in a Cross Stream," *International Journal of Heat and Mass Transfer*, Vol. 26, 1983, pp. 639–653.

19 Bergelin, O. P., Lexighton, M. D., Lafferty, W. L., and Pigford, R. L., "Heat Transfer and Pressure Drop During Viscous and Turbulent Flow Across Baffled and Unbaffled Tube Banks," University of Delaware, Engineering Experiment Station Bulletin No. 4, 1958.

Multidimensional Modeling of the Decay of Angular Momentum and Internal Energy in a Constant Volume Cylindrical Vessel

Q. C. Wang[1] and C. R. Ferguson[2]

Introduction

Heat loss and angular momentum decay in a constant volume cylindrical vessel is of interest because the flow has features similar to flows in internal combustion engines. The relationship of the ideal experiment to the more practical case is analogous to the relation between a flat plate and an airfoil.

A particularly noteworthy study is described by Dyer [1] wherein combustion is emphasized rather than heat transfer. The objective of his work, which is continuing at the Sandia National Laboratories in California, "is to provide a comprehensive set of simplified, well diagnosed experiments which can provide a critical validation of computer models." To this end he has measured the pressure and temperature, velocity and turbulence profiles in an unsteady, swirling flow bounded by a cylinder. Cloutman [2] input data at time zero as initial conditions to a computer program and the predicted evolution of velocity thereafter compared favorably with the measurements. As a study of heat transfer was not an explicit purpose of the research not all the data were presented nor were they analyzed to give the time-resolved heat loss from the flow.

We have extended the work of Cloutman [2] to realize not only a good match with the velocity field but also with the temperature field. The most important change we made was to change a constant employed in the law of the wall heat transfer analogy. Other differences include use of an improved subgrid scale turbulence model, extension of the time domain in the computations by a factor of two to more critically evaluate the model predictions, and a more comprehensive presentation and analysis of the computed results.

The KIVA code was developed at the Los Alamos National Laboratory for simulating two and three-dimensional flows in internal combustion engines [3]. In this note, we will discuss the methods used in KIVA only in terms of the user-specified constants. The governing equations and numerical methods used are discussed at length in the report by Amsden et al. [4].

Model Validation. The turbulence model used is a subgrid scale model which, unlike the KIVA code's predecessor CONCHAS, achieves closure with a transport equation for the turbulent kinetic energy q. The eddy viscosity ν_T is assumed to be

$$\nu_T = Aq^{1/2}L \tag{1}$$

where L is a characteristic length of the computational cell and

[1]Shanghai Marine Diesel Institute, China

[2]Purdue University, School of Mechanical Engineering, West Lafayette, IN 47907; correspondence should be addressed to this author.

Contributed by the Heat Transfer Division for publication in the JOURNAL OF HEAT TRANSFER. Manuscript recieved by the Heat Transfer Division May 24, 1985.

transfer in packed beds only in the range of voidage of 0.25 to 0.8 and at low Reynolds numbers [13, 14]. Similar restrictions may also be applicable to the tube bundles at crossflow. When the voidage is higher than 0.8 the prediction of creeping flow will deviate from the real situation seriously at $1 < \mathrm{Re}_d < 200$. The miscounted inertial effects in the wide opened space between tubes becomes significant. To illustrate this restriction, the heat transfer data of single tubes [8, 16, 18] are plotted in Fig. 5. The prediction of the present correlation in equation (25) gives good agreement when the pitch-to-diameter ratio is set at 2.0. When p/d is 2.0, the voidage is 0.8 in the bundle, and the fluid flow and heat transfer are very close to those of a single tube in infinite space. Therefore, as shown in Fig. 4, the present prediction will be suitable for $\beta^2 < 5.1$ (or $p/d < 2.0$). Beyond this, the prediction will come from setting $\beta^2 = 5.1$ in equation (25). Thus

$$\overline{\mathrm{Nu}}_d = 0.91 \mathrm{Re}_d^{0.6} \mathrm{Pr}^{1/3} (\mu_b/\mu_w)^{0.14} \tag{27}$$

for $\mathrm{Re}_d < 200$ and $p/d > 2.0$. This equation fits the data of single tubes within ± 30 percent.

Conclusions

At very low Reynolds numbers, the flow field can be approximated by the free surface model, together with a creeping flow approximation. Under conditions of high Peclet number, the average Nusselt number on a tube in a bundle is derived. Compared with the existing heat transfer data in the range of $\mathrm{Re}_d < 200$ and pitch-to-diameter ratios less than 2.0, a slightly modified correlation as shown in equation (25) is proposed which fits the data within ± 30 percent. For bundles with $p/d > 2.0$ and at $\mathrm{Re}_d < 200$, the heat transfer on a tube in a bundle is similar to the heat transfer of a single tube in an infinite pool. Therefore, the correlation in equation (27) is proposed which also fits the data within ± 30 percent.

References

1 Gnielinski, V., Zukauskas, A., and Skrinska, A., "Banks of Plain and Finned Tubes," in: *Heat Exchanger Design Handbook*, E. U. Schlunder, editor-in-chief, Section 2.5.3, Hemisphere, Washington, D.C., 1983.

2 Omohundro, G. A., Bergelin, O. P., and Colburn, A. P., "Heat Transfer and Fluid Friction During Viscous Flow Across Banks of Tubes," *Trans. ASME*, Vol. 71, 1949, pp. 27–34.

3 Bergelin, O. P., Colburn, A. P., and Hull, H. C., "Heat Transfer and Fluid Friction During Flow Across Banks of Tubes," University of Delaware, Engineering Experiment Station Bulletin No. 2, 1950.

4 Bergelin, O. P., Davis, E. S., and Hull, H. C., "A Study of Three Tube Arrangements in Unbaffled Tubular Heat Exchangers," *Trans. ASME*, Vol. 71, 1949, pp. 367–374.

5 Pierson, O. L., "Experimental Investigation of the Influence of Tube Arrangement on Convection Heat Transfer and Flow Resistance in Cross Flow of Gases Over Tube Banks," *Trans. ASME*, Vol. 59, 1937, pp. 563–572.

6 Bergelin, O. P., Brown, G. A., Hull, H. C., and Sullivan, F. W., "Heat Transfer and Fluid Friction During Viscous Flow Across Banks of Tubes," *Trans. ASME*, Vol. 72, 1950, pp. 881–888.

7 Kays, W., and London, A. L., *Compact Heat Exchanger*, 3rd ed., McGraw-Hill, New York, 1984.

8 Zukauskas, A., "Heat Transfer From Tubes in Crossflow," *Advances in Heat Transfer*, J. P. Hartnett and T. F. Irvine, Jr., eds., Academic Press, New York, 1972, Vol. 8, pp. 93–160.

9 Polley, G. T., Ralston, T., and Grand, J. D. R., "Forced Crossflow Boiling in an In-Line Tube Bundle," ASME Paper No. 80-HT-46.

10 Snyder, N. W., "Heat Transfer in Air from a Single Tube in a Staggered Tube Bank," *AIChE Symposium Series*, Vol. 49, No. 5, 1953, pp. 11–20.

11 McAdams, W. H., *Heat Transmission*, 3rd ed., McGraw-Hill, New York, 1954.

12 Whitaker, S., "Forced Convection Heat Transfer Correlation for Flow in Pipes, Past Flat Plates, Single Cylinders, Single Spheres, and Flow in Packed Beds and Tube Bundles," *AIChE Journal*, Vol. 18, 1972, pp. 361–371.

13 Happel, J., "Viscous Flow Relative to Arrays of Cylinders," *AIChE Journal*, Vol. 5, 1959, pp. 174–177.

14 Pfeffer, R., "Heat and Mass Transfer in Multiparticle System," *Industrial and Engineering Chemistry Fundamentals*, Vol. 3, 1964, pp. 380–383.

15 Hansen, A. G., "Generalized Similarity Analysis of Partial Differential Equations," *Nonlinear Partial Differential Equations*, W. F. Ames, ed., Academic Press, New York, 1967, pp. 1–17.

16 Dennis, S. C. R., Hudson, J. D., and Smith, N., "Steady Laminar Forced Convection From a Cylinder at Low Reynolds Numbers," *Physics of Fluids*, Vol. 11, 1968, pp. 933–940.

17 Collis, D. C., and Williams, M. J., "Two-Dimensional Convection From Heated Wires at Low Reynolds Numbers," *Journal of Fluid Mechanics*, Vol. 6, 1959, pp. 357–384.

18 Bader, H. M., "A Theoretical Study of Laminar Mixed Convection From a Horizontal Cylinder in a Cross Stream," *International Journal of Heat and Mass Transfer*, Vol. 26, 1983, pp. 639–653.

19 Bergelin, O. P., Lexighton, M. D., Lafferty, W. L., and Pigford, R. L., "Heat Transfer and Pressure Drop During Viscous and Turbulent Flow Across Baffled and Unbaffled Tube Banks," University of Delaware, Engineering Experiment Station Bulletin No. 4, 1958.

Multidimensional Modeling of the Decay of Angular Momentum and Internal Energy in a Constant Volume Cylindrical Vessel

Q. C. Wang[1] and C. R. Ferguson[2]

Introduction

Heat loss and angular momentum decay in a constant volume cylindrical vessel is of interest because the flow has features similar to flows in internal combustion engines. The relationship of the ideal experiment to the more practical case is analogous to the relation between a flat plate and an airfoil.

A particularly noteworthy study is described by Dyer [1] wherein combustion is emphasized rather than heat transfer. The objective of his work, which is continuing at the Sandia National Laboratories in California, "is to provide a comprehensive set of simplified, well diagnosed experiments which can provide a critical validation of computer models." To this end he has measured the pressure and temperature, velocity and turbulence profiles in an unsteady, swirling flow bounded by a cylinder. Cloutman [2] input data at time zero as initial conditions to a computer program and the predicted evolution of velocity thereafter compared favorably with the measurements. As a study of heat transfer was not an explicit purpose of the research not all the data were presented nor were they analyzed to give the time-resolved heat loss from the flow.

We have extended the work of Cloutman [2] to realize not only a good match with the velocity field but also with the temperature field. The most important change we made was to change a constant employed in the law of the wall heat transfer analogy. Other differences include use of an improved subgrid scale turbulence model, extension of the time domain in the computations by a factor of two to more critically evaluate the model predictions, and a more comprehensive presentation and analysis of the computed results.

The KIVA code was developed at the Los Alamos National Laboratory for simulating two and three-dimensional flows in internal combustion engines [3]. In this note, we will discuss the methods used in KIVA only in terms of the user-specified constants. The governing equations and numerical methods used are discussed at length in the report by Amsden et al. [4].

Model Validation. The turbulence model used is a subgrid scale model which, unlike the KIVA code's predecessor CONCHAS, achieves closure with a transport equation for the turbulent kinetic energy q. The eddy viscosity ν_T is assumed to be

$$\nu_T = Aq^{1/2}L \tag{1}$$

where L is a characteristic length of the computational cell and

[1]Shanghai Marine Diesel Institute, China

[2]Purdue University, School of Mechanical Engineering, West Lafayette, IN 47907; correspondence should be addressed to this author.

Contributed by the Heat Transfer Division for publication in the JOURNAL OF HEAT TRANSFER. Manuscript recieved by the Heat Transfer Division May 24, 1985.

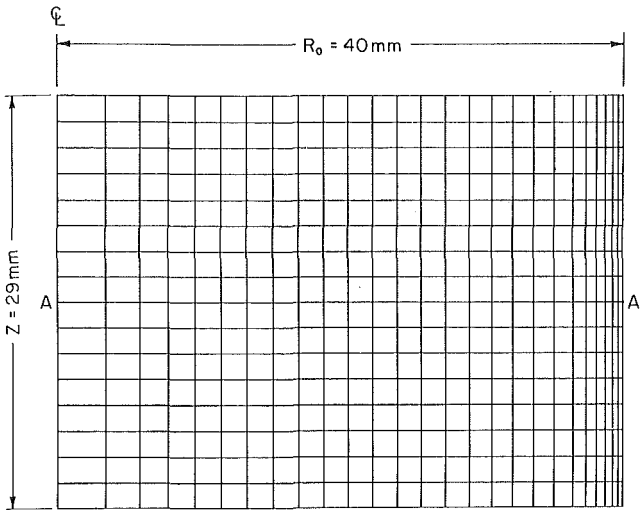

Fig. 1 Computation grid used to model swirling flow in a right circular cylinder. While the modeling could have assumed symmetry about the line A-A, a full solution was obtained to verify that solution was in fact symmetric.

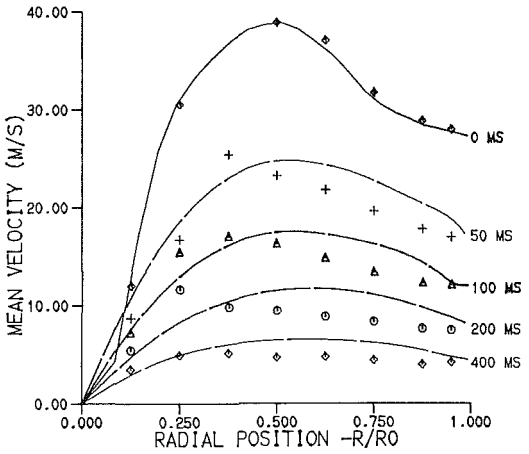

Fig. 2 Measured and computed swirl velocity at the midplane. The experimental data in this and all subsequent plots are from Dyer [1].

A is a constant that should be 0.05 if the model in the steady state is to reduce to the algebraic model described by Deardorff [5]. In our case the algorithm used for L reduces to $L = 2\Delta Z$. We found that to match the decaying swirl velocity as measured by Dyer [1] required that $A = 0.08$.

The boundary conditions employed are a modified law of the wall treatment wherein a velocity profile is assumed between the wall and the first vertex. Matching that profile to the tangential velocity (relative to the wall at that point) fixes the shear stress which is then imposed as the boundary condition. The thermal boundary layer is accounted for in a similar way. For more detail and treatment of kinetic energy dissipation by the wall the reader is referred to the report by Amsden et al. [4].

Figure 1 shows the two-dimensional grid we used. It was discovered that for a stable solution near the wall a finer grid was needed. However, in the KIVA code truncation errors will result from the interpolations used in differencing when a nonuniform grid is employed [6]; to minimize such errors the grid is not changed suddenly but is, instead, changed gradually.

The swirl velocity as a function of radius is shown in Fig. 2. The symbols denote experimental data of Dyer [1] and the solid curves are the computed results. There is perfect agreement between the data and the computation at time zero as the data were used for initial conditions. There is a slight

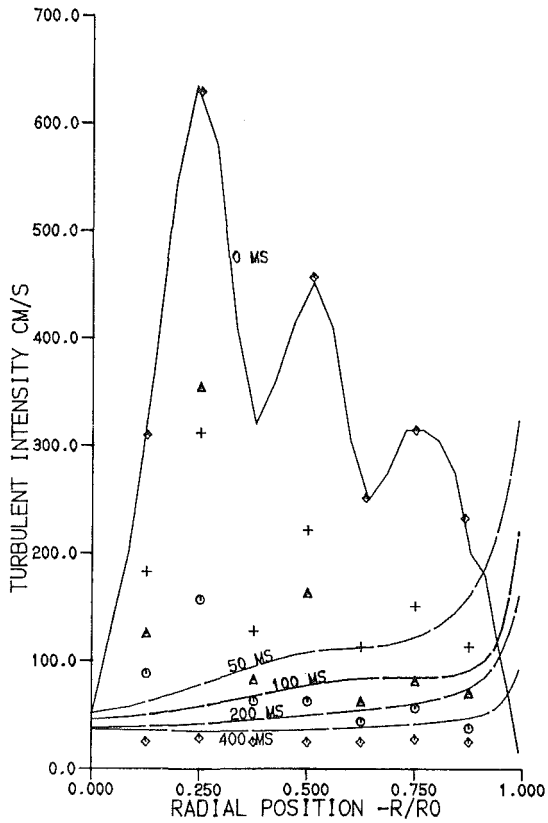

Fig. 3 Measured and computed turbulence at the midplane

discrepancy in the shape of the curves. The experimental data suggest the maximum velocity occus at radial locations near $R/R_0 = 3/8$ and moves slightly inward as time progresses. The computed maximum is closer to $R/R_0 = 1/2$ and the curve is flatter in its vicinity than was the experimental data in the vicinity of its maximum.

The calculation predicts no axial variation in the swirl velocity. The experimental half-radius velocity is decaying faster than the model predicts. Indeed we feel that choosing $A = 0.09$ might yield better results. The fitting of constants proved to be an expensive proposition so we did not get to try $A = 0.09$.

The radial distribution in the turbulent intensity at the midplane is shown in Fig. 3. We assumed at time zero that all of the turbulent kinetic energy was confined to scales smaller than the grid. The agreement between the experimental data and the calculated results is as good as can be hoped for. The turbulence can neither be measured nor calculated with the same precision as the mean flow. One conclusion that can be drawn from the calculation is that the turbulence quickly relaxes to a quasi-steady state and that at time zero it was probably in a quasi-steady state. The sudden change calculated between time zero and 50 ms later is an artifice due to the fact that had the calculation been able to start any earlier in the process it would have been predicting lower values at time zero.

To check the assumption that all the turbulence is confined to scales within the grid we plotted the calculated half-radius velocity as a function of time. The curve is smooth showing that the calculation is resolving none of the turbulence; therefore the comparison made in Fig. 3 is a fair one.

Before discussing the temperature field a comment on the initial conditions is in order. The experimental data set used did not include measurements of the radial or the axial velocities and they were assumed zero in the initial conditions. Approximately 2 ms later a small radial flow had established itself in the computations. The axial temperature distribution

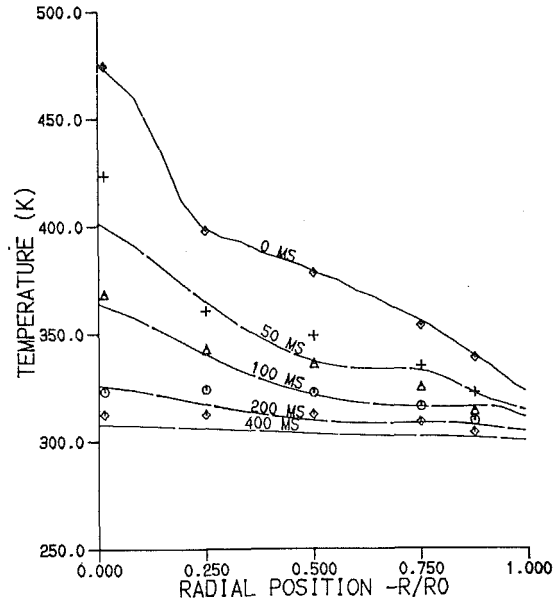

Fig. 4 Measured and computed gas temperature at the midplane

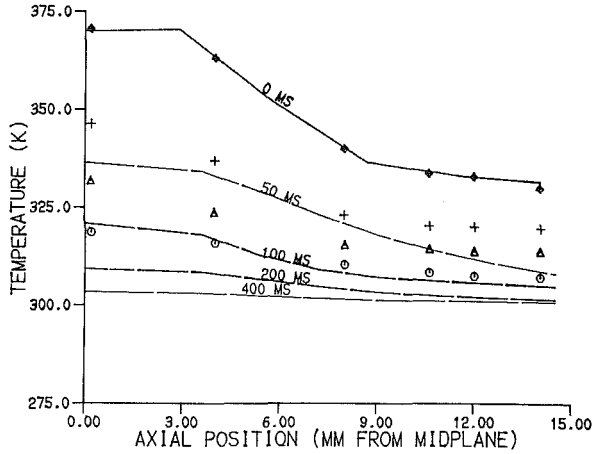

Fig. 5 Measured and computed gas temperature at the half-radius point

at time zero was assumed independent of radial position. Due to experimental error and incomplete knowledge of the initial state, the initial conditions actually used do not necessarily satisfy all the conservation equations. As a result the calculation has to be started with a very small time step to be stable. Using an interpolated donor cell differencing scheme (AO = 0.0, BO = 1.0 in the KIVA code) we had to cut the stability criterion on the time step by an order of magnitude (DTFC = 0.008 instead of DTFC = 0.10). As time progressed this could be relaxed and once 20 ms had elapsed the criterion was back to normal.

The temperature field is shown in Figs. 4 and 5. These results are for a turbulent Prandtl number of $\mathrm{Pr}_T = 0.9$ but with a multiplying constant in the boundary layer model changed from 1.125 to 3.0. Our boundary condition for the heat flux is then

$$J_w = 3.0\left(\frac{\tau}{U}\right)c_p(T - T_w) \tag{2}$$

where T is the temperature at the first grid point, τ is the wall shear stress, and U is the tangential gas speed at the location of T.

Implicit in equation (2) is the Reynolds analogy between heat and momentum transfer. It is only as valid as the boundary layer equations which require that the Prandtl number be of order unity and the pressure gradient be small. The modification proposed is attributed to the approximate nature of the analogy in this flow although we cannot dismiss the possibility that we may not have achieved a grid independent solution and it is accounting for this fact.

The heat transfer modeling needs more work. Diwakar [7] varied the turbulent Prandtl number to force agreement between measured and computed heat losses. Unfortunately he had to use a different value depending upon whether or not the flow was reacting. In our case we chose to modify a constant in the wall expression although we may have been able to effect an equally viable agreement by lowering the turbulent Prandtl number. A more critical experiment is needed wherein not only the flow parameters reported here are measured but also the heat flux distribution on the walls.

Global Correlations. As this is a constant volume system, the energy decay is due solely to heat loss $\dot{Q}_l$. Neglecting kinetic energy, we can write

$$\frac{dE}{dt} = -\dot{Q}_l \tag{3}$$

The pressure in the bomb is nearly uniform, which allows us to define at any time a mass average temperature according to

$$PV = mR\bar{T} \tag{4}$$

Using that mass-averaged temperature to define a heat transfer coefficient by

$$\dot{Q}_l = hA(\bar{T} - T_w) \tag{5}$$

we scaled the calculated results dimensionlessly to look for a correlation between the total instantaneous Nusselt number and a Reynolds number. In terms of a characteristic length and velocity defined by

$$l = V/A \tag{6}$$

$$U = U(r, z)\,|_{\substack{z=0 \\ r=R_0/2}} \tag{7}$$

we found that

$$\mathrm{Nu} = 0.54\mathrm{Re}^{0.5} \tag{8}$$

correlated the results very well. In this correlation all gas properties are evaluated at the mass-averaged temperature.

We also correlated the angular momentum Ω and kinetic energy KE of the flow and found

$$\frac{l/U}{\Omega}\frac{d\Omega}{dt} = 0.034\mathrm{Re}^{-0.3} \tag{9}$$

$$\frac{l/U}{KE}\frac{dKE}{dt} = 4.3\mathrm{Re}^{-0.6} \tag{10}$$

The exponents in these correlations are valid only within about ± 0.1. Further we believe the exponent on the Reynolds number is biased slightly low and the Nusselt numbers are slightly high due to our not optimizing the user constants but only getting them close. We observed in the baseline calculations a slope slightly greater than one. Had we used 2.7 instead of 3 in equation (2) and $A = 0.09$ in equation (1) the exponent would be closer to 0.7 and the other exponents would hardly change. A value of 0.7 would be consistent with a prediction based on equation (9) and employment of the Reynolds' analogy which in this case would be

$$\mathrm{Nu} = c\mathrm{Re}\,\frac{l/U}{\Omega}\frac{d\Omega}{dt} \tag{11}$$

where c is a constant which includes the Prandtl number and is essentially the constant adjusted in equation (2).

Finally, with respect to these exponents, if both the velocities characterizing angular momentum and kinetic energy each scaled perfectly linearly with the half-radius velocity, then the exponents in equations (9) and (10) on the

Reynolds number should be equal. That they are not is partly error and partly due to less-than-perfect correlation with the half-radius velocity.

Acknowledgments

Professor Ferguson was supported by the U.S. Department of Energy through its Engine Combustion Technology Program administered by the Sandia National Laboratories. Q. C. Wang was supported by the Chinese Educational Ministry as a visiting scholar at Purdue University. Computing Services on a CYBER-205 were provided by Purdue University. We are grateful to John Ramshaw and Anthony Amsden at the Los Alamos National Laboratory for providing us with the KIVA code as well as guidance in its use.

References

1 Dyer, T. M., "Characterization of One and Two-Dimensional Homogeneous Combustion Phenomena in a Constant Volume Bomb," SAE Paper No. 790353, Vol. 88, 1979, pp. 1196–1216.

2 Cloutman, L., "Numerical Simulation of Turbulent Reacting Flows," *International Conference Series on Advances in Numerical Methods in Engineering: Theory and Applications* (NUMETA 85), Swansea, United Kingdom, 1985.

3 Butler, T. D., Amsden, A. A., O'Rourke, P. J., and Ramshaw, J. D., "KIVA: A Comprehensive Model for 2-D and 3-D Engine Simulations," SAE Paper No. 850554, 1985.

4 Amsden, A. A., Ramshaw, J. D., O'Rourke, P. J., and Dukowicz, J. K., "KIVA: A Computer Program for Two-Dimensional and Three-Dimensional Fluid Flows With Chemical Reaction and Fuel Sprays," Los Alamos Report, 1984.

5 Deardorff, J. W., "On the Magnitude of the Subgrid Scale Eddy Coefficient," *J. Computer Physics*, Vol. 7, 1971, pp. 120–133.

6 Ramshaw, J. D., private communication, 1984.

7 Diwakar, R., "Assessment of the Ability of a Multidimensional Computer Code to Model Combustion in a Homogeneous-Charge Engine," SAE Paper No. 840230, 1984.

Heat Transfer From Circular Tubes in a Semi-infinite Medium

R. V. Arimilli,[1,2] M. Parang,[1,2] and P. R. Surapaneni[1,3]

Introduction

The use of buried utility lines for mass or energy transport is commonly encountered in various applications such as heat transfer from ground-coupled heat exchanger tubes [1], buried electrical power cables, and buried pipelines for the transportation of fluids involving thermal effects.

Boundary integral methods have been applied very successfully to problems governed by the Laplace equation. From an engineering point of view, in many problems only the solution on the boundary is of interest. The boundary integral method is well suited for such problems. For problems with circular interior boundaries, Barone and Caulk [2] have developed a special method in which the integrals around the circular boundaries were evaluated analytically. Using that method Arimilli and Parang [1] solved the problem of two parallel underground tubes each at the same constant surface temperature with convective boundary conditions at the surface of the half space.

In this note the results of a two-dimensional analysis based on the method of Barone and Caulk [2] are presented for steady heat transfer from a set of parallel tubes of arbitrary diameters and positions, located in a semi-infinite medium of uniform thermal conductivity k. Each of the tubes is considered to be at a uniform surface temperature, and the plane surface is assumed to be exposed to a specified uniform convective condition. At the far field, temperature in the semi-infinite medium is uniform and equal to the temperature of the convective medium T_a. The general nature of this analysis makes it applicable to many problems of this type.

In this method, the outward normal derivative of temperature q around each αth hole is expanded in the following harmonic-series form involving zeroth- and first-order terms

$$q^\alpha = q_0^\alpha + q_1^\alpha \sin\theta^\alpha + q_2^\alpha \cos\theta^\alpha$$

where

$$q_0^\alpha = \frac{Q_0^\alpha \; a_R}{2\pi \; a_\alpha \; k(T_R - T_a)}$$

Here q is dimensionless, Q_0^α is the rate of heat transfer per unit length from around the αth tube of radius a_α, T_R is the temperature of the reference tube surface, and a_R is the radius of the reference tube. The details of this formulation and the general computer program developed for the analysis may be found in [3].

Results and Discussion

The accuracy of the method is established by a comparison of the heat transfer results from the present analysis with those of the exact solution for the problem of a single tube in a semi-infinite medium with its plane surface maintained at a uniform temperature. In the analysis a Biot number (Bi = ha_R/k) of 10^5 is used in order to change the plane surface condition from convection to an effectively constant temperature case. The solution temperature distribution on the plane surface and the tube heat transfer were each found to be within one percent of the exact solution.

Three problems of interest were solved numerically using the present method. The first problem considered and solved is the problem of heat transfer from an array of n horizontal, equal-diameter tubes located at a depth D below the convection boundary. All the tubes are assumed for simplicity to have identical constant temperature T_R and equal spacing $2s$.

Figures 1 and 2 represent the zeroth order (q_{0s}) and first order (q_{1s}) solution of the normal derivative of temperature at tube surface for a single tube case ($n=1$). The second coefficient of expansion q_{2s} is identically zero for the $n=1$ case due to vertical symmetry in the problem. The results for q_{0s} and q_{1s} are plotted as a function of Biot number and depth D/a. It is observed that, in general, both q_0 and q_1 decrease with decreasing Biot number and increasing depth. The values of q_{0s} are at least one order of magnitude higher than those of q_{1s}. It is also observed that changes in heat transfer at the convection boundary have progressively smaller effects with increasing depth as expected.

Figure 3 shows the results for q_0 for the $n=1$ through $n=8$ tubes. In all these cases, Bi = 0.5 and $2s/a$ = 5.0 were taken as typical values encountered in buried heat exchanger tubes. Also the sum of q_0 for n tubes in each case is normalized with respect to n times the heat transfer from a single tube at the same conditions (nq_{0s}). These normalized values of total q_0 are presented as a function of D/a. The results show the same qualitative behavior as the single-tube case. However, it is clearly observed that increasing the number of tubes gives a progressively decreasing value for the normalized q_0 which is to be expected since the middle tubes in an array have a significantly lower heat transfer rate than the tubes located at the outer regions of the array. The q_1 and q_2 results may be found in [3, 4].

The second problem was chosen to illustrate the effect of variation of tube diameter on heat transfer rates. The two sub-

[1]Mechanical and Aerospace Engineering Department, The University of Tennessee, Knoxville, TN 37996-2210.

[2]Associate Professor.

[3]Graduate Student.

Contributed by the Heat Transfer Division for publication in the JOURNAL OF HEAT TRANSFER. Manuscript received by the Heat Transfer Division July 23, 1984.

Reynolds number should be equal. That they are not is partly error and partly due to less-than-perfect correlation with the half-radius velocity.

Acknowledgments

Professor Ferguson was supported by the U.S. Department of Energy through its Engine Combustion Technology Program administered by the Sandia National Laboratories. Q. C. Wang was supported by the Chinese Educational Ministry as a visiting scholar at Purdue University. Computing Services on a CYBER-205 were provided by Purdue University. We are grateful to John Ramshaw and Anthony Amsden at the Los Alamos National Laboratory for providing us with the KIVA code as well as guidance in its use.

References

1 Dyer, T. M., "Characterization of One and Two-Dimensional Homogeneous Combustion Phenomena in a Constant Volume Bomb," SAE Paper No. 790353, Vol. 88, 1979, pp. 1196–1216.

2 Cloutman, L., "Numerical Simulation of Turbulent Reacting Flows," *International Conference Series on Advances in Numerical Methods in Engineering: Theory and Applications* (NUMETA 85), Swansea, United Kingdom, 1985.

3 Butler, T. D., Amsden, A. A., O'Rourke, P. J., and Ramshaw, J. D., "KIVA: A Comprehensive Model for 2-D and 3-D Engine Simulations," SAE Paper No. 850554, 1985.

4 Amsden, A. A., Ramshaw, J. D., O'Rourke, P. J., and Dukowicz, J. K., "KIVA: A Computer Program for Two-Dimensional and Three-Dimensional Fluid Flows With Chemical Reaction and Fuel Sprays," Los Alamos Report, 1984.

5 Deardorff, J. W., "On the Magnitude of the Subgrid Scale Eddy Coefficient," *J. Computer Physics*, Vol. 7, 1971, pp. 120–133.

6 Ramshaw, J. D., private communication, 1984.

7 Diwakar, R., "Assessment of the Ability of a Multidimensional Computer Code to Model Combustion in a Homogeneous-Charge Engine," SAE Paper No. 840230, 1984.

Heat Transfer From Circular Tubes in a Semi-infinite Medium

R. V. Arimilli,[1,2] M. Parang,[1,2] and P. R. Surapaneni[1,3]

Introduction

The use of buried utility lines for mass or energy transport is commonly encountered in various applications such as heat transfer from ground-coupled heat exchanger tubes [1], buried electrical power cables, and buried pipelines for the transportation of fluids involving thermal effects.

Boundary integral methods have been applied very successfully to problems governed by the Laplace equation. From an engineering point of view, in many problems only the solution on the boundary is of interest. The boundary integral method is well suited for such problems. For problems with circular interior boundaries, Barone and Caulk [2] have developed a special method in which the integrals around the circular boundaries were evaluated analytically. Using that method Arimilli and Parang [1] solved the problem of two parallel underground tubes each at the same constant surface temperature with convective boundary conditions at the surface of the half space.

In this note the results of a two-dimensional analysis based on the method of Barone and Caulk [2] are presented for steady heat transfer from a set of parallel tubes of arbitrary diameters and positions, located in a semi-infinite medium of uniform thermal conductivity k. Each of the tubes is considered to be at a uniform surface temperature, and the plane surface is assumed to be exposed to a specified uniform convective condition. At the far field, temperature in the semi-infinite medium is uniform and equal to the temperature of the convective medium T_a. The general nature of this analysis makes it applicable to many problems of this type.

In this method, the outward normal derivative of temperature q around each αth hole is expanded in the following harmonic-series form involving zeroth- and first-order terms

$$q^\alpha = q_0^\alpha + q_1^\alpha \sin\theta^\alpha + q_2^\alpha \cos\theta^\alpha$$

where

$$q_0^\alpha = \frac{Q_0^\alpha \; a_R}{2\pi \; a_\alpha \; k(T_R - T_a)}$$

Here q is dimensionless, Q_0^α is the rate of heat transfer per unit length from around the αth tube of radius a_α, T_R is the temperature of the reference tube surface, and a_R is the radius of the reference tube. The details of this formulation and the general computer program developed for the analysis may be found in [3].

Results and Discussion

The accuracy of the method is established by a comparison of the heat transfer results from the present analysis with those of the exact solution for the problem of a single tube in a semi-infinite medium with its plane surface maintained at a uniform temperature. In the analysis a Biot number (Bi = ha_R/k) of 10^5 is used in order to change the plane surface condition from convection to an effectively constant temperature case. The solution temperature distribution on the plane surface and the tube heat transfer were each found to be within one percent of the exact solution.

Three problems of interest were solved numerically using the present method. The first problem considered and solved is the problem of heat transfer from an array of n horizontal, equal-diameter tubes located at a depth D below the convection boundary. All the tubes are assumed for simplicity to have identical constant temperature T_R and equal spacing $2s$.

Figures 1 and 2 represent the zeroth order (q_{0s}) and first order (q_{1s}) solution of the normal derivative of temperature at tube surface for a single tube case ($n=1$). The second coefficient of expansion q_{2s} is identically zero for the $n=1$ case due to vertical symmetry in the problem. The results for q_{0s} and q_{1s} are plotted as a function of Biot number and depth D/a. It is observed that, in general, both q_0 and q_1 decrease with decreasing Biot number and increasing depth. The values of q_{0s} are at least one order of magnitude higher than those of q_{1s}. It is also observed that changes in heat transfer at the convection boundary have progressively smaller effects with increasing depth as expected.

Figure 3 shows the results for q_0 for the $n=1$ through $n=8$ tubes. In all these cases, Bi = 0.5 and $2s/a$ = 5.0 were taken as typical values encountered in buried heat exchanger tubes. Also the sum of q_0 for n tubes in each case is normalized with respect to n times the heat transfer from a single tube at the same conditions (nq_{0s}). These normalized values of total q_0 are presented as a function of D/a. The results show the same qualitative behavior as the single-tube case. However, it is clearly observed that increasing the number of tubes gives a progressively decreasing value for the normalized q_0 which is to be expected since the middle tubes in an array have a significantly lower heat transfer rate than the tubes located at the outer regions of the array. The q_1 and q_2 results may be found in [3, 4].

The second problem was chosen to illustrate the effect of variation of tube diameter on heat transfer rates. The two sub-

[1]Mechanical and Aerospace Engineering Department, The University of Tennessee, Knoxville, TN 37996-2210.

[2]Associate Professor.

[3]Graduate Student.

Contributed by the Heat Transfer Division for publication in the JOURNAL OF HEAT TRANSFER. Manuscript received by the Heat Transfer Division July 23, 1984.

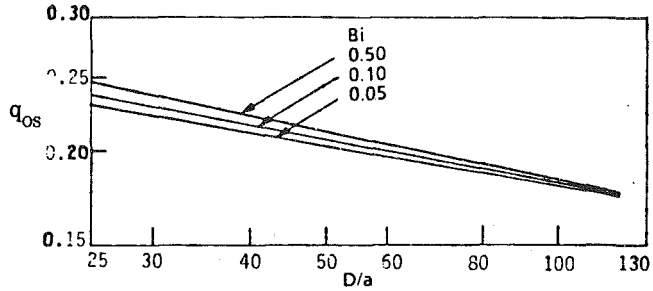

Fig. 1 Variation of q_0 with nondimensional depth at different Biot numbers for a single tube in a semi-infinite medium

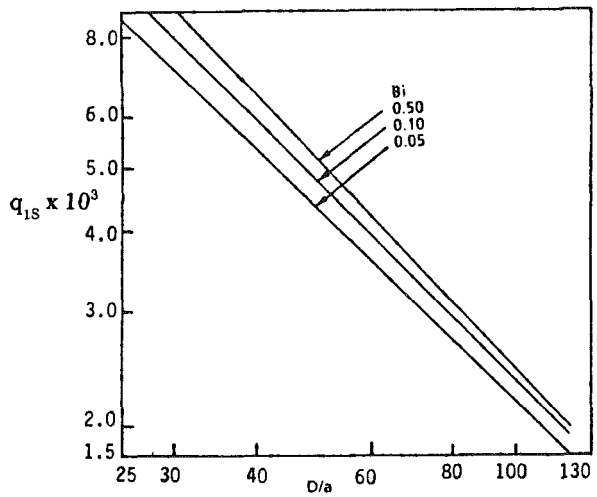

Fig. 2 Variation of q_1 with nondimensional depth at different Biot numbers for a single tube in a semi-infinite medium

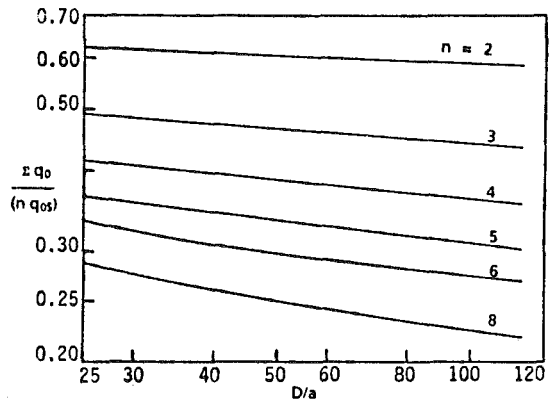

Fig. 3 Variation of normalized total value of q_0 with nondimensional depth for n uniformly spaced tubes in a row (Bi = 0.5, 2s/a = 5.0)

problems presented in Figs. 4(*a*) and 4(*b*) were considered. Here the total heat transfer rate from a set of four constant-diameter tubes as shown in Fig. 4(*a*) was compared to the total heat transfer rate from a set of four tubes illustrated in Fig. 4(*b*). The tube surface temperatures, spacing, and average depth in both cases are assumed equal, but the tube diameters are taken to be different in the two cases as shown. Here all length scales were nondimensionalized with respect to the tube radius in Fig. 4(*a*). The results for q_0, q_1, and q_2 are presented in Table 1 for tubes numbered 1, 3, 5, and 7. The symmetry condition can be readily used to obtain the values for tubes marked 2, 4, 6, and 8. The results indicate larger total values of q_0 in the arrangement of Fig. 4(*b*) relative to that in Fig. 4(*a*). However, it should be noted that the large values of q_0 (which is a nondimensional surface temperature gradient) at

Table 1 Results for q_0, q_1, and q_2, for various tubes in configurations shown in Figs. 4(a) and 4(*b*)

Tube No. α	Depth (D_{avg} / a_{max})	Diameter (a_α / a_{max})	q_0	q_1	q_2
1	50.0	1.0	0.1099	0.0137	0.0291
3	100.0	1.0	0.0831	-0.0033	0.0223
5	33.33	0.33	0.2649	0.0192	0.0353
7	66.67	1.0	0.0804	-0.0032	0.0313

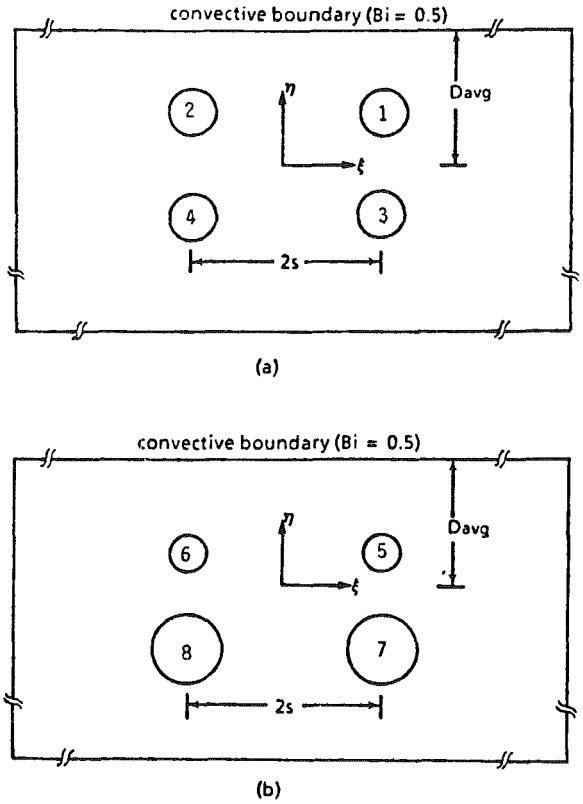

Fig. 4 Sketch of the problems considered (for comparative evaluation of q_0, q_1, and q_2 for two tube arrangements) are shown in (*a*) with $2s/a_{max} = 7.5$, and $a_1 = a_2 = a_3 = a_4 = a_{max} = a$ and in (*b*) with $2s/a_{max} = 5$, $a_7 = a_8 = a_{max}$, and $a_5 = a_6 = a_{max}/3$

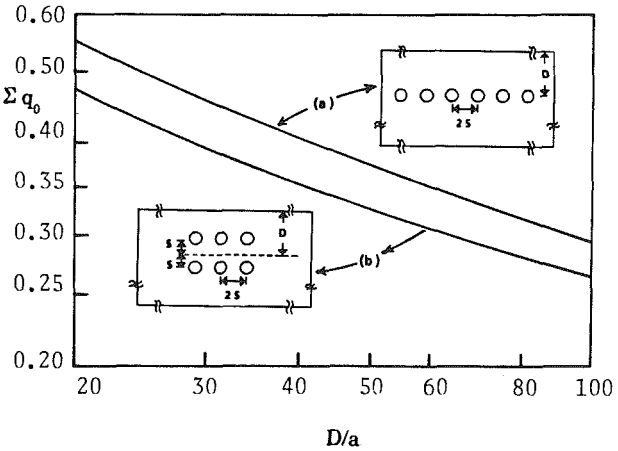

Fig. 5 Variation of total q_0 with nondimensional depth for configurations (a) and (*b*) shown (Bi = 0.5, 2s/a = 5.0)

tubes 5 and 6 do not imply higher heat transfer rates at these tubes since q_0 is scaled with tube diameters.

The third problem was selected to illustrate the effect of arrangement of tube arrays on the heat transfer rates. The problems shown in the insets of Fig. 5 were considered. Here all tubes were assumed to have same diameter, surface temperature, and spacing. However, the total heat transfer rate of a horizontal array of six tubes (inset *a*) was compared to that of two arrays of three tubes (inset *b*). The average depth in the second case (*b*) was kept the same as the depth of the single array case (*a*). The results for total values of q_0 are presented as a function of nondimensional depth D/a in Fig. 5. The results clearly indicate the advantage of single array arrangement at all depths in maximizing total heat transfer rates (approximately 10 percent increase in total heat transfer rates). It is also observed that increasing depth results in lower heat transfer rates. This trend is consistent with the results obtained for all other tube configurations discussed in this note, as well as those reported in [3].

Conclusions

A numerical model based on the boundary integral method was used for the analysis of steady-state, two-dimensional conduction heat transfer from isothermal, circular tubes in a semi-infinite medium. Using a model problem with a known closed-form solution, the error of the numerical model was found to be less than one percent. The high accuracy of the results and the efficiency associated with the boundary integral method makes the model presented a highly useful tool in solving the class of problems discussed.

References

1 Arimilli, R. V., and Parang, M., "Numerical Analysis of Heat Transfer in Buried Horizontal Heat Exchanger Tubes," *AIChE Symposium Series 225*, Vol. 79, 1983, pp. 121–129.

2 Barone, M. R., and Caulk, D. A., "Special Boundary Integral Equations for Approximate Solution of Laplace's Equation in Two-Dimensional Regions With Circular Holes," *The Quarterly Journal of Mechanics and Applied Mathematics*, Vol. XXXIV, Pt. 3, 1981, pp. 265–286.

3 Surapaneni, P. R., "Numerical Boundary Integral Analysis of Heat Transfer From Circular Tubes in a Semi-infinite Medium," M. S. Thesis, University of Tennessee, Knoxville, TN, 1985.

4 Arimilli, R. V., Parang, M., and Surapaneni, P. R., "Numerical Boundary Integral Analysis of Heat Transfer From Circular Tubes in a Semi-infinite Medium," *Heat Transfer in Heat Rejection Systems*, HTD-Vol. 37, ASME, 1984, pp. 65–71.

A Reappraisal of Measurement Errors Arising From the Use of a Thermal Conductivity Probe

H. R. Thomas[1] and J. Ewen[2]

Introduction

Experimental determination of the thermal conductivity of soil is required for the design of a number of engineering schemes. Of the various methods available the thermal conductivity probe has established itself as one of the most widely used techniques. It offers the user the advantage of rapid determination of the soil's property, both in the laboratory and in the field.

The mode of operation of the probe is related to the theoretical basis upon which the results are analyzed. As the probe is heated, the rate at which the temperature of the probe rises is a function, among other factors, of the thermal conductivity of the soil. A theoretical solution to the problem has been given by Blackwell [1] who showed that at sufficiently long periods of time the temperature response of the probe will be linear, when plotted as a function of natural logarithm of time. This fact is used to advantage in the operation of the test, the analysis of the collected data being delayed until this linearity condition is achieved.

Real probes differ from theoretical solutions in that a number of sources of error can arise. These include, for example, fluctuations in the power source [2], edge effects because the sample being tested is too small [3], deviations from radial flow because the length of the probe [4] is too small, and moisture migration effects [5]. Notwithstanding the potential importance of all these sources a further error can arise if temperature measurements take place before the linearity condition is achieved. This is an error related to purely theoretical considerations and in order to limit the overall error in the final measurement is it clearly necessary to ensure that the operation of the probe in practice matches the theoretical basis as closely as possible.

The purpose of this technical note is to examine the importance of this error and to show the relationship between measurement time and error levels. An analysis of the same problem has previously been given by Hartley and Black [6]. Guidelines were given as to the minimum required measurement time. Unfortunately the analysis presented is in error and consequently the guidelines presented are incorrect. It is the purpose of this technical note to re-assess this problem and present new correct guidelines.

Analysis

Retaining the same nomenclature as used by Hartley and Black, Blackwell's solution for the long-time response of the probe can be written as

$$\theta(t)=\frac{Q}{4\pi k_2}\left\{\ln 4\mathrm{Fo}-\gamma+\frac{2}{\mathrm{Bi}}+\frac{1}{2\mathrm{Fo}}\right.$$

$$\left.\times\left[\ln 4\mathrm{Fo}-\gamma+1-\phi\left(\ln 4\mathrm{Fo}-\gamma+\frac{2}{\mathrm{Bi}}\right)\right]+0\left(\frac{1}{\mathrm{Fo}^2}\right)\right\} \quad (1)$$

where θ is the temperature rise of the probe above the ambient temprature of the soil, t is the time, k_2 is the thermal conductivity of the soil, Q is the rate of heat input to the probe per unit length of probe, and γ is Euler's constant, 0.5772.

It can be seen that the temperature response of the probe is a function of the variables, the Fourier number Fo, the Biot number Bi, and ϕ. These parameters are defined by

$$\mathrm{Fo}=\alpha_2 t/b^2 \quad (2)$$

$$\mathrm{Bi}=bh/k_2 \quad (3)$$

$$\phi=[(k_1\alpha_2/k_2\alpha_1)][1-(a/b)^2] \quad (4)$$

k_1 is the thermal conductivity of the probe material, α_1 and α_2 are the thermal diffusivities of the probe material and the soil, respectively, a and b are the inside and outside radii of the thermal probe, and h is the thermal conductance at the soil–probe interface. In physical terms this means that the temperature response is considered to be a function of the duration of the test, the probe/soil thermal contact resistance and the heat capacity of the probe relative to the heat capacity of the soil.

It can be seen that since equation (1) contains terms in inverse powers of Fo, at large values of Fo the expression degenerates to a linear relationship between $\theta(t)$ and ln Fo.

To evaluate the significance of the error if the linearity condition is not achieved, Hartley and Black differentiated equa-

[1]Lecturer, Department of Civil and Structural Engineering, University College Cardiff, Cardiff, Wales, United Kingdom.

[2]Research Assistant, Solar Energy Unit, Department of Mechanical Engineering and Energy Studies, University College Cardiff, Cardiff, Wales, United Kingdom.

Contributed by the Heat Transfer Division for publication in the JOURNAL OF HEAT TRANSFER. Manuscript received by the Heat Transfer Division September 3, 1985.

tubes 5 and 6 do not imply higher heat transfer rates at these tubes since q_0 is scaled with tube diameters.

The third problem was selected to illustrate the effect of arrangement of tube arrays on the heat transfer rates. The problems shown in the insets of Fig. 5 were considered. Here all tubes were assumed to have same diameter, surface temperature, and spacing. However, the total heat transfer rate of a horizontal array of six tubes (inset *a*) was compared to that of two arrays of three tubes (inset *b*). The average depth in the second case (*b*) was kept the same as the depth of the single array case (*a*). The results for total values of q_0 are presented as a function of nondimensional depth D/a in Fig. 5. The results clearly indicate the advantage of single array arrangement at all depths in maximizing total heat transfer rates (approximately 10 percent increase in total heat transfer rates). It is also observed that increasing depth results in lower heat transfer rates. This trend is consistent with the results obtained for all other tube configurations discussed in this note, as well as those reported in [3].

Conclusions

A numerical model based on the boundary integral method was used for the analysis of steady-state, two-dimensional conduction heat transfer from isothermal, circular tubes in a semi-infinite medium. Using a model problem with a known closed-form solution, the error of the numerical model was found to be less than one percent. The high accuracy of the results and the efficiency associated with the boundary integral method makes the model presented a highly useful tool in solving the class of problems discussed.

References

1 Arimilli, R. V., and Parang, M., "Numerical Analysis of Heat Transfer in Buried Horizontal Heat Exchanger Tubes," *AIChE Symposium Series 225*, Vol. 79, 1983, pp. 121–129.

2 Barone, M. R., and Caulk, D. A., "Special Boundary Integral Equations for Approximate Solution of Laplace's Equation in Two-Dimensional Regions With Circular Holes," *The Quarterly Journal of Mechanics and Applied Mathematics*, Vol. XXXIV, Pt. 3, 1981, pp. 265–286.

3 Surapaneni, P. R., "Numerical Boundary Integral Analysis of Heat Transfer From Circular Tubes in a Semi-infinite Medium," M. S. Thesis, University of Tennessee, Knoxville, TN, 1985.

4 Arimilli, R. V., Parang, M., and Surapaneni, P. R., "Numerical Boundary Integral Analysis of Heat Transfer From Circular Tubes in a Semi-infinite Medium," *Heat Transfer in Heat Rejection Systems*, HTD-Vol. 37, ASME, 1984, pp. 65–71.

A Reappraisal of Measurement Errors Arising From the Use of a Thermal Conductivity Probe

H. R. Thomas[1] and J. Ewen[2]

Introduction

Experimental determination of the thermal conductivity of soil is required for the design of a number of engineering schemes. Of the various methods available the thermal conductivity probe has established itself as one of the most widely used techniques. It offers the user the advantage of rapid determination of the soil's property, both in the laboratory and in the field.

[1]Lecturer, Department of Civil and Structural Engineering, University College Cardiff, Cardiff, Wales, United Kingdom.

[2]Research Assistant, Solar Energy Unit, Department of Mechanical Engineering and Energy Studies, University College Cardiff, Cardiff, Wales, United Kingdom.

Contributed by the Heat Transfer Division for publication in the JOURNAL OF HEAT TRANSFER. Manuscript received by the Heat Transfer Division September 3, 1985.

The mode of operation of the probe is related to the theoretical basis upon which the results are analyzed. As the probe is heated, the rate at which the temperature of the probe rises is a function, among other factors, of the thermal conductivity of the soil. A theoretical solution to the problem has been given by Blackwell [1] who showed that at sufficiently long periods of time the temperature response of the probe will be linear, when plotted as a function of natural logarithm of time. This fact is used to advantage in the operation of the test, the analysis of the collected data being delayed until this linearity condition is achieved.

Real probes differ from theoretical solutions in that a number of sources of error can arise. These include, for example, fluctuations in the power source [2], edge effects because the sample being tested is too small [3], deviations from radial flow because the length of the probe [4] is too small, and moisture migration effects [5]. Notwithstanding the potential importance of all these sources a further error can arise if temperature measurements take place before the linearity condition is achieved. This is an error related to purely theoretical considerations and in order to limit the overall error in the final measurement is it clearly necessary to ensure that the operation of the probe in practice matches the theoretical basis as closely as possible.

The purpose of this technical note is to examine the importance of this error and to show the relationship between measurement time and error levels. An analysis of the same problem has previously been given by Hartley and Black [6]. Guidelines were given as to the minimum required measurement time. Unfortunately the analysis presented is in error and consequently the guidelines presented are incorrect. It is the purpose of this technical note to re-assess this problem and present new correct guidelines.

Analysis

Retaining the same nomenclature as used by Hartley and Black, Blackwell's solution for the long-time response of the probe can be written as

$$\theta(t)=\frac{Q}{4\pi k_2}\left\{\ln 4\mathrm{Fo}-\gamma+\frac{2}{\mathrm{Bi}}+\frac{1}{2\mathrm{Fo}}\right.$$

$$\left.\times\left[\ln 4\mathrm{Fo}-\gamma+1-\phi\left(\ln 4\mathrm{Fo}-\gamma+\frac{2}{\mathrm{Bi}}\right)\right]+0\left(\frac{1}{\mathrm{Fo}^2}\right)\right\} \quad (1)$$

where θ is the temperature rise of the probe above the ambient temprature of the soil, t is the time, k_2 is the thermal conductivity of the soil, Q is the rate of heat input to the probe per unit length of probe, and γ is Euler's constant, 0.5772.

It can be seen that the temperature response of the probe is a function of the variables, the Fourier number Fo, the Biot number Bi, and ϕ. These parameters are defined by

$$\mathrm{Fo}=\alpha_2 t/b^2 \quad (2)$$

$$\mathrm{Bi}=bh/k_2 \quad (3)$$

$$\phi=[(k_1\alpha_2/k_2\alpha_1)][1-(a/b)^2] \quad (4)$$

k_1 is the thermal conductivity of the probe material, α_1 and α_2 are the thermal diffusivities of the probe material and the soil, respectively, a and b are the inside and outside radii of the thermal probe, and h is the thermal conductance at the soil–probe interface. In physical terms this means that the temperature response is considered to be a function of the duration of the test, the probe/soil thermal contact resistance and the heat capacity of the probe relative to the heat capacity of the soil.

It can be seen that since equation (1) contains terms in inverse powers of Fo, at large values of Fo the expression degenerates to a linear relationship between $\theta(t)$ and ln Fo.

To evaluate the significance of the error if the linearity condition is not achieved, Hartley and Black differentiated equa-

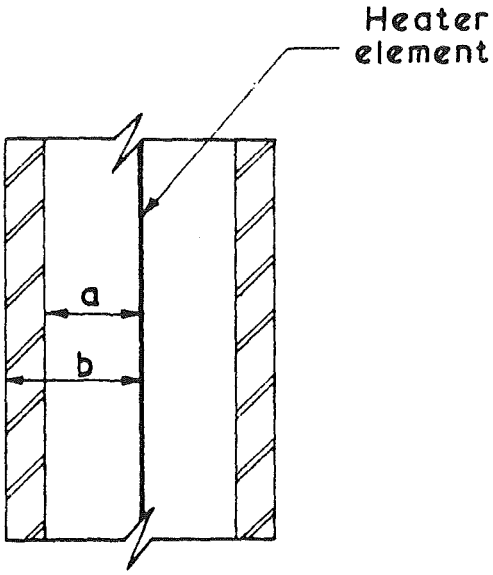

Fig. 1 Schematic of probe

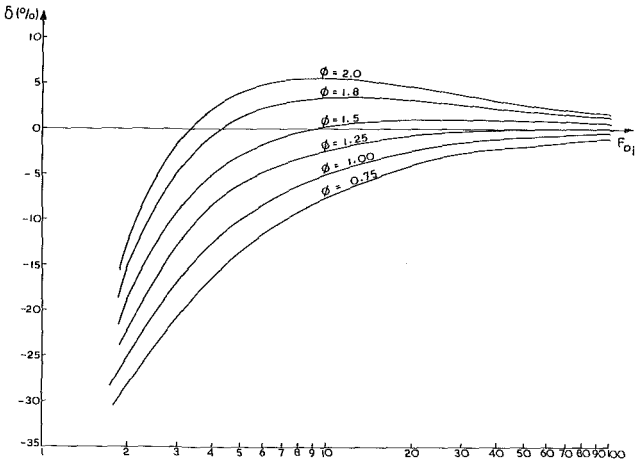

Fig. 2 Variation in the value of δ as a function of the initial Fourier number for various values of the probe design parameter ϕ, for the case of perfect thermal contact

tion (1) with respect to ln Fo. Following their procedure we obtain

$$\frac{d}{d\ln \mathrm{Fo}}\left(\frac{4\pi k_2\theta}{Q}\right) = 1 + \frac{1}{2\mathrm{Fo}}\left[(1-\phi)(\gamma - \ln 4\ \mathrm{Fo}) - \phi + \frac{2\phi}{\mathrm{Bi}}\right] \tag{5}$$

This differs from Hartley and Black's expression (their equation (8)). They appear to have differentiated equation (1) incorrectly and this represents the source of the error in their paper.

Rewriting (5) as

$$\frac{d}{d\ln \mathrm{Fo}}\left(\frac{4\pi k_2\theta}{Q}\right) = 1 + \delta \tag{6}$$

δ represents the fractional measurement error in $1/k_2$.

Hartley and Black present a set of curves showing the variation of δ as a function of Fo_i, the Fourier number at which initial readings are to be taken. The curves are in the main applicable to the case of perfect thermal contact between the probe and the soil, that is Bi = ∞. Various relationships are presented for various values of ϕ. These have been reworked using the correct expression (5) to produce the curves shown in Fig. 2.

It can be seen that the value of the error varies considerably

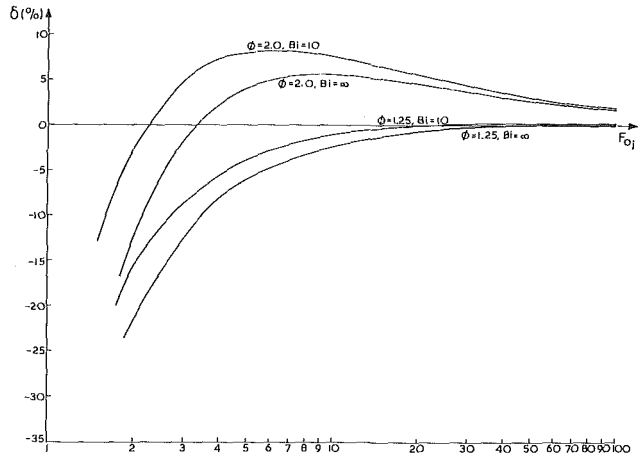

Fig. 3 Variation in the value of δ as a function of the initial Fourier number showing the effect of thermal contact resistance

at any particular time depending on the value of ϕ. It is generally considered that high probe heat capacity causes excessively long initial transient times [7]. This effect is illustrated clearly in Fig. 2 for ϕ values of 1.5, 1.8, and 2.0, for example. As the value of ϕ increases the absolute value of the error δ, within the time range of interest, also increases. Consequently the time required for the error level to decay to an acceptable level is increased.

However, the picture is more complex than hitherto revealed. At ϕ values of 0.75, 1.00, and 1.25 an increase in the value of ϕ, signifying an increase in the probe's heat capacity, reduces initial transient times. The error incurred at any particular time is lower for higher values of ϕ.

These two effects are interesting because an optimum value of ϕ appears to produce heat transfer rates which actually counteract the error introduced from the theoretical formulation. This pattern was not revealed in Hartley and Black's curves because of the error that had been incurred.

The curves in Fig. 2 are all for the case of perfect thermal contact between probe and soil. This is impossible to achieve in practice and the effect of this imperfection needs to be included in the analysis. In recognition of this Hartley and Black examined the case of Bi = 10 for the value of ϕ = 1.25. This example is represented here and is shown in Fig. 3. Furthermore the case of Bi = 10 and ϕ = 2.0 has been included.

Again the effect of contact resistance at the probe/soil interface is well known [7], being recognized as a source of a time delay in the attainment of the linear portion of the curve. The results shown in Fig. 3 for the case of ϕ = 2.0 illustrate this effect. The decrease in Biot number has caused an increase in the value of δ at all times. The effect of poorer soil-to-probe thermal contact at a value of ϕ equal to 1.25 is, however, contrary to that which might be expected since the absolute value of the error is generally reduced. This arises because the sign of the error associated with the heat capacity of the probe is opposite to the sign of the error due to poor contact. The two effects therefore counteract one another for this value of ϕ. This result would be equally true for lower values of ϕ.

Further decreases in the value of the Biot number can be expected to occur under field working conditions. Carslaw and Jaeger [8] give guidelines as to appropriate values of thermal conductance for various sizes of air gaps resulting from poor probe/soil fits. Using their values, further relationships between δ and Fo at decreased values of Bi can be evaluated. In general this effect will further increase the initial transient times for those cases where the error level was already positive. Where the error level was initially negative decreased values of Biot number will gradually decrease the error level until the overall error becomes positive. Thereafter further decreases in Biot number cause an increased positive error.

The results presented can be used in practice using the method described by Hartley and Black. This involves estimating the heat capacity of the soil so that ϕ can be evaluated and also estimating the value of the soil's thermal conductivity so that actual time can be determined from the Fourier number. Any differences between the estimated value of thermal conductivity and the measured value can be accommodated either by using conservative values of time or by repeating the test after equilibrium has been restored.

References

1 Blackwell, J. H., "A Transient-Flow Method for Determination of Thermal Constants of Insulating Materials in Bulk—Part 1—Theory," *J. Appl. Phys.*, Vol. 25, 1954, pp. 137–144.

2 Mitchell, J. K., and Kao, T. C., "Measurement of Soil Thermal Resistivity," *ASCE J. Geotech. Engng. Div.*, Vol. 104, 1978, pp. 1307–1320.

3 Anderson, P., and Blackstrom, G., "Thermal Conductivity of Solids Under Pressure by the Transient Hot-Wire Method," *Rev. Sci. Instr.*, Vol. 47, 1976, pp. 205–209.

4 Blackwell, J. H., "The Axial-Flow Error in the Thermal Conductivity Probe," *Canadian J. Physics*, Vol. 34, 1956, pp. 412–417.

5 Wechsler, A. E., "Development of Thermal Conductivity Probes for Soils and Insulations," U.S. Army Corps of Engineers, CRREL Technical Report 182, 1966.

6 Hartley, J. G., and Black, W. Z., "Minimization of Measurement Errors Involved in the Probe Method of Determining Soil Thermal Conductivity," ASME JOURNAL OF HEAT TRANSFER, Vol. 98, 1976, pp. 530–531.

7 Steinmanis, J. E., "Thermal Property Measurements Using a Thermal Probe," *Proc. Meeting on Underground Cable Thermal Backfill*, S. A. Boggs, F. Y. Chu, H. S. Radhakrishna, and J. E. Steinmanis, eds., Pergamon Press, New York, 1982, pp. 72–85.

8 Carslaw, H. S., and Jaeger, J. C., *Conduction of Heat in Solids*, Oxford University Press, 1959, p. 20.

Direct Exchange Areas for Calculating Radiation Transfer in Rectangular Furnaces

R. J. Tucker[1]

Nomenclature

K = attenuation or extinction coefficient of gas, m^{-1}
B = cube or square side, m
$\overline{S_iS_j}$ = direct exchange area between surfaces i and j, m^2
$\overline{g_iS_j}$ = direct exchange area between gas i and surface j, m^2
$\overline{g_ig_j}$ = direct exchange area between gas i and gas j, m^2
A = surface area, m^2
V = volume, m^3

Introduction

The prediction of the thermal performance of fuel-fired furnaces is dependent on an accurate calculation of radiant exchange between the combustion products, walls, and load within the heating chamber. The Hottel ZONE method [1] is a powerful technique for calculating radiation in furnaces provided the enclosure can be subdivided into well-defined surface and gas zones of uniform temperature. The technique requires an initial specification of the direct exchange areas between all gas and/or surface zone pairs which are in mutual radiative exchange. The radiant transfer originating from an emitting zone that arrives at (or is absorbed by) a receiving surface (or gas) zone is proportional to the difference in their blackbody emissive powers and to their mutual direct exchange area.

Fortunately, many furnace enclosures can be approximated geometrically by a collection of cubic gas zones bounded by walls comprising square surface zones. The exchange area between any two zones can then be generated by a simple summation of terms between component cubes and/or squares. This task can be made considerably easier if these are generated beforehand as charts, tables, or simple correlations accessible by a computer program. Charts providing direct exchange areas between pairs of cubes, pairs of squares, and cubes and squares in close proximity to each other have been prepared by Hottel and Cohen [2]. However, their data are limited to a range of optical path lengths (KB) of from zero to 1.4. In all multiple grey gas representations of the total emissivity or absorptivity of fossil-fuel combustion products, K for the high absorptivity grey gas component can exceed 20 m^{-1} for stoichiometric partial pressures of CO_2 and H_2O [3, 4]. This therefore limits the size of the cubes or squares for which exchange areas can be obtained to 0.07 m or less. Furthermore, some minor inaccuracies have been found in the above charts for a few of the configurations [5]. This paper presents more accurate data covering a wider range of KB from zero up to 18 (B_{max} = 0.9 m) and generated with the advantage of much faster digital computing capability than was presumably available when the original charts were prepared. The data are also presented in the form of simple exponential correlations which can easily be implemented into a computer file or subroutine.

Formulation of Direct Exchange Area

In the following formulations, the gas is assumed to be grey

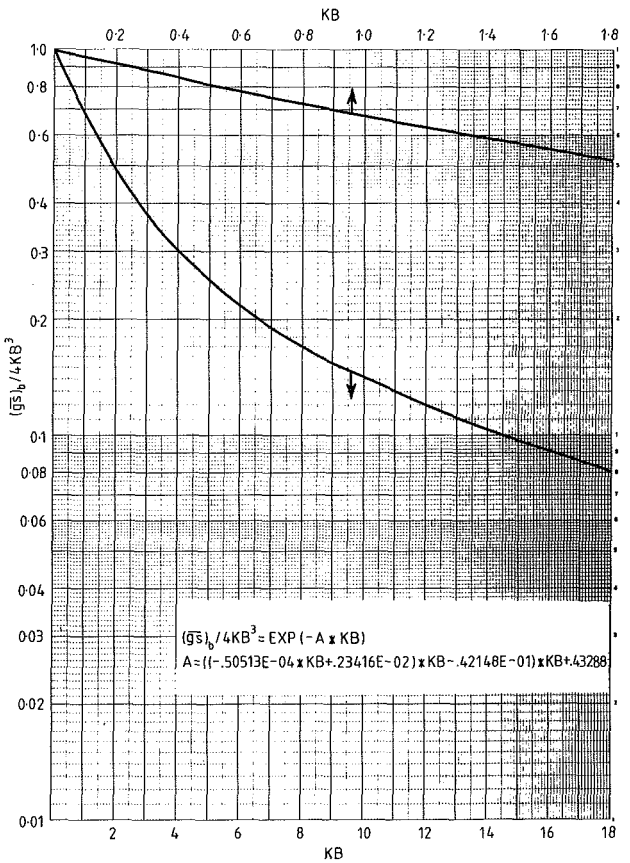

Fig. 1 The exchange area $(\overline{gs})_b$ between a cube of edge B and its six bounding surfaces

[1] British Gas Corporation, Midlands Research Station

Contributed by the Heat Transfer Division for publication in the JOURNAL OF HEAT TRANSFER. Manuscript received by the Heat Transfer Division January 29, 1985.

The results presented can be used in practice using the method described by Hartley and Black. This involves estimating the heat capacity of the soil so that ϕ can be evaluated and also estimating the value of the soil's thermal conductivity so that actual time can be determined from the Fourier number. Any differences between the estimated value of thermal conductivity and the measured value can be accommodated either by using conservative values of time or by repeating the test after equilibrium has been restored.

References

1 Blackwell, J. H., "A Transient-Flow Method for Determination of Thermal Constants of Insulating Materials in Bulk—Part 1—Theory," *J. Appl. Phys.*, Vol. 25, 1954, pp. 137–144.

2 Mitchell, J. K., and Kao, T. C., "Measurement of Soil Thermal Resistivity," *ASCE J. Geotech. Engng. Div.*, Vol. 104, 1978, pp. 1307–1320.

3 Anderson, P., and Blackstrom, G., "Thermal Conductivity of Solids Under Pressure by the Transient Hot-Wire Method," *Rev. Sci. Instr.*, Vol. 47, 1976, pp. 205–209.

4 Blackwell, J. H., "The Axial-Flow Error in the Thermal Conductivity Probe," *Canadian J. Physics*, Vol. 34, 1956, pp. 412–417.

5 Wechsler, A. E., "Development of Thermal Conductivity Probes for Soils and Insulations," U.S. Army Corps of Engineers, CRREL Technical Report 182, 1966.

6 Hartley, J. G., and Black, W. Z., "Minimization of Measurement Errors Involved in the Probe Method of Determining Soil Thermal Conductivity," ASME JOURNAL OF HEAT TRANSFER, Vol. 98, 1976, pp. 530–531.

7 Steinmanis, J. E., "Thermal Property Measurements Using a Thermal Probe," *Proc. Meeting on Underground Cable Thermal Backfill*, S. A. Boggs, F. Y. Chu, H. S. Radhakrishna, and J. E. Steinmanis, eds., Pergamon Press, New York, 1982, pp. 72–85.

8 Carslaw, H. S., and Jaeger, J. C., *Conduction of Heat in Solids*, Oxford University Press, 1959, p. 20.

Direct Exchange Areas for Calculating Radiation Transfer in Rectangular Furnaces

R. J. Tucker[1]

Nomenclature

- K = attenuation or extinction coefficient of gas, m^{-1}
- B = cube or square side, m
- $\overline{S_iS_j}$ = direct exchange area between surfaces i and j, m^2
- $\overline{g_iS_j}$ = direct exchange area between gas i and surface j, m^2
- $\overline{g_ig_j}$ = direct exchange area between gas i and gas j, m^2
- A = surface area, m^2
- V = volume, m^3

Introduction

The prediction of the thermal performance of fuel-fired furnaces is dependent on an accurate calculation of radiant exchange between the combustion products, walls, and load within the heating chamber. The Hottel ZONE method [1] is a powerful technique for calculating radiation in furnaces provided the enclosure can be subdivided into well-defined surface and gas zones of uniform temperature. The technique requires an initial specification of the direct exchange areas between all gas and/or surface zone pairs which are in mutual radiative exchange. The radiant transfer originating from an emitting zone that arrives at (or is absorbed by) a receiving surface (or gas) zone is proportional to the difference in their blackbody emissive powers and to their mutual direct exchange area.

Fortunately, many furnace enclosures can be approximated geometrically by a collection of cubic gas zones bounded by walls comprising square surface zones. The exchange area between any two zones can then be generated by a simple summation of terms between component cubes and/or squares. This task can be made considerably easier if these are generated beforehand as charts, tables, or simple correlations accessible by a computer program. Charts providing direct exchange areas between pairs of cubes, pairs of squares, and cubes and squares in close proximity to each other have been prepared by Hottel and Cohen [2]. However, their data are limited to a range of optical path lengths (KB) of from zero to 1.4. In all multiple grey gas representations of the total emissivity or absorptivity of fossil-fuel combustion products, K for the high absorptivity grey gas component can exceed 20 m^{-1} for stoichiometric partial pressures of CO_2 and H_2O [3, 4]. This therefore limits the size of the cubes or squares for which exchange areas can be obtained to 0.07 m or less. Furthermore, some minor inaccuracies have been found in the above charts for a few of the configurations [5]. This paper presents more accurate data covering a wider range of KB from zero up to 18 (B_{max} = 0.9 m) and generated with the advantage of much faster digital computing capability than was presumably available when the original charts were prepared. The data are also presented in the form of simple exponential correlations which can easily be implemented into a computer file or subroutine.

Formulation of Direct Exchange Area

In the following formulations, the gas is assumed to be grey

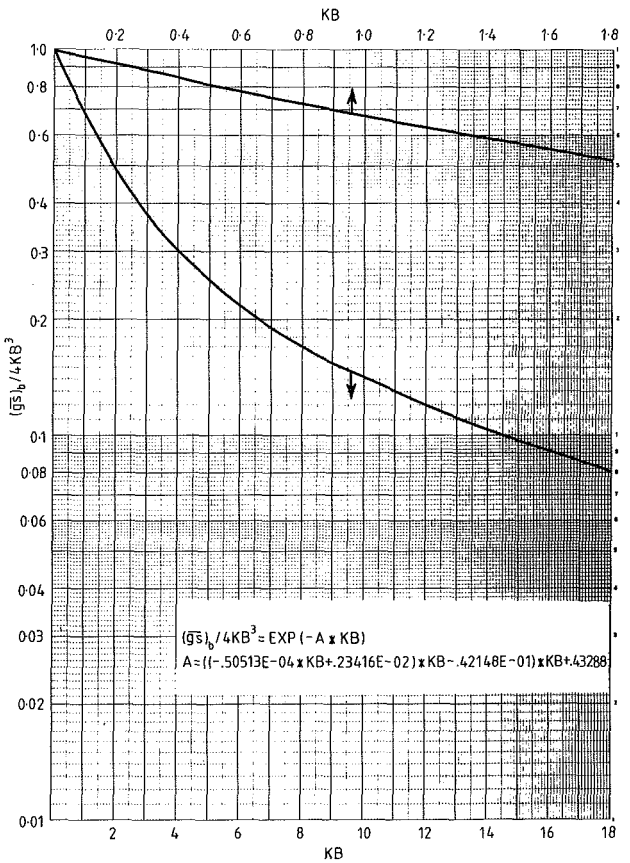

Fig. 1 The exchange area $(\overline{gs})_b$ between a cube of edge B and its six bounding surfaces

[1] British Gas Corporation, Midlands Research Station

Contributed by the Heat Transfer Division for publication in the JOURNAL OF HEAT TRANSFER. Manuscript received by the Heat Transfer Division January 29, 1985.

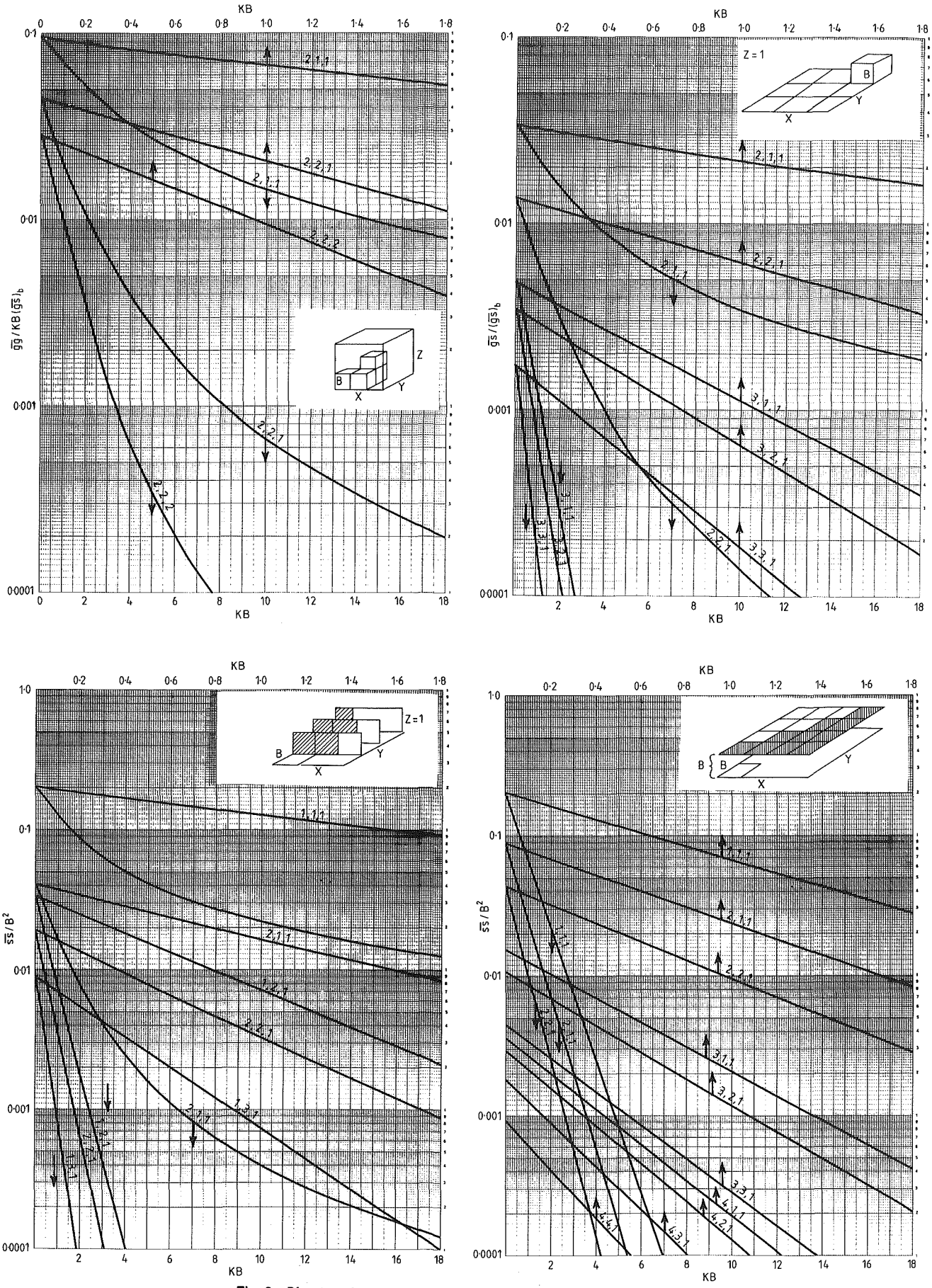

Fig. 2 Direct exchange areas between zones in close proximity (Nos. on curves are *X/B*, *Y/B*, *Z/B* where *B* = cube or square side)

Table 1 Correlation coefficients for direct exchange areas between parallel square surfaces; $\overline{ss}/B^2 = C * \exp(-A * KB)$

$\overline{ss}$ / B^2 = C * EXP(-A * KB)

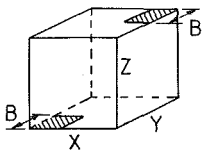

X/B	Y/B	Z/B	C	A	X/B	Y/B	Z/B	C	A
1	1	1	.1998	1.1053	1	1	4	.0191	4.0396
2	1	1	.0861	1.3014	2	1	4	.0171	4.1475
3	1	1	.0153	1.9987	3	1	4	.0126	4.4615
4	1	1	.0036	2.9351	4	1	4	.0082	4.9529
2	2	1	.0433	1.5172	2	2	4	.0153	4.2538
3	2	1	.0105	2.1959	3	2	4	.0114	4.5627
4	2	1	.0029	3.0880	4	2	4	.0076	5.0464
3	3	1	.0045	2.7513	3	3	4	.0088	4.8569
4	3	1	.0018	3.5187	4	3	4	.0061	5.3190
4	4	1	.0009	4.1511	4	4	4	.0045	5.7494
1	1	2	.0686	2.0710	1	1	5	.0124	5.0322
2	1	2	.0481	2.2368	2	1	5	.0115	5.1224
3	1	2	.0206	2.7286	3	1	5	.0093	5.3863
4	1	2	.0080	3.4595	4	1	5	.0068	5.8053
2	2	2	.0351	2.4015	2	2	5	.0107	5.2114
3	2	2	.0164	2.8812	3	2	5	.0087	5.4720
4	2	2	.0068	3.5899	4	2	5	.0065	5.8861
3	3	2	.0093	3.3165	3	3	5	.0073	5.7232
4	3	2	.0046	3.9625	4	3	5	.0055	6.1231
4	4	2	.0027	4.5268	4	4	5	.0043	6.5018
1	1	3	.0330	3.0512	1	1	6	.0087	6.0271
2	1	3	.0274	3.1838	2	1	6	.0082	6.1042
3	1	3	.0168	3.5683	3	1	6	.0071	6.3310
4	1	3	.0090	4.1582	4	1	6	.0056	6.6951
2	2	3	.0230	3.3140	2	2	6	.0078	6.1805
3	2	3	.0146	3.6906	3	2	6	.0067	6.4052
4	2	3	.0081	4.2680	4	2	6	.0054	6.7658
3	3	3	.0101	4.0432	3	3	6	.0059	6.6235
4	3	3	.0061	4.5855	4	3	6	.0048	6.9744
4	4	3	.0040	5.0783	4	4	6	.0039	7.3105

with a uniform attenuation coefficient. These restrictions are compatible with the multiple grey gas representation of a real furnace atmosphere.

The direct exchange areas between pairs of differential surface and/or volume elements i and j are given by the following expressions [1] where r is the separating distance between elements and θ their relative angle of orientation (measured relative to the normal to a surface element)

Surface-surface exchange

$$\overline{s_i s_j} = dA_i \cos\theta_i dA_j \cos\theta_j \exp(-Kr)/\pi r^2 \tag{1}$$

Volume-surface exchange

$$\overline{g_i s_j} = K\, dV_i dA_j \cos\theta_j \exp(-Kr)/\pi r^2 \tag{2}$$

Volume-volume exchange

$$\overline{g_i g_j} = K^2 dV_i dV_j \exp(-Kr)/\pi r^2 \tag{3}$$

Numerical Evaluation of Direct Exchange Areas

The integration of equations (1), (2), and (3) above must therefore be carried out to derive the exchange areas between finite square surfaces and/or cubic volume zones. Analytical solutions can only be derived when the gas is optically thin and therefore non-self-absorbing (i.e., when the $\exp(-Kr)$ term is unity, representing total transmittance). Where an absorbing gas is involved, numerical integration must be adopted. Indeed, for all evaluations carried out, including the surface-surface exchange in a nonabsorbing atmosphere, a simple numerical integration technique has been applied. Analytically derived formulae have been used, however, to verify the accuracy of the numerical technique, by providing exact exchange areas for the surface-surface configurations in a nonabsorbing atmosphere [6].

Table 2 Correlation coefficients for direct exchange areas between perpendicularly oriented square surfaces; $\overline{ss}/B^2 = C * \exp(-A * KB)$; $A = a_0 + a_1 * KB \ldots . a_4 * (KB)^4$

$\overline{ss}$ / B^2 = C * EXP(-A * KB)

A = a_0 + a_1*KB ..... a_4*(KB)^4

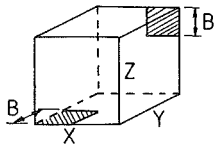

X/B	Y/B	Z/B	C	a_0	a_1	a_2	a_3	a_4
1	1	1	.2000	.5390	-.615E-01	.429E-02	-.151E-03	.206E-05
2	1	1	.0406	.9965	-.878E-1	.419E-02	-.773E-04	.000E+00
3	1	1	.0043	1.906				
1	2	1	.0328	1.571	-.391E-01	.208E-02	.000E+00	.000E+00
2	2	1	.0189	1.751				
3	2	1	.0059	2.384				
1	3	1	.0089	2.502				
2	3	1	.0069	2.665				
3	3	1	.0036	3.129				
1	2	2	.0329	2.055				
2	2	2	.0230	2.245				
3	2	2	.0101	2.780				
1	3	2	.0159	2.860				
2	3	2	.0129	3.010				
3	3	2	.0076	3.435				
1	3	3	.0124	3.481				
2	3	3	.0107	3.609				
3	3	3	.0073	3.976				

Results

The results of the numerical integrations are presented graphically in Figs. 1 and 2 for zones in close proximity to each other and as exponential correlations in Tables 1-4 for all configurations evaluated. Exchange areas are provided for squares in mutually parallel and perpendicular planes, as well as for cubes and squares and for pairs of cubes in a rectangular framework. These are all normalized as in the charts of Hottel and Cohen [2]. The "escape factor" $(\overline{gs})_b$ is the exchange area between a cube of edge B and its six bounding surfaces and is presented graphically and as a correlation in Fig. 1. $(\overline{gs})_b$ is itself normalized to the unit emittance $4KV$ in 4π steradians from a cube of volume V ($= B^3$). The plots in Fig. 2 for element pairs in very close proximity to each other are substantially "nonlinear." This is not evident in the Hottel and Cohen charts [2].

By comparison of the normalized surface–surface exchange areas for zero attenuation coefficient (factor C in Tables 1 and 2) with analytically derived data, the numerical technique was verified to be accurate to within ± 0.5 percent. The exponential correlations are themselves best-fit expressions derived by the method of least-squares and these are accurate to within three decimal places.

The above results relate to squares and/or cubes in close proximity to each other. Exchange areas between zones separated by larger distances can be approximated closely by assuming that the view and path length for absorption are the

Table 3 Correlation coefficients for direct exchange areas between cubic gas zones and square surface zones; $\overline{gs} / (\overline{gs})_b = C * \exp(-A * KB)$; $A = a_0 + a_1 * KB + a_2 * (KB)^2$

$\overline{gs} / (\overline{gs})_b = C * EXP(-A * KB)$

$A = a_0 + a_1 * KB + a_2 * (KB)^2$

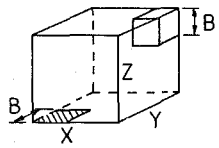

X/B	Y/B	Z/B	C	a_0	a_1	a_2
2	1	1	.0337	.4563	-.311E-01	.824E-03
3	1	1	.0048	1.457		
2	2	1	.0137	.8332	-.469E-01	.103E-02
3	2	1	.0034	1.674		
3	3	1	.0017	2.251		
1	1	2	.0313	1.062		
2	1	2	.0200	1.292		
3	1	2	.0078	1.933		
2	2	2	.0135	1.514		
3	2	2	.0062	2.089		
3	3	2	.0037	2.602		
1	1	3	.0120	2.033		
2	1	3	.0098	2.210		
3	1	3	.0060	2.666		
2	2	3	.0083	2.366		
3	2	3	.0053	2.806		
3	3	3	.0037	3.201		

Table 4 Correlation coefficients for direct exchange areas between pairs of cubic gas zones; $\overline{gg} / (KB\ (\overline{gs})_b) = C * \exp(-A * KB)$; $A = a_0 + a_1 * KB \ldots\ldots a_3 * (KB)^3$

$\overline{gg} / (KB\ (\overline{gs})_b) = C * EXP(-A * KB)$

$A = a_0 + a_1 * KB \ldots\ldots a_3 * (KB)^3$

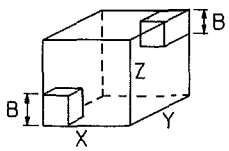

X/B	Y/B	Z/B	C	a0	a1	a2	a3
2	1	1	.0949	.3784	-.331E-01	.174E-02	-.360E-04
3	1	1	.0203	1.430			
2	2	1	.0445	.8190	-.599E-01	.235E-02	-.347E-04
3	2	1	.0161	1.657			
3	3	1	.0099	2.263			
2	2	2	.0283	1.147	-.620E-01	.132E-02	.000E+00
3	2	2	.0132	1.866			
3	3	2	.0090	2.458			

same for all points from within each zone, thus representing zones as differential elements. Equations (1)–(3) can in these cases be applied directly with the θ and r terms based on center-to-center orientation and distance.

Conclusions

Direct exchange areas are provided which can be used for the evaluation of radiation exchange within rectangular gas-filled enclosures. These are correlated in a form that can be incorporated easily into a computer library file or subroutine and should therefore be a valuable aid to the writing and development of mathematical models utilizing the zone method of analysis for radiant exchange.

Acknowledgments

This paper is published by permission of the British Gas Corporation. The author wishes to acknowledge John Truelove (formerly HTFS) for his helpful advice and collaboration at the start of this work.

References

1 Hottel, H. C., and Sarofim, A. F., *Radiative Transfer*, McGraw-Hill, New York, 1967.

2 Hottel, H. C., and Cohen, E. S., "Radiant Heat Exchange in a Gas-Filled Enclosure," AIChE, Mar. 1958, Vol. 4, p. 3.

3 Smith, T. F., Shen, Z. F., and Friedman, J. N., "Evaluation of Coefficients for the Weighted Sum of Grey Gases Model," ASME JOURNAL OF HEAT TRANSFER, Vol. 104, Nov. 1982, pp. 602–608.

4 Taylor, P. B., and Foster, P. J., "The Total Emissivities of Luminous and Non-luminous Flames," *Int. J. Heat Mass Transfer*, Vol. 17, 1974, pp. 1591–1605.

5 Becker, H. B., "A Mathematical Solution for Gas-to-Surface Radiative Exchange Area for a Rectangular Parallelepiped Enclosure Containing a Gray Medium," ASME JOURNAL OF HEAT TRANSFER, Vol. 99, May 1977.

6 Siegel, R., and Howell, J., *Thermal Radiation Heat Transfer*, McGraw-Hill, New York, 1972, Chap. 7.

Effective Absorptivity and Emissivity of Particulate Media With Application to a Fluidized Bed

M. Q. Brewster[1]

Nomenclature

- $\bar{a}$ = two-flux absorption coefficient
- B = back-scatter fraction
- c = mean particle clearance, μm
- d = particle diameter
- e_b = black hemispherical emissive power
- f_v = particle volume fraction
- q = heat flux, W/m^2 or W/m$^2 \cdot \mu$m
- T = particle temperature, K
- T_g = gas temperature, K
- U = superficial velocity (gas)
- x = semi-infinite slab normal coordinate
- α = absorptivity
- δ = nonisothermal layer thickness
- ϵ = emissivity or particle emissivity
- η = T_0/T_b
- λ = wavelength, μm
- ξ = constant defined in equation (9)
- $\bar{\sigma}$ = two-flux scattering coefficient
- ϕ = single scatter polar angle

[1]Department of Mechanical and Industrial Engineering, University of Utah, Salt Lake City, UT 84112; Assoc. Mem. ASME

Contributed by the Heat Transfer Division for publication in the JOURNAL OF HEAT TRANSFER. Manuscript received by the Heat Transfer Division February 5, 1985.

Table 3 Correlation coefficients for direct exchange areas between cubic gas zones and square surface zones; $\overline{gs} / (\overline{gs})_b = C * \exp(-A * KB)$; $A = a_0 + a_1 * KB + a_2 * (KB)^2$

$\overline{gs} / (\overline{gs})_b = C * EXP(-A * KB)$

$A = a_0 + a_1 * KB + a_2 * (KB)^2$

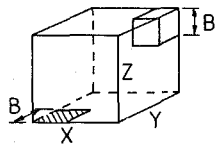

X/B	Y/B	Z/B	C	a_0	a_1	a_2
2	1	1	.0337	.4563	-.311E-01	.824E-03
3	1	1	.0048	1.457		
2	2	1	.0137	.8332	-.469E-01	.103E-02
3	2	1	.0034	1.674		
3	3	1	.0017	2.251		
1	1	2	.0313	1.062		
2	1	2	.0200	1.292		
3	1	2	.0078	1.933		
2	2	2	.0135	1.514		
3	2	2	.0062	2.089		
3	3	2	.0037	2.602		
1	1	3	.0120	2.033		
2	1	3	.0098	2.210		
3	1	3	.0060	2.666		
2	2	3	.0083	2.366		
3	2	3	.0053	2.806		
3	3	3	.0037	3.201		

Table 4 Correlation coefficients for direct exchange areas between pairs of cubic gas zones; $\overline{gg} / (KB\ (\overline{gs})_b) = C * \exp(-A * KB)$; $A = a_0 + a_1 * KB \ldots\ldots a_3 * (KB)^3$

$\overline{gg} / (KB\ (\overline{gs})_b) = C * EXP(-A * KB)$

$A = a_0 + a_1 * KB \ldots\ldots a_3 * (KB)^3$

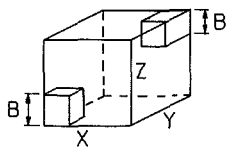

X/B	Y/B	Z/B	C	a0	a1	a2	a3
2	1	1	.0949	.3784	-.331E-01	.174E-02	-.360E-04
3	1	1	.0203	1.430			
2	2	1	.0445	.8190	-.599E-01	.235E-02	-.347E-04
3	2	1	.0161	1.657			
3	3	1	.0099	2.263			
2	2	2	.0283	1.147	-.620E-01	.132E-02	.000E+00
3	2	2	.0132	1.866			
3	3	2	.0090	2.458			

same for all points from within each zone, thus representing zones as differential elements. Equations (1)–(3) can in these cases be applied directly with the θ and r terms based on center-to-center orientation and distance.

Conclusions

Direct exchange areas are provided which can be used for the evaluation of radiation exchange within rectangular gas-filled enclosures. These are correlated in a form that can be incorporated easily into a computer library file or subroutine and should therefore be a valuable aid to the writing and development of mathematical models utilizing the zone method of analysis for radiant exchange.

Acknowledgments

This paper is published by permission of the British Gas Corporation. The author wishes to acknowledge John Truelove (formerly HTFS) for his helpful advice and collaboration at the start of this work.

References

1 Hottel, H. C., and Sarofim, A. F., *Radiative Transfer*, McGraw-Hill, New York, 1967.

2 Hottel, H. C., and Cohen, E. S., "Radiant Heat Exchange in a Gas-Filled Enclosure," AIChE, Mar. 1958, Vol. 4, p. 3.

3 Smith, T. F., Shen, Z. F., and Friedman, J. N., "Evaluation of Coefficients for the Weighted Sum of Grey Gases Model," ASME JOURNAL OF HEAT TRANSFER, Vol. 104, Nov. 1982, pp. 602–608.

4 Taylor, P. B., and Foster, P. J., "The Total Emissivities of Luminous and Non-luminous Flames," *Int. J. Heat Mass Transfer*, Vol. 17, 1974, pp. 1591–1605.

5 Becker, H. B., "A Mathematical Solution for Gas-to-Surface Radiative Exchange Area for a Rectangular Parallelepiped Enclosure Containing a Gray Medium," ASME JOURNAL OF HEAT TRANSFER, Vol. 99, May 1977.

6 Siegel, R., and Howell, J., *Thermal Radiation Heat Transfer*, McGraw-Hill, New York, 1972, Chap. 7.

Effective Absorptivity and Emissivity of Particulate Media With Application to a Fluidized Bed

M. Q. Brewster[1]

Nomenclature

- $\bar{a}$ = two-flux absorption coefficient
- B = back-scatter fraction
- c = mean particle clearance, μm
- d = particle diameter
- e_b = black hemispherical emissive power
- f_v = particle volume fraction
- q = heat flux, W/m^2 or W/m$^2 \cdot \mu$m
- T = particle temperature, K
- T_g = gas temperature, K
- U = superficial velocity (gas)
- x = semi-infinite slab normal coordinate
- α = absorptivity
- δ = nonisothermal layer thickness
- ϵ = emissivity or particle emissivity
- η = T_0/T_b
- λ = wavelength, μm
- ξ = constant defined in equation (9)
- $\bar{\sigma}$ = two-flux scattering coefficient
- ϕ = single scatter polar angle

[1]Department of Mechanical and Industrial Engineering, University of Utah, Salt Lake City, UT 84112; Assoc. Mem. ASME

Contributed by the Heat Transfer Division for publication in the JOURNAL OF HEAT TRANSFER. Manuscript received by the Heat Transfer Division February 5, 1985.

Subscripts

a = absorption
b = bulk or blackbody
bed = bed
eff = effective
0 = at wall (as in T_0)
s = scattering
w = wall
λ = monochromatic

Introduction

A simple, yet physically well-based and accurate model of radiative heat transfer in fluidized bed combustors would be of great help in the total heat transfer analysis of those systems. Many investigators have studied the radiative component in fluidized bed combustors trying to develop such a model [1–4].

The key parameter of interest in describing radiative transfer between a combusting fluidized bed and a cooled surface is the effective total, hemispherical emissivity of the bed based on the bed temperature ϵ_{eff}. It would be desirable to have a model giving the dependence of ϵ_{eff} on the pertinent parameters of wall temperature T_w, bed temperature T_b, bed particle volume fraction f_V, particle emissivity ϵ, and diameter d, which could be easily assimilated into a total heat transfer analysis. While raytracing [1] can be used to give ϵ_{eff} as a function of these parameters, the resulting equations are unwieldy. On the other hand, the radiative transfer equation as employed in [2, 4] is relatively straightforward and well based physically.

Transfer Equation

The problem which has prevented widespread consideration of the transfer equation as a model for packed and fluidized beds in the past is the argument that the condition of high particle number density in these systems ($f_v \sim 1$) contradicts the assumptions upon which the transfer equation is based. Indeed the transfer equation is derived assuming the existence of an elemental volume in which negligible shadowing and multiple scatter occur [5]. Furthermore, it is assumed that the particles interact independently with radiation (independent scattering). However, it has been shown experimentally [6] that the assumption of negligible multiple scatter and shadowing within an elemental volume containing many particles is merely an artifice in the derivation of the transfer equation and that the applicability of the transfer equation is limited only by the validity of the assumption of independent scattering. It has been shown that the onset of dependent scattering is best monitored by the ratio c/λ, the mean particle clearance to wavelength ratio [6, 7]. Since in fluidized beds this ratio is well above the recommended critical value of 0.3, the transfer equation should serve as an accurate model for radiative transfer in fluidized beds. Further support for this approach may be found in [6] where it is demonstrated that the two-flux solution of the transfer equation predicts measured transmittance in packed beds [8].

Two-Flux Model

The two-flux model is very familiar and has been extensively documented in the literature [9, 10]. Therefore the equations will not be given here. However, one point that should be emphasized is that as long as scattering is not acutely anisotropic [9], the two-flux parameters $\bar{a}$, $\bar{\sigma}$, and B can be calculated from fundamental properties of the particles, such as volume fraction f_v, diameter d, emissivity ϵ, and single-scatter phase function $p(\phi)$. It is not necessary or desirable to resort to using empirical or adjustable two-flux parameters, although this practice persists. For diffusely reflecting, opaque, geometric spheres with reflectivity independent of incident angle, the two-flux parameters are given in terms of the particle properties as follows [5, 10]

$$B = 0.667 \tag{1}$$

$$\bar{a} = 3f_v\epsilon/d \tag{2}$$

$$\bar{\sigma} = 3f_v(1-\epsilon)B/d \tag{3}$$

Solution by Superposition

The solution to the problem of heat transfer between a participating particulate medium and a cold plane wall can be conveniently obtained by using superposition of two simpler problems. The first problem involves emission by the particulate medium into a black body at zero degrees. The second problem involves absorption by the cold particulate medium of diffuse incident intensity. Linearity of the equations and boundary conditions [10] readily yields the result that the sum of the two simpler problems is a solution of the complete problem assuming that the properties are independent of temperature.

Formulation of the problem is completed by representing the heat transfer between the bed and wall as a classical surface interchange problem between two parallel plates. The net heat flux to the wall q is then given by equation (4) [1, 10]

$$q = \frac{\dfrac{\epsilon_{\text{eff}}}{\alpha_{\text{eff}}} e_b(T_b) - \dfrac{\epsilon_w}{\alpha_w} e_b(T_w)}{\dfrac{1}{\alpha_{\text{eff}}} + \dfrac{1}{\alpha_w} - 1} \tag{4}$$

In equation (4) ϵ_{eff} is the effective emissivity of the particulate medium based on bulk temperature T_b and α_{eff} is the effective absorptivity. Similarly ϵ_w and α_w are the corresponding properties for the wall.

Effective Absorptivity

The effective absorptivity is obtained by solving the equations for the cold medium, diffuse incidence problem [10]

$$\alpha_{\text{eff}} = \left[\frac{\epsilon}{(1-\epsilon)B}\left(\frac{\epsilon}{(1-\epsilon)B} + 2\right)\right]^{1/2} - \frac{\epsilon}{(1-\epsilon)B} \tag{5}$$

The results for α_{eff} are plotted in Fig. 1 for both isotropic scattering ($B = 0.5$) and diffusely reflecting particles ($B = 0.667$).

The effective absorptivity also plays the role of effective emissivity of an isothermal bed. This can be readily demonstrated by introducing a variable transformation to show that the equations for the cold medium, diffuse incidence problem are equivalent to the equations for the problem of emission into a blackbody at zero degrees for $T(x) = \text{const}$. This (perhaps obvious) result is Kirchhoff's Law for a participating medium. The importance of this observation lies in the fact that due to the high degree of solid mixing

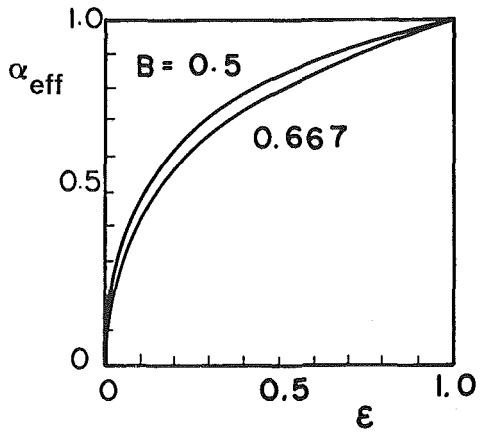

Fig. 1 Absorptivity/isothermal bed emissivity

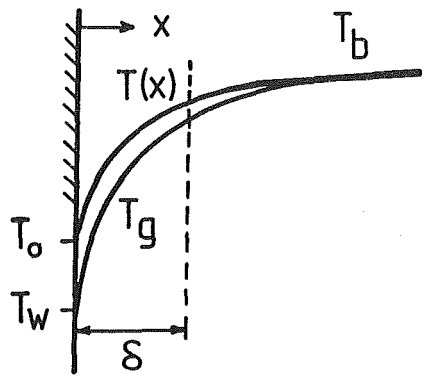

Fig. 2 Average particle and gas temperature profiles near the wall

in fluidized beds the assumption of an isothermal bed is a reasonable first approximation. Indeed for large particle beds ($d>1$ mm) it is a valid assumption [3]. Equation (5), which holds on either a total or spectral basis, indicates that for an isothermal bed the effective emissivity is only a function of particle emissivity ϵ and backscatter fraction B. It does not depend on temperature T_b, particle diameter d, or particle volume fraction f_v. As can be seen from Fig. 1, the effective emissivity of an isothermal bed is always greater than the particle emissivity, due to the blackbody or cavity effect of scattering by the particles.

Effective Emissivity

Experiments indicate both that ϵ_{eff} is not a function of ϵ and B alone and that a thin nonisothermal zone does exist in the bed near the wall. Furthermore, the time-averaged temperature profiles of the particles ($T(x)$) and the gas ($T_g(x)$) can be quite different (see Fig. 2). In general the larger the particles are the larger the difference will be between $T(x)$ and $T_g(x)$ due to the increased thermal time constant for larger particles. As a result the average particle temperature at the wall T_0 will be greater than the wall temperature T_w. To account for this nonisothermal zone an exponential particle temperature profile is assumed near the wall

$$\frac{T-T_0}{T_b-T_0}=1-\exp\left(-\frac{x}{\delta}\right) \tag{6}$$

Assuming gray particles with constant (temperature-independent) properties an analytic solution of the problem of emission into a black wall at zero degrees can be obtained using equation (6) to give the effective emissivity ϵ_{eff}

$$\epsilon_{\text{eff}}=\frac{\epsilon}{(1-\epsilon)B}\left\{\sum_{n=0}^{4}\frac{4!}{n!(4-n)!}\frac{(\eta-1)^n}{(\xi+n)}\left[\xi(1+\frac{2B(1-\epsilon)}{\epsilon}\right)^{1/2}+n\right]-\eta^4\right\} \tag{7}$$

where

$$\eta=\frac{T_0}{T_b} \tag{8}$$

and

$$\xi=\frac{3f_v\delta}{d}[\epsilon(2(1-\epsilon)B+\epsilon)]^{1/2} \tag{9}$$

Equations (7)–(9) indicate that ϵ_{eff} is a function of four dimensionless parameters, ϵ, B, $f_v\,\delta/d$, and T_0/T_b. From equations (2) and (3) the parameter $f_v\,\delta/d$ can be interpreted as the optical depth based on nonisothermal layer thickness. Figure 3 presents some sample calculations of ϵ_{eff} for the case of diffusely reflecting spherical particles, $B=0.667$. Also plotted in Fig. 3 are some experimental measurements of total effective bed emissivity from Baskakov et al. [11]. In general effective bed emissivity increases as T_0 increases for a given value of T_b. However for a given value of T_0 effective emissivity decreases with increasing T_b. These observed trends are also predicted by the nonisothermal gray model for ϵ_{eff}. The

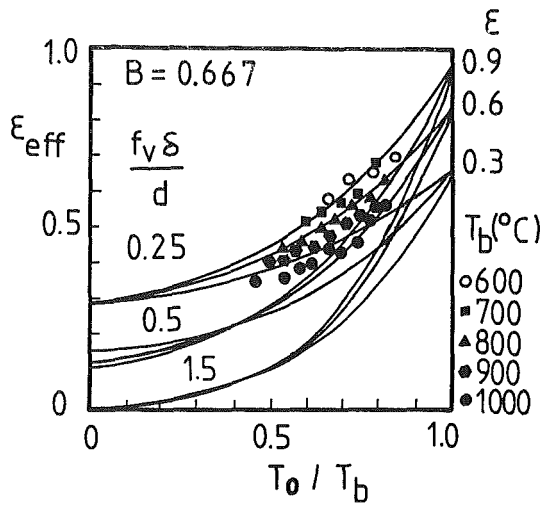

Fig. 3 Nonisothermal bed emissivity (experimental data from [11])

theoretical model for ϵ_{eff} also predicts that for $T_0/T_b\to 1$ the value of ϵ becomes of primary importance and $f_v\,\delta/d$ is insignificant. However, for $T_0/T_b\to 0$ the value of ϵ is unimportant while $f_v\,\delta/d$ is the dominating parameter (at least as long as $f_v\,\delta/d$ is not very small in which case ϵ does play a significant role).

One thing evident from the experimental data in Fig. 3 is that δ must be a function of T_0 and T_b independently since the data exhibit dependence on T_0 and T_b independently and not just on their ratio. Otherwise the data would fall on a single curve. Also, based solely on the results in Fig. 3, it would appear that $f_v\,\delta/d$ is of the order of 0.25 and therefore that $\delta/d\cong 0.5$ (since $f_v\cong 0.5$). Inspection of Fig. 3 indicates that this conclusion is reached independent of the particular value of ϵ. Plots similar to Fig. 3 but for other realistic values of B also indicate that this conclusion is reached independent of the particular value of B. However the value of $\delta/d\cong 0.5$ seems unrealistically low for an average value. [It certainly may not be low for an instantaneous value just after new (hot) particles have replenished the surface.] A partial explanation of the discrepancy is that the assumption is implicitly made in Fig. 3 that the particle temperature at the wall equals the wall temperature: $T_\sigma=T_w$. The data from [11] are based on the wall temperature T_w which would likely be substantially less than the particle temperature T_0. The data in Fig. 3 are plotted assuming $T_0=T_w$. Correcting for the actual condition $T_w<T_0$ would have the effect of shifting the experimental data to the right.

Conclusions

The total effective emissivity of a fluidized bed is a function of the particle emissivity ϵ, the back-scatter fraction B, the nonisothermal optical depth $f_v\,\delta/d$, and T_0/T_b. Experimental studies are needed to correlate δ/d and T_0/T_b in terms of appropriate dimensional and nondimensional parameters. The intent of this work has been to show from analysis which dimensionless parameters should be correlated in order to develop a simple yet accurate model for radiative transfer to cooled surfaces in fluidized beds.

References

1 Borodulya, V. A., and Kovensky, V. I., "Radiative Heat Transfer Between a Fluidized Bed and a Surface," *Int. J. Heat Mass Transfer*, Vol. 26, 1983, pp. 277–287.

2 Flamant, G., "Theoretical and Experimental Study of Radiant Heat Transfer in a Solar Fluidized Bed Receiver," *AIChE J.*, Vol. 28, No. 4, 1982, pp. 529–535.

3 Decker, N., and Glicksman, L. R., "Heat Transfer in Large Particle Fluidized Beds," *Int. J. of Heat Mass Transfer*, Vol. 26, No. 9, 1983, pp. 1307–1319.

4 Chen, J. C., and Chen, K. L., "Analysis of Simultaneous Radiative and

Conductive Heat Transfer in Fluidized Beds," *Chem. Eng. Commun.*, Vol. 9, 1981, pp. 255-271.

5 Siegel, R., and Howell, J. R., *Thermal Radiation Heat Transfer*, McGraw-Hill, New York, 1972, pp. 662-669.

6 Brewster, M. Q., and Tien, C.-L., "Radiative Transfer in Packed/Fluidized Beds: Dependent versus Independent Scattering," ASME JOURNAL OF HEAT TRANSFER, Vol. 104, No. 4, 1982, pp. 573-579.

7 Hottel, H. C., Sarofim, A. F., Dalzell, W. H., and Vasalos, I. A., "Optical Properties of Coatings. Effect of Pigment Concentration," *AIAA J.*, Vol. 9, No. 10, 1970, p. 1895.

8 Chen, J. C., and Churchill, S. W., "Radiant Heat Transfer in Packed Beds," *AIChE J.*, Vol. 9, 1963, p. 35.

9 Brewster, M. Q., and Tien, C. L., "Examination of the Two-Flux Model for Radiative Transfer in Particulate Systems," *Int. J. of Heat and Mass Transfer*, Vol. 25, No. 12, 1982, pp. 1905-1906.

10 Brewster, M. Q., "Effective Emissivity of a Fluidized Bed," Presented at ASME Winter Annual Meeting, New Orleans, LA, HTD-40, 1984, pp. 7-13.

11 Baskakov, A. P., Berg, B. V., Vitt, O. K., Filippovsky, N. F., Kirakosyan, V. A., Goldobin, J. M., and Maskaev, V. K., "Heat Transfer to Objects Immersed in Fluidized Beds," *Powder Technology*, Vol. 8, 1973, pp. 273-282.

The Effects of Turbulent Natural Convection on Thermal Explosion Critical Conditions

F. B. Cheung[1]

Introduction

Most studies of thermal explosion [1-3] have treated the process of heat transfer in the reacting medium as purely conductive, which is generally true for solid explosives. However, for reactions taking place in the liquid or gaseous phase, natural convection may sometimes be an important heat transfer mechanism, as indicated by the experiments of Ashmore et al. [4], and Merzhanov and Shtessel [5]. In such cases, the rate of cooling of the fluid medium may be enhanced markedly by the presence of convection, and predictions using the classical conduction theory may result in significant error.

The effects of natural convection on the critical conditions of thermal explosion have been studied numerically by Jones [6]. The ignition limit is found to be a strongly increasing function of the Rayleigh number, indicating that a higher rate of heat production can be accommodated without an explosion when convection occurs in the system in addition to conduction. With respect to convection, chemical kinetics is found to play a rather minor role in criticality. Thus the combustion reaction may be assumed to be of zero order, which in essence is equivalent to neglecting the consumption of reactants during the course of reaction.

The work of Jones [6], however, has been based on the laminar flow. In this study, the importance of turbulent convection in exothermic chemical reactions taking place in a fluid medium confined between two parallel plates is investigated. The presence of eddy heat transport in the reactant phase not only would enhance substantially the rate of cooling of the medium but also would result in a more uniform temperature profile in the interior region. This in turn would tend to lower the maximum temperature and with it the rate of energy release. Thus a much higher limit of ignition can be achieved, resulting in a system with much less tendency to explode. The purpose of this study is to provide an ignition criterion for the case in which heat transfer in the reacting medium is augmented by turbulent natural convection.

Analysis

In formulating the problem, the reacting medium is considered to be in the liquid or gaseous phase, confined between two parallel plates with infinite extent in the horizontal direction. The upper plate is isothermal whereas the lower plate is adiabatic. The Rayleigh number of the layer is sufficiently high that turbulence is the dominant mode of heat transfer in the medium. By combining the equations of continuity and conservation of energy and horizontally averaging, there results [7, 8]

$$\rho C_P\left(\frac{\partial \bar{T}}{\partial t}+\frac{\partial}{\partial z}\,\overline{w\theta}\right)=k\,\frac{\partial^2 \bar{T}}{\partial z^2}+q \tag{1}$$

with boundary conditions

$$z=0:\ \frac{\partial \bar{T}}{\partial z}=0,\ \overline{w\theta}=0 \quad \text{and} \quad z=L:\ \bar{T}=T_0,\ \overline{w\theta}=0 \tag{2}$$

where $\bar{T}$ and θ are the mean and fluctuating temperatures, respectively, w the vertical component of velocity, ρ the density, C_p the specific heat, k the thermal conductivity, L the depth of the fluid layer, and q the density of internal heat sources due to heat production by chemical reaction. The quantity $\overline{w\theta}$ represents the turbulent heat flux which is identically zero at the lower and upper walls as required by the no-slip condition.

To account for the thermal effects of the reaction, the heat production term q is represented as a function of the local fluid temperature according to Arrhenius' law

$$q=QA\,\exp\,(-E/R\bar{T}) \tag{3}$$

where Q is the exothermicity, A the pre-exponential factor, E the activation energy, and R the universal gas constant. In writing equation (3), the reaction has been assumed to be of zero order and the effects of reactant consumption have been neglected.

Stationary Method—Eddy Heat Transport Model

Under steady-state conditions, the transient term in equation (1) may be omitted. The equations governing the mean temperature field become

$$\frac{d}{dz}\left[\left(1+\frac{\epsilon_H}{\alpha}\right)\frac{d\bar{T}}{dz}\right]=-\,(QA/k)\,\exp([E/R\bar{T}) \tag{4}$$

$$z=0:\ dT/dz=0;\ z=L;\ \bar{T}=T_0 \tag{5}$$

where α is the thermal diffusivity and ϵ_H the eddy diffusivity for heat defined by $\overline{w\theta} = -\epsilon_H\, d\bar{T}/dz$. To close the above system, the eddy heat transport model of Cheung [7] is employed to provide an independent expression for ϵ_H. In this model, the process of turbulent natural convection is considered to be described well by a local Rayleigh number of the flow Ra*, which is characterized by a local buoyancy difference and a local length scale. The former is related to a local temperature drop according to the Boussinesq approximation and the latter, to local distances from the upper and the lower walls. From [7], we have

$$\frac{\epsilon_H}{\alpha}=0.051\ \mathrm{Ra}^{*0.87} \quad \text{and}$$

$$\mathrm{Ra}^*=\frac{g\beta(\bar{T}-T_0)L^3}{\alpha\nu}\left[\frac{z}{L}\left(1-\frac{z}{L}\right)\right]^{3.448} \tag{6}$$

where g is the acceleration due to gravity, β the coefficient of thermal expansion, and ν the kinematic viscosity. Equation (6) has been tested against the data reported in [9].

Following Jones [6], equations (4) to (6) may be combined and normalized in terms of a dimensionless distance $n=z/L$, a dimensionless temperature $\phi=E(\bar{T}-T_0)/RT_0^2$, the Frank-Kamenetskii parameter $\delta=QEL^2A\,\exp\,(-E/RT_0)/kRT_0^2$, the Rayleigh number of the system, $\mathrm{Ra}=g\beta L^3RT_0^2/\alpha\nu E$, and the parameter $\epsilon=RT_0/E$. This gives

$$\begin{aligned}\phi''=-\{1+0.051\ \mathrm{Ra}^{0.87}\phi^{0.87}[\eta(1-\eta)]^3\}^{-1}\{&\delta\,\exp[\phi/(1+\epsilon\phi)]\\&+0.153\ \mathrm{Ra}^{0.87}\phi^{0.87}(1-2\eta)[\eta(1-\eta)]^2\phi'\\&+0.044\ \mathrm{Ra}^{0.87}\phi^{-0.13}[\eta(1-\eta)]^3\phi'^2\}\end{aligned} \tag{7}$$

[1]Department of Mechanical Engineering, The Pennsylvania State University, University Park, PA 16802; Mem. ASME.

Contributed by the Heat Transfer Division for publication in the JOURNAL OF HEAT TRANSFER. Manuscript received by the Heat Transfer Division May 17, 1985.

Conductive Heat Transfer in Fluidized Beds," *Chem. Eng. Commun.*, Vol. 9, 1981, pp. 255-271.

5 Siegel, R., and Howell, J. R., *Thermal Radiation Heat Transfer*, McGraw-Hill, New York, 1972, pp. 662-669.

6 Brewster, M. Q., and Tien, C.-L., "Radiative Transfer in Packed/Fluidized Beds: Dependent versus Independent Scattering," ASME JOURNAL OF HEAT TRANSFER, Vol. 104, No. 4, 1982, pp. 573-579.

7 Hottel, H. C., Sarofim, A. F., Dalzell, W. H., and Vasalos, I. A., "Optical Properties of Coatings. Effect of Pigment Concentration," *AIAA J.*, Vol. 9, No. 10, 1970, p. 1895.

8 Chen, J. C., and Churchill, S. W., "Radiant Heat Transfer in Packed Beds," *AIChE J.*, Vol. 9, 1963, p. 35.

9 Brewster, M. Q., and Tien, C. L., "Examination of the Two-Flux Model for Radiative Transfer in Particulate Systems," *Int. J. of Heat and Mass Transfer*, Vol. 25, No. 12, 1982, pp. 1905-1906.

10 Brewster, M. Q., "Effective Emissivity of a Fluidized Bed," Presented at ASME Winter Annual Meeting, New Orleans, LA, HTD-40, 1984, pp. 7-13.

11 Baskakov, A. P., Berg, B. V., Vitt, O. K., Filippovsky, N. F., Kirakosyan, V. A., Goldobin, J. M., and Maskaev, V. K., "Heat Transfer to Objects Immersed in Fluidized Beds," *Powder Technology*, Vol. 8, 1973, pp. 273-282.

The Effects of Turbulent Natural Convection on Thermal Explosion Critical Conditions

F. B. Cheung[1]

Introduction

Most studies of thermal explosion [1-3] have treated the process of heat transfer in the reacting medium as purely conductive, which is generally true for solid explosives. However, for reactions taking place in the liquid or gaseous phase, natural convection may sometimes be an important heat transfer mechanism, as indicated by the experiments of Ashmore et al. [4], and Merzhanov and Shtessel [5]. In such cases, the rate of cooling of the fluid medium may be enhanced markedly by the presence of convection, and predictions using the classical conduction theory may result in significant error.

The effects of natural convection on the critical conditions of thermal explosion have been studied numerically by Jones [6]. The ignition limit is found to be a strongly increasing function of the Rayleigh number, indicating that a higher rate of heat production can be accommodated without an explosion when convection occurs in the system in addition to conduction. With respect to convection, chemical kinetics is found to play a rather minor role in criticality. Thus the combustion reaction may be assumed to be of zero order, which in essence is equivalent to neglecting the consumption of reactants during the course of reaction.

The work of Jones [6], however, has been based on the laminar flow. In this study, the importance of turbulent convection in exothermic chemical reactions taking place in a fluid medium confined between two parallel plates is investigated. The presence of eddy heat transport in the reactant phase not only would enhance substantially the rate of cooling of the medium but also would result in a more uniform temperature profile in the interior region. This in turn would tend to lower the maximum temperature and with it the rate of energy release. Thus a much higher limit of ignition can be achieved, resulting in a system with much less tendency to explode. The purpose of this study is to provide an ignition criterion for the case in which heat transfer in the reacting medium is augmented by turbulent natural convection.

Analysis

In formulating the problem, the reacting medium is considered to be in the liquid or gaseous phase, confined between two parallel plates with infinite extent in the horizontal direction. The upper plate is isothermal whereas the lower plate is adiabatic. The Rayleigh number of the layer is sufficiently high that turbulence is the dominant mode of heat transfer in the medium. By combining the equations of continuity and conservation of energy and horizontally averaging, there results [7, 8]

$$\rho C_P\left(\frac{\partial \bar{T}}{\partial t}+\frac{\partial}{\partial z}\,\overline{w\theta}\right)=k\,\frac{\partial^2 \bar{T}}{\partial z^2}+q \tag{1}$$

with boundary conditions

$$z=0:\ \frac{\partial \bar{T}}{\partial z}=0,\ \overline{w\theta}=0 \quad \text{and} \quad z=L:\ \bar{T}=T_0,\ \overline{w\theta}=0 \tag{2}$$

where $\bar{T}$ and θ are the mean and fluctuating temperatures, respectively, w the vertical component of velocity, ρ the density, C_p the specific heat, k the thermal conductivity, L the depth of the fluid layer, and q the density of internal heat sources due to heat production by chemical reaction. The quantity $\overline{w\theta}$ represents the turbulent heat flux which is identically zero at the lower and upper walls as required by the no-slip condition.

To account for the thermal effects of the reaction, the heat production term q is represented as a function of the local fluid temperature according to Arrhenius' law

$$q=QA\,\exp\,(-E/R\bar{T}) \tag{3}$$

where Q is the exothermicity, A the pre-exponential factor, E the activation energy, and R the universal gas constant. In writing equation (3), the reaction has been assumed to be of zero order and the effects of reactant consumption have been neglected.

Stationary Method—Eddy Heat Transport Model

Under steady-state conditions, the transient term in equation (1) may be omitted. The equations governing the mean temperature field become

$$\frac{d}{dz}\left[\left(1+\frac{\epsilon_H}{\alpha}\right)\frac{d\bar{T}}{dz}\right]=-\,(QA/k)\,\exp([E/R\bar{T}) \tag{4}$$

$$z=0:\ dT/dz=0;\ z=L;\ \bar{T}=T_0 \tag{5}$$

where α is the thermal diffusivity and ϵ_H the eddy diffusivity for heat defined by $\overline{w\theta} = -\epsilon_H\, d\bar{T}/dz$. To close the above system, the eddy heat transport model of Cheung [7] is employed to provide an independent expression for ϵ_H. In this model, the process of turbulent natural convection is considered to be described well by a local Rayleigh number of the flow Ra*, which is characterized by a local buoyancy difference and a local length scale. The former is related to a local temperature drop according to the Boussinesq approximation and the latter, to local distances from the upper and the lower walls. From [7], we have

$$\frac{\epsilon_H}{\alpha}=0.051\ \mathrm{Ra}^{*0.87} \quad \text{and}$$

$$\mathrm{Ra}^*=\frac{g\beta(\bar{T}-T_0)L^3}{\alpha\nu}\left[\frac{z}{L}\left(1-\frac{z}{L}\right)\right]^{3.448} \tag{6}$$

where g is the acceleration due to gravity, β the coefficient of thermal expansion, and ν the kinematic viscosity. Equation (6) has been tested against the data reported in [9].

Following Jones [6], equations (4) to (6) may be combined and normalized in terms of a dimensionless distance $n=z/L$, a dimensionless temperature $\phi=E(\bar{T}-T_0)/RT_0^2$, the Frank-Kamenetskii parameter $\delta=QEL^2A\,\exp\,(-E/RT_0)/kRT_0^2$, the Rayleigh number of the system, $\mathrm{Ra}=g\beta L^3RT_0^2/\alpha\nu E$, and the parameter $\epsilon=RT_0/E$. This gives

$$\begin{aligned}\phi''=-\{1+0.051\ \mathrm{Ra}^{0.87}\phi^{0.87}[\eta(1-\eta)]^3\}^{-1}\{&\delta\,\exp[\phi/(1+\epsilon\phi)]\\&+0.153\ \mathrm{Ra}^{0.87}\phi^{0.87}(1-2\eta)[\eta(1-\eta)]^2\phi'\\&+0.044\ \mathrm{Ra}^{0.87}\phi^{-0.13}[\eta(1-\eta)]^3\phi'^2\}\end{aligned} \tag{7}$$

[1]Department of Mechanical Engineering, The Pennsylvania State University, University Park, PA 16802; Mem. ASME.

Contributed by the Heat Transfer Division for publication in the JOURNAL OF HEAT TRANSFER. Manuscript received by the Heat Transfer Division May 17, 1985.

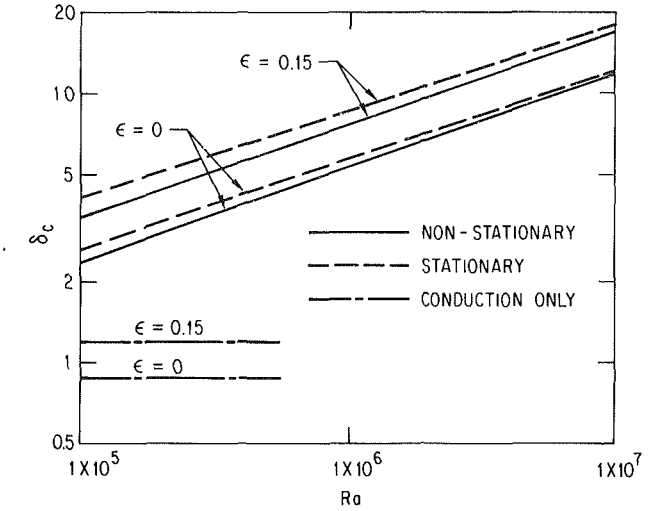

Fig. 1 The critical conditions of thermal explosion predicted by the stationary and nonstationary methods

where $\phi(1)=\phi'(0)=0$ and the prime denotes a total derivative with respect to η. This two-point boundary value problem is solved numerically using the Runge-Kutta method. The critical state, being specified by the maximum value of δ_c (Ra, ϵ), is identified with the one for which a steady-state solution ceases to exist if $\epsilon=0$, or with the one for which a jump phenomenon in the maximum temperature occurs if $\epsilon>0$.

Nonstationary Method—Boundary Layer Approximation

It has been shown that for turbulent natural convection in a volumetrically heated fluid layer, the gradient of the fluid temperature is important only in a region very close to the wall [9, 10]. Over the body of the layer, the temperature is relatively uniform as a result of intensive turbulent mixing. Heat transfer in the wall region of the layer is controlled principally by molecular diffusion. The thickness l of the thermal boundary layer at the wall can be conveniently defined as the equivalent diffusion length so as to offer the same local resistance by conduction as the actual boundary layer. This boundary-layer dominant aspect of turbulent flows has been employed by Cheung [8] to predict the transient temperature behavior of the layer. It is shown that mixing in the turbulent core region remains effective during the entire flow transition and that the rate of heat transfer is determined by the properties of the thermal boundary layer. These analytical results have later on been validated experimentally by Keyhani and Kulacki [10]. Accordingly, equation (1) may be integrated with respect to z over the entire fluid layer to obtain

$$\rho\, C_p \frac{dT_m}{dt} = -\frac{k(T_m - T_0)/L}{l} + QA \exp(-E/RT_m) \qquad (8)$$

where T_m is the transient temperature of the turbulent mixing core, which is practically the same as the instantaneous maximum temperature of the layer. The dimensionless boundary layer thickness is given by [8-10]

$$\frac{l}{L} = 0.74\ \mathrm{Ra}^{-1/3}\phi_m^{-1/3} \qquad (9)$$

where ϕ_m is the dimensionless turbulent core temperature. Equation (8) becomes

$$\frac{d\phi_m}{d\xi} = -0.135\ \mathrm{Ra}^{1/3}\phi_m^{4/3} + \delta \exp[\phi_m/(1+\epsilon\phi_m)] \qquad (10)$$

where $\xi = \alpha t/L^2$ is a dimensionless time. By specifying an initial value $\phi_m(0)$, the above equation may be integrated numerically using the Runge-Kutta method to obtain the time dependence of ϕ_m. The critical conditions for thermal explosion, being specified by the maximum value of δ_c (Ra, ϵ), is identified in this case with the one for which there is an upward inflection in the temperature versus time curve.

Results and Discussion

Figure 1 summarizes the critical conditions for thermal explosion predicted by the two different methods. For the case of $\epsilon=0$, the stationary and the nonstationary solutions may be represented by the following power laws over the range $1\times10^5 < \mathrm{Ra} < 1\times10^7$

$$\delta_c = 0.091\ \mathrm{Ra}^{0.30} \quad \text{and} \quad \delta_c = 0.052\ \mathrm{Ra}^{0.33} \qquad (11)$$

respectively. For $\epsilon = 0.15$, the ignition limit becomes higher. In this case, the stationary and nonstationary solutions may be correlated by

$$\delta_c = 0.127\ \mathrm{Ra}^{0.30} \quad \text{and} \quad \delta_c = 0.074\ \mathrm{Ra}^{0.33} \qquad (12)$$

respectively. The corresponding conduction solutions are also shown in the figure for comparison. At $\mathrm{Ra} = 1\times10^5$, the stationary and nonstationary solutions are found to be quite different. However, as Ra is increased, the difference becomes smaller and, for $\mathrm{Ra} = 1\times10^7$, the two solutions are almost identical. At this Rayleigh number, the values of δ_c are an order of magnitude higher than those predicted by the conduction theory [1-3]. At lower Rayleigh numbers (not shown in the figure), the values of δ_c become similar to those observed in the laminar regime [6] but are still several times higher than the conduction values. It should be noted that the 0.3 or 1/3 power-law dependence of δ_c on Ra is quite similar to the relation between the Nusselt number and Rayleigh number for turbulent flows. Physically, δ_c is related directly to the rate of cooling of the layer which in turn is measured by the Nusselt number. Thus it is quite logical to expect δ_c to be directly proportional to the value of Nu.

Although different physical assumptions have been employed in the stationary and nonstationary methods, the critical conditions predicted by these two approaches are reasonably consistent, especially at high Rayleigh numbers. This clearly illustrates the usefulness of the steady-state solutions in predicting criticality in a transient situation. The results of this study support the proposition of the existence of a stability limit defined by δ_c(Ra, ϵ), below which the time-dependent problem converges to the stable steady-state solution at large times. On the other hand, when conditions exist above the stability limit, explosion results after the induction time.

References

1 Frank-Kamenetskii, D. A., "The Theory of Thermal Explosion," *Diffusion and Heat Transfer in Chemical Kinetics*, 2nd ed., Plenum Press, New York, 1969, pp. 347-421.

2 Shouman, A. R., Donaldson, A. B., and Tsao, H. Y., "Exact Solution to the One-Dimensional Stationary Energy Equation for a Self-Heating Slab," *Combust. Flame*, Vol. 23, 1974, pp. 17-28.

3 Kordylewski, W., "Critical Parameters of Thermal Explosion," *Combust. Flame*, Vol. 34, 1979, pp. 109-117.

4 Ashmore, P. G., Tyler, B. J., and Wesley, T. A. B., "Experimental Investigations of Conductive and Convective Heat Transfer in Relation to Thermal Ignitions," *11th Symposium on Combustion*, The Combustion Institute, Pittsburgh, 1967, pp. 1133-1140.

5 Merzhanov, A. G., and Shtessel, E. A., "Thermal Explosions in a Liquid State Exposed to Natural Convection," *Dokl. Phys. Chem.*, Vol. 194, 1970, pp. 671-674.

6 Jones, D. R., "Convective Effects in Enclosed, Exothermically Reacting Gases," *Int. J. Heat Mass Transfer*, Vol. 17, 1974, pp. 11-21.

7 Cheung, F. B., "Natural Convection in a Volumetrically Heated Fluid Layer at High Rayleigh Numbers," *Int. J. Heat Mass Transfer*, Vol. 20, 1977, pp. 499-506.

8 Cheung, F. B., "Turbulent Natural Convection in a Horizontal Fluid Layer With Time Dependent Volumetric Energy Sources," *2nd AIAA/ASME Thermophysics and Heat Transfer Conference*, Palo Alto, 1978, Paper No. 78-HT-6.

9 Kulacki, F. A., and Nagle, M. Z., "Natural Convection in a Horizontal Fluid Layer With Volumetric Energy Sources," ASME JOURNAL OF HEAT TRANSFER, Vol. 97, 1975, pp. 204-211.

10 Keyhani, M., and Kulacki, F. A., "Experiments on Transient Thermal Convection with Internal Heating-Large Time Results," ASME JOURNAL OF HEAT TRANSFER, Vol. 105, 1983, pp. 261-266.

Journal of Heat Transfer

Discussion

Effect of Mass Transfer and Free Convection on the Flow Past a Vertical Porous Plate[1]

V. M. Soundalgekar.[2] I am sorry to see the referenced paper published in the JOURNAL OF HEAT TRANSFER. This very problem was published by us in the *Indian Journal of Pure and Applied Mathematics*, Vol. 13, 1982, pp. 393–410. I wish to state that our method of solution is far better than the one given by Hossain and Begum. It is very likely that the referees may not have seen our paper published in the *Indian Journal*. However, our paper was published long before the referenced paper was submitted to the JOURNAL OF HEAT TRANSFER.

[1]By M. A. Hossain and R. A. Begum, published in the August 1984 issue of the JOURNAL OF HEAT TRANSFER, Vol. 106, No. 3, pp. 664–668.

[2]Gulf Polytechnic, P. O. Box 32038, Isa Town, State of Bahrain.

Use of a Boundary-Fitted Coordinate Transformation for Unsteady Heat Conduction Problems in Multiconnected Regions With Arbitrarily Shaped Boundaries[1]

P. A. A. Laura.[2] The authors are to be congratulated for their extension of this coordinate transformation to unsteady heat conduction problems in two-dimensional, multiconnected, heterogeneous regions with arbitrarily shaped boundaries and their interesting application to a solidification problem in a large steel casting.

It is also the purpose of this Discussion to point out the existence of previous applications of a parallel approach: the conformal mapping method for solving non-steady-state heat conduction problems in isotropic and orthotropic media in the case of simple and doubly connected domains of complicated boundary shape. Admittedly Uchikawa and Takeda's approach is considerably more general in scope, but the conformal mapping technique is simpler, when applicable.

Some of the first applications of the conformal mapping technique to unsteady heat conduction problems were reported in the 1960s [11, 12]. The physical domain, of complicated boundary shape, was transformed onto a circular region. In the case of a doubly connected domain the transformation was performed onto an annular shape [13]. It was shown in [14] that the approach yields good engineering accuracy by obtaining independent solutions by means of a finite element code. The method was also applied in the case of a solid propellant rocket motor cross section [15]. References [16, 17] deal with applications of the conformal mapping method in the case of unsteady heat conduction problems in orthotropic media.

It was shown in [18, 19] that the conformal mapping approach is quite convenient in the case of heterogeneous domains of complicated geometry and also applicable in nonlinear problems [20]. Steady-state conditions are assumed in these two studies.

Reference [21] is probably the first study available in the open literature where the conformal mapping approach is used in order to tackle unsteady heat conduction in rods of arbitrary cross section and where heat generation occurs.

It may be also useful to the interested reader that the conformal mapping approach has been extensively used in mechanical vibration problems [22].

[1]By S. Uchikawa and R. Takeda, published in the May 1985 issue of the ASME JOURNAL OF HEAT TRANSFER, Vol. 107, No. 2, pp. 494–498.

[2]Director and Research Scientist, Institute of Applied Mechanics, Puerto Belgrano Naval Base, 8111—Argentina.

References

11 Laura, P. A. A., and Chi, M., "An Application of Conformal Mapping to a Three-Dimensional Unsteady Heat Conduction Problem," *The Aeronautical Quarterly*, Vol. XVI, Aug. 1965, pp. 221–230.

12 Laura, P. A. A., and Faulstich, A. J., "Unsteady Heat Conduction in Plates of Polygonal Shape," *International Journal of Heat and Mass Transfer*, Vol. 11, 1968, pp. 297–303.

13 Laura, P. A. A., and Ercoli, R., "A Solution of the Unsteady Diffusion Equation in an Arbitrary, Doubly Connected Region," *Nuclear Engineering and Design*, Vol. 23, 1972, pp. 1–9.

14 Laura, P. A. A., Sánchez Sarmiento, G., and Basombrio, F., "Numerical Experiments on the Determination of Unsteady State Temperature Distribution in Domains of Complicated Boundary Shape," *Nuclear Engineering and Design*, Vol. 47, 1978, pp. 231–237.

15 Laura, P. A. A., Sánchez Sarmiento, G., and Olivetto, M. E., "Numerical Experiments on the Determination of Unsteady State Temperature Distribution in a Solid Propellant Rocket Motor," *International Journal of Heat and Mass Transfer*, Vol. 22, 1979, pp. 625–628.

16 Laura, P. A. A., Gutierrez, R. H., Sánchez Sarmiento, G., and Tsuji, M., "Unsteady Heat Conduction in Orthotropic Plates of Arbitrary Shape With Geometrically Complicated Initial Conditions," *Fibre Science and Technology*, Vol. 13, 1980, pp. 465–476.

17 Laura, P. A. A., Gutierrez, R. H., and Sánchez Sarmiento, G., "Application of Conformal Mapping to the Determination of Unsteady Temperature Distribution in Orthotropic Plates," *Journal of Nuclear Engineering and Design*, Vol. 52, 1979, pp. 337–342.

18 Laura, P. A. A., and Sánchez Sarmiento, G., "Analytical Determination of Heat Flow Shape Factors for Composite, Prismatic Bars of Doubly-Connected Cross Section," *Nuclear Engineering and Design*, Vol. 50, 1978, pp. 379–385.

19 Laura, P. A. A., and Sánchez Sarmiento, G., "Temperature Distribution in a Composite Prismatic Rod in the Case of Heat Generation in the Circular, Concentric Core," *International Journal of Heat and Mass Transfer*, Vol. 22, 1979, pp. 341–343.

20 Laura, P. A. A., and Gutierrez, R. H., "Effect of Nonlinear Characteristics on Temperature Distribution in a Rocket Grain," *AIAA Journal*, Vol. 21, No. 7, 1983, pp. 1055–1056.

21 Laura, P. A. A., Gelos, R., and Sánchez Sarmiento, G., "Unsteady Temperature Distribution in Bars of Arbitrary Cross Section With Heat Generation," *Journal of Nuclear Engineering and Design*, Vol. 74, 1982, pp. 241–246.

22 Laura, P. A. A., "Applications of the Conformal Mapping Method to the Solution of Mechanical Vibrations Problem," *Shock and Vibration Digest*, Vol. 16, No. 12, 1984, pp. 3–7.